Classification of the nonlinear dynamics of ultrasonically excited bubbles and their effect on the acoustical properties of the medium: Theory, experiment and numerical simulations

by

AJ Sojahrood
Bachelors, Urmia University, 2008
Masters., Ryerson University, 2011

A dissertation
presented to Ryerson University
in partial fulfillment of
the requirements for the degree of
Doctor of Philosophy (Ph.D.)
in the Program of
Department of Biomedical Physics

Toronto, Ontario, Canada, 2020

Author's Declaration For Electronic Submission Of A Dissertation

I hereby declare that I am the sole author of this dissertation. This is a true copy of the dissertation, including any required final revisions, as accepted by my examiners.

I authorize Ryerson University to lend this dissertation to other institutions or individuals for the purpose of scholarly research

I further authorize Ryerson University to reproduce this dissertation by photocopying or by other means, in total or in part, at the request of other institutions or individuals for the purpose of scholarly research.

I understand that my dissertation may be made electronically available to the public.

CLASSIFICATION OF THE NONLINEAR DYNAMICS OF ULTRASONICALLY EXCITED BUBBLES AND THEIR EFFECT ON THE ACOUSTICAL PROPERTIES OF THE MEDIUM: THEORY, EXPERIMENT AND NUMERICAL SIMULATIONS

AJ Sojahrood

Doctor of Philosophy (Ph.D.)

Department of Biomedical Physics

Ryerson University, 2020

Abstract

Acoustically excited microbubbles (MBs) are the building blocks of several applications as diverse as underwater acoustics to sonochemistry and medicine. MBs are used in numerous diagnostic and therapeutic procedures. MBs dynamics are complex and nonlinear. Moreover, the presence of the MBs in a medium changes the medium's attenuation and sound speed. The changes are nonlinear and depend on the complex MB dynamics. Within this complexity lies great potential for applications. For instance, the nonlinear response of MBs is used to increase the contrast to tissue ratio in imaging. Achieving the full potential of MBs in applications requires not only understanding the MB behavior, but also a detailed knowledge on the effect of the MBs pulsations on the medium acoustical properties. For instance, increased attenuation due to MBs in the ultrasound beam path limits the focal ultrasound energy which can reach a target. In this work, nonlinear MB dynamics are studied with unprecedented detail over wide ranges of ultrasound exposure parameters. Methods of nonlinear dynamics and chaos including bifurcation diagrams and resonance curves are used to visualize the results. In tandem, the scattered pressure from single bubble oscillations was experimentally investigated. Nonlinear dynamics of the MBs is classified both experimentally and numerically. We show, for the first time, that higher order subharmonic oscillations can be generated at very low acoustic pressures (e.g. 1kPa) in the oscillations of the lipid coated MBs. We address one of the open problems in acoustics by developing a comprehensive model to calculate the nonlinear attenuation and sound speed of bubbly media. Unlike current models, our new model is not limited by any linear or semi-linear approximations. The predictions of the model are verified by comparing it to other simplified models and experimental observations

in bubbly media. We show, for the first time, the numerical and experimental evidence of the pressure dependent sound speed in bubbly media. The nonlinear attenuation and sound speed of the bubbly media are classified over a large range of acoustic exposure parameters. The classified regimes are then used to engineer the attenuation of a bubbly medium, during which ultrasound can pass through a highly dissipative bubbly medium with minimum loss.

Acknowledgments

This work would have not been possible without the help of several people during these years. First, I want to thank the support of my supervisors Prof. Michael C. Kolios and Dr. Raffi Karshafian. They helped me with strengthening several research skills and critical thinking. I want to acknowledge the strong leadership of Prof. Kolios from whom I learned valuable lessons in time and project management. His enthusiasm and energy in science and stimulating discussions helped with shaping of many ideas and results in this thesis. I want to thank my supervisory committee members Dr. David Goertz and Dr. Yuan Xu for the very useful insights and detailed discussions. Dr. David Goertz provided several practical insights and Dr. Yuan Xu helped me with critical signal processing analysis. Additionally I want to thank Dr. Tyrone Porter and Dr. Agata Exner for excellent collaboration, great one on one bouncing of ideas back and forth and for rigorous and fruitful discussions. I express many gratitude to Dr. Kevin Haworth not only for the elaborate discussions but also for facilitating the connection to other researchers in the filed. I have special regards to Dr. Glynn Holt from whom I learned many complex materials and enjoyed hours and hours of enthusiastic and fertile discussions. Many thanks to Prof. Michel Versluis whose works and discussions served like a lighthouse for many chapters in this thesis and his words encouraged me greatly to push against adversity. Many thanks to Mr. Hossein Haghi, Dr. Al deLeon, Ms. Qian Li, Dr. Christopher Hernandez and Ms. Elizabeth Brendl for the fruitful discussion and assistance during this time.

I express many thanks for my mother and father who provided tireless emotional and financial support during the years. Indeed we have not been able to physically meet for more than a decade and without their support this work would not be possible. I must thank and express my gratitude to Karen, who was there all the time and beside me during the hardships and struggles and lent me her immense assistance. Many thanks to Prof. Pedro Goldman for being by my side in the times of happiness and sadness; whom I enjoyed scientific and spiritual discussions and learned some of the best teaching skills I ever witnessed. The honor of being his teaching assistant not only helped me financially when I was in desperate need but also thought me lessons in patience, kindness and perseverance.

I want to thank Ms. Nora Farrell the Ombudsman of Ryerson University who helped me solve

some very significant problems on multiple occasions. And finally I want to thank members of the Parliament Mr. Thomas Mulcair, Ms. Jenny Kwan and Mr. Adam Vaughn for their immense efforts in helping me solve my immigration problems. Many gratitude to Ms. Miriam Taylor who tirelessly and patiently worked hand in hand with Mr. Thomas Mulcair and followed up my case with IRCC until my case was finally solved. Thank you very much Ms. Teresa Wright for your interview with me in Canadian Press which lead to finalization of my immigration case a day after the interview publication. Since the solution of my immigration case, 10 papers of this thesis were finalized in less than two years out of which 5 are published.

This work is supported by the Natural Sciences and Engineering Research Council of Canada (Discovery Grant RGPIN-2017-06496), NSERC and the Canadian Institutes of Health Research (Collaborative Health Research Projects) and the Terry Fox New Frontiers Program Project Grant in Ultrasound and MRI for Cancer Therapy (project #1034). A. J. Sojahrood is supported by a CIHR Vanier Scholarship.

Dedication

This thesis is dedicated to the 176 beautiful souls onboard of flight PS752 who left us so early. But will always be remembered.

Contents

List of Tables

List of Figures

Listings

List of Algorithms

List of Abbreviations and Symbols

α	attenuation
β	void fraction
AM	amplitude modulation
B	molecular co-volume
c	sound speed of the medium
Cd	dissipated power due to coating (shell) viscosity
c_l	sound speed in the liquid
C_v	heat capacity at constant volume
C_p	heat capacity at constant pressure
d	distance from bubble center
D	thermal diffusivity
δ_{total}	total thermal damping
δ_{Vis}	liquid viscosity damping constant
δ_{th}	thermal damping constant
δ_{rad}	radiation damping constant
δ_{int}	interfacial damping constant
δ_{sh}	shell viscosity damping constant
ϵ	shell thickness
f	frequency

f_r	Resonance frequency
f_{sh}	subharmonic resonance frequency
f_s	pressure dependent resonance frequency
FU	fundamental
G_s	Shell shear modulus
G	sediment shear modulus
k	polytropic exponent
K	Boltzman constant
K_l	liquid kinetic energy
χ	thermal diffusion length
L	thermal conductivity of gas
Ld	dissipated power due to liquid viscosity
LC	lipid coated
L_{th}	thickness of the thermal boundary layer
MB	microbubble
NB	nanobubble
US	ultrasound
$CEUS$	contrast enhanced ultrasound
UCA	ultrasound contrast agent
SN	saddle node bifurcation.
PD	period doubling
$P1$	period 1
$P2$	period 2

σ	surface tension
σ_0	initial surface tension
μ	viscosity
μ_l	liquid viscosity
μ_{sh}	shell viscosity
μ_s	sediment viscosity
μ_{th}	thermal viscosity
N	number of bubbles per unit volume
N_g	number of gas molecules
ω	angular frequency
ω_0	resonance angular frequency
P_0	atmospheric pressure
P_A	acoustic pressure amplitude
P	pressure
PDf_r	Pressure dependent resonance frequency
P_g	gas pressure
P_{sc}	scattered pressure
R	bubble radius
R_0	initial bubble radius
R_b	buckling radius
Rd	dissipated power due to radiation
R_r	rupture radius
$\dot{R}$	bubble wall velocity

$\dot{R}$	bubble wall acceleration
ρ	density
ρ_g	gas density
ρ_l	liquid density
SH	subharmonic
SuH	superharmonic
T	temperature
t	time
T_0	initial temperature
θ	shell thickness
Td	dissipated power due to thermal damping
UH	ultraharmonic
$v(r,t)$	velocity field
Sd	dissipated power due to scattering
W_{total}	total dissipated power

Chapter 1

Introduction

1.1 Background

A bubble is neither a gas or a liquid [1], nor a solid or a plasma. To form a bubble at least two phases of matter must exist. In this thesis a bubble is considered as a volume gas surrounded by a liquid, and in the case of coated microbubbles (MB) it is a volume of gas coated by a lipid, polymer or an albumin shell (Fig. 1.1). When exposed to an ultrasonic field the MB oscillates and emits sound. Bubbles can be introduced into the medium or they can be created by the deposition of energy into the medium. As an instance it can be created hydrodynamically [2] or in high frequency high pressure ultrasonics [3] or through focused laser light [4, 5].

The first mention of cavitation dates back to 1754 when Euler investigated the theory of turbines [6]. Cavitation can occur by applying tensile stress to the liquid elements using a pressure change. The first analysis of the cavitation for practical applications was made by Rayleigh in 1917 [2] in a hydrodynamics context. Hydrodyanmic cavitation occurs due to the changes in the ambient pressure and fluid. Ship propellers produce bubbles. When propellers rotate fast, the water ruptures and cavitation is produced. This diminishes the thrust and upon collapse of cavitation bubbles, the propellers erode. The bubble collapse is accompanied by underwater noise emissions. Early investigations studied the nature of these unwanted effects [2].

Later, it was found that when high intensity ultrasound is applied to an aqueous solution, the pressure achieved in the the rarefaction cycle can exceed the attractive forces among the liquid molecules. This ruptures the water and acoustic cavitation is generated [4, 5]. In response to the sound filled the generated MBs begin nonlinear oscillations which can be accompanied by intense noise emission which is called the acoustic cavitation noise [4].

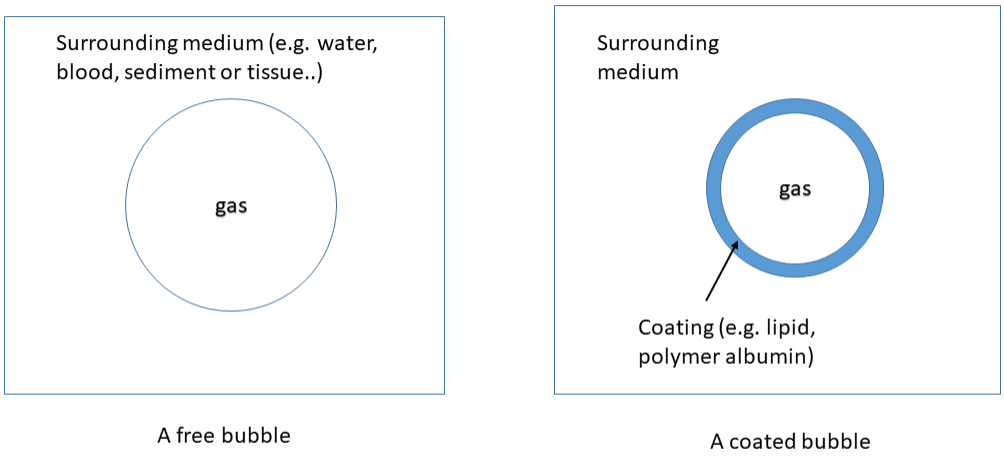

Figure 1.1: A schematic representation of a free (left) and coated bubble (right)

More recent investigations revealed that strong light waves can cause MBs to appear in a liquid through a phenomenon called dielectric breakdown. This phenomenon is called optical cavitation. Bubbles and cavitation are closely connected and often both are discussed together (e.g. in the book by Brennen [7]). The processes upon which cavitation can be generated are summarized in Fig. 1.2, which is adopted from [5].

Lord Rayleigh's theory [2] only considers the bubbles that collapse freely. His work was extended by Plesset [8] by adding an acoustic excitation term. His work formed the building blocks of the Rayleigh-Plesset equation [8], which forms the basis of the equations for modeling the acoustically excited bubbles.

In the presence of an acoustical excitation, the bubble expands and contracts. This is shown in Fig. 1.3 adapted from [9]. The bubble expands with the negative pressure and contracts with the positive pressure. The bubble may reach an unstable size and the collapse can lead to bubble destruction. The radius time curve will be used often in this thesis to study the bubble dynamics. The contraction and expansion of the bubble in the form of radius-time curve is shown in Fig. 1.4. The MB oscillations as simplified in Figs. 1.3 & 1.4, forms the building block of several applications

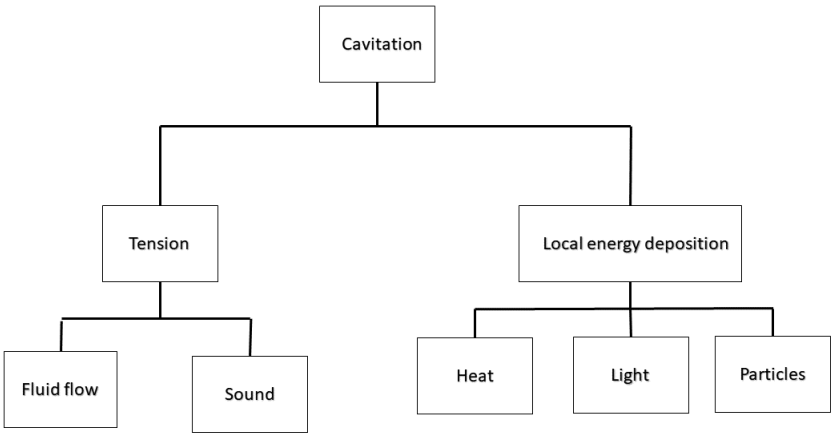

Figure 1.2: Classification scheme for different types of cavitation adopted from [5].

and phenomena. Oscillations of the MBs and the rapid collapse during the compression phase leads to the generation of a flow filled around the oscillating bubble and emitting of shockwaves to the surrounding medium. Moreover, the collapse of the bubble results in the elevation of the gas temperature [1, 7]. These effects, when exploited controllably, form the basis for several industrial, chemical, food science and medical applications of MBs.

1.2 Nonlinear MB dynamics, applications and challenges

MBs excited by ultrasound waves are highly nonlinear oscillators [11]. It has been shown both numerically and experimentally that MBs exhibit complex and chaotic dynamics [11, 12, 13, 14, 15, 16, 17, 18, 19, 20, 21]. MBs encapsulated by a shell are being used in diagnostic ultrasound as contrast agents (UCAs) [22]. The dynamics of the UCAs (coated MBs) has also been associated with complex and chaotic oscillations [18, 21].

Despite their complex behavior, MBs and UCAs have become instrumental in a wide variety of fields. MBs are used in sonochemistry to increase chemical yields [23], in surface cleaning applications [24] and material science [25]. In the context of medical ultrasound, studies have shown the potential of the UCAs to target and enhance drug/gene delivery [26], reversibly open blood–brain barrier to deliver drugs to the brain [27] and in ultrasound diagnostic imaging to enhance the

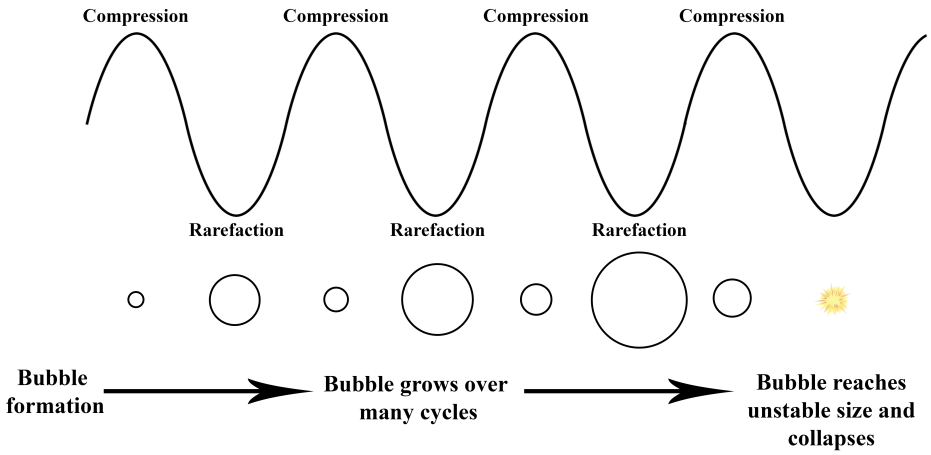

Figure 1.3: The process of bubble oscillations adapted from [9].

detection of cancer even at early stages and with increased sensitivity [28].

However, despite the many applications of the UCAs and MBs, due to the complexity in modeling their interaction with ultrasound fields [1], the relationship between the ultrasound exposure parameters (e.g., frequency and pressure) and the UCA and bubble behavior is not well understood [1]. The UCA response to ultrasound is nonlinear and complex; thus, the ultrasound exposure conditions for some applications may not be optimized. A comprehensive understanding of the dynamics of the UCAs over a large range of relevant ultrasound exposure parameters can be achieved using methods of nonlinear physics.

Fundamental insights into the dynamical properties of the UCAs can lead to the optimization of the exposure parameters for specific applications. However, many of the numerical and experimental studies on the UCA dynamics have been carried out for a limited range of ultrasound frequencies and pressures [1]. Due to the complexity and sensitivity of the UCA oscillations to the exposure parameters, the limited information acquired in these studies does not provide a comprehensive framework that can be used further for the unification and classification of the UCAs and bubble dynamics. Furthermore, many potential exposure parameter combinations may be overlooked due to the discrete nature and limited range of the parameters that have been investigated. Thus, a more comprehensive analysis of the parameter space is required.

In addition to the complexity of the dynamics of the MBs and UCAs, the introduction of the MBs

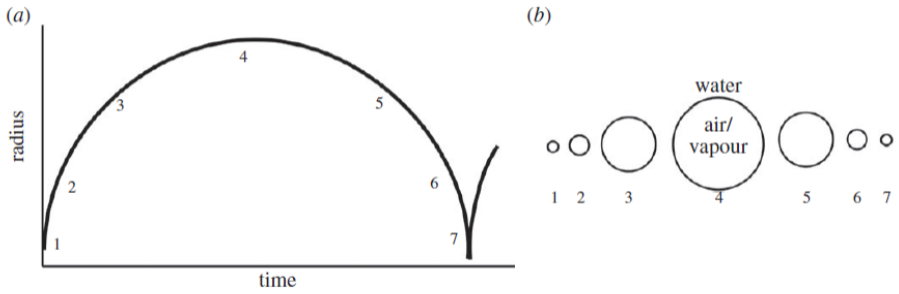

Figure 1.4: a) Radius time curve of bubble oscillations, b) corresponding phase of the bubble oscillations adapted [10].

to the medium changes the acoustical properties of the medium [29, 30, 31]. The oscillations of the MBs increase the attenuation of the medium and change the speed of sound. The increase in attenuation is directly proportional to the dissipation of the acoustic energy during bubble oscillations which is nonlinear and complex. Experimental studies and semi linear models have shown that the attenuation of a bubbly medium deviates largely from linear predictions [28,29,30]. For a given frequency, the oscillation of the MBs at the target location largely depends on the pressure that the MBs are exposed to at the time of their oscillations. Thus a better understanding of the attenuation of a bubbly medium, one in which changes in the medium properties that are dependent on pressure of bubbles are taken into account, is necessary for optimizing and controlling the dynamics of the MBs.

Despite the importance of the attenuation phenomenon in a bubbly medium, models that are used to predict the attenuation are based on linear oscillations of the MBs [29] which are only valid for small amplitude MB oscillations (e.g. 1% expansion ratio of the bubble). The improved model by Louisnard [30] is also based on semi linear assumptions and thus cannot accurately predict the speed of sound and attenuation during nonlinear MB oscillations. As shown in previous

works [30, 31], the nonlinear attenuation of the MBs above a pressure threshold can completely shield the acoustic waves from reaching the target location. In addition, comprehensive knowledge of the nonlinear attenuation and its dependence on pressure and frequency may allow one to choose parameter ranges that may decrease the pre-focal attenuation with advantages for ultrasound imaging and drug delivery which use focused ultrasound beams. Increasing the attenuation at the focal location, while minimizing attenuation outside the focal point, can be advantageous for applications related to bubble enhanced heating [32, 33].

Thus, in order to better understand the bubble related phenomena and optimize and control the behavior of the MBs and UCAs in applications we need:

1- A comprehensive knowledge of the the MBs oscillations for a large range of ultrasound exposure parameters; so that the potential parameter ranges (e.g. frequency and pressure) for stable nonlinear MB oscillations can be calculated and applied to the relevant application.

2- A detailed understanding of the nonlinear attenuation of the bubbly medium to deliver the sufficient acoustic energy at the target location to ensure adequate MB oscillations.

These two phenomena are interwoven. As will be seen in this thesis, the propagation of sound waves through dense bubble clouds can be engineered if we can mathematically model the interactions mentioned above. This thesis will describe how the two goals above are approached.

1.3 Examples of the nonlinear bubble behavior and related applications

In this section we introduce instances of the nonlinear bubble behavior. Radial oscillations of the bubble as a function of the driving periods of the acoustic field will be visualized alongside the scattered pressure by the bubbles and the power spectrum of the scattered pressure. We will show how an increase in the excitation pressure can change the oscillatory behavior of the bubble. Then we will introduce the method of bifurcation analysis and relate some of the introduced nonlinear phenomena to diagnostic applications of ultrasound.

1.3.1 Keller-Miksis model

The nonlinear behavior of an uncoated bubble will be used as an example. The radial oscillations of the uncoated bubbles can numerically simulated by solving the well known Keller-Miksis equation [34]:

$$\rho\left(1-\frac{\dot{R}}{c}\right)R\ddot{R}+\frac{3}{2}\rho\dot{R}^2\left(1-\frac{\dot{R}}{3c}\right)=$$

$$\left(1+\frac{\dot{R}}{c}+\frac{R}{c}\frac{d}{dt}\right)\left((p_0+\frac{2\sigma}{R_0})\left(\frac{R_0}{R}\right)^{3k}-\frac{2\sigma}{R}-\frac{4\mu\dot{R}}{R}-P_0+P_a sin\left(2\pi ft\right)\right) \tag{1.1}$$

In this equation, R is radius at time t, R_0 is the initial bubble radius, $\dot{R}$ is the wall velocity of the bubble and $\ddot{R}$ is the wall acceleration ρ is the liquid density (998 $\frac{kg}{m^3}$), c is the sound speed (1481 m/s), P_0 is the atmospheric pressure (101 kPa), σ is the surface tension (0.0725 $\frac{N}{m}$), μ is the liquid viscosity (0.001 Pa.s), P_a and f are the amplitude and frequency of the applied acoustic pressure. The values in the parentheses are for water at 293 K and are used in all the simulations. The gas inside the bubble is air with polytropic exponent of k=1.4.

1.3.2 Scattered pressure by bubbles

Oscillations of the bubbles generate a scattered pressure (P_{Sc}) which can be calculated by [35]:

$$P_{sc}=\rho\left(\frac{R}{d}\right)\left(R\ddot{R}+2\dot{R}^2\right) \tag{1.2}$$

where d is the distance from the center of the bubble (and for simplicity is considered as 1m in this thesis unless otherwise mentioned). Calculation of the scattered pressure is of great importance since in several applications the scattered pressure (P_{sc}) resulting from bubble oscillations plays a critical role. For example, in imaging applications the P_{sc} is detected and analyzed to form images. In majority of the applications and phenomena involving bubble dynamics, monitoring the behavior of the bubbles is through recording the P_{sc} signal and analyzing its frequency components.
In this Chapter, Eq. 1.1 is solved using the 4^{th} order Runge-Kutta technique for an air bubble with $R_0=2\mu m$ sonicated with $f=1.8MHz$. The simulations were done using the ode45 function of

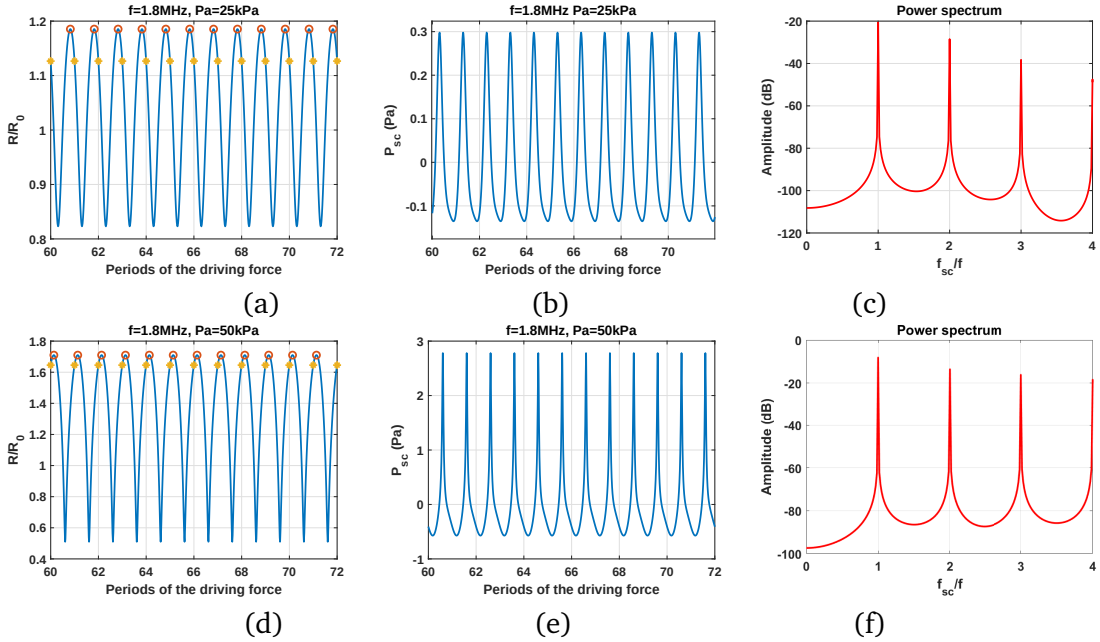

Figure 1.5: Oscillations of an air bubble with $R_0 = 2\mu m$ sonicated with $f = 1.8MHz$ at different pressures of: a-c) 25 kPa and d-f) 50 kPa. The left column is the radial oscillations as a function of driving periods, the middle column represents the P_{sc} and the right column represents the power spectrum of the P_{sc}

MATLAB and the relative and absolute tolerance of the integration was set to 1e-12 and 1e-13. The solutions were recorded at time steps of $\frac{0.001}{f}$. The initial conditions of the problem were set to $R_0(t = 0) = R_0$ and $\dot{R}(t = 0) = 0$ m/s.

1.3.3 Radial oscillations, P_{sc} and power spectrum at different ultrasound excitation pressures

Fig. 1.5a shows the radial oscillations of an air bubble with $R_0 = 2\mu m$ where $f = 1.8MHz$ and $P_a = 25kPa$. The red and yellow circles highlight the peaks and radial amplitude of the bubble at the start of each period respectively. The radial oscillations have one maximum and the yellow circles also have one value. The corresponding P_{sc} and its power spectrum are shown in Figs. 1.5b-c respectively.

Fig. 1.5.d shows the radial oscillations when $P_a = 50kPa$. The corresponding P_{sc} and its power spectrum are shown in Figs. 1.5e-f respectively. Compared to the previous case, although the amplitude of the excitation pressure is only doubled, the maximum amplitude of the P_{sc} increased approximately 10 folds. The corresponding fundamental and harmonic components respectively at

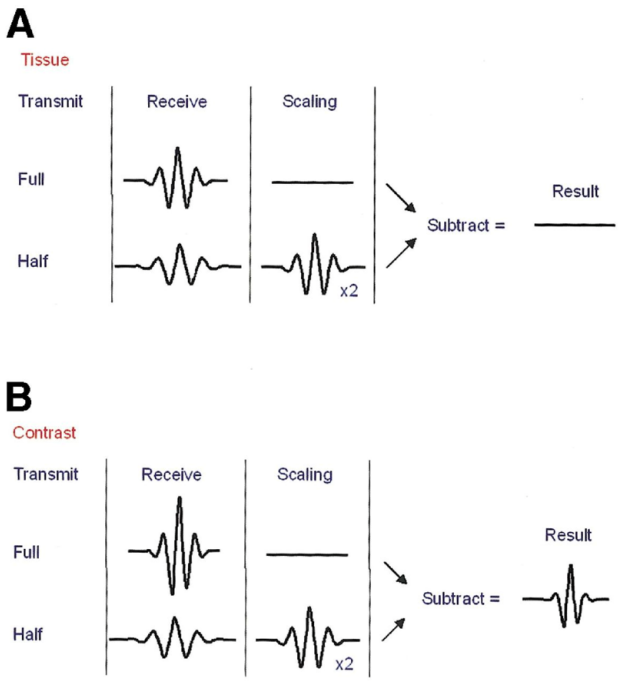

Figure 1.6: Schematic of the amplitude modulation technique: a) case of the tissue and b) case of the bubbles.

f and $2f$ have increased about 10 dB. This shows one of the nonlinear responses of the bubble to changes in ultrasonic excitation amplitude.

The asymmetrical increase in the scattered pressure from bubbles forms the foundations of the amplitude modulation techniques [36, 37] in contrast enhanced diagnostic ultrasound. The schematic of this technique is shown in Fig. 1.6. In this technique two pulses are sent with one having half the amplitude of the other. The scattered signals are scaled and subtracted upon receive. The signals from tissue cancel due to the linear response of the tissue and thus the tissue signal is suppressed. However, there is a residual signal due to the nonlinear bubble behavior, thus the contrast to tissue ratio increases.

Fig. 1.7.a displays the radial oscillations of the bubble when excitation pressure is increased to 230 kPa. The oscillations have two peaks and the yellow circles have two values. These values repeat themselves once every two acoustic cycles. Thus the period of the oscillations is 2. The corresponding P_{sc} has two maxima. The occurrence of P2 is concomitant with the generation of 1/2 order subharmonics (SHs) and 3/2 ultraharmonics (UHs) in the power spectrum of the P_{sc} (Fig. 1.7c). This behavior is exclusive to the bubbles and the tissue can not produce SHs or UHs. SHs oscillations are used to increase the contrast to tissue ratio in contrast enhanced ultrasound

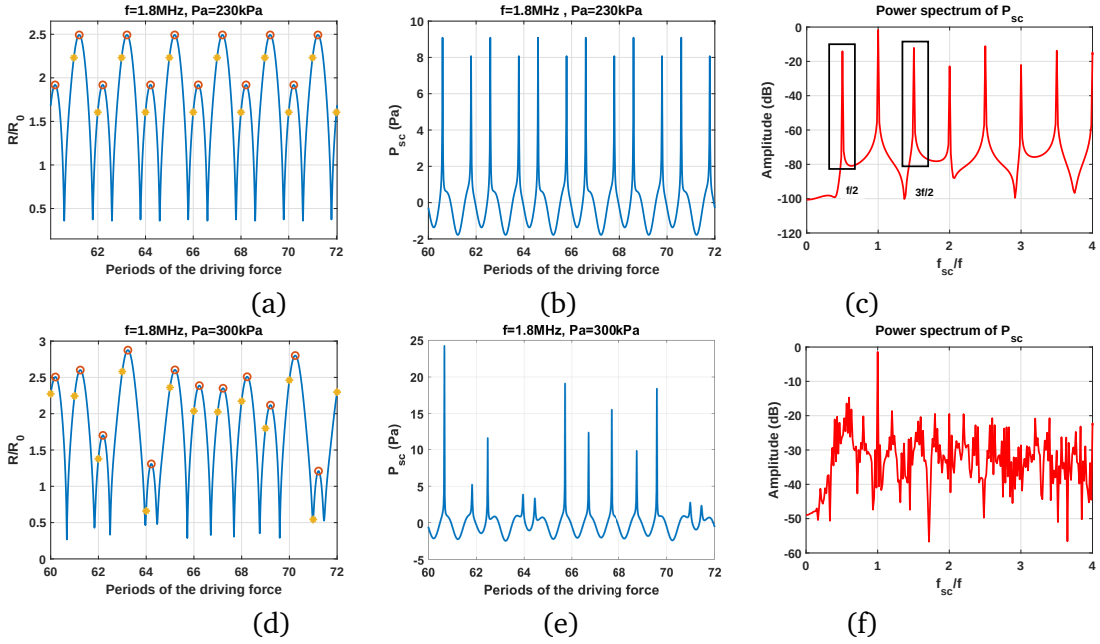

Figure 1.7: Oscillations of an air bubble with $R_0 = 2\mu m$ sonicated with $f = 1.8MHz$ at different pressures of: a-c) 230 kPa and d-f) 300 kPa. The left column is the radial oscillations as a function of driving periods, the middle column represents the P_{sc} and the right column represents the power spectrum of the P_{sc}

[38]. The signals are filtered upon receive and only the SH frequency component is kept in the image. Thus contrast to tissue ratio increases. Fig. 1.8 shows the SH image of a rabbit ear. The signal from the tissue is suppressed and the vessels are displayed with high contrast.

When pressure is increased to 300 kPa (Fig. 1.7d) the oscillations have several peaks. The yellow circles have many distinct values and it is very difficult to distinguish a period or a pattern in the bubble oscillations. This is referred to as chaotic oscillations. Occurrence of chaos is undesirable as the oscillations are unpredictable and the strength of the nonlinear components (e.g. SH) of the power spectrum decrease. This is because the signal energy is distributed over a large frequency range leading to a broadband spectrum (Fig, 1.7f).

Figs. 1.5 and 1.7 show that the behavior of the bubble strongly depends on the excitation amplitude. The discrete nature of the analysis in these figures. does not allow for a comprehensive understanding of the bubble dynamics. Moreover, some of the parameter ranges with potential for applications may be overlooked. Thus, in this thesis we will use the bifurcation diagrams to analyze the bubble behavior over a large range of parameters (frequency, pressure, size and initial surface tension of the bubbles). In Chapter 3, we will introduce in detail a comprehensive

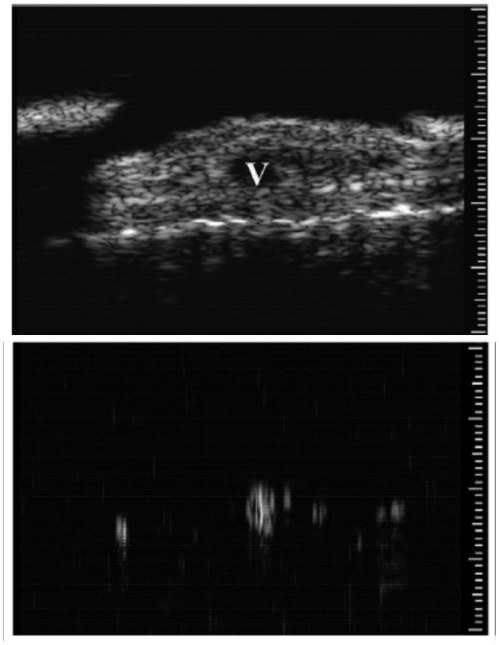

Figure 1.8: In vivo demonstration of SH imaging in the microvasculature of a rabbit ear. Top, 20 MHz fundamental mode image of a rabbit ear in cross section, in which the presence of a 300–400 μm diameter microvessel (V) is evident relative to the surrounding tissue before bubble injection. Bottom, SH image at 10 MHz of the same region after the injection of bubbles. The tissue signal has been suppressed, leaving the image of the 400 μm vessel as well as signals from several smaller vessels that were not visible in the original scan [38].

method of generating the bifurcation diagrams. Here we will show the bifurcation diagram of the bubble in Figs. 1.5 and 1.7 alongside the fundamental, harmonic, 1/2 order SH and 3/2 order UH components of the power spectrum.

Fig. 1.9a displays the bifurcation structure of an air bubble with $R_0 = 2\mu m$ sonicated with $f = 1.8MHz$ as a function of pressure. The red curve represent the peaks of the radial oscillations at each pressure and the blue curve represents the amplitude of bubble oscillations at the beginning of each period. The analysis is performed within the last 40 cycles of a 240 cycles pulse to avoid the transient bubble oscillations.

Oscillations are P1 for pressures below 220 kPa. The red and blue curve have one value. Point A ($P_a = 25kPa$), corresponds to the radial oscillations in Fig. 1.5a. At $P_a \approx 30kPa$ the radial oscillation amplitude undergoes a rapid increase. This causes a discontinuity in the bifurcation diagram and is referred to as a saddle node (SN) bifurcation. The radial oscillations at point B are shown in Fig. 1.5.d. The sudden increase in the radial oscillations at the SN pressure have potential applications in amplitude modulation techniques as the residual signal from bubbles will be higher

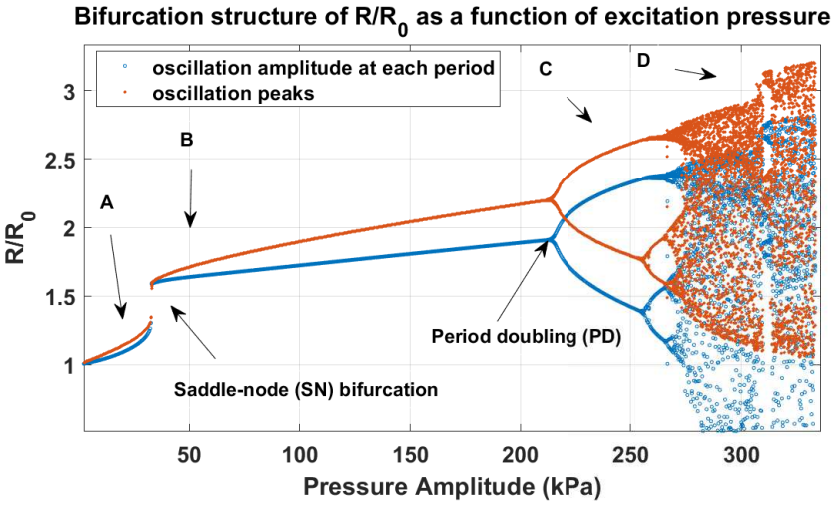

(a)

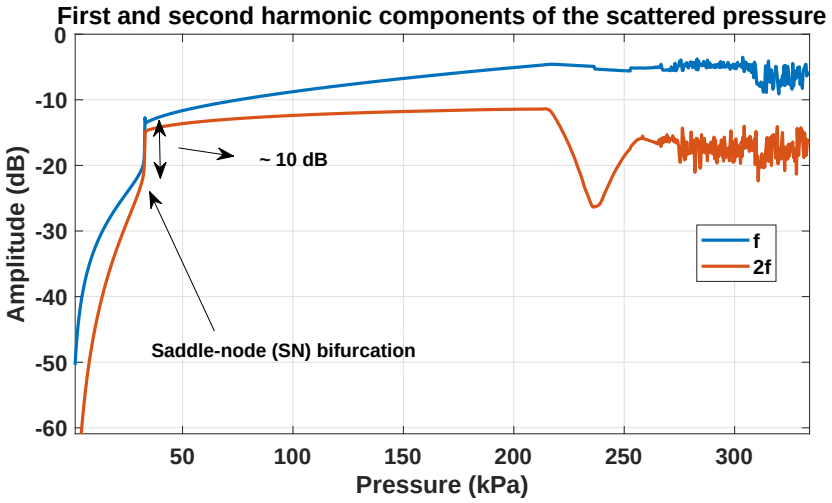

(b)

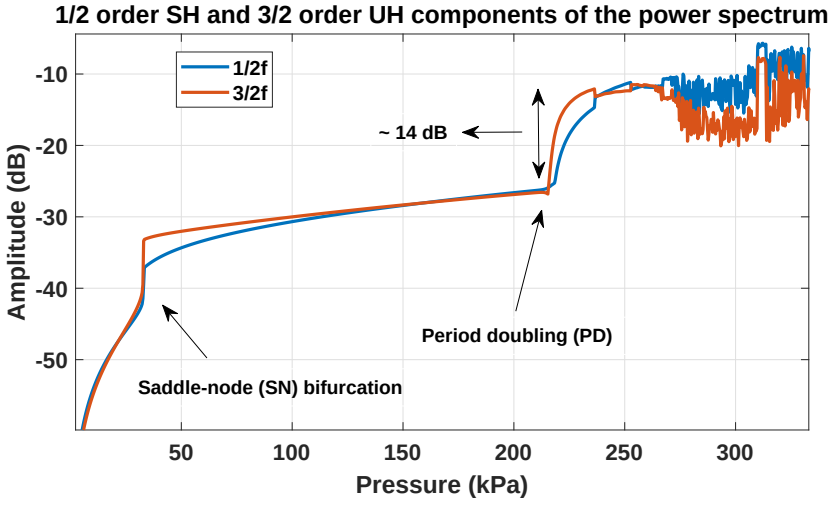

(c)

Figure 1.9: Case of an air bubble with $R_0 = 2\mu m$ sonicated with f=1.8 MHz: a) bifurcation structure of the $\frac{R}{R_0}$ as a function of the driving acoustic pressure, b) harmonic components of the power spectrum of the P_{sc} as a function of the driving pressure and c) subharmonic (SH) and ultraharmonic (UH) components of the power spectrum of the P_{sc} as a function of the driving acoustic pressure.

in amplitude.

Further increase in excitation pressure results in a monotonic increase in the bubble amplitude and at $P_a \approx 220kPa$ a period doubling (PD) bifurcation takes place. Oscillations becomes period 2 (P2) and there are two distinct values for the blue curve. Radial oscillations of the point C are shown in Fig. 1.7.a. There are two yellow circles (the two blue values in the bifurcation diagram) and the oscillations also have two peaks. Above a pressure threshold chaotic oscillations appear. This phenomenon usually occurs through successive Pds. Point D in the chaotic window corresponds to the radial oscillations in Fig. 1.7d. The oscillations have many distinct values at each period of the driving pressure, thus when they are plotted versus the acoustic pressure in Fig. 1.9 they resemble a continuous vertical line.

The fundamental and the 2nd harmonic components of the power spectrum are shown in Fig. 1.9.b. The occurrence of the SN bifurcation is simultaneous with a sudden 10 dB increase in the fundamental and 2nd order harmonic components of the power spectrum which can be used to enhance the contrast in amplitude modulation techniques [36, 37].

Fig. 1.9.c shows that concomitant with the Pd in the bifurcation diagram, the amplitude of the 1/2 order SH and 3/2 UH of the power spectrum increases significantly (14 dB). Moreover, occurrence of the chaotic oscillations are simultaneous with a drop in the SH and UH strength. Additionally, due to the higher pressures required for chaotic oscillations, the scattered signal will be higher from tissue, thus signal to noise may also decrease.

The application of the bifurcation diagrams reveals valuable information about the radial oscillations of the bubbles. In this thesis, this information will be used to classify the nonlinear bubble dynamics and relate each nonlinear regime to the relevant applications of bubbles.

1.4 Thesis structure

The thesis has 10 chapters which constitute either published papers, or papers that have been submitted for publication or are being prepared for submission. To avoid duplication, the relevant background context is presented in each individual chapter instead of the introduction.

In Chapter 2, the influence of the pressure dependent resonance frequency (PDf_r) on the bubble dynamics will be investigated. The bifurcation structure of the radial oscillations of the MBs when

sonicated with their PDf_r will be analyzed. The non-destructive (stable oscillations) scattered pressure by UCAs will be investigated in tandem with bifurcation diagrams and the conditions for amplification of the non-destructive scattered pressure by MBs and wall velocities will be identified. The work is published in Nonlinear Dynamics [39]

In Chapter 3, we will introduce a more comprehensive method to study the bifurcation diagrams of the bubble oscillators. Current methods cannot differentiate the exposure parameter regions where the oscillations are in ultraharmonic regimes from the exposure parameter regions where the bubble oscillations are in subharmonic regimes. Moreover, using current methods, superharmonic regimes of oscillations cannot be identified. We will introduce a comprehensive method that tackles the problems associated with the conventional bifurcation methods. The work is published in Ultrasonics Sonochemistry [40]

In Chapter 4, we will use the method developed in Chapter 3, and will classify the bifurcation structure of an uncoated bubble that is sonciated with its resonance frequency (f_r) and its subharmonic (SH) resonance frequency ($f_{sh} = 2f_r$). Conditions for the generation, amplification and stability of 1/2 order subharmonics (SHs) will be investigated comprehensively. This paper is published in Physics Letters A [41].

In Chapter 5, the pressure dependence of the SH resonance frequency (f_{sh}) will be investigated. The dynamics of the uncoated MBs sonicated with their pressure dependent f_{sh} (PDf_sh) will be investigated using the comprehensive method developed in Chapter 3. Conditions for the enhancement of the upper limit of the SH power during non-destructive bubble oscillations will be identified. This paper is under review in Nonlinear Dynamics [42].

In Chapter 6, we will provide critical corrections to the formulations of the pressure dependent dissipation mechanisms in the oscillations of the uncoated MBs. The corrections are critical for the models that will be used for calculating the propagation of ultrasound through bubbly media. This paper is published in Ultrasonics Sonochemistry [43].

In Chapter 7, we will introduce a simple model for the dynamics of the coated bubble including radiation effects. Using the approach in Chapter 6, the formulations for the pressure dependent dissipation mechanisms in the bubble oscillator will be derived. Through analyzing the pressure dependent dissipation mechanisms, the nonlinear scattering to dissipation ratio will be calculated and conditions for its maximization scattering and minimizing attenuation. This paper is published

in Ultrasonics Sonochemistry [44].

In Chapter 8, the nonlinear dynamics of the uncoated and coated MBs (with linear visco-elasticity) will be classified by using and extending the analysis in chapters 2,3,4 and 5. Then, using the derived nonlinear formulations and the classified behavior, the dissipation mechanisms due to thermal damping, radiation damping, damping due to the viscosity of the shell and the liquid viscosity will be classified. This chapter will be submitted as two papers.

In Chapter 9, we will present a model for calculating the pressure dependent attenuation and sound speed in bubbly media. The model uses no linear approximations. The accuracy of the model will be verified numerically and experimentally. Using the classification scheme in Chapter 8, we will classify the nonlinear regimes of the attenuation and sound speed in bubbly media. The important information obtained ins this classification scheme is then related to possible optimization of exposure parameters for relevant applications. This chapter will be submitted as two papers. This work won the 2nd **best paper award** in the 171st Meeting of the Acoustical Society of America in Salt Lake City, Utah in 2016 [45].

In Chapter 10, we will report the first time experimental observations of the higher order non-linearity in the oscillations of lipid coated MBs at low excitation pressures. Physical reasons for the enhanced non-linearity will be given by comparing the experimental results with numerical predictions. This paper has been submitted to the International Journal of Engineering Science. This work won the **best paper award** in the joint congress of the 21st International Congress on Acoustics, 165th Meeting of the Acoustical Society of America and the 52nd meeting of the Canadian Acoustical Society in Montreal, Canada in 2013 [46].

In Chapter 11, we will classify the dynamics of the lipid coated MBs. The buckling and rupture of the lipid coating, significantly enhance the nonlinear behavior and make the dynamics of lipid coated bubble very complex. Using the information of the chapters 2,3,4,5 and 8 and by analyzing the bifurcation structure of the lipid coated MBs with different initial surface tensions, we will examine the influence of the coating on the nonlinear bubble behavior. Finally, a simple classification scheme is provided for the complex coated bubble system. This paper is planned to be submitted soon.

The thesis will end with a summary of the contributions of each chapter.

Bibliography

[1] Lauterborn, Werner, and Thomas Kurz. ”Physics of bubble oscillations.” Reports on progress in physics 73, no. 10 (2010): 106501.

[2] Lord Rayleigh 1917 On the pressure developed in a liquid during the collapse of a spherical cavity Phil. Mag. Ser. 6 34 94–8

[3] Lauterborn W 1974 Kavitation durch Laserlicht (Cavitation by laser light) Acustica 31 51–78.

[4] Lauterborn W, Suchla E. Bifurction structure in a model of acoustic turbulence. Phys Rev Lett 1984;53(24):2304–7.

[5] Lauterborn, W. and Ohl, C.D., 1997. Cavitation bubble dynamics. Ultrasonics sonochemistry, 4(2), pp.65-75.

[6] J.-B. Dumas, Histoire de l’Académie royale des sciences, belles-lettres et arts de Lyon, vol. 1. Giberton et Brun, 1839

[7] Brennen C E 1995 Cavitation and Bubble Dynamics (Oxford: University Press)

[8] M. S. Plesset, “The Dynamics of Cavitation Bubbles,” Journal of Applied Mechanics, vol. 16, pp. 277–282, 1949.

[9] Leong, T., Ashokkumar, M. and Kentish, S., 2011. The fundamentals of power ultrasound-A review. Acoustics Australia, Vol.39, No. 2 - 43

[10] Ohl, S.W., Klaseboer, E. and Khoo, B.C., 2015. Bubbles with shock waves and ultrasound: a review. Interface focus, 5(5), p.20150019.

[11] Parlitz, U., Englisch, V., Scheczyk, C., Lauterborn, W.:Bifurcation structure of bubble oscillators. J. Acoust. Soc.Am. 88(2), 106177 (1990)

[12] Lauterborn,W., Suchla, E.: Bifurctionstraucture in a modelof acoustic turbulence. Phys. Rev. Lett. 53(24), 2304–2307(1984)

[13] Esche, R.: Untersuchungderschwingungs kavitation inussigkeiten. Acustica 2, 20818 (1952)

[14] Luterborn, W., Cramer, L.: Subharmonic route to chaos observed in acoustics. Phys. Rev. Lett. 47(20), 14458 (1981)

[15] Lauterborn, W., Koch, A.: Holographic observation of period-doubled and chaotic bubble oscillations in acoustic cavitation. Phys. Rev. A 35(4), 19746 (1987)

[16] Holt, R.G.,Gaitan, D.F.,Atchley,A.A., Holzfuss, J.:Chaotic sonoluminescence. Phys. Rev. Lett. 72(9), 13769 (1994)

[17] Hegedus, F., Hos, C., Kullmann, L.: Stable period 1, 2 and3 structures of the harmonically excited Rayleigh–Plesset equation applying low ambient pressure. IMAJ.Appl.Math.78(6), 1179–1195 (2013)

[18] Macdonald, C.A., Gomatam, J.: Chaotic dynamics of microbubbles in ultrasonic elds. Proc. IMechE. 220, 333–343 (2006)

[19] Behnia, S., Jafari,A., Soltanpoor,W., Jahanbakhsh, O.: Nonlinear transitions of a spherical cavitation bubble. Chaos, Solitons Fractal 41, 818–828 (2009)

[20] Behnia, S., Jafari,A., Soltanpoor, W., Sarkhosh, L.: Towards classification of the bifurcation structure of a spherical cavitation bubble. Ultrasonics 49, 605–610 (2009)

[21] Sojahrood, A.J., Kolios, M.C.: Classification of the nonlinear dynamics and bifurcation structure of ultrasound contrast agents excited at higher multiples of their resonance frequency. Phys. Lett. A 376(33), 2222–2229 (2012)12.

[22] Cosgrove, D.: Ultrasound contrast agents: an overview. Eur.J. Radiol 60, 324–330 (2006)

[23] Suslick, K.S.: Sonochemistry. In: Kroschwitz, J. (ed.) Kirk-Othmer concise encyclopedia of chemical technology, 4thedn., pp. 1867–1868. Wiley, New York (1999)

[24] Maisonhaute, E., Prado, C., White, P.C. and Compton, R.G., 2002. Surface acoustic cavitation understood via nanosecond electrochemistry. Part III: Shear stress in ultrasonic cleaning. Ultrasonics sonochemistry, 9(6), pp.297-303.

[25] Suslick, K.S., Price, J.G.:Application of ultrasound to materials chemistry. Ann. Rev. Mater. Sci. 29, 295–326 (1999)

[26] Ferrara, K., Pollard, R., Borden, M.: Ultrasound microbubble contrast agents: fundamentals and application to geneand drug delivery. Ann. Rev. Biomed. Eng. 9, 415–447 (2007)

[27] Nhan, T., et al.: Drug delivery to the brain by focused ultrasound induced blood brain barrier disruption: quantitative evaluation of enhanced permeability of cerebral vasculatureusing two-photon microscopy. J. Control. Release 172,274280 (2013)

[28] Stieger, S.S., et al.: Imaging of angiogenesis using Cadence contrast pulse sequencing and targeted contrast agents. Contrast Media Mol. Imaging 3(1), 9–18 (2008)

[29] K.W. Commander, A. Prosperetti, Linear pressure waves in bubbly liquids: Comparison between theory and experiments J. Acoust. Soc. Am., 85 (2) (1989), pp. 732–746

[30] O. Louisnard, A simple model of ultrasound propagation in a cavitating liquid. Part I: Theory, nonlinear attenuation and traveling wave generation, Ultrasonics Sonochemistry, Volume 19, Issue 1, (2012) Pages 56-65

[31] R. Jamshidi et al.Dissipation of ultrasonic wave propagation in bubbly liquids considering the effect of compressibility to the first order of acoustical Mach number, Ultrasonics, 53(4)Pages 842–848 (2013)

[32] R. G. Holt, R. A. Roy, Measurements of bubble-enhanced heating from focused, mhz-frequency ultrasound in a tissue-mimicking material, Ultrasound in Medicine & Biology Volume 27, Issue 10, October 2001, Pages 1399–1412

[33] Sokka, S.D., King, R. and Hynynen, K., 2003. MRI-guided gas bubble enhanced ultrasound heating in in vivo rabbit thigh. Physics in Medicine & Biology, 48(2), p.223.

[34] Keller, J.B. and Miksis, M., 1980. Bubble oscillations of large amplitude. The Journal of the Acoustical Society of America, 68(2), pp.628-633.

[35] Hilgenfeldt, S., Lohse, D. and Zomack, M., 1998. Response of bubbles to diagnostic ultrasound: a unifying theoretical approach. The European Physical Journal B-Condensed Matter and Complex Systems, 4(2), pp.247-255.

[36] Brock-Fisher AG, Poland M and Rafter P Means for increasing sensitivity in nonlinear imaging systems. US Patent **5577505** (1996).

[37] Dijkmans, P.A., Senior, R., Becher, H., Porter, T.R., Wei, K., Visser, C.A. and Kamp, O., 2006. Myocardial contrast echocardiography evolving as a clinically feasible technique for accurate, rapid, and safe assessment of myocardial perfusion: the evidence so far. Journal of the American College of Cardiology, 48(11), pp.2168-2177.

[38] Goertz, D.E., Cherin, E., Needles, A., Karshafian, R., Brown, A.S., Burns, P.N. and Foster, F.S., 2005. High frequency nonlinear B-scan imaging of microbubble contrast agents. IEEE transactions on ultrasonics, ferroelectrics, and frequency control, 52(1), pp.65-79.

[39] Sojahrood, A.J., Falou, O., Earl, R., Karshafian, R. and Kolios, M.C., 2015. Influence of the pressure-dependent resonance frequency on the bifurcation structure and backscattered pressure of ultrasound contrast agents: a numerical investigation. Nonlinear Dynamics, 80(1-2), pp.889-904.

[40] Sojahrood, A.J., Wegierak, D., Haghi, H., Karshfian, R. and Kolios, M.C., 2019. A simple method to analyze the super-harmonic and ultra-harmonic behavior of the acoustically excited bubble oscillator. Ultrasonics sonochemistry, 54, pp.99-109.

[41] Sojahrood, A.J., Earl, R., Kolios, M.C. and Karshafian, R., 2020. Investigation of the 1/2 order subharmonic emissions of the period-2 oscillations of an ultrasonically excited bubble. Physics Letters A, p.126446.

[42] Sojahrood, A.J., Earl, R., Li, Q., Porter, T.M., Kolios, M.C. and Karshafian, R., 2019. Nonlinear dynamics of acoustic bubbles excited by their pressure dependent subharmonic

resonance frequency: oversaturation and enhancement of the subharmonic signal. arXiv preprint arXiv:1909.05071.

[43] Sojahrood, A.J., Haghi, H., Karshfian, R. and Kolios, M.C., Critical corrections to models of nonlinear power dissipation of ultrasonically excited bubbles, 2020, Ultrasonics Sonochemistry, 66, 10589. https://doi.org/10.1016/j.ultsonch.2020.105089

[44] Sojahrood, A.J., Haghi, H., Li, Q., Porter, T.M. Karshfian, R. and Kolios, M.C., 2020, Nonlinear power loss in the oscillations of coated and uncoated bubbles: Role of thermal, radiation and encapsulating shell damping at various excitation pressures, Ultrasonics Sonochemsitry, 66, 105070.

[45] Jafari Sojahrood, A., Li, Q., Burgess, M., Karshafian, R., Porter, T. and Kolios, M.C., 2016. Development of a nonlinear model for the pressure dependent attenuation and sound speed in a bubbly liquid and its experimental validation. The Journal of the Acoustical Society of America, 139(4), pp.2175-2175.

[46] Jafari Sojahrood, A., Karshafian, R. and C. Kolios, M., 2013, June. Bifurcation structure of the ultrasonically excited microbubbles undergoing buckling and rupture. In Proceedings of Meetings on Acoustics ICA2013 (Vol. 19, No. 1, p. 075097). Acoustical Society of America.

Chapter 2

Influence of the pressure dependent resonance frequency on the bifurcation structure and backscattered pressure of ultrasound contrast agents: A Numerical investigation

2.1 Abstract

The bifurcation structure of the oscillations of ultrasound contrast agents (UCAs) was studied as a function of the driving pressure for excitation frequencies that were determined using the UCAs pressure dependent resonances (f_s). It was shown that when excited by the (f_s), the UCA can undergo a saddle node bifurcation (SNB) to higher amplitude oscillations. The driving pressure at which the SNB occurs is controllable and depends on the (f_s) magnitude. Utilizing the appropriate (f_s), the scattering cross section of the UCAs can significantly be enhanced (e.g. $\sim$ 9 fold) while at the same time avoiding potential UCA destruction (by limiting the radial expansion ratio < 2). This offers significant advantages for optimizing UCA mediated imaging and therapeutic ultrasound applications[1].

[1]Published as: Sojahrood, A.J., Falou, O., Earl, R., Karshafian, R. and Kolios, M.C., 2015. Influence of the pressure-dependent resonance frequency on the bifurcation structure and backscattered pressure of ultrasound contrast agents: a numerical investigation. Nonlinear Dynamics, 80(1-2), pp.889-904.

2.2 Introduction

Bubbles excited by ultrasound waves are highly nonlinear oscillators [1]. It has been shown both numerically and experimentally that bubbles exhibit complex and chaotic dynamics [1, 2, 3, 4, 5, 6, 7, 8, 9, 10, 11]. Bubbles encapsulated by a shell are being used in diagnostic ultrasound as contrast agents (UCAs) [12]. The dynamics of the UCAs has also been associated with complex and chaotic oscillations [8, 11].

Despite the complex behavior, bubbles and UCAs have become instrumental in a wide variety of fields. UCAs are used in sonoluminscence [6], in sonochemistry to increase chemical yields [13], and material science [14]. In the context of medical ultrasound, studies have shown the potential of the UCAs to target and enhance drug/gene delivery [15], reversibly open blood brain barrier to deliver drugs to the brain [16] and in ultrasound diagnostic imaging to enhance the detection of cancer even at early stages and with molecular sensitivity [17].

Despite of the many applications of UCAs, the relationship between the ultrasound exposure parameters (e.g. frequency and pressure) and the UCA behavior is not well understood. The UCA response to ultrasound is nonlinear and complex; thus the exposure conditions in some applications may not be optimized. A comprehensive understanding of the dynamics of the UCAs for the large range of relevant exposure parameters can be achieved using methods of nonlinear physics.

Fundamental insights into the dynamical properties of the UCAs can lead to optimization of the exposure parameters for particular applications. However, many of the numerical and experimental studies on the UCA dynamics have been carried out for a limited range of ultrasound frequencies and pressures. Due to the complexity and sensitivity of the exposure and the UCA parameters on the UCA oscillation dynamics, the limited information acquired in these studies does not provide a comprehensive framework that can be used further for the unification and classification of the UCAs dynamics. Furthermore, many potential exposure parameter combinations may be excluded due to the discrete nature of the parameters that have been investigated.

In most UCA applications, resonant UCA oscillations are of fundamental importance as they result in the highest energy transfer from the ultrasonic field to the UCAs [18]. As an example, in ultrasonic imaging when UCAs are driven with their resonance frequency they generate a significant backscattered signal which will enhance the signal compared to the background signal [19]. Previous

studies for free [20] and encapsulated [21, 22, 23, 24] bubbles have shown a shift in the UCA resonance occurs for different driving ultrasound amplitudes. Higher driving pressures have shown to decrease the resonance frequency of the free and encapsulated bubbles [20, 21, 22, 23, 24]. Despite the well-known fact of this shift in the resonant frequency for free bubbles [2] and the recent detailed observations of this shift for contrast agents [21, 22, 23, 24], to our best knowledge no study has been published that examines the consequences of this shift in the UCA resonant frequency on the dynamical behavior of the UCAs. The dynamics of the system over a wide continuous range of the pressure and frequency has not been studied. To address the effect of the excitation frequency and the applied acoustic pressure on the dynamics of the UCAs, these two parameters must be investigated together, taking into account the nonlinear relation between the acoustic pressure and the UCA resonance frequency.

The focus of this study is to investigate the dynamics of the resonant UCAs (excited by linear and pressure dependent resonance frequencies). The aim of this work is to build a fundamental understanding of the dynamics of the ultrasound contrast agents for the identification and classification of the nonlinear signatures of the resonant UCAs. This is studied firstly by calculating the UCA resonance curves at different ultrasound driving pressures. In the second step, these resonance frequencies are used to drive the UCA excitation and the dynamical behavior of the UCAs are visualized by the aid of the bifurcation diagrams of the radial oscillations of the UCAs as a function of the driving acoustic pressures. In the third step, the maximum backscattered pressure is calculated with the aid of bifurcation diagrams to investigate the effect of the nonlinear resonance on the backscattered pressure in the regime of non-destructive UCA oscillations.

2.3 Methods

2.3.1 The Bubble model

The radial oscillations of the UCAs were simulated by solving the Church-Hoff model [25] for UCAs through applying the $4th$-order Runge-Kutta technique :

$$\rho(\ddot{R}R + \frac{3}{2}\dot{R}^2) = P_0((\frac{R_0}{R})^{3\Gamma} - 1) - p_A(t)$$

$$-4\mu_L\frac{\dot{R}}{R}-12\mu_s\theta\frac{{R_0}^2}{R^3}\frac{\dot{R}}{R}-12G_s\theta\frac{{R_0}^2}{R^3}(1-\frac{\dot{R}_0}{R}) \tag{2.1}$$

In this equation R is the UCA radius at time t, R_0 is the initial radius of the unexcited UCA, $\dot{R}$ is the UCA wall velocity at time t, $\ddot{R}$ is the UCA wall acceleration at time t, ρ is the density of liquid and is equal to 998 $\frac{kg}{m^3}$ and μ_L is the density of the surrounding liquid which is equal to 0.001 $\frac{N.s}{m^2}$, P_0 is the equilibrium gas pressure within the bubble which is $1.01*10^5Pa$, Γ is polytropic exponent which is equal to 1.095 for SF_6. The symbol μ_s stands for the shell viscosity, θ is the shell thickness and G_s is the shear modulus of the shell. The values for these parameters are given in section 2.2. The driving ultrasound pulse, $p_A(t)$, is a sinusoidal signal consisting of 80 cycles at varying acoustic pressure amplitudes ($1kPa-1MPa$) and frequencies ($0.5-10MHz$):

$$p_A(t)=P_A\sin(2\pi ft) \tag{2.2}$$

In the above equation, $p_A(t)$ is the driving sound field where P_A is the acoustic pressure amplitude, f is the driving frequency and t is time. In addition, the backscattered acoustic pressure (P_{sc}) at a distance d from the center of the UCA, was calculated using [26]:

$$P_{sc}=\rho_L\frac{R}{d}(2\dot{R}^2+R\ddot{R}) \tag{2.3}$$

In this paper, the backscatter pressure of different UCAs was calculated at a normalized distance $d=1$ as discussed in [27]. The maximum scattering cross section was calculated using [28]:

$$SCS_{max}=(4\pi{R_0}^2)|\frac{P_{sc}}{P_A}|^2_{max} \tag{2.4}$$

Where SCS_{max} is the maximum scattering cross section.

2.3.2 Simulation parameters

Four UCAs with initial radii of $1,2,3$ and $4\mu m$ were considered. The sample shell parameters of $G_s=50MPa$, $\theta=4nm$ and $\mu_{sh}=\frac{1.49(R_0(\mu m)-0.86)}{\theta(nm)}$ were chosen. The shell viscosity was based on the values reported in [29] that take into account the increase in the shell viscosity for larger UCAs. These parameters were chosen based on published values for a generic UCA; this is done since the

main purpose of the paper is to investigate a general characteristic of the UCA system excited by its pressure dependent resonance frequency and not the behavior of one particular UCA. The results may therefore be generalized to all the UCAs whose dynamics are governed by equations like Eq. 1.

2.4 Results

2.4.1 Pressure dependent resonance

First the resonance frequencies of the UCAs were calculated by solving $Eq.1$. For each UCA, the primary linear resonance frequency was calculated by assuming a weak driving pressure amplitude of $P_A = 1kPa$. To calculate the maximum amplitude of the radial oscillations, the last 40 cycles of a 80 cycle sonication were used. In practice attenuation measurements are used to determine the resonance frequency of the UCAs [23]. In these experiments, the ultrasound pulse hits the UCAs which are initially at rest. Thus, at each frequency step (0.01 MHz), the Hoff model was solved with the initial conditions of $R(t = 0)$=R_0 and $\dot{R}(t = 0)$=0 to emulate UCA experimental conditions. The dynamics of a highly nonlinear system like UCA is strongly dependent on the initial conditions (ICs) [7, 30]. The effect of the ICs on the resonance curves is studied in section 4. After calculating the linear resonance frequency for $P_A = 1kPa$, for each UCA, the P_A was increased and the new resonance frequencies were calculated for 5 different P_As. Again at each frequency step the ICs is set as $R(t = 0)$=R_0 and $\dot{R}(t = 0)$=0. The maximum pressure amplitude was set based on a maximum ratio the radial oscillations of the UCA of R_n = 1.9 ($R_n = \frac{R_{max}}{R_0}$). This upper limit was used since the UCA disruption threshold is estimated to be $R_n \sim 2.0$ [31].Complete discussion about the threshold for UCA destruction is given in the discussion section. This limit can be considered a limit below which UCA destruction will be at a minimum.

The normalized maximum radial oscillation (R_n) as a function of frequency at varying acoustic pressures (P_A) for UCAs with R_0 of $1\ \mu m$ and $4\ \mu m$ are shown in Figure 2.1a and 2.1b, respectively. The resonance frequency of the UCA decreased and the radial oscillation increased with acoustic pressure. For the 1 μm UCA, the resonance frequency decreased from the linear resonance frequency (f_r) of 8.21 MHz at $1kPa$ to 5.46 MHz (f_s) at 340 kPa acoustic pressure ($R_n = 1.9$). This corresponds to 33% decrease in the resonant frequency (Figure 2.1a). For the 4 μm UCA,

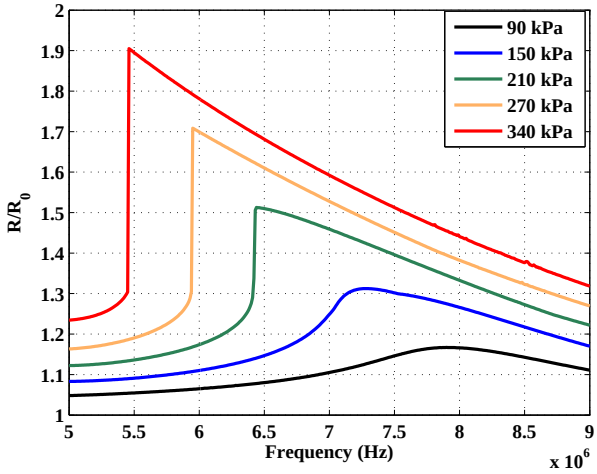

(a)

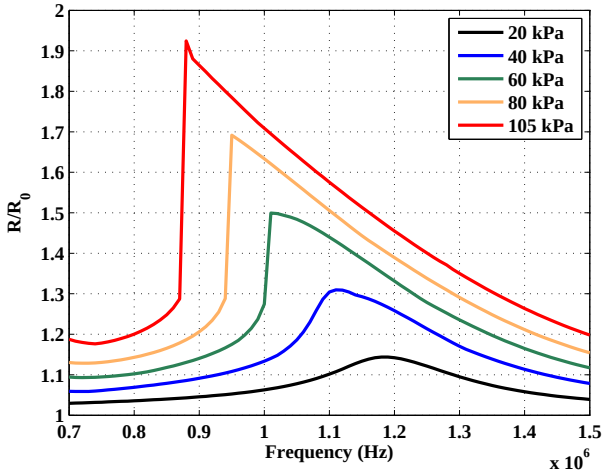

(b)

Figure 2.1: Resonance curves at different driving pressures for a) R_0=1 μm (linear resonance=8.21 MHz), b) R_0=4 μm (linear resonance=1.21 MHz). The driving pressures used in the simulation are shown in the figure caption.

the resonance frequency decreased from 1.21 MHz (f_r) to 0.88 MHz (f_s) at 105 kPa ($R_n = 1.9$) corresponding to 27% decrease in the resonant frequency (Figure 2.1b).

The ratios of f_s to f_r ($\frac{f_s}{f_r}$) as a function of acoustic pressure for four UCA sizes (1-to-4 μm) are shown in Figure 2.2. The ratio $\frac{f_s}{f_r}$ decreased as the acoustic pressure increased. Moreover, the $\frac{f_s}{f_r}$ ratio decreased for increasing UCA size at a given acoustic pressure exposure. The rate of decrease of $\frac{f_s}{f_r}$ is approximately 3 times higher for UCA with $R_0 = 4$ μm compared to $R_0 = 1$ μm. On average, the resonance frequency changed by 30-35% from the linear resonance frequency as the

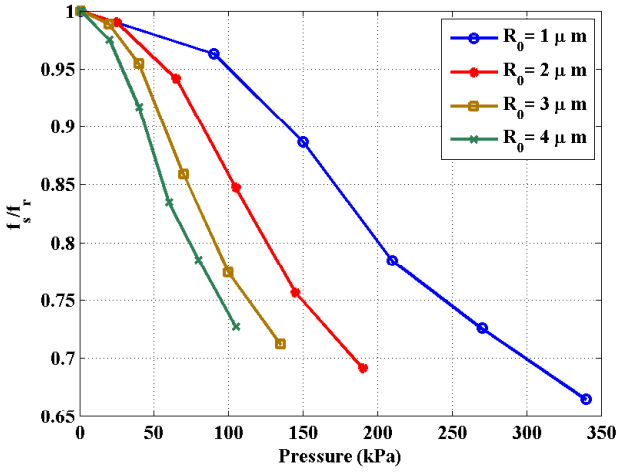

Figure 2.2: Variation of the resonance frequencies versus acoustic pressure for UCAs with R_0= 1,2,3 and 4 μm.

acoustic pressure increased. The larger UCAs reach the threshold of $R_n = 1.9$ at lower pressures compared to smaller UCAs (105 kPa vs 340 kPa for the 4 μm and 1 μm UCA, respectively). This is mainly due to the larger effect of viscosity and surface tension for the smaller UCA oscillations [32].

2.4.2 Bifurcation structure of the UCA driven with linear and pressure dependent resonance frequencies

The bifurcation structures of the radial oscillations of the 4 UCAs (representing 4 initial radii) were plotted as a function of R_n versus the driving acoustic pressure P_A. The driving frequencies were chosen firstly based on the linear resonance frequency and then the calculated pressure dependent resonance frequencies for the appropriate ultrasound driving pressure. The bifurcation analysis was performed over the 40 cycles of the 80 cycle pulse to eliminate the transient behavior.

In order to investigate the effects of the shift in the resonance frequency on the behavior of the UCAs, the bifurcation diagrams of the UCAs were generated as a function of R_n versus driving acoustic pressure (P_A). In each diagram the driving frequency used was based on the pressure dependent resonance frequency (f_s in Fig. 2.1). The generated bifurcation diagrams were compared to the case of insonification with linear resonance frequency ($f = f_r$, $P_A = 1\ kPa$). The results of this comparison are shown in Fig. 2.3 for UCAs of $R_0 = 1$ (left column) and 4 μm (right column) respectively.

The bifurcation diagrams of 1 μm and 4 μm size UCAs with varying acoustic pressures (P_A) at their corresponding resonance frequencies (f_s) are shown in Figure 2.3.

The bifurcation diagram for the 1 μm UCA excited at its linear resonance frequency (f_r = 8.21 MHz) is shown in Figure 2.3a. The UCA (1 μm) undergoes period doubling bifurcation at P_A of 546 kPa and R_n of 1.54, and exhibits $\frac{1}{2}$ subharmonics up to 661 kPa (P_A). With increasing pressure, the UCA shows period doubling cascades and chaos at P_A of 700 kPa and R_n of 1.88. The disruption threshold occurs at 790 kPa pressure with R_n = 2. According to Fig. 2.3a the maximum R_n which is obtained in the regime of period one is 1.54 (The red line indicates the destruction threshold).

A similar response is observed for the 4 μm UCA at its linear resonance frequency (f_r = 1.21 MHz) (Figure 2.3b). The 4 μm UCA exhibits period-one oscillations with increasing amplitude up to P_A of 240 kPa (R_n = 1.7), and above which the 4 μm UCA undergoes successive period doubling (P_A = 320 kPa) to chaos. The destruction occurs at 280 kPa. As depicted in Fig. 2.3b, driving the UCA with R_0=4 μm with its linear resonance frequency results in a maximum period one R_n of 1.7.

Fig. 2.3c shows the bifurcation structure of the UCA with R_0= 1 μm driven with f = 7.25 MHz (the resonance frequency f_s at P_A = 150kPa, Fig. 2.1a). Compared to Fig. 2.3a, a change in the slope of increase in R_n versus pressure is noticeable at P_A = 150 kPa. The UCA driven with f_r exhibits a monotonic increase in R_n as P_A is increased. As illustrated in Fig. 2.3b, for P_A<P_s (P_s= 150 kPa), R_n is smaller than the case depicted in Fig. 2.3a. After the P_A is increased above the P_s, the R_n undergoes a rapid growth and gets larger than the R_n of that UCA driven with f_r (Fig. 2.3a). The oscillatory behavior follows a period one regime with a higher R_n compared to the case of the UCA driven with f_r. Period doubling occurs at P_A =506 kPa while R_n reaches $\sim$ 1.7. Compared to the UCA driven with f = f_r, R_n reaches a higher value when the period doubling occurs. The UCA exhibits period two before the occurrence of further period doubling cascades above P_A = 606 kPa. The onset of chaos and destruction are concomitant at P_A = 630 kPa with R_n = 2. Like the onset of period doubling, the pressure threshold for chaotic behavior is lower compared to the case of f= f_r.

Fig. 2.3d shows the bifurcation structure of the UCA with R_0= 4 μm driven with f = 1.11 MHz (the resonance frequency f_s at P_A = 40 kPa, Fig. 2.1a). The dynamics are very similar to the UCA in Fig. 2.3c. The oscillation amplitude is below the oscillation amplitude of the UCA sonicated

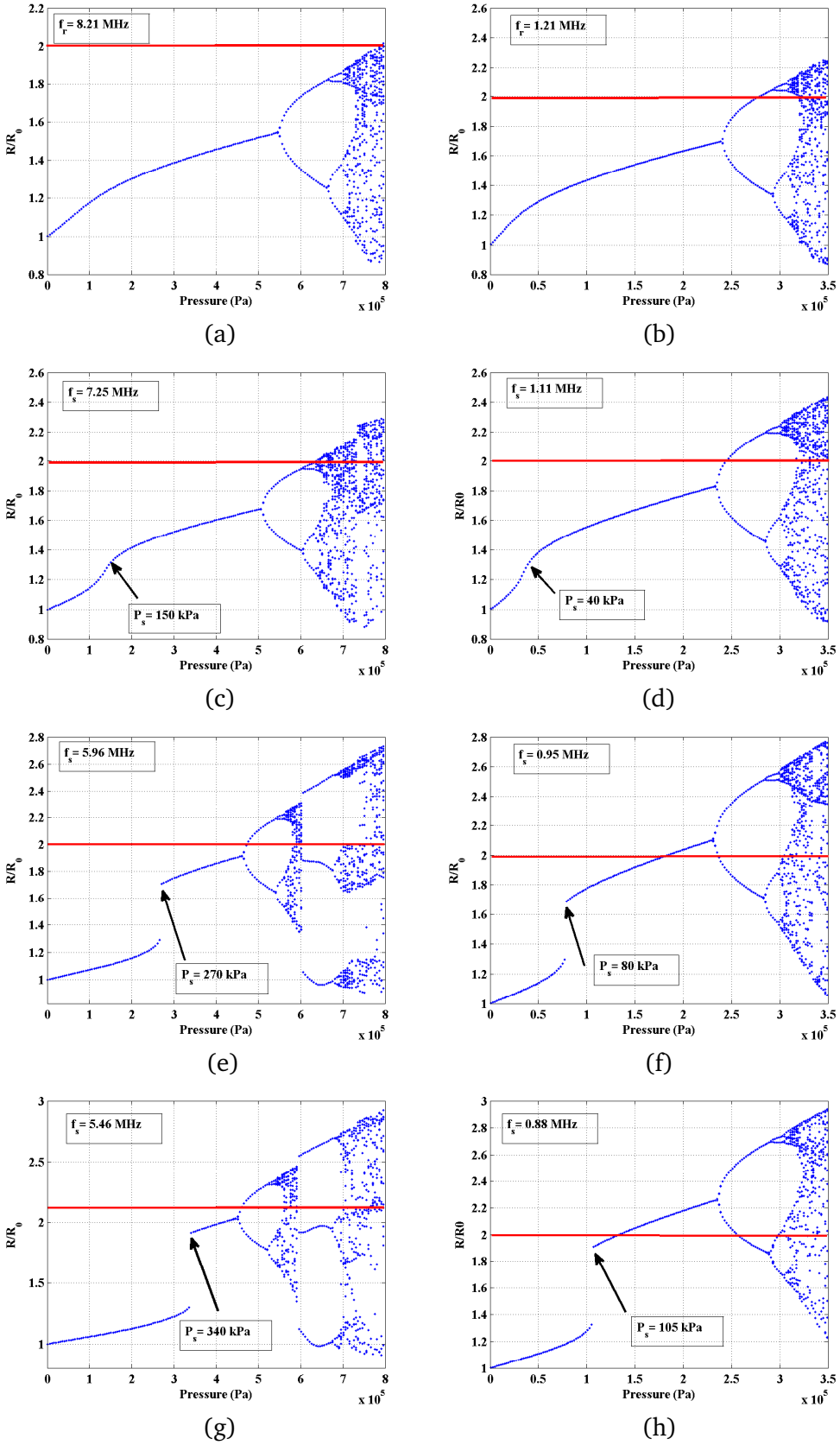

Figure 2.3: Bifurcation diagram of the $\frac{R}{R_0}$ of the UCAs verses the driving acoustic pressure. In the left column, the UCA have an initial radius $R_0 = 1\ \mu m$, while in the right column they have an initial radius of 4 μm, and are driven at the frequencies in the figure inset. The initial radius and excitation frequencies are: a) R_0=1 μm f=8.21 MHz, b) R_0=4 μm f=1.21 MHz, c) R_0=1 μm f=7.25 MHz, d)R_0=4μm f=1.11 MHz, 2 e) R_0=1μm f=5.96 MHz, f) R_0=4μm f=0.95 MHz, g) R_0=1μm f=5.46 MHz and h R_0=4μm f=0.88 MHz. (Red line shows the destruction threshold).

with $f = f_r$ but only for P_A<P_s=40 kPa. For acoustic pressure amplitudes greater than P_s, the oscillations undergo a significant increase in amplitude and in a manner similar to that presented in Fig. 2.3b. For these conditions, the destruction of the UCA with R_0= $4\mu m$ occurs at 247 kPa.

Fig. 2.3e depicts the bifurcation diagram of the UCA with R_0 =1 μm when driven with f = 5.96 MHz (f_s at P_A = 270 kPa). Compared to Fig. 2.3a, R_n is lower for $P_A < P_s$ = 270 kPa. Once the P_A is increased above 270 kPa, R_n undergoes a rapid growth and exhibits a saddle node bifurcation to a higher oscillation amplitude ($R_n \sim$ 1. 71), which is 23% larger than the R_n in Fig. 2.3a (at the same P_A). The UCA continues period one oscillations at a higher R_n compared to Figs 2.3a and 2.3c and undergoes period doubling at $P_A \sim$ 461 kPa at which point the R_n reaches 1.91. This is 24% larger than the maximum period one R_n in Fig. 2.3a. The chaotic behavior appears at P_A = 577 kPa with R_n 2.20. The threshold P_A for the onset of period doubling, destruction (at 475 kPa) and chaotic oscillations is lower than both the threshold P_A for f_r = 8.21 MHz and f_s = 7.25 MHz.

Fig. 2.3f illustrates the bifurcation diagram of the UCA with R_0 =4 μm when driven with f= 0.95 MHz (f_s at P_A = 80 kPa). Compared to Fig. 2.3b, R_n is lower for a $P_A < P_s$=80 kPa. Once the P_A is increased above P_s=60 kPa, R_n undergoes a rapid growth and exhibits a saddle node bifurcation to a higher oscillation amplitude ($R_n \sim$ 1.68), which is 26% larger than the R_n in Fig. 2.3b at the same P_A. The UCA continues period one oscillations at a higher R_n compared to Figs 2.3b and 2.3d. The radial oscillations pass the destruction threshold at 183 kPa. The UCA undergoes period doubling at P_A 231 kPa while R_n reaches $\sim$ 2.2. The maximum period one oscillations in this case is 17% larger than the maximum period one R_n in Fig. 2.3b. The chaotic behavior appears at P_A = 300 kPa with $R_n \sim$ 2.6. The threshold P_A for the onset of period doubling and chaotic oscillations is lower than both the f_r = 1.21 MHz and f_s = 1.11 MHz. There is a high degree of similarity in the dynamics between Fig. 2.3f and Fig. 2.3e. This indicates a general behavior for the UCAs sonicated with their pressure dependent resonance frequency.

The bifurcation diagram of the UCA with R_0 =1 μm sonicated with f = 5.46 MHz (the f_s at P_A = 340 kPa) is presented in Fig. 2.3g. As shown, the R_n is less than the previous cases (Figs. 2.3a, 2.3c and 2.3e) for $P_A < P_s$ =340 kPa. However, once the P_A is increased above 340 kPa, R_n exhibits a significant growth and becomes larger than the R_n in Figs. (2.3a, 2.3c and 2.3e). At this P_A amplitude, the R_n is 35% larger than when driven with f_r. The oscillation is of period one

for $P_A < 451\ kPa$ with a larger R_n (in $330 < P_A < 451 kPa$) compared to the previous cases. The radial oscillations of the UCA passes the destruction threshold at 416 kPa. The UCA undergoes period doubling at 451 kPa and $R_n \sim 2.04$. Finally, the oscillations become chaotic after a series of successive period doubling bifurcations at $\sim 546\ kPa$. In this case a full nondestructive amplitude (R_n=2) of period one is developed before the UCA undergoes period doubling.

Fig. 2.3h depicts the bifurcation diagram of the UCA with R_0 =4 μm insonified with $f = 0.88\ MHz$ (the f_s at $P_A = 105\ kPa$). As shown, the R_n is less than the previous cases (Figs. 2.3b, 2.3d, 2.3f) for $P_A < P_s = 105\ kPa$. However, once the P_A is increased above 105 kPa, R_n exhibits a significant growth and becomes larger than the R_n in Figs. (2.3a, 2.3d, 2.3f). At $P_A = P_s = 105\ kPa$ amplitude, the R_n is $\sim 30\%$ larger than when driven with f_r. The oscillation is of period one for $P_A < 231\ kPa$ with a larger R_n (in $105 < P_A < 231\ kPa$) compared to the previous cases. The destruction threshold occurs at 137 kPa The UCA undergoes period doubling at 232 kPa ($R_n \sim 2.32$). Finally, the oscillations become chaotic after a series of successive period doubling bifurcations at 310 kPa. Again, the similarity between Fig. 2.3g and 2.3h is noticeable indicating a general trend in the UCA behavior sonicated with pressure dependent resonance. In both cases a full amplitude period one oscillation is achieved. The importance of the full amplitude period one oscillations is in the backscattered pressure and will be discussed in the next section.

2.4.3 Maximum backscattered pressure in the regime of stable UCA oscillations

The backscattered pressure amplitude (P_{sc}) was numerically calculated using Eq. 3 for all of the exposure parameters. In each case the excitation pressure range was chosen so that the R_n remained below the UCA destruction threshold ($R_n = 2$). This range was chosen by examination of the bifurcation diagrams and ensuring that $\frac{R_{max}}{R_0} < 2$ (red line in figure 2.3). The results are shown in $Figs. 2.4a - d$ for UCAs with R_0= 1, 2, 3 and 4 μm.

The backscattered pressure amplitude (P_{sc}) from UCAs of different sizes (1-to-4 μm) at varying resonance frequencies is shown in Figure 2.4. The P_{sc} increases with acoustic pressure for all UCA sizes and acoustic frequencies. At low acoustic pressures, a higher P_{sc} is achieved at the UCA's linear resonance frequency (f_r). However, with increasing acoustic pressure and at pressure dependent resonance frequency, the P_{sc} amplitude significantly increases.

As shown in Figs. 2.4a-d, driving the UCA with its linear resonance frequency (f_r) results in a

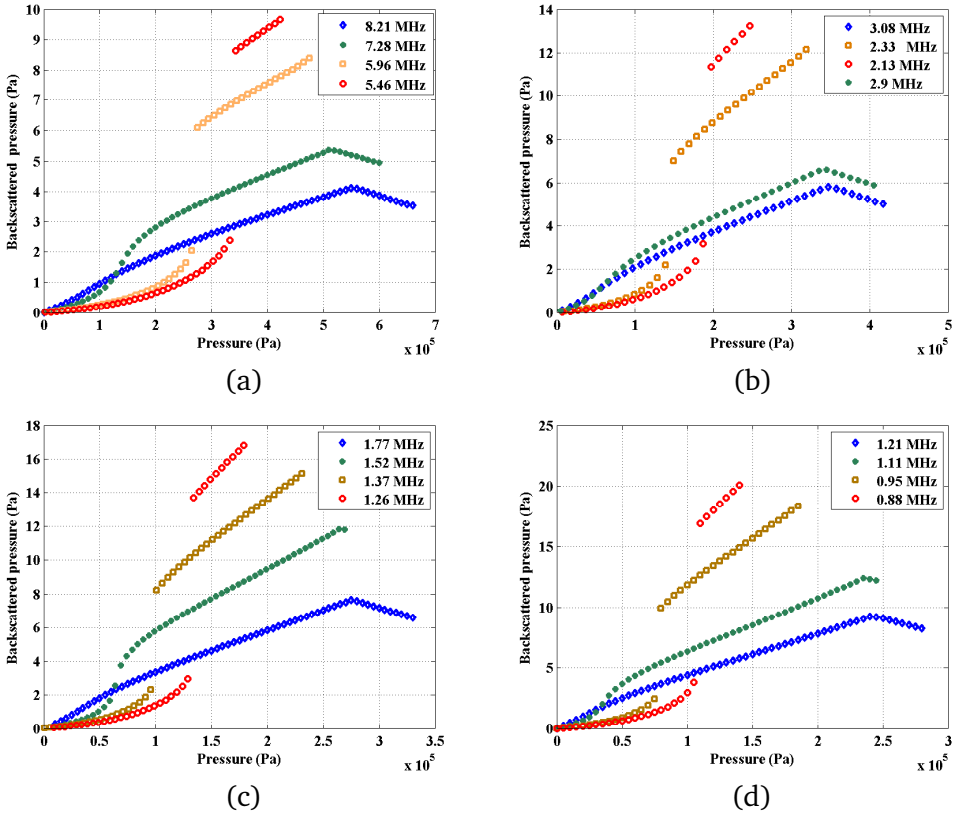

Figure 2.4: Backscattered pressure amplitude as a function of pressure for linear and pressure dependent resonance frequencies when a) R_0= 1 μm, b) R_0=2 μm, c) R_0=3 μm and d) R_0=4 μm. The pressure dependent resonance frequencies are in the figure legends.

higher backscattered pressure amplitude (P_{sc}), but only at low pressures of insonification. When sonicated with its linear resonance frequency, the P_{sc} increases linearly alongside the driving acoustic pressure until the UCA undergoes the period doubling bifurcation. The occurrence of the period doubling bifurcation is concomitant with a decrease in the P_{sc} although the UCA displays a higher R_n. This will be explained in the next section.

Figs. 2.4a-d illustrate that when a UCA is sonicated with its pressure dependent resonance frequency (f_s), the diagram has two distinct regions, $P_A < P_s$ and $P_A > P_s$. For $P_A < P_s$ the P_{sc} is less than the backscattered pressure amplitude of a UCA driven with f_r. However, as soon as the pressure is increased above P_s, the P_{sc} increases significantly becoming much larger than the P_{sc} of a UCA driven with its linear resonance frequency f_r. For example in Fig. 2.4a, the P_{sc} of a R_0 =1 μm UCA driven with f_s =5.46 MHz (P_s=340 kPa) becomes $\sim$ 3 fold larger than the P_{sc} of the same UCA driven with f_r=8.21 MHz as soon as the pressure increases above 340 kPa.

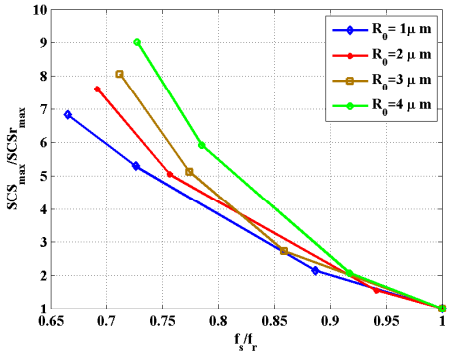

Figure 2.5: The normalized maximum possible scattering cross section while avoiding the UCA destruction as a function of $\frac{f_s}{f_r}$. In each case the maximum possible scattering cross section (SCS_{max}) is normalized by the maximum possible scattering cross section for a UCA driven with its linear resonance frequency ($SCSr_{max}$).

A comparison between Figs. 2.3 and 2.4 shows that the sudden increase in P_{sc} is concomitant with the saddle node bifurcation in R_n-P_A bifurcation diagrams. The increase is more significant for higher P_s and lower f_s. In this regard, if f_{s1}, f_{s2} and f_{s3} are the pressure dependent resonance frequencies of the UCA at the acoustic pressures of P_{s1}, P_{s2} and P_{s3} where P_{s1}<P_{s2}<P_{s3}; the P_{sc} follows the order of P_{sc3}>P_{sc2}>P_{sc1} as soon as P_A increases above P_{s3}.

Fig. 2.4 contains very important information regarding the maximum possible backscatter from an UCA (P_{scmax}). Driving the UCA with its linear resonance frequency does not result in the maximum backscatter. When the pressure dependent resonance frequency is used and the pressure is increased above P_s, the P_{sc} increases significantly. The backscattered pressure amplitude continues to increase alongside pressure until the UCA is destroyed ($R_n > 2$). Just below this critical pressure for UCA destruction the maximum possible backscattered pressure (P_{scmax}) is at its highest for the UCA driven with f_s.

For example, in Fig. 2.4a, the P_{scmax} for R_0=1 μm driven with f_r=8.15 MHz is 4 Pa and occurs at P_A= 542 kPa. However, when the same UCA is driven with f_s=5.4 MHz the P_scmax reaches 9.3 Pa and happens at P_A= 408 kPa. It should be noted that not only is the backscatter pressure maximized, but also it is occurring at a lower driving pressure. This can have significant advantages in increasing the signal to noise ratio (SNR) and contrast to tissue ratio (CTR) in medical imaging applications. This is because the SNR decreases for linear scatterers (such as tissues) at lower sonication pressures while at the same time the P_{sc} from the UCA increases at these lower excitation pressures..

In summary, it is observed that in the region of nondestructive oscillations (R_n<2), the maximum possible backscattered pressure has an upper limit when the UCA is driven with f_r. This limit can significantly be enhanced through optimizing the driving frequency in terms of the pressure dependent resonant frequency f_s and applying an acoustic pressure that is greater than a threshold P_s. The maximum possible nondestructive backscattered pressure occurs in the region of the period one oscillations. Occurrence of the period doubling is concomitant with a decrease in the backscattered pressure.

2.4.4 Comparison between the maximum possible backscatter cross section

In order to investigate the effect of the pressure dependent resonance on the scattering properties of the UCAs, the maximum possible scattering cross section (SCS_{max}) was calculted using Eq. 4. The maximum possible backscattered pressure derived in Fig. 2.4 was used in the calculation of the SCS_{max}. These values were then normalized by the maximum possible SCS in the case of excitation with the linear resonance frequency ($SCSr_{max}$). These values were plotted as a function of $\frac{f_s}{f_r}$ in Fig. 2.5.

As it is illustrated in Fig. 2.5, driving the UCA with f_s results in a larger scattering cross section compared to excitation with f_r. The SCS_{max} increases as f_s decreases. As an example, exciting an R_0=4 μm UCA with f_s= 0.86 MHz results in a SCS_{max} which is 9 times greater than the SCS_{max} of f_r=1.21 MHz. It can also be concluded from Figure 2.5 that the SCS_{max} increases faster versus $\frac{f_s}{f_r}$ for the larger UCAs.

2.4.5 The concomitant decrease in maximum backscattered pressure with period doubling

In section 3.3 it was shown that the backscattered pressure decreases when the period doubling occurs. At the first glance, this appears counterintuitive as the decrease occurs for a higher R_n. After period doubling, while pressure increases, R_n keeps increasing but the backscattered pressure decreases. Comparing the radial oscillations between the period one regime and the period two regime (after the period doubling has taken place) shows that when period doubling occurs, the magnitude of the UCA contraction decreases, thus the UCA velocity and acceleration during the contraction phase of the UCA oscillation are smaller compared to the period one oscillations prior

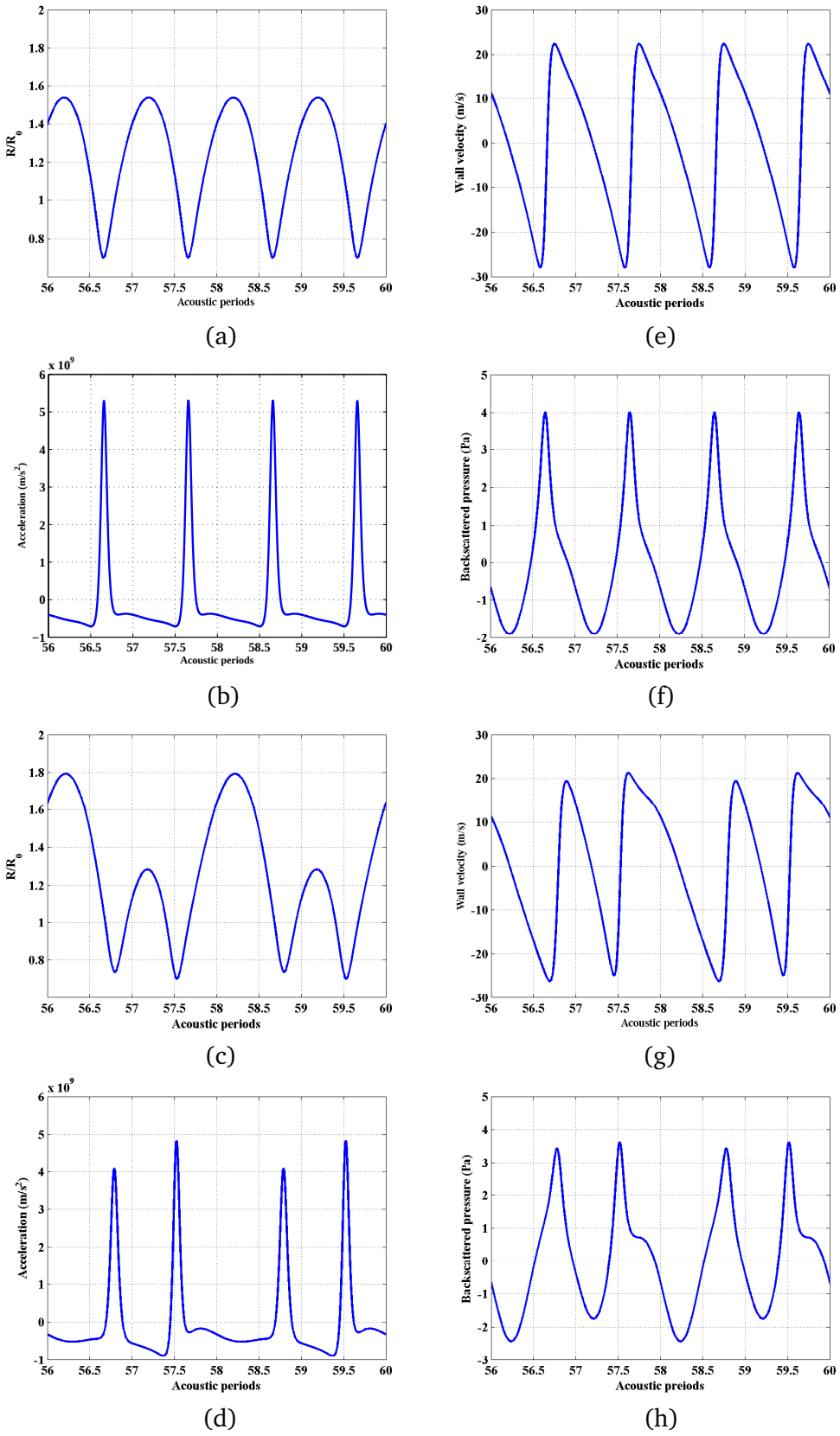

Figure 2.6: Comparison between the period 1 and 2 behaviors of the UCA with R_0=1 μm driven with 8.21 MHz of frequency. In left column P_A=533 kPa: a) radial oscillations, b) velocity, c) acceleration, d) Backscattered pressure. In right column P_A=640 kPa: e) radial oscillations, f) velocity, g) acceleration, and h) Backscattered pressure..

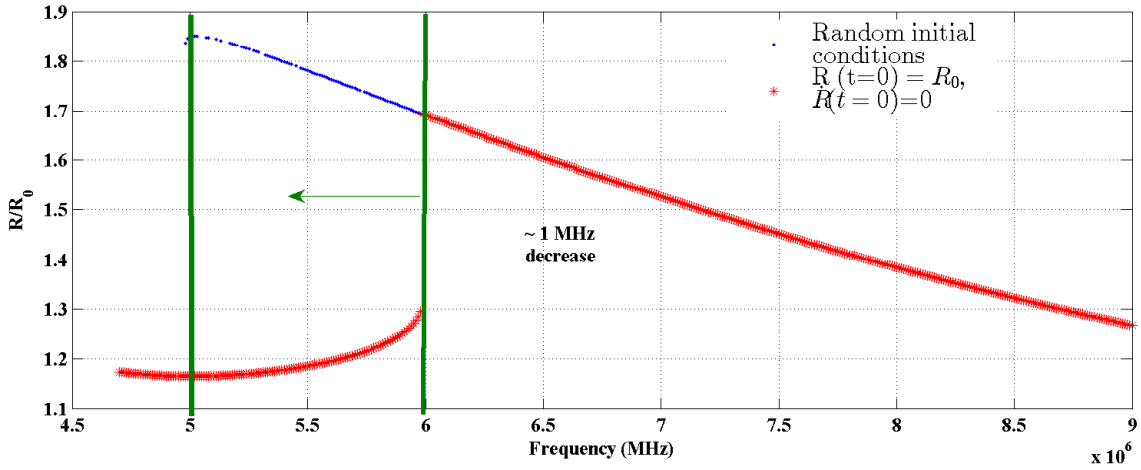

Figure 2.7: The pressure dependent resonance frequency of the UCA with $R_0 = 1\ \mu m$ at $P_A = 264kPa$ with 10 random initial conditions (blue superimposed) and when the initial conditions are $R(t=0)$=R_0 and $\dot{R}(t=0)$=0 (red).

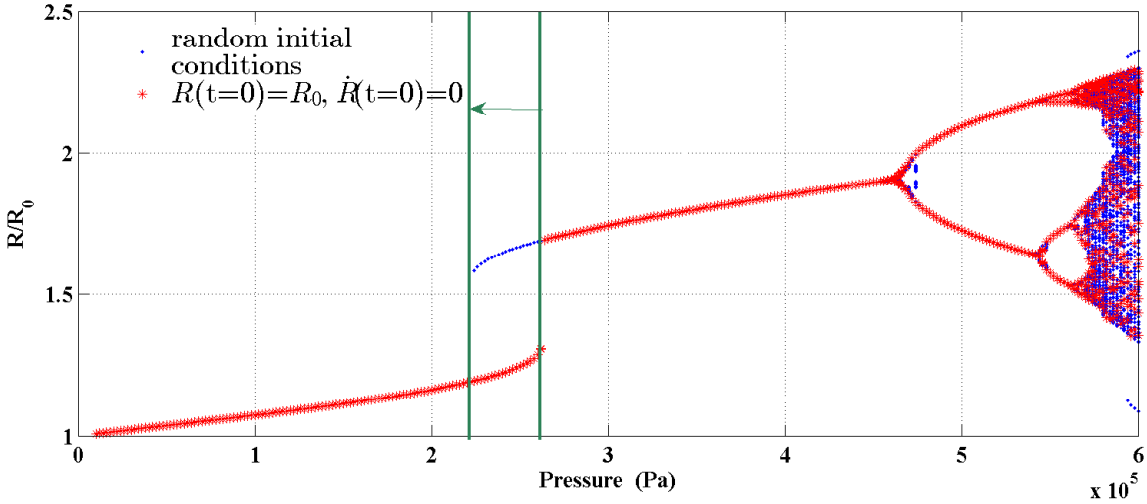

Figure 2.8: The bifurcation diagram of the UCA with $R_0 = 1\ \mu$ m sonicated with $f = 6\ MHz$ with 10 random initial conditions (blue superimposed) and when the initial conditions are $R(t=0)$=R_0 (red).

to period doubling.

This phenomenon is shown in detail in Figs. 2.6a-d. Fig. 2.6a shows the radial oscillations of the UCA with R_0=1 μm driven with f_r=8.21 MHz and acoustic pressure of 533 kPa as a function of the driving acoustic periods. This corresponds to a UCA undergoing period one oscillations before the occurrence of the period doubling (Fig. 2.3a). The corresponding wall velocity, acceleration and backscattered pressure are shown in Figs. 2.6b-d. Fig. 2.6e illustrates the radial oscillations of the same UCA when driven with an acoustic pressure of 640 kPa. According to Fig. 2.3a this condition corresponds for period two oscillations after the period doubling bifurcation. The corresponding wall velocity, acceleration and backscattered pressure are shown in Figs. 2.6f-h. It can be observed in Fig. 2.6d that despite the increasing UCA radius, the magnitude of the contraction is smaller than in Fig. 2.6a. This results in a smaller velocity and acceleration for the UCA as shown in Fig. 2.6f-g. As a consequence the corresponding backscattered pressure is larger for the UCA undergoing period one oscillation (Fig. 2.6d).

The concomitant decrease in the P_{sc} amplitude with period doubling was only shown for the frequency range that was studied in this paper. The decrease in P_{sc} was shown only for UCAs being sonicated with their resonance and pressure dependent resonance frequencies. The frequencies which are considered in our study are between the resonance frequency (f_r) and the pressure dependent resonance frequency (f_s) down to $0.665 * f_r$. It should be noted that in different cases like sonication of the UCA with its $2nd$ harmonic resonance frequency ($0.5 * f_r$) or sonication with the subharmonic resonance frequency $\sim 2 * f_r$ the behavior of the UCA will be different and one may not see the same decrease in the backscattered pressure concomitant with period doubling. However, as the main purpose of this study is the understanding of the dynamics of the resonant UCAs, we have not studied the above mentioned frequency ranges. Investigation of the behavior of the harmonically or subharmonically resonant UCAs are beyond the scope of this paper.

2.5 Effect of the initial condition on the resonance curves and bifurcation structure of the UCAs

As it was discussed earlier, to generate the resonance curves and the bifurcation diagrams, the initial conditions were chosen to be $R(t = 0)$=R_0 and $\dot{R}(t = 0)$=0. However, the dynamics of

a nonlinear system like UCA is heavily dependent on the initial conditions. The effect of random initial conditions on the dynamics and resonance curves of bubble oscillators have been investigated in [1, 7, 30]. The results of these studies have shown that there can be coexisting stable solutions for a given parameter range. In order to visualize all the solutions for a given parameter range, the effect of random initial conditions should be studied. In order to complete the analysis on the dynamics of the UCAs driven with their pressure dependent resonance frequency and test the effect of the initial condition on the solutions of the system in this regime, we have calculated one resonance curve and one bifurcation diagram considering 10 random initial conditions [30] at each step.

Figure 2.7 shows the resonance frequency of a UCA with $R_0 = 1\ \mu m$, sonicated with an ultrasound pulse whose pressure amplitude is $P_A = 264$ kPa. At each frequency step, the radial dynamics of the UCA is simulated for 10 random initial conditions (ICs) and the $\frac{R_{max}}{R_0}$ is plotted for every IC. Compared to the case of sonication with ICs of $R(t=0)=R_0$, the resonance frequency may occur at a lower frequency ($\sim 1\ MHz$ lower) with a higher amplitude. Also note the coexisting attractors for the frequency range of $\sim$ 5 to 6 MHz.

Figure 2.8 shows the bifurcation diagrams of the UCA with $R_0 = 1\ \mu$ m for two different set of ICs. The blue curve shows the bifurcation diagram for the IC of $R(t=0)=R_0$ and $\dot{R}(t=0)=0$ while the red curve shows the bifurcation diagram for 10 random initial condition at each pressure step. The sonication frequency is 6 MHz which is the pressure dependent resonance frequency of the UCA (f_s) at $P_A = 264\ kPa$ for $R(t=0)=R_0$ and $\dot{R}(t=0)=0$ calculated in fig. 2.7. As it is illustrated, the UCA starting with $R(t=0)=R_0$ and $\dot{R}(t=0)=0$ (red), starts with period one oscillations which undergo a saddle node bifurcation at $P_A = 264$ kPa to a higher amplitude. However, the UCA starting with the random initial conditions, exhibit a slight different behavior. There is coexisting period one oscillations in for $224kPa \leq P_A < 264kPa$. Depending on the IC, the UCA exhibit the saddle node bifurcation to a higher amplitude for a lower P_A.

2.6 Discussion and conclusion

The resonance frequency of the UCAs decreases with increasing acoustic pressure. It was shown that the shift in the resonance significantly influences the oscillatory behavior of the UCA. The key

findings can be summarized as follows:

When the bifurcation diagrams of the ($R_n = \frac{R}{R_0}$) versus acoustic pressure (P_A) of an UCA driven with its linear resonance frequency (f_r) are compared to the case of insonification with f_s (resonance frequency at the acoustic pressure P_s), it is seen that R_n undergoes either a steep rise or a saddle node bifurcation at the excitation pressure P_s. After a saddle node bifurcation, the UCA continues oscillations in the same way as the UCA driven with f_r but with a higher R_n. Both UCAs undergo a period doubling transition to chaos, however the UCAs driven with f_s exhibit period doubling and chaotic oscillations at lower pressure thresholds.

When the R_n -P_A bifurcation diagrams are compared for UCAs driven with f_{s1} and f_{s2} (non-linear resonance frequencies corresponding to P_{s1} and P_{s2} with $P_{s2} > P_{s1}$), both UCAs exhibit the saddle node bifurcation with the difference of a saddle node bifurcation to a higher amplitude in case of the UCA driven with f_{s2}. In addition, the UCA destruction ($R_n > 2$) and the transition to chaos occur at a lower pressure threshold for the UCA driven with P_{s2}. When the backscattered pressures are compared, it was shown that the acoustic pressure range can be divided into two distinct regions ($P_A < P_s$ and $P_A > P_s$). For $P_A < P_s$, the backscattered pressure is higher for the UCA driven with f_r. However, for the UCA driven with f_s, while $P_A > P_s$ the backscattered pressure undergoes a significant increase and is greater than for the case of the excitation with $f = f_r$. This is true for all of the applied driving acoustic pressure values for which $P_A > P_s$. The main advantage of sonication with f_s is the increased backscatter from UCAs at lower driving acoustic pressures. This can result in an enhanced signal to noise ratio and contrast to tissue ratio in a clinical imaging setting.

The threshold for destruction was set based on the criteria which was formulated by Flynn [33] and later was used in [31]. According to the formulation by FLynn, when $\frac{R_{max}}{R_0}$>2, inertial forces dominate the collapse of the UCA, and increasing quantities of kinetic energy will be transferred to the collapsing bubble as the surrounding liquid converges while at the same time decreasing amount of this energy is lost as a result of dissipation. Transient collapse is defined as a phenomenon where significant amount of energy is concentrated in the bubble and the effect of the energy supply outweighs the energy dissipation [34]. So the destruction criterion by Flynn is set as $\frac{R_{max}}{R_0}$>2.

There is also another criterion based on the ratio of $\frac{R_{max}}{R_0}$ which is developed by Apfel [35]. In this criterion transient collapse occurs when $\frac{R_{max}}{R_0}$ is between 2 and 2.3 . In this work we have used

the Flynn's criterion to ensure there is no transient collapse, as it predicts the minimum expansion ratio for bubble destruction.

There have been a number of experimental studies on the destruction of the ultrasound contrast agents. These studies employed mainly two techniques: 1- fast optical measurements of the UCA radius [36, 37, 38, 39], 2- Acoustical method by analyzing the post excitation signal after collapse [40, 41, 42]. Results of the large number of optical measurements of the UCA oscillations in [36, 37, 38, 39] has shown that although some UCAs may undergo large amplitude oscillations and are not destroyed when $\frac{R_{max}}{R_0}>2$, however, there is no or very little evidence of UCA destruction when $\frac{R_{max}}{R_0}<2$. In other words, the majority of the UCAs are destroyed once $\frac{R_{max}}{R_0}>2$ although some few UCAs may exhibit higher expansion ratios. In another series of acoustical investigations on the UCA destruction, the post excitation signal by UCA has been used as an indicator for UCA destruction [40, 41, 42]. The results of these studies, illustrated no evidence of UCA destruction when $\frac{R_{max}}{R_0}<2$. The UCA destruction only happened once $\frac{R_{max}}{R_0}>2$, although again some of the UCAs exhibited higher amplitude of oscillations. Based on these results we have chosen the destruction threshold to be equal to 2 to avoid UCA destruction.

It should be noted that the results of our study at the destruction point also satisfies the criteria developed by Mitchell and Plesset [43]. According to this theoretical study, the bubble is stable if $\frac{R_{max}}{R_{min}}<5$ and it is unstable if $\frac{R_{max}}{R_{min}}>10$. In our study the maximum $\frac{R_{max}}{R_{min}}$ in the nondestructive regime is 4.11 (R_0= 4 μm, f_s= 0.88 MHz and P_A = 137 kPa) which is below the limit of this criterion. Thus the identified parameter ranges for nondestructive oscillations in this study also satisfy this criterion of bubble stability.

It should be noted that another potentially better indicator for UCA destruction is the UCA wall velocity. However, there has not been a criterion set based on the UCA wall velocity limit. There have been experimental studies in which the bubble wall velocity has been recorded or estimated during the collapse. We have also compared the maximum simulated UCA wall velocity at the destruction threshold with the published destructive bubble wall velocities. The bubble wall velocities of -51 m/s in [36] ("apparently sufficient to destroy very small bubbles" [36]), -350 m/s in [37] and -144, -329 and -456 m/s in [44] are reported to be sufficient for bubble destruction. The maximum negative and positive wall velocity in our simulations are respectively -48.92 m/s and 36.47 m/s for (R_0= 1 μm, f_s= 5.46 MHz and P_A = 340 kPa), which are smaller than the

reported velocities for the bubble destruction.

In this paper it was shown that the main feature of the UCA oscillations driven with f_r is that R_n grows monotonically with pressure up to a pressure threshold and beyond which the UCA oscillations undergoes successive period doubling bifurcations leading to eventual chaotic oscillations. The occurrence of the period doubling is concomitant with counterintuitive decrease in the backscatter pressure. This is due to the fact that the magnitude of the UCA contraction decreases with period doubling (Figure 2.6), which results in lower wall velocity and acceleration when compared to the case of the period one oscillation. Thus, in order to maximize the backscatter pressure during nondestructive oscillations, period one oscillations of full amplitude (R_n = 2) are needed.

It was shown that through driving the UCA with f_r, radial oscillations of period one with the full amplitude (R_n=2) are not developed. In this regard, application of f_s will be of great advantage. If f_s is optimized correctly, period one oscillations with full amplitude (R_n=2) can be generated. This results in significant enhancement of the backscattered pressure without the UCA destruction. In addition, because the maximum backscatter pressure occurs at a lower applied acoustic pressure, the background noise is minimized, which may lead to a superior SNR and CTR. Calculation of the maximum possible scattering cross section (SCS_{max}) showed that through optimizing f_s, nondestructive SCS_{max} can be enhanced up to 9 fold.

The backscattered pressure amplitude was calculated using eq. 3, however the frequency dependent attenuation that will occur in tissue was not considered. Thus, high-frequency components that will be preferentially diminished in tissue were persevered. As the main goal of the paper was the study of the dynamical characteristics of the UCA which is independent from attenuation, we have not considered the spreading loss due to attenuation. However, in applications, we may expect a better enhancement in case of the sonication with the pressure dependent resonance frequency compared to the values predicted here. This is because the pressure dependent resonance frequency is smaller ($\sim 30 - 35\ \%$ in this study) compared to the linear resonance frequency, thus the backscatter signal from UCAs experiences less attenuation.

In many investigations, the resonance frequency of the UCAs is experimentally selected through attenuation measurements. The applied pressure amplitude may significantly shift the resonance frequency with larger UCAs experiencing a more drastic effect. The results indicate that in order to

increase the efficiency of the UCA applications, either corrections should be made for the measured resonance frequency, or the pressure amplitude of the sonication should be chosen higher than the pressure amplitude used for measuring the resonance frequency of the UCA. This is because choosing pressures below the value (P_s) used in the measurements, the backscattered pressure is significantly reduced (Figs. 2.4a-d).

The sudden increase in the radial oscillations of the UCA for $P_A > P_s$ may provide advantages to current diagnostic and therapeutic applications of the UCA. One of the diagnostic applications that can benefit from this phenomenon is the amplitude modulation (AM) UCA imaging technique [45,46,47]. This method is based on the nonlinear increase in the backscatter pressure when pulses of different amplitude are applied. In AM two pulses are sent to the tissue with the first having twice the amplitude of the second. The backscattered pressure from the second pulse is scaled by multiplying its magnitude by two and subtracted from the backscattered from the first pulse. Due to the linear response of the tissue, the residual from the tissue will be minimal, however there will be a significant residual from the UCAs, which leads to a superior CTR. The sudden jump will be large when increasing the nonlinearity of the UCA system by choosing the half amplitude signal below P_s and the full amplitude above P_s.

Another benefit may be in the case of imaging a region of interest (ROI) deep within the body. Because the UCAs are distributed within all the vessels among the pre-target tissue layers, they may shield the signals on the beam path and from the target tissue and UCA in the ROI. Specifically this tends to be more problematic in cases of deeper targets. This is because the signal encounters more UCAs on its path to the target and back, therefore the signal significantly loses its strength. Consequently the ultrasonic beams become attenuated by the superficial pre-focal tissue, which causes the loss of the strength of the signal from the UCAs at the target, thus limits the visualization of the tissue layers at deeper locations [48, 49]. The accuracy of tissue perfusion measurement is largely affected by this shadowing effect [48, 49]. To allow accurate quantification, removal of shadowing artifact is crucial [47, 49]. Near resonance, the attenuation is higher because of increased scattering and energy absorption by the UCAs [18]. In this regard the imaging procedure can be optimized by using focused transducers that produce the pressures greater than P_s at the ROI (focal region) and less than P_s at the superficial tissue. This will decrease the prefocal shadowing effect (because pre-focal UCAs will be non-resonant) and at the same time increases the backscatter

at the ROI (the UCAs at the ROI are resonant because the focal pressure is more than P_s) which can ultimately improve the SNR and CTR.

One of the therapeutic applications that can benefit from this nonlinear behavior of UCAs is the microbubble enhanced drug delivery. In drug delivery UCA oscillations are used to enhance the permeability of the cell to the drug [15]. However, multiple scattering of the UCAs coming from pre-focal regions will attenuate the ultrasonic beams and have undesirable effects on the healthy (non-targeted) tissue while also distorting the focus at the target tissue [50]. Because of the steep pressure gradient of the therapy transducers, pressures above P_s can be generated at the target while the pressure in the surrounding tissue can be kept below P_s. This way, the microbubbles in the non-focal surrounding tissue will oscillate below resonance and therefore the pre-focal scattering effects and attenuations are minimized. In addition, the microbubble activity will be enhanced in the focal region, due to enhanced oscillations in pressure dependent resonance regime. This can lead to a more effective and precise treatment and enhanced safety.

This work considered single size microbubbles. However, location of the saddle node bifurcation is highly size dependent. Thus, in case of a polydisperse solution of microbubbles (which is generally the case in clinical investigations), only a fraction of microbubble sizes will be active in the pressure dependent resonance regime. One possible way to partially take advantage of the pressure dependent resonance can be to choose a frequency which excite the majority of the microbubbles around the resonance peak. The other method could be the use of centrifugation techniques to stack the micobubbles in narrow size ranges [51], then the driving frequency can be chosen so that it drives the majority of each stack into pressure dependent resonance regime. Through using monodisperse microbubbles [23, 52, 53] one may fully take advantage of exciting all the microbubbles in the pressure dependent resonance regime.

Another factor that should be considered is the microbubble growth due to rectified diffusion. In applications where long high amplitude pulses are used for sonication, the effect of rectified diffusion may become significant. This can displace the pressure for saddle node bifurcation in the microbubble system as the microbubble can grow beyond the active size range due to rectified diffusion. One possible way to solve this problem is modifying the pulsing sequences by choosing a suitable combination of ”pulse on time” / ”pulse off time” strategy [54]. The duration of the pulse on time may ensure the microbubbles are still in effective pressure dependent resonance

regime, while the ”pulse off” time duration may ensure that there is enough partial dissolution of microbubbles. The ”pulse off” time duration may allow reactivation of the microbubbles which have grown beyond the active size range at the beginning of the subsequent pulse [54].

Bibliography

[1] Parlitz U, Englisch V, Scheczyk C, Lauterborn W Bifurcation structure of bubble oscillators. J. Acoust. Soc. Am. **88**(2) 106177 (1990).

[2] Lauterborn W and Suchla E Bifurction strauctureinamodel of acoustic turbulence. Phys. Rev. Lett. **53**(24) 2304-2307 (1984).

[3] Esche R Untersuchungder schwingungs kavitation in ussigkeiten. Acustica **2** 20818 (1952).

[4] Luterborn W and Cramer L Subharmonic route to chaos observed in acoustics. Phys. Rev. Lett. **47**(20) 14458 (1981).

[5] Lauterborn W and Koch A Holographic observation of period-doubled and chaotic bubble oscillations in acoustic cavitation. Phys. Rev. A **35**(4) 19746 (1987).

[6] Holt RG, Gaitan DF, Atchley AA and Holzfuss J Chaotic sonoluminescence. Phys. Rev. Lett. **72**(9) 13769 (1994).

[7] F Hegedűs, C Hős, L Kullmann Stable period 1, 2 and 3 structures of the harmonically excited Rayleigh - Plesset equation applying low ambient pressure IMA Journal of Applied Mathematics Volume **78**(6) 1179-1195 (2013).

[8] Macdonald CA and Gomatam J Chaotic dynamics of microbubbles in ultrasonic elds, Proc. IMechE. 220 333-343 (2006).

[9] Behnia S, Jafari. A, Soltanpoor W and Jahanbakhsh O Nonlinear transitions of a spherical cavitation bubble. Chaos, Solitons & Fractal **41** 818-828 (2009)

[10] Behnia S, Jafari. A, Soltanpoor W and Sarkhosh L Towards classificationof the bifurcation structure of a spherical cavitation bubble. Ultrasonics 49 605-610 (2009)

[11] Sojahrood AJ, and Kolios MC Classification of the nonlinear dynamics and bifurcation structure of ultrasound contrast agents excited at higher multiples of their resonance frequency, Phys. Lett. A **376**(33) 2222-2229 (2012)

[12] Cosgrove D Ultrasound contrast agents: An overview, European Journal of Radiology **60** 324-330 (2006).

[13] Suslick KS *Sonochemistry, Kirk-Othmer Encyclopedia of Chemical Technology* DOI: 10.1002/0471238961.1915141519211912.a01 (2000)

[14] Suslick KS and Price JG Application of ultrasound to materials chemistry. Ann. Rev. Mater. Sci. **29** 295-326 (1999)

[15] Ferrara K, Pollard R and Borden M Ultrasound microbubble contrast agents: fundamentals and application to gene and drug delivery, Annual Review of Biomedical Engineering **9** 415-447 (2007).

[16] Nhan, Tam, Alison Burgess, Eunice E. Cho, Bojana Stefanovic, Lothar Lilge, and Kullervo Hynynen. "Drug delivery to the brain by focused ultrasound induced blood–brain barrier disruption: Quantitative evaluation of enhanced permeability of cerebral vasculature using two-photon microscopy." Journal of Controlled Release **72** 274-280 (2013).

[17] Stieger, Susanne M., Paul A. Dayton, Mark A. Borden, Charles F. Caskey, Stephen M. Griffey, Erik R. Wisner, and Katherine W. Ferrara. "Imaging of angiogenesis using Cadence contrast pulse sequencing and targeted contrast agents." Contrast media & molecular imaging 3 (2008): 9-18.

[18] Deng CX and Lizzi FL A review of the physical phenomena associated with ultrasonic contrast agents and illustrative clinicalapplications, Ultrasound in Medicine & Biology **28**(3) 277-286 (2002).

[19] Schrope BA, Newhouse VL, and Uhlendorf V Simulated capillary blood flow measurement using a nonlinear ultrasonic contrast agent, Ultrasonic Imaging **14** 134-158 (1992).

[20] Lauterborn W Numerical investigation of nonlinear oscillations of gas bubbles in liquids, J. Acoust. Soc. Am. **59**(2) 283-293 (1976).

[21] MacDonald CA, Sboros V, Gomatam J, Pyec SD, Moran CM and McDicken WN A numerical investigation of the resonance of gas filled microbubbles: resonance dependence on acoustic pressure amplitude, Ultrasonics **43** 113-122 (2004).

[22] Doinikov AA, Haac JF and Dayton PA Resonance frequencies of lipid-shelled microbubbles in the regime of nonlinear oscillations , Ultrasonics **49**(2) 263-268 (2009).

[23] Gong Y, Cabodi M and Porter T Pressure-dependent Resonance Frequency for Lipid-coated Microbubbles at Low Acoustic Pressures, IEEE International Ultrasonics Symposium Proceedings, 10.1109/ULTSYM.2010.0488 (2010)

[24] Helfield BL and Goertz DE Nonlinear resonance behavior and linear shell estimates for Definity and MicroMarker assessed with acoustic microbubble spectroscopy, J. Acoust. Soc. Am. **133** 1158- 1168 (2013)

[25] Hoff L, Sontum PC, Hovem JM Oscillations of polymeric microbubbles:Effect of the encapsulating shell, *J. Acoust. Soc. Am.*, 107(4) 2272-2280 (2000).

[26] Hilgenfeldt S, Lohse D and Zomack M 2000 Sound scattering and localized heat deposition of pulse-driven microbubbles J. Acoust. Soc. Am., **107**(6) 3530-3539

[27] Kvikliene A et al. Modeling of nonlinear effects and the response of ultrasound contrast micro bubbles: simulation and experiment, Ultrasonics **42** 301-307 (2004).

[28] Church CC, The effects of an elastic solid surface layer on the radial pulsations of gas bubbles, J. Acous. Soc. Am. **97**(3) 1510-1521 (1995)

[29] Morgan KE, Allen JS, Dayton PA, Chomas JE, Klibanov AL, and Ferrara KW Experimental and Theoretical Evaluation of Microbubble Behavior: Effect of Transmitted Phase and Bubble Size IEEE transactions on ultrasonics, ferroelectrics, and frequency control **47**(6) 1494-1509 (2000).

[30] F Hegedűs Stable bubble oscillations beyond Blake's critical threshold, Ultrasonics **54**(4) 1113 - 1121 (2014)

[31] Flynn HG and Church CC Transient pulsations of small gas bubbles in water, J. Acoust. Soc. Am. **84** 985-998 (1988).

[32] Akhatov I, Gumerov N, Ohl CD, Parlitz U, Lauterborn W The role of surface tension in stable single-bubble sonoluminescence , Phys. Rev. Lett **78** 227-230 (1997)

[33] Flynn Hg, Cavitation dynamics.II. Free pulsations and models of cavitation bubbles, J. Acoust. Soc. Am. **58** 1160-1170 (1975)

[34] Leighton TG, The Acoustic bubble. 1994, Academic Press Limited, London, UK

[35] Apfel RE, Some new results on cavitation threshold prediction and bubble dynamics. In: Cavitation and inhomogeneities in underwater acoustics. (Lauterborn W, ed.). Springer, Berlin, 79-83 (1980)

[36] Chomas JE, Dayton PA, May D, and Ferrara K, Threshold of fragmentation for ultrasonic contrast agents, J. Biomed. Optics **6**(2) 141-150, (2001)

[37] Chomas JE, Dayton PA, May D, Klibanov A and Ferrara K, Optical observation of contrast agent destruction, Applied Physics Letters, **77** 1056 (2000)

[38] Bloch H, Wan M, Dayton PA and Ferrara K, Optical observation of lipid- and Polymer-shelled ultrasound microbubbles, Applied Physics letters, **84** 631 (2004)

[39] Chomas J, Dayton P, May D and Ferrara K, Nondestructive subharmonic imaging,IEEE Trans. Ultrasonics, Ferroelectrics and frequency control, **9**(7) 883-892 (2002)

[40] Santin MD, King DA, Foiret J, Haak A, O'Brien Jr WD and Bridal SL, Encapsulated contrast microbubble radial oscillation associated with postexcitation pressure peaks, J. Acoust. Soc. Am. **127** 1156 (2010)

[41] King DA, and W O'Brien Jr WD, Comparison between maximum radial expansion of ultrasound contrast agents and experimental postexcitation signal results, J. Acoust. Soc. Am. 129, **114** (2011)

[42] King DA, Malloy MJ, Roberts AC, Haak A, Yoder CC and O'Brien WD ,Determination of postexcitation thresholds for single ultrasound contrast agent microbubbles using double passive cavitation detection, J. Acoust. Soc. Am. **127** 3449 (2010)

[43] Plesset MS, Mitchell TP, On the stability of the spherical shape of a vapor cavity in a liquid - Quart. Appl. Math, 13419-430 (1956)

[44] Church CC and Cartensen E, ”Stable” inertial cavitation, Ultrasound in medicine and Biology, **27**(10), 1435-1437 (2001)

[45] Philips P and Gardner E Contrast-agent detection and quantification, Eur.Radiol Suppl **14**(8) 4-10 (2004).

[46] Brock-Fisher AG, Poland M and Rafter P Means for increasing sensitivity in nonlinear imaging systems. US Patent **5577505** (1996).

[47] Eckersley RJ, Chin CT and Burns PN Optimizing phase and amplitude modulation schemes for imaging microbubble contrast agents at low acoustic power, Ultrasound in Med. Biol. **6**(31) 213-219 (2005).

[48] Bos LJ , Piek JJ and Spaan JA Effects of shadowing on the time-intensity curves in contrast echocardiography: a phantom study., Ultrasound in Med. & Biol. **22**(2) 217-227 (1996).

[49] Tang MX, Eckersley RJ and Noble JA Regularized estimation of contrast agent attenuation to improve the imaging of microbubbles in small animal studies, Ultrasound in Med. & Biol. **34**(6) 938-948 (2008).

[50] Coussios CC, Farny CH, Ter Haar G and Roy RA Role of acoustic cavitation in the delivery and monitoring of cancer treatment by high-intensity focused ultrasound (HIFU), International Journal of Hyperthermia **23**(2) 105-120 (2007).

[51] Feshitan JA, Chen CC, Kwan JJ, Borden MA. Microbubble size isolation by differential centrifugation. J Colloid Interface Sci. **329**(2) 316-24 (2009)

[52] Yanjun Gong, Mario Cabodi, Tyrone M Porter , Acoustic investigation of pressure-dependent resonance and shell elasticity of lipid-coated monodisperse microbubbles, Applied Physics Letters 104(7) 074103 2014

[53] Parrales MA et. al, Acoustic characterization of monodisperse lipid-coated microbubbles: Relationship between size and shell viscoelastic properties, J. Acoust. Soc. Am. **136** (3) 1077 2014

[54] M. Hauptmann, H. Struyf, De Gendt,, C. Glorieux and S. Brems, Importance of Bubble Size Control in Ultrasonic Surface Cleaning by Pulsed High-Frequency Sound Fields, ECS J. Solid State Sci. Technol. **3**(1) N3032-N3040 (2014)

Chapter 3

A simple method to analyze the super-harmonic and ultra-harmonic behavior of the acoustically excited bubble oscillator

3.1 Abstract

The bubble oscillator is a highly nonlinear system, which makes it difficult to generate a comprehensive understanding of its oscillatory behavior. One method used to investigate such complex dynamical systems is the bifurcation analysis. Numerous investigations have employed the method of bifurcation diagrams to study the effect of different control parameters on the bubble behavior. These studies, however, focused mainly on investigating the subharmonic (SH) and chaotic oscillations of the bubbles. Super-harmonic (SuH) and ultra-harmonic (UH) bubble oscillations remain under-investigated. One reason is that the conventional method used for generating bifurcation diagrams cannot reliably identify features that are responsible for the identification of SuH and UH oscillations. Additionally, the conventional method cannot distinguish between the UHs and SHs. We introduce a simple procedure to address this shortcoming. In this method, the maxima of the bubble oscillatory response were selected and plotted alongside the traditional bifurcation points for the corresponding control parameter. Results show that depending on the control parameters the conventional method or the method of maxima may miss intricate details of the oscillations. In order to have a comprehensive knowledge on the rich dynamics of the system, the two methods should be employed side by side. Through plotting the two bifurcation structures in tandem, the oscillatory behavior of the bubble was analyzed with more detail, and stable SuH and UH bubble

oscillations were investigated. Based on this new analysis, the conditions for the generation and amplification of UH and SuH regimes are discussed[1].

3.2 Introduction

The acoustic bubble [1,2,3,4,5,6,7,8,9,10,11,12] oscillator is present in many physical phenomena and applications. Bubbles are involved in physical phenomena associated with underwater acoustics and oceanography [2,12]. Bubbles are used as catalysts for chemical reactions in sonochemistry [13, 14, 15, 16] and several non-chemical cleaning applications [17]. Bubble oscillations drive sonoluminscence [15], and are the basis of several medical applications including, but not limited to, blood vessel imaging and treatment monitoring [18,19], drug delivery [20], blood brain barrier opening [21], high intensity focused ultrasound [22], shock wave lithotripsy [23] and histotripsy and clot lysis [24].

The bubble oscillator is a highly nonlinear dynamical system [1, 2, 3, 4, 5, 6, 7, 8, 9, 10, 11, 12, 25, 26, 27, 28, 29, 30, 31, 32, 33, 34, 35, 36, 37, 38, 39, 40, 41]; the oscillatory bubble behavior has been referred to as chaotic and complex [1, 2, 3, 4, 5, 6, 7, 8, 9, 10, 11, 12, 25, 26, 27, 28, 29, 30, 31, 32, 33, 34, 35, 36, 37, 38, 39, 40, 41]. Due to the complex behavior, a comprehensive understanding of the phenomena associated with bubble dynamics is difficult. Consequently, the optimization of applications is a challenging task. Moreover, due to the incomplete knowledge on the nonlinear behavior of bubbles, many applications are not optimized and this limits progress in the associated fields (e.g., enhanced drug delivery [20]).

Methods of nonlinear dynamics (e.g. resonance curves and bifurcation diagrams) have been extensively applied to investigate bubble behavior [1, 2, 3, 4, 5, 6, 7, 25, 26, 27, 28, 29, 30, 31, 32, 33,34,35,36,37,38,39,40,41]. It has been shown that the bubble oscillator can exhibit $\frac{1}{2},\frac{1}{3},\frac{1}{4},\frac{1}{5}$ or higher order SHs, as well as period doubling route to chaos [1, 2, 3, 4, 5, 6, 7, 25, 26, 27, 28, 29, 30, 31, 32, 33, 34, 35, 36, 37, 38, 39, 40, 41]. These studies have shed light on the nonlinear dynamics and bifurcation structure of the bubbles; however, the approaches used in these publications have provided insights primarily on SH and chaotic bubble oscillations.

[1]Published as: Sojahrood, A.J., Wegierak, D., Haghi, H., Karshfian, R. and Kolios, M.C., 2019. A simple method to analyze the super-harmonic and ultra-harmonic behavior of the acoustically excited bubble oscillator. Ultrasonics sonochemistry, 54, pp.99-109.

Recently the dynamics of a 0.1 mm gas bubble immersed in glycerine with varying temperature was studied in [42, 43, 44] where the effect of high viscosity on the bubble dynamics and the evolution of the harmonic and UH resonances were presented. Results of these studies have emphasized that knowledge of the oscillatory behavior of the bubble (including SHs and UHs) is necessary to optimize the bubble applications.

Despite many investigations of the nonlinear behavior of acoustically excited bubbles using the methods of chaos physics and nonlinear dynamics, details of the super-harmonic (SuH) and ultra-harmonic (UH) oscillations including the characteristics of the radial oscillation, phase portraits and the backscattered pressure have received less attention. The conventional analysis method only extracts the data after every period of acoustic driving pressure [1, 5]. The alternative method of bifurcation analysis which is based on analyzing the peaks of the radial oscillations (e.g. employed in [25, 26, 27, 28, 38]) can not by itself produce information to help identify the SuH and/or UH behavior of the bubble.Thus, analysis methods need to be developed to identify and explore SuH and UH oscillations alongside the SH and chaotic regimes.

In this work, we introduce a more comprehensive and simple method to study the SuH and UH bubble oscillations. The bifurcation structure of the bubble oscillator is constructed using the two well-known methods in tandem. This is done by plotting the maxima of the stable oscillations of the bubble alongside the conventional bifurcation points at each corresponding control parameters in the bifutcation diagrams. Through plotting the two bifurcation curves we were able to straightforwardly identify the SuH and UH oscillations and explore the conditions that are required to generate and amplify the SuH and UH oscillations.This method establishes a framework that provides a more comprehensive understanding of the rich nonlinear behavior of bubbles; consequently, it may help in optimizing current applications and/or can be used to discover new nonlinear bubble behaviors that may result in new applications.

3.3 Methods

3.3.1 The Bubble model

The radial oscillations of the bubbles are numerically simulated by solving the well known Keller-Miksis equation [45]:

$$\rho\left(1-\frac{\dot{R}}{c}\right)R\ddot{R}+\frac{3}{2}\rho\dot{R}^2\left(1-\frac{\dot{R}}{3c}\right)=$$

$$\left(1+\frac{\dot{R}}{c}+\frac{R}{c}\frac{d}{dt}\right)\left((p_0+\frac{2\sigma}{R_0})\left(\frac{R_0}{R}\right)^{3k}-\frac{2\sigma}{R}-\frac{4\mu\dot{R}}{R}-P_0+P_A sin\left(2\pi ft\right)\right) \tag{3.1}$$

In this equation, R is radius at time t, R_0 is the initial bubble radius, $\dot{R}$ is the wall velocity of the bubble and $\ddot{R}$ is the wall acceleration ρ is the liquid density (998 $\frac{kg}{m^3}$), c is the sound speed (1481 m/s), P_0 is the atmospheric pressure (101 kPa), σ is the surface tension (0.0725 $\frac{N}{m}$), μ is the liquid viscosity (0.001 Pa.s), P_A and f are the amplitude and frequency of the applied acoustic pressure. The values in the parentheses are for water at 293 ^{0}K and are used in all the simulations. The gas inside the bubble is air with polytropic exponent of k=1.4.

Oscillations of a bubble generates a backscattered pressure (P_{Sc}) which can be calculated by [46]:

$$P_{Sc}=\rho\left(\frac{R}{d}\right)\left(R\ddot{R}+2\dot{R}^2\right) \tag{3.2}$$

where d is the distance from the center of the bubble (and for simplicity is considered as 1m in this paper) [46].Backscattered pressure is directly related to the radial oscillations of the bubble but is a more complex function of the radial oscillations and also will be affected by the freqeuncy depdendent attenuation in tissue [47]. Calculation of the backscattered pressure is of great importance since in several applications the backscattered pressure resulting from bubble oscillations plays a critical role. For example, in imaging applications the backscattered pressure is detected and analyzed to form images. In shock wave lithotripsy the backscattered pressure is used to break and disintegrate kidney stones. In majority of the applications and phenomena involving bubble dynamics, monitoring the behavior of the bubbles is through recording the backscatterd signal and analyzing its frequency components.

Equation 1 is solved using the 4th order Runge-Kutta technique; the control parameters of interest are R_0, f and P_A. The resulting radial bubble oscillations are visualized using the bifurcations diagrams. The simulations were done using the ode45 function of MATLAB and the relative and absolute tolerance of the integration was set to 1e-12 and 1e-13. The solutions were recorded at time steps of $\frac{0.001}{f}$. The initial conditions of the problem were set to $R_0(t=0)=R_0$ and

$\dot{R}(t=0) = 0$ m/s. Bifurcation diagrams of the normalized bubble oscillations $\frac{R}{R_0}$ are presented as a function of driving pressure. Detailed analysis is presented at select control parameters using a) the radius versus time curves, b) phase portrait analysis and c) the frequency spectrum of the backscattered pressure.

3.3.2 Bifurcation diagrams

For highly nonlinear systems like bubble oscillators, small changes in the initial conditions of the system or control parameters can result in large changes in the behavior of the system. Due to the complexity and sensitivity of the bubble dynamics to the exposure parameters (frequency and acoustic pressure) and the initial conditions, a comprehensive understanding of the bubble dynamics is a challenging task and requires investigation of the behavior of the system over a wide range of the control parameters. Bifurcation diagrams are valuable tools to analyze the dynamics of nonlinear systems where the qualitative and quantitative changes of the dynamics of the system can be investigated effectively over a wide range of the control parameters.

3.3.2.1 Conventional bifurcation analysis

When dealing with systems responding to a driving force, to generate the points in the bifurcation diagrams vs. the control parameter, one option is to sample from a specific point in each driving period. The approach can be summarized in:

$$Q \equiv (R(\Theta))\{(R(t), \dot{R}(t)) : \Theta = \frac{n}{f}\} \quad where \quad n = 100, 101...150 \tag{3.3}$$

Where Q denotes the points in the bifurcation diagram, R and $\dot{R}$ are the time dependentradius and wall velocity of the bubble at a given set of control parameters of (R_0, P_0, P_A, c, k, μ, σ, f) and Θ is given by $\frac{n}{f}$. Points on the bifurcation diagram are constructed by plotting the solution of $R(t)$ at time points that are multiples of the driving acoustic period. The results are plotted for $n = 100 - 150$ to ensure a steady state solution has been reached.

3.3.2.2 Method of peaks

As a more general method, bifurcation points can be constructed by setting one of the phase space coordinates to zero:

$$Q \equiv max(R)\{(R, \dot{R}) : \dot{R} = 0\} \tag{3.4}$$

In this method, the steady state solution of the radial oscillations for each control parameter is considered. The maxima of the radial peaks ($\dot{R} = 0$) are identified (determined within 100-150 cycles of the stable oscillations) and are plotted versus the given control parameter in the bifurcation diagrams. The bifurcation diagrams of the normalized bubble oscillations ($\frac{R}{R_0}$) are calculated using both methods a) and b). When the two results are plotted alongside each other, it is easier to uncover more important details about the SuH and UH oscillations, as well as the SH and chaotic oscillations.

3.4 Results

To illustrate how the method of constructing the bifurcation diagram can influence the classification of the oscillatory patterns, we have considered a bubble with initial diameter of 4 microns. The linear resonance frequency (f_r) of the bubble is ˜2.04 MHz. f_r is calculated by numerically solving equation 1 for $P_A = 1kPa$ and finding the frequency that results in the maximum expansion ratio. We have studied the bifurcation structure of the bubble in the form of $\frac{R}{R_0}$ as a function of the driving acoustic pressure for (400kHz<f<6MHz) and (1kPa<P_A< 3MPa). For simplicity we focus on the stable non-destructive regime of oscillations and results are only presented for pressure ranges that leads to radial oscillations with $\frac{R}{R_0} \leqq 2$ [27].

3.4.1 Example of SHs, UHs and SuHs oscillations

To gain a better insight of the oscillation characteristics that the conventional bifurcation analysis method will be unable to reveal, first we will show different regime of oscillations in detail. In this regard a) radial oscillations vs. driving acoustic periods, b) phase portraits, c)backscattered pressure vs. driving periods and d) backscattered frequency spectra are examined in detail. Exposure parameters relevant to biomedical applications were chosen. Fig. 3.1a depicts the radial

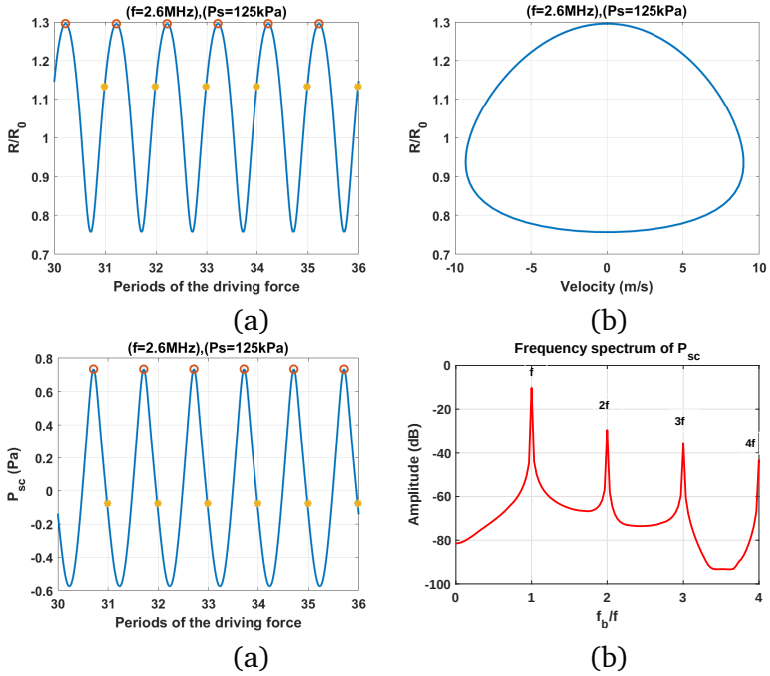

Figure 3.1: Oscillation characteristics of a 4 micron bubble driven at f=2.6 MHz and 125 kPa of pressure: a) Radial oscillations versus driving periods. Yellow dots correspond to R(t) values at each period (conventional method) and Red dots (peaks method) are positioned at the peaks of the R(t) curve. b) phase portrait diagrams c) Backscattered pressure aand d) frequency spectrum of the backscattered pressure. .

oscillations of the bubble for P_A=125 kPa and f=2.6MHz. The yellow stars represent the amplitude of radial oscillations after every period, and the red circle illustrates the maxima of the curve. There exists only one value for all red circles and yellow stars; therefore, the behavior is a period-1 (P1) signal with one maximum. In this case both methods predict the same behavior. The corresponding phase portrait in Fig. 3.1b is a semi circular orbit with one loop. The backscattered pressure has one peak and is shown in Fig. 3.1c and the corresponding fundamental component of the P_{Sc} in Fig. 3.1d is stronger than the SuHs.

Fig. 3.2a shows the R-T curve that corresponds to P_A=78 kPa and f=1.2 MHz. The signal has two maxima, while the amplitude of the signal at each driving period remains the same. In this case the two methods do not provide the same results. This suggests a P1 signal with two maxima. Fig. 3.2b shows that the phase portrait of the bubble undergoes an internal bend; depicting a similar behavior when SHs are present in the curve. However, the absence of SHs are evident in the frequency spectra (Fig. 3.2d) of the corresponding P_{Sc} shown in Fig 3.2c while the 2^{nd} harmonic has the highest value (2^{nd} harmonic resonance). In this case examination of the maxima provides

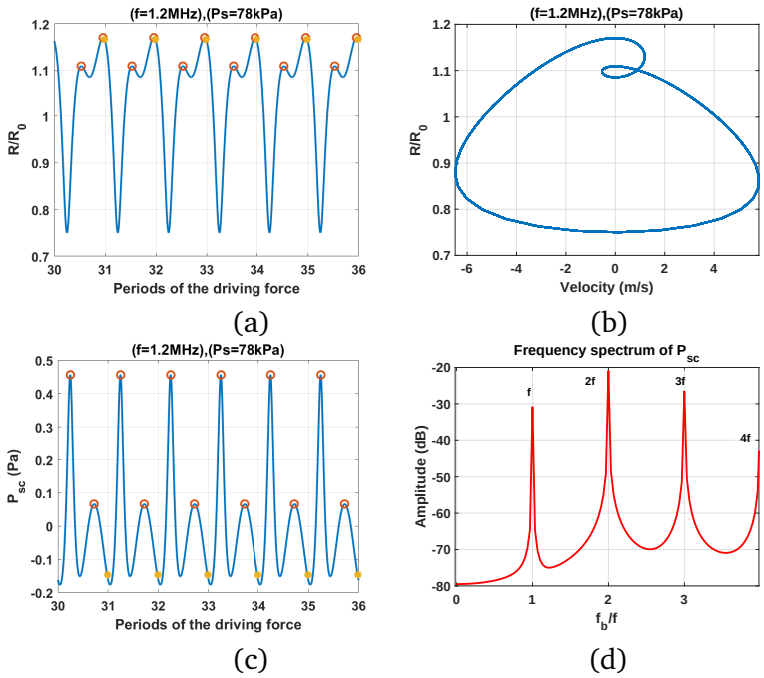

Figure 3.2: Oscillation characteristics of a 4 micron bubble driven at f=1.2 MHz and 78 kPa of pressure: a) Radial oscillations versus driving periods. Yellow dots correspond to R(t) values at each period (conventional method) and Red dots (peaks method) are positioned at the peaks of the R(t) curve. b) phase portrait diagrams c) Backscattered pressure aand d) frequency spectrum of the backscattered pressure. .

more complete information about the oscillation characteristics, identifying a 2^{nd} SuH resonance. Figure 3.3 and 3.4 compare the characteristics of two P2 oscillations; one has two maxima while the other has 4 maxima. Fig 3.3a shows the R-T curve of the bubble for f=2.6 MHz and P_A=275kPa. The signal has two maxima (two red dots), and the signal repeats its pattern once every two acoustic driving periods (two yellow stars). The phase portrait (Fig 3.3b) consists of two circular orbits with one creating another and enclosing it within itself. The backscattered pressure is shown in Fig. 3.3c and has 2 maxima. Fig. 3.3d depicts the existence of $\frac{1}{2}$ order SH which is stronger than the UH components. Fig. 3.4a shows the R-T curve of the bubble for f=1.2 MHz and P_A=145kPa; the signal is of P2 but with 4 distinct maxima. The radial oscillations repeat their pattern once every two acoustic periods (two yellow stars), and each pattern has 4 maxima (4 red dots). The phase portrait has two circular orbits similar to Fig 3.3b; however, each of these circular orbits underwent an internal bend. The backscattered pressure is shown in Fig. 3.4c and has 4 maxima. The frequency content of the P_{Sc} in Fig. 3.4f has $\frac{1}{2}$ order SHs as well as UHs; the 2^{nd} order SuH is the strongest signal, and $\frac{5}{2}$ and $\frac{7}{2}$ UHs are stronger than $\frac{1}{2}$ order SH and other UHs.

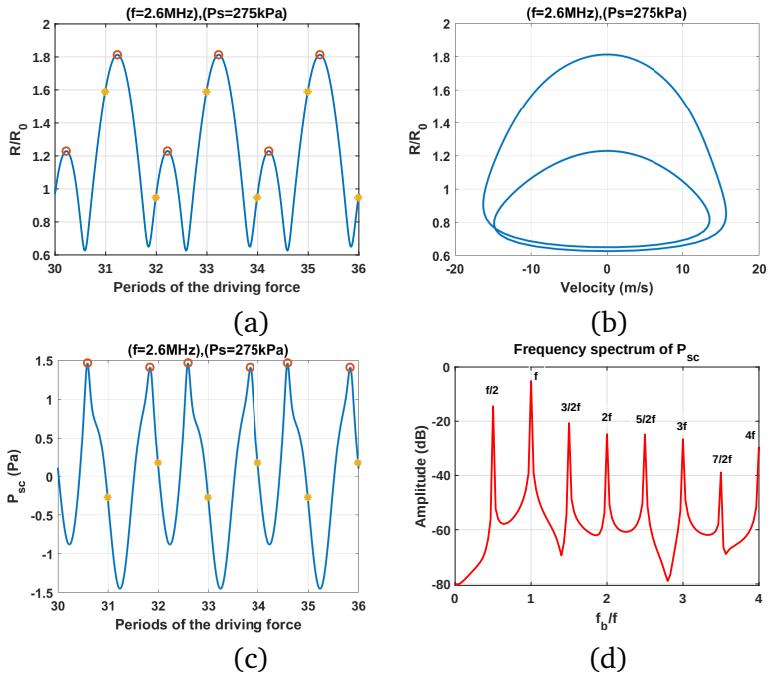

Figure 3.3: Oscillation characteristics of a 4 micron bubble driven at f=2.6 MHz and 275 kPa of pressure: a) Radial oscillations versus driving periods. Yellow dots correspond to R(t) values at each period (conventional method) and Red dots (peaks method) are positioned at the peaks of the R(t) curve. b) phase portrait diagrams c) Backscattered pressure aand d) frequency spectrum of the backscattered pressure. .

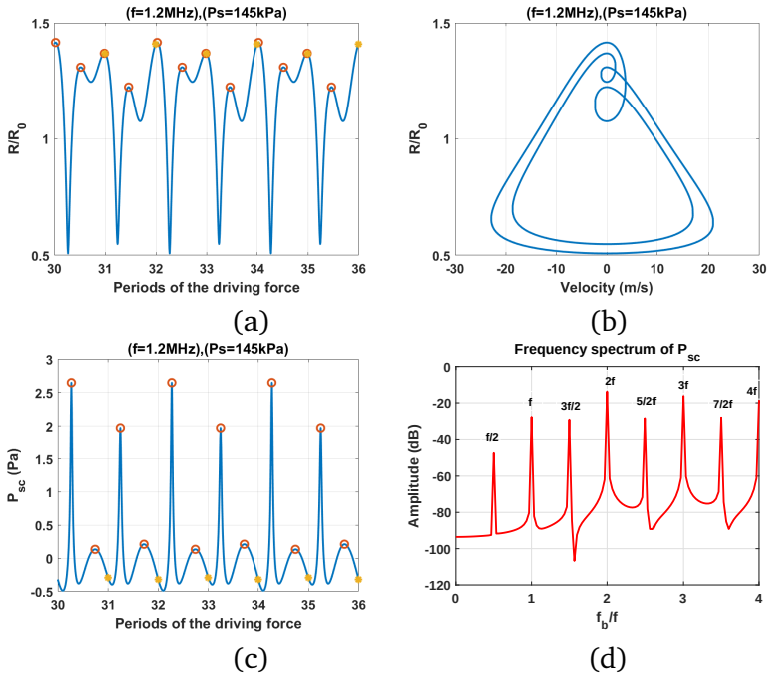

Figure 3.4: Oscillation characteristics of a 4 micron bubble driven at f=1.2 MHz and 145 kPa of pressure: a) Radial oscillations versus driving periods. Yellow dots correspond to R(t) values at each period (conventional method) and Red dots (peaks method) are positioned at the peaks of the R(t) curve. b) phase portrait diagrams c) Backscattered pressure aand d) frequency spectrum of the backscattered pressure. .

Fig. 3.5a shows the R-T curve that corresponds to P_A=135 kPa and f=4.068 MHz. The signal has only one maxima, while the amplitude of the signal at each driving period has two distinct values. This suggests a P2 signal with one maximum. Fig. 3.5b shows that the phase portrait of the bubble consists of rotated semi heart shape loop. The corresponding backscattered pressure has two maxima (Fig. 3.5c) and the frequency component of the P_{Sc} (Fig. 3.5d) has a very strong SH near the fundamental level while the 2^{nd} SuH and $\frac{3}{2}$ order UH are relatively weaker. This is an example of a case that the method of peaks fails to capture intricate details of the oscillations however the conventional method reveals the $\frac{1}{2}$ order SH resonance clearly.

Figure 3.6 is another example in which the method of peaks can not capture the nature of oscillations clearly however the conventional method captures the details that the peaks method missed. Fig. 3.6a shows the R-T curve that corresponds to P_A=400 kPa and f=5.8986 MHz. The signal has only one maxima, while the amplitude of the signal at each driving period has three distinct values. This suggests a P3 signal with one maximum. Fig. 6b shows that the phase portrait of the bubble consists of a duck shape loop. The corresponding backscattered pressure has three maxima (Fig. 3.6c) and the frequency component of the signal has a very strong $\frac{1}{3}$ and $\frac{2}{3}$ SH near the fundamental level while the 2^{nd} SuH and other UHs and SHs are relatively weaker.

3.4.2 Bifurcation diagrams and power spectrum

After introducing a few examples in figures 3.1-6 here we examine the bifurcation structure of the $\frac{R}{R_0}$ of bubble as a function of pressure that is constructed by the two methods in tandem. The frequency components of the backscattered pressure are also plotted along side the bifurcation diagrams to visualize the evolution of the frequency spectra as pressure increases. To focus on more practical and stable oscillation regimes, we have omitted the parameter ranges that result in chaotic oscillations or bubble destruction ($\frac{R}{R_0} > 2$). As it is discussed in detail in [16], $\frac{R}{R_0} > 2$ seems to be the minimum estmated expansion ratio for bubble destruction. The bifurcation structures that are produced using the conventional method are presented in blue, and the ones produced by the method of peaks are shown in red. Results are shown in Figures 3.7-11.

Fig. 3.7a shows the response of the bubble when f=0.7 MHz. The conventional method reveals a period 1 solution for P_A<118 kPa and detects the generation of period 2 solution for P_A>120 kPa. On the other hand, the peaks method reveals the generation of two maxima at 24 kPa<P_A<56 kPa

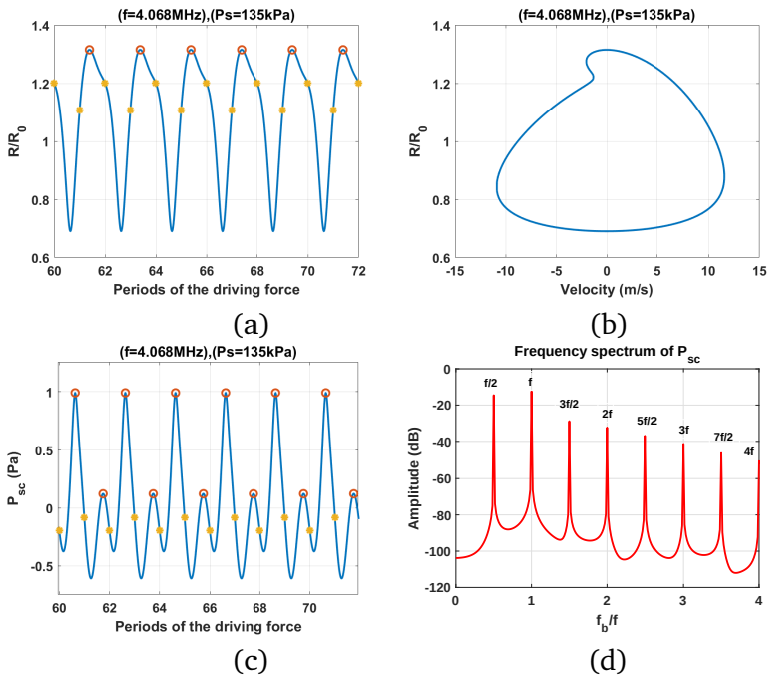

Figure 3.5: Oscillation characteristics of a 4 micron bubble driven at f=4.068 MHz and 135 kPa of pressure: a) Radial oscillations versus driving periods. Yellow dots correspond to R(t) values at each period (conventional method) and Red dots (peaks method) are positioned at the peaks of the R(t) curve. b) phase portrait diagrams c) Backscattered pressure aand d) frequency spectrum of the backscattered pressure. .

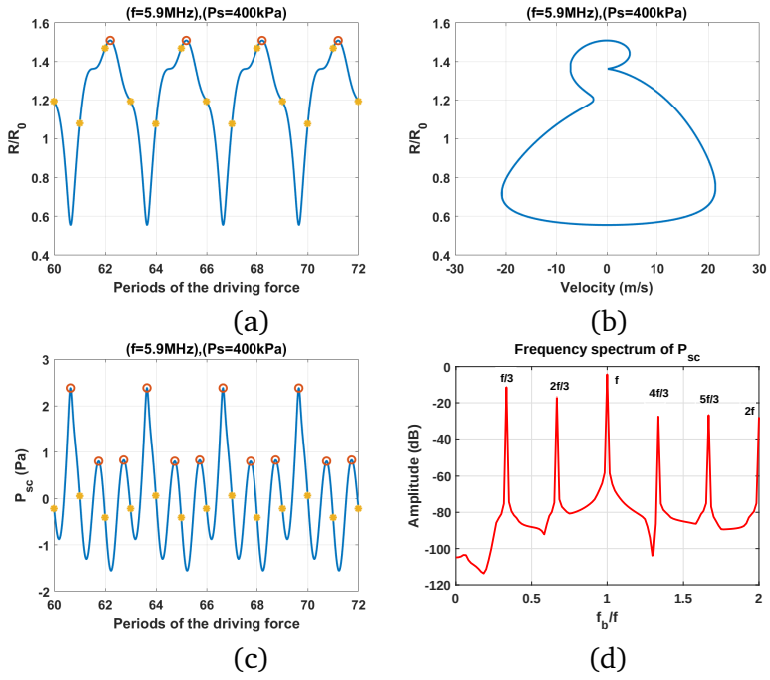

Figure 3.6: Oscillation characteristics of a 4 micron bubble driven at f=5.9 MHz and 400 kPa of pressure: a) Radial oscillations versus driving periods. Yellow dots correspond to R(t) values at each period (conventional method) and Red dots (peaks method) are positioned at the peaks of the R(t) curve. b) phase portrait diagrams c) Backscattered pressure aand d) frequency spectrum of the backscattered pressure. .

and three maxima for 56 kPa<P_A<118 kPa. The three maxima undergo period doublings (PDs) resulting in a solution with 6 maxima for $P_A > 118$ kPa.

Examination of the frequency content of the backscattered pressure reveals the underlying phenomenon which results in the discrepancy between the two methods. Figure 3.7b shows the amplitude of the harmonics and UHs of the backscattered signal. The occurrence of the maxima correlates with the resonance of the harmonic contents of the signal. After a pressure threshold (˜25 kPa), the 3^{rd} SuH of the backscattered signal becomes stronger than the fundamental and other SuH harmonics, showing a 3^{rd} SuH resonance. The 3^{rd} SuH saturates for $P_A > 56$ kPa concomitant with the occurrence of 3 maxima in the peaks methods. The SH and UH contents of the backscattered signal are shown in Fig. 3.7c. The simultaneous appearance of period doublings (PDs) in the blue curve and multiple PDs in the red curve are coincident with a sharp increase in the SH and UH content of the backscattered signal (Fig. 3.7c, arrow); the backscatter at the $\frac{7}{2}$ (purple) and $\frac{9}{2}$ UHs (green) are the strongest whit the $\frac{1}{2}$ SH (blue) the weakest component.
Fig. 3.8a shows that when sonication frequency is 1.2 MHz the conventional method depicts a similar behavior to f=0.7 MHz (fig. 3.1a); a linear response is observed for $P_A < 110$kPa and radial oscillations undergo a PD for $P_A > 110$ kPa. The method of peaks reveals a solution with one maximum for PA $<$ 51 kPa which is similar to the conventional method; above this pressure, however, 2 maxima occur in the bifurcation diagram up until $P_A = 110$kPa which are not detected in the conventional method. For PA $>$ 110 kPa, the oscillations undergo two concomitant PDs resulting in a solution with 4 maxima. The conventional method predicted the same behavior for the two frequencies (0.7 MHz(Fig 3.7a) and 1.2 MHz (Fig 3.8a)), however, the method of peaks revealed more intricate details of the bubble dynamics. Fig. 3.8b shows that the second harmonic of the backscattered signal has the strongest amplitude and saturates concomitant with the generation of the initial two maxima at ˜52 KPa. Fig. 3.8c illustrates a sharp increase in the amplitude of SH and UHs concomitant with the generation of PDs (arrow) in the blue and red curves as shown in Fig. 3.1b. UH components of the signal are stronger than the SHs (˜20 dB) with $\frac{5}{2}$ and $\frac{3}{2}$ UHs being the strongest while the $\frac{1}{2}$ SH is the weakest component.

Fig. 3.9a shows that when f= 2.6 MHz the conventional method (blue) and method of peaks (red) depict a similar behavior to f=0.7 MHz and f=1.2 MHz (Fig. 3.7a, 3.8a). The oscillations are of period 1 in both graphs until P_A=243 kPa; above this pressure, PD occurs in both methods.

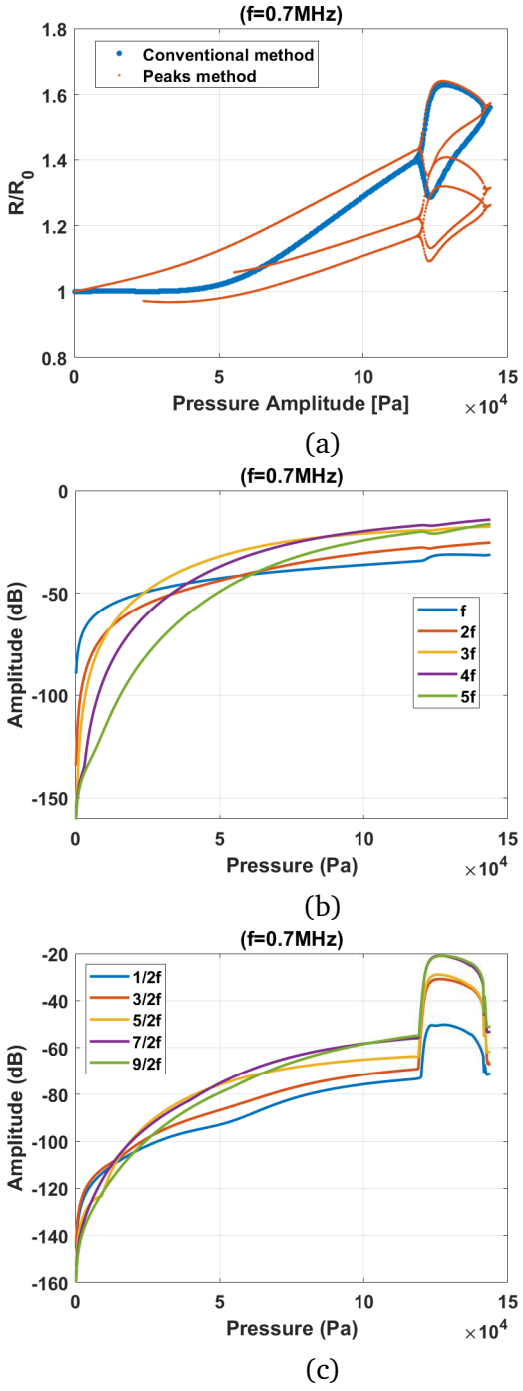

Figure 3.7: a) Bifurcation structure of the normalized radial oscillations versus acoustic pressure of a 4 micron air bubble immersed in water as constructed by the conventional method (blue) and the peaks method (red) when f=0.7 MHz, b) harmonics of the backscattered pressure versus acoustic pressure, c)SH and UH amplitudes of the backscattered pressure versus the acoustic pressure

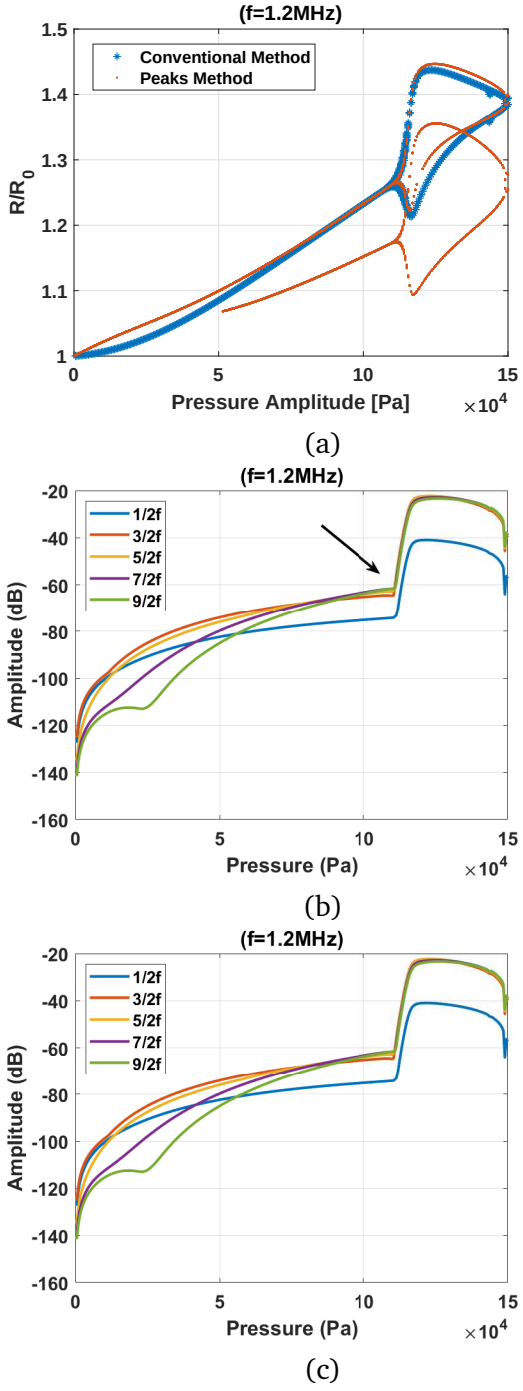

Figure 3.8: a) Bifurcation structure of the normalized radial oscillations versus acoustic pressure of a 4 micron air bubble immersed in water as constructed by the conventional method (blue) and the peaks method (red) when f=1.2 MHz, b) harmonics of the backscattered pressure versus acoustic pressure, c)SH and UH amplitudes of the backscattered pressure versus the acoustic pressure

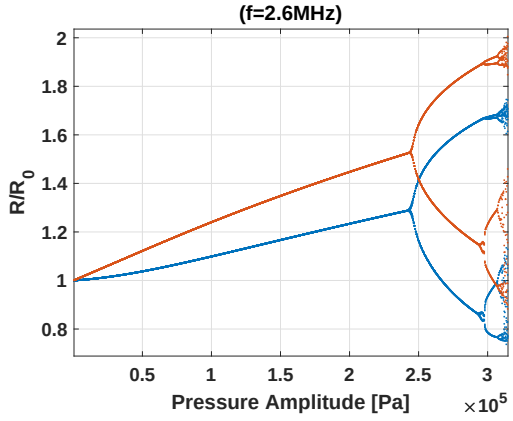

(a)

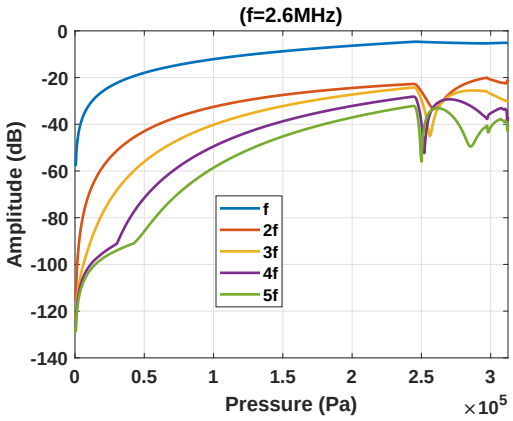

(b)

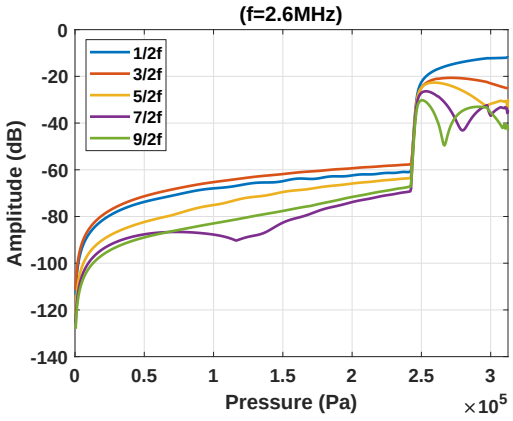

(c)

Figure 3.9: a) Bifurcation structure of the normalized radial oscillations versus acoustic pressure of a 4 micron air bubble immersed in water as constructed by the conventional method (blue) and the peaks method (red) when f=2.6 MHz, b) harmonics of the backscattered pressure versus acoustic pressure, c)SH and UH amplitudes of the backscattered pressure versus the acoustic pressure

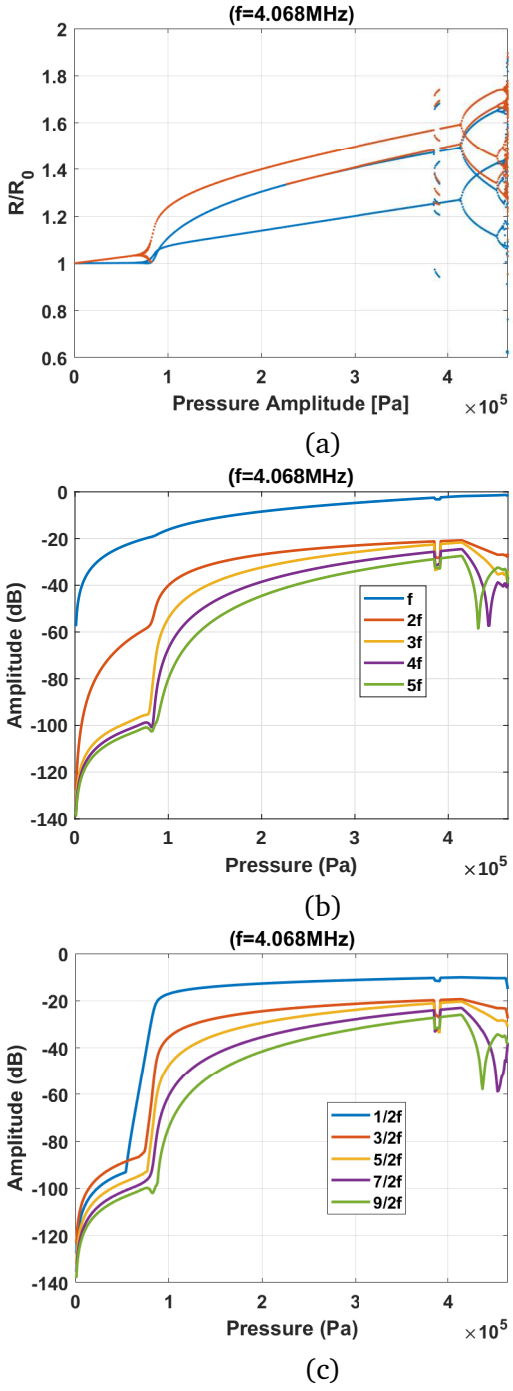

Figure 3.10: a) Bifurcation structure of the normalized radial oscillations versus acoustic pressure of a 4 micron air bubble immersed in water as constructed by the conventional method (blue) and the peaks method (red) when f=4.068 MHz, b) harmonics of the backscattered pressure versus acoustic pressure, c)SH and UH amplitudes of the backscattered pressure versus the acoustic pressure

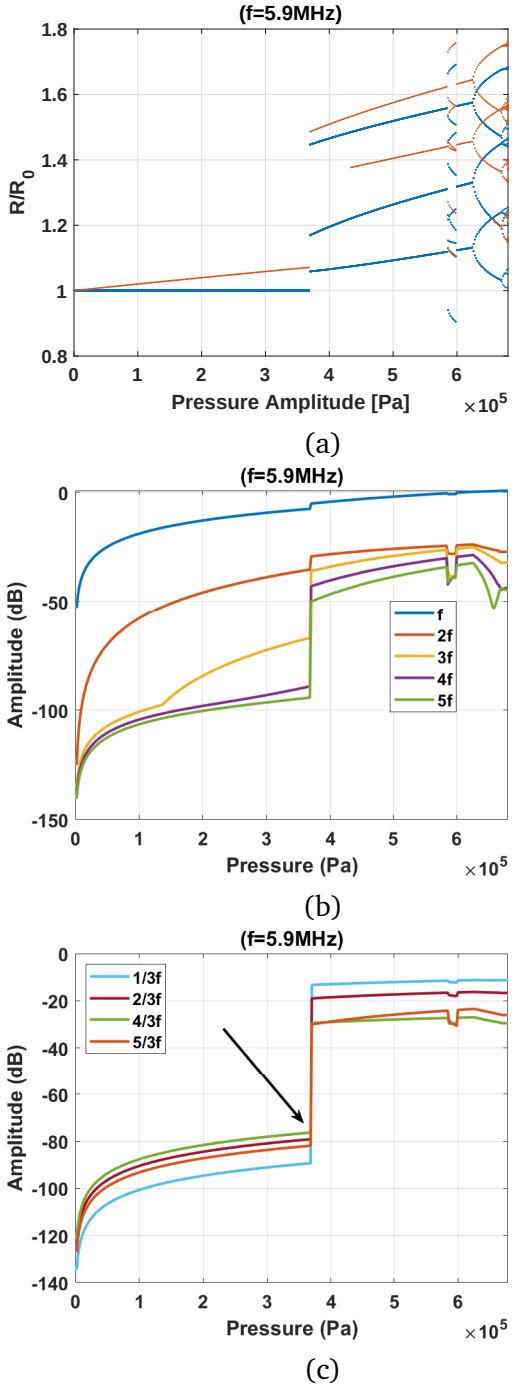

Figure 3.11: a) Bifurcation structure of the normalized radial oscillations versus acoustic pressure of a 4 micron air bubble immersed in water as constructed by the conventional method (blue) and the peaks method (red) when f=5.9 MHz, b) harmonics of the backscattered pressure versus acoustic pressure, c)SH and UH amplitudes of the backscattered pressure versus the acoustic pressure

The fundamental frequency is the strongest frequency component in the backscattered signal as is shown in Fig. 3.9b. Figure 3.9c indicates that the SH and UH components of the signal increase rapidly at pressures at which the PD occurs in Fig. 3.1c ; the SH component is stronger than all the UHs.

Fig. 3.10a shows that when f= 4.068 MHz and for P_A less than 66 kPa the conventional method (blue) and method of peaks (red) depict a similar behavior to f=0.7 MHz,f=1.2 MHz and f=2.6 MHz (Fig. 3.7a, 3.8a, 3.9a). The oscillations are of period 1 in both graphs until P_A=66 kPa; above this pressure, PD occurs in both methods. The fundamental frequency is the strongest frequency component in the backscattered signal as is shown in Fig. 3.10b. Figure 3.10c indicates that the SH and UH components of the signal increase rapidly (shown by arrow) at pressures at which the PD occurs in Fig. 3.10a; the SH component is stronger than all the UHs. However, as the pressure increase above P_A=66 kPa, one of the maxima disappears while the conventional method still depicts a P2 solution. In this case the maxima method fails to capture all the details of the oscillations. Above P_A=228 kPa the second maxima returns and oscillations become again P2 with two maxima.

Figure 3.11a shows the bifurcation structure of the $\frac{R}{R_0}$ as a function of pressure when f=5.9 MHz. For P_A less than 370 kPa he conventional method (blue) and method of peaks (red) depict a similar behavior to f=0.7 MHz ,f=1.2 MHz, f=2.6 MHz and 4.068 MHz (Fig. 3.7a, 3.8a, 3.9a and 3.10a). The oscillations are of period 1 in both graphs and as soon as P_A increases above 370 kPa the oscillations undergo a saddle node bifurcation in both graphs. However, the method of peaks (red) displays a saddle node bifurcation from a solution with one maxima to higher amplitude solution with one maxima while the conventional method reveals more details by capturing a saddle node bifurcation from a P1 to a P3 solution. Thus oscillations are of P3 with one maxima. As the pressure increases a second maxima appears for P_A higher than 444 kPa. These solution undergo concomitant PD at P_A=626 kPa; the red curve shows that the signal has 4 maxima while the blue curve depicts a P6 solution. At frequencies above resonance the maxima method was unable to reveal some intricate details of oscillations while for frequencies around and below resonance it was the conventional method that failed to reveal the intricate oscillation details. We conclude that for a comprehensive analysis of the bubble dynamics the two methods should be employed in tandem and the analysis will be incomplete in case that only one of the methods is used.

3.5 Discussion and summary

We have shown that the conventional method of generating bifurcation diagrams cannot reveal the hidden details of the oscillations that typically result in UH and SuH resonance. We have introduced a simple alternative method to generate the bifurcation diagrams; the method extracts the peaks of the oscillations and plots it as a function of the given control parameter. When this method is applied alongside the conventional method one can reveal hidden details of the bubble oscillations and identify the parameter ranges where SuH, UH or SH oscillations occur. We can briefly categorize the scenarios shown in this paper as follows:

1. The conventional method depicts a P1 oscillation regime, and the maxima method only reveals one maximum. In this case, the oscillation has a P1 resonance and the fundamental frequency component is the strongest in the backscattered signal. $\frac{1}{2}$ order SH and UHs are generated concomitant with PD in both graphs (constructed by conventional method and method of maxima) and $\frac{1}{2}$ order SHs, or $\frac{3}{2}$ UHs are stronger than other UHs.

2. The conventional method depicts a P1 oscillation regime, but maxima method reveals n=2,3,... maxima. In this case, the n-th order SuH frequency component is the strongest in the backscattered signal. Generation of PD in the conventional method is concomitant with the generation of n-PDs in the diagram constructed by the peaks method; this correlates with an UH resonance behavior of $\frac{(2n-1)}{2}$ or $\frac{(2n+1)}{2}$; in other words, these UHs are stronger than the $\frac{1}{2}$ order SHs and other UHs.

3. The conventional method depicts a P2 oscillation regime, but the maxima method reveals only 1 maximum; in this case, we have a P2 resonance; $\frac{1}{2}$ order SH frequency component is the stronger than UHs.

4. UH and SHs only exist when the conventional method predicts a P2 oscillations; however, the method of maxima needs to be applied alongside of traditional method to determine whether SH or UH resonance are present, as well as the order of UHs.

Heat and mass transfer across the bubble influence the dynamics of the bubble oscillations [48, 49, 50, 51, 52]. Heat and mass transfer in turn are nonlinear and depend on the nonlinear dynamics

of the bubble. Since the main purpose of this paper was to introduce a simple and more comprehensive method to identify the SuH and UH oscillations of the bubble, for simplicity, the effects of heat and mass transfer were neglected. Nonlinear dynamics of heat and mass transfer requires further investigation and is beyond the scope of this paper. However, for accurate optimization of the applications and understanding of the associated phenomena with bubble dynamics, these effects must be considered.

Detailed studies on the effect of initial conditions (ICs) (R(0) and $\dot{R}(0)$) on the dynamical evolution of the bubble oscillations [28,29,30,31,32,33,34] have resulted in the discovery of new nonlinear features [29,30,31,32,33,34]. For example, depending on the ICs, the bubble has shown to exhibit period 1 (P1), P2 or P3 oscillations [31,33]. Application of the method proposed in this paper can help to better understand and categorize these nonlinear features, especially in the SuH and UH oscillation regimes. These results may be used to optimize applications by sending the proper pre-conditioning pulses to manipulate the ICs of the bubble to achieve the desirable behavior.

In contrast enhanced ultrasound imaging SH component of the backscattered signal is used to enhance the contrast to tissue ratio since the tissue does not produce SHs and UHs [53]. UHs oscillations, however have the advantage of generating images with higher resolution due to higher frequency [53]. Understating the ultrasound exposure parameters for the generation and enhancement of UHs will help to acquire images with high contrast to tissue ratio and resolution. Pre-conditioning pulses may help in enhancing the UH signal and using the methods described in this work can help in identification of optimum pre-conditioning pulses to enhance UHs. Another important application of bubbles in medicine is in molecular acoustic angiography [54] where the high frequency response of the bubbles is used to acquire images with superior resolution. In this regard higher order SuHs [54, 55] or higher order UHs can be used to achieve high contrast and high resolution due to higher frequency response of the bubbles. Due to the lack of tissue SuHs and significant UHs only the bubble response is detected and micro-vessels can be visualized with superior detail and resolution. Identification of the exposure parameters for the SuH and UH responses of the bubbles can be used in these applications.

The nonlinear behavior of the lipid shell enhances the generation of SHs ($\frac{1}{2}$, $\frac{1}{3}$, $\frac{2}{3}$, $\frac{1}{4}$, $\frac{3}{4}$ ...) at very low acoustic pressures and over a more extensive frequency range [56, 57]. The behavior of lipid shell MBs are more complex due to the nonlinear response of the encapsulating shell. For example

the buckling of the lipid shell can result in compression only behavior [58]. Implementation of the proposed method in this paper can shine a brighter light on the behavior of lipid coated MBs. Our proposed approach can be used to optimize the wide range of applications that employ lipid coated MBs (for example: blood brain barrier opening [59], UH imaging [53], SuH imaging [54, 55], Passive acoustic Imaging [60] and treatment monitoring [61]). The pressure radiated by the SuHs is attenuated much faster due to the higher attenuation of the higher harmonics [62, 63]. This property can be used to enhance the heat deposition in therapeutic applications of ultrasound [62, 63] especially for thermal therapy in regions with higher blood perfusion or tissue located beyond an obstacle like bone where delivery of acoustic energy is limited. Furthermore, SuH oscillations may result in better mixing; identification of the of the relative frequencies and pressures can help in setting up a specific shape oscillation to increase the efficacy of these applications. Furthermore, the anatomy of the giant resonances [4] and their nonlinear properties can be studied with more detail; the lower bound of frequency to create a desired giant resonance can be identified. Since knowledge of the bifurcation structure is critical for non-feedback techniques [30] to control the multi-stability of the bubble system a more detailed understanding of the system bifurcation structure can be helpful in such control techniques by identifying the proper exposure parameters.

Bibliography

[1] U. Parlitz, et al., Bifurcation structure of bubble oscillators, *The Journal of the Acoustical Society of America* 88 (1990): 1061-1077.

[2] A. Prosperetti, L.A. Crum, and K.W. Commander, Nonlinear bubble dynamics, *The Journal of the Acoustical Society of America* 83 (1988): 502-514.

[3] T.G. Leighton. *The acoustic bubble*. Academic press, 2012.

[4] W. Lauterborn, and T. Kurz, Physics of bubble oscillations, *Reports on progress in physics* 73 (2010): 106501.

[5] W. Lauterborn, and U. Parlitz, Methods of chaos physics and their application to acoustics, *The Journal of the Acoustical Society of America* 84 (1988): 1975-1993.

[6] W. Lauterborn, and E. Cramer, Subharmonic route to chaos observed in acoustics, *Physical Review Letters* 47 (1981): 1445.

[7] W. Lauterborn, and J. Holzfuss, Acoustic chaos, *International Journal of bifurcation and Chaos* 1 (1991): 13-26.

[8] A. Prosperetti, and A. Lezzi, Bubble dynamics in a compressible liquid. Part 1. First-order theory, *Journal of Fluid Mechanics* 168 (1986): 457-478.

[9] L. Hoff, *Acoustic characterization of contrast agents for medical ultrasound imaging*. Springer Science & Business Media, 2001.

[10] S.M. van der Meer, et al., Microbubble spectroscopy of ultrasound contrast agents, *The Journal of the Acoustical Society of America* 121 (2007): 648-656.

[11] A. Muthupandian, et al, Bubbles in an acoustic field: an overview, *Ultrasonics Sonochemistry* 14 (2007): 470-475.

[12] T. G. Leighton, From seas to surgeries, from babbling brooks to baby scans: The acoustics of gas bubbles in liquids, International Journal of Modern Physics B 18.25 (2004): 3267-3314.

[13] K.S. Suslick ,Sonochemistry, *science* 247 (1990): 1439-1445.

[14] B.D. Storey, and A.J. Szeri, Water vapour, sonoluminescence and sonochemistry, *Proceedings of the Royal Society of London A: Mathematical, Physical and Engineering Sciences*. Vol. 456. No. 1999. The Royal Society, 2000.

[15] L. Crum et al., eds. *Sonochemistry and sonoluminescence*. Vol. 524. Springer Science & Business Media, 2013.

[16] K. Yasui, et al., Theoretical study of single-bubble sonochemistry, *The Journal of chemical physics* 122 (2005): 224706.

[17] H. Lais, et al., Numerical modelling of acoustic pressure fields to optimize the ultrasonic cleaning technique for cylinders, *Ultrasonics sonochemistry* 45 (2018): 7-16.

[18] T. Segers et al., Monodisperse Versus Polydisperse Ultrasound Contrast Agents: Non-Linear Response, Sensitivity, and Deep Tissue Imaging Potential, *Ultrasound in medicine & biology* 44 (2018): 1482-1492.

[19] K.J. Haworth, et al., Passive imaging with pulsed ultrasound insonations, *The Journal of the Acoustical Society of America*, 132(1) (2012): 544-553.

[20] K. Ferrara, R. Pollard, and M. Borden, Ultrasound microbubble contrast agents: fundamentals and application to gene and drug delivery, *Annu. Rev. Biomed. Eng.* 9 (2007): 415-447.

[21] M.A. O'Reilly, et al, Focused-ultrasound disruption of the blood-brain barrier using closely-timed short pulses: influence of sonication parameters and injection rate, *Ultrasound in medicine & biology* 37 (2011): 587-594.

[22] R. G. Holt, and R.A. Roy, Measurements of bubble-enhanced heating from focused, MHz-frequency ultrasound in a tissue-mimicking material, *Ultrasound in medicine & biology*27 (2001): 1399-1412.

[23] S. Yoshizawa, et al., High intensity focused ultrasound lithotripsy with cavitating microbubbles, *Medical & biological engineering & computing* 47 (2009): 851-860.

[24] K.B. Bader., K.J. Haworth, H. Shekhar, A.D. Maxwell, T. Peng, D.D. McPherson, and C.K. Holland, Efficacy of histotripsy combined with rt-PA in vitro. *Physics in Medicine & Biology* 61, (2016): 5253.

[25] A.J. Sojahrood and M.C. Kolios, Classification of the nonlinear dynamics and bifurcation structure of ultrasound contrast agents excited at higher multiples of their resonance frequency, *Physics Letters A* 376 (2012): 2222-2229.

[26] S. Behnia, AJ Sojahrood, W. Soltanpoor and O. Jahanbakhsh, Suppressing chaotic oscillations of a spherical cavitation bubble through applying a periodic perturbation, *Ultrasonics sonochemistry* 16 (2009): 502-511.

[27] A.J. Sojahrood et al., Influence of the pressure-dependent resonance frequency on the bifurcation structure and backscattered pressure of ultrasound contrast agents: a numerical investigation, *Nonlinear Dynamics* 80 (2015): 889-904.

[28] S. Behnia, A.J. Sojahrood, W. Soltanpoor, and L. Sarkhosh, Towards classification of the bifurcation structure of a spherical cavitation bubble, *Ultrasonics* 49(8) (2009): 605-610.

[29] F. Hegedűs, and L. Kullmann, Basins of attraction in a harmonically excited spherical bubble model, *Periodica Polytechnica Mechanical Engineering* 56 (2012): 125-132.

[30] F. Hegedűs, et al, Non-feedback technique to directly control multistability in nonlinear oscillators by dual-frequency driving, *Nonlinear Dynamics* (2018): 1-21.

[31] F. Hegedűs, and C. Kalmár, Dynamic stabilization of an asymmetric nonlinear bubble oscillator, *Nonlinear Dynamics*: 1-18.

[32] F. Hegedűs, Topological analysis of the periodic structures in a harmonically driven bubble oscillator near Blake's critical threshold: Infinite sequence of two-sided Farey ordering trees, *Physics Letters A* 380-10 (2016): 1012-1022.

[33] R.Varga, and F. Hegedűs, Classification of the bifurcation structure of a periodically driven gas bubble, *Nonlinear Dynamics* 86 (2016): 1239-1248.

[34] F. Hegedűs, C. Hős, and L. Kullmann, Stable period 1, 2 and 3 structures of the harmonically excited Rayleigh–Plesset equation applying low ambient pressure, *The IMA Journal of Applied Mathematics* 78 (2012): 1179-1195.

[35] Y. Zhang, Chaotic oscillations of gas bubbles under dual-frequency acoustic excitation, *Ultrasonics sonochemistry*40 (2018): 151-157.

[36] Y. Zhang, Y. Gao, and X. Du, Stability mechanisms of oscillating vapor bubbles in acoustic fields, *Ultrasonics sonochemistry* 40 (2018): 808-814.

[37] Y. Zhang, and S. Li. Bubble dynamics under acoustic excitation with multiple frequencies, *IOP Conference Series: Materials Science and Engineering*. Vol. 72. No. 1. IOP Publishing, 2015.

[38] Y. Zhang, Y. Zhang and S. Li, Combination and simultaneous resonances of gas bubbles oscillating in liquids under dual-frequency acoustic excitation, *Ultrasonics sonochemistry* 35 (2017): 431-439.

[39] S.A. Suslov, A.Ooi, and R. Manasseh, Nonlinear dynamic behavior of microscopic bubbles near a rigid wall, *Physical Review E* 85 (2012): 066309

[40] F. Dzaharudin , A. Ooi, & R. Manasseh, Effects of boundary proximity on monodispersed microbubbles in ultrasonic fields. *Journal of Sound and Vibration* 410, (2017): 330-343

[41] F. Dzaharudin , S.A. Suslov, R. Manasseh and A. Ooi, Effects of coupling, bubble size, and spatial arrangement on chaotic dynamics of microbubble cluster in ultrasonic fields, *The Journal of the Acoustical Society of America* 134 (2013): 3425-3434.

[42] F. Hegedűs and K. Klapcsik, The effect of high viscosity on the collapse-like chaotic and regular periodic oscillations of a harmonically excited gas bubble. *Ultrasonics sonochemistry* 27, (2015): 153-164

[43] F. Hegedűs and K. Klapcsik, The effect of high viscosity on the evolution of the bifurcation set of a periodically excited gas bubble. *Chaos, Solitons & Fractals* 104, (2017) 198-208.

[44] K. Klapcsik, R. Varga, F. Hegedűs, Bi-parametric topology of subharmonics of an asymmetric bubble oscillator at high dissipation rate, *Nonlinear Dynamics* (2018) 1-17 DOI: http://doi.org/10.1007/s11071-018-4497-2.

[45] J.B. Keller, and M. Miksis, Bubble oscillations of large amplitude, *The Journal of the Acoustical Society of America* 68 (1980): 628-633.

[46] S. Hilgenfeldt, D. Lohse, and M. Zomack, Sound scattering and localized heat deposition of pulse-driven microbubbles, *The Journal of the Acoustical Society of America* 107 (2000): 3530-3539.

[47] Y. Zhang, A generalized equation for scattering cross section of spherical gas bubbles oscillating in liquids under acoustic excitation. *Journal of Fluids Engineering* 135(9), (2013) 091301.

[48] Y. Zhang, Heat transfer across interfaces of oscillating gas bubbles in liquids under acoustic excitation. *International Communications in Heat and Mass Transfer* 43, (2013) 1-7.

[49] Y. Zhang, Y. Gao, Z. Guo and X. Du, Effects of mass transfer on damping mechanisms of vapor bubbles oscillating in liquids, *Ultrasonics sonochemistry*, 40, (2018) 120-127.

[50] F. Hegedűs, C. Hos and L. Kullmann, Influence of heat transfer on the dynamic response of a spherical gas/vapour bubble, *International Journal of Heat and Fluid Flow* 31(6) (2010): 1040-1049.

[51] A. Prosperetti, The thermal behaviour of oscillating gas bubbles., *Journal of Fluid Mechanics* 222 (1991): 587-616.

[52] A. Prosperetti, L.A. Crum and K.W. Commander, Nonlinear bubble dynamics, *The Journal of the Acoustical Society of America* 83(2) (1988): 502-514.

[53] V. Daeichin, et al., Subharmonic, non-linear fundamental and ultraharmonic imaging of microbubble contrast at high frequencies, *Ultrasound in medicine & biology* 41 (2015): 486-497.

[54] S.E. Shelton, et al., Molecular acoustic angiography: A new technique for high-resolution superharmonic ultrasound molecular imaging, *Ultrasound in medicine & biology* 42 (2016): 769-781.

[55] A. Bouakaz, et al., Super harmonic imaging: a new imaging technique for improved contrast detection, *Ultrasound in medicine & biology* 28 (2002): 59-68.

[56] A.J Sojahrood R. Karshafian, and M.C. Kolios, Bifurcation structure of the ultrasonically excited microbubbles undergoing buckling and rupture, *Proceedings of Meetings on Acoustics ICA2013*. Vol. 19. No. 1. ASA, 2013.

[57] A.J Sojahrood R. Karshafian, and M.C. Kolios, Detection and characterization of higher order nonlinearities in the oscillations of Definity at higher frequencies and very low acoustic pressures, *Ultrasonics Symposium (IUS), 2012 IEEE International*. IEEE,2012.

[58] P. Marmottant, S. van der Meer, M. Emmer, M. Versluis, N. de Jong, S. Hilgenfeldt and D. Lohse, A model for large amplitude oscillations of coated bubbles accounting for buckling and rupture, *The Journal of the Acoustical Society of America*, 118(6), (2005) 3499-3505.

[59] M.A. O'Reilly and K. Hynynen, Blood-brain barrier: real-time feedback-controlled focused ultrasound disruption by using an acoustic emissions-based controller, *Radiology* 263, (2012)96–106

[60] K.J. Haworth, et al., Passive imaging with pulsed ultrasound insonations, *The Journal of the Acoustical Society of America*, 132(1) (2012) 544-553.

[61] C.C Coussios, et al. Role of acoustic cavitation in the delivery and monitoring of cancer treatment by high-intensity focused ultrasound (HIFU), *International Journal of Hyperthermia* 23(2) (2007) 105-120.

[62] R.G., Holt, and R.A. Roy, Measurements of bubble-enhanced heating from focused, MHz-frequency ultrasound in a tissue-mimicking material, *Ultrasound in medicine & biology*, 27(10), (2001) 1399-1412.

[63] A.J. Sojahrood, and M.C. Kolios, The utilization of the bubble pressure dependent harmonic resonance frequency for enhanced heating during high intensity focused ultrasound treatments. In AIP Conference Proceedings (Vol. 1481, No. 1, (2012, October) pp. 345-350). AIP.

Chapter 4

Investigation of the 1/2 order subharmonic emissions of the period-2 oscillations of an ultrasonically excited bubble.

4.1 Abstract

In this work, through applying a comprehensive bifurcation method, we study the nonlinear radial oscillations of the bubble oscillator. The frequency of the driving force is chosen as the linear resonance frequency (f_r) and linear subharmonic (SH) resonance frequency ($f_{sh} = 2f_r$) of the bubble. Results show that, when the bubble is sonicated with $2f_r$, period doubling is more likely to result in non-destructive oscillations. The evolution of the bubble period-2 (P2) oscillations makes the shape of a bowtie for bubbles with an initial diameter of 0.74 μm and above. When $f = 2f_r$, the phase portrait of the P2 attractor is distinctly different from a P2 attractor when $f = f_r$, and subharmonic component of the backscattered pressure is maximum. When sonicated by $2f_r$, due to lower oscillation amplitude and gentler bubble collapse, the bubble can sustain stable P2 oscillations for a longer duration and over a broader range of applied acoustic pressure [1].

4.2 Introduction

An acoustically excited bubble is an example of a highly nonlinear and complex oscillator [1, 2, 3, 4, 5, 6, 7, 8, 9, 10, 11, 12, 13]. Pioneering works of [1, 5, 6, 7] investigated the complex behavior

[1]Published as: Sojahrood, A.J., Earl, R., Kolios, M.C. and Karshafian, R., 2020. Investigation of the 1/2 order subharmonic emissions of the period-2 oscillations of an ultrasonically excited bubble. Physics Letters A, p.126446.

of the bubbles in the realm of nonlinear dynamics and chaos. Despite the numerous studies that shed light on the bubble behavior, due to the complexity of the system, the bubble behavior is not yet fully describable [4]. Thus, following the pioneering studies on the nonlinear bubble behavior, investigation is yet ongoing with several studies in the last decade [14, 15, 16, 17, 18, 19, 20, 21, 22, 23, 24, 25, 26, 27]. [13] and [15] investigated the bifurcation structure of ultrasound contrast agents (UCAs) that are coated with a stabilizing shell. Occurrence of the oscillations with higher periods in the bubble behavior were investigated in [13, 17, 20, 22]. Application of a dual frequency acoustic excitation to control the chaotic bubble behavior was first proposed in [14]. Nonlinear behavior of the bubble under excitation with multiple frequencies were investigated in detail in [18, 23, 25, 26]. [13] and [21] investigated possible ways to classify the complex bubble behavior. Stability mechanisms of vapor bubbles were investigated in [24] and the influence of strong nonlinear coupling on the dynamics of interacting bubbles were probed in [27].

Bubbles exist in several phenomena in nature; they are involved in underwater acoustics [3, 12] and oceanography studies [12, 27, 28]; they have a key role in enhanced chemical reaction in sonochemistry [29, 30, 31, 32]; they are the building block of sonoluminescence [30, 31] and they have several advantageous applications in medical ultrasound [33, 34, 35, 36, 37, 38, 39, 40](e.g. contrast-enhanced imaging [33, 34, 35, 36], drug delivery [34, 35], blood-brain barrier (BBB) opening [37], enhanced heating in high-intensity ultrasound treatments [38], shock wave lithotripsy [39], histotripsy [40] and sonothrombolysis [41, 42]).

The complex dynamics of the bubbles have been the subject of numerous numerical [1, 2, 3, 4, 5, 6, 7, 8, 9, 10, 11, 12, 13, 14, 15, 16, 17, 18, 19, 20, 21, 22, 23, 24, 25, 26, 27] and experimental studies [4, 43, 44, 45, 46, 47, 48, 49, 50, 51]. The pioneering work of [1] extensively studied the bifurcation structure of the bubble oscillator and revealed the nonlinear nature of the system and period doubling route to chaos. The chaotic dynamics of the bubble oscillator has recently been extensively studied using the methods of nonlinear dynamics [15, 16, 17, 18, 19, 20, 21, 22, 23, 24, 25, 26]. The existence of period 2,3, 4 and higher periods have been confirmed in several numerical and recent experimental studies of single bubble dynamics [1, 2, 3, 4, 5, 6, 7, 8, 9, 10, 11, 12, 13, 14, 15, 16, 17, 18, 19, 20, 21, 22, 23, 24, 25, 26, 27].

One of the main characteristics of nonlinear oscillators is the period doubling route to chaos [1, 4]. The occurrence of period doubling in the oscillations of the bubbles is concomitant with

the generation of 1/2 order subharmonics (SHs) and ultraharmonics (UHs) in the backscattered pressure signal from the bubbles. 1/2 order SHs has been used as an indicator for stable cavitation to monitor treatments [52, 53, 54]; in bubble sizing [55], in contrast-enhanced ultrasound to detect the signal from blood [54, 55, 56, 57, 58], for non-invasive measurement of pressure inside vessels [59, 60, 61] and as an indicator for the pressure threshold of BBB opening [62, 63] among several other applications.

It is known that as the acoustic pressure is increased, the nonlinear response will become chaotic and bubble radius grows beyond a limit that may result in bubble destruction. When chaos occurs, the SH amplitude experiences fluctuations or may even disappear. Because of the spread of the signal energy over a wider frequency range, chaotic oscillations won't be useful in imaging methods or monitoring treatments as they may not be distinguishable from broadband noise due to bubble destruction. Thus, in this paper, SH oscillations are of main interest for acoustic pressures between two limit values: the threshold for the onset of SH oscillations and the critical pressure at which the nonlinear response becomes chaotic or results in bubble destruction. Knowledge of these limits is essential for the optimization of applications that depend on the SH oscillations of the bubbles.

Pioneering theoretical work of Eller [64] and Prosperetti [65, 66, 67, 68] investigated the pressure threshold for the generation of subharmonics for uncoated free bubbles. Later, studies have theoretically and experimentally investigated the pressure threshold for the generation of SHs in the encapsulated bubbles [69, 70, 71, 72]. The focus of these studies was on the determination of the conditions required to achieve the lowest pressure threshold that can produce 1/2 order SHs. In the theoretical works [64,65,66,67,68,69,70], the equations for the bubble radial oscillations were linearized and used to determine the lowest pressure threshold.

Pioneering theoretical work [64, 65, 66, 67, 68, 69] has shown that sonication of uncoated bubbles with twice their linear resonance frequency (f_r) will result in the generation of SHs at the lowest pressure threshold. This frequency can be referred to as the linear $1/2$ order SH resonance frequency ($f_{sh} = 2f_r$). Recent numerical works [71, 72] investigated the SH threshold in uncoated and encapsulated bubbles. Their method was based on calculating the SH component of the backscattered pressure from different bubble sizes. They found that at low pressures, there is no SH component that is distinguishable from the noise level; however, by increasing the acoustic pressure, the SH component appears and grows quickly. This is followed by a gradual saturation of

the SH component and eventual disappearance. In their work, the excitation pressure just above which a distinct subharmonic peak appears was selected as the SH threshold. They found that for small bubbles (less than 1 micron), increased damping weakens the bubble response at twice the resonance frequency, leading to a shift of the minimum SH pressure threshold from twice the resonance frequency toward the resonance frequency.

Recent theoretical work of Prosperetti [67] investigated the SH threshold of coated bubbles and showed that the subharmonic threshold can be considerably lowered with respect to that of an uncoated free bubble if the mechanical response of the coating varies rapidly in the neighborhood of certain specific values of the bubble radius (e.g. changes in shell parameters due to buckling of the shell). [73] numerically investigated the ambient pressure dependence of the SH generation from contrast bubbles.

Despite the studies investigating the SH threshold of the bubbles [64, 65, 66, 67, 68, 69, 70, 71, 72], the bifurcation structure of the bubble oscillator in the regime of $1/2$ order SHs (especially when sonicated with f_{sh}) has not been investigated in detail. Additionally, the evolution of the nonlinear bubble dynamics at higher amplitudes of period 2 (P2) oscillations and the exposure conditions to generate sustainable non-destructive high amplitude P2 bubble oscillations are not understood in detail.

Detailed investigation of the period doubling (PD) phenomenon in the bubble oscillator and the dynamical properties of P2 oscillations will help in better understanding and optimization of 1/2 order SHs emissions. This study investigates the dynamics of the bubble oscillator by closer examination of the dynamics of the bubbles undergoing period doubling (PD). The bifurcation structure of the bubble radial oscillations has been investigated as a function of pressure under sonication with f_r and $2f_r$. In [74, 75] we have shown that when two methods of bifurcation constructions are applied in tandem more intricate details of the oscillations are revealed (e.g. ultraharmonics (UHs) and Superharmonics). Therefore, in this study, we have used this method to reveal the conditions for the generation, amplification and stability of P2 oscillations and the phase structure of the bubble oscillations. Effects of the bubble size on the behavior of P2 oscillations is investigated by considering bubbles with R_0 between $0.2\mu m - 10\mu m$. This study provides fundamental insight over the characteristics of period 2 oscillations when the bubble is sonicated with $f = f_r$ and $f = 2f_r$. These insights will help in selecting the appropriate ultrasound

exposure parameters for imaging or therapeutic applications that use bubbles. Moreover, they will provide a foundation for a better understanding of the PD phenomenon in case of more complex systems like encapsulated microbubbles with nonlinear shell behavior [76] or bubbles entrapped in tissues [77, 78, 79].

4.3 Methods

Since the purpose of this study is the detailed investigation of the nature of P2 oscillations and their fundamental characteristics in a bubble system, we have chosen the uncoated bubble as the oscillator of interest. Addition of the encapsulating shells will add more complexity to the dynamics and will be the subject of future studies. The fundamental information about the bubble dynamics in the absence of the shell will help provide a better understanding of the more complex features that will appear in case of the coated bubbles and will help in separating the shell effects from the abstract bubble system.

4.3.1 The Bubble model

The dynamics of the bubble model including the compressibility effects to the first order of Mach number can be modelled using Keller-Miksis equation [80]:

$$\rho[(1-\frac{\dot{R}}{c})R\ddot{R}+\frac{3}{2}\dot{R}^2(1-\frac{\dot{R}}{3c})]=(1+\frac{\dot{R}}{c})(G)+\frac{R}{c}\frac{d}{dt}(G) \tag{4.1}$$

where G is given by

$$G=P_g-\frac{4\mu_L\dot{R}}{R}-\frac{2\sigma}{R}-P_0-P_A sin(2\pi ft) \tag{4.2}$$

where P_g is the gas pressure in the bubble and is given by $P_g=(P_0+\frac{2\sigma}{R})*(\frac{R_0}{R})^{3\gamma}$
In this equation, R is radius at time t, R_0 is the initial bubble radius, $\dot{R}$ is the wall velocity of the bubble and $\ddot{R}$ is the wall acceleration, ρ is the liquid density (998 $\frac{kg}{m^3}$), c is the sound speed (1481 m/s), P_0 is the atmospheric pressure, σ is the surface tension (0.0725 $\frac{N}{m}$), μ is the liquid viscosity (0.001 Pa.s), P_A and f are the amplitude and frequency of the applied acoustic pressure. The values in the parentheses are for water at 293^0K. In this paper the gas inside the bubble is air (γ=1.4) and water is the host media.

The undamped resonance frequency of the bubble ($f_{undamped}$) can be calculated using linearization ([3] P. 372):

$$f_{undamped} = \frac{1}{2\pi}\sqrt{\frac{3\gamma(P_0 + \frac{2\sigma}{R})}{\rho R_0^2} - \frac{2\sigma}{\rho R_0^3}} \tag{4.3}$$

4.3.2 Backscattered pressure

Oscillations of a bubble generate a backscattered pressure (P_{Sc}) which can be calculated by [81]:

$$P_{sc} = \rho\frac{R}{d}(R\ddot{R} + 2\dot{R}^2) \tag{4.4}$$

where d is the distance from the center of the bubble (and for simplicity is considered as 1m in this paper) [15]. Eq. 4.1 is solved using the 4th order Runge-Kutta technique using the ode45 function in Matlab (this function also has a 5th order error estimation). The control parameters of interest are R_0, f and P_A. The resulting radial bubble oscillations are visualized using bifurcations diagrams. Bifurcation diagrams of the normalized bubble oscillations R/R_0 are presented as a function of driving pressure (P_A is investigated between $1kPa - 3.5MPa$ with in steps of $1kPa$) at $f = f_r$ and $f = 2f_r$ (f_r is the linear damped resonance frequency) and for bubbles with R_0 between $0.2\mu m$-$10\mu m$. Detailed analysis is presented for selected control parameters using a) the radius versus time curves, b) phase portrait analysis and c) the frequency spectrum of the backscattered pressure.

4.3.3 Investigation techniques

Bifurcation diagrams are valuable tools to analyze the dynamics of nonlinear systems where the qualitative and quantitative changes of the dynamics of the system can be investigated effectively over a wide range of the control parameters. In this paper, we employ a more comprehensive bifurcation analysis method introduced in [74, 75].

2.3.a) Poincaré section

When dealing with systems responding to a driving force, to generate the points in the bifurcation diagrams vs. the control parameter, one option is to sample the R(t) curves using a specific point

in each driving period. The approach can be summarized in:

$$P \equiv (R(\Theta))\{(R(t), \dot{R}(t)) : \Theta = \frac{n}{f}\} \tag{4.5}$$

Where P denotes the points in the bifurcation diagram, R and $\dot{R}$ are the time dependent radius and wall velocity of the bubble at a given set of control parameters of (R_0, P_A and f), Θ is given by $\frac{n}{f}$ and n=1,2,....440. Points on the bifurcation diagram are constructed by plotting the solution of $R(t)$ at time points that are multiples of the driving acoustic period. The results are plotted for $n = 400 - 440$ to ensure a steady state solution has been reached for all bubbles and thus 40 Poincaré point are stored for each solution. Due to smaller viscous effects, bigger bubbles require longer cycles to reach steady state.

2.3.b) Method of peaks

Another way of constructing bifurcation points is by setting one of the phase space coordinates to zero:

$$Q \equiv max(R)\{(R, \dot{R}) : \dot{R} = 0\} \tag{4.6}$$

In this method, the steady state solution of the radial oscillations for each control parameter is considered. The maxima of the radial peaks ($\dot{R} = 0$ and $\ddot{R} > 0$) are identified (determined within 400-440 cycles of the stable oscillations) and are plotted versus the given control parameter in the bifurcation diagrams.

The bifurcation diagrams of the normalized bubble oscillations (R/R_0) are calculated using both methods a) and b). When the two results are plotted alongside each other, it is easier to uncover more important details about the SuH and UH oscillations, as well as the SH and chaotic oscillations.

4.3.4 Investigation steps and criteria

Damping changes the resonance frequency of the bubble and Eq. 9.3 can loose accuracy [83]. Moreover, the radiation effects in Keller-Miksis model affect the stiffness of the bubble oscillator through the momentum it gives to the liquid [3] (P. 372). To calculated the linear damped resonance frequency including all these effects, resonance curves of the bubbles were calculated

by numerically solving Eq. 1 for different frequency values and for an acoustic pressure of 1 kPa. The frequency values which were solved to find the frequency of maximum response were chosen between $0.5f_{undamped} - 1.5f_{undamped}$ in steps sizes of $f_{undamped}/500$ where $f_{undamped}$ was calculated using Eq.9.3. An acoustic pressure of 1 kPa is chosen as it results in very low oscillation amplitudes ($\frac{R_{max}}{R_0} < 1.02$) and thus nonlinear effects can be neglected. The linear damped resonance frequency (f_r) was determined as the frequency by which the oscillation amplitude was maximum. To avoid transient oscillations, for each simulation parameter, all analysis was performed within the last 40 cycles of a 440 cycle acoustic pulse. The process of choosing the maximum resonance frequency is similar to [82].

The bifurcation structure of the bubble radial oscillations were then plotted as a function of (R/R_0) with respect to the applied acoustic pressure when the driving frequencies were f_r and $f_{sh} = 2f_r$. f_{sh} is called the 1st SH resonance frequency. Results were compared for $f = f_r$ and $f = f_sh$. The evolution of the two different period 2 attractors was studied in more detail by examination of the time-series of the radial oscillations, maximum wall velocities, phase portraits and frequency spectra of the backscattered pressure at different stages of the dynamical evolution of the system. For each sonication frequency and pressure, the maximum wall velocity and maximum non-destructive wall velocity ($\frac{R}{R_0} \leq 2$ [84], for a review on the minimum threshold of bubble destruction refer to [15]) were calculated for the regimes of non-chaotic oscillations. The results were compared for cases of $f = f_r$ and $f = f_{sh}$. The pressure ranges which result in non-destructive bubble oscillations ($\frac{R}{R_0} \leq 2$ [15, 82]) and non-chaotic oscillations were determined. For these determined parameter ranges, the maximum fundamental (FU), subharmonic (SH) and ultraharmonic (UH) amplitude of the backscattered acoustic pressure wave were calculated. The results were compared for cases of $f = f_r$ and $f = f_{sh}$.

4.4 Results

4.4.1 Period doubling and SH initiation, growth and saturation

In order to have a better understanding on the effect of period doubling and chaos on the 1/2 order SH and 3/2 order UH emissions of the bubble oscillations, Figure 4.1 plots the bifurcation structure of R/R_0 (the red curve represents the Poincaré section points at each acoustic period, and blue

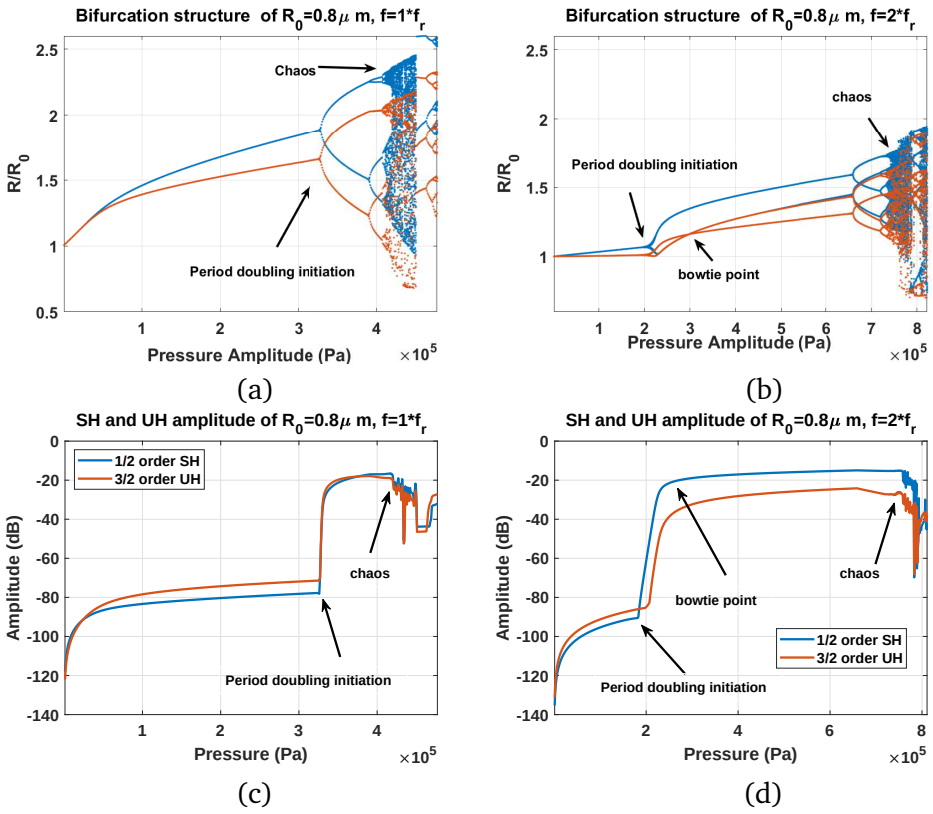

Figure 4.1: Bifurcation structure of bubble with $R_0 = 0.8\mu m$ driven by a) its resonance frequency (f_r), b)$2f_r$. 1/2 order SH and 3/2 order UH component of the backscattered signal when c)$f = f_r$, d)$f = 2f_r$.

curve represents the peaks of the oscillations) as a function of pressure and the corresponding SH and UH amplitude of the backscattered pressure side by side. The SH and the UH components are calculated by finding the frequency spectrum of the P_{sc} (Eq.9.4) The bubble has an initial radius of $0.8\mu m$ (this size has been chosen as a sample and because different stages of the dynamical process can be seen more clearly). The left column shows the dynamics of the bubble when $f = f_r$ and the right column represents the case of $f = 2f_r$. Period doubling in both cases results in the initiation and fast growth of SH amplitudes; as pressure increases, the SH and UH components grow in magnitude and reach a saturation value. This behavior (initiation, growth and saturation) has been also observed experimentally [67]. The P2 oscillations undergo further period doubling cascades to chaos; the occurrence of chaotic oscillations is concomitant with a decrease in SH and UH amplitude which continue rapid fluctuation in amplitude for chaotic oscillations. In case of sonication with $f = f_r$ and when PD occurs, 3/2 order UH component of the P_{sc} grows faster than the 1/2 order SH component of the P_{sc}; however, for $f = 2f_r$, the SH component of the backscattered pressure grows faster than the UH component and becomes stronger in magnitude.

4.4.2 Different stages of the P2 oscillations when $f = f_r$ and $f = f_{sh}$

Focusing on a narrow pressure range allows us to better understand the mechanism of the two different PDs and the corresponding dynamics of SH and UH components of the backscattered signal (Fig. 4.2). In this figure, the bubble has $R_0 = 0.8\mu m$; the left column represents the case in which $f = f_r$ and the right column represents the case in which $f = 2f_r$.

When bubble is sonicated with $f = f_r$ (Fig. 4.2a) the bifurcation structure of the bubble has 3 different oscillation regions; the P1 oscillation stage (black arrow), the initiation of PD stage (blue arrow) and the P2 oscillations stage (red arrow). The bifurcation structures that are generated using the Poincaré section at every acoustic period and maxima methods have concomitant PD and P2 oscillations, indicating the bubble oscillation is a P2 oscillation with two maxima. The corresponding SH and UH components of the backscattered pressure are plotted in Fig. 4.2b and can be categorized in 3 regions which can be described by the absence of SHs and UHs (black arrow), the initiation and fast growth of SH and UH of the P_{sc} concomitant with period doubling in Fig. 4.2a (blue arrow) and the region of UH and SH amplitude saturation (red arrow). Fig. 4.2c shows the maximum amplitude of the wall velocity. The velocity increases monotonically with

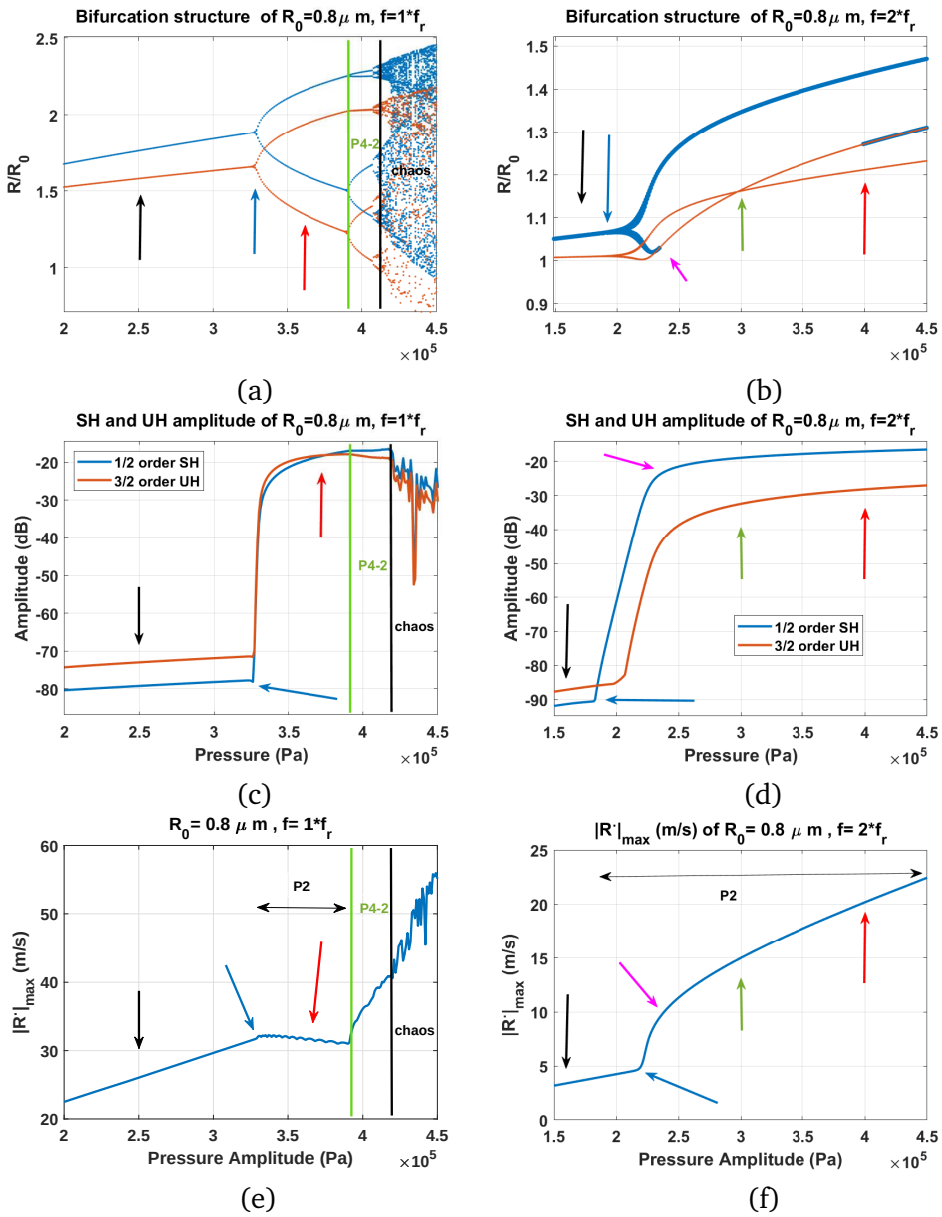

Figure 4.2: A closer look at the evolution of the P2 attractor when a) $f = f_r$ and b) $f = 2f_r$. The SH and UH component of the signal when c) $f = f_r$, and d) $f = 2f_r$. Wall velocity as a function of pressure when e) $f = f_r$, and f) $f = 2f_r$ (Maximum wall velocity of oscillations with periods higher than 2 are not displayed)

pressure elevation and undergoes a decrease concomitant with PD. The decrease of wall velocity concomitant with PD when the bubble is sonicated with a frequency close to f_r is studied in detail in [15].Occurrence of further PDs results in P4-2 oscillations followed by successive PDs to chaos. Generation of P4-2 does not increase the SH or UH amplitude, however, the bubble wall velocity increases. Occurrence of chaos leads to a substantial decrease in SH and UH strength, although the maximum wall velocity increases.

Fig. 4.2b shows the bifurcation structure of the R/R_0 of the bubble when it is sonicated with $f = 2f_r$. The dynamics of the PD bifurcation is different from the case of sonication with $f = f_r$ (Fig. 4.2a). The bubble initially starts with period 1 (black arrow). At 165 kPa the bubble undergoes a PD and oscillations become P2 with 2 maxima. As soon as PD occurs, the SH amplitude and wall velocity undergo a rapid increase (Fig. 4.2d and Fig. 4.2f). As the pressure increases, one of the local maxima in the bifurcation structure (blue curve) disappears while the red bifurcation curve still keeps P2 oscillations (purple arrow). Just before the disappearance, the value of the maxima (blue curve) overlaps one of the solutions in the red curve; this implies one of the time points in which the bubble wall velocity becomes zero is once every two acoustic cycles. The disappearance of the second maxima (at 245 kPa) is concomitant by a fast increase in the UH amplitude (purple arrow). Above this pressure, the growth rate of SH amplitude changes and starts to plateau. As the pressure increases, the two branches in the Poincaré section bifurcation diagram (red curve) converge at $\approxeq$ 297 kPa. At this pressure there is only one point in the red curve (green arrow). This is concomitant with further decrease of the growth rate of the SH and UH components of the backscattered pressure.

To more thoroughly examine the dynamics of PD when $f = f_r$, Fig. 4.3 shows the time-series, phase portraits and the frequency spectra of the backscattered pressure at three different pressures (black, blue, and red arrows in Fig. 4.2a). When $P_A = 250$ kPa, the oscillations are P1; Fig. 4.3a shows that the signal has one maximum (red circle) and R/R_0 has one single value at the end of each period of the acoustic driving force. The phase portrait (constructed over the last 40 cycles of a 200 cycle pulse) shown in Fig. 4.3b is a bell shape orbit consisting of only one loop. There is no distinct SH component in the frequency spectrum of the P_{sc} shown in Fig. 4.3c.

At $P_A = 330$ kPa (Fig. 4.3d) corresponding to the blue arrow in Figs. 4.2a and c, oscillations are of P2. There are two maxima and two distinct values for R/R_0 at the end of each driving period

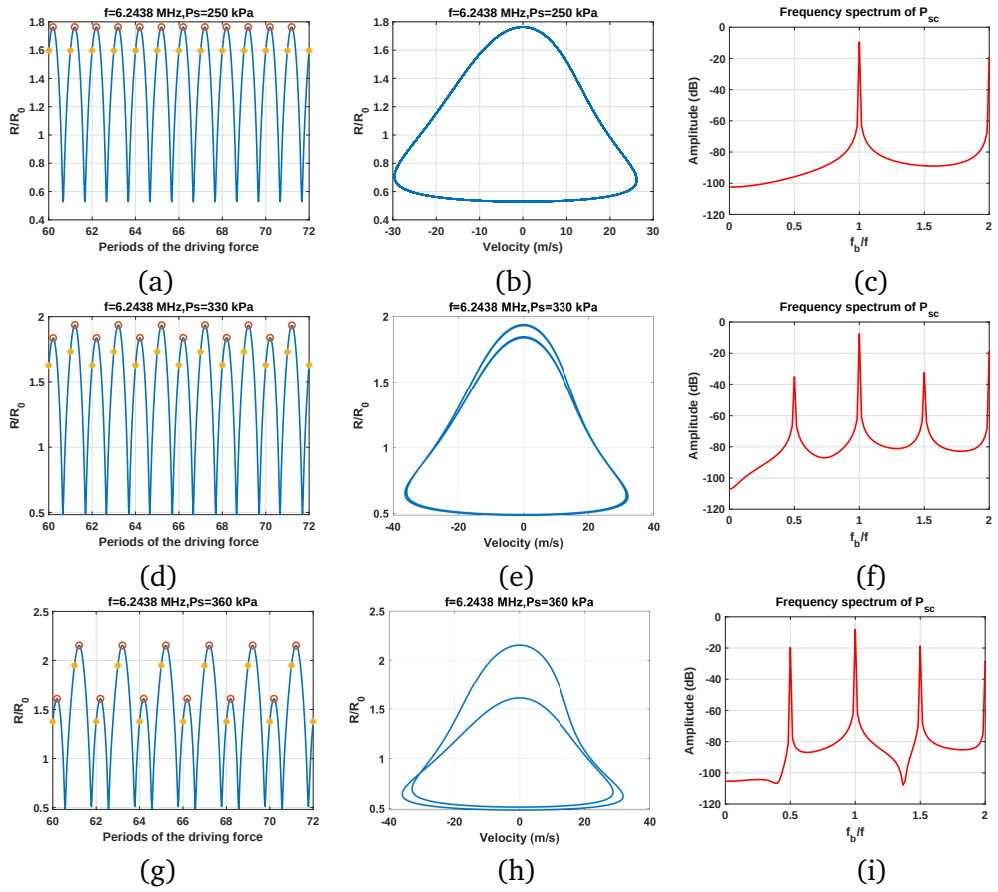

Figure 4.3: Evolution of the dynamics of the bubble with $R_0 = 0.8\mu m$ when $f = f_r$. Diagrams are plotted for three difference pressures of interest (250, 330 and 360 kPa, see Figure 2a). a) Radial oscillations, b) phase portrait diagram and c) frequency spectrum of the P_{sc} when P_s=250 kPa. The d) radial oscillations, e) the phase portrait diagram and f) the frequency spectrum of the P_{sc} are plotted when P_s=330kPa.The g) radial oscillations, h) the phase portrait diagram and i) the frequency spectrum of the P_{sc} are plotted when P_s=360kPa.

(shown in red and yellow circles respectively). The phase portrait in Fig. 4.3e, consists of a bell shape orbit which undergoes a bell shaped loop within itself. The frequency spectrum of the P_{sc} in Fig. 4.3f now has distinct SH and UH components with UH component stronger than the SH component. As pressure increases the separation between the two distinct peaks of the R/R_0 curve increases (Fig. 4.3g), as do the two loops of the phase portrait (Fig. 4.3h). In this case, the SH and UH components of the P_{sc} grow stronger with increasing pressure.

When sonicated with $f = 2f_r$, the period doubling can be analyzed in 5 pressure ranges (indicated by the black, blue, purple, green and red arrows in Fig. 2b).

Fig. 4.4 shows the time series, phase portraits and the frequency spectrum of the P_{sc} of a bubble with $R_0 = 0.8\mu m$ when $f = 2f_r$. Fig. 4.4a-c shows the time series, phase portrait and the frequency spectrum of the P_{sc} when P_A=205 kPa; the oscillations are of P1, the phase portrait is an ellipsoidal orbit of only one loop and the frequency spectrum lacks any distinct SH or UH component.

Right after the generation of PD at P_A=205 kPa, the radial oscillations have two maxima (red circles) and R/R_0 has two distinct values at the end of each period (yellow circles). When PD occurs radial oscillations are much smaller ($R_{max}/R_0 < 1.08$) when $f = 2f_r$ (Fig. 4.4d) compared to when $f = f_r$ with $R_{max}/R_0 = 1.95$ (Fig. 4.4d). The phase portrait in Fig. 4.4e consists of one ellipsoidal orbit undergoing and ellipsoidal loop within itself. The frequency spectrum of the P_{sc} in Fig. 4.4f shows a distinct SH component indicating the generation of SH oscillations.

When pressure is increased one of the maxima of the R/R_0 oscillations disappear while the oscillations remain P2 oscillations. Fig. 4.4g shows a representative R/R_0 time series of this stage of oscillations (purple arrow in Fig. 4.2b) when P_A=240 kPa. The radial oscillations have only one maximum however there are two distinct values (yellow circles) for R/R_0 at the end of every period. The phase portrait has an interesting heart like shape, which is rotated by -90 degrees around the y-axis shown in Fig. 4.4h. The frequency spectrum of P_{sc} illustrates distinct SH and UH peaks in Fig. 4.4i.

As the pressure further increases, the yellow circle with lower amplitude in the radial oscillation curve (Fig. 4.4a) grows quicker than the initially higher amplitude yellow circle. Thus, at a pressure that is shown by green arrow in Fig. 4.2b, the bifurcation diagram constructed by setting Poincaré section at each acoustic period (red curve) only shows one point as the two solutions have the same amplitude.

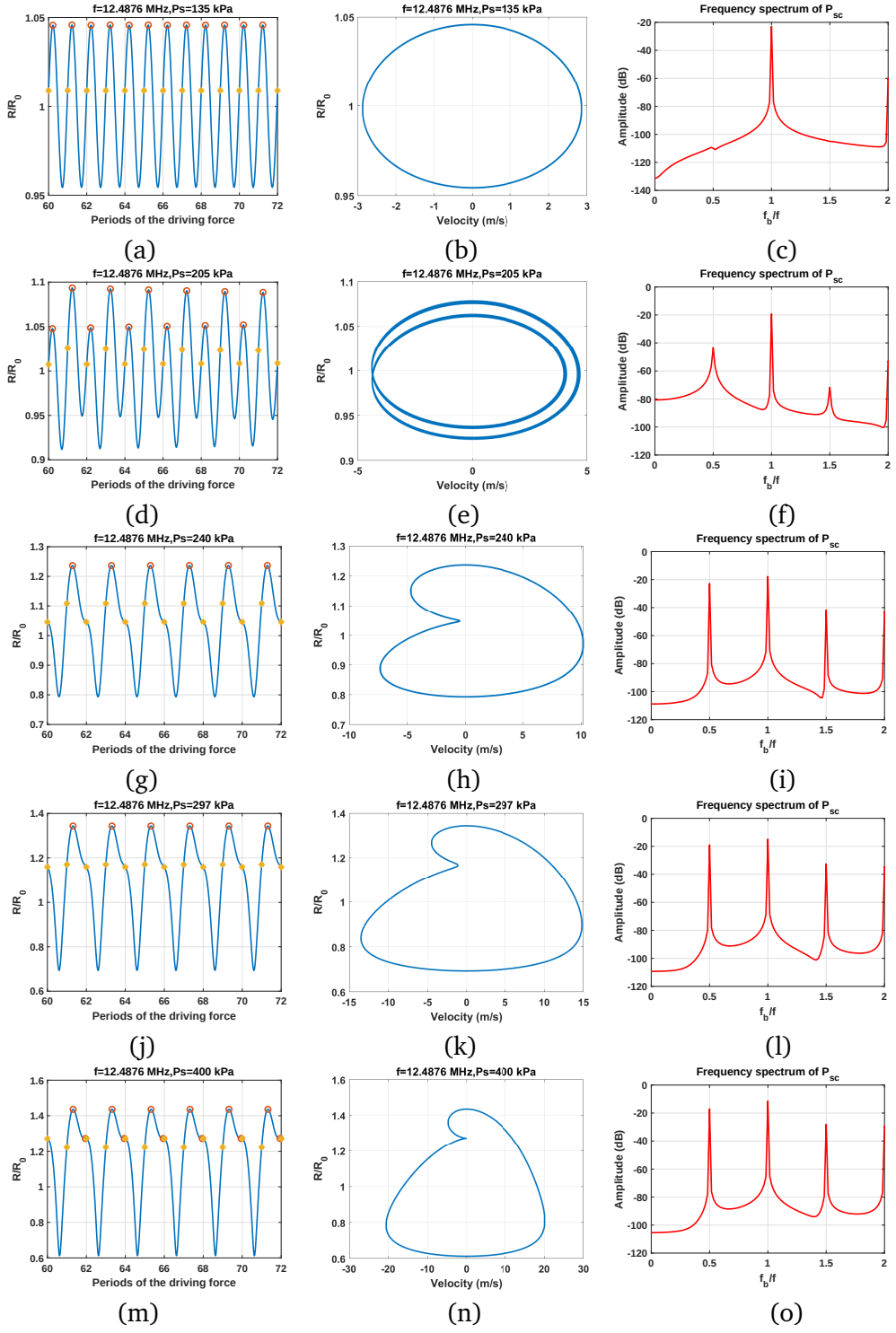

Figure 4.4: Evolution of the dynamics of the bubble with $R_0 = 0.8\mu m$ when $f = 2f_r$. Diagrams are plotted for four difference pressures of interest (see Figure 4.2b). Radial oscillations are plotted in the left column, phase portrait diagrams in the middle column and the frequency spectrum of the P_{sc} in the right column. The top row is for P_s=135 kPa, and the rows after for 205, 240, 297 and 400 kPa.

To shed a better light on the dynamics of the bubble shown by the green arrow in Fig. 4.2b, the time series of R/R_0 as a function of periods is shown in Fig. 4.4j. The signal has one maxima and repeats its shape once every two acoustic cycles; the amplitude of R/R_0 (yellow circle) at each period is the same; however, one yellow circle is located at the growth stage (positive wall velocity) while the second one is located at the collapse stage of the oscillations (negative wall velocity). The phase portrait still is in a heart shape form with one loop and SH and UH components are grown stronger as a function of pressure (Fig. 4.4k and 4.4l respectively).

As the pressure increases, the second maxima re-appears. Fig. 4.4m shows that the R/R_0 oscillations of the bubble (P_A=400 kPa) have two maxima (red circles) and R/R_0 represent two distinct values after every period. One of the maxima (red circles) is located exactly on one of the (yellow circles) indicating velocity becomes zero once every two acoustic cycles and right at the end of the acoustic driving period.

4.4.3 Bifurcation structure of bubbles with different sizes when $f = f_r$ and $f = 2f_r$

Figure 4.5 shows the bifurcation structure of the normalized radial oscillations of the three bubble sizes chosen ($R_0 = 0.5, 1.5$ and $2.5\mu m$) with respect to the excitation pressure amplitude; the left column represents the case where the sonication frequency is f_r and right column represents the case where the sonication frequency is f_{sh} ($f_{sh} = 2f_r$). The red graphs represent the structure constructed by the by setting the Poincaré section at each acoustic period and blue graphs represent the structure constructed by the maxima method.

Comparison between the two columns reveals 3 important findings:

1- The pressure threshold for P2 oscillations are lower when $f = f_{sh}$ and the possible pressure range of P2 oscillations are considerably larger.

2- When $f = f_{sh}$, P2 oscillations exist for a larger pressure range and evolve in the shape of a bowtie.

3- The amplitude of P2 oscillations are considerably ($\approx 80\%$) smaller when $f = f_{sh}$.

Figures 4.5a, 4.5c, and 4.5e show that when $f = f_r$, the period-1 (P1) oscillations monotonically increase with pressure increase; then at a pressure threshold bubble oscillations undergo period doubling (PD). For lower pressure values (e.g. 1kPa-10 kPa in Fig. 4.5a) the two bifurcation diagrams are on top of each other. This means that the wall velocity of bubble oscillations is in

phase with the driving acoustic filed and oscillations are resonant [27]. As the pressure increases, the two curves diverge; this is because at higher pressures resonance frequency decreases [15] and oscillations become off-resonant. The pressure threshold for PD is size dependent and is higher for smaller bubbles due to the stronger viscous effects on smaller bubbles which is consistent with analytical predictions [62, 63, 64, 65, 66]. The bubble with $R_0 = 2.5\mu m$ underwent a period doubling at 208 kPa while the pressure threshold for the bubble with $R_0 = 0.5\mu m$ was 446 kPa. Both methods of bifurcation construction show a period doubling succeeding linear oscillations. When $f = f_r$, the period doubling phenomenon however occurs when the R/R_0 amplitude is very close to 2; indicating that bubble would be more likely to undergo inertial collapse.

Figures 4.5b, 4.5d and 4.5f show the bifurcation structure of the bubble when $f = 2f_r$ for R_0=2.5, 1.5 and 0.5 μm respectively. Compared to sonication with $f = f_r$, the linear oscillation amplitude and R/R_0 growth rate with pressure increase are smaller. The pressure threshold of PD is lower than sonication with $f = f_r$; the bubble with $R_0 = 2.5\mu m$ and the bubble with $R_0 = 0.5\mu m$ underwent PD at 62 kPa (Fig. 4.5b) and 388 kPa (Fig. 4.5f) respectively. The R/R_0 oscillation amplitude of the P2 oscillations are much smaller than 2 indicating that the bubble may sustain long-lasting P2 oscillations without destruction. Additionally, the pressure range that results in P2 oscillations is broader (e.g. when $R_0 = 2.5\mu m$, for $f = f_r$ pressure range of P2 oscillations is $\approx$ 40 kPa while for $f = 2f_r$ this pressure range increases to 400 kPa).

Fig. 4.5 shows that the pressure range of P2 oscillations becomes broader as R_0 decreases, likely due to the stronger effects of viscous damping (e.g. when f=2fr the pressure range of P2 oscillations are $\approx$ 400kPa, $\approx$ 480 kPa and $\approx$ 600 kPa respectively for R_0= 2.5, 1.5 and 0.5 μm).

One of the differences between the cases of sonication with $f = f_r$ (left column) and $f = 2f_r$ (right column) is the occurrence of the bowtie point (Fig. 4.5). When $f = 2f_r$, P2 oscillations occur over a larger pressure range and at a pressure (see insets in graphs) the two red curves meet. At this pressure, radial oscillations of the bubble have the same value after every period (see Fig. 4.4j as an instance), however one point has a positive wall velocity and one point has a negative wall velocity. After the occurrence of PD and with increasing pressure the two branches of the red curve converge until they meet and then diverge. This makes the evolution of the P2 oscillations to form a shape that looks like a bowtie.

When the blue curve (representing the maxima of the R/R_0) is analyzed, it is seen that the bubble

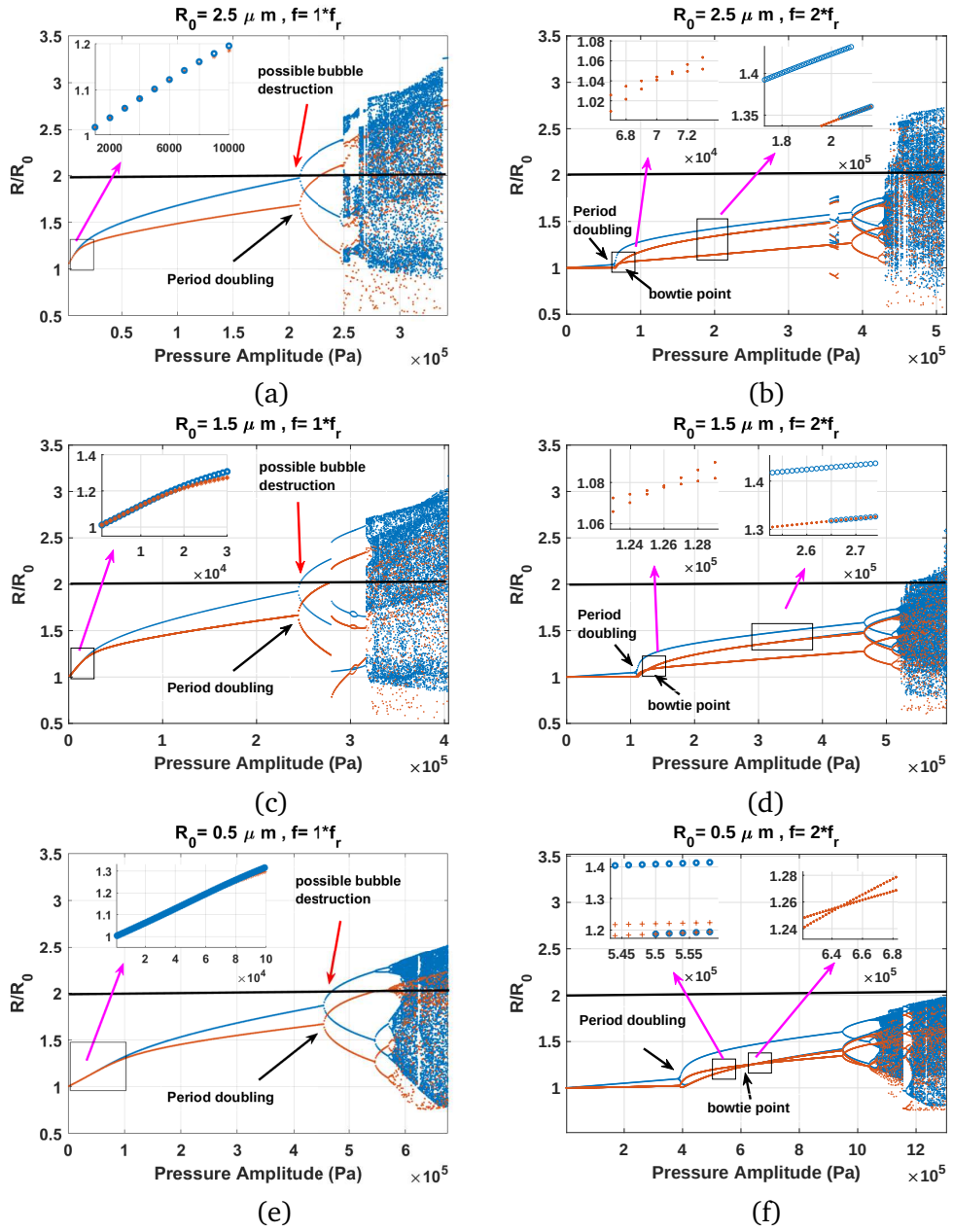

Figure 4.5: Bifurcation structure (conventional method in red and method of peaks in blue) of the normalized radial oscillations (R/R_0) of the bubble as a function of pressure for a) R_0=2.5 μm *and* $f = f_r$ b) $R_0 = 2.5\mu m$ *and* $f = 2f_r$, c) $R_0 = 1.5\mu m$ *and* $f = f_r$, d)$R_0 = 1.5\mu m$ *and* $f = 2f_r$, e) $R_0 = 0.5\mu m$ *and* $f = f_r$, f) $R_0 = 0.5\mu m$ *and* $f = 2f_r$.

has two maxima when PD occurs in the red curve. But one of the maxima of the blue curve disappears quickly as the pressure increases (see Fig. 4.4g as an example of a time series). This indicates that the period of oscillations is 2; however, the R/R_0 oscillations vs time have only one maximum. Above a second pressure threshold (highlighted by zooming in the Figs. 4.5b,d and f), the second maxima re-emerges and its amplitude is exactly equal to the highest amplitude of the R/R_0 branch of the P2 oscillations in red curve (see Fig. 4.4m as an instance).

In case of $f = f_r$ and $R_0 = 1.5\mu m$ (Fig. 4.5c) we see a short window of P3 oscillations and for the bubble with $R_0 = 2.5\mu m$, we see a short pressure window of P6 oscillations for $f = 2f_r$ (Fig. 4.5b). These will be discussed in more detail in the Appendix.

Fig. 4.6, shows the bifurcation structure of R/R_0 of the bubbles with R_0 of 0.4, 0.3, and 0.2 μm (top to bottom respectively) versus acoustic pressure. The left column represent the case where the sonication frequency is set to the linear resonance of the bubble (f_r) and right column represent the case of sonication with $2f_r$.

When the bubble is sonicated with f_r; the radial oscillations increase monotonically with pressure elevation and the bubble undergoes PD route to chaos above a pressure threshold (e.g. 700 kPa for the bubble with R_0=0.3 μm). The blue curve and red curve are initially on top of each other (wall velocities are in phase with the driving acoustic pressure) but they diverge as the pressure increases. For smaller bubbles the pressure range where the red and blue curve have the same value are wider (e.g. 200 kPa for the R_0=0.3 μm bubble and 460 kPa for the R_0=0.2 μm bubble). When $f = f_r$, the R/R_0 amplitude of bubble oscillations at the time of PD is very close to 2; this indicates that bubbles may not be able to sustain non-destructive oscillations. The bifurcation diagrams generated by both methods demonstrate concomitant PD. This shows that the oscillations are of P2 with two maxima. It should be noted that the occurrence of PD does not necessarily mean that the oscillations will have two maxima, nor does a P1 oscillations necessarily have 1 maximum [75].

When bubbles are sonicated with $f = 2f_r$ however, R/R_0 amplitude is well below the value of 2 when PD occurs. The bubble keeps P2 oscillations with an amplitude relatively below 2 (e.g. 1.15 at 0.1 MPa in Fig. 4.6f) indicating that the bubble is more likely to sustain non-destructive P2 oscillations when sonicated with $2f_r$. Additionally the pressure range of P2 oscillations are much broader compared to the case of sonication with fr (e.g. 1 MPa in Fig. 4.6d). Unlike the cases of bubbles with R_0 larger than 0.5 μm when sonicated with $f = 2f_r$, the bubble oscillations

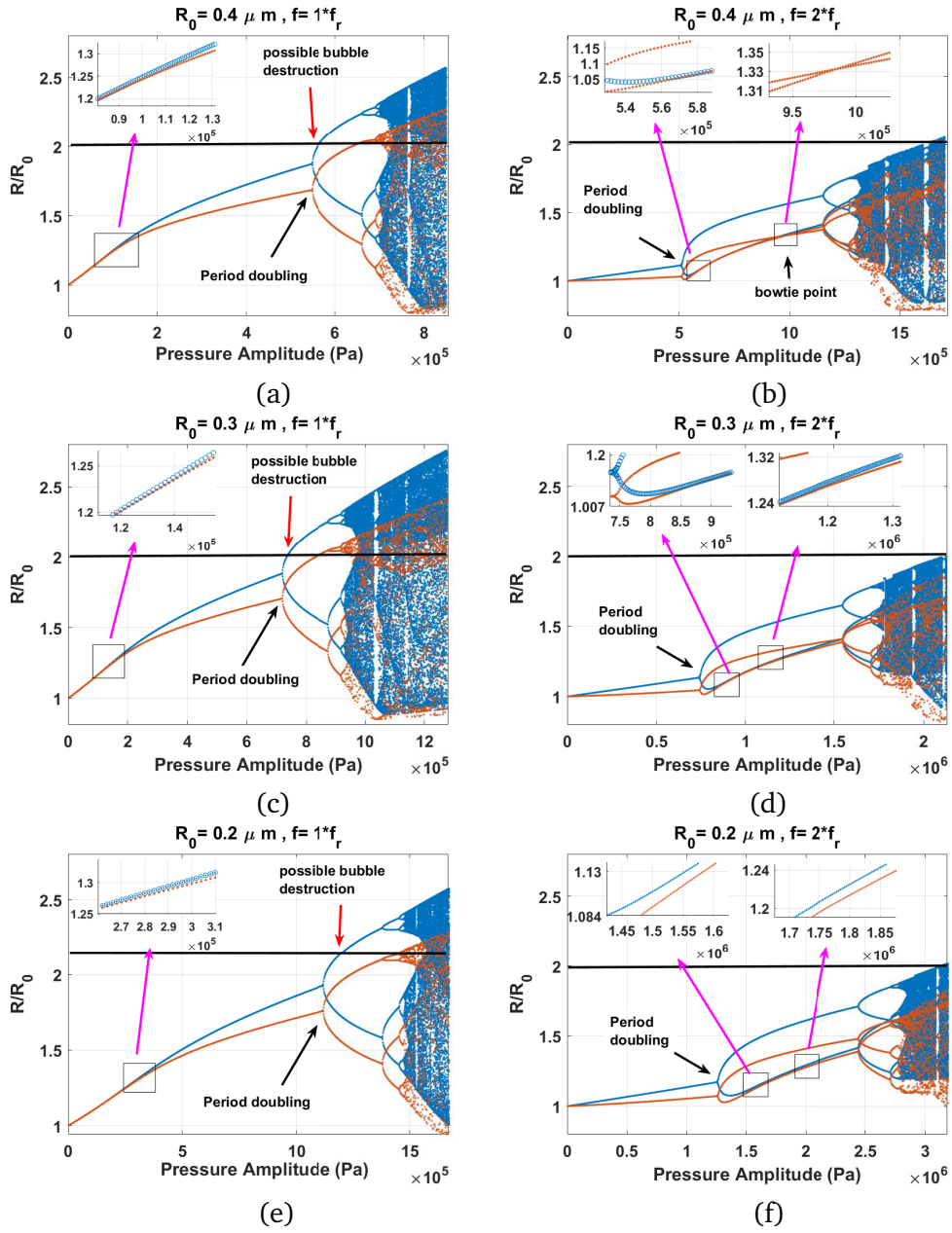

Figure 4.6: Bifurcation structure (conventional method in red and method of peaks in blue) of the normalized radial oscillations (R/R_0) of the bubble as a function of pressure for a) $R_0 = 0.4\mu m \; and \; f = f_r$ b) $R_0 = 0.4\mu m \; and \; f = 2f_r$, c) $R_0 = 0.3\mu m \; and \; f = f_r$, d) $R_0 = 0.3\mu m \; and \; f = 2f_r$, e) $R_0 = 0.2\mu m \; and \; f = f_r$, f) $R_0 = 0.2\mu m \; and \; f = 2f_r$.

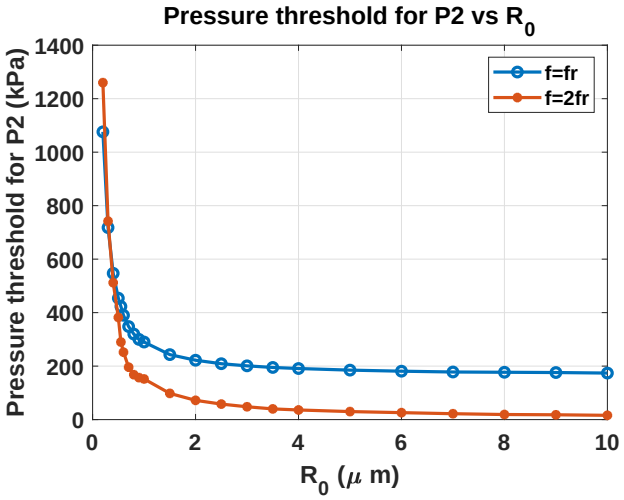

(a)

Figure 4.7: Pressure threshold of P2 oscillations as a function of R_0 when bubble is sonicated with $f = f_r$ and $f = 2f_r$.

exhibit two maxima for the whole range of P2 oscillations. After a pressure threshold, the lower maxima of the P2 oscillations lies on top of one of the branches of the P2 oscillations in the conventional bifurcation diagram; this indicates that one of the time points where the velocity of bubble oscillations is zero is exactly once every two acoustic cycles. Furthermore, the evolution of P2 oscillations for bubbles with $R_0 \leq 0.37\ \mu m$ does not have the bowtie point; in other words, when sonicated with $2f_r$ a bowtie point only happens for bubbles with R_0 larger than 0.37 μm. Comparing figs 4.5 and 6, when $f = f_r$, chaotic oscillations only develop when $R/R_0 > 2.3$; thus, in practice, resonant bubbles may not sustain chaotic oscillations due to the high possibility of destruction. However, when $f = 2f_r$, and for bubbles with $R_0 \lessapprox 2.5\mu m$, chaotic oscillations can develop when $R/R_0 \leq 2$; thus, these bubbles may sustain chaotic oscillations when $f = 2f_r$. As the bubble size gets smaller, the pressure threshold for the PD increases for both $f = f_r$ and $f = 2f_r$. Although, PD typically occurs at a lower pressure when $f = 2f_r$ however, for the bubbles with $R_0 = 0.3$ and $0.2\ \mu m$ pressure threshold for PD is lower when $f = f_r$. It is hypothesized in [71, 72] that increased damping is the reason behind this effect.

4.4.4 Pressure threshold and range of P2 oscillations

Figure 4.7 illustrates the pressure threshold of period doubling (PD) as a function of R_0 for $f = f_r$ and $f = 2f_r$ and is created by analyzing the bifurcation diagrams of bubbles with initial radii

between 0.2-10 μm (Appendix: Figs 4.12a and A.13a). The pressure threshold (P_t) of PD is lower when the bubble is sonicated with $2f_r$; however, as R_0 decreases the difference between the $P_t(f_1)$ and $P_t(f_2)$ decreases and for bubbles with initial radii of $R_0 = 0.3$ and 0.2 μm pressure threshold for PD is lower when $f = f_r$. The pressure threshold of PD is lower for bigger bubbles; this is due to weaker effects of viscosity on larger bubbles. These results are in agreement with analytical predictions of Prosperetti [66].

Figure 8 is made by analyzing the bifurcation diagrams of bubbleswith initial radii of 0.2-10 μm size (Appendix: Figs 4.12a and 4.13a). Figure 4.8a demonstrates the range of P2 oscillations as a function of R_0 for $f = f_r$ and $f = 2f_r$. To construct Fig. 4.8a we have identified the lower pressure limit (the pressure threshold) and the upper pressure limit of P2 oscillations and then plotted the value of their subtraction as a function of radius. In Fig. 4.8b the upper pressure limit is chosen so that $R_{max}/R_0 < 2$. When bubble is sonicated with 2fr, the range of acoustic pressures that can result in P2 oscillations are broader than when compared to $f = f_r$ by an order of magnitude (e.g. for $R_0 = 4\mu m$, the P2 pressure range is 34 and 304 kPa for $f = f_r$ and $f = 2f_r$ respectively). Figure 4.8b demonstrates the pressure range of P2 oscillations when $R/R_0 \leq 2$. When $f = f_r$, bubbles with R_0>2.5 μm undergo PD when R/R_0>2, thus they may not exhibit non-destructive SH oscillations; however, when $f = 2f_r$, all the studied bubble sizes (0.2 $\mu m \leq R_0 \leq$10 μm) exhibit non-destructive P2 oscillations over a broad range of acoustic pressures. Thus, if non-destructive SH oscillations are desired in an application where ($R(t = 0s) = R_0$ and $\dot{R}(t = 0s) = 0m/s$ a condition that is typically seen during imaging applications), preferred sonciation frequency between $f = f_r$ and $f = 2f_r$ is the latter one. However, the choice of frequency may be different depending on the initial conditions and in case of liquids with higher viscosity [85].

4.4.5 Absolute wall velocity of the period 2 oscillation regimes

Wall velocity is an important measure of the bubble collapse and strongly contributes to the bubble backscatter in (Eq. 9.4). To compare the magnitudes of the bubble wall velocities, the absolute wall velocities for bubbles of initial radii between $0.2\mu m$-10 μm were plotted alongside their bifurcation diagram as a function of pressure (Appendix: Fig. 4.12 and Fig. 4.13). The absolute value of the bubble wall velocity when PD occurs and the maximum achievable P2 absolute wall velocities were

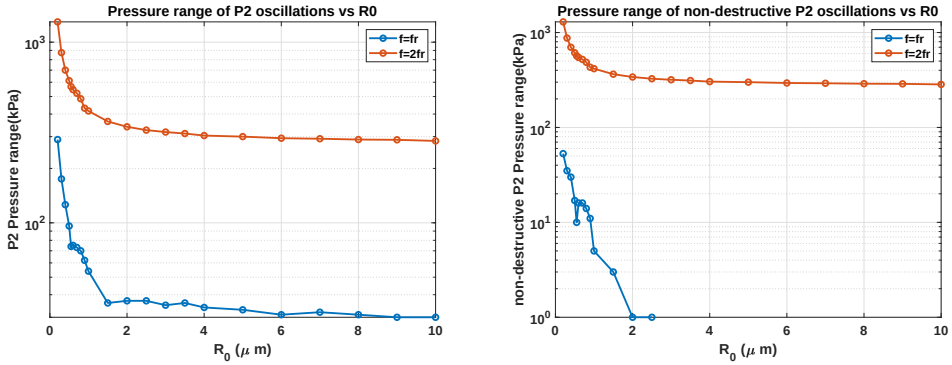

Figure 4.8: a) Acoustic pressure range of P2 oscillations as a function of R_0, b) Non-destructive ($\frac{R}{R_0} \leq 2$) acoustic pressure range of P2 oscillations as a function of R_0.

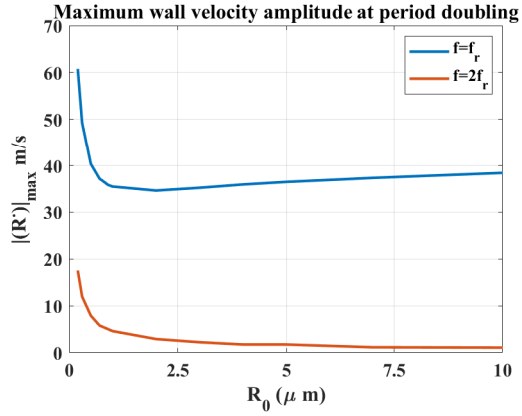

Figure 4.9: Maximum wall velocity amplitude ($|\dot{R}(t)|_{max}$) when period doubling occurs as a function of R_0. Blue is for $f = f_r$, and red denotes the case of $f = 2f_r$.

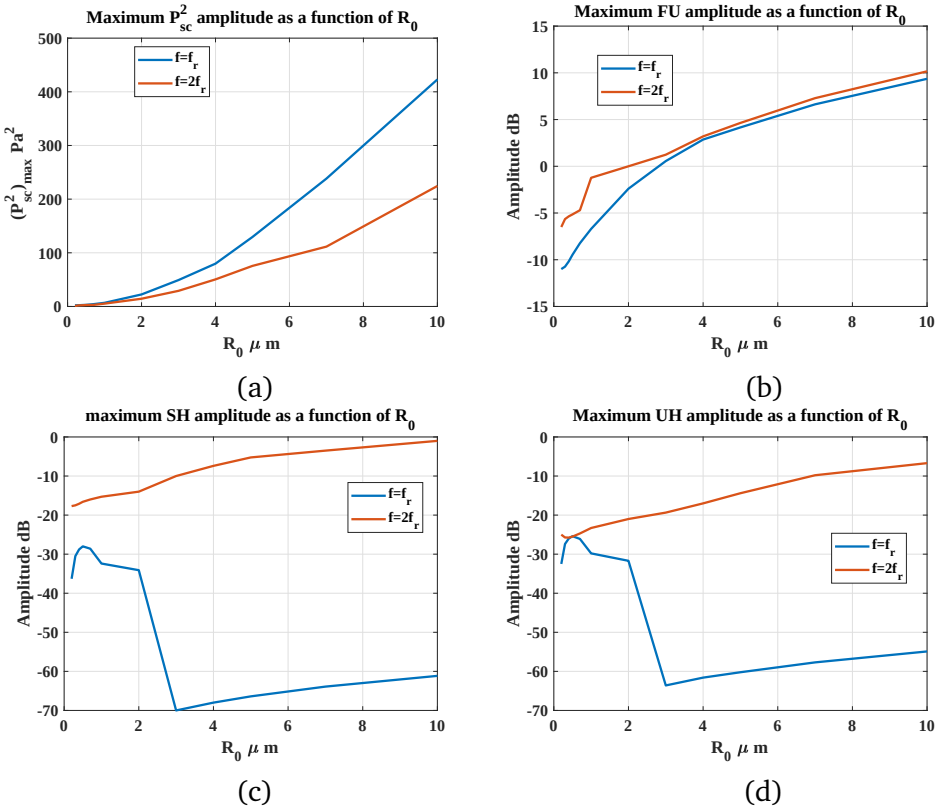

Figure 4.10: Maximum possible non-destructive: a)P_{sc}^2, b) Fu amplitude, c) SH amplitude and d) UH amplitude as a function of R_0.

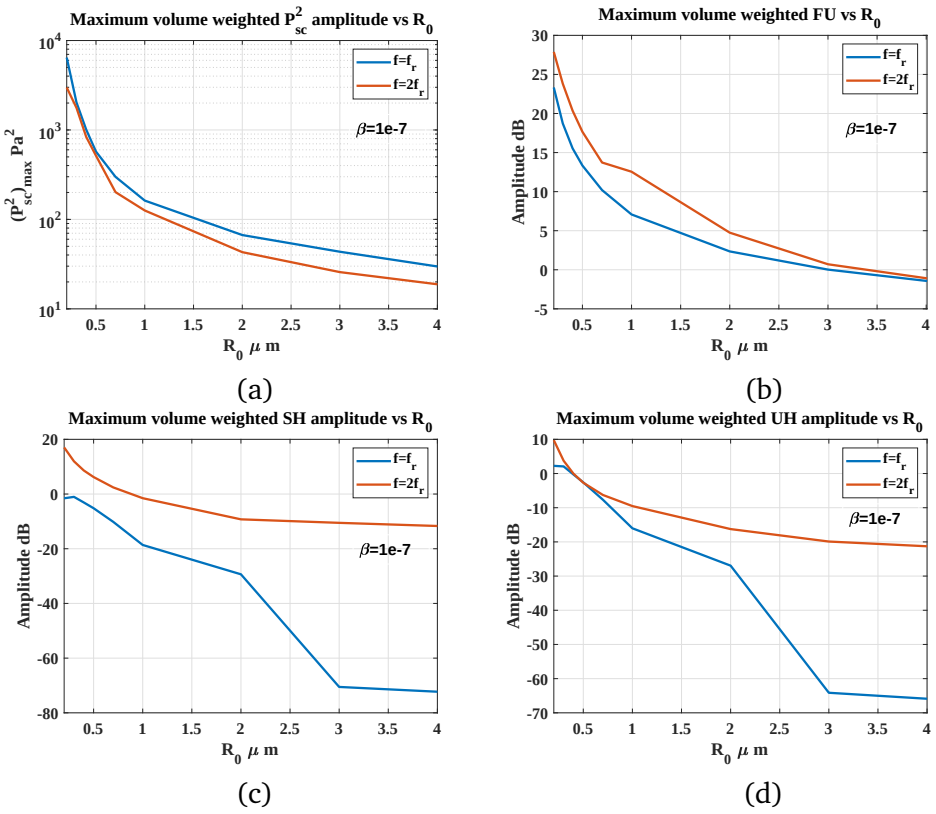

Figure 4.11: Gas volume weighted (β=1e-7) maximum possible non-destructive: a) P_{sc}^2, b) FU amplitude, c) SH amplitude and d)UH amplitude as a function of R_0.

extracted from Fig. 4.12 and 4.13 and are plotted as a function of bubble size in Figure 4.9. Figure 4.9 depicts the bubble absolute wall velocity when PD occurs as a function of size. The blue line shows the case of $f = f_r$ and the red line represents $f = 2f_r$. For the micron size bubbles when $f = f_r$, the wall velocity is $\approx$ 34-40 m/s when PD occurs. For nanobubbles the PD wall velocity rapidly increases as the size decreases, reaching velocities greater than 60 m/s for the bubble with $R_0 = 0.2\mu m$. The same trend is seen when $f = 2f_r$; the PD wall velocity is less than $\approx$ 6 m/s for micron size bubbles and rapidly increases for nanobubbles approaching 20 m/s for the bubble with $R_0 = 0.2\mu m$. In comparison to bubbles sonicated by $f = f_r$, bubbles sonicated with $f = 2f_r$ exhibit much smaller wall velocities when PD occurs (e.g. for bubbles with initial radii $> 0.5\mu m$, 6-36 times smaller and for bubbles with initial radii $< 0.5\mu m$, about 3-5 times smaller). Thus due to lower collapse velocities, this suggests that bubbles sonicated with $f = 2f_r$ are more likely to sustain P2 non-destructive oscillations.

4.4.6 Analysis of the backscatter signal for the two types of Period two oscillations

To identify the maximum achievable non-destructive backscattered signal strength and it's fundamental (FU), $1/2$ order subharmonic (SH) and $3/2$ order ultraharmonic (UH) components, the maximum nondestructive ($R/R_0 \leq 2$) values for each bubble size when $f = f_r$ and $f = 2f_r$ were plotted (Fig. 4.10). These values are extracted from Figs 4.14-4.17 in Appendix.

The maximum value of P_{sc}^2 (P_{sc}^2 is used instead of P_{sc} to better relate to the signal intensity) and the fundamental component of the P_{sc} are stronger when the bubble is sonicated with $f = f_r$ (Fig. 4.10a-b), with bigger bubbles scattering stronger than smaller bubbles. However, the maximum non-destructive SH and UH amplitude of P_{sc} are stronger when $f = 2f_r$ (Fig. 4.10c-d).

When $f = 2f_r$ nondestructive SH_{max} and UH_{max} are greater for bigger bubbles; however, when $f = f_r$ nondestructive SH_{max} and UH_{max}, of the 1 micron bubble (R_0=0.5 μm) exhibits the strongest possible nondestructive SH_{max}(-28 dB) and UH_{max} ($\approx$ -25.5 dB). Nondestructive SH_{max} and UH_{max} are highest for bubbles with ($0.3\mu m < R_0 < 2$ μm) when $f = f_r$. As is discussed in Fig. 4.4, when $f = f_r$, only a small range of bubble sizes can undergo non-destructive PD and consequently SH and UH emissions when $R/R_0 \leq 2$.

Gas volume plays an important role in many applications. For a given volume a greater number of smaller bubbles are possible. The volume fraction is given by $\beta = \frac{4}{3}\pi N R^3$ where β is the volume

fraction that the gas occupies, N is the number of bubbles per unit volume and R is the radius of the bubbles at time t. To consider the effect of gas volume on the maximum achievable signal from bubbles, the results of figure 4.10 are normalized for a case of β=10^{-7} and, the signal intensities were calculated for a 1 mm cube in figure 4.11 (assuming negligible interaction between bubbles). Results of the bubbles bigger than 8 micron in diameter ($R_0 = 4\mu m$) were omitted as the average capillary diameter in human body is approximately 8 μm [86].

Fig. 4.11 shows that smaller bubbles (e.g. nanobubbles) have the potential to provide stronger signals in specific situations (e.g. when $f = 2f_r$ and β=10^{-7}). If one assumes monodispersity and that all signals arrive in phase, then the bubbles with $R_0 = 0.2\mu m$ bubbles produce SH_{max} and UH_{max} of 15 dB and 18 dB higher than the 3 μm bubbles when controlled for gas volume.

4.5 Discussion

Period doubling (PD) and chaos are one of the well-known characteristics of nonlinear dynamical systems including bubble oscillators [1,2,3,4,5,6,7]. PD results in bubble subharmonic oscillations which are of great importance in applications including but not limited to contrast-enhanced ultrasound imaging [54, 55, 56], monitoring therapeutic applications of ultrasound [50, 51, 52], non-destructive testing [53, 64, 65, 66], sonoluminescence [41] and other applications. The nonlinear and chaotic dynamics of the bubble oscillator have been the subject of many recent studies [15, 16, 17, 18, 19, 20, 21, 22, 23, 24, 25, 26].

However, the two main period-2 regimes in the bubble oscillator have not been studied in detail. Because of the importance of bubble 1/2 order SH oscillations, comprehensive knowledge of the mechanisms of PD and 1/2 order SH oscillations can help in optimizing current applications or explore new potential parameters to be used in applications.

In this work the bifurcation structure of the R/R_0 of the bubble oscillator was studied as a function of pressure; two important cases of sonication with linear resonance frequency (f_r) and subharmonic resonance frequency ($2f_r$) were studied in detail for bubbles with initial radii of 0.2 μm up to 10 μm. The SH, ultraharmonic (UH) and fundamental (FU) components of the backscattered pressure, as well as the R/R_0 vs time and phase portraits of the signals, were analyzed.

It was shown that the bubbles sonicated with $f = 2f_r$ are most likely to sustain non-destructive

oscillations as the period doubling occurs at a very gentle oscillation regime and at very small expansion ratios ($R_{max}/R_0 < 1.1R_0$). To the contrary, sonication with $f = f_r$ may not result in non-destructive period doubling as the period doubling occurs at expansion ratio of $R_{max}/R_0 \gtrapprox 2$. Expansion ratio of 2 is reported by Flynn [84] as the minimum threshold of transient cavitation where inertial forces dominate the collapse of the bubble. In another study, Apfel [87] suggested the threshold of $R_{max}/R_0 \approx 2.3$ as the transient cavitation threshold. Another criteria was developed by Mitchell and Plesset [88] which is based on the R_{max}/R_{min} ratio. According to this theoretical study, the bubble is stable if $R_{max}/R_{min} < 5$ and it is unstable if $R_{max}/R_{min} > 10$. In our previous study [15] and for coated bubbles with pure viscoelastic behavior of the coating, stability condition of $R_{max}/R_0 \lessapprox 2$ also satisfied the stability criteria of $R_{max}/R_{min} < 5$ by Mitchell and Plesset [88]. For a review on the studies on transient cavitation threshold one can refer to [3] (P. 316-335). Several experimental studies [89, 90, 91, 92] have reported stable oscillations of coated bubbles beyond the minimum stability threshold of $R_{max}/R_0 \approx 2$. In these studies, which are based on optical measurements of the bubble radius during oscillations, the majority of the coated bubbles were destroyed once $R_{max}/R_0 > 2$. These results were also supported by acoustic measurements of the destruction of coated bubbles [93, 94, 95] where the destruction only happened when $R_{max}/R_0 > 2$, although some bubbles survived higher expansion ratios. Based on the experimental observations, the minimum threshold for transient cavitation used in this work is a reasonable choice. However, since the criteria of $R_{max}/R_0 = 2$ is the minimum value, this does not guarantee that destruction will happen at this exact value, thus some bubbles may survive period 2 oscillations when they are sonicated with $f = f_r$. This criteria is considered to be a sufficient condition to ensure bubbles do not undergo transient collapse which may need to be avoided for SH imaging applications. The conclusions of the study are based on a model in the absence of coating. The increased viscosity and change in the nonlinear bubble behavior due to the coating will affect the conclusions.

Another advantage of sonication with $f = 2f_r$ is the higher amplitude of the 1/2 order SHs and 3/2 order UHs which leads to a higher contrast to tissue ratio. Moreover, due to the lower pressure threshold of the period 2 oscillations, sonication with $2f_r$ may lead to superior signal to noise ratio of the SH and UH images.

We showed that when $f = f_r$, increasing the exciation pressure amplitude leads to a monotonic

increase in the scattered pressure (P_{sc}) by bubbles (Fig. 4.14a). However, when $f = 2f_r$, P_{sc} undergoes a rapid increase (> 10 fold) when excitation pressure is increased above the pressure threshold for period doubling (Fig. 4.14b). This property can be exploited for amplitude modulation imaging techniques [96].

SH emissions of isolated coated bubbles have been studied experimentally through high speed optical observations of bubble oscillations [92]. They showed that when $f = f_r$, the pressure threshold of SH generation is greater than the bubble destruction threshold. When $f = f_r$ we showed that PD only occurs when R_{max}/R_0 is close to 2 and thus stable SH oscillations may not occur. Thus our results are in agreement with the results of optical observations in [92]. Moreover, [92] concludes that when $f = 2f_r$ the bubble exhibits SH emissions while exhibiting maximum stability. This conclusion is in agreement with the results of our study.

In this study we only focused on 1/2 order SHs regime of oscillations when $f = f_r$ and $f = 2f_r$ and to replicate the initial conditions that we expect during imaging applications, we chose $R(t = 0s) = R_0$ and $\dot{R}(t = 0s) = 0$ [15]. However, the initial conditions of the system heavily influences the pressure threshold and order of the SHs [85]. Through, GPU accelerated simulations, nonlinear dynamics of the bubble with different initial conditions (25 random initial conditions) has been investigated using 2 dimensional bifurcation diagrams in [85]. The stability conditions of the P2 and higher order SH oscillations, may change depending on the initial condition of the system.

The model that used in this paper is the Keller-Miksis model [80] for uncoated bubbles. Analysis of the complex dynamics of the uncoated bubble builds the fundamental knowledge that is needed to investigate the more complex coated bubble models. The buckling and rupture of the coating and the dynamic variation of the effective surface tension of the bubbles can be modeled using the Marmottant model [76]. In the Marmottant model when the coating buckles the effective surface tension on the bubble drops to zero. The coating behaves like an elastic material when the bubble radius is between the buckling and rupture radii. When the radial amplitude exceeds the rupture radius, the effective surface tension becomes equal to that of the uncoated bubble. The effect of strain softening of the coating have been analyzed in [97]. In this model interfacial elasticity decreases with increasing area fraction of the coating of the bubble. The strain softening is due to the decreasing association between the constitutive molecules of the encapsulation. This model do not necessarily incorporate buckling/rupturing radii however has been able to predict

subharmonic oscillations. [97] concludes that the use of the strain softening model improves the ability to predict subharmonic response. Moreover, similar to Marmottant model [76], this model can also predict compression only behavior when buckling occurs. In a comparative study of the SH emissions [98] of the coated bubbles at higher frequencies, both the [76] and [97] were applied to undertsand the SH emissions. Paul et al. [97] concludes that similar results can be achieved for both "compression-only" and "expansion dominated" oscillations and thus, this emphasizes the fact that the exact form of the coating elasticity relation to radius still remains unknown.

Experimental results have shown that the buckling of the lipid coating enhances the generation of SH oscillations at very low acoustic pressures [99,100]. These pressures are below the thresholds of SH generation for uncoated bubbles even though coated bubbles have higher viscosity. Prosperetti's theoretical analysis [67] attributed this effect to the dynamic variation of the effective surface tension on the bubble.

Faez et al. [101] investigated the SH response of individual coated bubbles (diameters between 1 and 4 μm) for the excitation frequency between 4-12 MHz at pressures of 50, 100 and 120 kPa. Among their 390 analyzed bubbles 40 percent exhibited SH response. The SH resonance frequency for bubbles smaller than 3 μm increased up to 10 $\%$ with increasing acoustic pressure from 50 to 120 kPa (a hardening effect of the coating). This was just the opposite of what was observed for the fundamental response. Faez et al [102] investigated the SH response of biotinylated lipid coated bubbles in vivo in a chicken embryo model. Bubble diameters between 1-3.5 μm were sonicated in the frequency range of 4–7 MHz and applied pressure amplitudes of 300 kPa and 400 kPa. 44 $\%$ of the total studied bubble population showed a subharmonic response in the applied driving frequency range. All the bubbles showed (strain) hardening behavior of the coating. Moreover, transmit at $f = f_r$ was responsible for the SH response of the bubbles. These results indicate the strong and complex effects of the coating on the nonlinear behavior of the bubble.

In this work effect of non-spherical oscillations of the bubble [103, 104, 105, 106] were neglected. Holt et al. [104] investigated the subharmonic behavior of larger bubbles ($\approx 100 - 200\mu m$ in size) and have experimentally observed the shape oscillations concomitant with subharmonic oscillations. They showed that, since the frequency of the first shape oscillation is 1/2 of the driving frequency, its appearance could be phenomenologically mistaken for a simple period-doubling of the radial mode. At higher pressure amplitudes, the oscillations were shown to be very complex,

with many subharmonic components conjectured to the result from nonlinear volume resonances and shape oscillations of undetermined mode [104]. Recently Klapcsik and Hegedűs [103] through GPU accelerated large parameter investigations and 2 dimensional bifurcation diagrams, have studied the dependence of the active cavitation threshold on the shape instability of the bubble. Shape instability can affect the subharmonic threshold and nonlinear behavior of bubbles. More accurate predictions of the oscillations requires the incorporation of the shape instability during bubble oscillations. Versluis et al. [105] through using high speed optical observations were able to identify shape oscillations of mode n= 2 to 6 in the behavior of single air bubbles with radii between $10\mu m$ and 45 μm. Their study [105] concluded that the close to resonance bubbles were found to be most vulnerable toward shape instabilities. For coated bubbles, nonspherical bubble oscillations were investigated in [106] through high speed optical observations. It was shown that non-spherical bubble oscillations are significantly present in medically relevant ranges of bubble radii and applied acoustic pressures. Non-spherical oscillations develop preferentially at the resonance radius and may be present during SH oscillations [106]. Thus, for a more accurate modeling of the MB oscillations, deeper theoretical modeling of bubble coating, accounting for membrane shear and bending is required [106].

Another factor that can affect the pressure threshold for PD and amplitude of P2 oscillations is thermal damping. However, thermal damping is nonlinear [107] and application of the generally used linear models may lead to inaccurate predictions of large amplitude nonlinear oscillations. Thermal effects are shown [107] to become more important in uncoated bubble oscillations. However, for coated bubbles enclosed with gases like C3F8 thermal effects may be neglected [107] without impairing the solutions.

4.6 Summary of the results and conclusion

The findings of this study can be summarized as follows:

1- When $f = f_r$, the R/R_0 oscillations of the bubble increases monotonically with pressure, and above a pressure threshold PD occurs. This is concomitant with the appearance of SH oscillations.

2- When $f = f_r$, the occurrence of PD is most likely concomitant with bubble destruction as R/R_0 is very close to, or above, 2. Only bubbles with initial radii between 0.2 μm and 2.5 μm may

sustain stable P2 oscillations ($R/R_0 \leq 2$) and only for a narrow pressure range. The bubble with $R_0 = 0.2\mu m$ has the widest pressure range for non-destructive SH oscillations ($\approx$ 60 kPa)

3- For the majority of the bubble sizes studied, PD occurs at lower pressures when $f = 2f_r$ compared to $f = f_r$. The difference between the two pressure thresholds is 180-190 kPa for bubbles with R_0 bigger than 0.5 μm. As the bubble size decreases, the two pressure thresholds converge and then diverge with bubbles with R_0=0.2 and 0.3 μm having a lower pressure threshold when $f = f_r$.

4- When the bubbles are sonicated with $2f_r$, PD is more likely to result in non-destructive oscillations as $R/R_0 <$1.2. Even as pressure increases, the R_{max}/R_0 of the P2 oscillations does not exceed 2.

5- When $f = 2f_r$ and for bubbles with initial radii greater than 0.37 μm the evolution of the P2 oscillations exhibits a bowtie point. At this point, the two points on the Poincaré section have the same amplitude for R/R_0, however one point has a positive $\dot{R}$ while the other one has a negative $\dot{R}$.

6- When $f = 2f_r$, the period doubling happens over a much wider pressure range when compared to $f = f_r$. This makes the period doubling shape to be elongated in the bifurcation diagrams. Due to the lower oscillation amplitude and gentle bubble collapse (lower bubble wall velocities), the bubble can sustain stable P2 oscillations for a longer duration and over a broader range of acoustic pressures.

7- The occurrence of PD is concomitant with the initiation of the growth of SH and UH component of the signal. When $f = f_r$, the UH component of the signal undergoes the initiation first; however, when $f = 2f_r$ the SH component of the signal grows first.

8- Different stages of the PD when bowtie point occurs correspond to the initiation (start of the PD), growth and saturation of the SH and UH signals (at bowtie point when two red curves overlap) and then overlap of one of the maxima with one of the points of the Poincaré section at each period. The phenomena of initiation, growth and saturation of subharmonics have also been confirmed by experimental observations [68].

9- When $f = f_r$, the occurrence of PD is concomitant with a decrease in bubble wall velocity; however, when $f = 2f_r$, the bubble wall velocity undergoes a rapid increase as soon as PD occurs.

10- For bubbles with initial radii $> 0.3\mu m$ when PD occurs wall velocity is approximately 30-45 m/s; however, when $f = 2f_r$, the PD wall velocity is less than 10 m/s. This is another reason as to

why P2 oscillations are more likely non-destructive when $f = 2f_r$.

11- When sonicated with $2f_r$, the phase portrait of the P2 attractor differs from the P2 attractor that is generated through sonication with f_r. When $f = f_r$, the phase portrait consists of one bell shape orbit that undergoes a bell shape loop within itself. When $f = 2f_r$, the phase portrait of the P2 oscillations looks like a rotated heart (Fig. 4.4).

12- The SH component of the P_{sc} is higher when the bubble is sonicated with $2f_r$; however, maximum P_{sc} amplitude, FU and UH component of the P_{sc} are higher when $f = f_r$.

13- Bigger bubbles scatter sound more strongly; however, for a given gas volume smaller microbubbles may produce stronger scattering due to their greater numbers compared to bigger bubbles.

4.7 Appendix

4.7.1 Bifurcation structure and the dynamical properties of the bubbles with $R_0 = 0.2\mu m - 10\mu m$

Figure 4.12(a), displays the bifurcation structure of the R/R_0 of the bubbles as a function of pressure for bubbles with $R_0 = 0.2\mu m - 10\mu m$ when $f = f_r$. We have omitted the chaotic range of oscillations as the main focus here is to compare the mechanism of PD of bubbles of different sizes. The bifurcation curves are plotted using the conventional bifurcation analysis method as here we are only interested in the period of the bubble oscillations. All bubbles undergo a period doubling from P1 to P2; the pressure threshold for PD increases as the bubble size decreases. Fig. 4.12 (b), shows the corresponding maximum wall velocity. The wall velocity increases monotonically with pressure until the occurrence of PD. As soon as PD occurs, the maximum wall velocity starts decreasing with increasing pressure for bubbles with $R_0 > 0.4\mu m$. For bubbles with $R_0 \leq 0.4\mu m$ in diameter, the growth rate of wall velocity as a function of pressure elevation is reduced as soon as PD occurs. Smaller bubbles reach a higher P2 maximum wall velocities.

Fig. 4.13(a) displays the bifurcation structure of the R/R_0 oscillations of the bubble a function of pressure presented for bubbles with $R_0 = 0.2\mu m - 10\mu m$ when $f = 2f_r$. Bigger bubbles undergo PD at lower pressures and lower R/R_0 amplitude because of less constrictions imposed by viscous forces. The mechanism of PD is through a PD bifurcation that evolves in a form of bow tie shape for bubbles with $R_0 > 0.37\mu m$. The corresponding wall velocities in Fig. 4.13b exhibit an exact

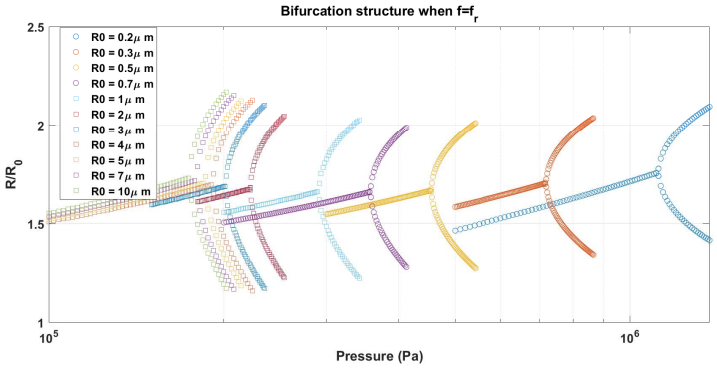

(a)

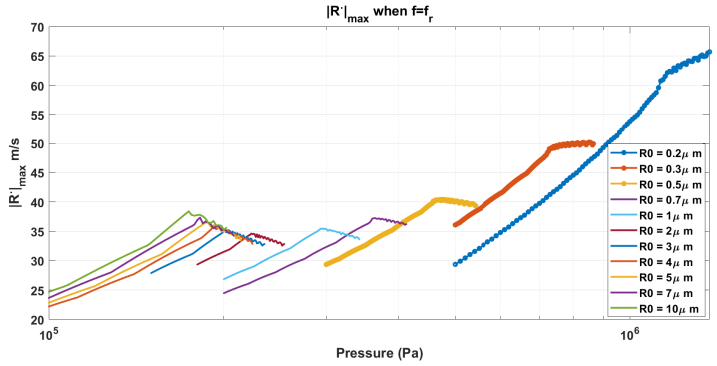

(b)

Figure 4.12: Bifurcation structure of R/R_0 of the bubble oscillations as a function of pressure when $f = f_r$ ($R_0 = 0.2\mu m - 10\mu m$). b) The corresponding maximum wall velocity amplitude ($|\dot{R(t)}|_{max}$) .

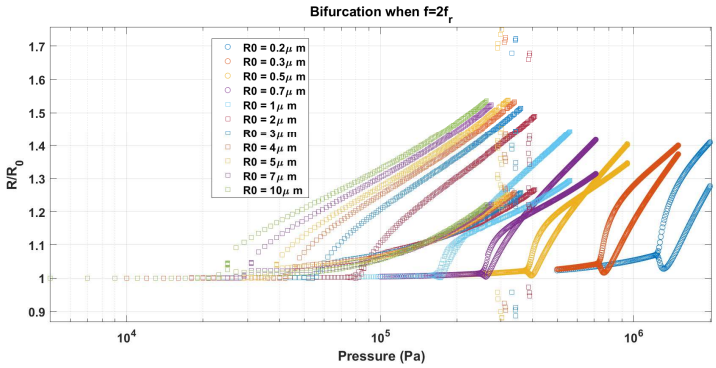

(a)

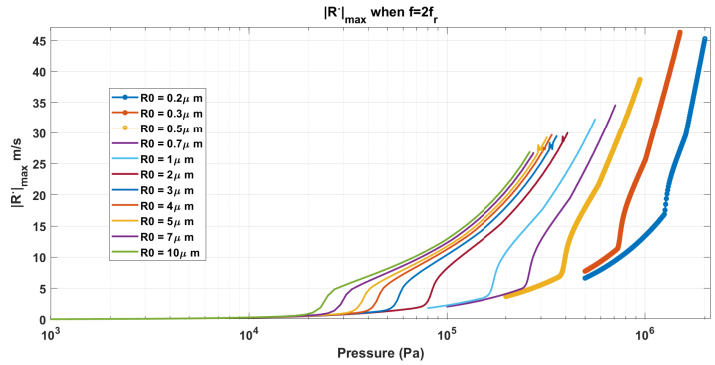

(b)

Figure 4.13: Bifurcation structure of R/R_0 of the bubble oscillations as a function of pressure when $f = 2f_r$ ($R_0 = 0.2\mu m - 10\mu m$). b) The corresponding maximum wall velocity amplitude ($|\dot{R(t)}|_{max}$) .

opposite behavior when compare with the case of sonication with $f = f_r$ (Fig. 4.12b). The wall velocity grows very slowly as pressure increases until PD occurs. As soon as PD occurs, the growth rate of the wall velocity dramatically increases. Additionally, when PD coccus, wall velocities are 3-36 times smaller compared to when the bubbles are sonicated with $f = f_r$. Lower wall velocity is an important factor for the sustainable non-destructive oscillations of bubbles.

Figure 4.14(a) shows the maximum value of $(P_{sc}^2)_{max}$ in the regime of non-destructive oscillations ($\frac{R}{R_0} \leq 2$). The maximum value of $(P_{sc}^2)_{max}$ increases monotonically with pressure. For bubbles that are able to exhibit PD while ($\frac{R}{R_0} \leq 2$), $(P_{sc}^2)_{max}$ undergo a decrease as soon as PD occurs consistent with the predictions of [15] for coated bubbles. This phenomenon is discussed in full detail in [15]. Bigger bubbles achieve higher $(P_{sc}^2)_{max}$ and can be destroyed at lower pressures.

When $f = 2f_r$ the maximum $(P_{sc}^2)_{max}$ increases monotonically with increasing pressure. As soon as PD occurs maximum $(P_{sc}^2)_{max}$ undergoes a rapid increase. For bubbles that exhibit the bow tie shape bifurcation ($R_0 > 0.37\mu m$) the $(P_{sc}^2)_{max}$ continues increasing rapidly until a second pressure

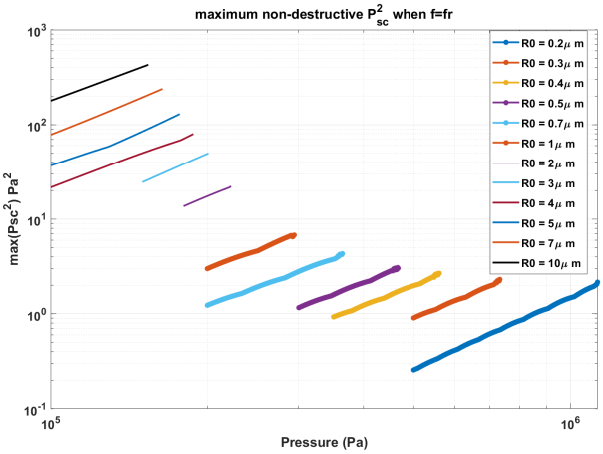

(a)

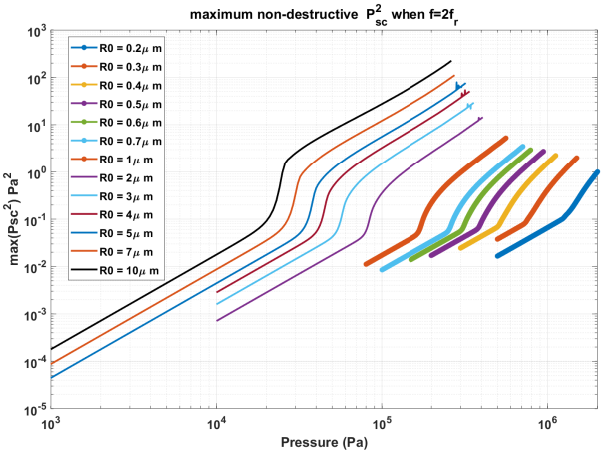

(b)

Figure 4.14: Maximum value of non-destructive P_{sc}^2 ($\frac{R}{R_0} \leq 2$) when : a) $f = f_r$, and b) $f = 2f_r$.

threshold. Above the second pressure threshold, the rate of change of $(P_{sc}^2)_{max}$ decreases. This pressure threshold is the same as the pressure where the bow tie point occurs in the conventional bifurcation diagram.

Figure 4.15a-b shows the fundamental component of the non-destructive $(P_{sc}^2)_{max}$ for $f = f_r$ and $f = 2f_r$ respectively. The fundamental component of the (P_{sc}) exhibit the same behavior as $(P_{sc}^2)_{max}$ as a function of pressure.

Figure 4.16 shows the amplitude of the SH component of the (P_{sc}) when $f = f_r$ and $f = 2f_r$ respectively. When f=fr, only a fraction of the bubble sizes that are shown ($R_0 < 4\mu m$) are able to undergo non-destructive PD ($\frac{R}{R_0} \leq 2$); this is seen as a rapid increase in the SH component as the pressure increases above the PD threshold. However, the pressure range of P2 oscillations

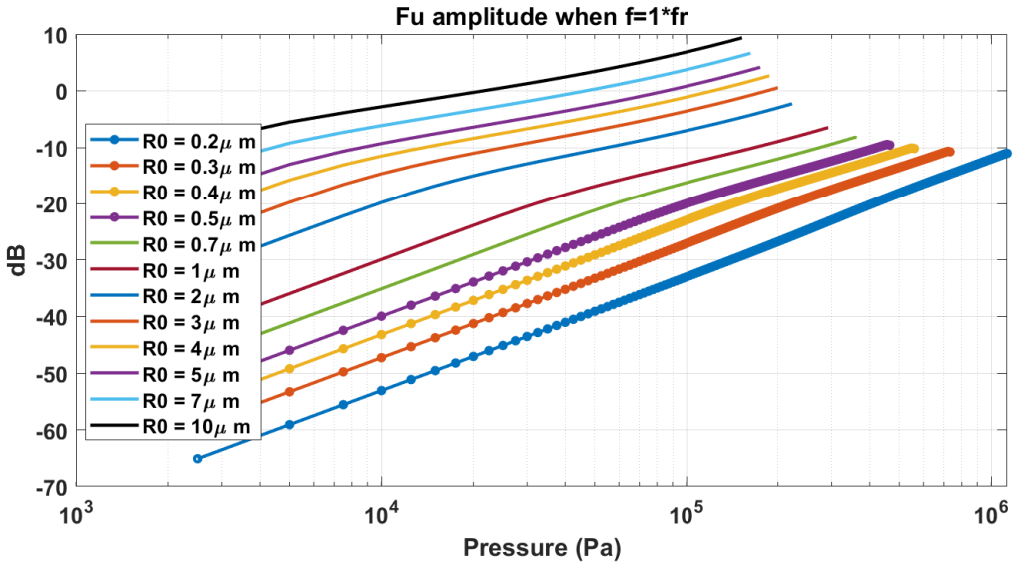

(a)

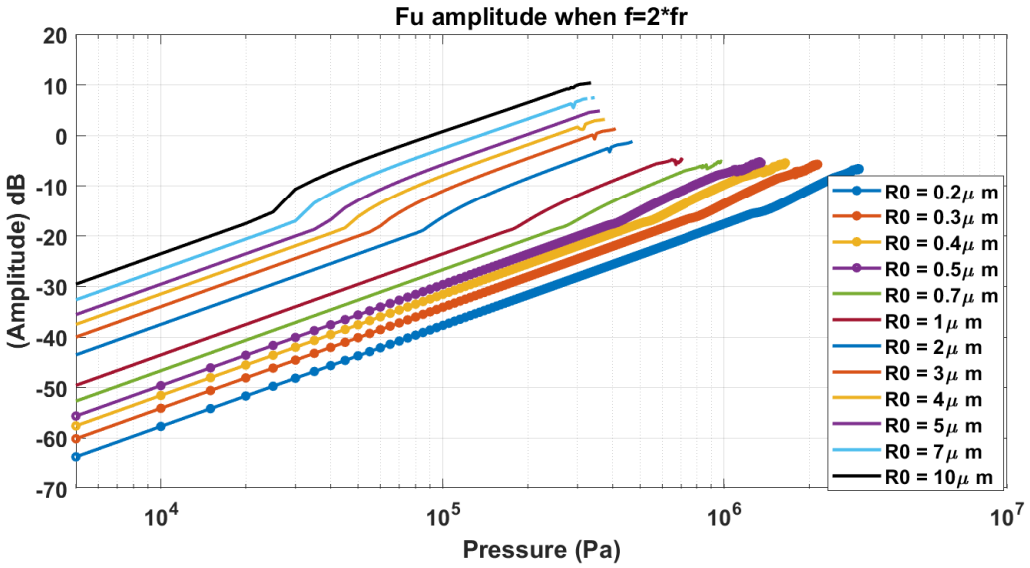

(b)

Figure 4.15: Fundamental (FU) amplitude of the intensity of non-destructive ($\frac{R}{R_0} \leq 2$) P_{sc} when : a) $f = f_r$, and b) $f = 2f_r$.

for non-destructive oscillations is very small. When $f = 2f_r$ (Fig. 4.16b), the SH component of the signal grows rapidly when PD occurs and the rate of increase decreases above a second pressure threshold. Fig. 4.17, illustrates the UH component of the (P_{sc}) when $f = f_r$ and $f = 2f_r$ respectively. The UH component of the signal exhibits the same trend as the SH component shown in Fig. 4.16.

4.7.2 higher order attractors at f_r and $2f_r$

Figure 4.18 pays a closer attention on the P6 behavior that is seen for bubbles ($2.5 < R_0 < 5$) when $f = 2f_r$ and initial conditions are $R(0) = R_0$ and $\dot{R(0)} = 0$. This is a condition which is common in biomedical imaging applications [15]). Figure 4.18a shows the generation of the P6 behavior (black arrow) through a saddle node bifurcation from P2 that only lasts for a small pressure window. The radial oscillations of $\frac{R}{R_0} \leq 2$ as a function of period are shown in figure 4.18b; the signal exhibits 6 maxima (red circles) that repeat themselves once every 6 acoustic cycles. The phase portrait of the signal has 3 loops; each are enclosing a smaller loop in Fig. 4.18c. The back-scatter frequency spectrum is shown in Figure 4.18d, depicting the existence of 5 SHs of f/6, f/3, f/2, 2f/3 and 5f/6 (with the f/2 component the strongest). The period 6 shown here (we name it P6-2) has distinct differences from the P6 that can be generated by sonicating a bubble with a frequency that is about 6 times the resonance frequency of the bubble [13]. The later is generated through a saddle node bifurcation [13] from a period 1 oscillations (we name it P6-1) while the former that is shown in figure 4.18 is generated through a saddle node bifurcation from period 2 oscillations. Additionally, the P6-1 R/R_0 signal has one envelope with 6 or 5 maxima while a P6-2 R/R_0 signal has three envelopes each with 2 maxima. When the frequency spectrum of the P_{sc} is considered, the f/6 is the strongest SH component of a P6-1 oscillation [13] while f/2 is the strongest SH component of a P6-2 oscillations.

Another interesting nonlinear oscillation that was observed in this paper is a P3 signal that is generated through a saddle node bifurcation from P2 oscillations when $f = f_r$. This behavior was observed for bubbles of size $1\mu m < R_0 < 2\mu m$. Figure 4.19a shows the P3 oscillation (black arrow) that is generated through a saddle node bifurcation from a P2 oscillation. The radial oscillations shown in Fig. 4.19b display a signal with three maxima with two repeating envelopes once every 3 acoustic cycles; one has two maxima and one has one maxima. The phase portrait in Fig. 4.19c

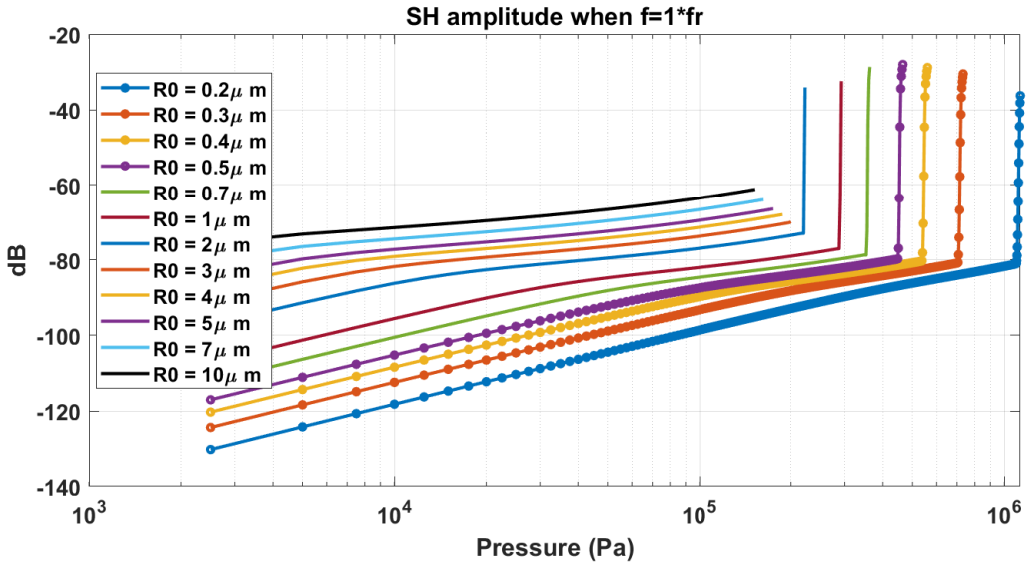

(a)

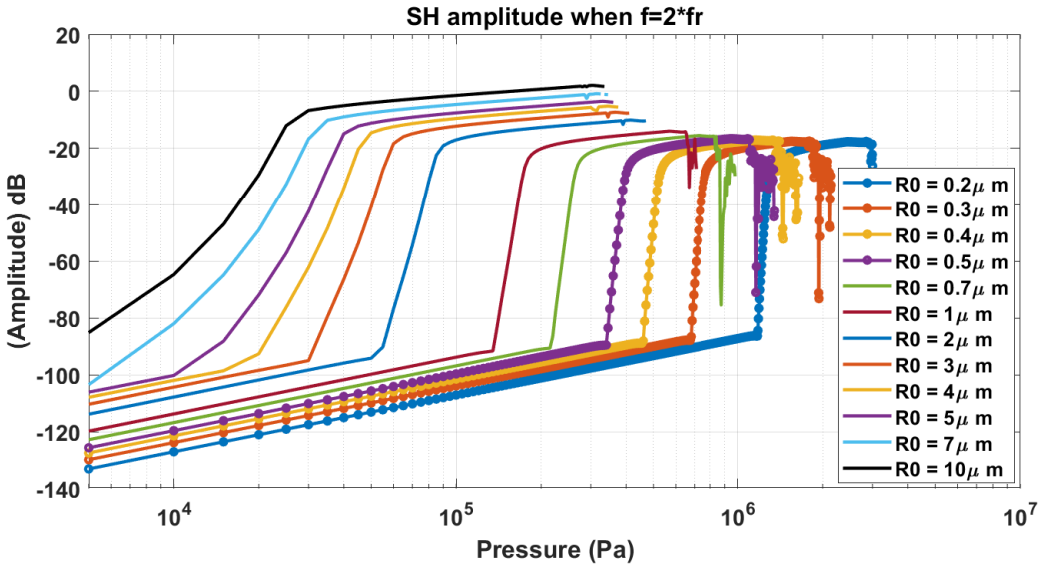

(b)

Figure 4.16: Sub-harmonic (SH) amplitude of the intensity of non-destructive ($\frac{R}{R_0} \leq 2$) P_{sc} when : a) $f = f_r$, and b) $f = 2f_r$.

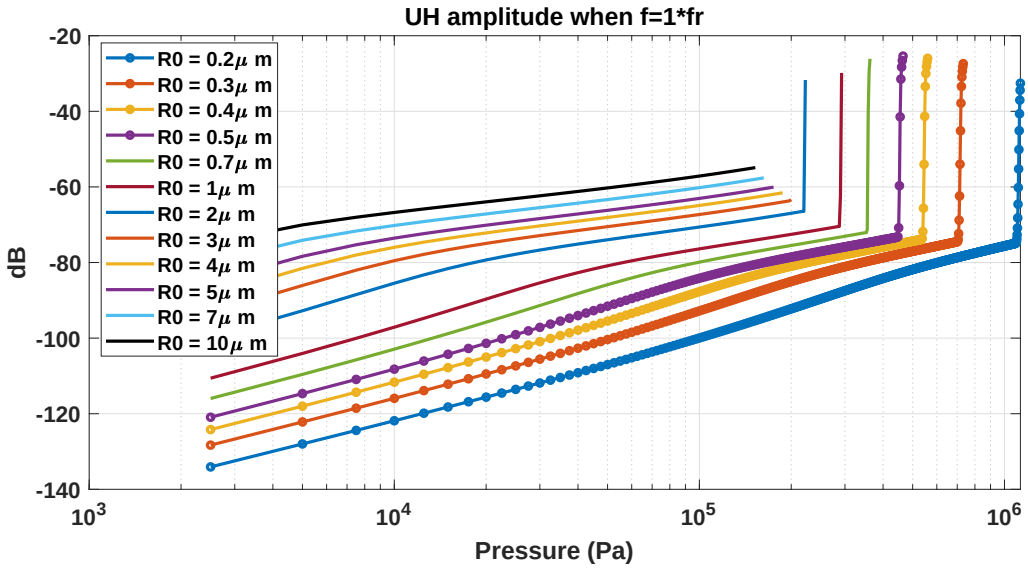

(a)

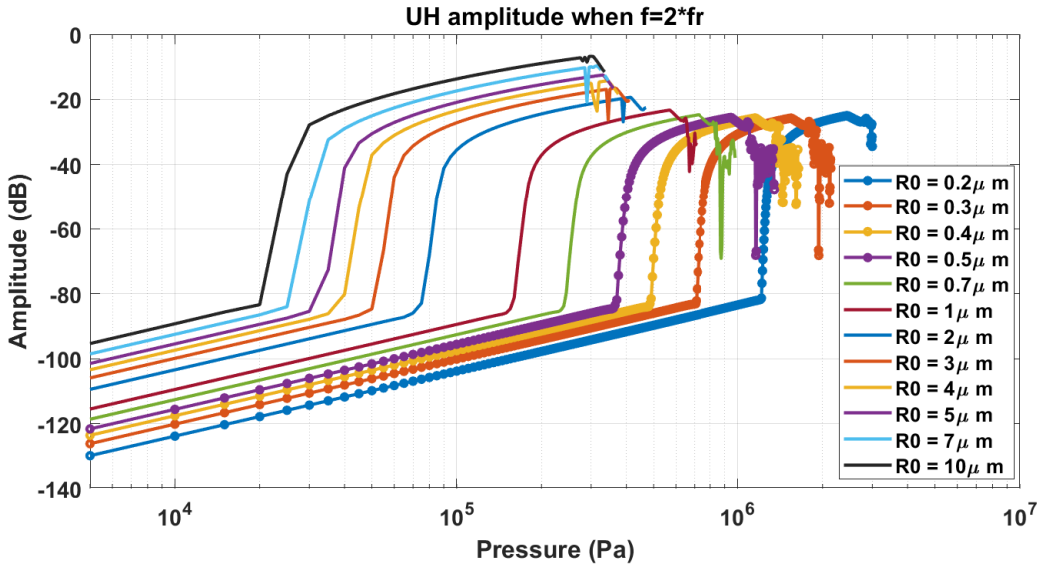

(b)

Figure 4.17: Ultra-harmonic (UH) amplitude of the intensity of non-destructive ($\frac{R}{R_0} \leq 2$) P_{sc} when : a) $f = f_r$, and b) $f = 2f_r$.

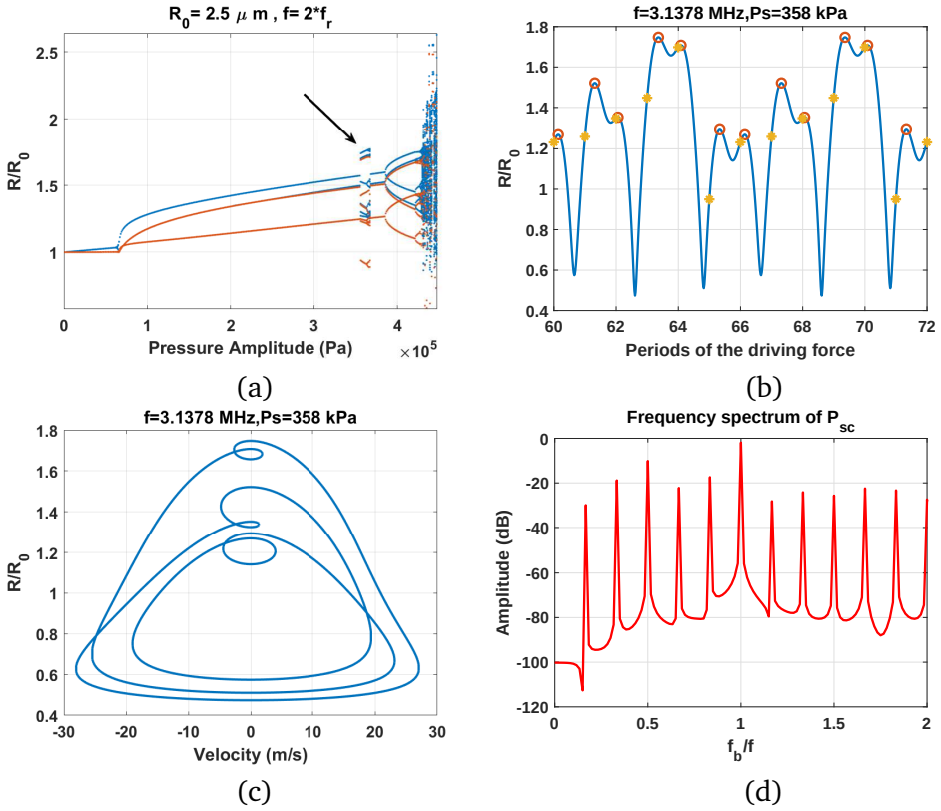

Figure 4.18: Bifurcation structures of the bubble with $R_0 = 2.5\mu m$ and $f = 2f_r$ as a function of pressure highlighting a period 6 signal (black arrow). Time-series of the P6 R/R_0 oscillation as a function of the driving acoustic period when $f = 2f_r$ and P_A=358 kPa. C) Phase portrait of the P6 attractor. d) the corresponding frequency spectrum of the backscattered pressure.

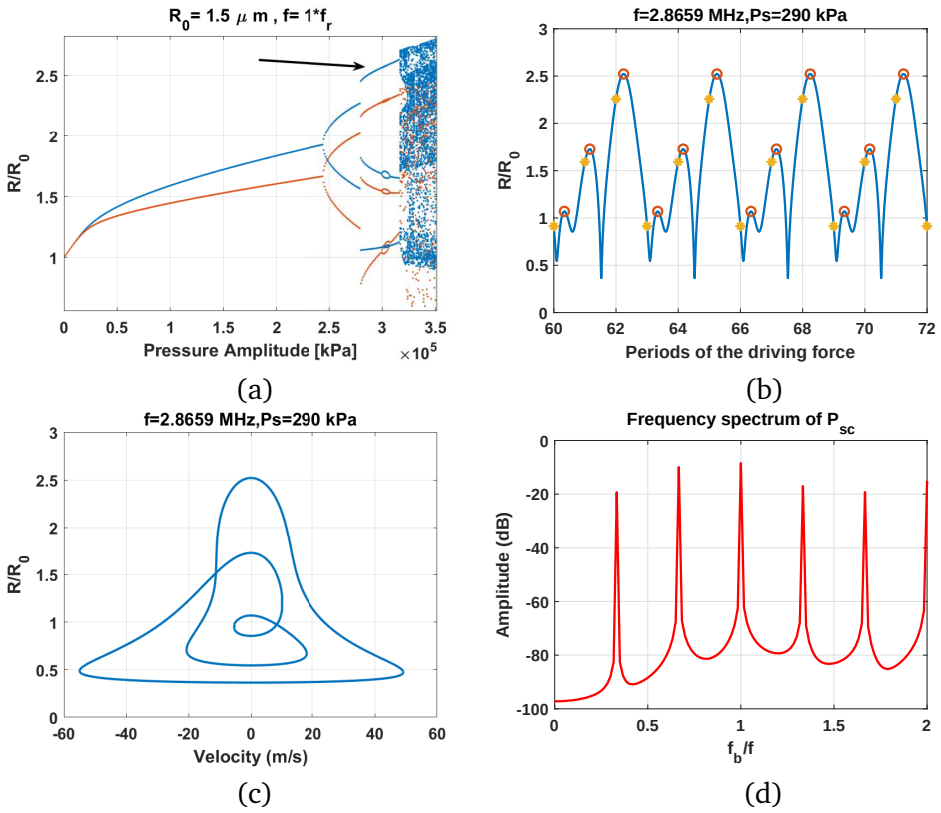

Figure 4.19: Bifurcation structures of the bubble with $R_0 = 1.5\mu m$ and $f = f_r$ as a function of pressure highlighting a period 3 signal (black arrow). Time-series of the P3 R/R_0 oscillation as a function of the driving acoustic period when $f = 2f_r$ and P_A=290 kPa. C) Phase portrait of the P3 attractor. d) the corresponding frequency spectrum of the backscattered pressure..

consists of two orbits sharing an internal bend. The frequency spectrum in Fig. 4.19d, depicts three SHs with frequencies of f/3 and 2f/3 with 2f/3 stronger than the f/3 component. We name this a P3-2 oscillation and it has distinct differences from a P3-1 oscillation (a P3-1 occurs when a bubble is sonicated with a frequency that is approximately 3 times its resonance frequency and is generated via a saddle node bifurcation from a P1 oscillation [13]). The main difference is mechanism of generation as it is discussed above. The second difference is the shape of the radial oscillations; P3-1 has one envelope with 2 or 3 peaks that repeat itself once every three acoustic cycle. The phase portrait of a P3-1 oscillation consists of one orbit with two distinct internal bends and the f/3 component of the frequency spectrum is stronger than the 2f/3 component.

Bibliography

[1] Parlitz, U., et al. ”Bifurcation structure of bubble oscillators.” The Journal of the Acoustical Society of America 88.2 (1990): 1061-1077.

[2] Prosperetti, Andrea, Lawrence A. Crum, and Kerry W. Commander. ”Nonlinear bubble dynamics.” The Journal of the Acoustical Society of America 83.2 (1988): 502-514.

[3] Leighton, Timothy. The acoustic bubble. Academic press, 2012.

[4] Lauterborn, Werner, and Thomas Kurz. ”Physics of bubble oscillations.” Reports on progress in physics 73.10 (2010): 106501.

[5] Lauterborn, W., and U. Parlitz. ”Methods of chaos physics and their application to acoustics.” The Journal of the Acoustical Society of America 84.6 (1988): 1975-1993.

[6] Lauterborn, Werner, and Eckehart Cramer. ”Subharmonic route to chaos observed in acoustics.” Physical Review Letters 47.20 (1981): 1445.

[7] Lauterborn, Werner, and Joachim Holzfuss. ”Acoustic chaos.” International Journal of bifurcation and Chaos 1.01 (1991): 13-26.

[8] Prosperetti, A., and A. Lezzi. ”Bubble dynamics in a compressible liquid. Part 1. First-order theory.” Journal of Fluid Mechanics 168 (1986): 457-478.

[9] Hoff, Lars. Acoustic characterization of contrast agents for medical ultrasound imaging. Springer Science & Business Media, 2001.

[10] van der Meer, Sander M., et al. ”Microbubble spectroscopy of ultrasound contrast agents.” The Journal of the Acoustical Society of America 121.1 (2007): 648-656.

[11] Ashokkumar, Muthupandian, et al. ”Bubbles in an acoustic field: an overview.” Ultrasonics Sonochemistry 14.4 (2007): 470-475.

[12] Leighton, T. G. ”From seas to surgeries, from babbling brooks to baby scans: The acoustics of gas bubbles in liquids.” International Journal of Modern Physics B 18.25 (2004): 3267-3314.

[13] Sojahrood, Amin Jafari, and Michael C. Kolios. ”Classification of the nonlinear dynamics and bifurcation structure of ultrasound contrast agents excited at higher multiples of their resonance frequency.” Physics Letters A 376.33 (2012): 2222-2229.

[14] Behnia, S., Sojahrood, A.J., Soltanpoor, W. and Jahanbakhsh, O., 2009. Suppressing chaotic oscillations of a spherical cavitation bubble through applying a periodic perturbation. Ultrasonics sonochemistry, 16(4), pp.502-511.

[15] Sojahrood, Amin Jafari, et al. ”Influence of the pressure-dependent resonance frequency on the bifurcation structure and backscattered pressure of ultrasound contrast agents: a numerical investigation.” Nonlinear Dynamics 80.1-2 (2015): 889-904.

[16] Behnia S., Jafari A., Soltanpoor W. and Jahanbakhsh O. Nonlinear transitions of a spherical cavitation bubble, Choas, Solitons & Fractals, 41 (2), (2009): 818-828.

[17] Hegedus, Ferenc, and László Kullmann. ”Basins of attraction in a harmonically excited spherical bubble model.” Periodica Polytechnica Mechanical Engineering 56.2 (2012): 125-132.

[18] Hegedus, Ferenc, et al. ”Non-feedback technique to directly control multistability in nonlinear oscillators by dual-frequency driving.” Nonlinear Dynamics (2018): 1-21.

[19] Hegedűs, Ferenc, and Csanád Kalmár. ”Dynamic stabilization of an asymmetric nonlinear bubble oscillator.” Nonlinear Dynamics: 1-18.

[20] Hegedűs, Ferenc. ”Topological analysis of the periodic structures in a harmonically driven bubble oscillator near Blake’s critical threshold: Infinite sequence of two-sided Farey ordering trees.” Physics Letters A 380.9-10 (2016): 1012-1022.

[21] Varga, Roxána, and Ferenc Hegedűs. ”Classification of the bifurcation structure of a periodically driven gas bubble.” Nonlinear Dynamics 86.2 (2016): 1239-1248.

[22] Hegedűs, F., Cs Hős, and L. Kullmann. ”Stable period 1, 2 and 3 structures of the harmonically excited Rayleigh–Plesset equation applying low ambient pressure.” The IMA Journal of Applied Mathematics 78.6 (2012): 1179-1195.

[23] Zhang, Yuning. ”Chaotic oscillations of gas bubbles under dual-frequency acoustic excitation.” Ultrasonics sonochemistry40 (2018): 151-157.

[24] Zhang, Yuning, Yuhang Gao, and Xiaoze Du. ”Stability mechanisms of oscillating vapor bubbles in acoustic fields.” Ultrasonics sonochemistry 40 (2018): 808-814.

[25] Zhang, Y. N., and S. C. Li. ”Bubble dynamics under acoustic excitation with multiple frequencies.” IOP Conference Series: Materials Science and Engineering. Vol. 72. No. 1. IOP Publishing, 2015.

[26] hang, Yuning, and Shengcai Li. ”Combination and simultaneous resonances of gas bubbles oscillating in liquids under dual-frequency acoustic excitation.” Ultrasonics sonochemistry 35 (2017): 431-439.

[27] Pandey, V., 2019. Asymmetricity and sign reversal of secondary Bjerknes force from strong nonlinear coupling in cavitation bubble pairs. Physical Review E, 99(4), p.042209.

[28] Dogan, Hakan, Paul R. White, and Timothy G. Leighton. ”Acoustic wave propagation in gassy porous marine sediments: The rheological and the elastic effects.” The Journal of the Acoustical Society of America 141.3 (2017): 2277-2288.

[29] Suslick, Kenneth S. ”Sonochemistry.” science 247.4949 (1990): 1439-1445.

[30] Storey, Brian D., and Andrew J. Szeri. ”Water vapour, sonoluminescence and sonochemistry.” Proceedings of the Royal Society of London A: Mathematical, Physical and Engineering Sciences. Vol. 456. No. 1999. The Royal Society, 2000.

[31] Crum, Lawrence A., et al., eds. Sonochemistry and sonoluminescence. Vol. 524. Springer Science & Business Media, 2013.

[32] Yasui, Kyuichi, et al. ”Theoretical study of single-bubble sonochemistry.” The Journal of chemical physics 122.22 (2005): 224706.

[33] Segers, Tim, et al. ”Monodisperse Versus Polydisperse Ultrasound Contrast Agents: Non-Linear Response, Sensitivity, and Deep Tissue Imaging Potential.” Ultrasound in medicine & biology 44.7 (2018): 1482-1492.

[34] Perera, Reshani, et al. ”Ultrasound Contrast Agents and Delivery Systems in Cancer Detection and Therapy.” Advances in Cancer Research (2018).

[35] Ferrara, Katherine, Rachel Pollard, and Mark Borden. ”Ultrasound microbubble contrast agents: fundamentals and application to gene and drug delivery.” Annu. Rev. Biomed. Eng. 9 (2007): 415-447.

[36] Forsberg, Flemming, William T. Shi, and B. B. Goldberg. ”Subharmonic imaging of contrast agents.” Ultrasonics 38.1-8 (2000): 93-98.

[37] McDannold, N., N. Vykhodtseva, and K. Hynynen. ”Targeted disruption of the blood–brain barrier with focused ultrasound: association with cavitation activity.” Physics in Medicine & Biology 51.4 (2006): 793.

[38] Holt, R. Glynn, and Ronald A. Roy. ”Measurements of bubble-enhanced heating from focused, MHz-frequency ultrasound in a tissue-mimicking material.” Ultrasound in medicine & biology27.10 (2001): 1399-1412.

[39] Yoshizawa, Shin, et al. ”High intensity focused ultrasound lithotripsy with cavitating microbubbles.” Medical & biological engineering & computing 47.8 (2009): 851-860.

[40] Roberts, William W., et al. ”Pulsed cavitational ultrasound: a noninvasive technology for controlled tissue ablation (histotripsy) in the rabbit kidney.” The Journal of urology 175.2 (2006): 734-738.

[41] H., Kleven, R.T., Peng, T., Palaniappan, A., Karani, K.B., Huang, S., McPherson, D.D. and Holland, C.K., 2019. In vitro characterization of sonothrombolysis and echocontrast agents to treat ischemic stroke. Scientific reports, 9(1), p.9902.

[42] Bader, K.B., Bouchoux, G. and Holland, C.K., 2016. Sonothrombolysis. In Therapeutic Ultrasound (pp. 339-362). Springer, Cham.

[43] Holt, R. Glynn, and D. Felipe Gaitan. ”Observation of stability boundaries in the parameter space of single bubble sonoluminescence.” Physical review letters 77.18 (1996): 3791.

[44] Holt, R. Glynn, et al. ”Chaotic sonoluminescence.” Physical review letters 72.9 (1994): 1376.

[45] Gaitan, D. Felipe, and R. Glynn Holt. ”Experimental observations of bubble response and light intensity near the threshold for single bubble sonoluminescence in an air-water system.” Physical Review E 59.5 (1999): 5495.

[46] Holt, R. Glynn, and Lawrence A. Crum. ”Acoustically forced oscillations of air bubbles in water: Experimental results.” The Journal of the Acoustical Society of America 91.4 (1992): 1924-1932.

[47] Sijl, J., Dollet, B., Overvelde, M., Garbin, V., Rozendal, T., de Jong, N., Lohse, D. and Versluis, M., 2010. Subharmonic behavior of phospholipid-coated ultrasound contrast agent

[48] Lauterborn, Werner, and Thomas Kurz. ”The Bubble Challenge for High-Speed Photography.” The Micro-World Observed by Ultra High-Speed Cameras. Springer, Cham, 2018. 19-47.

[49] Lauterborn, Werner, and Claus-Dieter Ohl. ”Cavitation bubble dynamics.” Ultrasonics sonochemistry 4.2 (1997): 65-75.

[50] Jafari Sojahrood, Amin, Raffi Karshafian, and Michael C. Kolios. ”Bifurcation structure of the ultrasonically excited microbubbles undergoing buckling and rupture.” Proceedings of Meetings on Acoustics ICA2013. Vol. 19. No. 1. ASA, 2013.

[51] Sojahrood, Amin Jafari, Raffi Karshafian, and Michael C. Kolios. ”Detection and characterization of higher order nonlinearities in the oscillations of Definity at higher frequencies and very low acoustic pressures.” Ultrasonics Symposium (IUS), 2012 IEEE International. IEEE, 2012.

[52] Coussios, CC, et al. ”Role of acoustic cavitation in the delivery and monitoring of cancer treatment by high-intensity focused ultrasound (HIFU).” International Journal of Hyperthermia 23.2 (2007): 105-120.

[53] K.J. Haworth, et al., Passive imaging with pulsed ultrasound insonations, The Journal of the Acoustical Society of America, 132(1) (2012): 544-553.

[54] M.A. OReilly, et al, Focused-ultrasound disruption of the blood-brain barrier using closely-timed short pulses: inflence of sonication parameters and injection rate, Ultrasound in medicine & biology 37 (2011): 587-594.

[55] Leighton, T. G., et al. "Acoustic bubble sizing by the combination of subharmonic emissions with an imaging frequency." Ultrasonics 29.4 (1991): 319-323.

[56] Goertz, David E., et al. "High frequency nonlinear B-scan imaging of microbubble contrast agents." IEEE transactions on ultrasonics, ferroelectrics, and frequency control 52.1 (2005): 65-79.

[57] Goertz, David E., et al. "Subharmonic contrast intravascular ultrasound for vasa vasorum imaging." Ultrasound in medicine & biology 33.12 (2007): 1859-1872.

[58] Forsberg, Flemming, et al. "Breast lesions: imaging with contrast-enhanced subharmonic US—initial experience." Radiology 244.3 (2007): 718-726.

[59] Shi, WilliamT, et al. "Pressure dependence of subharmonic signals from contrast microbubbles." Ultrasound in medicine & biology 25.2 (1999): 275-283.

[60] Forsberg, Flemming, et al. "In vivo pressure estimation using subharmonic contrast microbubble signals: Proof of concept." IEEE transactions on ultrasonics, ferroelectrics, and frequency control 52.4 (2005): 581-583.

[61] Dave, Jaydev K., et al. "Noninvasive LV pressure estimation using subharmonic emissions from microbubbles." JACC: Cardiovascular Imaging 5.1 (2012): 87-92

[62] O'Reilly MA, Hynynen K. Blood-brain barrier: real-time feedback-controlled focused ultrasound disruption by using an acoustic emissions-based controller. Radiology. 2012;263:96–106

[63] Tsai, C.-H., Zhang, J.-W., Liao, Y.-Y. & Liu, H.-L. Real-time monitoring of focused ultrasound blood-brain barrier opening via subharmonic acoustic emission detection: implementation of confocal dual-frequency piezoelectric transducers. Phys. Med. Biol. 61, 2926–2946 (2016)

[64] Eller, Anthony, and H. G. Flynn. ”Generation of subharmonics of order one-half by bubbles in a sound field.” The Journal of the Acoustical Society of America 46.3B (1969): 722-727.

[65] Prosperetti, Andrea. ”Nonlinear oscillations of gas bubbles in liquids: steady-state solutions.” The Journal of the Acoustical Society of America 56.3 (1974): 878-885.

[66] Prosperetti, Andrea. ”Application of the subharmonic threshold to the measurement of the damping of oscillating gas bubbles.” The Journal of the Acoustical Society of America61.1 (1977): 11-16.

[67] Prosperetti, Andrea. ”A general derivation of the subharmonic threshold for non-linear bubble oscillations.” The Journal of the Acoustical Society of America 133.6 (2013): 3719-3726

[68] Krishna, P. D., P. M. Shankar, and V. L. Newhouse. ”Subharmonic generation from ultrasonic contrast agents.” Physics in Medicine & Biology 44.3 (1999): 681.

[69] Shankar, P. M., P. D. Krishna, and V. L. Newhouse. ”Subharmonic backscattering from ultrasound contrast agents.” The Journal of the Acoustical Society of America106.4 (1999): 2104-2110.

[70] Kimmel, Eitan, et al. ”Subharmonic response of encapsulated microbubbles: Conditions for existence and amplification.” Ultrasound in medicine & biology 33.11 (2007): 1767-1776.

[71] Katiyar, Amit, and Kausik Sarkar. ”Effects of encapsulation damping on the excitation threshold for subharmonic generation from contrast microbubbles.” The Journal of the Acoustical Society of America 132.5 (2012): 3576-3585.

[72] Katiyar, Amit, and Kausik Sarkar. ”Excitation threshold for subharmonic generation from contrast microbubbles.” The Journal of the Acoustical Society of America 130.5 (2011): 3137-3147.

[73] Jiménez-Fernández, J. ”Dependence of the subharmonic signal from contrast agent microbubbles on ambient pressure: A theoretical analysis.” The Journal of the Acoustical Society of America 143.1 (2018): 169-179.

[74] Sojahrood, A. J., et al. ”A comprehensive bifurcation method to analyze the super-harmonic and ultra-harmonic behavior of the acoustically excited bubble oscillator.” arXiv preprint arXiv:1810.01239 (2018).

[75] A.J. Sojahrood, D. Wegierak, H. Haghi, R. Karshfian, and M. C. Kolios. A simple method to analyze the super-harmonic and ultra-harmonic behavior of the acoustically excited bubble oscillator. Ultrasonics sonochemistry, 54 (2019); 99-109.

[76] Marmottant, P., van der Meer, S., Emmer, M., Versluis, M., de Jong, N., Hilgenfeldt, S., andLohse, D. (2005). A model for large amplitude oscillations of coated bubbles accounting for buckling and rupture. The Journal of the Acoustical Society of America, 118(6), 3499-3505.

[77] Allen, J. S., & Roy, R. A. (2000). Dynamics of gas bubbles in viscoelastic fluids. I. Linear viscoelasticity. The Journal of the Acoustical Society of America, 107(6), 3167-3178.

[78] Yang, X. and Church, C.C., 2005. A model for the dynamics of gas bubbles in soft tissue. The Journal of the Acoustical Society of America, 118(6), pp.3595-3606.

[79] Allen, J. S., and Roy, R. A. (2000). Dynamics of gas bubbles in viscoelastic fluids. II. Nonlinear viscoelasticity. The Journal of the Acoustical Society of America, 108(4), 1640-1650.

[80] Keller, Joseph B., and Michael Miksis. ”Bubble oscillations of large amplitude.” The Journal of the Acoustical Society of America 68.2 (1980): 628-633.

[81] Hilgenfeldt, Sascha, Detlef Lohse, and Michael Zomack. ”Sound scattering and localized heat deposition of pulse-driven microbubbles.” The Journal of the Acoustical Society of America 107.6 (2000): 3530-3539.

[82] Haghi, H., Sojahrood, A.J. and Kolios, M.C., 2019. Collective nonlinear behavior of interacting polydisperse microbubble clusters. Ultrasonics Sonochemistry, p.104708.

[83] Khismatullin, D.B., 2004. Resonance frequency of microbubbles: Effect of viscosity. The Journal of the Acoustical Society of America, 116(3), pp.1463-1473.

[84] Flynn, H.G., Church, C.C.: Transient pulsations of small gas bubbles in water. J. Acoust. Soc. Am. 84, 985–998 (1988).

[85] Varga, R., Klapcsik, K. and Hegedűs, F., 2020. Route to shrimps: Dissipation driven formation of shrimp-shaped domains. Chaos, Solitons & Fractals, 130, p.109424.

[86] Freitas, R.A., 1999. Nanomedicine, volume I: basic capabilities (Vol. 1). Georgetown, TX: Landes Bioscience. (P. 124 and P. 211)

[87] Apfel, R.E., 1980. Some new results on cavitation threshold prediction and bubble dynamics. In Cavitation and inhomogeneities in underwater acoustics (pp. 79-83). Springer, Berlin, Heidelberg.

[88] Plesset, M.S., Mitchell, T.P.: On the stability of the spherical shape of a vapor cavity in a liquid. Quart. Appl. Math. 13419–430 (1956).

[89] Chomas, J.E., Dayton, P.A., May, D., Ferrara, K., Threshold of fragmentation for ultrasonic contrast agents. J. Biomed. Opt. 6(2), 141–150 (2001).

[90] Chomas, J.E., Dayton, P.A., May, D., Klibanov, A., Ferrara,K., Optical observation of contrast agent destruction. Appl. Phys. Lett. 77, 1056 (2000).

[91] Bloch, H.,Wan, M., Dayton, P.A., Ferrara, K., Optical observation of lipid- and polymer-shelled ultrasound microbubbles. Appl.Phys. lett. 84, 631 (2004).

[92] Chomas, J., Dayton, P., May, D., Ferrara, K., Nondestructive subharmonic imaging. IEEE Trans. Ultrason. Ferroelectr. Freq. Control 9(7), 883–892 (2002).

[93] Santin, M.D., King, D.A., Foiret, J., Haak, A., O'Brien Jr, W.D., Bridal, S.L., Encapsulated contrast microbubble radial oscillation associated with postexcitation pressure peaks. J. Acoust. Soc. Am. 127, 1156 (2010).

[94] King, D.A., W O'Brien Jr, W.D.: Comparison between maximum radial expansion of ultrasound contrast agents and experimental postexcitation signal results. J. Acoust. Soc. Am. 129, 114 (2011).

[95] King, D.A., Malloy, M.J., Roberts, A.C., Haak, A., Yoder, C.C., O'Brien, W.D.: Determination of postexcitation thresholds for single ultrasound contrast agent microbubbles using double passive cavitation detection. J. Acoust. Soc. Am. 127, 3449 (2010).

[96] Brock-Fisher, A.G., Poland, M., Rafter, P. Means for increasing sensitivity in nonlinear imaging systems. US Patent 5577505 (1996).

[97] Paul, S., Katiyar, A., Sarkar, K., Chatterjee, D., Shi, W.T. and Forsberg, F., 2010. Material characterization of the encapsulation of an ultrasound contrast microbubble and its subharmonic response: Strain-softening interfacial elasticity model. The Journal of the Acoustical Society of America, 127(6), pp.3846-3857.

[98] Helfield, B.L., Cherin, E., Foster, F.S. and Goertz, D.E., 2012. Investigating the subharmonic response of individual phospholipid encapsulated microbubbles at high frequencies: A comparative study of five agents. Ultrasound in medicine & biology, 38(5), pp.846-863.

[99] Frinking, P.J., Gaud, E., Brochot, J. and Arditi, M., 2010. Subharmonic scattering of phospholipid-shell microbubbles at low acoustic pressure amplitudes. IEEE transactions on ultrasonics, ferroelectrics, and frequency control, 57(8), pp.1762-1771.

[100] Sijl, J., Dollet, B., Overvelde, M., Garbin, V., Rozendal, T., de Jong, N., Lohse, D. and Versluis, M., 2010. Subharmonic behavior of phospholipid-coated ultrasound contrast agent microbubbles. The Journal of the Acoustical Society of America, 128(5), pp.3239-3252.

[101] Faez, T., Emmer, M., Docter, M., Sijl, J., Versluis, M. and de Jong, N., 2011. Characterizing the subharmonic response of phospholipid-coated microbubbles for carotid imaging. Ultrasound in medicine & biology, 37(6), pp.958-970.

[102] Faez, T., Skachkov, I., Versluis, M., Kooiman, K. and de Jong, N., 2012. In vivo characterization of ultrasound contrast agents: microbubble spectroscopy in a chicken embryo. Ultrasound in medicine & biology, 38(9), pp.1608-1617.

[103] Klapcsik, K. and Hegedűs, F., 2019. Study of non-spherical bubble oscillations under acoustic irradiation in viscous liquid. Ultrasonics sonochemistry, 54, pp.256-273.

[104] Holt, R.G. and Crum, L.A., 1992. Acoustically forced oscillations of air bubbles in water: Experimental results. The Journal of the Acoustical Society of America, 91(4), pp.1924-1932.

[105] Versluis, M., Goertz, D.E., Palanchon, P., Heitman, I.L., van der Meer, S.M., Dollet, B., de Jong, N. and Lohse, D., 2010. Microbubble shape oscillations excited through ultrasonic parametric driving. Physical review E, 82(2), p.026321.

[106] Dollet, B., Van Der Meer, S.M., Garbin, V., De Jong, N., Lohse, D. and Versluis, M., 2008. Nonspherical oscillations of ultrasound contrast agent microbubbles. Ultrasound in medicine & biology, 34(9), pp.1465-1473.

[107] Sojahrood, A.J., Haghi, H., Li, Q., Porter, T.M., Karshafian, R. and Kolios, M.C., 2019. Nonlinear energy loss in the oscillations of coated and uncoated bubbles: Role of thermal, radiation damping and encapsulating shell at various excitation pressures. arXiv preprint arXiv:1909.08793.

Chapter 5

Nonlinear dynamics of acoustic bubbles excited by their pressure dependent subharmonic resonance frequency: oversaturation and enhancement of the subharmonic signal

5.1 Abstract

The acoustic bubble is an example of a highly nonlinear system which is the building block of several applications and phenomena ranging from underwater acoustics to sonochemistry and medicine. Nonlinear behavior of bubbles, and most importantly $\frac{1}{2}$ order subharmonics (SH), are used to increase the contrast to tissue ratio (CTR) in diagnostic ultrasound (US) and to monitor bubble mediated therapeutic US. It is shown experimentally and numerically that when bubbles are sonicated with their SH resonance frequency ($f_{sh} = 2f_r$ where f_r is the linear resonance frequency), SHs are generated at the lowest excitation pressure. SHs then increase rapidly with pressure increase and reach an upper limit of the achievable SH signal strength. Numerous studies have investigated the pressure threshold of SH oscillations; however, conditions to enhance the saturation level of SHs has not been investigated. In this paper nonlinear dynamics of bubbles excited by frequencies in the range of $f_r < f < 2f_r$ is studied for different sizes of bubbles (400nm-8 μm). We show that the SH resonance frequency is pressure dependent and decreases as pressure increases. When a bubble is sonicated with its pressure dependent SH resonance frequency, oscillations undergo a saddle node bifurcation from a P1 or P2 regime to a P2 oscillation

regime with higher amplitude. The saddle node bifurcation is concomitant with over saturation of the SH and UH amplitude and eventual enhancement of the upper limit of SH and UH strength (e.g. $\approx$ 7 dB in UH amplitude). This can increase the CTR and signal to noise ratio in applications. Here, we show that the highest non-destructive SH amplitude occurs when $f \cong 1.5 - 1.8 f_r$[1].

5.2 Introduction

A bubble is a nonlinear oscillator that can exhibits complex and chaotic dynamics [1,2,3,4,5,6,7,8]. Bubbles are the building block of several applications and phenomena; they have applications in sonochemistry [9, 10, 11, 12, 13, 14, 15], ultrasonic cleaning [16, 17] , sonoluminscence [14, 15] and medical ultrasound [18, 19, 20, 21, 22, 23]. Pioneering works of [1, 2, 3, 4, 5, 6, 7, 8] have shown the nonlinear and chaotic properties of forced bubble oscillations which are followed by recent extensive studies on the nonlinear behavior of bubbles in water [23, 24, 26, 27], coated bubbles [24, 26] , bubbles in highly viscous media [28, 29, 30, 31, 32, 33]; and bubbles sonicated with asymmetrical driving acoustic forces [34, 37]. Complexity of the bubble dynamics makes it very difficult to effectively implement bubbles in applications; however, within this complexity there exists an opportunity for beneficial bubble behavior in applications.

Period doubling (PD) is an example of a beneficial nonlinear behavior. In the bubble oscillator PD results in generation of $\frac{1}{2}$ order SHs and $\frac{3}{2}$ order UHs. SH oscillations of bubbles are highly desirable due to unique properties that makes them very useful in several applications. Ultrasound contrast agents (coated bubbles) are clinically used on a daily basis to image microvascular blood flow and quantify blood perfusion (e.g. in the liver, kidney and the myocardium) [38, 39, 40]. Due the absence of SHs and UHs in tissue's response to diagnostic ultrasound [20, 41, 42, 43]; SH and UH emissions by bubbles allow the detection of blood flow with exceptional contrast enhancement [20, 41, 42, 43]. Furthermore, SH emissions have lower frequencies and are attenuated less by the tissue.

In therapeutic ultrasound SH emissions are used for monitoring therapeutic applications of ultrasound and as an indicator for stable cavitation [44, 45]. SHs and UHs are employed to measure the

[1]Submitted to Nonlinear dynamics in Nov 2019 as: Sojahrood, A.J., Earl, R., Li, Q., Porter, T.M., Kolios, M.C. and Karshafian, R., 2019. Nonlinear dynamics of acoustic bubbles excited by their pressure dependent subharmonic resonance frequency: oversaturation and enhancement of the subharmonic signal. arXiv preprint arXiv:1909.05071.

efficacy of blood brain barrier opening [46, 47]. SHs are proposed for the non-invasive measurement of the pressure inside vessels [48, 49, 50], to image the microvasculature [41, 51, 52] and can be utilized in bubble sizing [53], among other applications.

Esche [54] was the first to characterize the SH bubble behavior through experimental observations in 1952. Pioneering theoretical works of Eller [55] and Prosperetti [56, 57, 58, 59] showed through a weakly non-linear analysis of the Rayleigh-Plesset model [60] that the subharmonic behavior of bubbles can only exist if the driving pressure amplitude exceeds a threshold pressure; it has been predicted theoretically that the pressure threshold is minimum for sonications with twice the linear resonance frequency (f_r) of the bubbles. This frequency is referred to as the linear $\frac{1}{2}$ order SH resonance frequency (f_{sh}=2f_r). Recently, several experimental [61, 62, 63], numerical [64, 65] and theoretical [59, 62] studies have investigated the pressure threshold of SH generation in bubble oscillations. These works have shown that SH oscillations in bubbles have three stages: initiation, rapid growth and saturation. Numerical Investigation of the SH threshold in uncoated and coated bubbles in [64, 65]; have shown that for small bubbles (less than 500nm), increased damping weakens the bubble response at f_{sh}. This leads to a shift of the minimum SH pressure threshold from f_{sh} towards f_r.

We have recently studied the bifurcation structure of the bubbles excited with their f_r and f_{sh} [66]. We have shown that for uncoated bubbles in water, non-destructive ($\frac{R}{R_0}$ <2 [67]) stable SH oscillations are less likely to develop if the bubble is sonicated with f_r. This is because when $f = f_r$, SHs oscillations only developed for $\frac{R}{R_0}$ >2. When the bubble is sonicated with f_{sh}, PD occurs through a bow-tie shape bifurcation and at very gentle oscillation regimes ($\frac{R}{R_0} < 1.05$). This suggest that bubbles are more likely to sustain stable SHs at f_{sh} [66]. The generation of PD in bifurcation diagrams was concomitant with the initiation of SHs which rapidly grow with increased pressure and get saturated. In other words, there is an upper limit for the achievable SHs and UHs strength and acoustic pressure increase will not necessarily result in SHs increase. To the contrary, a pressure increase can result in chaotic oscillations and/or bubble destruction which will lead to subsequent decrease in SHs and UHs strength [50, 66]. Despite several studies investigating the SH threshold of the bubbles [56, 57, 58, 59, 61, 62, 63, 64, 65], conditions for the enhancement of the upper limit of non-destructive SHs and UHs oscillations are under-investigated. Furthermore, the bifurcation structure of the bubble oscillator in the regime of $\frac{1}{2}$ order SHs when $f_r < f <\approx f_{sh}$ is not

studied in detail. Due to the importance of the SH and UH oscillations of bubbles, comprehensive knowledge of the resonant period 2 (P2) oscillations and conditions to enhance non-destructive P2 oscillations can aid in understanding and optimizing bubble applications.

In this study, which follows upon our previous work [26] where pressure dependent resonance (PDf_r) was used to increase the non-destructive scattered pressure (P_{sc}) by bubbles, we investigate the pressure dependence of SH resonance (Pdf_{sh}). Through numerically simulating the resonance curves of bubbles at different pressures, linear (f_{sh}) and pressure dependent (Pdf_{sh}) SH resonance frequencies of bubble diameters ranging from 400nm up to 8 microns are calculated (8 microns can be considered the upper limit of size used in biomedical applications [19]). The bifurcation structure of the bubble oscillations as a function of pressure is studied when $f = Pdf_{sh}$. The corresponding SH and UH strength of the P_{sc} are calculated and studied in conjunction with the bifurcation diagrams. We show that Pdf_{sh} decreases as pressure increases. Sonication of the bubble with Pdf_{sh} results in a saddle node bifurcation from a period 1 (P1) or a P2 oscillation regime to a P2 oscillation of higher amplitude. This is concomitant by the oversaturation of the SHs and UHs strength of up to ≈4 and ≈7 dB. Additionally for each bubble size there is an optimum frequency between $1.5f_r - 1.8f_r$which results in the maximum SH scattering cross section.

5.3 Methods

Similar to [66], we have chosen the uncoated bubble as the bubble oscillator of interest. Effect of coating is neglected as addition of the encapsulation introduces more complexity to the bubble dynamics. In order to have a detailed understanding on the dynamics of the bubble its preferable to separate the nonlinear effects of coating from that of the bubble itself. This makes it easier to understand the dynamics of the system and understand the basis of the bubble behavior. Furthermore, in future studies where coating is involved, information of the system behavior in the absence of coating will allow for a more straightforward understanding of the complex effects of coating on the system behavior.

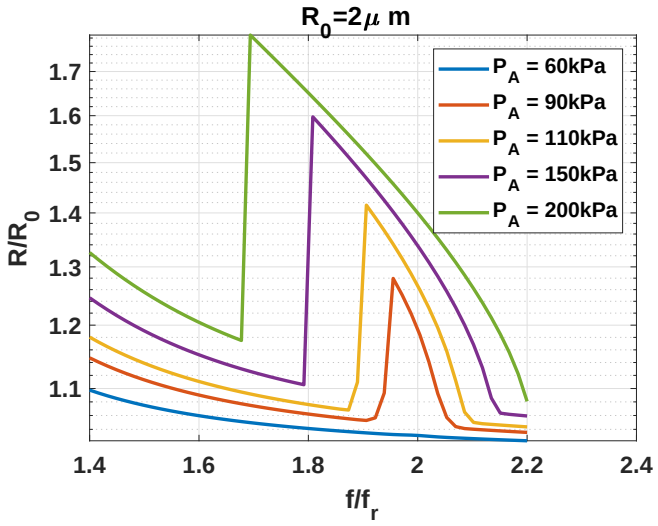

(a)

Figure 5.1: SH resonance frequency of a bubble with $R_0 = 2\mu m$ at different pressure amplitudes.

5.3.1 The Bubble model

The radial oscillations of the bubbles are numerically simulated by solving the Keller-Miksis equation [68]:

$$\rho[(1-\frac{\dot{R}}{c})R\ddot{R}+\frac{3}{2}\dot{R}^2(1-\frac{\dot{R}}{3c})] = (1+\frac{\dot{R}}{c})(G)+\frac{R}{c}\frac{d}{dt}(G) \tag{5.1}$$

where $G = P_g - \frac{4\mu_L\dot{R}}{R} - \frac{2\sigma}{R} - P_0 - P_A sin(2\pi ft)$. P_g is the gas pressure in the bubble and is given by $P_g = (P_0 + \frac{2\sigma}{R}) * (\frac{R}{R_0})^{3\gamma}$

In this equation, R is radius at time t, R_0 is the initial bubble radius, $\dot{R}$ is the wall velocity of the bubble and $\ddot{R}$ is the wall acceleration ρ is the liquid density (998 $\frac{kg}{m^3}$), c is the sound speed (1481 m/s), P_g is the gas pressure, σ is the surface tension (0.0725 $\frac{N}{m}$), μ is the liquid viscosity (0.001 Pa.s), $P_A =$ and f are the amplitude and frequency of the applied acoustic pressure. The values in the parentheses are for water at 293^0K. In this paper the gas inside the bubble is Air (γ=1.4) and water is the host media.

5.3.2 Resonance curves

It is shown that above a pressure threshold SH oscillations are generated and the threshold is minimum at f_{sh} ($f = 2f_r$). The radial oscillations of free uncoated air bubbles (R_0=200nm-4 μm)

were numerically simulated by solving equation 1, for $f_r < f < 2.2f_r$ and for a range of pressure amplitudes. The resonance curves were only calculated for pressure amplitude and frequency combinations that result in non-destructive bubble oscillations $\frac{R}{R_0} < 2$ [26, 67]. The maximum bubble radius was calculated in the last 20 cycles of a 200 cycle driving pulse to ensure that there was no transient behavior (similar analysis to [66]) and then plotted as a function of frequency in each graph. At each pressure,f_{sh} and Pdf_{sh} were selected from the graphs and used to generate the bifurcation diagrams in the next step.

5.3.3 Bifurcation diagrams

Bifurcation diagrams are valuable tools to analyze the dynamics of nonlinear systems where the qualitative and quantitative changes of the dynamics of the system can be investigated effectively over a wide range of the control parameters. In this paper, we employ a more comprehensive bifurcation analysis method introduced in [74, 75].

5.3.3.1 Conventional bifurcation analysis

When dealing with systems responding to a driving force, to generate the points in the bifurcation diagrams vs. the control parameter, one option is to sample the R(t) curves using a specific point in each driving period. The approach can be summarized in:

$$P \equiv (R(\Theta))\{(R(t), \dot{R}(t)) : \Theta = \frac{n}{f}\} \; where \; n = 400, 401...440 \tag{5.2}$$

Where P denotes the points in the bifurcation diagram, R and $\dot{R}$ are the time dependentradius and wall velocity of the bubble at a given set of control parameters of (R_0, P_0, P_A, c, k, μ, σ, f) and Θ is given by $\frac{n}{f}$. Points on the bifurcation diagram are constructed by plotting the solution of $R(t)$ at time points that are multiples of the driving acoustic period. The results are plotted for $n = 400 - 440$ to ensure a steady state solution has been reached for all bubbles. Due to smaller viscous effects, bigger bubbles require longer cycles to reach steady state.

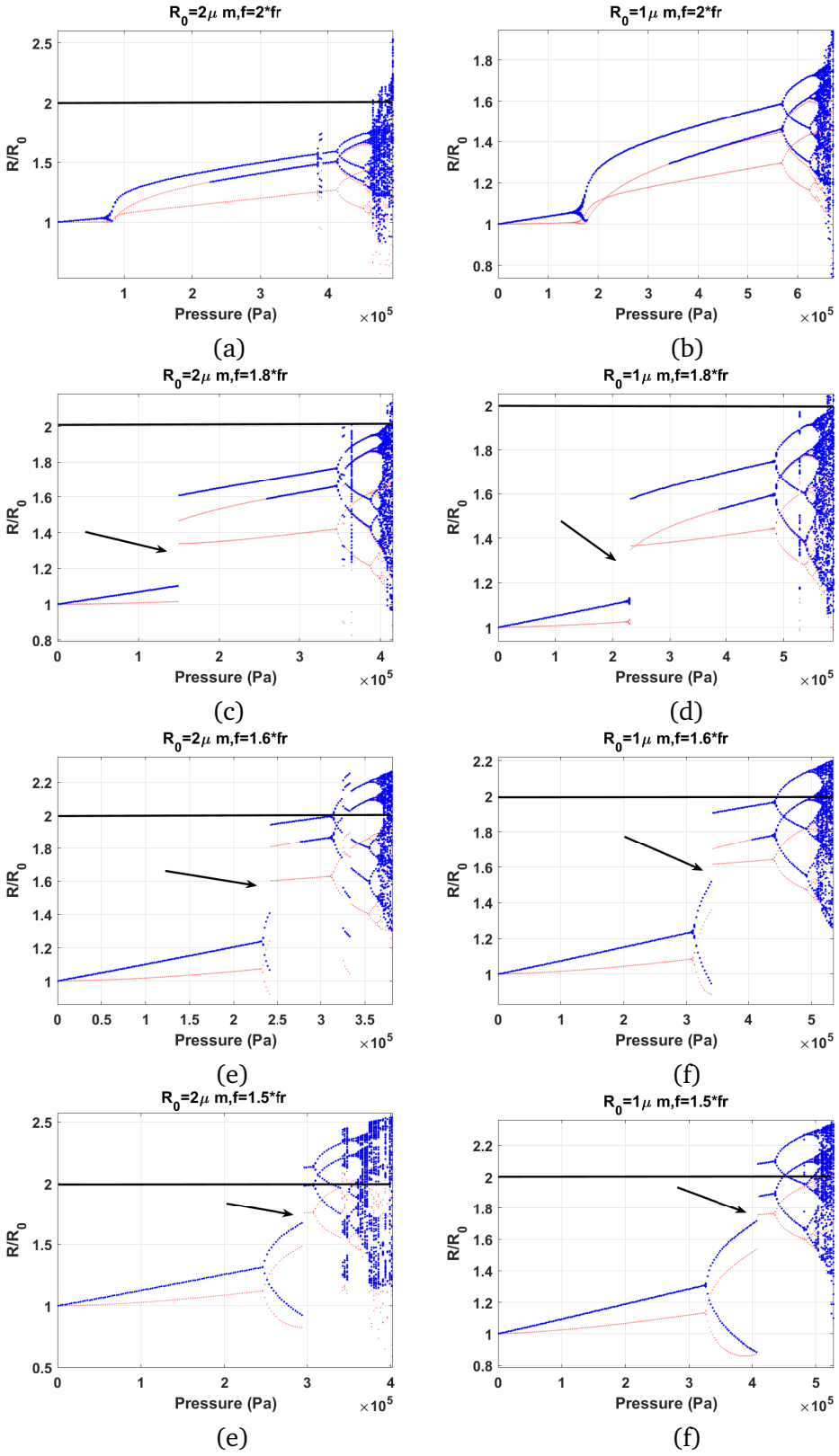

Figure 5.2: Bifurcation structure (blue: method of peaks, red: conventional method) of the micron-size bubbles as a function of pressure when sonicated with f_{sh} and Pdf_{sh}. Left column is for $R_0 = 2\mu m$ and Right column is for $R_0 = 1\mu m$ (arrow shows the pressure responsible for SN bifurcation)

5.3.3.2 Method of peaks

As a more general method, bifurcation points can be constructed by setting one of the phase space coordinates to zero:

$$Q \equiv max(R)\{(R, \dot{R}) : \dot{R} = 0\} \tag{5.3}$$

In this method, the steady state solution of the radial oscillations for each control parameter is considered. The maxima of the radial peaks ($\dot{R} = 0$) are identified (determined within 400-440 cycles of the stable oscillations) and are plotted versus the given control parameter in the bifurcation diagrams. The bifurcation diagrams of the normalized bubble oscillations ($\frac{R}{R_0}$) are calculated using both methods a) and b). When the two results are plotted alongside each other, it is easier to uncover more important details about the SuH and UH oscillations, as well as the SH and chaotic oscillations.

5.3.4 Backscattered pressure

Oscillations of a bubble generates a scattered pressure (P_{sc}) which can be calculated by [71]:

$$P_{sc} = \rho \frac{R}{d}(R\ddot{R} + 2\dot{R}^2) \tag{5.4}$$

where d is the distance from the center of the bubble (and for simplicity is considered as 1m in this paper) [26]. Equation 1 is solved using the 4th order Runge-Kutta technique using the ode45 function in Matlab (this function also has a 5th order estimation); the control parameters of interest are R_0, f and P_A. The resulting radial bubble oscillations are visualized using resonance curves and bifurcations diagrams. Bifurcation diagrams of the normalized bubble oscillations $\frac{R}{R_0}$ are presented as a function of the driving pressure in conjunction with the SH and UH amplitude of the P_{sc}. The scattered pressure (P_{sc}) is calculated alongside the bifurcation structure only for pressures that result in non-destructive oscillations ($\frac{R}{R_0} < 2$) [26, 67]. SH and UH amplitude of the P_{sc} is plotted alongside each bifurcation diagram to highlight the effect of nonlinearities on the changes in the SH and UH strength.

5.4 Results

5.4.1 Pressure dependent SH resonance frequency (PDSH)

First we explored the bubble expansion ratio ($\frac{R}{R_0}$) as a function of peak excitation pressure for a range of frequencies between 1.4f_r- 2f_r, where f_r is the linear resonance frequency. It has been hypothesized that a local maximum in the expansion ratio would be observed at $2f_r$, which would represent the subharmonic response of the bubble. However, the maximum response shifted to lower frequencies as the excitation pressure was increased (Fig. 5.1). Theoretical studies have reported that the resonance frequency, which equates to f_r only at very low excitation pressures (i.e. $< 50kPa$) for a microbubble is inversely related with excitation pressure. We postulate this can explain the shift in the subharmonic response to lower frequencies relative to $2f_r$. Figure 5.1 shows the SH resonance frequency of a R_0=2μm bubble sonicated with different pressure amplitudes. The linear SH resonance frequency is generated at 60 kPa and f=$2f_r$. As the pressure increases, similar to the case of pressure dependent resonance [26], SH resonance frequency decreases. For example the SH resonance frequency is $\approxeq 2f_r$ at 60 kPa and is 1.7f_r at 200 kPa. We call this shifted SH resonance frequency "pressure dependent SH resonance frequency (Pdf_{sh})". In the next section, we will show the mechanism of SH enhancement when bubbles of different sizes are sonicated with their Pdf_{sh}.

5.4.2 Bifurcation structure of the micron size bubbles (SH enhancement region)

Figures 5.2a and 5.2b show the bifurcation structure of the R_0=2μm and R_0=1μm bubbles as a function of pressure when f=$2f_r$. The radial oscillations of the bubbles undergo period doubling at the lowest pressure threshold (60 kPa for R_0=2 μm), which evolve in the form of a bowtie to P2 oscillations of higher amplitude as the acoustic pressure increases. The oscillations undergo further period doubling before the appearance of chaos. In this case full amplitude ($\frac{R}{R_0}$=2) P2 non-destructive oscillations do not develop.

Figures 5.2c and 5.2d show the bifurcation structure of the R_0=2 μm and R_0=1 μm bubbles as a function of pressure when $f = 1.8f_r$. The radial oscillations undergo a saddle node bifurcation from P1 to P2 oscillations of higher amplitude. The P2 oscillations have one maximum (red curve),

above a second pressure threshold the second maximum appears (oscillations become P2 with two maxima); the maxima are exactly on top of one of the branches of the conventional method which implies the wall velocity is in phase with the driving signal once every two acoustic cycles. Compared to the case of $f = f_{sh}$, bubbles sonicated by their Pdf_{sh} have a higher pressure threshold for P2 oscillations; however, the amplitude of the P2 oscillations are higher. The oscillations undergo further period doubling and chaos eventually occurs. Similar to $f = 2f_r$, when $f = 1.8f_r$ full amplitude ($\frac{R}{R_0}$=2) P2 non-destructive oscillations did not develop.

Figures 5.2c and 5.2d show the bifurcation structure of the R_0=2 μm and R_0=1 μm size bubbles as a function of pressure when $f = 1.6f_r$. The radial oscillations undergo a saddle node bifurcation from P2 (with two maxima) oscillations to P2 oscillations of higher amplitude (with one maxima). Compared to the case of f=f_{sh}, and f=1.8f_r bubbles sonicated by their Pdf_{sh}=1.6f_r have a higher pressure threshold (Pt) for P2 oscillations (e.g. for R_0=2μm Pt$\approxeq$ 230 kPa). The amplitude of the P2 oscillations are higher than the previous cases at the occurrence of SN bifurcation (e.g. for R_0=2μm P$\approxeq$ 242 kPa the $\frac{R_{max}}{R_0}$=1.94).b Similar to the previous cases, as pressure increases a second maximum re-emerges in the blue curve with its value being the same as one of the branches of the red curve. P2 oscillations then grow by pressure increase and P2 oscillations reach a large amplitude that result in non-destructive oscillations (e.g. for R_0=2μm R=1.99 R_0at P_A =309 kPa). Figures 5.2g and 5.2h show the bifurcation structure of the R_0=2 μm and R_0=1 μm bubbles as a function of pressure when $f = 1.5f_r$. PD initiation is at the highest pressure threshold (e.g. for R_0=2μm Pd occurs at 245 kPa). Above a second pressure threshold (e.g. for R_0=2 μm at P_A =295 kPa) P2 oscillations (with two maxima) undergo a SN bifurcation to P2 oscillations (with two maxima) of higher amplitude (($\frac{R_{max}}{R_0} \approxeq 2.13$). In this case occurrence of PD is concomitant with bubble destruction as $\frac{R}{R_0} > 2$ for both bubbles.

5.4.3 Bifurcation structure of the nano-bubbles (SH enhancement region)

Figures 5.3a and 5.3b show the bifurcation structure of the bubbles with $R_{=}0 = 400nm$ & $R_0 = 200nm$ as a function of pressure when $f = 2f_r$. The radial oscillations of the bubbles undergo period doubling at the lowest pressure threshold ($\approxeq$ 470 kPa for R_0=400 nm). P2 oscillations grow in amplitude as pressure increase and undergo further period doubling before the appearance of chaos. When $f = 2f_r$ full amplitude ($\frac{R_{max}}{R0}$=2) non-destructive P2 oscillations do not develop.

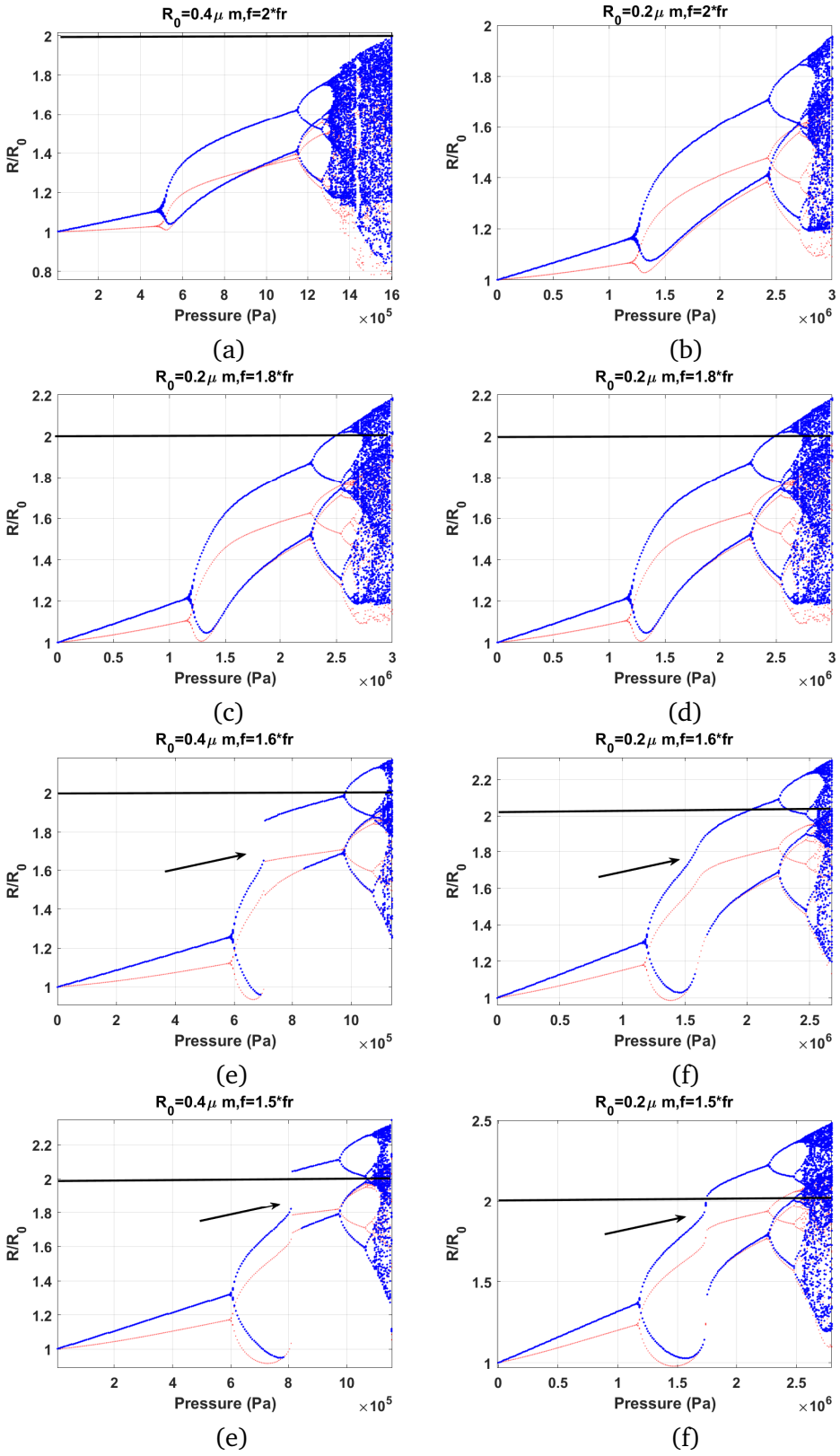

Figure 5.3: Bifurcation structure (blue: method of peaks, red: conventional method) of the nano-size bubbles as a function of pressure when sonicated with f_{sh} and Pdf_{sh}. Left column is for $R_0 = 0.4\mu m$ and Right column is for $R_0 = 0.2\mu m$ (arrow shows the pressure responsible for SN bifurcation)

Figures 5.3c and 5.3d show the bifurcation structure of $R_{=}0 = 400nm$ & $R_0 = 200nm$ bubbles as a function of pressure when $f = 1.8f_r$. P2 oscillations undergo a sharp increase in amplitude (e.g. for R_0=400 nm at P_A ≈600 kPa). Compared to the case of $f = f_{sh}$, bubbles sonicated by their Pdf_{sh} have a higher pressure threshold for P2 oscillations; however, the amplitude of the P2 oscillations are higher (similar for micron size bubbles in Fig 5.2c-d). The oscillations undergo further period doubling and chaos eventually occurs. Similar to $f = 2f_r$, when $f = 1.8f_r$, bubble doesn't reach full amplitude ($\frac{R_{max}}{R0}$=2) P2 non-destructive oscillations (similar to the case of micron size bubbles). Unlike micron size bubbles, SN bifurcation is not observed; this is due to the stronger effect of liquid viscosity on smaller bubbles.

Figures 5.3e and 5.3f show the bifurcation structure of the R_0=400 nm and R_0=200 nm size bubbles as a function of pressure when $f = 1.6f_r$. Radial oscillations undergo a saddle node bifurcation from P2 oscillations to P2 oscillations of higher amplitude. Compared to the case of $f = f_{sh}$, and $f = 1.8f_r$, nano-bubbles sonicated by their Pdf_{sh}=1.6f_r have a higher pressure threshold (P_t) for P2 oscillations (e.g. for R_0=400 nm $P_t \approxeq 570kPa$). In this case the amplitude of the P2 oscillations are higher than the previous cases after the occurrence of SN bifurcation (e.g. for R_0=400nm $P_A \approxeq 710kPa$ and ($\frac{R_{max}}{R0} = 1.86$). P2 oscillations then grow as pressure increases and P2 oscillations reach large amplitude of non-destructive oscillations (e.g. for $R_0 = 400nm$ $R_{max} = 1.98R_0$ at P_A =976 kPa).

Figures 5.3g and 5.3h show the bifurcation structure of the $R_0 = 400nm$ and $R_0 = 200nm$ size bubbles as a function of pressure when $f = 1.5f_r$. PD initiation is at the highest pressure threshold (e.g. for R_0=400 nm Pd occurs at 597 kPa). Above a second pressure threshold (e.g. for $R_0 = 400nm$ at P_A = 815 kPa) P2 oscillations undergo a SN bifurcation to P2 oscillations of higher amplitude ($\frac{R}{R_0} \approxeq 2.04$). In this case occurrence of PD is concomitant with bubble destruction as $\frac{R_{max}}{R0} > 2$ for both bubbles.

5.4.4 Enhancement of the SH saturation level

In order to investigate the consequence of the occurrence of SN on the strength of the SH and UHs of the P_{sc}, figure 5.4 displays the bifurcation structure of the bubble with R_0=1 μm when $f = 2f_r$and $f = 1.6f_r$ together with the SH and UH amplitude as well as the maximum value of both the P_{sc}^2 and $|\dot{R}|$. When $f = 2f_r$, PD (P_A ≈135 kPa) is concomitant with SH and UH initiation.

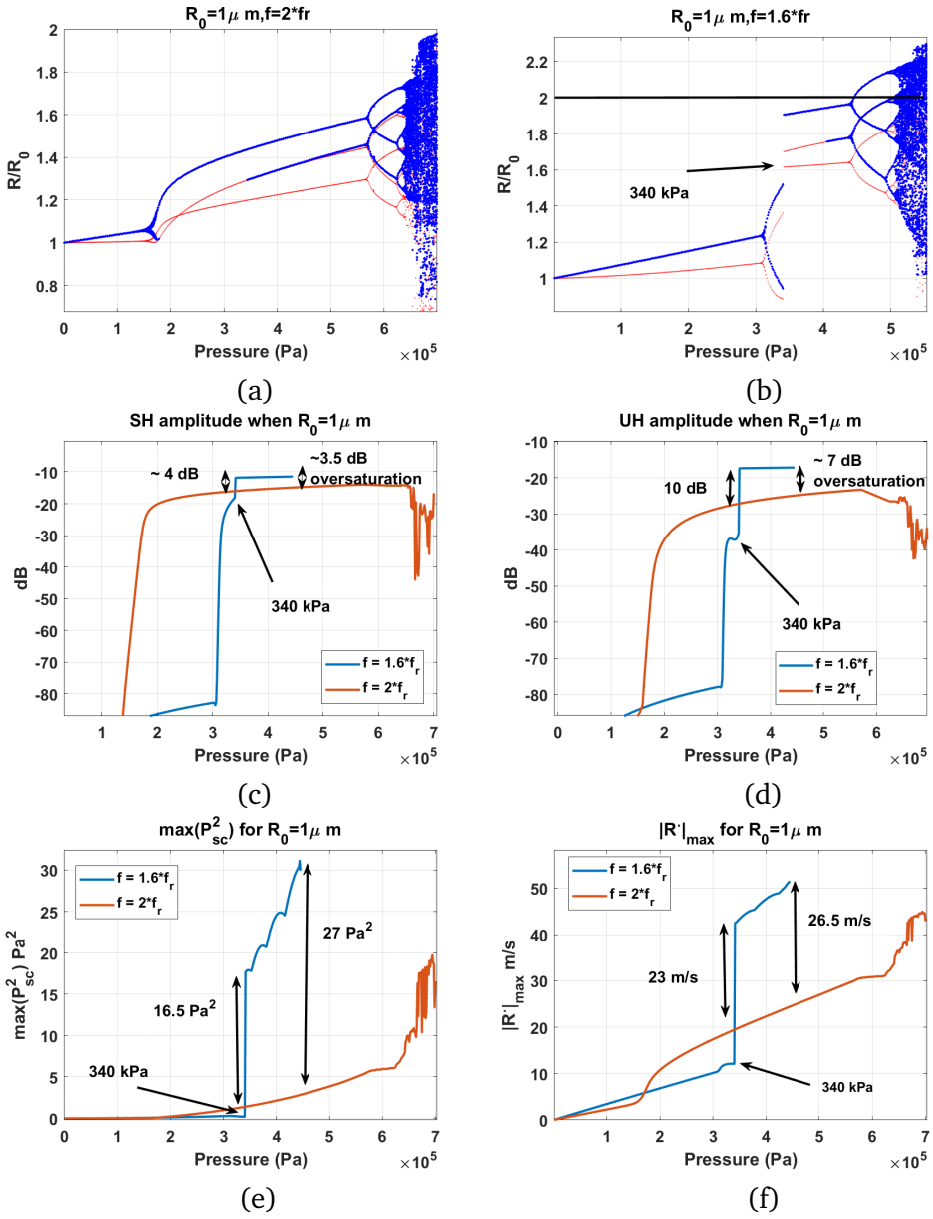

Figure 5.4: Period doubling and the corresponding bifurcation structure: a) bifurcation structure of the bubble when $f = 2f_r$,b) bifurcation structure of the bubble when $f = 1.6f_r$ and c) corresponding SH component of the P_{sc}, d) corresponding UH component of the P_{sc}, e) Maximum non-destructive P_{sc}^2 ($\frac{R_{max}}{R_0} < 2$) and f) maximum absolute value of the wall velocity

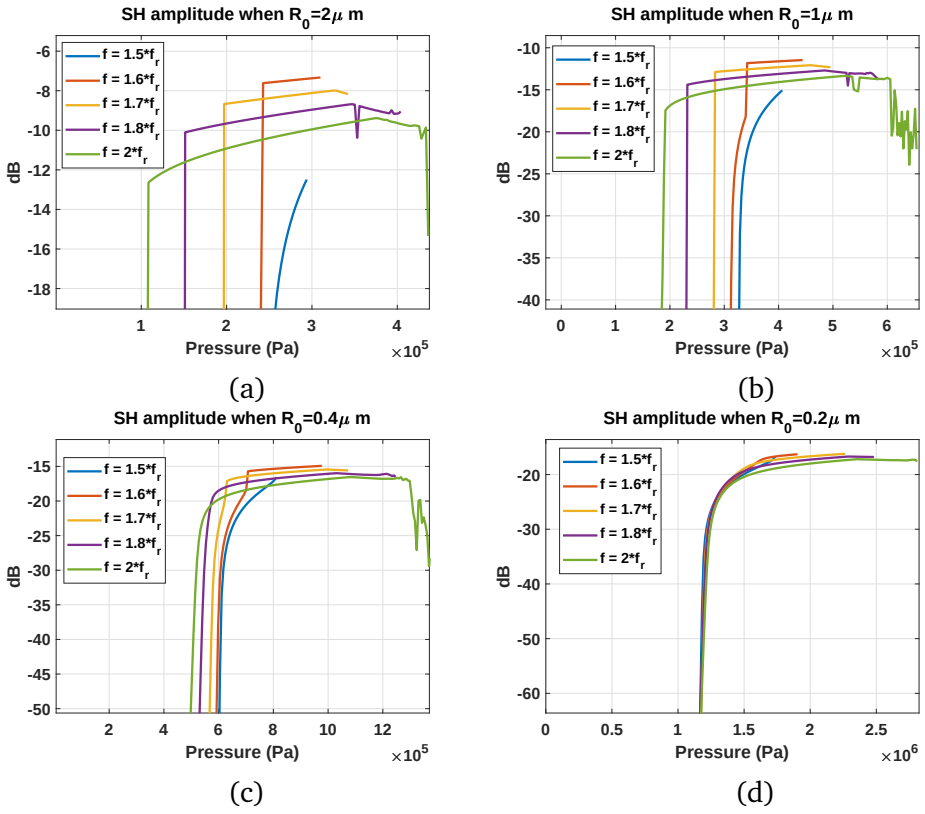

Figure 5.5: Non-destructive ($\frac{R_{max}}{R_0} < 2$) SH component of the P_{sc} for f_{sh} and Pdf_{sh} of: a) $R_0 = 2\mu m$, b) $R_0 = 1\mu m$, c) $R_0 = 0.4\mu m$ and d) $R_0 = 0.2\mu m$.

Consistent with experimental observations [61,62,63], SH and UH component of P_{sc} grow quickly with pressure increase and are saturated. The amplitude of SHs and UHs decrease simultaneous with P4 oscillations ($P_A \approxeq$ 568 kPa) and chaos ($P_A \approxeq$ 651 kPa). Chaos result in increase in P_{sc}^2 and wall velocity; however, SHs and UHs amplitude of the P_{sc} decrease.

When $f = 1.6f_r$, initiation of SH and UH oscillations are concomitant with P2 generation in the bifurcation diagram ($P_A \approxeq$ 310 kPa). When the SN bifurcation occur($P_A \approxeq$ 342kPa), SH and UH amplitude of P_{sc} undergo a significant increase (4 dB and 10 dB larger than the case of sonication with $f = 2f_r$). This results in oversaturation of the SH and UH amplitude. When $f = 1.6f_r$, the occurrence of a SN in the bifurcation diagram is concomitant with a significant increase in the maximum amplitude of P_{sc}^2 (P_{sc}^2 becomes 88 times larger than its value before the occurrence of SN) . At P_A =340 kPa (the pressure at the SN bifurcation) P_{sc}^2 and maximum wall velocity amplitude are respectively 16.5 Pa^2 and 23 m/s larger than the case of sonication with $f = 2f_r$ (by a factor of $\approxeq$ 80 and 4 times respectively). Moreover, when $f = 1.6f_r$, the maximum achievable non-destructive ($\frac{R}{R_0} < 2$) SH and UH amplitude are respectively 3.5 and 7 dB larger than the case of $f = 2f_r$. Thus, application of the Pdf_{sh} (in this case $f = 1.6f_r$) resulted in the oversaturation of the SH and UH amplitude. Maximum non-destructive P2 P_{sc}^2 and P2 non-destructive wall velocity amplitude are respectively 27 and 26.5 m/s higher than $f = 2f_r$.

Figure 5.5a-d illustrates the SH amplitude of the P_{sc} as a function of acoustic pressure at different frequencies ($f = 2f_r$, $1.8f_r$, $1.7f_r$, $1.6f_r$and $1.5f_r$) for R_0=2 μm (5.5a), R_0=1 μm (5.5b), R_0=400 nm (5.5c) and R_0=200 nm (5.5d). The SH amplitude of the P_{sc} are only shown for non-destructive oscillation regimes where $\frac{R}{R_0} < 2$. When bubbles are sonicated with f=$2f_r$, SHs are initiated at the lowest pressure, and the SHs amplitude grows with increasing pressure and then saturate. At higher pressures where P4 oscillations or chaos occurs, the SH amplitude decreases rapidly. When bubbles are sonicated with their Pdf_{sh}, SHs are initiated at higher acoustic pressures. However, SHs grow rapidly after initiation (concomitant with SN bifurcation) and the SH amplitude becomes larger than the case of sonication with $f = 2f_r$. For the frequencies shown in Fig. 5.5, the maximum SH amplitude occurs when $f = 1.6f_r$ (red line). For all the bubble sizes studied here, when f=$1.5f_r$(blue line in Fig. 5.5), the SN bifurcation is concomitant with bubble destruction ($\frac{R}{R_0} > 2$), therefore sonication with $f = 1.5f_r$ does not result in any SH enhancement over the conventional method of sonication with $f = 2f_r$. For frequencies less than $2f_r$ the bubble undergoes destruction

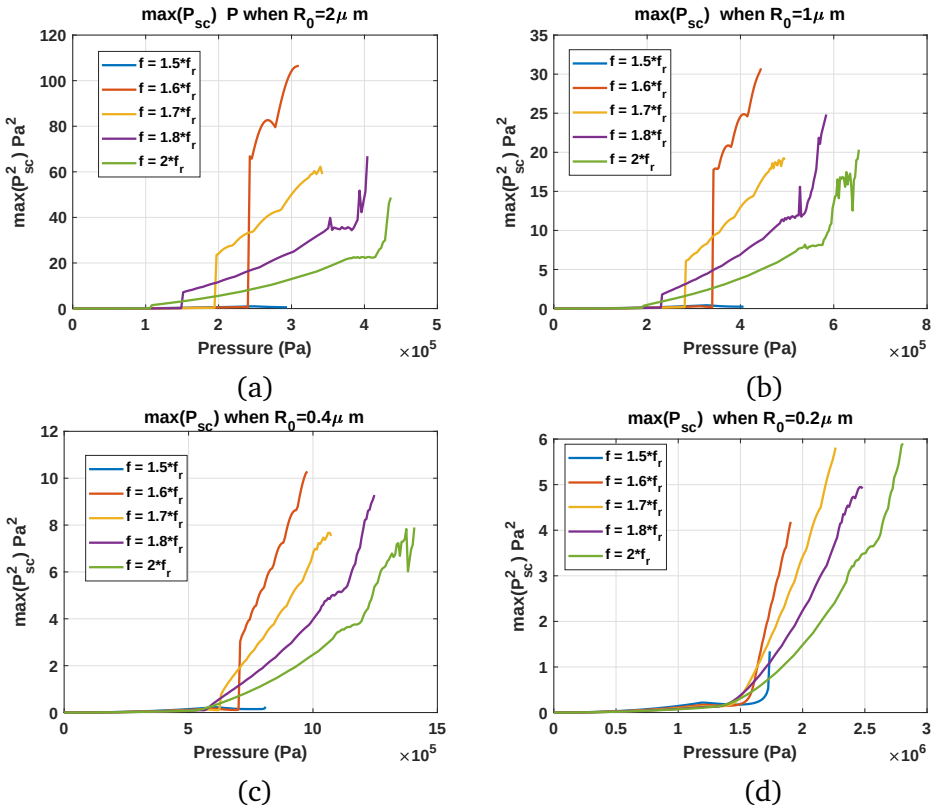

Figure 5.6: Maximum value of Non-destructive P_{sc}^2 for f_{sh} and Pdf_{sh} of: a) $R_0 = 2\mu m$, b) $R_0 = 1\mu m$, c) $R_0 = 0.4\mu m$ and d) $R_0 = 0.2\mu m$.

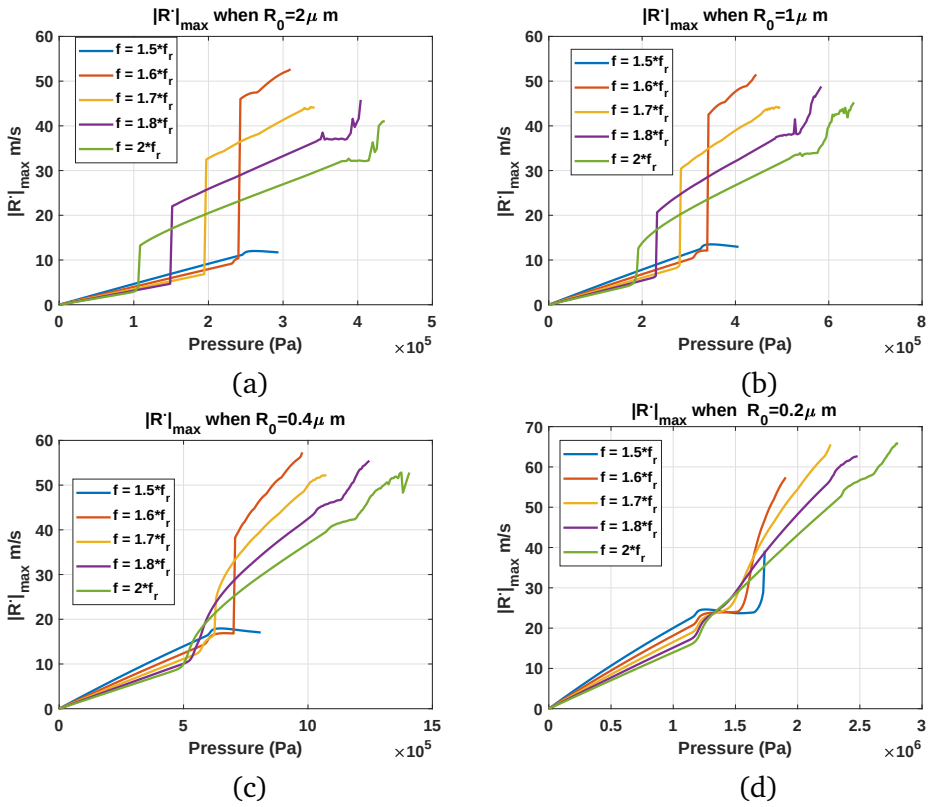

Figure 5.7: Maximum value of Non-destructive absolute wall velocity for f_{sh} and Pdf_{sh} of: a) $R_0 = 2\mu m$, b) $R_0 = 1\mu m$, c) $R_0 = 0.4\mu m$ and d) $R_0 = 0.2\mu m$.

at a lower acoustic pressures.

Figure 5.6 displays the maximum non-destructive ($\frac{R}{R_0} < 2$) P_{sc}^2 at different frequencies (f=$2f_r$, $1.8f_r$, $1.6f_r$ and $1.5f_r$) for R_0=2 μm (6a), R_0=1 μm (6b), R_0=400 nm (6c) and R_0=200 nm (6d). When f=$2f_r$, P_{sc}^2 is very small for pressures below PD; concomitant with generation of PD, P_{sc}^2 undergoes a rapid increase and then increases linearly with acoustic pressure. When P4 oscillations occur, P_{sc}^2 decreases for micron size bubbles (the growth rate decreases for nano-size bubbles); this is similar to the decrease of P_{sc} concomitant with P2 oscillations when f=f_r [26]. Further increase in the acoustic pressure results in chaotic oscillations which lead to significant enhancement of the P_{sc}^2; however, this enhancement in amplitude is associated with a rapid decrease in SH and UH amplitude (Fig 4 and 5).

When $f = Pdf_{sh}$ ($f = 1.8f_r$, $1.7f_r$ and $1.6f_r$), P_{sc}^2 is smaller than its counter part when $f = 2f_r$. Above a pressure threshold, the SN bifurcation results in the generation of higher amplitude P2 oscillations. The SN bifurcation is coincident with a rapid increase in P_{sc}^2. P_{sc}^2 becomes significantly

larger than the case of sonication with $f = 2f_r$ (e.g. for the bubble with R_0=2 μm and $f = 1.6f_r$, when SN occurs at $\approxeq$ 242 kPa, P_{sc}^2 becomes 8.4 times larger than its counterpart when $f = 2f_r$). After the SN, P_{sc}^2 increase monotonically with pressure increase until the bubble is destroyed ($\frac{R_{max}}{R_0} > 2$).

Figure 5.7 displays the maximum non-destructive wall velocity at different frequencies ($f = 2f_r$, $1.8f_r$, $1.6f_r$ and $1.5f_r$) for R_0=2 μm (6a), R_0=1 μm (6b), R_0=400 nm (6c) and R_0=200 nm (6d). Maximum wall velocity amplitude increases monotonically with pressure; however, as soon as PD occurs, the wall velocity undergoes a rapid increase and continues to increase monotonically after. The occurrence of P4 oscillations results in a decrease in the maximum wall velocities for micron size bubbles (or decrease in the growth rate of wall velocity for nano-size bubbles) which is similar to the decrease of wall velocity concomitant with the occurrence of P2 when $f = f_r$ [26]. At higher pressures, the generation of chaotic oscillations leads to a rapid increase in wall velocity; however, as seen before this is simultaneous with a decrease in SH and UH amplitudes. For the bubble with R_0=0.2 μm the occurrence of SN bifurcation does not have a pronounced effect on the maximum wall velocity amplitude which is due to the dominant effect of liquid viscosity on smaller bubbles.

5.4.5 Bifurcation structure of the micro-bubbles (for $fr < f < 1.5f_r$)

In the previous sections we saw that when $f \approxeq 1.5f_r$, SN bifurcation results in bubble destruction ($\frac{R}{R_0} > 2$) and sonication with $1.5fr < f < 2f_r$ results in an enhancement of the SH amplitude. In this section, we closely examine the bifurcation structure of the micro-bubbles when sonicated with $f_r < f < 1.5f_r$. Figure 5.8 shows the bifurcation structure of the micron-size bubbles with R_0=2μm and R_0=1μm as a function of pressure. The frequencies are $1.4f_r$, $1.2f_r$ and $1.1f_r$. Unlike the case of sonication with $1.5f_r < f < 2f_r$; within the parameter ranges studies here (and for $\frac{R}{R_0} < 2$), there is no SN bifurcation taking place in the diagrams. The evolution of the dynamics of the system is through a simple PD to P2 oscillations followed by a cascade of PDs to chaos. In case of $f = 1.2f_r$and $1.1f_r$ full amplitude ($\frac{R_{max}}{R0}$=2) non-destructive P2 oscillations are developed; however, unlike $1.5f_r < f < 2f_r$, PD is simultaneous with a decrease in wall velocity and scattered pressure. We have previously shown that when bubble is sonicated with $f = f_r$, the occurrence of PD is concomitant with a decrease in the scattered pressure and maximum wall velocity [26]. The red curve in figure 5.8 (constructed by conventional method) never meets the

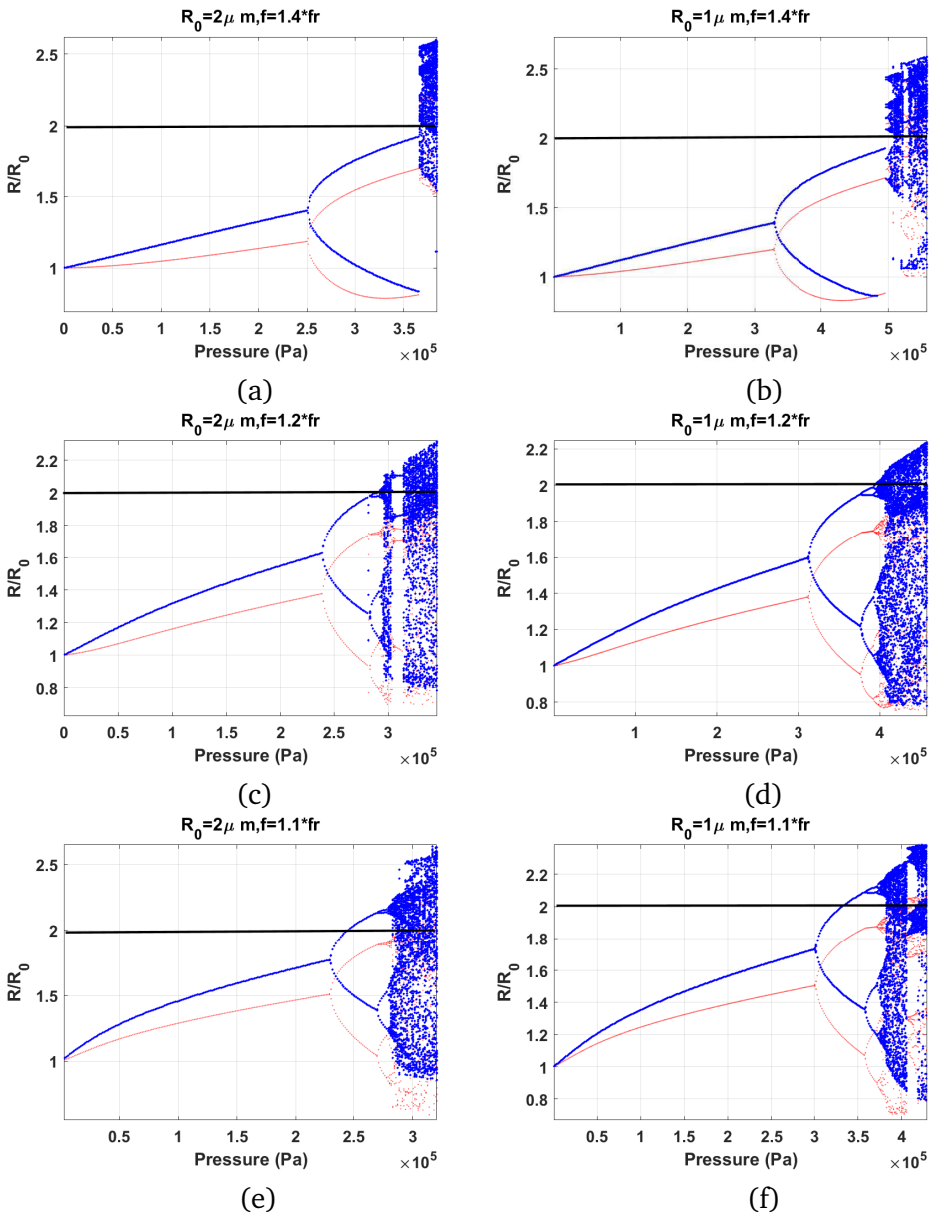

Figure 5.8: Bifurcation structure (blue: method of peaks, red: conventional method) of the micron-size bubbles as a function of pressure when sonicated with $f = 1.4f_r, 1.2f_r \& 1.1f_r$. Left column is for $R_0 = 2\mu m$ and Right column is for $R_0 = 1\mu m$ (arrow shows the pressure responsible for SN bifurcation)

blue curve (constructed by the maxima method) suggesting that the wall velocity of the bubble never gets in phase with the acoustic driving force.

5.4.6 Bifurcation structure of the nano-bubbles (for $f_r < f < 1.5f_r$)

Figure 5.9 shows the bifurcation structure of the nano-size bubbles as a function of pressure. Bubbles have initial radii of R_0= 400nm (left column) and R_0=200nm (right column). When $f = 1.4f_r$, P1 bubble oscillations grow monotonically with increasing pressure and above a pressure threshold bubbles undergo a PD to P2 oscillations. P2 oscillations grow in amplitude and above a second pressure threshold; there is a SN bifurcation to P2 oscillations of higher amplitude. The SN bifurcation results in P2 oscillations that are resonant (one of the maxima in blue curve is on top of one of the branches of the red curve), however, similar to the case of the $f = 1.5f_r$, the SN results in bubble destruction ($\frac{R_{max}}{R0} > 2$). When $f = 1.2f_r$ and $f = 1.1f_r$, SN bifurcation does not take place and the bubble oscillations undergo a PD bifurcation to P2 oscillations followed by a cascade of PDs to chaos.

5.4.7 Maximum achievable P_{sc}^2, wall velocity, SH and UH as a function of frequency

In many applications, it is of interest to find exposure parameters that maximize the scattered pressure or enhances a specific frequency component in the scattered pressure. Figure 5.10a-b show the normalized value of maximum non-destructive P_{sc}^2 ($\frac{R}{R_0} < 2$) and wall velocity in the regime of P2 oscillations as a function of frequency. P_{sc}^2 and wall velocity reach their maximum at $f = 1.6f_r$ for bubbles with R_0=0.4, 1 and 2μm and it is maximum for $f = 1.65f_r$ when R_0=0.2 μm. For all bubbles there is a universal minimum for P_{sc}^2 and wall velocity when $f = 1.5 - 1.55fr$. We show that conventional practice of sonication with SH resonance frequency (f_{sh}=$2f_r$) does not lead to the generation of the maximum P2 scattered pressure or wall velocity. Instead there is a frequency range ($1.55 < f < 1.7$) that results in the maximum value of the two parameters. Figure 5.10c-d presents the maximum non-destructive ($\frac{R}{R_0} < 2$) SH and UH amplitude as a function of frequency. For all bubble sizes examined, the conventional sonication with the $f_{sh}(2f_r)$ does not result in the strongest SH or UH amplitude. The bubble with R_0=2μm reaches the strongest SH and UH amplitude when $f = 1.6f_r$; the bubbles with R_0=1μm and R_0=0.4μm reach the maximum at $f = 1.55f_r$. For bubbles with R_0=2μm, 1μm and 0.4μm there exist a universal minimum for SH

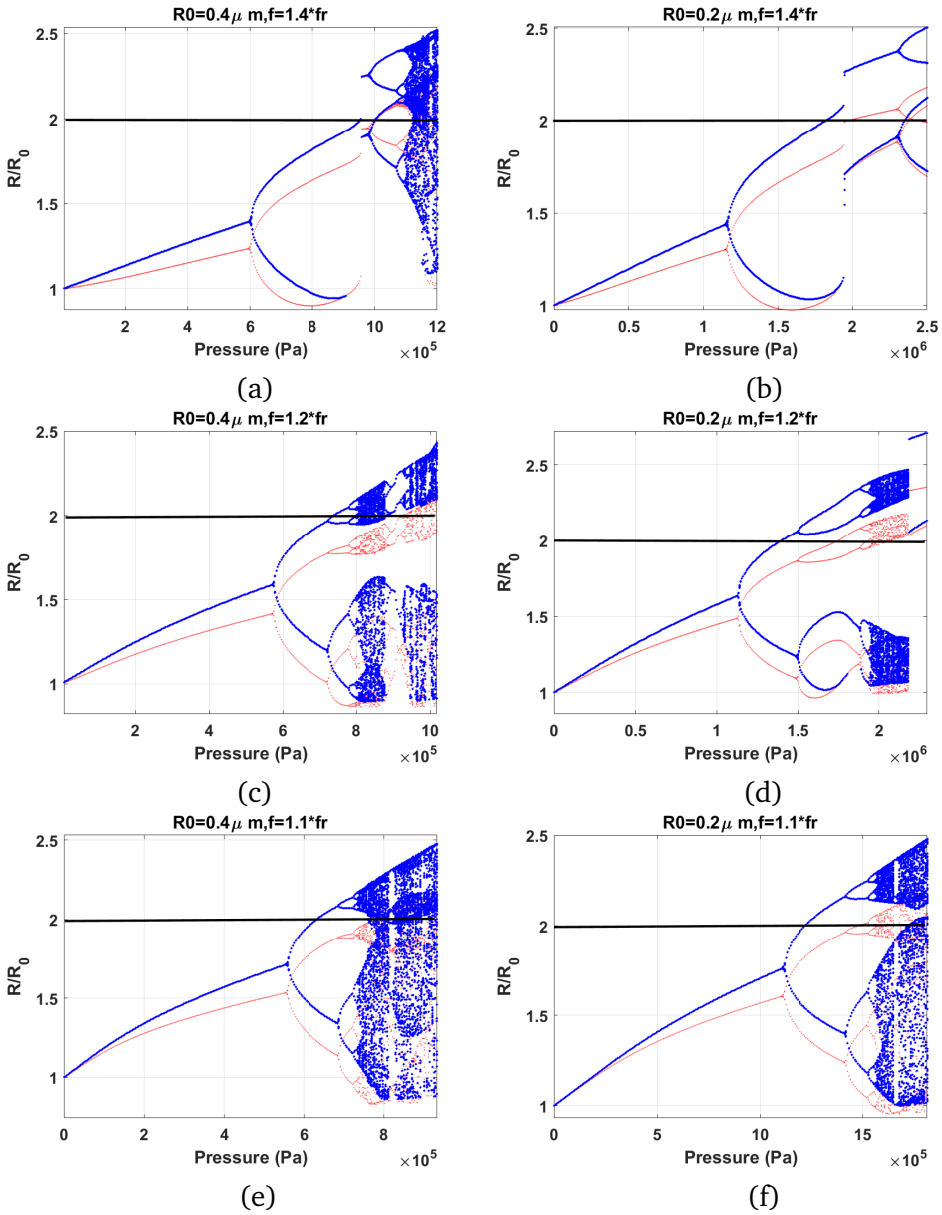

Figure 5.9: Bifurcation structure (blue: method of peaks, red: conventional method) of the micron-size bubbles as a function of pressure when sonicated with $f = 1.4f_r, 1.2f_r \& 1.1f_r$. Left column is for $R_0 = 0.4\mu m$ and Right column is for $R_0 = 0.2\mu m$ (arrow shows the pressure responsible for SN bifurcation)

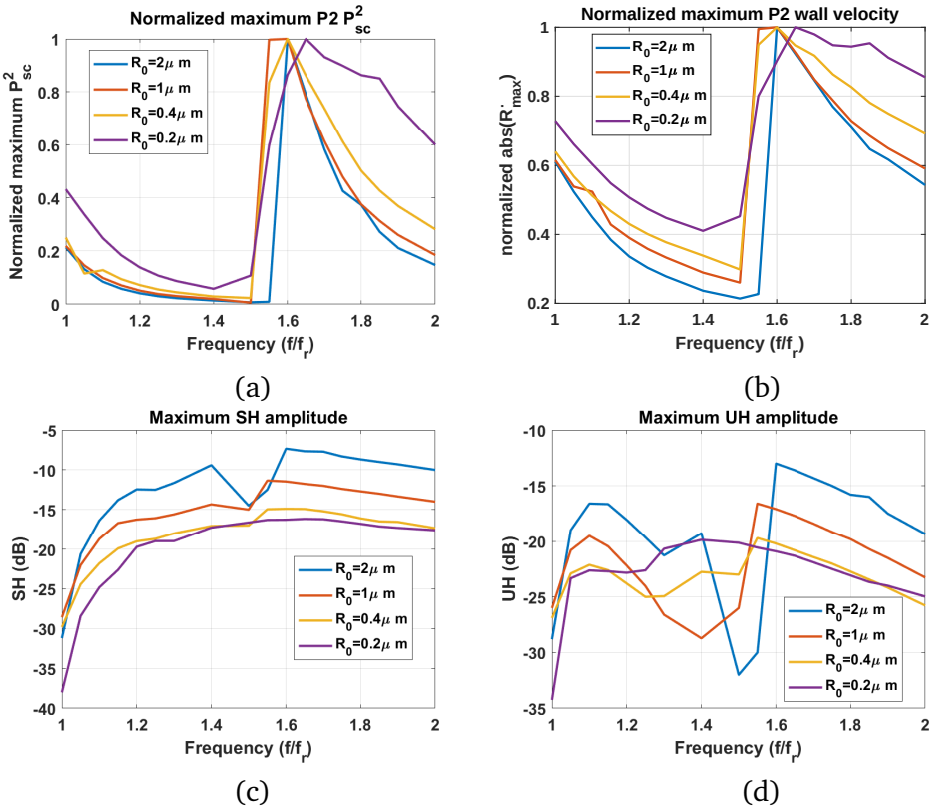

Figure 5.10: a) Normalized maximum non-destructive P2 P_{sc}^2, b) Normalized maximum non-destructive P2 wall velocity, c) Maximum non-destructive SH amplitude, and d) Normalized maximum UH amplitude.

and UH at $1.5f_r$; this is because the SN bifurcation leads to bubble destruction at this frequency, thus non-destructive full amplitude P2 oscillations are not developed in this case. For R_0=200 nm, maximum SH and UH amplitudes occurs respectively at $f = 1.6f_r$ and $1.4f_r$.

5.5 Discussion and summary

SH oscillation of bubbles are one of the most important nonlinear signatures of bubbles which are used in several medical and industrial applications [18, 19, 20, 21, 22, 23, 38, 39, 40, 41, 42, 43, 44, 45, 46, 47, 48, 49, 50, 51, 52]. Despite the importance of SH oscillations, most studies have only focused on investigating the minimum pressure threshold for SH oscillations [56, 57, 58, 59, 61, 62, 63, 64, 65]. Conditions to maximize the SH power remain uncertain. When the bubble is sonicated with twice its linear resonance frequency (f_r), SHs are developed at the lowest pressure threshold [54, 55, 56, 57, 58, 59]. SHs grow quickly above this pressure threshold, however, they are saturated and any further increase in incident pressure may even lead to weakening of the SHs due to the occurrence of chaos or bubble destruction. Knowledge of the conditions and exposure parameters that enhance the saturation level would allow to select exposure parameters that increase the contrast to tissue ratio (CTR) and signal to noise ratio (SNR) in applications. We have previously studied the two main routes of period doubling (PD) in the bubble oscillator and showed that due to the very high oscillation amplitude ($\frac{R}{R_0} > 2$ [67] and a for detailed review please see the discussion in [26]), non-destructive SH oscillations are less likely to be developed when bubbles are sonicated with f_r. However, sonication with f_{sh}=$2f_r$, results in the generation of SHs at very gentle oscillation regimes which increases the chance of the bubble survival during SH regime of oscillations. We have also previously shown that the scattered signal from bubbles can be enhanced if the bubbles are sonicated with its pressure dependent resonance frequency [26]. In this work the bifurcation structure of bubbles sonicated by its pressure dependent resonance frequencies (Pdf_{sh}) was investigated in detail.

SH and UH amplitudes were examined between two pressure limits: The threshold for the onset of SH oscillations and the critical pressure at which the nonlinear response becomes chaotic (or results in bubble destruction). Knowledge of these limits is essential for the optimization of applications related to SHs as the SH amplitude drops rapidly when chaos occurs. The findings of this study can

be summarized as follows:

1- When bubbles are sonicated with f_{sh}=$2f_r$, bubble oscillations undergo period doubling (PD) at the lowest pressure threshold. Period 2 (P2) oscillations result in the generation of SHs and UHs which then grow quickly with increasing pressure reaching a saturation value. Thus, there is an upper limit of achievable SH and UH strength under conventional exposure parameters for SH imaging.

2- When sonicated with f_{sh} or Pdf_sh, the occurrence of P4 or chaotic oscillations lead to a drop in the SH and UH amplitude. Thus, in a clinical setting CTR decreases for these exposure conditions. Furthermore since P4 and chaos occur at higher acoustic pressures, higher backscatter from tissue will result in a decrease of bubble contrast enhancement compared to the tissue signal. Thus, the limit for the occurrence of P4 or chaos should be determined and avoided in practical situations where the goal is higher CTR and SNR.

3- Pressure increase leads to a decrease in SH resonance frequency. This is similar to the decrease in resonance frequency with pressure [26].

4- When the bubble is sonicated with Pdf_sh, PD initiation is at higher pressures compared to $f = f_{sh}$. Bubble oscillations undergo a SN bifurcation from P1 to P2 or from a P2 to P2 oscillations of higher amplitude. This is concomitant with a rapid growth of signal and oversaturation of the SH level.

5- When $f = Pdf_sh$, the SN bifurcation results in a sudden increase in the scattered pressure and wall velocity; this effect is more pronounced in bubbles $> 800nm$ as the higher viscous forces on smaller bubbles increases the pressure required for the onset of nonlinear oscillations.

6- In this study for bubble sizes $> 800nm$, the maximum non-destructive SH, UH, backscatter pressure and wall velocity are generated when bubbles are sonicated with f≅1.55-1.6f_r. Conversely, there is a universal minimum for all these values at f≅1.4-1.5f_r.

7- When sonicated with $1.5f_r < f < 2f_r$, the occurrence of PD is concomitant with an increase in the wall velocity and scattered pressure. This is in contrast to sonication with $f_r < f < 1.5f_r$, where PD is simultaneous with a drop in scattered pressure and wall velocity. We have also previously shown that when bubble is sonicated with its pressure dependent resonance (PDf_r) and $f = f_r$, the maximum wall velocity drops when PD occurs [26]. This can be one of the reasons for the loss of echogenecity observed concomittant with Pd [72].

8- When sonicated with $1.5f_r < f < 2f_r$, the occurrence of P4 or chaotic oscillations lead to an increase in maximum scattered pressure and wall velocity; however, this increase is simultaneous with a drop in SH and UH strength; thus it is not an ideal situation for SH imaging applications.

9- For bubble sizes $> 400nm$ when sonicated with $f_r < f < 1.5f_r$; oscillations undergo a simple PD from P1 to P2 oscillations which is followed by a PD cascade to chaos.

We have shown that exposure parameters ($f = 2f_r$) that are used in conventional SH imaging do not result in the maximum SH or UH strength. We conclude that sonication with $f \approxeq 1.6f_r$ generates the highest achievable non-destructive ($\frac{R}{R_0} < 2$) SH and UH amplitude (e.g. depending on pressure, for the bubble with R_0=1μm the enhancement in SH and UH were respectively 3.5-4 dB and 7-10 dB).

In this paper, we have derived the exposure parameters that maximize the enhancement of the SHs, UHs, scattered pressure and wall velocities. The fundamental findings of this study can be used to optimize the outcome of ultrasound applications based on SH oscillations. Furthermore, in drug delivery applications, sonication parameters that lead to non-destructive oscillations with elevated wall velocities can be used to increase the long lasting shear stress on the nearby cells.

SN bifurcation is concomitant with a fast increase in the scattered pressure. For example when the bubble with R_0=1μm was sonicated with $f = 1.6f_r$ scattered pressure underwent a 9.4 times increase as soon as SN occurred (Fig. 5.6b). This has several advantages for amplitude modulation imaging used in medical ultrasound [73, 74, 75]. Amplitude modulation (AM) is a method that takes advantage of the nonlinear response of the bubble to increase in acoustic pressure; in this method, two pulses are sent to the target with one having twice the amplitude of the other. The signals are scaled and subtracted upon return. Because of the linear response of tissue to pressure increase the signal from the tissue cancels and the residual signal from the bubble enhances the CTR. When bubble is sonicated with Pdf_{sh}, sonication with pressures below and above the pressure threshold for the SN can significantly enhance the residual signal; furthermore, because of the higher frequencies of PDsfh compared to conventional AM sonication at f_r, higher resolution is expected.

In this paper, we have analyzed the nonlinear dynamics of the free bubble in the absence of coating (shell). Coated bubbles and most importantly lipid shell bubbles [76] are used in medical applications of ultrasound from SH imaging [40] to blood brain barrier opening [46] and thrombolysis

[77]. The nonlinear behavior of lipid coating (e.g. buckling and rupture) makes the dynamics of the bubble system more complex. In other words, the nonlinear shell dynamics are interwoven with the inherent nonlinear behavior of the bubble. This makes it very difficult to understand the behavior of the system and decouple effects due to the shell compared to nonlinear effects inherent in the forced bubble oscillator. It has been shown experimentally and numerically [40,52,78,79,80,81,82,83,84] that addition of the lipid shell reduces the pressure threshold for nonlinear oscillations including SH oscillations [59, 64, 65]. Followed by experimental observations of the pressure threshold of SH oscillations [78] and numerical results [64, 65], Prosperetti [59] theoretically investigated the SH threshold of coated bubbles. He showed that consistent with experimental observations [78], the SH threshold can be considerably lowered with respect to that of an uncoated free bubble. This happens when the mechanical response of the coating varies rapidly in the neighbourhood of certain specific values of the bubble radius (e.g. changes in shell parameters due to buckling of the shell [76]).

In this paper, we have neglected the shell effects. To better understand the dynamics of the more complex coated bubble, we first need to establish the nonlinear response of the less complex uncoated system. In this regard, understanding the nonlinear dynamics of the bubble system in the absence of the shell is the first step in developing a comprehensive framework for the understanding of the complex nonlinear behavior of bubbles. Future studies will include the effect of coating and since we know the behavior of the free bubble system, it is much easier to understand the shell effects on the bubble system.

We have neglected the effects of thermal damping [85, 86, 87, 88]. Thermal damping especially in bigger bubbles can potentially have a strong effect on the dynamics of the system and changes the resonant behavior of the system. At higher frequencies (above resonance), the effect of thermal damping is weaker and neglecting the thermal effects in this paper may not change the general conclusions presented here. A more complete understanding of the thermal damping, however, is necessary for accurate prediction of the bubble behavior. Another important factor that should be considered is the interaction between bubbles [89, 90, 91, 92, 93]. In applications bubbles exist in poly-disperse clusters and their oscillations affect each other. We have recently shown that SH behavior of a polydisperse interacting cluster of bubbles is dictated by the SH response of the bigger bubbles in the cluster. Conclusions of this study can be useful in optimizing the SH strength of a

poly-disperse cluster by optimizing the exposure parameters required to enhance the SH response of the clusters bigger bubbles.

Bibliography

[1] Parlitz, U., et al. ”Bifurcation structure of bubble oscillators.” The Journal of the Acoustical Society of America 88.2 (1990): 1061-1077.

[2] Prosperetti, Andrea, Lawrence A. Crum, and Kerry W. Commander. ”Nonlinear bubble dynamics.” The Journal of the Acoustical Society of America 83.2 (1988): 502-514.

[3] , Timothy. The acoustic bubble. Academic press, 2012.

[4] Lauterborn, Werner, and Thomas Kurz. ”Physics of bubble oscillations.” Reports on progress in physics 73.10 (2010): 106501.

[5] Lauterborn, W., and U. Parlitz. ”Methods of chaos physics and their application to acoustics.” The Journal of the Acoustical Society of America 84.6 (1988): 1975-1993.

[6] Lauterborn, Werner, and Eckehart Cramer. ”Subharmonic route to chaos observed in acoustics.” Physical Review Letters 47.20 (1981): 1445.

[7] Lauterborn, Werner, and Joachim Holzfuss. ”Acoustic chaos.” International Journal of bifurcation and Chaos 1.01 (1991): 13-26.

[8] Prosperetti, A., and A. Lezzi. ”Bubble dynamics in a compressible liquid. Part 1. First-order theory.” Journal of Fluid Mechanics 168 (1986): 457-478.

[9] Suslick, Kenneth S. ”Sonochemistry.” science 247.4949 (1990): 1439-1445.

[10] Storey, Brian D., and Andrew J. Szeri. ”Water vapour, sonoluminescence and sonochemistry.” Proceedings of the Royal Society of London A: Mathematical, Physical and Engineering Sciences. Vol. 456. No. 1999. The Royal Society, 2000.

[11] Crum, Lawrence A., et al., eds. Sonochemistry and sonoluminescence. Vol. 524. Springer Science & Business Media, 2013.

[12] Yasui, Kyuichi, et al. ”Theoretical study of single-bubble sonochemistry.” The Journal of chemical physics 122.22 (2005): 224706

[13] Suslick, Kenneth S. ”Sonochemistry.” science 247.4949 (1990): 1439-1445.

[14] Storey, Brian D., and Andrew J. Szeri. ”Water vapour, sonoluminescence and sonochemistry.” Proceedings of the Royal Society of London A: Mathematical, Physical and Engineering Sciences. Vol. 456. No. 1999. The Royal Society, 2000.

[15] Crum, Lawrence A., et al., eds. Sonochemistry and sonoluminescence. Vol. 524. Springer Science & Business Media, 2013.

[16] Cd Ohl, M. Arora, R. Dijkink, V. Janve, and D. Lohse. ”Surface cleaning from laser-induced cavitation bubbles.” Applied physics letters 89, no. 7 (2006): 074102

[17] E. Maisonhaute, C. Prado, P.C. White, and R.G. Compton. ”Surface acoustic cavitation understood via nanosecond electrochemistry. Part III: Shear stress in ultrasonic cleaning.” Ultrasonics sonochemistry 9, no. 6 (2002): 297-303.

[18] Roovers, S., Segers, T., Lajoinie, G., Deprez, J., Versluis, M., De Smedt, S.C. and Lentacker, I., 2019. The role of ultrasound-driven microbubble dynamics in drug delivery: from microbubble fundamentals to clinical translation. Langmuir.

[19] Ferrara, Katherine, Rachel Pollard, and Mark Borden. ”Ultrasound microbubble contrast agents: fundamentals and application to gene and drug delivery.” Annu. Rev. Biomed. Eng. 9 (2007): 415-447.

[20] Forsberg, Flemming, William T. Shi, and B. B. Goldberg. ”Subharmonic imaging of contrast agents.” Ultrasonics 38.1-8 (2000): 93-98.

[21] McDannold, N., N. Vykhodtseva, and K. Hynynen. ”Targeted disruption of the blood–brain barrier with focused ultrasound: association with cavitation activity.” Physics in Medicine & Biology 51.4 (2006): 793.

[22] Holt, R. Glynn, and Ronald A. Roy. ”Measurements of bubble-enhanced heating from focused, MHz-frequency ultrasound in a tissue-mimicking material.” Ultrasound in medicine & biology27.10 (2001): 1399-1412.

[23] Yoshizawa, Shin, et al. ”High intensity focused ultrasound lithotripsy with cavitating microbubbles.” Medical & biological engineering & computing 47.8 (2009): 851-860.

[24] Sojahrood, Amin Jafari, and Michael C. Kolios. ”Classification of the nonlinear dynamics and bifurcation structure of ultrasound contrast agents excited at higher multiples of their resonance frequency.” Physics Letters A 376.33 (2012): 2222-2229.

[25] Behnia, Sohrab, et al. ”Suppressing chaotic oscillations of a spherical cavitation bubble through applying a periodic perturbation.” Ultrasonics sonochemistry 16.4 (2009): 502-511.

[26] Sojahrood, Amin Jafari, et al. ”Influence of the pressure-dependent resonance frequency on the bifurcation structure and backscattered pressure of ultrasound contrast agents: a numerical investigation.” Nonlinear Dynamics 80.1-2 (2015): 889-904.

[27] Behnia S., Jafari A., Soltanpoor W. and Jahanbakhsh O. Nonlinear transitions of a spherical cavitation bubble, Choas, Solitons & Fractals, 41 (2), (2009): 818-828.

[28] Hegedűs, Ferenc, and László Kullmann. ”Basins of attraction in a harmonically excited spherical bubble model.” Periodica Polytechnica Mechanical Engineering 56.2 (2012): 125-132.

[29] Hegedűs, Ferenc, et al. ”Non-feedback technique to directly control multistability in nonlinear oscillators by dual-frequency driving.” Nonlinear Dynamics (2018): 1-21.

[30] Hegedűs, Ferenc, and Csanád Kalmár. ”Dynamic stabilization of an asymmetric nonlinear bubble oscillator.” Nonlinear Dynamics: 1-18.

[31] Hegedűs, Ferenc. ”Topological analysis of the periodic structures in a harmonically driven bubble oscillator near Blake’s critical threshold: Infinite sequence of two-sided Farey ordering trees.” Physics Letters A 380.9-10 (2016): 1012-1022.

[32] Varga, Roxána, and Ferenc Hegedűs. ”Classification of the bifurcation structure of a periodically driven gas bubble.” Nonlinear Dynamics 86.2 (2016): 1239-1248.

[33] Hegedűs, F., Cs Hős, and L. Kullmann. ”Stable period 1, 2 and 3 structures of the harmonically excited Rayleigh–Plesset equation applying low ambient pressure.” The IMA Journal of Applied Mathematics 78.6 (2012): 1179-1195.

[34] Zhang, Yuning. ”Chaotic oscillations of gas bubbles under dual-frequency acoustic excitation.” Ultrasonics sonochemistry40 (2018): 151-157.

[35] Zhang, Yuning, Yuhang Gao, and Xiaoze Du. ”Stability mechanisms of oscillating vapor bubbles in acoustic fields.” Ultrasonics sonochemistry 40 (2018): 808-814.

[36] Zhang, Y. N., and S. C. Li. ”Bubble dynamics under acoustic excitation with multiple frequencies.” IOP Conference Series: Materials Science and Engineering. Vol. 72. No. 1. IOP Publishing, 2015.

[37] Zhang, Yuning, and Shengcai Li. ”Combination and simultaneous resonances of gas bubbles oscillating in liquids under dual-frequency acoustic excitation.” Ultrasonics sonochemistry 35 (2017): 431-439.

[38] Quaia, Emilio. ”Assessment of tissue perfusion by contrast-enhanced ultrasound.” European radiology 21, no. 3 (2011): 604-615.

[39] Correas, Jean-Michel, Michel Claudon, François Tranquart, and Olivier Hélénon. ”The kidney: imaging with microbubble contrast agents.” Ultrasound quarterly 22, no. 1 (2006): 53-66.

[40] Sijl, Jeroen, Benjamin Dollet, Marlies Overvelde, Valeria Garbin, Timo Rozendal, Nico De Jong, Detlef Lohse, and Michel Versluis. ”Subharmonic behavior of phospholipid-coated ultrasound contrast agent microbubbles.” The Journal of the Acoustical Society of America 128, no. 5 (2010): 3239-3252.

[41] Needles, A., D. E. Goertz, R. Karshafian, E. Cherin, A. S. Brown, P. N. Burns, and F. S. Foster. ”High-frequency subharmonic pulsed-wave Doppler and color flow imaging of microbubble contrast agents.” Ultrasound in medicine & biology 34, no. 7 (2008): 1139-1151.

[42] Liu, Ji-Bin, Daniel A. Merton, Flemming Forsberg, and Barry B. Goldberg. ”Contrast-Enhanced Ultrasound Imaging.” In Diagnostic Ultrasound, pp. 51-74. CRC Press, 2019.

[43] Forsberg, Flemming, Maria Stanczak, Andrej Lyshchik, David Loren, Patrick O'kane, Ali Siddiqui, Thomas E. Kowalski et al. "Subharmonic and Endoscopic Contrast Imaging of Pancreatic Masses: A Pilot Study." Journal of Ultrasound in Medicine 37, no. 1 (2018): 123-129.

[44] Coussios, CC, et al. "Role of acoustic cavitation in the delivery and monitoring of cancer treatment by high-intensity focused ultrasound (HIFU)." International Journal of Hyperthermia 23.2 (2007): 105-120.

[45] K.J. Haworth, et al., Passive imaging with pulsed ultrasound insonations, The Journal of the Acoustical Society of America, 132(1) (2012): 544-553.

[46] M.A. OReilly, et al, Focused-ultrasound disruption of the blood-brain barrier using closely-timed short pulses: inflence of sonication parameters and injection rate, Ultrasound in medicine & biology 37 (2011): 587-594.

[47] Jones, Ryan M., and Kullervo Hynynen. "Advances in acoustic monitoring and control of focused ultrasound-mediated increases in blood-brain barrier permeability." The British journal of radiology 92, no. xxxx (2019): 20180601.

[48] Gupta, Ipshita, John R. Eisenbrey, Priscilla Machado, Maria Stanczak, Kirk Wallace, and Flemming Forsberg. "On Factors Affecting Subharmonic-aided Pressure Estimation (SHAPE)." Ultrasonic imaging 41, no. 1 (2019): 35-48.

[49] Dave, Jaydev K., Valgerdur G. Halldorsdottir, John R. Eisenbrey, Daniel A. Merton, Ji-Bin Liu, Jian-Hua Zhou, Hsin-Kai Wang et al. "Investigating the efficacy of subharmonic aided pressure estimation for portal vein pressures and portal hypertension monitoring." Ultrasound in medicine & biology 38, no. 10 (2012): 1784-1798.

[50] Jimenez-Fernandez, J. "Dependence of the subharmonic signal from contrast agent microbubbles on ambient pressure: A theoretical analysis." The Journal of the Acoustical Society of America 143, no. 1 (2018): 169-179.

[51] Goertz, David E., et al. "Subharmonic contrast intravascular ultrasound for vasa vasorum imaging." Ultrasound in medicine & biology 33.12 (2007): 1859-1872.

[52] Helfield, Brandon L., Emmanuel Cherin, F. Stuart Foster, and David E. Goertz. ”Investigating the subharmonic response of individual phospholipid encapsulated microbubbles at high frequencies: A comparative study of five agents.” Ultrasound in medicine & biology 38, no. 5 (2012): 846-863.

[53] Leighton, T. G., et al. ”Acoustic bubble sizing by the combination of subharmonic emissions with an imaging frequency.” Ultrasonics 29.4 (1991): 319-323.

[54] R. Esche, “Investigations on oscillating cavities in liquids,” Acustica 2, 208–218 1952.

[55] Eller, Anthony, and H. G. Flynn. ”Generation of subharmonics of order one-half by bubbles in a sound field.” The Journal of the Acoustical Society of America 46.3B (1969): 722-727.

[56] Prosperetti, Andrea. ”Nonlinear oscillations of gas bubbles in liquids: steady-state solutions.” The Journal of the Acoustical Society of America 56.3 (1974): 878-885.

[57] Prosperetti, Andrea. ”Application of the subharmonic threshold to the measurement of the damping of oscillating gas bubbles.” The Journal of the Acoustical Society of America61.1 (1977): 11-16.

[58] Prosperetti, Andrea. ”Application of the subharmonic threshold to the measurement of the damping of oscillating gas bubbles.” The Journal of the Acoustical Society of America61.1 (1977): 11-16.

[59] Prosperetti, Andrea. ”A general derivation of the subharmonic threshold for non-linear bubble oscillations.” The Journal of the Acoustical Society of America 133.6 (2013): 3719-3726

[60] M. S. Plesset and A. Prosperetti, “Bubble dynamics and cavitation,” Annu. Rev. Fluid Mech. 9, 145–185 1977.

[61] Krishna, P. D., P. M. Shankar, and V. L. Newhouse. ”Subharmonic generation from ultrasonic contrast agents.” Physics in Medicine & Biology 44.3 (1999): 681.

[62] Shankar, P. M., P. D. Krishna, and V. L. Newhouse. ”Subharmonic backscattering from ultrasound contrast agents.” The Journal of the Acoustical Society of America106.4 (1999): 2104-2110.

[63] Kimmel, Eitan, et al. ”Subharmonic response of encapsulated microbubbles: Conditions for existence and amplification.” Ultrasound in medicine & biology 33.11 (2007): 1767-1776.

[64] Katiyar, Amit, and Kausik Sarkar. ”Effects of encapsulation damping on the excitation threshold for subharmonic generation from contrast microbubbles.” The Journal of the Acoustical Society of America 132.5 (2012): 3576-3585.

[65] Katiyar, Amit, and Kausik Sarkar. ”Excitation threshold for subharmonic generation from contrast microbubbles.” The Journal of the Acoustical Society of America 130.5 (2011): 3137-3147.

[66] Sojahrood, A.J., Earl, R., Kolios, M.C. and Karshafian, R., 2020. Investigation of the 1/2 order subharmonic emissions of the period-2 oscillations of an ultrasonically excited bubble. Physics Letters A, p.126446.

[67] Flynn, H.G., Church, C.C.: Transient pulsations of small gas bubbles in water. J. Acoust. Soc. Am. 84, 985–998 (1988)

[68] Keller, Joseph B., and Michael Miksis. ”Bubble oscillations of large amplitude.” The Journal of the Acoustical Society of America 68.2 (1980): 628-633.

[69] Sojahrood, A. J., et al. ”A comprehensive bifurcation method to analyze the super-harmonic and ultra-harmonic behavior of the acoustically excited bubble oscillator.” arXiv preprint arXiv:1810.01239 (2018).

[70] A.J. Sojahrood, D. Wegierak, H. Haghi, R. Karshfian, and M. C. Kolios. A simple method to analyze the super-harmonic and ultra-harmonic behavior of the acoustically excited bubble oscillator. Ultrasonics sonochemistry, 54 (2019); 99-109.

[71] Hilgenfeldt, Sascha, Detlef Lohse, and Michael Zomack. ”Sound scattering and localized heat deposition of pulse-driven microbubbles.” The Journal of the Acoustical Society of America 107.6 (2000): 3530-3539.

[72] Radhakrishnan, K., Bader, K.B., Haworth, K.J., Kopechek, J.A., Raymond, J.L., Huang, S.L., McPherson, D.D. and Holland, C.K., 2013. ”Relationship between cavitation and loss of echogenicity from ultrasound contrast agents.” Physics in Medicine & Biology, 58(18), p.6541.

[73] Philips, P., Gardner, E.: Contrast-agent detection and quantification. Eur. Radiol. Suppl. 14(8), 4–10 (2004)

[74] Brock-Fisher, A.G., Poland, M., Rafter, P.: Means for increasing sensitivity in nonlinear imaging systems. US Patent 5577505 (1996)

[75] Eckersley, R.J., Chin, C.T., Burns, P.N.: Optimizing phase and amplitude modulation schemes for imaging microbubble contrast agents at low acoustic power. Ultrasound Med. Biol. 6(31), 213–219 (2005)

[76] Marmottant, P., van der Meer, S., Emmer, M., Versluis, M., de Jong, N., Hilgenfeldt, S., & Lohse, D. (2005). A model for large amplitude oscillations of coated bubbles accounting for buckling and rupture. The Journal of the Acoustical Society of America, 118(6), 3499-3505.

[77] Kleven, R.T., Karani, K.B., Salido, N.G., Shekhar, H., Haworth, K.J., Mast, T.D., Tadesse, D.G. and Holland, C.K., 2019. The effect of 220 kHz insonation scheme on rt-PA thrombolytic efficacy in vitro. Physics in Medicine & Biology in Press.

[78] Frinking, Peter JA, Emmanuel Gaud, Jean Brochot, and Marcel Arditi. "Subharmonic scattering of phospholipid-shell microbubbles at low acoustic pressure amplitudes." IEEE transactions on ultrasonics, ferroelectrics, and frequency control 57, no. 8 (2010): 1762-1771.

[79] Faez, Telli, Marcia Emmer, Margreet Docter, Jeroen Sijl, Michel Versluis, and Nico de Jong. "Characterizing the subharmonic response of phospholipid-coated microbubbles for carotid imaging." Ultrasound in medicine & biology 37, no. 6 (2011): 958-970.

[80] Sijl, Jeroen, Marlies Overvelde, Benjamin Dollet, Valeria Garbin, Nico De Jong, Detlef Lohse, and Michel Versluis. ""Compression-only" behavior: A second-order nonlinear response of ultrasound contrast agent microbubbles." The Journal of the Acoustical Society of America 129, no. 4 (2011): 1729-1739.

[81] Helfield, Brandon L., Emmanuel Cherin, F. Stuart Foster, and David E. Goertz. "Investigating the subharmonic response of individual phospholipid encapsulated microbubbles at high frequencies: A comparative study of five agents." Ultrasound in medicine & biology 38, no. 5 (2012): 846-863.

[82] Sijl, Jeroen, Hendrik J. Vos, Timo Rozendal, Nico de Jong, Detlef Lohse, and Michel Versluis. ”Combined optical and acoustical detection of single microbubble dynamics.” The Journal of the Acoustical Society of America 130, no. 5 (2011): 3271-3281.

[83] Jafari Sojahrood, Amin, Raffi Karshafian, and Michael C. Kolios. ”Bifurcation structure of the ultrasonically excited microbubbles undergoing buckling and rupture.” In Proceedings of Meetings on Acoustics ICA2013, vol. 19, no. 1, p. 075097. ASA, 2013.

[84] Sojahrood, Amin Jafari, Raffi Karshafian, and Michael C. Kolios. ”Detection and characterization of higher order nonlinearities in the oscillations of Definity at higher frequencies and very low acoustic pressures.” In 2012 IEEE International Ultrasonics Symposium.

[85] Prosperetti, Andrea, Lawrence A. Crum, and Kerry W. Commander. ”Nonlinear bubble dynamics.” The Journal of the Acoustical Society of America 83, no. 2 (1988): 502-514.

[86] Stricker, Laura, Andrea Prosperetti, and Detlef Lohse. ”Validation of an approximate model for the thermal behavior in acoustically driven bubbles.” The Journal of the Acoustical Society of America 130, no. 5 (2011): 3243-3251.

[87] Zhang, Yuning, and S. C. Li. ”Notes on radial oscillations of gas bubbles in liquids: Thermal effects.” The Journal of the Acoustical Society of America 128, no. 5 (2010): EL306-EL309.

[88] Hegedűs, Ferenc, Csaba Hős, and László Kullmann. ”Influence of heat transfer on the dynamic response of a spherical gas/vapour bubble.” International Journal of Heat and Fluid Flow 31, no. 6 (2010): 1040-1049.

[89] Haghi, H., Sojahrood, A.J. and Kolios, M.C., 2019. Collective nonlinear behavior of interacting polydisperse microbubble clusters. Ultrasonics Sonochemistry, p.104708.

[90] Pandey, V., 2019. Asymmetricity and sign reversal of secondary Bjerknes force from strong nonlinear coupling in cavitation bubble pairs. Physical Review E, 99(4), p.042209.

[91] Pandey, V., 2018. Simulated cavitation noise from strong nonlinear coupling in a multi-bubble system. The Journal of the Acoustical Society of America, 144(3), pp.1985-1985.

[92] Pandey, V., 2018. Strong nonlinear coupling between two cavitation bubbles in an acoustic field. The Journal of the Acoustical Society of America, 144(3), pp.1984-1984.

[93] Nguyen, D.M., Sanathanan, M.S., Miao, J., Rivas, D.F. and Ohl, C.D., 2019. In-phase synchronization between two auto-oscillating bubbles. Physical review fluids, 4(4), p.043601.

Chapter 6

Critical corrections to formulations of nonlinear power dissipation of ultrasonically excited bubbles

6.1 Abstract

Current models for calculating nonlinear power dissipation during the oscillations of acoustically excited bubbles generate non-physical values for the radiation damping (Rd) term for some frequency and pressure regions that include near resonance oscillations. Moreover, ratio of the dissipated powers significantly deviate from the values that are calculated by the linear model at low amplitude oscillations (acoustic excitation pressure of $P_A = 1kPa$ and expansion ratio of $<\approxeq 1.01$) . In high amplitude oscillation regimes ($P_a \geq 20kPa$), the dissipated power due to Rd deviates largely from the dissipated power as calculated by the widely accepted approach that uses the scattered power by the bubbles. We provide critical corrections to the present models. The validity of the results were examined in regimes of low amplitude oscillations and high amplitude oscillations. In the low amplitude regime, the ratio of the dissipated powers as calculated by the current and proposed model were compared with the linear model predictions. At higher amplitude oscillations, the dissipated power by radiation loss as calculated by the current and the proposed model were compared with the dissipated power calculated using the scattered energy by the bubbles. We show that non-physical values are absent in the proposed model. Moreover, predictions of the proposed approach are identical to the predictions of the linear model and the dissipated power estimated using the scattered pressure by the bubble. We show that damping due

to thermal effects, liquid viscosity and radiation heavily depend on the excitation pressure and that the linear model estimations are not valid even at pressures as low as 20 kPa[1].

6.2 Introduction

Bubbles attenuate ultrasound through radiation damping (Rd), thermal damping (Td) and damping due to liquid viscosity ($L_{vis}d$) [1,2,3,4,5,6]. Radiation damping is due to the energy re-radiated away from the bubble as acoustic waves due to bubble oscillations ([4]- p. 175). Td occurs due to the temperature loss from thermal conduction between the gas and the surrounding liquid ([4]- p. 175). $L_{vis}d$ occurs due to the work that the bubble wall does against the viscous forces of the liquid.

Numerous studies have investigated the mechanisms of damping in bubbly media; using linear approximations (limited to very small bubble oscillation amplitudes) and neglecting the dependence of the dissipated energy on the local pressure [4, 5, 6, 7, 8]. Semi-linear approaches have also been developed that only considered the pressure dependence of the radiation damping while using linear terms for the other damping factors (thermal and viscous damping) [9].

In many bubble dynamic studies, thermal effects are either neglected or simplified using models that are derived based on linear approximations [4, 5, 6, 7, 8, 9]. Zhang and Li [10] investigated the thermal effects on the nonlinear radial oscillations of bubbles. Although they used the linear estimations for thermal effects, their study showed that the nonlinear bubble behavior was significantly influenced by thermal effects.

In their linear form, Rd, Td, and $L_{vis}d$ are functions of bubble initial radii and acoustic driving frequency. Linear thermal effects have been studied in detail in [11]. Prosperetti [12], numerically investigated the linear damping constants of bubbles with $10^{-4} - 0.1cm$ over a frequency range of $10Hz - 10^{8}Hz$. He showed that damping due to viscosity is higher in smaller bubbles while radiation damping and thermal damping show a frequency dependent behavior. For a given bubble size, radiation damping is small at lower frequencies and increases with frequency. Thermal damping is stronger at lower frequencies and deceases with frequency. In terms of the Péclet number (defined as $P_{eb} = \frac{\omega R_0^2}{D_b^T}$ where ω is the angular frequency of the acoustic field, R_0 is the

[1]Published as: Sojahrood, A.J., Haghi, H., Karshafian, R. and Kolios, M.C., 2020. Critical corrections to models of nonlinear power dissipation of ultrasonically excited bubbles. Ultrasonics Sonochemistry, 66, pp.105089-105089.

bubble initial radius and D_b^T is the thermal diffusivity inside the bubble), viscous damping is the typical dominating damping mechanism for small Péclet numbers, thermal damping is stronger for medium Péclet numbers and radiation damping is larger for larger Péclet numbers [13].

The damping terms Td, $L_{vis}d$ and Rd, however, are nonlinear and pressure dependent [1,2]. These parameters are functions of the bubble radial oscillations which are shown to exhibit nonlinear behavior including subharmonic, superharmonic and chaotic oscillations [14, 15, 16, 17, 18, 19, 20, 21]. Moreover, bubble oscillations are nonlinear in the majority of applications (e.g. [22, 23, 24, 25, 26, 27, 28, 29, 30, 31]). In these applications, the higher acoustic pressures result in nonlinear large amplitude bubble oscillations; thus, linear approximations fail to accurately model the medium dissipation and therefore attenuation. A more complete estimation of the wave dissipation in bubbly media requires an accurate estimation of the power dissipated by the nonlinear oscillations of the bubbles that includes pressure dependent effects of the dissipation mechanisms [1, 2, 3, 32, 33].

Louisnard [1], starting with mass and momentum conservation equations for a bubbly liquid and using Rayleigh-Plesset equation [34] has derived the nonlinear energy terms for Td and $L_{vis}d$. He showed that damping from nonlinear oscillations of the bubbles can be several orders of magnitude higher than the damping estimated by linear models. Jamshidi and Brenner [2] used the approach introduced by Louisnard [1] in conjunction with the Keller-Miksis equation [35] accounting for the compressibility of the medium to the first order of acoustical Mach number. Incorporation of the changes in the compressibility of the medium allowed for the derivation of Rd and small modifications in Td and $L_{vis}d$. It was shown [2, 3] that radiation damping increases significantly above Blake threshold and becomes one of the major contributors to total damping and cannot be neglected. However, as it will be shown here, the terms that are derived in [2], have errors and need to be corrected. Rd at its current form in [2] leads to negative values near resonance and in some frequency and pressure ranges. Additionally, the ratio of dissipated powers (e.g. $\frac{<Td>}{<Rd>}$ and $\frac{<L_{vis}d>}{<Rd>}$ where $<>$ stands for time-averaged) at linear regimes ($P_a \leq 1kPa$) significantly deviate from the linear power ratios. Predictions of $< Rd >$ significantly deviate from the results of the acoustic power radiated by the bubbles ($< Sd >$). A damping factor should always have positive values; it can not be negative. Moreover, in linear oscillation regimes, the ratio of dissipated powers must be in agreement with linear predictions. Finally, $< Rd >$ and $< Sd >$ should have the same

values. This is because $< Rd >$ and $< Sd >$ both describe the same phenomenon which is damping due to the acoustic energy radiated by the bubbles.

In this work, the nonlinear terms for Td, Rd and $L_{vis}d$ were re-arranged and new expressions were proposed. The proposed terms do not return negative values for damping terms. The solutions using the new approach were verified in the linear regime. In the pressure dependent regime, using the pressure radiated by pulsating bubbles [4, 36, 37, 38], the acoustic power radiated by the bubbles were calculated and the accuracy of the new model were verified.

6.3 Methods

6.3.1 Mass and momentum equations for bubbly media

van Wijngaardan [39] and Caflisch et al. [40] presented the mass and momentum conservation equations for a bubbly liquid as:

$$\frac{1}{\rho c^2}\frac{\partial P}{\partial t} + \nabla . v = \frac{\partial \beta}{\partial t} \tag{6.1}$$

and

$$\rho \frac{\partial v}{\partial t} = -\nabla P \tag{6.2}$$

where c is the sound speed, ρ is the density of the medium, $v(r,t)$ is the velocity field, $P(r,t)$ is the acoustic pressure, $\beta = \frac{4}{3}N\pi R(t)^3$ is the void fraction where N is number of bubbles per unit volume, and $R(t)$ is the radius of the bubble at time t. Eqs. 1 and 2, can be re-written into an equation of energy conservation, by multiplying (1) by P and (2) by v:

$$\frac{\partial}{\partial t}\left(\frac{1}{2}\frac{P^2}{\rho c^2} + \frac{1}{2}\rho v^2\right) = NP\frac{\partial V}{\partial t} \tag{6.3}$$

Where V is the volume occupied by gas.

Thermal parameters of the Air at 1 atm [42]			
L ($\frac{W}{m^0C}$)	$C_p \frac{kJ}{kg^0C}$	C_v $\frac{kJ}{kg^0C}$	ρ_g $\frac{kg}{m^3}$
0.01165+C*T	1.0049	0.7187	1.025

Table 6.1: Thermal properties used in simulations. (C=$5.528 * 10^{25}$ $\frac{W}{mK^2}$)

6.3.2 The Bubble model

The dynamics of the bubble model including the compressibility effects to the first order of Mach number can be modelled using Keller-Miksis equation [35]:

$$\rho[\left(1-\frac{\dot{R}}{c}\right)R\ddot{R}+\frac{3}{2}\dot{R}^2\left(1-\frac{\dot{R}}{3c}\right)]=\left(1+\frac{\dot{R}}{c}\right)G+\frac{R}{c}\frac{dG}{dt} \tag{6.4}$$

where $G = P_g - \frac{4\mu_L\dot{R}}{R} - \frac{2\sigma}{R} - P_0 - P_A sin(2\pi ft)$.

In this equation, R is radius at time t, R_0 is the initial bubble radius, $\dot{R}$ is the wall velocity of the bubble, $\ddot{R}$ is the wall acceleration, ρ is the liquid density (998 $\frac{kg}{m^3}$), c is the sound speed of the medium (1481 m/s), P_g is the gas pressure, σ is the surface tension (0.0725 $\frac{N}{m}$), μ is the liquid viscosity (0.001 Pa.s), and P_A and f are the amplitude and frequency of the applied acoustic pressure. The values in the parentheses are for pure water at 293 K. In this paper the gas inside the bubble is air and water is the host media.

P_g is given by Eq. 5 [41]:

$$P_g = \frac{N_g KT}{\frac{4}{3}\pi R(t)^3 - NB} \tag{6.5}$$

where N_g is the total number of the gas molecules, K is the Boltzman constant and B is the molecular co-volume. The average temperature inside the gas can be calculated using Eq. 6:

$$\dot{T} = \frac{4\pi R(t)^2}{C_v}(\frac{L(T_0 - T)}{L_{th}} - \dot{R}P_g) \tag{6.6}$$

Where C_v is the specific heat at constant volume, T_0=$300K$ is the initial gas temperature, L_{th} is the thickness of the thermal boundary layer. L_{th} is given by $L_{th} = min(\sqrt{\frac{DR(t)}{|\dot{R}(t)|}}, \frac{R(t)}{\pi})$ where D is the thermal diffusivity of the gas. D can be calculated using $D = \frac{L}{C_p\rho_g}$ where L is the gas thermal conductivity, C_p is specific heat at constant pressure and ρ_g is the gas density.

To calculate the radial oscillations of the bubble Eqs. 4, 5 and 6 are coupled and solved using

the ode45 solver of MATLAB with relative and absolute tolerances of $1e-12$ and $1e-13$ respectively. The time steps of each solution was $\frac{1e-4}{f}$ where f is the sonication frequency in Hz. The initial conditions of $R(t=0s)=R_0$, $\dot{R}(t=0s)=R_0$, $P_g(t=0s)=P_0+\frac{2\sigma}{R_0}$ where $P_0=101kPa$ is the atmospheric pressure and $T(t=0s)=300K$.

6.3.3 Derivation of the damping terms

Multiplying both sides of Eq.4 by $\frac{N\partial V}{\partial t}$ and summation with equation 3 yields:

$$\rho N\left(R\ddot{R}+\frac{3}{2}\dot{R}^2\right)\frac{\partial V}{\partial t}-\rho N\frac{\dot{R}}{c}\left(R\ddot{R}+\frac{1}{2}\dot{R}^2\right)\frac{\partial V}{\partial t}+\frac{\partial}{\partial t}\left(\frac{1}{2}\frac{P^2}{\rho c^2}+\frac{1}{2}\rho v^2\right)+\nabla.(Pv)$$

$$=N\left(P_g+\frac{\dot{R}}{c}P_g+\frac{R}{c}\frac{dP_g}{dt}\right)\frac{\partial V}{\partial t}-N\left(\frac{4\mu_L\dot{R}}{R}+\frac{\dot{R}}{c}\frac{4\mu_L\dot{R}}{R}+\frac{R}{c}\frac{d(\frac{4\mu_L\dot{R}}{R})}{dt}\right)\frac{\partial V}{\partial t}$$

$$-N\left(\frac{2\sigma}{R}+\frac{\dot{R}}{c}\frac{2\sigma}{R}+\frac{R}{c}\frac{d(\frac{2\sigma}{R})}{dt}\right)\frac{\partial V}{\partial t}-N\left(\frac{\dot{R}}{c}P+\frac{R}{c}\frac{dP}{dt}\right)\frac{\partial V}{\partial t} \tag{6.7}$$

The kinetic energy of the liquid around bubble can be written as [2]:

$$K_l=2\pi\rho R^3\dot{R}^2 \tag{6.8}$$

using Eqs. 7 and 8 and re-arranging terms we will have:

$$\frac{\partial}{\partial t}\left(\frac{1}{2}\frac{P^2}{\rho c^2}+\frac{1}{2}\rho v^2+NK_l+4N\pi R^2\sigma\right)+\nabla.(Pv)=N\left(P_g\right)\frac{\partial V}{\partial t}-N\left(\frac{4\mu_L\dot{R}}{R}\right)-$$

$$N\left(\left(\frac{\dot{R}}{c}P+\frac{R}{c}\frac{dP}{dt}-\frac{\dot{R}}{c}P_g-\frac{R}{c}\frac{dP_g}{dt}+\frac{\dot{R}}{c}\frac{4\mu_L\dot{R}}{c}+\frac{R}{c}\frac{d(\frac{4\mu_L\dot{R}}{R})}{dt}\right)\frac{\partial V}{\partial t}-\frac{\dot{R}}{c}\frac{\partial K_l}{\partial t}\right) \tag{6.9}$$

Eq.9 can be written as:

$$\frac{\partial}{\partial t}\left(\frac{1}{2}\frac{P^2}{\rho c^2}+\frac{1}{2}\rho v^2+NK_l+4N\pi R^2\sigma\right)+\nabla.(Pv)=-N\left(Td+L_{vis}d+Rd\right) \tag{6.10}$$

where Td, $L_{vis}d$ and Rd are time dependent thermal, liquid and radiation damping respectively. $\frac{1}{2}\frac{P^2}{\rho c^2}$ is the elastic potential energy that is stored in the liquid and $\frac{1}{2}\rho v^2$ is the kinetic energy per unit volume of the liquid [2] For N=1, Jamshidi and Brenner presented the damping terms in Eq. 9 as:

$$\begin{cases} Td = (-P_g - \dfrac{\dot{R}}{c}P_g - \dfrac{R}{c}\dot{P_g})\dfrac{\partial V}{\partial t} \\ L_{vis}d = \left(\dfrac{4\mu_L\dot{R}}{R} + \dfrac{\dot{R}}{c}\dfrac{4\mu_L\dot{R}}{c} + \dfrac{R}{c}\dfrac{d(\frac{4\mu_L\dot{R}}{R})}{dt}\right)\dfrac{\partial V}{\partial t} \\ Rd = \left(\dfrac{\dot{R}}{c}P + \dfrac{R}{c}\dfrac{dP}{dt}+\right)\dfrac{\partial V}{\partial t} - \dfrac{\dot{R}}{c}\dfrac{\partial K_l}{\partial t} \end{cases} \tag{6.11}$$

Integrating Eq.11 over one acoustic period T results in:

$$\frac{1}{T}\int_0^T \frac{\partial}{\partial t}\left(\frac{1}{2}\frac{P^2}{\rho c^2} + \frac{1}{2}\rho v^2 + K_l + 4\pi R^2\sigma\right) + \nabla.< Pv >= -< (Td + L_{vis}d + Rd) > \tag{6.12}$$

The first term on the left hand side of Eq. 12 cancels over time T ($T = \frac{n}{f}$ where n=1,2,...) [1, 2]. Assuming periodic oscillations of the bubbles and averaging over T, the first two terms of the LHS of Eq. 10 cancel due to their periodic nature [1, 2].

However, the last two terms of the LHS of Eq. 10 do not necessarily cancel out depending on the oscillations [2]. NK_l is the kinetic energy per unit volume of the liquid due to its radial movement around the bubbles and $4\pi N\sigma R^2$ is the interfacial potential energy per unit volume. Taking integration over time $T = \frac{n}{f}$:

$\frac{1}{T}\int_0^T \frac{\partial}{\partial t}\left(NK_l\right)dt = \frac{2\pi N}{T}\rho\left(R(T)^3\dot{R}(T)^2 - R(0)^3\dot{R}(0)^2\right)$

$\frac{1}{T}\int_0^T \frac{\partial}{\partial t}\left(4\pi N\sigma R^2\right)dt = \frac{4\pi N}{T}\sigma\left(R(T)^2 - R(0)^2\right)$

In the case of stable bubble behavior, the bubble oscillates nonlinearly around R_0. At the end of each cycle, the radius is approximately equal to R_0 and the next cycle starts similar to the previous one. Thus, we can assume $R(T) \approxeq R_0$ and $\dot{R}(0) = 0m/s$ & $\dot{R}(T) \approxeq 0\ m/s$ [2] and thus, the integrals become zero or very small in magnitude [2]. If the bubble transiently collapses, the bubble will collapse before reaching the end of a cycle. After a violent collapse it starts to ring-down with the bubble resonance frequency in a series of after bounces to the end of the cycle. In this situation, again, $R(T) \approxeq R_0$ and $\dot{R}(0) = 0\ m/s$ and $\dot{R}(T) \approxeq 0\ m/s$ and the integrals can be neglected due to very small amplitudes [2]. In the case of a collapse before reaching to the end of an acoustic cycle

[2]For information on the derivation of the $\frac{1}{2}\frac{P^2}{\rho c^2}$ and $\frac{1}{2}\frac{P^2}{\rho c^2}$ one can refer to [38] p. 255.

(above the Blake threshold), an energy of approximately $4\pi R^2\sigma$ is dissipated [2]. For a bubble with the R_0 in the μm range, this energy is approximately ten orders of magnitude less than the other dissipated energies [2] and can also be neglected.

Thus the dissipated powers become:

$$\begin{cases} < Td >= \dfrac{-1}{T}\displaystyle\int_0^T (P_g + \frac{\dot{R}}{c}P_g + \frac{R}{c}\dot{P}_g)\frac{\partial V}{\partial t}dt \\ \\ < L_{vis}d >= \dfrac{16\pi\mu_L}{T}\displaystyle\int_0^T (R\dot{R}^2 + \frac{R^2\dot{R}\ddot{R}}{c})dt \\ \\ < Rd >= \dfrac{1}{T}\displaystyle\int_0^T \left[\frac{4\pi}{c}\left(R^2\dot{R}\left(\dot{R}P + R\dot{P} - \frac{1}{2}\rho\dot{R}^3 - \rho R\dot{R}\ddot{R}\right)\right)\right]dt \end{cases} \tag{6.13}$$

where $< Td >$, $< L_{vis}d >$ and $< Rd >$ are total energy loss over time T (Dissipated power). In this paper, the integrations are performed over the last 40 cycles of a 240 cycle pulse to ensure transient behavior has subsided. However, Eq. 13 in its current form is not correct and several terms need to be re-arranged. Every term that contains the sound speed represents the compressibility effects to the first order of Mach number and should be added to the radiation damping term. Thus the proposed damping terms will be in the form of Eq. 14:

$$\begin{cases} < Td >= \dfrac{-1}{T}\displaystyle\int_0^T (P_g)\,\frac{\partial V}{\partial t}dt \\ \\ < L_{vis}d >= \dfrac{16\pi\mu_L}{T}\displaystyle\int_0^T \left(R\dot{R}^2\right)dt \\ \\ < Rd >= \dfrac{1}{T}\displaystyle\int_0^T \left[\frac{4\pi}{c}\left(R^2\dot{R}\left(\dot{R}P + R\dot{P} - \frac{1}{2}\rho\dot{R}^3 - \rho R\dot{R}\ddot{R}\right)\right)\right. \\ \qquad\qquad \left. - \left(\frac{\dot{R}}{c}P_g + \frac{R}{c}\dot{P}_g\right)\frac{\partial V}{\partial t} + \frac{16\pi\mu_L R^2\dot{R}\ddot{R}}{c}\right]dt \end{cases} \tag{6.14}$$

6.3.4 Ratio of dissipated powers during low amplitude oscillation regimes

One way to validate Eq. 13 and Eq. 14 is to focus on the linear oscillation regimes ($P_a = 1kPa$) and compare the ratios of the dissipated powers $\frac{<Td>}{<Rd>}$ and $\frac{<L_{vis}d>}{<Rd>}$ with the ratios of the dissipated

powers from the analytical expressions of the linear model [5, 11, 12]. In the linear regime, the ratio of the dissipated powers equals the ratio of the damping constants [4](p.296). The constants of the bubble oscillations for radiation, thermal and viscous damping are given by the following analytical expressions [5, 11, 12]:

$$\begin{cases} \beta_{L_{vis}} = \dfrac{2\mu}{\rho R_0^2} \\ \\ \beta_{th} = \dfrac{2\mu_{th}}{\rho R_0^2} \\ \\ \beta_{rd} = \dfrac{\omega^2 a}{2c} \end{cases} \tag{6.15}$$

In Eq. 21, $\beta_{L_{vis}}$, β_{th} and β_{rd} are respectively damping constants due to liquid viscosity, thermal and radiation. In this equation, μ_{th} is thermal viscosity [5, 11, 12] and ω is the acoustic angular frequency. μ_{th} is given by:

$$\mu_{th} = \frac{P_{g0}\Im(\phi)}{4\omega} \tag{6.16}$$

where P_{g0} is the initial gas pressure, $\Im$ is the imaginary part and the complex term ϕ is calculated from [11]:

$$\phi = \frac{3\gamma}{1 - 3\left(\gamma - 1\right) i\chi \left[\left(\frac{i}{\chi}\right)^{\frac{1}{2}} coth\left(\frac{i}{\chi}\right)^{\frac{1}{2}} - 1\right]} \tag{6.17}$$

where γ is the polytropic exponent and $\chi = \frac{D}{\omega R_0^2}$ represents the thermal diffusion length where D is the thermal diffusivity of the gas.

The ratio of the dissipated powers in the linear regime should thus follow: $\frac{<Td>}{<Rd>} = \frac{\beta_{th}}{\beta_{rd}}$ and $\frac{<L_{vis}d>}{<Rd>} = \frac{\beta_{L_{vis}}}{\beta_{rd}}$.

6.3.5 Acoustic power due to scattered pressure by bubbles

Radiation damping is due to the re-radiated (scattered) pressure by the bubble. Thus, $< Rd >$ should be equal to the acoustic power that is scattered by the bubble [22, 23, 24, 37]. Here, we will first introduce the derivation of the energy that the spherical bubble radiates. Vokurka [36] started

with the Euler's equation ([38] p.3 Eq. 2.4):

$$\frac{1}{\rho}\frac{\partial p}{\partial r} = -\frac{\partial v}{\partial t} - v\frac{\partial v}{\partial r} \tag{6.18}$$

where ρ is the liquid density, p is pressure, r is the distance and v is the fluid velocity. This equation, relates the pressure in the liquid p to the fluid velocity v.

The incompressibility relation is given as:

$$\frac{\dot{r}}{\dot{R}} = \frac{R^2}{r^2} \tag{6.19}$$

This equation is derived and discussed in detail in [4](Eq. 2.25-page 87) where R is the bubble instantaneous radius and over dot denotes the derivative with respect to time. Vokurka [36] used Eq. 2, and integrated the Euler's equation and obtained the pressure at a distance r from the bubble center. The process is given as follows and note that $\dot{r} = v$:

Inserting the value of v into Eq. 15 we have:

$$\frac{R^2\dot{R}}{r^2}\frac{\partial}{\partial r}\left(\frac{R^2\dot{R}}{r^2}\right) + \frac{\partial}{\partial t}\left(\frac{R^2\dot{R}}{r^2}\right) = -\frac{1}{\rho}\frac{\partial p}{\partial r} \tag{6.20}$$

after taking the derivatives and omitting higher order terms due to their small contributions for the frequencies and pressures that are considered here, one arrives at:

$$\frac{\partial p}{\partial r} = -\frac{\rho}{r}(R^2\ddot{R} + 2R\dot{R}^2) \tag{6.21}$$

Integrating Eq. 21 one arrives at the expressions for the pressure scattered by the bubble at a distance r from the bubble center:

$$P_{sc} = \rho\frac{R}{r}(R\ddot{R} + 2\dot{R}^2) \tag{6.22}$$

The acoustic power (W_{sc}) scattered (re-radiated) by the bubble thus can be calculated as [4,22,23, 24,37]:

$$W_{sc} = \frac{4\pi r^2}{\rho c}{P_{sc}}^2 = \frac{4\pi\rho}{c}R^2(R\ddot{R} + 2\dot{R}^2) \tag{6.23}$$

This quantity represents dissipated power due to scattering by the bubble (we will use $< Sd >$ for its representation for simplicity) and can be calculated using:

$$< Sd >= \frac{1}{T}\int_0^T W_{sc}dt \tag{6.24}$$

The dissipated power due to radiation should have the same value as the acoustic scattered power by the bubble. Therefore, one can compare $< Rd >$ and $< Sd >$ to validate the predictions of Eq. 14.

6.4 Results

6.4.1 Low amplitude oscillation regimes ($P_a = 1kPa$)

In this section, the predictions of the ratio of the dissipated powers are compared in the linear regime of oscillations (very small amplitude bubble oscillations, $\frac{R_{max}}{R_0} \approxeq 1.01$ at resonance). Eq. 4 is coupled to Eq. 5 and Eq. 6 and solved for a $R_0 = 3\mu m$ air bubble sonicated with $P_A = 1kP$ and for frequencies between $0.5f_r - 2.5f_r$ (f_r is the frequency of maximum response at 1 kPa). $< Td >$, $< L_{vis}d >$ and $< Rd >$ are calculated using Eq. 13 (Jamshidi and Brenner model [2]) and Eq. 14 (proposed model) and the acoustic power radiated by the bubble $< Sd >$ is calculated using Eq. 24. Calculations are performed over for the last 40 cycles of a 240 cycle pulse to ensure the transient behavior has subsided. The damping constants were calculated using Eq. 15. The thermal properties of the air as given in Table 1 were used for all the calculations.

Fig. 6.1a shows $\frac{<Td>}{<Rd>}$ and $\frac{\beta_{th}}{\beta_{rd}}$ as a function of frequency. The predictions of the proposed model (red) are in excellent agreement with the results of the analytical expressions (yellow). However, predictions of the Jamshidi and Brenner model (Eq. 13) significantly deviate from the linear model, especially for frequencies below resonance. Moreover, negative values appear for $f < 0.87f_r$ which can not be shown in the log graph. Fig. 6.1b shows the $\frac{<L_{vis}d>}{<Rd>}$ and $\frac{\beta_{L_{vis}}}{\beta_{rd}}$ as a function of frequency. Once again, the predictions of the proposed model (red) are in excellent agreement with the results of the analytical expressions (yellow). However, predictions of the Jamshidi and Brenner model (blue) significantly deviate from linear model predictions.

Figs. 6.2a-b show the dissipated powers of $< Td >$, $< L_{vis}d >$, $< Rd >$ and $< Sd >$ as a function

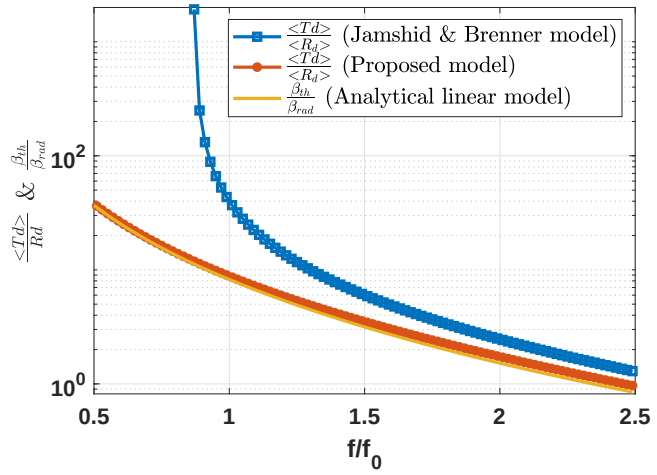

(a)

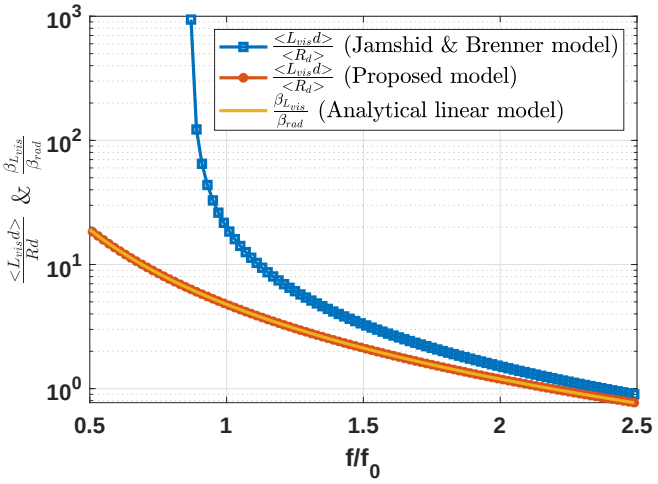

(b)

Figure 6.1: Ratio of the dissipated powers of a) $\frac{<Td>}{<Rd>}$ and b) $\frac{<L_{vis}d>}{<Rd>}$ as calculated by the proposed model (Eq. 14) and Jamshidi and Brenner model (Eq. 13) and compared to analytical linear damping constants of $\frac{\beta_{th}}{\beta_{rd}}$ and $\frac{\beta_{L_{vis}}}{\beta_{rd}}$. $< Td >$, $< Rd >$ and $< L_{vis}d >$ are respectively dissipated powers due to thermal, radiation and liquid viscosity damping. β_{th}, β_{rd} and $\beta_{L_{vis}}$ are respectively the damping constants for thermal, radiation and liquid viscosity. The bubble is an air bubble with $R_0 = 3\mu m$. The dissipated powers are averaged over the last 40 cycles of a 240 cycle acoustic pulse with $P_a = 1kPa$.

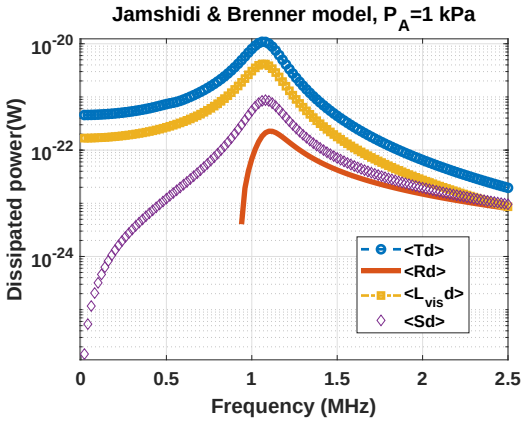

(a)

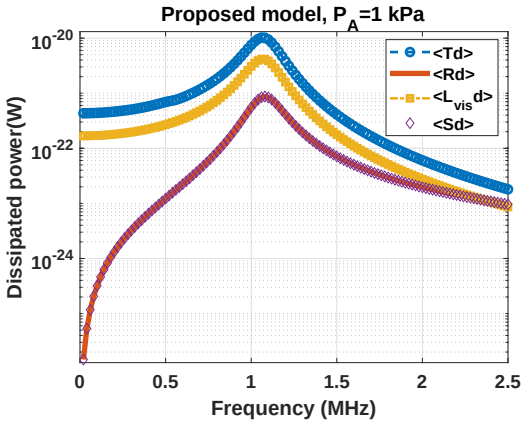

(b)

Figure 6.2: The dissipated powers due to thermal damping ($< Td >$), radiation damping ($< Rd >$), liquid viscosity damping ($< L_{vis}d >$) and damping due to the scattered pressure by bubbles $< Sd >$ when P_A=1 kPa as a function of frequency for an air bubble with R_0= 3 μ m calculated by a) the Jamshidi and Brenner model (Eq. 13) and b) the proposed model (Eq. 14). The dissipated powers are averaged over the last 40 cycles of a 240 cycle acoustic pulse with $P_a = 1kPa$.

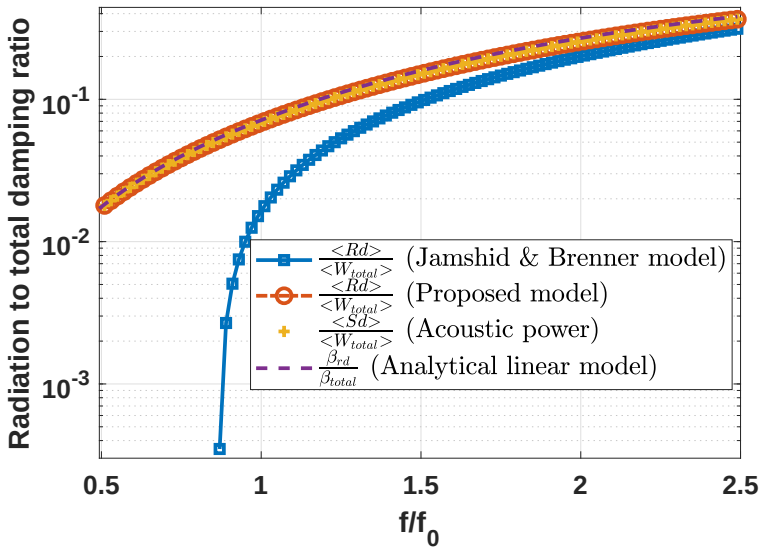

Figure 6.3: Radiation to total damping ratio as a function of frequency. $P_A = 1kPa$ to ensure low amplitude oscillations. The bubble is an air bubble with $R_0 = 3\mu m$. In this figure, $< Rd >$ and $< Sd >$ are the dissipated powers due to radiation damping and damping due to the scattered pressure by bubbles respectively. $< W_{total} >=< Td >+< Rd >+< L_{vis}d >$ is the total dissipated power where $< Td >$ and $< L_{vis}d >$ are respectively dissipated powers due to thermal damping and liquid viscosity damping. β_{rd} is the radiation damping constant and $\beta_{total} = \beta_{rd} + \beta_{th} + \beta_{L_{vis}}$ where β_{th} and $\beta_{L_{vis}}$ are respectively constants for thermal and liquid viscosity damping. The dissipated powers are averaged over the last 40 cycles of a 240 cycle acoustic pulse.

of frequency at $P_A = 1kPa$. $< Rd >$ (red) as calculated by Jamshidi and Brenner model (Eq. 13) in Fig. 6.2a is negative for frequencies below resonance. Additionally, it significantly deviates from the predictions of acoustic power theory $< Sd >$ (purple diamonds). $< Rd >$ as calculated by the proposed model of Eq. 14 (red curve in Fig. 6.2b) is in great agreement with the predictions of the $< Sd >$ (purple diamonds) and negative values are absent.

For the last comparison in the linear regime, Fig. 6.3 shows $\frac{Rd}{W_{total}}$, $\frac{Sd}{W_{total}}$ and $\frac{\beta_{rd}}{\beta_{total}}$ as calculated by Eq. 13, 14, 24 and 15. $W_{total} =< Rd + Td + L_{vis}d >$ and $\beta_{total} = \beta_{rd} + \beta_{th} + \beta_{L_{vis}}$. Predictions of the Jamshidi and Brenner model significantly deviate from the other models. The deviation is higher for lower frequencies.

6.4.2 Large amplitude nonLinear oscillation regimes

At higher pressures, predictions of the nonlinear model deviate from the linear model [1,2,3]. Figs. 6.4a-b shows the dissipated power at P_A= 20 kPa due to $< Td >$, $< L_{vis}d >$, $< Rd >$ and $< Sd >$ calculated using Eq. 13, Eq. 14 and Eq. 24. For frequencies below resonance, $< Rd >$ becomes negative. Moreover, $< Rd >$ as calculated by Jamshidi and Brenner model (Eq. 13) deviates from

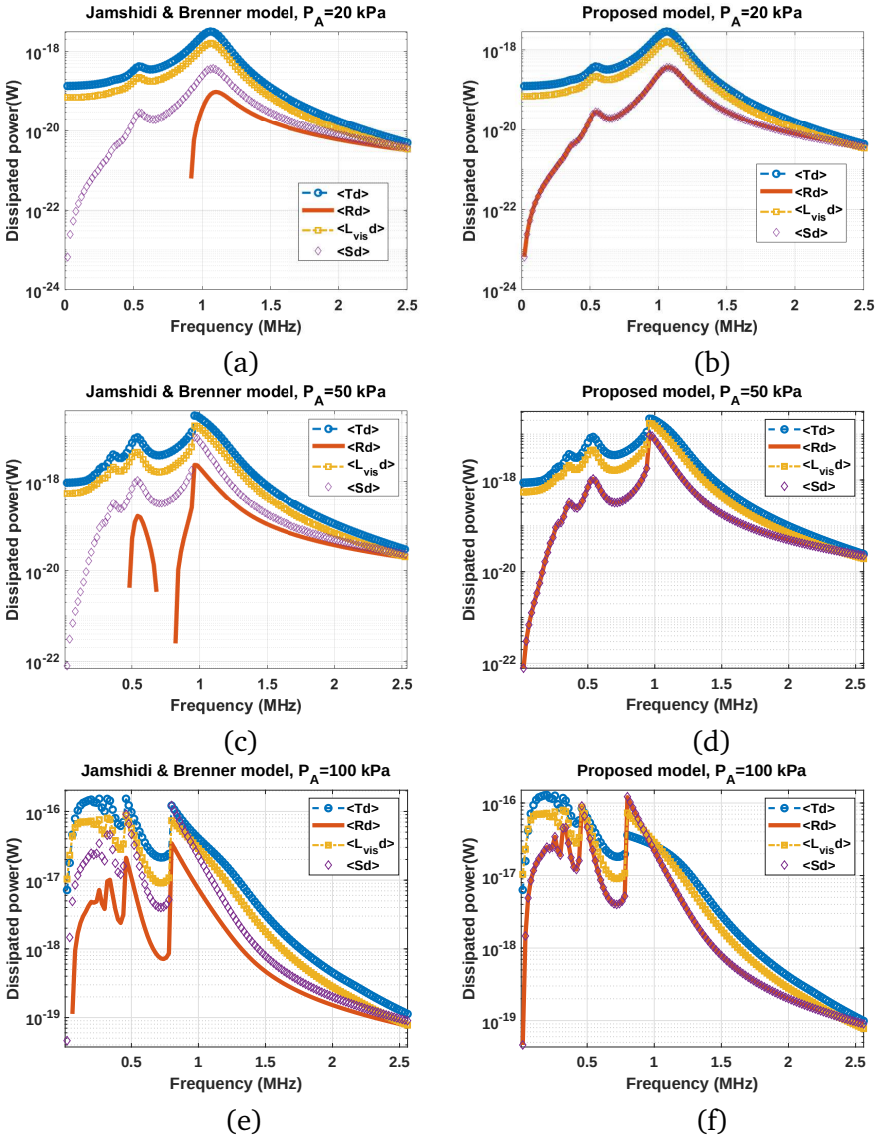

Figure 6.4: The dissipated power due to thermal damping ($< Td >$), radiation damping ($< Rd >$), liquid viscous damping ($< L_{vis}d >$) and damping due to the scattered pressure by bubbles ($< Sd >$) as a function of frequency for an air bubble with R_0=3 μm as calculated by the Jamshidi and Brenner model (left column) and the proposed model (right column): a-b) $P_A = 20kPa$, c-d) $P_A = 50kPa$ and e-f) $P_A = 100kPa$. The dissipated powers are averaged over the last 40 cycles of a 240 cycle acoustic pulse with $P_a = 1kPa$.

values of $< Sd >$ calculated by Eq. 24. Fig. 6.4b shows that the proposed model described by Eq. 14 predicts the correct values for $< Rd >$ which are in agreement with $< Sd >$. We also see the generation of 2nd harmonic resonance frequency due to the pressure increase at ≈ 540 kHz.

Figures 6.4c-d, represent the predictions of Eqs. 13, 14 and 24 when P_A=50 kPa. Increasing the acoustic pressure shifted the fundamental frequency of the bubble to lower values. Damping values increased by an order of magnitude. Moreover, a 3rd harmonic resonance peak at 360 kHz is generated. Once again, Eq. 13 predicts negative values for $< Rd >$ for some frequencies below the fundamental resonance frequency and there is discrepancy between $< Sd >$ and the $< Rd >$. Eq. 14 accurately captures the value of $< Rd >$ (Fig. 6.4d). Figures 6.4e-f show the predictions of Eq. 13, 14 and 24 when P_A= 100 kPa. Fig. 6.4e shows that solutions of Eq. 13 for $< Rd >$ are not in agreement with $< Sd >$. However, the proposed model (Eq. 14) predicts the correct value for $< Rd >$ (Fig. 6.4f) which is in good agreement with $< Sd >$. Increasing the pressure to P_A= 100 kPa results in further shifting of the resonance frequencies of the system to lower frequencies, and 4th and 5th harmonic resonance peaks are observable in the graphs. Radiation damping grows faster than the other damping factors as pressure increases. At the pressure dependent resonance ($f = 800kHz$) and pressure dependent 2nd harmonic resonance ($f = 460kHz$), radiation damping becomes stronger than the other damping factors. Thermal damping remains the strongest damping term for the rest of frequencies.

The values for $< Rd >$, $< Td >$ and $< L_{vis}d >$ are pressure and frequency dependent. $< Rd >$ grows with a faster rate than the other damping factors by pressure increase and there are regions in frequency and pressure domain in which $< Rd >$ is stronger than other damping factors. The different contributions of the damping factors can have significant consequences in selecting the optimal ultrasound exposure parameters for different applications.

Figs 6.5a-d show the ratio of the dissipated powers due to the thermal and liquid viscosity damping as calculated by the Jamshidi and Brenner model to the ones as calculated by the proposed model. $< Td_{JB} >$ and $< L_{vis}d_{JB} >$ are the dissipated powers due to thermal and liquid viscosity as calculated by Jamshidi and Brenner model (Eq. 13) respectively. $< Td_{PM} >$ and $< L_{vis}d_{PM} >$ are respectively the dissipated powers due to thermal and liquid viscosity as calculated by proposed model (Eq. 14). The ratio of the dissipated powers due to liquid viscosity($\frac{<L_{vis}d_{JB}>}{<L_{vis}d_{PM}>}$ represented by red line) is $\approxeq 1$ which indicates that the two models return approximately identical results over

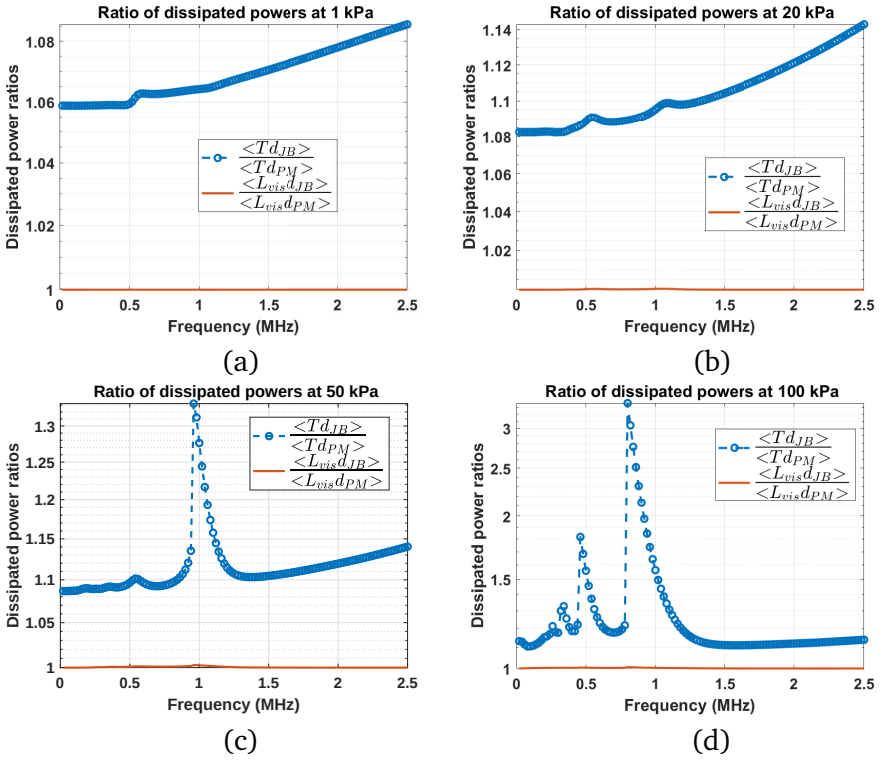

Figure 6.5: The ratios of the dissipated powers due to the thermal and liquid viscosity as calculated by the proposed and Jamshidi and Brenner models as a function of frequency for an air bubble with $R_0 = 3\mu m$ at P_A=: a) $1kPa$, b) $20kPa$, c) $50kPa$ and d) $100kPa$. (In the legends $< Td_{JB} >$ and $< L_{vis}d_{JB} >$ are respectively dissipated powers due to thermal and liquid viscosity as calculated by Jamshidi and Brenner model (Eq. 13). $< Td_{PM} >$ and $< L_{vis}d_{PM} >$ are respectively the dissipated powers due to thermal and liquid viscosity the values calculated by the proposed model (Eq. 14).

the frequency ($20kHz - 2.5MHz$) and pressure (1kPa-100kPa) ranges that are studied here. However, the dissipated powers due to the thermal damping are quite different between the two models. The ratio of the dissipated powers due to the thermal damping ($\frac{<Td_{JB}>}{<Td_{PM}>}$, represented by blue line) grows with frequency increase. At 1 kPa this value is between $1.06 - 1.0825$ with a peak at resonance. The ratios grow as pressure increases ($1.08 - 1.14$ at 20 kPa to $1.1 - 3.7$ at 100 kPa) with peaks at the pressure dependent resonance and super harmonic resonances of the system. The Jamshidi and Brenner model overestimates the thermal damping between 6 $\%$ to 300 $\%$.

6.5 Discussion

The dissipated powers due to the radiation damping ($< Rd >$), thermal damping ($< Td >$) and damping due to the friction by the liquid viscosity ($< L_{vis}d >$) are nonlinear and depend on the excitation pressure and frequency [1, 2]. Accurate predictions of bubble oscillations and bubble related phenomena in sound fields requires an accurate estimation for the dissipation mechanisms. However, the majority of studies considered linear estimations (valid only for very small amplitude bubble oscillations) for the damping mechanisms in a bubble oscillator (e.g. [4, 5, 6, 7, 8, 9, 10, 11, 12]).

Some models have been proposed that take into account the nonlinearities of the bubble oscillator. Jamshidi and Brenner [2] used the Lousinard's method [1] and derived the pressure dependent terms for $< Rd >$, $< Td >$, and $< L_{vis}d >$. However, we showed here that the Jamshidi and Brenner model needs corrections. We showed that:

1- $< Rd >$ as derived by Jamshidi and Brenner [2] generates negative values for some frequencies below bubble resonance and at a wide range of applied pressures. A dissipation mechanism should not be negative. A negative value is analogous to a phenomenon that pumps energy to the system and this contradicts the definition of dissipation.

2- For low amplitude bubble oscillations (e.g. $P_A = 1kPa$ and $\frac{R_{max}}{R_0} \approxeq 1.01$) the ratios of the dissipated powers $\frac{<L_{vis}d>}{<Rd>}$, $\frac{<Td>}{<Rd>}$ and $\frac{<Rd>}{<W_{total}>}$ as calculated by Jamshidi and Brenner [2], significantly deviate from the predictions of the linear model [5, 11] even when $< Rd >$ returns positive values.

3- For large amplitude bubble oscillations at higher pressures, $< Rd >$ as calculated by Jamshidi and Brenner model [2], significantly deviates from the dissipation power calculated by the scattered

(re-radiated) pressure by the bubble ($< Sd >$). Since these two parameters refer to the same mechanism, they should have the same value.

We provided critical corrections to the terms derived by the Jamshidi and Brenner. Negative values were absent in the results of the proposed model for the range of frequencies and pressures studied here. In the low amplitude oscillation regime, the predictions of the proposed model for the ratio of energies are in excellent agreement with the predictions of the linear model. Moreover, predictions of $< Rd >$ are in excellent agreement with the predictions of $< Sd >$ both in low amplitude and high amplitude regimes of oscillations.

In agreement with linear model, it was shown that for the $R_0 = 3\mu m$ bubble and for ultrasound frequencies $20kHz < f < 2.5MHz$, $< Td >$ and $< Rd >$ are respectively the strongest and weakest dissipation mechanisms at lower pressures (e.g. $P_A < 20kPa$). However, as pressure increases, $< Rd >$ grows at a faster rate compared to $< Td >$ and $< L_{vis}d >$. At specific frequencies (e.g. pressure dependent resonance frequency [18]) $< Rd >$ becomes the dominant dissipation mechanism. This shows that compressibility effects are very important even at moderate pressures (e.g. 100 kPa (Fig. 6.1h)). Thus models for free bubbles and ultrasound contrast agents (UCAs) [6] that neglect or simplify liquid compressibility effects may loose accuracy even at moderate pressures.

At 100 kPa (Fig. 6.4f), and at the pressure dependent resonance frequency (0.8 MHz) $< Rd >$ is larger than $< L_{vis}d >$, which is larger than $< Td >$. This is in contradiction with the linear model results. The physical reason for the higher values for $< Rd >$ is that at pressure dependent resonance the collapse occurs over a shorter duration and bubble wall velocity and acceleration are higher. Thus the scattered pressure by the bubble and the dissipation due to viscosity are stronger. However, because the collapse occurs faster, the average available surface are for the temperature diffusion decreases which results in smaller $< Td >$ compared to other damping mechanisms. Same phenomenon occurs for pressure dependent 2nd order SuH resonance (460 kHz) at 100 kPa.

In this study we focused on damping mechanisms due to $< Td >$, $< L_{vis}d >$ and $< Rd >$. However, there are other damping mechanisms that can become important depending on the exposure conditions and the gas inside the bubble. Mass transfer effects have been shown to significantly alter the damping mechanisms of vapor bubbles [10]. Mass transfer in vapor bubbles can become the dominant damping phenomenon [10]. Phase change effects in a gas-vapour bubbly liquid can

have a major effect on the behavior of the system [43]. In this regard the temperature of the solution can heavily alter the dissipation mechanisms. A correct model for dissipation mechanisms for large amplitude vapor bubble oscillations should incorporate these effects.

In this study we only considered the free bubble model as the focus was to correct the energy dissipation calculations for linear and nonlinear bubble oscillations. In the case of bubbles that are coated [6] or in case of bubbles that are immersed in viscoelastic materials like tissue [44, 45] or sediments [7, 8] there are additional damping mechanisms due to the viscoelasticty of the coating or the surrounding medium that needs to be derived by applying the process described in this work on the right bubble oscillation model.

Accurate knowledge of the pressure dependent dissipation effects can help in optimization of the excitation frequency and pressure for enhanced energy distribution in ultrasonic fields. Increased attenuation of ultrasonic waves due to the presence of bubbles, limits the delivery of sufficient energy to activate bubbles that are at the focus and/or limits the regions of enhanced bubble activity. In therapeutic applications of ultrasound (e.g. drug delivery [30], high intensity focused ultrasound [23, 24]) the increased attenuation of pre-focal bubbles may result in undesirable heating in the intervening tissue. In diagnostic applications of ultrasound, the increased attenuation of bubbles in the beam path creates shadowing effects that deteriorate the images of underlying tissues [25, 30]. In sonochemical reactors, inhomogeneous pressure distributions inside reactors from pressure dependent attenuation reduces the efficacy. Accurate models for nonlinear damping in the presence of the bubbles significantly assists in understanding the mechanism of nonlinear attenuation and aids in designing protocols that minimize the unwanted effects.

Scattered pressure by the bubbles is a function of the bubble radial oscillations, wall velocity and acceleration; thus, there is a direct correlation between the intensity of bubble activity and the scattered pressure [4]. Scattered pressure by bubbles and attenuation (directly proportional to total dissipation) [1, 2, 3, 4, 5, 6] are parameters that can be measured in real time and also can be calculated theoretically. Two characteristics typically define the efficacy of an application; enhanced bubble activity (e.g. scattering or micro-streaming) and attenuation caused by the bubble activity. The scattering to attenuation ratio (STAR) was proposed in [25] as a measure of the scattering effectiveness of contrast enhanced ultrasound. However, in that work and subsequent studies, linear parameters were used to calculate STAR, thus the pressure dependence of the STAR was not

examined.

Knowledge on the scattered (re-radiated) energy from the bubbles can be used as a measure of the bubble activity. To this end, the scattering to dissipation ratio (STDR) can not only provide a measure of the effectiveness of imaging applications of ultrasound, but it may also be used as a measure of the effectiveness of several other applications (e.g. sonochemistry and therapeutic ultrasound) where the goal is selective maximization of bubble activity and reducing unwanted dissipation. Decreasing the dissipation of bubbly media increases the power that can be delivered to bubbles.

STDR is nonlinear and depends on the complex bubble dynamics. We observed in Fig. 6.4 that Rd can overcome the other damping factors for specific pressure and frequency ranges, and thus there are potential exposure parameters for which the STDR can be maximized. Using the nonlinear model represented by Eq. 14 for the damping terms, we can define a similar term to STAR which can also be used for nonlinear regimes of oscillations:

$$STDR = \frac{< Rd >}{< Td + L_{vis}d + Rd >} \tag{6.25}$$

The accurate calculation of STDR can help in selecting optimized frequency and pressure ranges to reduce unwanted pre-focal dissipation and enhance bubble activity at focus. For example, in case of the bubble presented in Fig. 6.4, by taking advantage of the steep pressure gradients of focused transducers and setting the focal pressure slightly above 100 kPa, this property can be used to reduce the absorption of the ultrasound in pre-focal regions while maximizing the absorption and bubble activity in the target focal region [18, 33] that have higher pressures.

6.6 Conclusion and future work

This study provides critical corrections for the calculation of power dissipation during the propagation of ultrasonic waves through a bubbly medium. The accuracy of the proposed models were verified against the linear analytical expressions for low amplitude oscillation regimes and against acoustic power theory for higher amplitude oscillation regimes. The correct models can be used to study the dissipation mechanisms related to thermal damping, radiation loss and damping due

to liquid viscosity. This can help in revealing the exposure parameters for which bubble activity is maximized. It was shown that, at specific frequencies and pressures, the dissipation due to radiation becomes higher than other dissipation mechanisms. Thus the exposure parameters of the applications can be optimized to enhance a particular effect of interest. Investigation of the pressure dependence of STDR and acoustic excitation parameters that can potentially maximize the STDR are of great importance and can be the subject of future studies.

This study only focused on correcting the dissipation terms for a free bubble in a liquid like water. Thus, the applications of the proposed model are limited to free bubbles immersed in Newtonian fluids like water and organic solvents. The approach presented here, can be applied in combination with the appropriate bubble models for coated bubbles (e.g. [6]) or bubbles in sediments (e.g. [7,8]) or bubbles in tissue (e.g. [44,45]) to derive the additional damping effects due to the coating and the visco-elasticity of the surrounding medium. This can help in accurate pressure dependent predictions in studies related to characterization of bubbles in underwater acoustics [4, 7, 8] and characterization of shell parameters of encapsulated bubbles [9, 46, 47, 48, 49, 50] or propagation of waves in bubbly tissue [44, 45].

6.7 Acknowledgments

The work is supported by the Natural Sciences and Engineering Research Council of Canada (Discovery Grant RGPIN-2017-06496), NSERC and the Canadian Institutes of Health Research (Collaborative Health Research Projects) and the Terry Fox New Frontiers Program Project Grant in Ultrasound and MRI for Cancer Therapy (project #1034). A. J. Sojahrood is supported by a CIHR Vanier Scholarship.

Bibliography

[1] Louisnard, O., A simple model of ultrasound propagation in a cavitating liquid. Part I: Theory, nonlinear attenuation and traveling wave generation. *Ultrasonics sonochemistry* 19(1), 56-65. (2012): 1061-1077.

[2] Jamshidi, R., and Brenner, G. Dissipation of ultrasonic wave propagation in bubbly liquids considering the effect of compressibility to the first order of acoustical Mach number. *Ultrasonics* 53(4) (2013): 842-848.

[3] Dogan, H., and Popov, V. Numerical simulation of the nonlinear ultrasonic pressure wave propagation in a cavitating bubbly liquid inside a sonochemical reactor. *Ultrasonics sonochemistry* 30 (2016): 87-97.

[4] T.G. Leighton. *The acoustic bubble*. Academic press, 2012.

[5] Commander, K. W., and Prosperetti, A. Linear pressure waves in bubbly liquids: Comparison between theory and experiments, *The Journal of the Acoustical Society of America* 85(2) (1989): 732-746.

[6] Hoff, L., Sontum, P. C., and Hovem, J. M. Oscillations of polymeric microbubbles: Effect of the encapsulating shell. *The Journal of the Acoustical Society of America* 107(4) (2000): 2272-2280.

[7] Mantouka, A., Dogan, H., White, P. R., and Leighton, T. G. Modelling acoustic scattering, sound speed, and attenuation in gassy soft marine sediments. *The Journal of the Acoustical Society of America* 140(1) (2016):274-282.

[8] Dogan, H., White, P. R., and Leighton, T. G. Acoustic wave propagation in gassy porous marine sediments: The rheological and the elastic effects. *The Journal of the Acoustical Society of America,* 141(3) (2017): 2277-2288.

[9] Segers, T., de Jong, N., and Versluis, M. Uniform scattering and attenuation of acoustically sorted ultrasound contrast agents: Modeling and experiments. *The Journal of the Acoustical Society of America* 140(4) (2016): 2506-2517.

[10] Zhang, Y. and Li, S., 2014. Thermal effects on nonlinear radial oscillations of gas bubbles in liquids under acoustic excitation. International Communications in Heat and Mass Transfer, 53, pp.43-49.

[11] Prosperetti, A., Crum, L.A. and Commander, K.W., 1988. Nonlinear bubble dynamics. The Journal of the Acoustical Society of America, 83(2), pp.502-514.

[12] Prosperetti, A., 1984. Bubble phenomena in sound fields: part one. Ultrasonics, 22(3), pp.115-124.

[13] Zhang, Y., Gao, Y., Guo, Z. and Du, X., 2018. Effects of mass transfer on damping mechanisms of vapor bubbles oscillating in liquids. Ultrasonics sonochemistry, 40, pp.120-127.

[14] F. Hegedűs, Topological analysis of the periodic structures in a harmonically driven bubble oscillator near Blake's critical threshold: Infinite sequence of two-sided Farey ordering trees, *Physics Letters A* 380-10 (2016): 1012-1022.

[15] F. Hegedűs and K. Klapcsik, The effect of high viscosity on the collapse-like chaotic and regular periodic oscillations of a harmonically excited gas bubble. *Ultrasonics sonochemistry* 27, (2015): 153-164

[16] S.A. Suslov, A.Ooi, and R. Manasseh, Nonlinear dynamic behavior of microscopic bubbles near a rigid wall, *Physical Review E* 85 (2012): 066309

[17] Sojahrood, A.J., Wegierak, D., Haghi, H., Karshfian, R., and Kolios, M. C. A simple method to analyze the super-harmonic and ultra-harmonic behavior of the acoustically excited bubble oscillator. *Ultrasonics sonochemistry* 54 (2019):99-109

[18] A.J. Sojahrood et al., Influence of the pressure-dependent resonance frequency on the bifurcation structure and backscattered pressure of ultrasound contrast agents: a numerical investigation, *Nonlinear Dynamics* 80 (2015): 889-904.

[19] Jafari Sojahrood, Amin, and Michael Kolios. "The use of pressure dependent subharmonic resonance to increase the signal to noise ratio of ultrasound contrast agent imaging." The Journal of the Acoustical Society of America 129, no. 4 (2011): 2511-2511.

[20] A.J. Sojahrood, R. Earl, M.C. Kolios and R. Karshafian. Notes on the two main routes of period doubling and 1/2 order subharmonic oscillations in a bubble oscillator (2019) arXiv:1909.02694

[21] Sojahrood, A.J. and Kolios, M.C., 2012. Classification of the nonlinear dynamics and bifurcation structure of ultrasound contrast agents excited at higher multiples of their resonance frequency. Physics Letters A, 376(33), pp.2222-2229.

[22] Umemura, S.I., Kawabata, K.I. and Sasaki, K., 2005. In vivo acceleration of ultrasonic tissue heating by microbubble agent. IEEE transactions on ultrasonics, ferroelectrics, and frequency control, 52(10), pp.1690-1698.

[23] Holt, R.G. and Roy, R.A., 2001. Measurements of bubble-enhanced heating from focused, MHz-frequency ultrasound in a tissue-mimicking material. Ultrasound in medicine and biology, 27(10), pp.1399-1412.

[24] S. Yoshizawa, et al., High intensity focused ultrasound lithotripsy with cavitating microbubbles, *Medical and biological engineering and computing* 47 (2009): 851-860.

[25] A. Bouakaz, N. De Jong, and C. Cachard,. Standard properties of ultrasound contrast agents. Ultrasound in medicine and biology, 24(3), (1998): 469-472.

[26] K.B. Bader., K.J. Haworth, H. Shekhar, A.D. Maxwell, T. Peng, D.D. McPherson, and C.K. Holland, Efficacy of histotripsy combined with rt-PA in vitro. *Physics in Medicine & Biology* 61, (2016): 5253.

[27] C.C Coussios, et al. Role of acoustic cavitation in the delivery and monitoring of cancer treatment by high-intensity focused ultrasound (HIFU), *International Journal of Hyperthermia* 23(2) (2007) 105-120.

[28] M.A. O'Reilly and K. Hynynen, Blood-brain barrier: real-time feedback-controlled focused ultrasound disruption by using an acoustic emissions-based controller, *Radiology* 263, (2012)96–106

[29] K.J. Haworth, et al., Passive imaging with pulsed ultrasound insonations, *The Journal of the Acoustical Society of America*, 132(1) (2012) 544-553.

[30] K. Ferrara, R. Pollard, and M. Borden, Ultrasound microbubble contrast agents: fundamentals and application to gene and drug delivery, *Annu. Rev. Biomed. Eng.* 9 (2007): 415-447.

[31] Sojahrood, A. J., Li, Q., Haghi, H., Karshafian, R., Porter, T. M., and Kolios, M. C. Pressure dependence of the ultrasound attenuation and speed in bubbly media: Theory and experiment. *arXiv preprint arXiv:* (2018): 1811.07788.

[32] Sojahrood, A. J., Li, Q., Haghi, H., Karshafian, R., Porter, T. M., and Kolios, M. C. Investigation of the nonlinear propagation of ultrasound through a bubbly medium including multiple scattering and bubble-bubble interaction: Theory and experiment. *In 2017 IEEE International Ultrasonics Symposium (IUS)* IEEE (2017) pp. 1-4.

[33] Segers, Tim, Pieter Kruizinga, Maarten P. Kok, Guillaume Lajoinie, Nico De Jong, and Michel Versluis. "Monodisperse versus polydisperse ultrasound contrast agents: Non-linear response, sensitivity, and deep tissue imaging potential." Ultrasound in medicine & biology 44, no. 7 (2018): 1482-1492.

[34] Plesset, M.S. The dynamics of cavitation bubbles. *ASME J. Appl. Mech.* 16 (1949): 228–231.

[35] Keller, J.B. and Miksis M., Bubble oscillations of large amplitude, ., *J. Acoust. Soc. Am.* 68 (1980) 628–633.

[36] Vokurka, K. On Rayleigh's model of a freely oscillating bubble. I. Basic relations. Czechoslovak Journal of Physics B, 35(1), (1985): 28-40.

[37] Hilgenfeldt, S., Lohse, D., and Zomack, M. Response of bubbles to diagnostic ultrasound: a unifying theoretical approach. The European Physical Journal B-Condensed Matter and Complex Systems, 4(2), (1998):247-255.

[38] L. D. Landau and E. M. Lifshitz, Fluid Mechanics (Pergamon Press, Oxford, 1987).

[39] Caflisch, R.E., Miksis, M.J., Papanicolaou, G.C., Ting L., Effective equations for wave propagation in bubbly liquids, *J. Fluid Mech.* 153 (1985): 259–273.

[40] Wijngaarden, L.V., On the equation of motion for mixtures of liquid and gas bubbles, *J. Fluid Mech.*33 132(1) (1968): 465–474.

[41] R. Toegel, B. Gompf, R. Pecha, D. Lohse, Does water vapor prevent upscaling sonoluminescence?, *Phys Rev. Lett.* 85(2000): 3165–3168.

[42] Lide, D.R., and Kehiaian, H. V., CRC Handbook of Thermophysical and Thermochemical Data, *CRC Press, Boca Raton, FL,* (1994)

[43] Prosperetti, A., 2015. The speed of sound in a gas–vapour bubbly liquid. Interface focus, 5(5), p.20150024.

[44] Allen, J.S. and Roy, R.A., 2000. Dynamics of gas bubbles in viscoelastic fluids. I. Linear viscoelasticity. The Journal of the Acoustical Society of America, 107(6), pp.3167-3178.

[45] Allen, John S., and Ronald A. Roy. ”Dynamics of gas bubbles in viscoelastic fluids. II. Nonlinear viscoelasticity.” The Journal of the Acoustical Society of America 108, no. 4 (2000): 1640-1650.

[46] Kopechek, Jonathan A., Kevin J. Haworth, Jason L. Raymond, T. Douglas Mast, Stephen R. Perrin Jr, Melvin E. Klegerman, Shaoling Huang, Tyrone M. Porter, David D. McPherson, and Christy K. Holland. ”Acoustic characterization of echogenic liposomes: Frequency-dependent attenuation and backscatter.” The Journal of the Acoustical Society of America 130, no. 5 (2011): 3472-3481.

[47] Raymond, J.L., Haworth, K.J., Bader, K.B., Radhakrishnan, K., Griffin, J.K., Huang, S.L., McPherson, D.D. and Holland, C.K., 2014. Broadband attenuation measurements of phospholipid-shelled ultrasound contrast agents. Ultrasound in medicine & biology, 40(2), pp.410-421.

[48] Shekhar, Himanshu, Nathaniel J. Smith, Jason L. Raymond, and Christy K. Holland. ”Effect of temperature on the size distribution, shell properties, and stability of Definity®.” Ultrasound in medicine & biology 44, no. 2 (2018): 434-446.

[49] Goertz, D.E., de Jong, N. and van der Steen, A.F., 2007. Attenuation and size distribution measurements of Definity™ and manipulated Definity™ populations. Ultrasound in medicine & biology, 33(9), pp.1376-1388.

[50] Helfield, B.L., Leung, B.Y., Huo, X. and Goertz, D.E., 2014. Scaling of the viscoelastic shell properties of phospholipid encapsulated microbubbles with ultrasound frequency. Ultrasonics, 54(6), pp.1419-1424.

Chapter 7

Nonlinear power loss in the oscillations of coated and uncoated bubbles: Role of thermal, radiation and encapsulating shell damping at various excitation pressures

7.1 Abstract

This study presents the fundamental equations governing the pressure dependent disipation mechanisms in the oscillations of coated bubbles. A simple generalized model (GM) for coated bubbles accounting for the effect of compressibility of the liquid is presented. The GM was then coupled with nonlinear ODEs that account for the thermal effects. Starting with mass and momentum conservation equations for a bubbly liquid and using the GM, nonlinear pressure dependent terms were derived for energy dissipation due to thermal damping (Td), radiation damping (Rd) and dissipation due to the viscosity of liquid (Ld) and coating (Cd). The pressure dependence of the dissipation mechanisms of the coated bubble have been analyzed for the first time. The dissipated energies were solved for uncoated and coated 2- 20 μm in bubbles over a frequency range of $0.25f_r - 2.5f_r$ (f_r is the bubble resonance) and for various acoustic pressures (1kPa-300kPa). Thermal effects were examined for air and C3F8 gas cores. In the case of air bubbles, as pressure increases, the linear thermal model looses accuracy and accurate modeling requires inclusion of the full thermal model. However, for coated C3F8 bubbles of diameter 1-8 μm, which are typically used in medical ultrasound, thermal effects maybe neglected even at higher pressures. For uncoated

bubbles, when pressure increases, the contributions of Rd grow faster and become the dominant damping mechanism for pressure dependent resonance frequencies (e.g. fundamental and super harmonic resonances). For coated bubbles, Cd is the strongest damping mechanism. As pressure increases, Rd contributes more to damping compared to Ld and Td. For coated bubbles, the often neglected compressibility of the liquid has a strong effect on the oscillations and should be incorporated in models. We show that the scattering to damping ratio (STDR), a measure of the effectiveness of the bubble as contrast agent, is pressure dependent and can be maximized for specific frequency ranges and pressures [1].

7.2 Introduction

Acoustically excited bubbles are oscillating gas or vapor cores that are found in free (uncoated) or coated form (e.g. encapsulated by a lipid or polymer shell). They form the core of several applications in liquids [1], and in soft and palpable matter (e.g. tissue [1,2,3] or sediments[1,4,5]). When excited by a sound field they can oscillate with amplitudes large enough to destroy most materials [1, 6, 7]; enhance chemical reactions [8, 9, 10], and act as healing or diagnostic agents in medicine [11, 12, 13]. During these high amplitude oscillations, temperatures reached in the gas core are high enough to turn the bubbles into tiny light bulbs [9, 10, 14].

Dynamics of the acoustically excited bubbles are nonlinear and chaotic. These dynamics have been the subject of numerous experimental [1, 15, 17, 18, 19, 20] and numerical [21, 22, 23, 24, 25, 26, 27, 28, 29, 30] studies. Achieving the full potential of bubbles in applications and understanding their role in the associated phenomena not only requires a detailed knowledge over their complex behavior but also on the effect of bubble oscillations on the propagation of acoustic waves.

Propagation properties of acoustic waves in bubbly media are considerably different from those in single-phase media (e.g. pure water) [31, 32, 33, 34, 35, 36]. Derivation of the correct medium properties are essential for the understanding and predicting bubble oscillations in different locations of the media and consequently optimization of bubble related applications.

One of the characteristic properties of bubble oscillations in a medium is the increased attenuation.

[1] Published as: Sojahrood, A.J., Haghi, H., Li, Q., Porter, T.M., Karshafian, R. and Kolios, M.C., 2020. Nonlinear power loss in the oscillations of coated and uncoated bubbles: Role of thermal, radiation and encapsulating shell damping at various excitation pressures. Ultrasonics sonochemistry, 66, p.105070.

Bubbles attenuate ultrasound through viscous damping due to liquid (Ld) and coating (Cd) viscous effects, radiation damping (Rd) and thermal damping (Td) [33, 34, 35, 36, 37, 38, 39]. The changes in attenuation of bubbly media has significance in studies related to oceanography [4, 5] and acoustic characterization of coated bubbles used as ultrasound contrast agents (UCAs) [38, 39, 40, 41, 42, 43]. Furthermore, knowledge of the nonlinear attenuation in the medium will help in optimization of applications related to sonochemistry [35, 36, 37] and medical ultrasound [11, 12, 13, 44, 45] by enhancing and controlling the acoustic energy at the target.

The majority of the previous studies employed linear approximations [33, 38, 39, 40, 41, 42] (limited to very small bubble oscillation amplitudes) to calculate the damping parameters during bubble oscillations. Thus, linear models neglect the dependence of the dissipated energy on the local pressure [33, 34, 35, 36] and are not applicable to conditions under which bubbles are excited in most applications. To properly account for the pressure dependence of attenuation new approaches are developed that only consider the pressure dependence of the radiation damping while using linear terms for the rest of the damping factors (thermal and viscous damping) [39]. However other damping factors are also pressure dependent and linear approximations reduce the accuracy of model predictions.

To account for the pressure dependence of all of the damping parameters, mass and momentum conservation equations were used by Louisnard [34] and nonlinear energy terms for Td and Ld were derived for a bubbly liquid using the Rayleigh-Plesset equation [46]. Jamshidi and Brenner [35] used Louisnards approach [34] and the Keller-Miksis (KM) equation [47] to capture the nonlinear damping term for re-radiated energy by bubbles (Rd). Louisnard [34] and Jamshidi's [35] study showed that damping from nonlinear oscillations of bubbles can be several orders of magnitude higher than the damping estimated by linear models.

We have shown in [36], that the derived terms in [35] are incorrect as they can lead to non-physical values for Rd; moreover, predictions of their model were not consistent with the results of radiation damping due to re-radiated pressure (Sd) by bubbles [36]. We have corrected the nonlinear damping terms in [36] and predictions of Rd were in excellent agreement with Sd. We have shown that as pressure increases, Rd grows faster than other damping factors and there exist frequency and pressure domains in which Rd is stronger than other damping parameters.

Despite the importance of nonlinear thermal losses when it comes to modeling the bubble os-

cillations, most studies simplify the role of thermal losses on bubble behavior by using models that are derived based on linear approximations [4, 5, 33, 34, 35, 36]. In addition, for coated bubbles, the role of radiation damping is not completely captured as effects of the compressibility of the liquid are often neglected or simplified [38, 48]. It is shown in [35, 36, 37] that radiation damping is pressure dependent and can be a major contributor to the total damping and should not be neglected. A more complete estimation of the wave attenuation in bubbly media must incorporate the effects of thermal and radiation damping on bubble oscillations and the total dissipated power [34, 35, 36, 37].

In this work we present a generalized model (GM) for the oscillations of coated bubbles. Compressibility effects (similar to the KM model [47]) are added to the Church-Hoff model [38]. We can call this model the KMCH model. KMCH is then coupled with the ordinary differential equations (ODEs) [49] that take into account the thermal effects. In case of uncoated bubbles, to capture the thermal and radiation effects on the oscillations, the Keller-Miksis (KM) model is also coupled with thermal ODEs [49]. Using the equations for conservation of mass and momentum in bubbly liquids and applying the KMCH model, our proposed approach in [36] was applied to derive all the damping terms Rd, Cd, Td and Ld for the oscillations of a coated bubble.

The total dissipated power by bubble oscillations was then studied as a function of frequency for various excitation pressures. In each case (free uncoated and coated bubbles) three thermal models were considered; these models were solved for an air gas core and C3F8 gas core that is generally used in UCAs. The first model neglects the thermal effects. The second model includes the thermal effects using linear approximations by introducing an artificial thermal viscosity [50]. The third model includes the full ordinary differential equations (ODEs) that describe the average temperature elevation within the bubble and heat loss at the bubble boundary [49, 51, 52, 53]. The second model has widely been used in studies related to oceanography [4, 5] or ultrasound contrast agent characterization [38, 39, 40, 41, 42]). In this paper we refer this model the linear thermal model and we refer to the third model the full thermal model.

Here we will show that for uncoated bubbles, thermal effects are very important; at very low acoustic pressures ($P_A \approx 1kPa$) predictions of the linear thermal model are in good agreement with the full thermal model. However, as pressure increases predictions of the full thermal and linear thermal model deviate for both gas cores; thus the full thermal model must be used for

accurate bubble modeling. In case of C3F8 coated bubbles, however, thermal effects are masked by large dissipation due to the bubble coating and are negligible. Even at high pressures (e.g. 100 kPa), predictions of the linear thermal, full thermal and non-thermal model are in good agreement. However, for coated bubbles with air, thermal effects are important and the full thermal model must be used for accurate prediction of bubble behavior at higher pressures and at frequencies and pressures in which subharmonic (SH) oscillations are generated.

For both cases (uncoated and coated bubble) and for both gas types, mechanisms of energy dissipation were studied as a function of frequency and pressure. We show that increasing the excitation pressure leads to a faster growth in Rd compared to other damping mechanisms; thus, optimum frequency and pressure ranges exist in which scattering to total damping ratio (STDR) is maximized.

7.3 Methods

7.3.1 Coated bubble model

The dynamics of a coated bubble oscillator can be modeled using the Church-Hoff model [38]:

$$\rho\left[R\ddot{R}+\frac{3}{2}\dot{R}^2\right]= \left(P_g-\frac{4\mu_L\dot{R}}{R}-\frac{12\mu_{sh}\epsilon R_0^2\dot{R}}{R^4}-12G_s\epsilon R_0^2\left(\frac{1}{R^3}-\frac{R_0}{R^4}\right)-P_0-P\right) \tag{7.1}$$

Where ρ is the density of the medium, R is the radius at time t, $\dot{R}$ is the bubble wall velocity, $\ddot{R}$ is the bubble wall acceleration, R_0 is the initial radius of the bubble, μ and μ_{sh} are the viscosity of the liquid and shell (coating) respectively, ϵ is the thickness of the coating, G_s is the shell shear modulus, P_g is the gas pressure inside the bubble, P_0 is the atmospheric pressure (101.325 kPa) and P is the acoustic pressure given by $P = P_a sin(2\pi ft)$ with P_a and f are respectively the excitation pressure and frequency. Church-Hoff model (Eq. 1) does not incorporate the effects of the compressibility of the medium. Similar to the KM model [47] we added the effects of the compressibility of the medium to the first order of Mach number. The generalized model (GM) can

be called Keller-Miksis-Church-Hoff (KMCH) model and is written as:

$$\rho\left[\left(1-\frac{\dot{R}}{c}\right)R\ddot{R}+\frac{3}{2}\dot{R}^2\left(1-\frac{\dot{R}}{3c}\right)\right]= \\ \left(1+\frac{\dot{R}}{c}+\frac{R}{c}\frac{d}{dt}\right)\left(P_g-\frac{4\mu_L\dot{R}}{R}-\frac{12\mu_{sh}\epsilon R_0^2\dot{R}}{R^4}-12G_s\epsilon R_0^2\left(\frac{1}{R^3}-\frac{R_0}{R^4}\right)-P_0-P\right) \tag{7.2}$$

Here c is the sound speed in the liquid. In this paper for all of the simulations related to coated bubbles G_s=45 MPa and $\mu_{sh}=\frac{1.49(R_0(\mu m)-0.86)}{\theta(nm)}$ [54] (sh stands for shell (coating)) with $\theta=4$ nm.

7.3.2 Uncoated Bubble model

The dynamics of the bubble model including the compressibility effects to the first order of Mach number can be modeled using Keller-Miksis (KM) equation [47]:

$$\rho\left[\left(1-\frac{\dot{R}}{c}\right)R\ddot{R}+\frac{3}{2}\dot{R}\left(1-\frac{R}{3c}\right)\right]=\left(1+\frac{\dot{R}}{c}\right)(G)+\frac{R}{c}\frac{d}{dt}(G) \tag{7.3}$$

where $G=P_g-\frac{4\mu_L\dot{R}}{R}-\frac{2\sigma}{R}-P_0-P_A sin(2\pi ft)$.

In this equation, R is radius at time t, R_0 is the initial bubble radius, $\dot{R}$ is the wall velocity of the bubble, $\ddot{R}$ is the wall acceleration, ρ is the liquid density (998 $\frac{kg}{m^3}$), c is the sound speed (1481 m/s), P_g is the gas pressure, σ is the surface tension (0.0725 $\frac{N}{m}$), μ is the liquid viscosity (0.001 Pa.s), and P_A and f are the amplitude and frequency of the applied acoustic pressure. The values in the parentheses are for pure water at 293 K. In this paper the gas inside the bubble is either air or C3F8 and water is the host media. Depending on which model is used for the simulation of the thermal effects , P_g will be a function that will be defined in the next 3 subsections.

7.3.3 Non-thermal model

If the terms related to thermal damping are neglected, P_g in Eq. 2 and 3 can be written in the form of:

$$P_g=P_{g0}(\frac{R_0}{R})^{3\gamma} \tag{7.4}$$

Thermal parameters of the gases at 1 atm				
Gas type	L($\frac{W}{mK}$)	$c_p(\frac{kJ}{kgK})$	c_v $(\frac{kJ}{kgK})$	ρ_g $(\frac{kg}{m^3})$
Air [55]	$0.01165 + C \times T^2$	1.0049	0.7187	1.025
C3F8 [56]	0.012728	0.79	0.7407	8.17

Table 7.1: Thermal properties of the gases used in simulations.[2] C=5.528×10^{25} $\frac{W}{mK^2}$.

Where γ is the polytropic exponent and is given by $\frac{c_p}{c_v}$. According to the Church-Hoff Model [38] for a coated bubble $P_{g0} = P_0$ where P_0 is the atmospheric pressure. For an uncoated bubble as given by Keller-Miksis equation [47]. $P_{g0} = P_0 - \frac{2\sigma}{R_0}$. In this work we have neglected the small effect of vapor pressure.

7.3.4 Full thermal effects

If thermal effects are considered, P_g is given by Eq. 5 [49, 50, 51, 52, 53]:

$$P_g = \frac{N_g K T}{\frac{4}{3}\pi R(t)^3 - N_g B} \tag{7.5}$$

Where N_g is the total number of the gas molecules, K is the Boltzman constant and B is the molecular co-volume of the gas inside the bubble. The average temperature inside the gas can be calculated using Eq. 6 [49]:

$$\dot{T} = \frac{4\pi R(t)^2}{C_v}\left(\frac{L\,(T_0 - T)}{L_{th}} - \dot{R}P_g\right) \tag{7.6}$$

where C_v is the heat capacity at constant volume, T_0=293K is the initial gas temperature, L_{th} is the thickness of the thermal boundary layer. L_{th} is given by $L_{th} = min(\sqrt{\frac{aR(t)}{|\dot{R}(t)|}}, \frac{R(t)}{\pi})$ where a is the thermal diffusivity of the gas which can be calculated using $a = \frac{L}{c_p \rho_g}$ where L is the gas thermal conductivity and c_p is specific heat capacity at constant pressure and ρ_g is the gas density.

Predictions of the full thermal model have been shown to be in good agreement with predictions of the models that incorporate the thermal effects using the PDEs [51] that incorporate the temperature gradients within the bubble. To incorporate the full thermal effects, Eqs. 2 and 3 are coupled with Eq. 5, to calculate the radial oscillations of the coated and uncoated bubbles respectively. The coupled ODEs are solved using the ODE45 solver of MATLAB.

7.3.5 Linear thermal model

The linear thermal model [33, 50] is a popular model that has been widely used in studies related to oceanography [4, 5] and the modeling and characterization of coated bubble oscillations [38, 39, 40, 41, 42]. In this model through linearization thermal damping is approximated by adding an artificial viscosity term to the liquid viscosity. Furthermore, a variable isoentropic index is used instead of the polytropic exponent of the gas.

In this model P_g is given by:

$$P_g = P_{g0}\left(\frac{R_0}{R}\right)^{3k} \tag{7.7}$$

Where the polytropic exponent γ is replaced by isoentropic indice (k):

$$k = \frac{1}{3}\Re(\phi) \tag{7.8}$$

liquid viscosity is artificially increased by adding a thermal viscosity (μ_{th}) to the liquid viscosity. This thermal viscosity (μ_{th}) is given by:

$$\mu_{th} = \frac{P_{g0}\Im(\phi)}{\omega} \tag{7.9}$$

In the above equations the complex term ϕ is calculated from

$$\phi = \frac{3\gamma}{1 - 3\left(\gamma - 1\right) i\chi\left[\left(\frac{i}{\chi}\right)^{\frac{1}{2}} coth\left(\frac{i}{\chi}\right)^{\frac{1}{2}} - 1\right]} \tag{7.10}$$

where γ is the polytropic exponent and $\chi = \frac{D}{\omega R_0^2}$ represents the thermal diffusion length where D is the thermal diffusivity of the gas. $D = \frac{L}{\gamma c_p \rho_g}$ where c_p, ρ_g, and L are specific heat capacity in constant pressure, density and thermal conductivity of the gas inside the bubble.

To calculate the radial oscillations of the coated bubble and uncoated bubble while including the linear thermal effects Eqs. 2 and Eq. 3 are respectively coupled with Eq. 7 and liquid viscosity is increased by μ_{th}.

7.3.6 Nonlinear terms of dissipation for the KMCH model (the coated bubble)

Using the approach in [36], the nonlinear dissipation terms for the KMCH model is derived. The derivation is presented in Appendix. Fig. 7.1 represents a schematic of the process of the acoustic energy loss by the bubbles. The nonlinear dissipation powers for the KMCH model are given by Eq. 11:

$$\begin{cases} Td = \dfrac{-4\pi}{T}\displaystyle\int_0^T R^2\dot{R}P_g dt \\ \\ Ld = \dfrac{16\pi\mu_L}{T}\displaystyle\int_0^T R\dot{R}^2 dt \\ \\ Cd = \dfrac{48\pi\mu_{sh}\varepsilon R_0^2}{T}\displaystyle\int_0^T \frac{\dot{R}^2}{R^2} dt \\ \\ Gd = \dfrac{48\pi G_s\varepsilon R_0^2}{T}\displaystyle\int_0^T \left(\frac{\dot{R}}{R} - \frac{R_0\dot{R}}{R^2}\right) dt \\ \\ Rd = \dfrac{1}{T}\displaystyle\int_0^T \left(4\pi\left[\frac{R^2\dot{R}^2}{c}\left(P - P_g\right) + \frac{R^3\dot{R}}{c}\left(\dot{P} - \dot{P}_g\right) + \frac{4\mu_L R^2\dot{R}\ddot{R}}{c}\right.\right. \\ \left. +12\mu_{sh}\varepsilon R0^2\left(\frac{\dot{R}\ddot{R}}{cR} - \frac{3\dot{R}^3}{cR^2}\right) + 12G_s\varepsilon R0^2\left(\frac{-2\dot{R}^2}{cR} + \frac{3R_0\dot{R}^2}{cR^2}\right)\right] \\ \left. -\frac{\rho R^2\dot{R}^4}{2c} - \frac{\rho R^3\dot{R}^2\ddot{R}}{c}\right) dt \end{cases} \tag{7.11}$$

Where Td, Ld, Cd, Gd and Rd are the dissipation powers due to the thermal, liquid viscosity, coating viscosity, coating elasticity (returns zero for the parameters that are studied in this paper) and radiation damping respectively. T is the integration time and can be given as n/f where n=1,2..... . In this paper the integrals are performed over the last 20 cycles of a 200 cycles pulses. It should be noted that in this paper we considered the dissipation mechanisms of only a single bubble. In real cases, however, bubbles exists in polydisperse clusters with variable number density for each bubble size. In such case, accurate modeling requires consideration of bubble interactions on the radial dynamics of each bubble [22]. Dissipation powers then can be calculated by solving Eq. 11 for each size separately and then summing the contribution of each bubble. Another assumption in Eq. 11 is

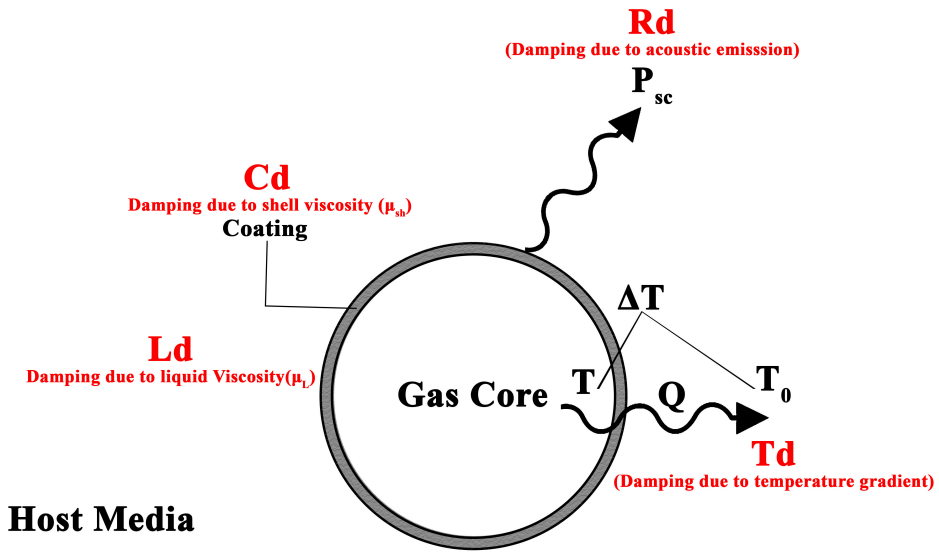

Figure 7.1: Schematic diagram showing the different damping mechanisms for a coated bubble. The nonlinear damping terms are due to the liquid viscosity (Ld), viscosity of the coating (Cd), the heat loss due to the temperature gradient between the bubble and the host media (Td) and the damping due to the re-radiation of acoustic waves by the bubble (Rd). These terms are represented by Eq. 12. In the diagram P_{sc} is the scattered (re-radiated) pressure by the bubble (radiated spherically away from bubble), T is the internal gas temperature, T_0 is the temperature of the host media and Q represents heat energy loss due to the temperature gradient ΔT.

that its accuracy is limited to the regime of low Mach numbers [35] where both Keller-Miksis [47] and Caflisch [31] equations are valid. The regime of large amplitude bubble oscillations that lead to wall velocities in the order of sound speed of the medium are beyond the focus of this study.

In case of the non-thermal model (Eq. 4) Td=0. In case of the LTM model (Eq. 7-10), Td is replaced by $Td = \frac{16\pi\mu_{th}}{T}\int_0^T \left(R\dot{R}^2\right) dt$.

7.3.7 Nonlinear terms of dissipation for the KM model (the uncoated bubble)

The dissipation terms for an uncoated bubble were derived in our previous work [36] and are given by Eq. 12:

$$\begin{cases} Td = \dfrac{-4\pi}{T}\displaystyle\int_0^T P_g \dot{R} R^2 dt \\ \\ Ld = \dfrac{16\pi\mu_L}{T}\displaystyle\int_0^T \left(R\dot{R}^2\right) dt \\ \\ Rd = \dfrac{1}{T}\displaystyle\int_0^T \left[\dfrac{4\pi}{c}\left(R^2\dot{R}\left(\dot{R}P + R\dot{P} - \dfrac{1}{2}\rho\dot{R}^3 - \rho R\dot{R}\ddot{R}\right)\right)\right. \\ \qquad \left. - \left(\dfrac{\dot{R}}{c}P_g + \dfrac{R}{c}\dot{P}_g\right)4\pi\dot{R}R^2 + \dfrac{16\pi\mu_L R^2\dot{R}\ddot{R}}{c}\right] dt \end{cases} \tag{7.12}$$

In case of using the model with no thermal damping effects Td=0 and in case of incorporating the linear thermal effects $Td = \frac{16\pi\mu_{th}}{T}\int_0^T \left(R\dot{R}^2\right) dt$ All the dissipated powers were calculated for the last 20 cycles of pulses with 200 cycles length. Simulations were carried out in Matlab using ODE45. The minimum time size for integration in each simulation was $\frac{10^{-5}}{f}$ where f is the excitation frequency. Similar to Eq. 11, in case of the non-thermal model (Eq. 4) Td=0. In case of the LTM model (Eq. 7-10), Td is replaced by $Td = \frac{16\pi\mu_{th}}{T}\int_0^T \left(R\dot{R}^2\right) dt$.

7.3.8 Acoustic power due to scattered pressure by bubbles

Radiation damping is due to the re-radiated (scattered) energy by the bubble. The acoustic energy scattered by an oscillating bubble can be calculated using [57, 58]:

$$W_{sc} = \frac{4\pi r^2}{\rho c} P_{sc}^2 \tag{7.13}$$

where P_{sc} is the pressure scattered (re-radiated) by the oscillating bubble [57, 58]:

$$P_{sc} = \rho\frac{R}{r}\left(R\ddot{R} + 2\dot{R}^2\right) \tag{7.14}$$

here r is the distance from the bubble center. Using Eqs.13 and 14 we can write:

$$W_{sc} = \frac{4\pi\rho}{c} R^2 \left(R\ddot{R} + 2\dot{R}^2 \right)^2 \tag{7.15}$$

The dissipated power due to radiation should have the same value of the acoustic scattered power by the bubble. To calculate the power loss due to the scattered pressure by the bubble one can take the time average of the Eq. 15:

$$Sd = \frac{1}{T} \int_0^T W_{sc} dt \tag{7.16}$$

where Sd is the dissipated power due to the scattered pressure by the bubble. This term should have the same value of as Rd. Therefore, one can compare $< Rd >$ and $< Sd >$ to validate the predictions of Rd in Eq. 11. In this paper, Eq. 16 was used to validate the predictions of Rd in Eq. 11, similar to our previous approach in [36]. Rd and Sd were in good agreement within the parameter ranges that are studied in this paper.

7.4 Results

7.4.1 Total dissipated power by uncoated bubbles

In order to get a better understanding of the effect of thermal dissipation on the uncoated bubble oscillations, Fig. 7..2 presents the total dissipated power as a function of frequency for different excitation pressures. The bubble has an initial radius of $R_0 = 2\mu$m. At each pressure and frequency, first the radial oscillations as a function of time are calculated. This is done for three cases by solving the coupled KM model (Eq. 3) with the full thermal (FTM) (Eqs. 5-6), linear thermal (LTM) (Eqs. 7-10) and non-thermal model (NTM) (Eq. 4). Then the radial oscillations are used as input in to Eq. 12 to calculate the dissipation mechanisms. In Fig. 7..2, the left column is for an air gas core and right column represents the C3F8 gas core. At $P_a = 1$ KPa (Figs 7..2a-b), predictions of FTM and LTM are in good agreement ; however, the NTM over estimates the dissipated power and also over estimates the resonance frequency. The resonance energy curves are wider when thermal effects are present which is due to the increased damping. Furthermore, due to lower thermal damping in the case of a C3F8 gas core, the resonance energy curves in Fig. 7..2b are narrower

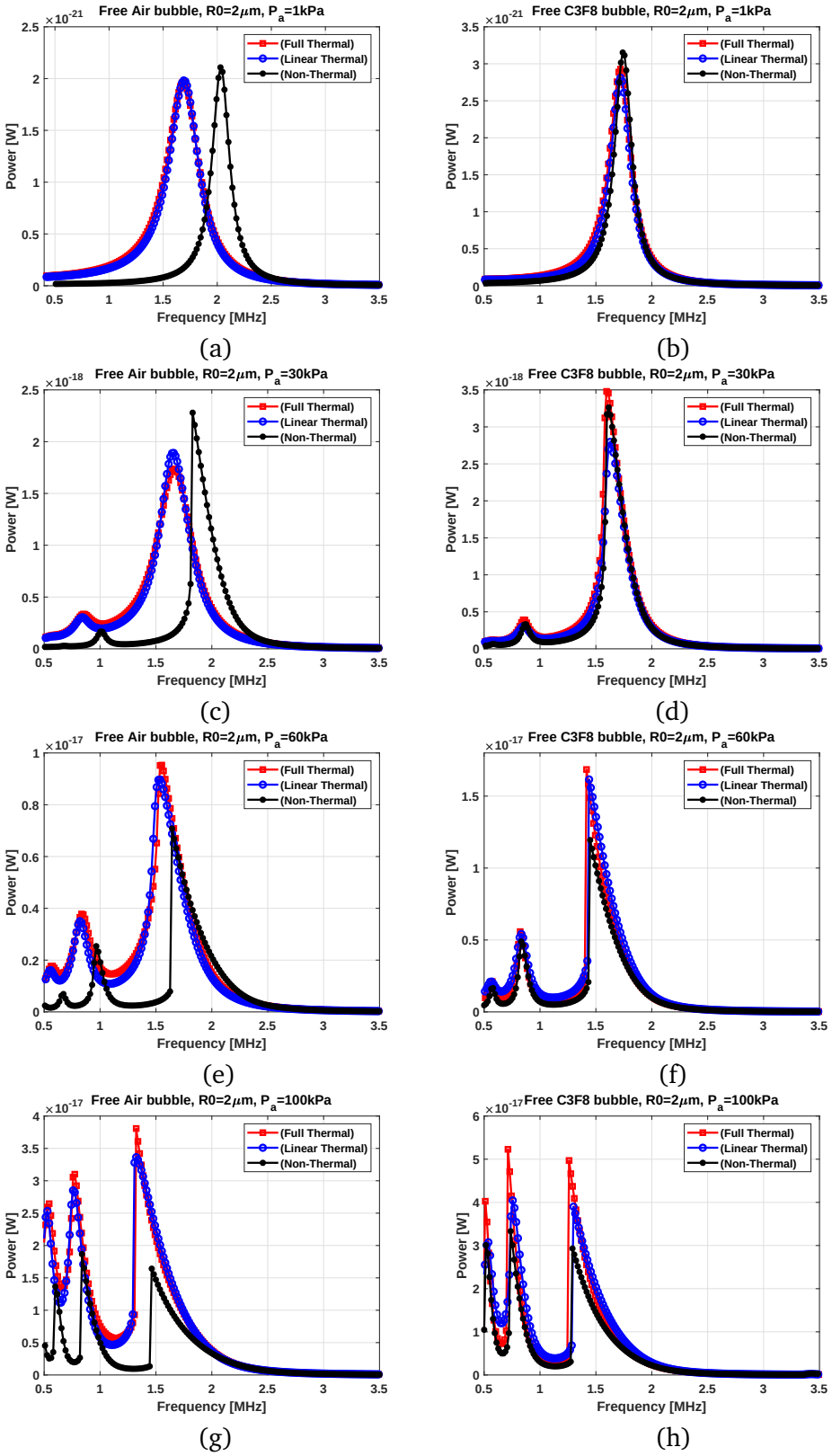

Figure 7.2: Total dissipated power as predicted by the non-thermal, linear thermal, and full thermal model as a function of frequency for an uncoated bubble with $R_0 = 2\ \mu$ m at various pressures (left column is for air gas core and right column is for C3F8 gas core).

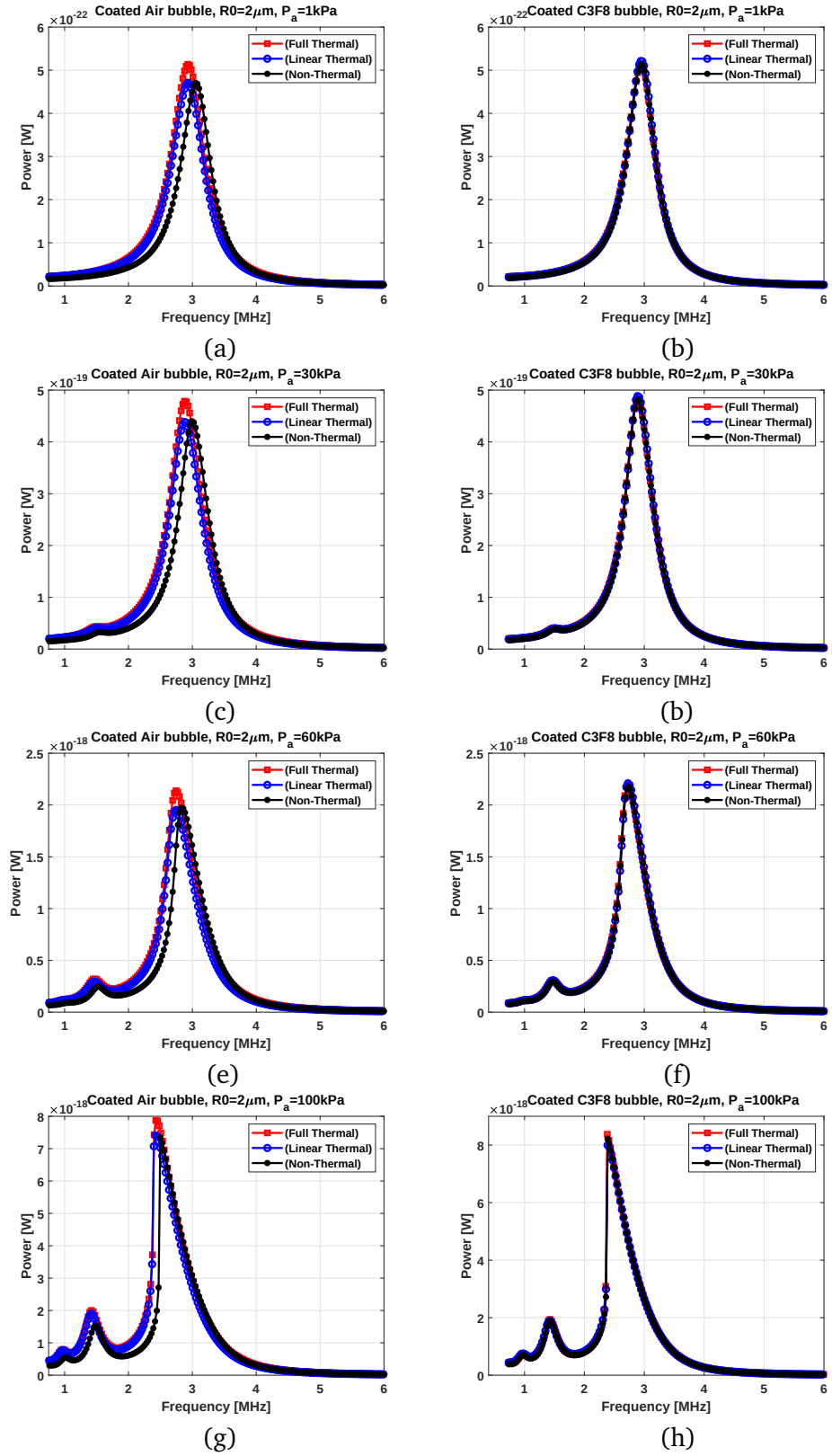

Figure 7.3: Total dissipated power as predicted by the non-thermal, linear thermal, and full thermal model as a function of frequency for a coated bubble with $R_0 = 2$ μ m at various pressures (left column is an uncoated air bubble and right column is a C3F8 coated (left column is for air gas core and right column is for C3F8 gas core)).

compared to Fig. 7..2a.

Nonlinear effects increase with increasing pressure and at $P_a = 30$kPa (Figs 7..2c-d) predictions of the FTM and LTM start deviating. We also observe a 2nd superharmonic (SuH) resonance peak below resonance frequency. At $P_a = 60$kPa (Figs. 7..2e-f) nonlinear effects result in further disagreement between the FTM and the LTM. Moreover, the damping predicted by LTM and FTM are $\approx 30\%$ higher than the predictions of the NTM models. At higher pressure the total dissipated power grows at resonance and the 2nd SuH resonance while both resonance frequencies decrease in magnitude; this is a phenomenon known as pressure dependent (PD) resonance [24]. We also observe the generation of a third peak below 2nd SuH resonance which indicates the 3rd SuH resonance frequency. NTM underestimates the total dissipated power by about 250 $\%$ at the main resonance. NTM predicts the correct value for the resonance frequencies of the bubble with C3F8 gas core; however, it over-predicts the resonance frequencies of the air bubble.

At $P_a = 100$kPa predictions of the FTM for the total dissipated power deviate by up to 20 $\%$ from those made by the LTM model. However, for all pressures, the FTM and the LTM predict the same resonance frequencies. The NTM underestimates the total dissipated power and over-predicts the resonance frequencies.

We see here that for pressures above 1 kPa and for air and C3F8 uncoated bubbles FTM must be applied for more accurate predictions of the dissipated powers and bubble oscillations. In case of gases with higher thermal damping like Ar usage of the FTM becomes more important as thermal effects become even more significant.

7.4.2 Total dissipated power by coated bubbles

In order to get a better understanding on the effect of thermal dissipation on the uncoated bubble oscillations, Fig. 7..3 shows the total dissipated power as a function of frequency and gas core composition for a coated bubble with $R_0 = 2\mu$m, G_s=45 MPa and $\mu_{sh} = \frac{1.49(R_0(\mu m)-0.86)}{\theta(nm)}$ with $\theta = 4$nm. The right column represents the dissipation results for a bubble with air gas core and the left column illustrates the dissipated power for a C3F8 gas core. When $P_a = 1$kPa (Figs. 7.3a-b) and with air as the gas core, the NTM over estimates the value of the resonance frequency while the FTM and LTM predict the same resonance frequency. However, the LTM slightly under-predicts

($\approx 6\%$ at resonance peak) the dissipated power. In case of a C3F8 gas core, the NTM, FTM and LTM predict the same value for resonance frequency and total dissipated power. The total dissipated power increases with an increase in the excitation pressure (Figs. 7.3c-h), and the main resonance frequency shifting to lower frequencies. In case of an air gas core, the LTM slightly underestimates the total dissipated power at resonance; however, the LTM and FTM predict the same value for the dissipated power at other frequencies (Fig. 7.3). For the studied pressures in Fig. 7.3 (1-100 kPa) even when 2nd order SuH occurs, predictions of the LTM and FTM are in good agreement. This is because unlike the uncoated bubble where the thermal damping is the major contributor to the total dissipated power, in case of coated bubble thermal effects are largely overwhelmed by the strong dissipation due to Cd. In case of a C3F8 gas core, predictions of the NTM, FTM and LTM are in excellent agreement at all excitation pressures examined. This is because C3F8 has smaller Td compared to air, therefore Td is overwhelmed by the strong Cd. For the characterization of UCAs that enclose gases like C3F8 (coated bubbles with $R_0 < 4\mu m$), thermal effects can fully be neglected. For larger bubbles, Td increases as the surface area for Td increases; however, UCA sizes are limited to bubbles smaller than 8 μm [12]. Fig. 7.3 however shows that FTM is the appropriate model for more accurate prediction of the behavior of uncoated bubbles.

7.4.2.1 Mechanisms of damping in coated bubbles at different pressure amplitudes

In order to highlight the pressure dependence of the dissipation mechanisms in a coated bubble, the dissipation due to Rd, Td, Ld and Cd of a coated bubble with $R_0 = 4\mu m$ is studied as a function of frequency ($0.25f_r < f < 2.5f_r$) at different pressures between $1-240kPa$ and results are plotted in Fig. 7.4. More information on the mechanisms of damping considering the effect of size for both the coated and uncoated bubbles can be found in the Appendix. Fig. 7.4 plots the dissipated power due to the damping from coating (Cd), Td, Rd and Ld for a coated bubble with R_0=4 μm ,G_s=45 MPa, θ=9 nm and $\mu_{sh} = \frac{1.49(R_0(\mu m)-0.86)}{\theta(nm)}$. This was chosen as it is the upper limit of the coated bubbles that can be used in biomedical ultrasound and thus has the highest Td. The right column represents the air gas core and the left column represents the C3F8 gas core. When P_a=1 kPa and for the air as the filling gas (Fig. 7.4a) the damping due to Cd is the major damping factor at the main resonance and frequencies below ($Cd > Td > Ld > Rd$). For frequencies above $1.5f_r$ Rd

contributes more to damping with Rd≈Cd at $f = 2.5f_r$. At $f \approx f_r$, Cd is 3 times stronger than Td and Ld. For the bubble filled a C3F8 core (Fig. 7.4b) Cd is the major dissipation factor with $Cd > Ld > Rd > Td$; Cd is ≈ 3.8 larger than Ld and 40 times larger than Td. Thus use of C3F8 as the gas core significantly reduces the Td at resonance.

For the coated bubble filled an air core at an increased $P_a = 80$kPa (Fig. 7.4c), we see the generation of 2nd and 3rd SuH resonances and a large shift of the main resonance to PDf_r (pressure dependent resonance frequency) at $f = 0.79f_r$. Cd is the major damping factor (≈ 4.5 times larger than Ld) with $Ld \approx Rd \approx Td$. At frequencies below resonance $Cd > Td > Ld > Rd$ and at frequencies above $1.5f_r$ $Rd > Ld \approx Td$. For the bubble filled a C3F8 gas core (Fig. 7.4d) the shift in main resonance is more significant due to less thermal damping effects ($PDf_r = 0.76f_r$) and $Cd > (Ld \approx Rd) > Td$. Here Cd is 64 times stronger than Td at the PDf_r.

Fig. 7.4e-f displays the case of sonication with P_a= 160 kPa. For the air bubble (Fig. 7.4e) $Cd > Rd > Ld > Td$ at frequencies near and below PDf_r. When the growth rate of the dissipation factors are compared in Fig. 7.4, we see that Rd grows the fastest with pressure increase and Td has the slowest growth rate. As pressure increases Rd grows faster and eventually becomes the second major dissipation factor while the initially strong Td lags behind the rest of the damping factors. Due to the high bubble oscillation amplitude $\frac{R_{max}}{R_0} > 2$ the bubble may not sustain stable non-destructive oscillations for $f < f_r$ at 160 kPa. At this pressure and at $f_r < f < 1.5f_r$ Ld ≈Td≈Rd. For the C3F8 bubble, due to the smaller damping from thermal effects we can see the generation of SH resonance peak at $f \approx 2f$ (Fig. 7.4f). For the frequency range that is studied here, $Cd > Rd \approx Ld$. Cd is ≈ 100 times and 600 times stronger than Td, respectively at PDf_r and PDf_{sh} (pressure dependent SH resonance at ≈ $1.86f_r$).

At P_a=240 kPa the SH resonance peak is seen for the coated air bubble (Fig. 7.4g). The bubble oscillation amplitude has exceeded the threshold of destruction $\frac{R_{max}}{R_0} > 2$ for $f < f_r$. At $f = PDf_{sh}$ ($1.67f_r$ at P_a=240 kPa) $Cd > Rd > Td \approx Ld$. Cd is about 46 times stronger than Td. For the coated bubble enclosing C3F8 (Fig. 7.4h) thermal effects are much weaker at PDf_{sh} ($1.62f_r$ at P_a=240 kPa) with $Cd > Rd > Ld > Td$ and Cd is about 72 times stronger than Td. For frequencies below f_r, the bubble can not sustain stability at this pressure.

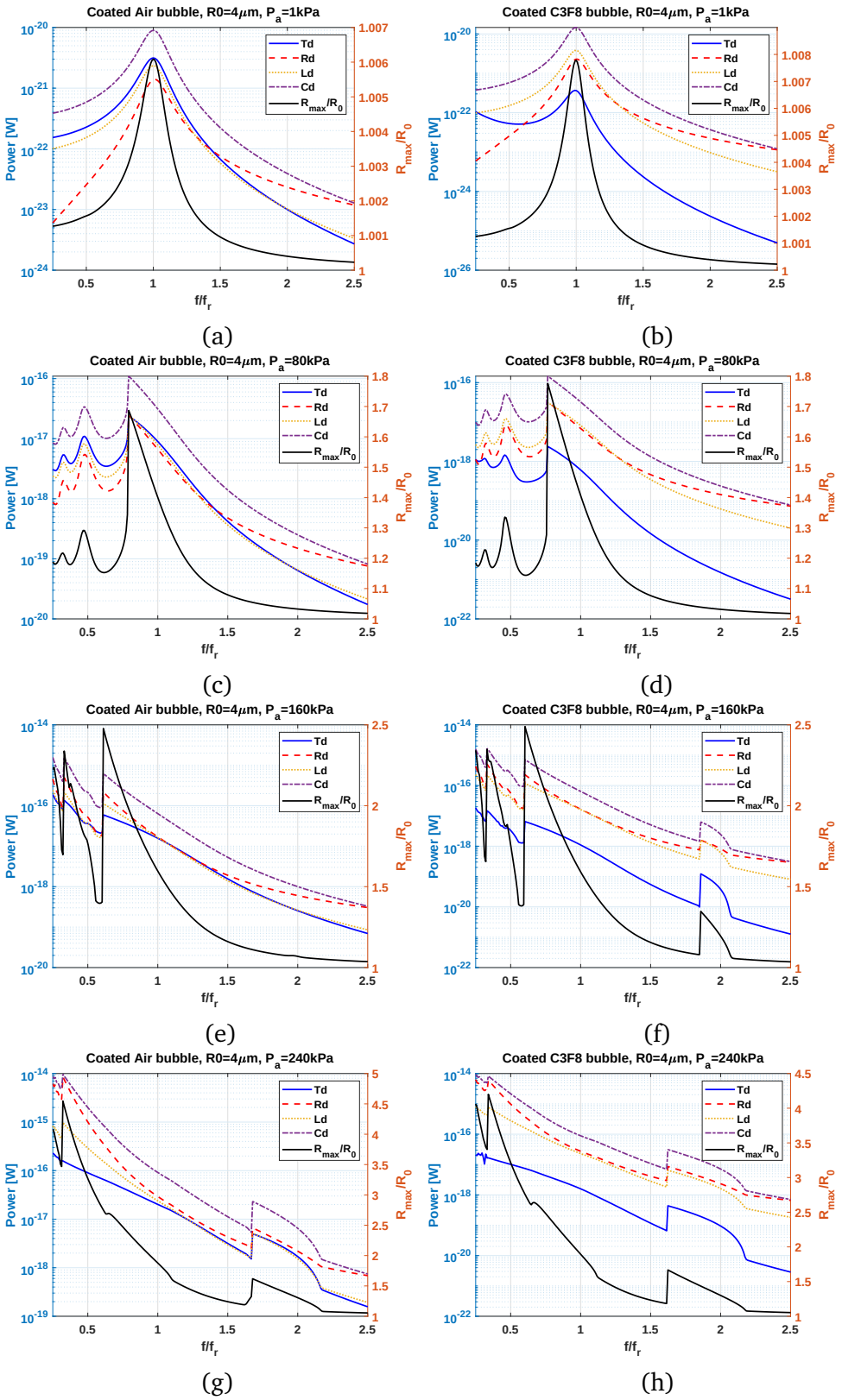

Figure 7.4: Dissipated power due to Cd, Td, Ld and Rd as predicted by the full thermal model as a function of frequency for a coated bubble with $R_0 = 4\ \mu$ m at various pressures (left column is for an air gas core and right column is for a C3F8 gas core).

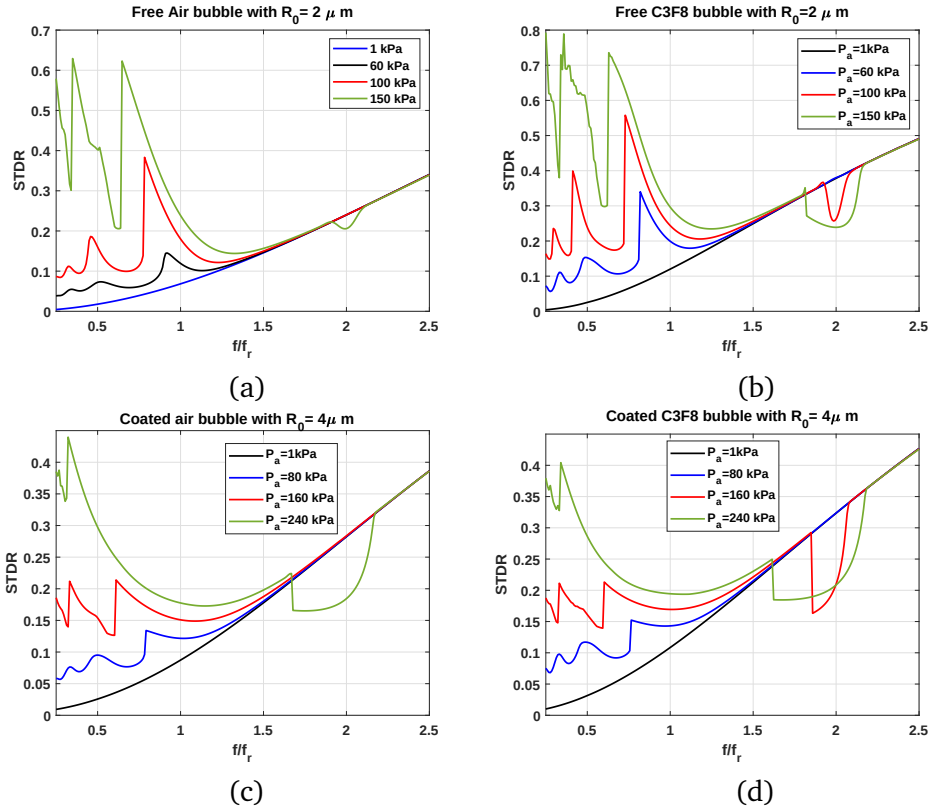

Figure 7.5: Scattering to damping ratio (STDR) as a function of frequency at various excitation pressures. Top row is for an uncoated bubble with $R_0 = 2\mu m$ and bottom row is for a coated bubble with $R_0 = 4\mu m$. (left column is an uncoated air bubble and right column is a C3F8 coated bubble).

7.4.2.2 Scattering to damping ratio (STDR)

One of the important reasons for the valuation of the nonlinear dissipation terms (Eqs. 11 & 12) is the calculation of the pressure dependent scattering to dissipation ratio (STDR). In the previous sections and the results presented in the Appendix, it was shown that dissipation due to Cd, Ld, Rd and Td are pressure dependent. We showed that as pressure increases, Rd can grow faster than the other damping factors and can become the dominant or the second major dissipation mechanism in the total dissipation. This will increase the scattering to dissipation ratio (STDR), which would be desirable for applications in which a larger scattering to dissipation is desired. In this section we investigate the pressure dependence of the STDR and present the regions for which STDR can be enhanced. The graphs are calculated using Eqs. 11 and 12 and inputting the radial oscillations that are solved by coupling the KMCH (Eq. 2) or the KM (Eq. 3) models with the FTM.

Fig. 5a shows the STDR of an air uncoated bubble with $R_0 = 2\mu$m as a function of frequency

at various pressures. At 1 kPa (the blue line), the STDR diagram doesn't show any distinct peak; STDR grows as a function of frequency. At higher frequencies the bubble oscillations are very weak; thus Ld and Td are negligible compared to active scattering Rd. This is because even for weak bubble oscillations, the bubble re-radiates and scatters sound waves. However, the very weak oscillation leads to near zero wall velocities thus Ld becomes very small. Similarly, due to the near zero temperature elevation inside bubble, Td becomes very small as well. Thus, the STDR is higher at higher frequencies and lower excitation pressures. An increase in pressure leads to increase in the STDR. The STDR is very high at PDf_r [24] (e.g. 0.4 at 100 kPa). As pressure increases, the STDR at the SuH resonance frequencies and PDf_r increases. This is due the faster growth of Rd as incident pressure increases when compared to other damping factors. At 150 kPa and concomitant with the generation of $\frac{1}{2}$ SH resonance [60] (green curves $f/f_r > 1.5$), the STDR decreases. This is because when the bubble oscillation amplitude increases, Ld and Td become significant, decreasing the STDR. We have shown the same effect for the case of sonication with pressure dependent SH resonance [61] when $\frac{1}{3}$ [62,63] order SH resonance occurs [36]. For the investigated bubble when $f > 1.5f_r$, the STDR does not change as pressure increases, unless SH oscillations appear (in which case STDR decrease by pressure increase).

Fig. 7.5b shows the STDR of a C3F8 uncoated bubble with $R_0 = 2\mu$m as a function of frequency at various pressures. The evolution of STDR with pressure is similar to that of the air bubble; however, SH oscillations occur at lower pressures than the air gas core due to smaller effects of Td. Furthermore, the STDRs at PDf_r and SuH resonances are stronger than those for the air bubble due to weaker contributions from Td. Thus, for uncoated bubbles one may get larger STDRs if a gas like C3F8 is used.

Fig. 7.5c shows the STDR as a function of frequency of a coated air bubble with $R_0 = 4\mu$m. The evolution of the STDR with pressure increase is very similar to that of the uncoated bubble; however, the STDR is considerably reduced compared to the uncoated counterpart. This is because of the increased damping due to coating friction. In Fig. 7.4 we showed that Cd is the major damping factor for the coated bubble. We see the same trend in the STDR of the bubble with a C3F8 gas core (Fig. 7.5d). The values of STDR are very close to the ones of the air gas core for $f < 1.5f_r$. This is because Cd is the major contributor to total damping and changes in Td do not affect the W_{total} significantly. At higher frequencies however, the C3F8 bubble exhibit SH

oscillations at a lower pressure.

7.5 Discussion

Bubbles are the building blocks of several applications from material science and sonochemsitry [6,7,8,9,10] to oceanography [4,5] and medicine [11,12,13]. Dynamics of bubbles are nonlinear and complex [15, 17, 18, 19, 20] and to achieve their full potential in applications a detailed and quantitative understanding of the bubble response to acoustic excitation as well as scattering and damping mechanisms are needed. The presence of bubbles however, changes the acoustic properties of the medium [31, 32, 33, 34, 35, 36, 37]. Changes in the acoustic properties are nonlinear and are a function of bubble size, excitation frequency and pressure [34, 35, 36, 37]. Because of the changes in the acoustic properties of the medium (e.g. increased pressure dependent attenuation [34,37,43,45]), knowledge of the nonlinear bubble behavior is not enough to control and optimize applications. One must have sufficient knowledge on the relationship between the nonlinear bubble oscillations and changes in the acoustic properties of the medium. For example, increased attenuation from bubbles in the beam path can limit the energy that the bubbles at the target are exposed to [34,45] and decrease the efficacy of sonochemical applications [34,35, 37], drug delivery [65] and enhanced heating in HIFU [44]. Increased attenuation of bubbles can also create shielding of the post-focal tissue and bubbles in contrast enhanced diagnostic ultrasound and deteriorate the ultrasound images [65,66]. In bubble characterization applications like oceanography studies [4,5] or characterization of ultrasound contrast agents [38,39,40,41, 42,43] pressure dependent changes in the attenuation are of significant importance and should be understood in detail.

In this study we present a simple model for coated bubbles that accounts for the compressibility effects up to the first order of Mach number. The model is called CHKM model as it is a hybrid of Church-Hoff model [38] and Keller-Miksis (KM) model [47]. The goal of incorporating the compressibility effects was to investigate the dissipation of acoustic energy due to re-radiation (Rd) effects [35, 36, 37]. Rd is a important pressure dependent dissipation mechanism [35, 36, 37]; however, it is simplified [48] or fully neglected [38] in models that are used to study the coated

bubble behaviors. To model the oscillations of coated bubbles and uncoated bubbles, CHKM and KM models were respectively solved; in each case three forms were considered for the gas pressure inside the bubble. First, CHKM was coupled to nonlinear ordinary differential equations (ODEs) that model the thermal behavior of gas bubbles [49, 51, 52, 53]. Second, thermal effects were incorporated using linear approximations that include the thermal effects [33, 53]. The linear thermal model has been widely used in studies related to coated bubble characterization and characterization of bubbles in oceanography [4, 5, 39, 40]. Third, thermal effects were fully neglected.

The relationship between excitation pressure and damping mechanisms for an oscillating coated bubble has not been investigated thoroughly. Thus, in this work, using our previous approach [36] we derived the nonlinear pressure dependent terms for the energy dissipation of the coated bubbles, which were derived for the first time. Dissipation terms stemming from thermal effects (Td), viscosity of coating (Cd), liquid viscosity (Ld) and re-radiation of acoustic waves (Rd) by coated bubbles were derived.

In order to investigate the effect of thermal damping on bubble oscillations and choose the proper model for bubble oscillations, the total dissipated acoustic energy was modeled using the three models described above for both uncoated and coated bubbles of different sizes. For each bubble size energy curves were displayed as a function of frequency at various pressures and for two gas cores of air and C3F8.

Results showed that in case of uncoated bubbles thermal effects are significant and cannot be neglected. Furthermore, linear approximations are only valid for small excitation pressures (e.g. 1 kPa). For higher pressures (e.g. $>$ 10 kPa) predictions of the linear thermal model and the full thermal model deviate and full thermal model should be used to model bubble oscillations. The deviation arises due to the growth of nonlinear effects in the bubble oscillations. The linear thermal model is derived by assuming very small bubble oscillation amplitude [10] (e.g. $R_{max}/R_0 < 1.02$) and for symmetric expansion and compression (the bubble oscillates around R_0). However, as pressure increases, the radial oscillations grow above the size limit where linear assumptions are valid. The bubble expansion and compression phases are no longer symmetric. Higher internal temperatures are created during significant compression or collapse (larger R_{max}/R_{min}) and the average surface area available for temperature escape becomes smaller or enhanced depending on

the regime of oscillations. This causes the predictions of the two models to deviate. As an example, below resonance (e.g. at pressure dependent resonance frequency) the collapse of the bubble into a smaller radius decreases the surface area for the heat to dissipate into the surrounding liquid. At the same time, the bubble collapses with a higher wall velocity and rebounds quicker, thus the time duration available for the temperature escape will be limited as well. The average surface area for thermal conduction decreases. Thus, the initially stronger Td in the linear oscillation regime (e.g. $P_A = 1kPa$ in Fig. 7.4a), becomes weaker than Rd and Ld in the PDf_r regime (e.g. Fig. 7.4e and 4g). This effect can only be captured using the full thermal model (Eqs. 4 and 5). It should be noted that the more complete thermal model uses the full partial differential equations (PDEs) [51] for heat loss which incorporates the temperature gradients within the oscillating bubble. The full thermal model in ODE form (Eqs. 4 and 5) has the advantage of faster computation time, however it simplifies the PDE form by assigning a uniform average temperature within the gas. For the moderate pressures used in this study, predictions of the full thermal model in the ODE form have been shown to be in good agreement with the thermal model in the PDE form [51].

In case of the coated bubbles with air gas core the ODE thermal model (Eq. 5 & 6) [51] is a more precise model to incorporate the thermal effects at higher pressures compared to simplified linear model [33, 50] (Fig. 7.3). Because of very high dissipation due to coating, Cd is the dominant dissipation mechanisms within the frequency and pressure ranges that were studied in this paper. As the driving pressure increases, the ratio of the Td to other damping factors decreases for $< 1.5f_r$ (Figs. 7.4c,7.4e & 7.g). For the air coated bubble with $R_0 = 4\mu m$ and at 1kPa, and in agreement with linear estimations [38] $Cd > Td > Ld > Rd$. However, when $P_A = 80$ kPa (Fig. 7.4c) and at $f = PDf_r(\approx 0.8f_r)$, $Cd > Td \cong Ld \cong Rd$; when $P_A = 160$ kPa (Fig. 7.4e) and at $f = PDf_r(\approx 0.61f_r)$ $Cd > Rd > Ld > Td$. The reason for the larger increase in Ld and Rd compared to Td is because of the faster bubble collapses (higher wall velocities) and higher wall accelerations. Thus, Rd and Ld exhibit very large growth with pressure, meanwhile due to lower average surface area for thermal conduction stemming from rapid collapse and rebound, Td can not grow as fast as the other dissipation mechanisms. Td estimated by the linear thermal approximations (Eqs. 7-10) cannot capture this effect as it is proportional only to the wall velocity ($Td = \frac{16\pi\mu_{th}}{T}\int_0^T \left(R\dot{R}^2\right) dt$), and thus behaves similar to Ld and in this case will remain stronger than Ld at all pressures. At higher pressures, these results are in contradiction with the predictions

of the linear model and emphasize the importance of using the full thermal model (Eqs. 5 and 6) in modeling the radial oscillations together with Eq. 11 and 12 in modeling the dissipation mechanisms. For frequencies $> 1.5f_r$ and for pressure and frequency ranges where SH oscillations occur (e.g. [60, 61]), Td of the air gas core is very important and can not be ignored (Fig. 7.4g).

In case of C3F8 coated bubbles, and for the pressure and frequency ranges that are investigated here, thermal effects can be neglected (Figs. 7.3a, 7.b, 7.f, & 7.h) as it is 10-100 times smaller than the major dissipation factor Cd (Figs. 7.4b, 7.4d, 7.4e and 7.4f). The reason for much smaller Td of the C3F8 gas core compared to the air gas core is that the heat capacity of the C3F8 at constant volume is about 8.2 times higher. This consequently results in much smaller temperature elevations inside the bubble. Therefore, the temperature gradient at the bubble wall decreases and thus thermal loss becomes smaller.

The pressure ranges studied here (1 kPa-100 kPa) are often used to characterize the shell parameters of coated bubbles in medical ultrasound. The previous studies [39, 67, 68]; considered an artificial viscosity term and added it to the liquid viscosity to consider the thermal effects in the bubble oscillations. The viscosity is usually twice that of the water viscosity [39, 67, 68]. Here, we show that such approximation leads to considerable overestimation of the Td especially in case of C3F8 or similar gasses like C4F10 (Fig. 7.4). Thus estimated values for the viscosity of coating in [39, 67, 68] and pressure threshold of SH oscillations may be inaccurate.

In the Appendix, we investigated the dependence of Cd, Ld, Rd and Td for different bubble sizes as a function of frequency and at different pressures. We showed that the dissipated energy depends on size, frequency and pressure. In case of uncoated bubbles, it is shown in the Appendix that Td is very important for the larger air bubbles (e.g. $10\mu m$); however at higher pressures Rd can exceed Td. For C3F8 uncoated large bubbles Td is only the major damping factor for $f < f_r$ and lower pressures (e.g. $P_a < 10kPa$). Rd is the major damping factor at $f > 1.5f_r$ and for all the pressures studied here. For the uncoated C3F8 large bubble (e.g. $10\mu m$) Rd becomes the major damping factor for $f < f_r$ (e.g. PDf_r and super harmonic resonance ($SuHf_r$)) as pressure increases ($P_a > 40kPa$). For smaller uncoated air and C3F8 bubbles ($R_0 < 2\mu m$) Td is not the major damping factor. Rd, Ld and Td grow as pressure increases; Rd exhibits the fastest growth rate and Td the slowest. At higher pressures (e.g. $P_a > 100kPa$) Rd and Ld become an order of magnitude higher than Td (for the studied frequency range here $0.25f_r < f < 2.5f_r$).

For coated bubbles Cd is the major damping factor for the pressure and frequency ranges that were studied here (except for $f > 2f_r$ and for the coated bubble with $R_0 = 1\mu$m where Rd is the most significant dissipation mechanism). Similar to the uncoated bubble, Rd grows faster than other damping factors with pressure increases while Td has the slowest growth rate. The reason for the faster growth of Rd with pressure increase is its strong dependence on the fourth power of the wall velocity and second power of the wall acceleration (Rd $\propto R^2\left(R\ddot{R}+2\dot{R}^2\right)^2$ Eq. 16 [2]). Ld and Cd are only dependent on the second power of the wall velocity (Ld$\propto (R\dot{R}^2)$ and Cd $\propto (\frac{\dot{R}^2}{R^2})$). At higher pressures and specially at frequencies below resonance, the bubble attains very high wall velocities upon collapse and due to the stronger dependence of the Rd on wall velocity compared to Cd and Ld, it demonstrates a larger growth. Because of the very strong effect of Cd on the damping (which increases for smaller bubbles) and due to the reduction of Td with size, Td becomes less important for smaller coated bubbles (compare Fig. 7.4 with the Fig. 7.9 of the appendix).

The bubble scattered pressure (P_{sc}) and attenuation can be measured in real time. P_{sc} depends on $R(t)$, $\dot{R(t)}$ and $\ddot{R(t)}$; thus there is a direct relation between the enhanced bubble activity and increased P_{sc}. Power loss due to radiation (P_{sc}) can be calculated using Eqs. 11 and 12 for coated and uncoated bubbles respectively or Eq. 15 and is related to the scattered pressure measured in real time during applications. Total damping can be calculated using Eqs. 11 and 12 and attenuation which is directly related to damping [34, 35, 37] can be calculated using the total damping [34, 35, 37]. The scattering to damping ratio ($STDR = \frac{Rd}{W_{total}}$ where W_{total} is the total dissipated power due to bubble oscillations) can be defined as a dimensionless parameter that can be used to assess the ratio of the energy re-radiated by the bubble as a fraction of the total attenuation.

We derive the nonlinear terms to calculate the STDR and investigated the pressure dependence of the STDR for without any linear assumptions. We showed that scattering to damping ratio (STDR) is pressure dependent; STDR grows with pressure at pressure dependent resonance frequencies (PDf_r [24]) and at super harmonic resonances of the system ($SuHf_r$ [23]). The increase in STDR with pressure was due to the faster growth in Rd relative to the other damping factors. STDR is generally higher at $f > f_r$. For the bubble size and frequency examined in this paper pressure

[2] Eq. 16 is used here for simplicity of comparison. Note that the Rd in Eq. 11 and the Sd in Eq. 16 are the same phenomena and have the same value

ranges here, elevation in excitation pressure does not change the value of STDR for $f > 1.5f_r$, until the occurrence of SH resonance which leads to a decrease in STDR. At $f \approx 2f_r$ and when SH oscillations are initiated, due to the gentler collapses [60] and larger available surface area for thermal conduction the Td undergoes a larger enhancement compared to Rd and Ld (e.g. Figs. 7.4g-h, and in Appendix see Figs. 7.7f-h and 4.8f-h) which consequently results in a decrease in STDR (when SHs are initiated Td exhibits the largest growth). For coated bubbles, and for the stable non-destructive bubble oscillations $\frac{R_{max}}{R_0} \leq 2$, STDR can be higher than PDf_r and $SuHf_r$ even when SH oscillations occur (Figs. 7.5c and 7.d).

Coated bubbles are used as ultrasound contrast agents (UCAs) in ultrasound imaging [11,12,13,40, 45,65,66,67,68] where higher scattering and small attenuation are desired. The scattering defines the ability of UCA to enhance the echogenicity of the target. However, the presence of bubbles increases the damping of the acoustic energy in the beam path and reduces the energy available for the bubbles to be activated at the focal point. Thus higher scattering ability of UCAs and lower total damping is desired. In this regard STDR expresses the ability of the UCA to enhance the visualization of the tissue containing the UCAs and the underlying tissues [45, 65]. In therapeutic applications like drug delivery shear stress resulted from micro-streaming due to bubble oscillations are used to increase the drug delivery to cells in the target [64]. In drug delivery higher wall velocities and higher P_{sc} are desired. Compared to imaging applications, in therapeutic applications higher concentration of bubbles are used to achieve desirable effects [64]; thus damping effects are more significant [13, 44]. Higher STDR and P_{sc} are good indicators of a faster bubble wall velocity and lower total damping. In High Intensity Focused Ultrasound the re-radiated energy by bubbles is used to enhance the heating in the target area [44]; re-radiated pressure often have strong higher harmonics content which have higher absorption rate in tissue [44]. This results in localized efficient enhanced heating [44]. In these applications as well, higher P_{sc} and lower energy damping due to pre-focal bubble oscillations are desired. Same conclusions can be made for active bubbles in sonochemistry and other applications. Decreasing the pre-focal power dissipation becomes more important in treatment of locations where delivery of energy is more difficult (e.g. presence of pre-focal bone in blood brain barrier opening [69, 70]). One of the important applications of the derived nonlinear energy terms in this paper is the ability to calculate the pressure dependent STDR and thus optimize the acoustic exposure parameters to increase the focal bubble activity

while reducing pre-focal dissipation.

It should however be noted that STDR by itself is not a sufficient parameter to asses efficient bubble activity for a particular application. We have shown here and in [36] that the STDR is higher at frequencies above f_r, however, at higher frequencies bubbles are only active when pressure exceeds a threshold (e.g. above the pressure threshold of P3 or P4 oscillations [62, 63, 71, 72, 73]). Thus, depending on the application [36], the STDR must be used in tandem with P_{sc} or Rd to determine the regions of higher bubble activity and lower total damping.

7.6 Summary and conclusion

Despite the importance of radiation effects, the majority of the models for coated bubble oscillations neglect or simplify radiation effects. Moreover, thermal effects are often approximated using linear models or are fully neglected. Additionally, pressure dependent dissipation effects during bubble oscillations are not fully understood. In this work we first introduced a simple and comprehensive model for coated bubble oscillations. The model incorporates the compressibility of the medium to the first order of Mach number. Secondly, the equations for the dissipation effects due to thermal damping, liquid viscous damping, coating viscous damping and radiation damping are derived with no linear simplifications. The dissipation mechanisms were then studied as a function of frequency and at different excitation pressures. We showed that radiation effects are important and can not be neglected. Radiation damping becomes more important with pressure increase. Even at frequencies below resonance, dissipation due to radiation can become the major dissipation mechanism with pressure increase. This is in stark contradiction to the predictions of linear models. For uncoated bubbles, thermal effects are very important and can not be neglected. With pressure increase, predictions of the linear thermal model loses accuracy and inclusion of the full thermal effects are recommended. In case of coated bubbles that encapsulate gas cores similar to C3F8, thermal effects are not important and can be neglected even at higher pressures. We also showed that scattering to damping ratio is pressure dependent and there exists frequency and pressure ranges in which the STDR is higher. The basic equations provided here and the presented fundamental information can be used to optimize the exposure parameters in applications and for more accurate characterization

of bubbly media and coated bubbles.

7.7 Acknowledgments

The work is supported by the Natural Sciences and Engineering Research Council of Canada (Discovery Grant RGPIN-2017-06496), NSERC and the Canadian Institutes of Health Research (Collaborative Health Research Projects) and the Terry Fox New Frontiers Program Project Grant in Ultrasound and MRI for Cancer Therapy (project #1034). A. J. Sojahrood is supported by a CIHR Vanier Scholarship.

7.8 Appendix

7.8.1 Derivation of the nonlinear terms of dissipation for the GM

Van Wijngaardan [32] and Caflisch et al. [31] presented the mass and momentum conservation equations for a bubbly liquid as:

$$\frac{1}{\rho c^2}\frac{\partial P}{\partial t} + \nabla.v = \frac{\partial \beta}{\partial t} \tag{7.17}$$

and

$$\rho\frac{\partial v}{\partial t} = -\nabla P \tag{7.18}$$

where c is the sound speed, ρ is the density of the medium, $v(r,t)$ is the velocity field, $P(r,t)$ is acoustic pressure, $\beta = \frac{4}{3}N\pi R(t)^3$ is the void fraction where N is number of bubbles per unit volume, and $R(t)$ is the radius of the bubble at time t. These two equations can be re-written into an equation of energy conservation, by multiplying (1) by P and (2) by v:

$$\frac{\partial}{\partial t}\left(\frac{1}{2}\frac{P^2}{\rho c^2} + \frac{1}{2}\rho v^2\right) = NP\frac{\partial V}{\partial t} \tag{7.19}$$

Multiplying Eq.2 by $N\frac{\partial V}{\partial t}$ results in:

$$\begin{aligned}
&\rho N\left(R\ddot{R}+\frac{3}{2}\dot{R}^2\right)\frac{\partial V}{\partial t}-\rho N\frac{\dot{R}}{c}\left(R\ddot{R}+\frac{1}{2}\dot{R}^2\right)\frac{\partial V}{\partial t}\\
&=N\left(P_g+\frac{\dot{R}}{c}P_g+\frac{R}{c}\frac{dP_g}{dt}\right)\frac{\partial V}{\partial t}-N\left(\frac{4\mu_L\dot{R}}{R}+\frac{\dot{R}}{c}\frac{4\mu_L\dot{R}}{R}+\frac{R}{c}\frac{d}{dt}\left(\frac{4\mu_L\dot{R}}{R}\right)\right)\frac{\partial V}{\partial t}\\
&-N\left(12\mu_{sh}\epsilon R_0^2\frac{\dot{R}}{R^4}+\frac{\dot{R}}{c}12\mu_{sh}\epsilon R_0^2\frac{\dot{R}}{R^4}+\frac{R}{c}\frac{d}{dt}\left(12\mu_{sh}\epsilon R_0^2\frac{\dot{R}}{R^4}\right)\right)\frac{\partial V}{\partial t}\\
&-N\left(12G_s\epsilon R_0^2\left(\frac{1}{R^3}-\frac{R_0}{R^4}\right)+\frac{\dot{R}}{c}12G_s\epsilon R_0^2\left(\frac{1}{R^3}-\frac{R_0}{R^4}\right)+\frac{R}{c}\frac{d}{dt}\left(12G_s\epsilon R_0^2\left(\frac{1}{R^3}-\frac{R_0}{R^4}\right)\right)\right)\frac{\partial V}{\partial t}\\
&-N\left(P+\frac{\dot{R}}{c}P+\frac{R}{c}\frac{dP}{dt}\right)\frac{\partial V}{\partial t}
\end{aligned}\tag{7.20}$$

if we add Eq.18 and Eq.19:

$$\begin{aligned}
&\rho N\left(R\ddot{R}+\frac{3}{2}\dot{R}^2\right)\frac{\partial V}{\partial t}-\rho N\frac{\dot{R}}{c}\left(R\ddot{R}+\frac{1}{2}\dot{R}^2\right)\frac{\partial V}{\partial t}+\frac{\partial}{\partial t}\left(\frac{1}{2}\frac{P^2}{\rho c^2}+\frac{1}{2}\rho v^2\right)\\
&=N\left(P_g+\frac{\dot{R}}{c}P_g+\frac{R}{c}\frac{dP_g}{dt}\right)\frac{\partial V}{\partial t}-N\left(\frac{4\mu_L\dot{R}}{R}+\frac{\dot{R}}{c}\frac{4\mu_L\dot{R}}{R}+\frac{R}{c}\frac{d}{dt}\left(\frac{4\mu_L\dot{R}}{R}\right)\right)\frac{\partial V}{\partial t}\\
&-N\left(12\mu_{sh}\epsilon R_0^2\frac{\dot{R}}{R^4}+\frac{\dot{R}}{c}12\mu_{sh}\epsilon R_0^2\frac{\dot{R}}{R^4}+\frac{R}{c}\frac{d}{dt}\left(12\mu_{sh}\epsilon R_0^2\frac{\dot{R}}{R^4}\right)\right)\frac{\partial V}{\partial t}\\
&-N\left(12G_s\epsilon R_0^2\left(\frac{1}{R^3}-\frac{R_0}{R^4}\right)+\frac{\dot{R}}{c}12G_s\epsilon R_0^2\left(\frac{1}{R^3}-\frac{R_0}{R^4}\right)+\frac{R}{c}\frac{d}{dt}\left(12G_s\epsilon R_0^2\left(\frac{1}{R^3}-\frac{R_0}{R^4}\right)\right)\right)\frac{\partial V}{\partial t}\\
&-N\left(\frac{\dot{R}}{c}P+\frac{R}{c}\frac{dP}{dt}\right)\frac{\partial V}{\partial t}
\end{aligned}\tag{7.21}$$

The mass of the liquid around the bubble can be calculated as

$$M_l=\frac{1}{2}\int_R^\infty \rho 4\pi r^2 dr \tag{7.22}$$

Keller-Miksis type models are derived by assuming that the flow of the liquid [47] around the bubble is non-rotational $\vec{\nabla}\times v=0$. This assumption leads to definition of the velocity potential φ, which is given by:

$$v=\frac{\partial\varphi}{\partial r} \tag{7.23}$$

Furthermore the kinetic energy of the liquid around the bubble can be written as [35]:

$$K_l = \frac{1}{2}\int_R^\infty \rho\left(\frac{\partial\varphi}{\partial r}\right)^2 4\pi r^2 dr = 2\pi\rho R^3\dot{R}^2 \tag{7.24}$$

inserting K_l in to Eq. 20:

$$\begin{aligned}
&\frac{\partial}{\partial t}\left(\frac{1}{2}\frac{P^2}{\rho c^2}+\frac{1}{2}\rho v^2\right)+N\left(\left(1-\frac{\dot{R}}{c}\right)\frac{\partial K_l}{\partial t}+\frac{\rho\dot{R}^3}{c}\frac{\partial V}{\partial t}\right)+\nabla.(Pv)\\
&=N\left(P_g+\frac{\dot{R}}{c}P_g+\frac{R}{c}\frac{dP_g}{dt}\right)\frac{\partial V}{\partial t}-N\left(\frac{4\mu_L\dot{R}}{R}+\frac{\dot{R}}{c}\frac{4\mu_L\dot{R}}{R}+\frac{R}{c}\frac{d}{dt}\left(\frac{4\mu_L\dot{R}}{R}\right)\right)\frac{\partial V}{\partial t}\\
&-N\left(12\mu_{sh}\epsilon R_0^2\frac{\dot{R}}{R^4}+\frac{\dot{R}}{c}12\mu_{sh}\epsilon R_0^2\frac{\dot{R}}{R^4}+\frac{R}{c}\frac{d}{dt}\left(12\mu_{sh}\epsilon R_0^2\frac{\dot{R}}{R^4}\right)\right)\frac{\partial V}{\partial t}\\
&-N\left(12G_s\epsilon R_0^2\left(\frac{1}{R^3}-\frac{R_0}{R^4}\right)+\frac{\dot{R}}{c}12G_s\epsilon R_0^2\left(\frac{1}{R^3}-\frac{R_0}{R^4}\right)+\frac{R}{c}\frac{d}{dt}\left(12G_s\epsilon R_0^2\left(\frac{1}{R^3}-\frac{R_0}{R^4}\right)\right)\right)\frac{\partial V}{\partial t}\\
&-N\left(\frac{\dot{R}}{c}P+\frac{R}{c}\frac{dP}{dt}\right)
\end{aligned} \tag{7.25}$$

Eq.24 can be re-arranged as:

$$\begin{aligned}
&\frac{\partial}{\partial t}\left(\frac{1}{2}\frac{P^2}{\rho c^2}+\frac{1}{2}\rho v^2+NK_l\right)+\nabla.(Pv)=\\
&N\left(P_g\right)\frac{\partial V}{\partial t}-N\left(\frac{4\mu_L\dot{R}}{R}\right)\frac{\partial V}{\partial t}-N\left(12\mu_{sh}\varepsilon R_0^2\frac{\dot{R}}{R^4}\right)\frac{\partial V}{\partial t}-N\left(12G_s\varepsilon R_0^2\left(\frac{1}{R^3}-\frac{R_0}{R^4}\right)\right)\frac{\partial V}{\partial t}\\
&-N\left(\left[\frac{\dot{R}}{c}P+\frac{R}{c}\dot{P}-\frac{\rho\dot{R}^3}{c}-\frac{\dot{R}}{c}P_g-\frac{R}{c}\dot{P}_g+\frac{\dot{R}}{c}\frac{4\mu_L\dot{R}}{R}+\frac{R}{c}\left(\frac{4\mu_L\ddot{R}}{R}-\frac{4\mu_L\dot{R}^2}{R^2}\right)\right.\right.\\
&+\frac{\dot{R}}{c}12\mu_{sh}\varepsilon R_0^2\frac{\dot{R}}{R^4}+\frac{R}{c}12\mu_{sh}\varepsilon R_0^2\left(\frac{\ddot{R}}{R^4}-\frac{4\dot{R}^2}{R^5}\right)\\
&\left.\left.\frac{\dot{R}}{c}12G_s\varepsilon R_0^2\left(\frac{1}{R^3}-\frac{R_0}{R^4}\right)+\frac{R}{c}12G_s\varepsilon R_0^2\left(\frac{-3\dot{R}}{R^4}+\frac{4R_0\dot{R}}{R^5}\right)\right]\frac{\partial V}{\partial t}-\frac{\dot{R}}{c}\frac{\partial K_l}{\partial t}\right)
\end{aligned} \tag{7.26}$$

We then can simplify Eq. 25 as

$$\frac{\partial}{\partial t}\left(\frac{1}{2}\frac{P^2}{\rho c^2}+\frac{1}{2}\rho v^2\right)+\nabla.(Pv)=-N\left(\pi_{Thermal}+\pi_{Liquid}+\pi_{Shell}+\pi_{Gs}+\pi_{Radiation}\right) \tag{7.27}$$

where

$$\begin{cases} \pi_{Thermal} = -P_g \dfrac{\partial V}{\partial t} \\ \\ \pi_{Liquid} = \left(\dfrac{4\mu_L \dot{R}}{R} \right) \dfrac{\partial V}{\partial t} \\ \\ \pi_{coating} = \left(12\mu_{sh} \varepsilon R_0^2 \dfrac{\dot{R}}{R^4} \right) \dfrac{\partial V}{\partial t} \\ \\ \pi_{Gs} = \left(12 G_s \varepsilon R_0^2 \left(\dfrac{1}{R^3} - \dfrac{R_0}{R^4} \right) \right) \dfrac{\partial V}{\partial t} \\ \\ \pi_{Radiation} = \left(\left[\dfrac{\dot{R}}{c} P + \dfrac{R}{c} \dot{P} - \dfrac{\rho \dot{R}^3}{c} - \dfrac{\dot{R}}{c} P_g - \dfrac{R}{c} \dot{P}_g + \dfrac{\dot{R}}{c} \dfrac{4\mu_L \dot{R}}{R} + \dfrac{R}{c} \left(\dfrac{4\mu_L \ddot{R}}{R} - \dfrac{4\mu_L \dot{R}^2}{R^2} \right) \right. \right. \\ \qquad + \dfrac{\dot{R}}{c} 12\mu_{sh} \varepsilon R_0^2 \dfrac{\dot{R}}{R^4} + \dfrac{R}{c} 12\mu_{sh} \varepsilon R_0^2 \left(\dfrac{\ddot{R}}{R^4} - \dfrac{4\dot{R}^2}{R^5} \right) \\ \left. \left. \dfrac{\dot{R}}{c} 12 G_s \varepsilon R_0^2 \left(\dfrac{1}{R^3} - \dfrac{R_0}{R^4} \right) + \dfrac{R}{c} 12 G_s \varepsilon R_0^2 \left(\dfrac{-3\dot{R}}{R^4} + \dfrac{4R_0 \dot{R}}{R^5} \right) \right] \dfrac{\partial V}{\partial t} - \dfrac{\dot{R}}{c} \dfrac{\partial K_l}{\partial t} \right) \end{cases} \tag{7.28}$$

where time dependent $\pi_{Thermal}$, π_{Liquid}, $\pi_{coating}$ and $\pi_{Radiation}$ describe damping due to thermal, liquid viscosity, coating viscosity and re-radiation. The term π_{Gs} can be referred to as the damping due to the stiffness of the coating. When averaged over all acoustic cycles this damping term always return zero.

Averaging Eq. 26 over a time period T yields:

$$\frac{1}{T} \int_0^T \frac{\partial}{\partial t} \left(\frac{1}{2} \frac{P^2}{\rho c^2} + \frac{1}{2} \rho v^2 \right) dt + \nabla . < Pv >= -N \left(Td + Ld + Cd + Gd + Rd \right) \tag{7.29}$$

Where Td,Ld,Cd,Rd and Gd are the dissipated powers due to thermal, Liquid viscosity , coating viscosity, re-radiation and stiffness of the coating.

$$\begin{cases} Td = \dfrac{-4\pi}{T}\displaystyle\int_0^T R^2\dot{R}P_g dt \\ \\ Ld = \dfrac{16\pi\mu_L}{T}\displaystyle\int_0^T R\dot{R}^2 dt \\ \\ Cd = \dfrac{48\pi\mu_{sh}\varepsilon R_0^2}{T}\displaystyle\int_0^T \frac{\dot{R}^2}{R^2} dt \\ \\ Gd = \dfrac{48\pi G_s\varepsilon R_0^2}{T}\displaystyle\int_0^T \left(\frac{\dot{R}}{R} - \frac{R_0\dot{R}}{R^2}\right) dt \\ \\ Rd = \dfrac{1}{T}\displaystyle\int_0^T \Bigg(4\pi\Bigg[\frac{R^2\dot{R}^2}{c}(P-P_g) + \frac{R^3\dot{R}}{c}\left(\dot{P}-\dot{P}_g\right) + \frac{4\mu_L R^2\dot{R}\ddot{R}}{c} \\ \quad +12\mu_{sh}\varepsilon R0^2\left(\frac{\dot{R}\ddot{R}}{cR} - \frac{3\dot{R}^3}{cR^2}\right) + 12G_s\varepsilon R0^2\left(\frac{-2\dot{R}^2}{cR} + \frac{3R_0\dot{R}^2}{cR^2}\right)\Bigg] \\ \qquad\qquad -\frac{\rho R^2\dot{R}^4}{2c} - \frac{\rho R^3\dot{R}^2\ddot{R}}{c}\Bigg) dt \end{cases} \tag{7.30}$$

In case of using the model with no thermal damping effects Td=0 and in case of incorporating the linear thermal effects $Td = \frac{16\pi\mu_{th}}{T}\int_0^T \left(R\dot{R}^2\right) dt$

7.8.2 Mechanisms of damping in uncoated and coated bubbles at different pressure amplitudes and sizes

7.8.2.1 The uncoated bubble with $R_0 = 10\mu m$

In this section we investigate the dependence of Td, Ld, and Rd on pressure, frequency, bubble size and gas core composition for 3 bubble sizes ($R_0 = 10$, 2 and $1\mu m$).

Fig. 7.7 shows Td, Rd, Ld and resonance frequency ($\frac{R_{max}}{R_0}$) of an uncoated bubble with $R_0 = 10\mu m$ as a function of frequency for different pressure amplitudes. The right column plots the data for an air bubble and the left column plots the data for the C3F8 gas core. All of the calculations are

performed using the FTM. When the gas core is air (Fig. 7.7a), Td is the major energy dissipation factor for frequencies below $2f_r$. These results are consistent with analytical predictions [50] where Td>Ld>Rd. For a C3F8 gas core (Fig. 7.7b) , Ld is the dominant damping factor at $0.5f_r < f < 1.4f_r$ below which Td becomes dominant and above which Rd becomes dominant. The width of the curve is considerably narrower due to weaker damping effects; for the bubble with $R_0 = 10\mu m$ thermal damping for the air gas core is very high and leads to widening of the curve. Due to smaller damping effects (Fig. 7.7b), the bubble is able to grow larger $\frac{R_{max}}{R_0}$ and achieve higher wall velocities, thus energy dissipation due to Ld becomes significant at resonance.

Figs. 7.7c-d show the case of P_a=40 kPa. For the air gas core bubbles (Fig. 7.7c) there is a shift of the resonance frequency to lower values as well as the generation of 2nd and 3rd SuH resonance. Td is still the major damping factor for $f < 2f_r$; however, Rd has grown faster compared to Ld at resonance and is now stronger than Ld at pressure dependent resonance (PDf_r) and higher frequencies. This may increase the scattering to damping ratio (STDR); a parameter that we would like to maximize in imaging applications. For bubble with C3F8 gas core (Fig. 7.7d), we witness the generation of sub-harmonic (SH) resonance peak at $\approx 2f_r$. The SH peak occurs at lower pressures for C3F8 due to weaker damping compared to air. Rd is the major damping factor at PDf_r and 2nd SuH resonance and Rd and Ld are comparable at $2f_r$ and 3rd SuH resonance. Due to a weaker Td (an order of magnitude smaller compared to Fig. 7.7c) in case of the C3F8 bubble (Fig. 7.7d) amplitude of the bubble oscillations are higher at the resonances. Application of C3F8 as the gas core can potentially increase STDR in bigger bubbles by suppressing the effect of Td.

For an air bubble, when P_a=80 kPa Rd dominates damping at frequencies below PDf_r (Fig. 7.7e). This shows that compared to Ld and Td, Rd grows at a faster rate with P_a. Thus contrary to predictions of the linear models, we can find a pressure and frequency region in which Rd is higher than Td and Ld and thus the STDR is optimized. For C3F8 (Fig. 7.7f) and at P_a=80 kPa Rd is the strongest contributor to the dissipated power at the frequencies studied. At this pressure we also witness the generation of $\frac{3}{2}$ and $\frac{5}{2}$ UH resonance (e.g. the peak between PDf_r and 2nd SuH) with Rd as the strongest damping factor.

For P_a=110 kPa, Fig. 7.7g shows that SH resonance peak appears at $f = \approx 2f_r$. Rd becomes the major damping factor at frequencies below f_r; however, due to the fact that $\frac{R_{max}}{R_0}$ have exceeded 2 the bubble can not sustain long lasting stable oscillations and will undergo destruction [24,59]. We

observe the same phenomenon in the C3F8 gas core bubbles (Fig. 7.7h) with Rd being the strongest damping mechanism. In case of the C3F8, Rd>Ld>Td and in case of air gas core, Rd>Td>Ld.

7.8.2.2 The uncoated bubble with $R_0 = 2\mu m$

Fig. 7.8 shows the dissipated power due to Td, Ld and Rd in the oscillations of a 2 μm bubble. The left column represents an air bubble and the right column represents the C3F8 bubble. Fig. 7.8a shows that at $P_a = 1kPa$, Td and Ld are the major mechanisms of energy dissipation in the bubble oscillations. Because the bubble is smaller than the previous case (see Fig. 7.8a where Td is an order of magnitude greater than Ld), Td and Ld have equal contributions to damping. Fig. 7.8b represents the C3F8 bubble. Due to further weakening of the thermal effects, Ld is an order of magnitude higher than Td.

Increasing P_a to 40 kPa leads to the generation of 2nd and 3rd SuH resonance frequencies and the decrease in the fundamental resonance (PDf_r) (Fig 7.8c-d). Due to a weaker Td in the case of the C3F8 bubble (Fig. 7.8d), the amplitude of the bubble oscillations are higher at the resonances. For the air bubble Td and Ld are the major dissipation mechanisms for $f < 2f_r$. For C3F8 $Ld > Rd > Td$ for frequencies of and above the $2ndSuH$; this suggests that the STDR can be higher for the C3F8 bubble.

For P_a=100 kPa and for an air bubble (Fig. 7.8e) Td becomes less significant at f=PDf_r; with $Ld > Rd > Td$. This implies a higher STDR at this frequency and pressure. For f=2nd SuH and f=3rd SuH we witness a fast growth of Rd however still $Ld > Td > Rd$. These results indicate that as pressure increases Rd grows faster than Ld and Td. In case of C3F8 (Fig. 7.8f) bubble we see the generation of SH resonance at $f \approx 2f_r$ and $Ld > Sd \gg Td$. Because of a higher Rd, when the gas core is C3F8, a higher STDR may be expected. Further increasing the pressure to 150 kPa leads to the generation of SH resonance peak at $f \approx 2f_r$ (Fig. 7.8g) for the air bubble. The later appearance of the SH peak is due to the higher Td in the air bubble. For an air bubble at P_a=100 kPa, $Rd > Ld > Td$ at PDf_r , $2ndSuH$ and $3rdSuH$ and $\frac{3}{2}UH$ resonances. However, for frequencies above f_r, Td and Ld are the major damping factors. Results of Figs. 7.7 and 7.8 suggest a relationship between $\frac{R_{max}}{R_0}$ and the order of damping factors for the air bubble. With an increase in the incident pressure, Rd grows faster than other damping factors; at $\frac{R_{max}}{R_0} \approx 2$, Rd becomes stronger than the other damping factors. These results suggest that in the case of air bubbles, in

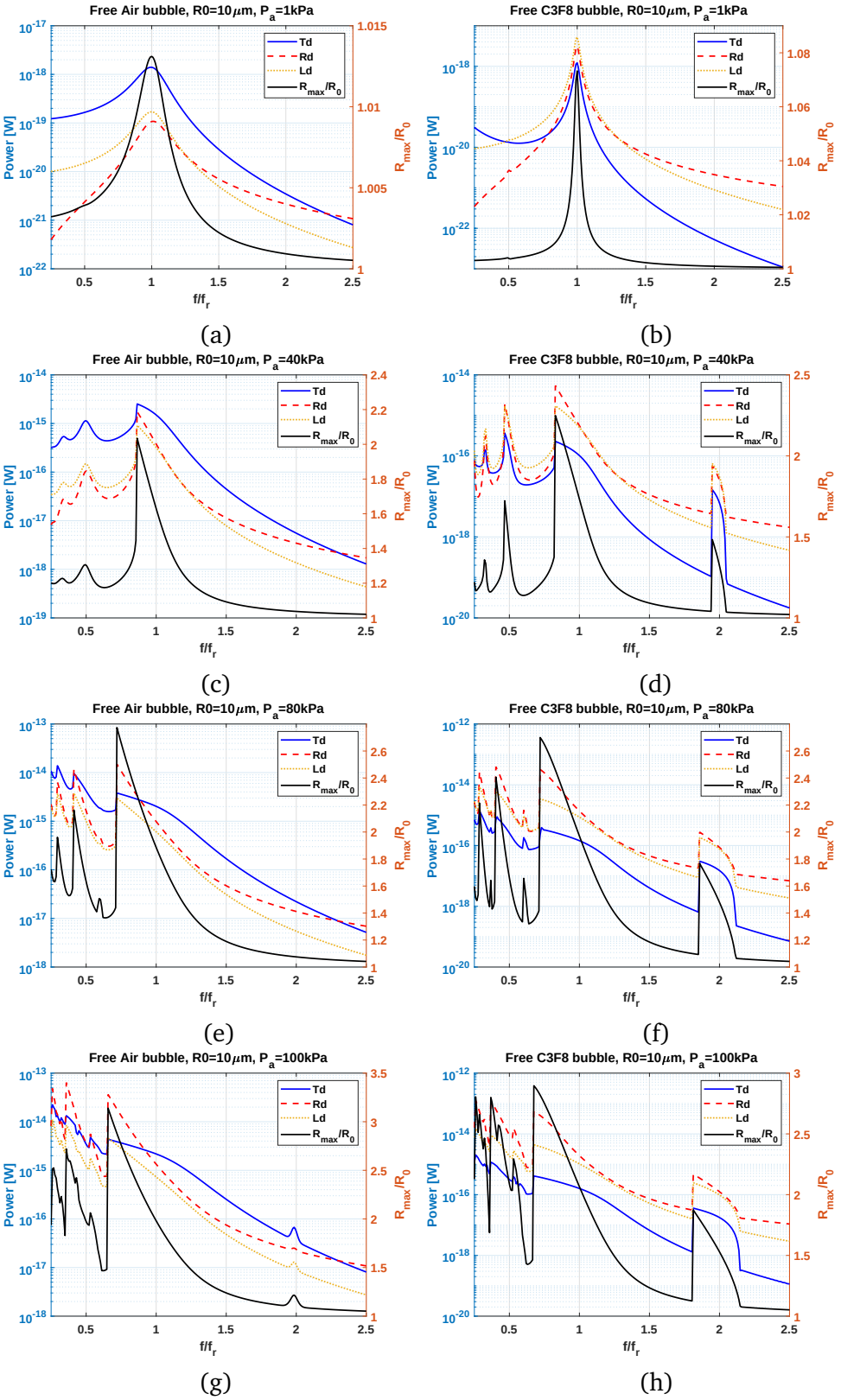

Figure 7.6: Dissipated power due to Cd, Td, Ld and Rd as predicted by the full thermal model as a function of frequency for an uncoated bubble with $R_0 = 10\ \mu m$ at various pressures (left column is for an air gas core and right column is for a C3F8 core).

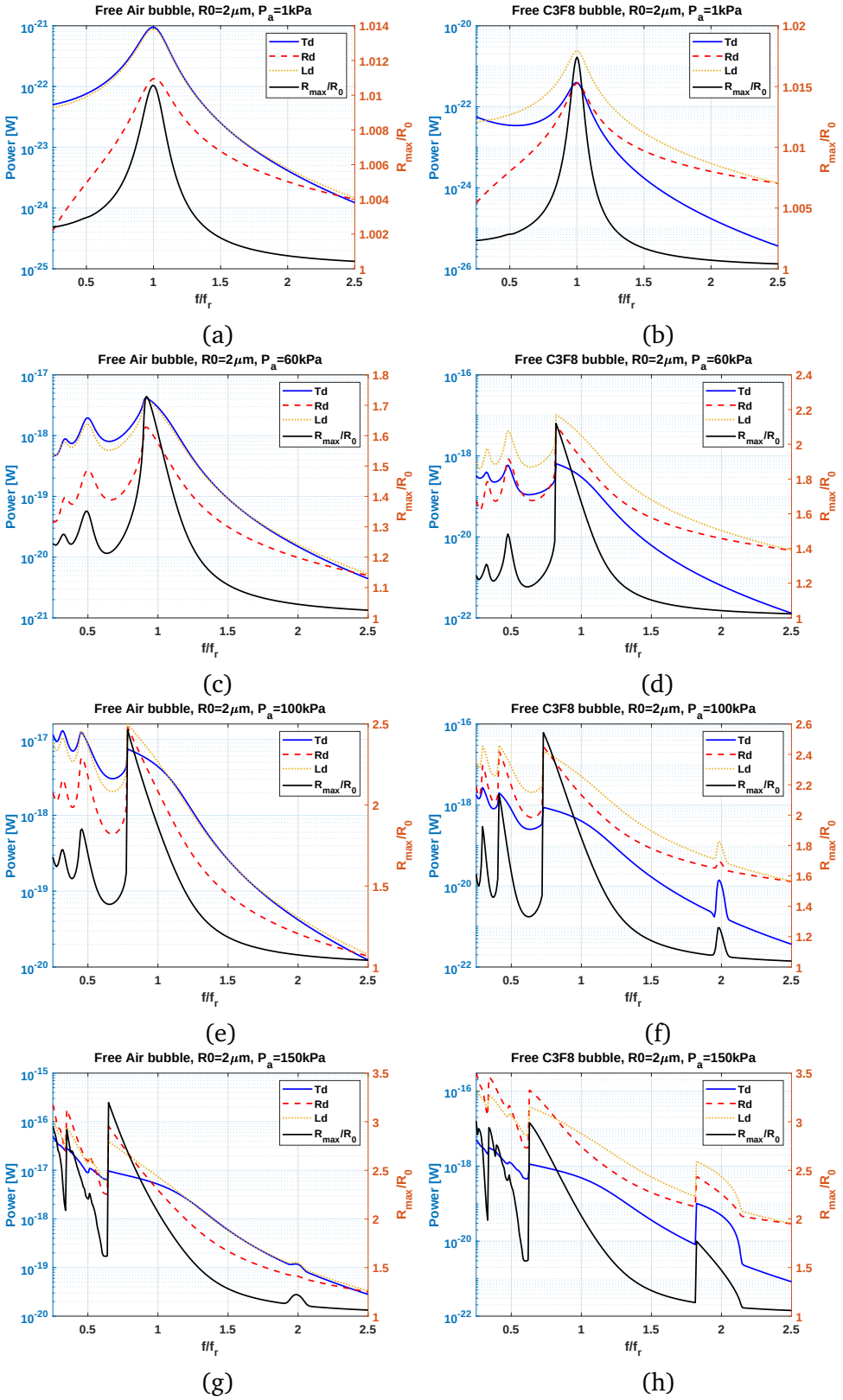

Figure 7.7: Dissipated power due to Td, Ld and Rd as predicted by the full thermal model as a function of frequency for an uncoated bubble with $R_0 = 2\ \mu$ m at various pressures (left column is for an air gas core and right column is for a C3F8 gas core).

order to increase the STDR one needs to sufficiently increase the pressure; however we should also consider the lower threshold of bubble destruction which is $\frac{R_{max}}{R_0} > 2$. At P_a=100 kPa and in case of C3F8 bubble (Fig. 7.8h), $Rd > Ld > Td$ for the studied frequency range. Also we see a stronger SH oscillations compared to the air bubble.

7.8.2.3 The coated (encapsulated) bubble with $R_0 = 1\mu m$

Fig. 7.9 shows the power dissipated due to Cd, Ld, Rd and Td for a coated bubble with $R_0 = 1\mu m$, G_s=45 MPa, θ=4 nm and $\mu_{sh} = \frac{1.49(R_0(\mu m)-0.86)}{\theta(nm)}$. The right column represents the air gas core bubble and the left column represents the C3F8 gas core bubble. Compared to Fig. 7.9, Td is further suppressed as the smaller bubble has smaller surface area for temperature exchange. At $P_a = 1kPa$ (Fig. 7.9a-b), we see a similar behavior for the air and C3F8 gas core. $\frac{R_{max}}{R_0}$, Cd, Ld and Rd are similar for both cases;this is because the bubble with $R_0 = 1\mu m$ Td is negligible and change of gas doesn't make a big difference in the oscillation amplitudes or the dissipated powers. $Cd > Ld > Rd > Td$ with Cd $\approx$ 20 and 62 times larger than Td for the air and C3F8 bubble respectively.

Increasing the pressure to 100 kPa (Fig. 7.9c-d) results in the generation of 2nd SuH frequency with $Cd > Ld > Rd > Td$ for $0.2f_r < f < 1.5f_r$. At higher frequencies ($f > 2f_r$) Rd becomes the strongest damping factor.

When P_a=200 kPa a shift in the fundamental frequency occurs (f=f_r at 1kPa) to PDf_r (0.756f_r and 0.76f_r for air (Fig. 7.9e) and C3F8 (Fig. 7.9f) bubbles, respectively). Furthermore, a 3rd SuH resonance also appears below the 2nd SuH resonance frequency. For $f < 1.5f_r$ $Cd > Ld > Rd > Td$ with Rd becoming the major damping factor at $f > 2f_r$. At this pressure Cd is 22.5 and 100 times larger than Td for air and C3F8 respectively.

Increasing the pressure to 300 kP_a (Figs 7.9g-h) leads to a higher $\frac{R_{max}}{R_0}$ at 3rd SuH, 2nd SuH and PDf_r and a decrease in the value of the resonances of the system. For example at 300 kPa PDf_r is $\approx 0.65f_r$ and $0.66f_r$ respectively for air and C3F8. For $f < 1.5f_r$, Cd is the major damping factor with $Cd > Ld > Rd > Td$. As the pressure increases, Rd grows faster and approaches Ld and will eventually have a greater contribution to the total damping compared to Ld. Td on the other hand has the slowest growth with P_a increase at the main resonance. At P_a =300 kPa unlike at the lower

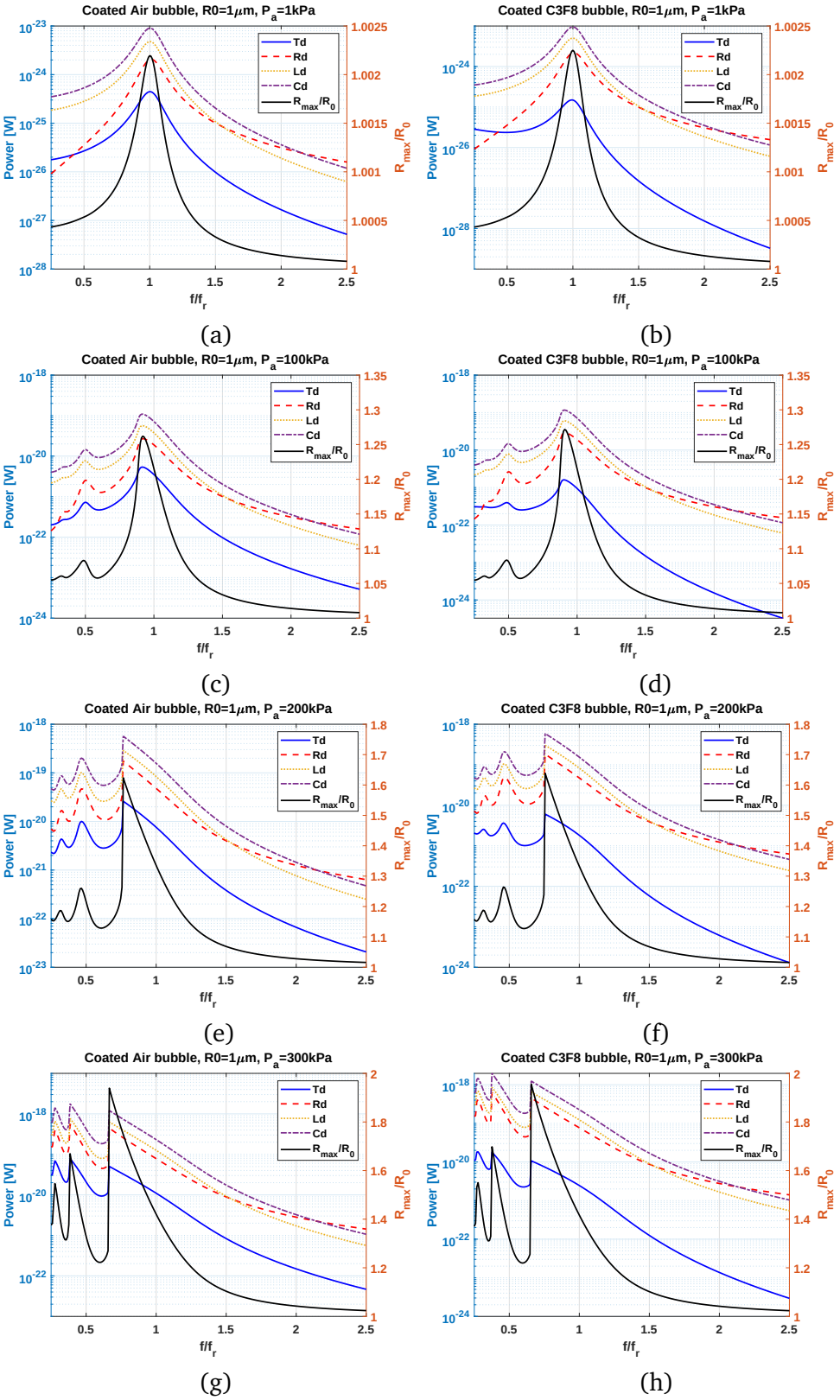

Figure 7.8: Dissipated power due to Cd, Td, Ld and Rd as predicted by the full thermal model as a function of frequency for a coated bubble with $R_0 = 1$ μ m at various pressures (left column is for an air gas core and right column is for a C3F8 gas core).

pressures, the highest dissipation occurs at 2nd SuH resonance and not at the main resonance.

Bibliography

[1] Lauterborn, W., & Kurz, T. (2010). Physics of bubble oscillations. Reports on progress in physics, 73(10), 106501.

[2] Yang, X., & Church, C. C. (2005). A model for the dynamics of gas bubbles in soft tissue. The Journal of the Acoustical Society of America, 118(6), 3595-3606.

[3] Xu, Zhen, Timothy L. Hall, J. Brian Fowlkes, and Charles A. Cain. "Effects of acoustic parameters on bubble cloud dynamics in ultrasound tissue erosion (histotripsy)." The Journal of the Acoustical Society of America 122, no. 1 (2007): 229-236.

[4] Dogan, H., & Popov, V. Numerical simulation of the nonlinear ultrasonic pressure wave propagation in a cavitating bubbly liquid inside a sonochemical reactor. *Ultrasonics sonochemistry* 30 (2016): 87-97.

[5] Mantouka, Agni, Hakan Dogan, P. R. White, and T. G. Leighton. "Modelling acoustic scattering, sound speed, and attenuation in gassy soft marine sediments." The journal of the acoustical society of America 140, no. 1 (2016): 274-282.

[6] Collings, Anthony F., Anthony D. Farmer, Paul B. Gwan, AP Sosa Pintos, and Chin Jian Leo. "Processing contaminated soils and sediments by high power ultrasound." Minerals Engineering 19, no. 5 (2006): 450-453.

[7] Bigelow, Timothy A., Trevor Northagen, Thomas M. Hill, and Frances C. Sailer. "The destruction of Escherichia coli biofilms using high-intensity focused ultrasound." Ultrasound in medicine & biology 35, no. 6 (2009): 1026-1031.

[8] Suslick, Kenneth S. "Sonochemistry." science 247, no. 4949 (1990): 1439-1445.

[9] Storey, Brian D., and Andrew J. Szeri. "Water vapour, sonoluminescence and sonochemistry." Proceedings of the Royal Society of London. Series A: Mathematical, Physical and Engineering Sciences 456, no. 1999 (2000): 1685-1709.

[10] Crum, Lawrence A., Timothy J. Mason, Jacques L. Reisse, and Kenneth S. Suslick, eds. Sonochemistry and sonoluminescence. Vol. 524. Springer Science & Business Media, 2013.

[11] Roovers, Silke, Tim Segers, Guillaume Lajoinie, Joke Deprez, Michel Versluis, Stefaan C. De Smedt, and Ine Lentacker. "The role of ultrasound-driven microbubble dynamics in drug delivery: from microbubble fundamentals to clinical translation." Langmuir (2019).

[12] Qin, Shengping, Charles F. Caskey, and Katherine W. Ferrara. "Ultrasound contrast microbubbles in imaging and therapy: physical principles and engineering." Physics in medicine & biology 54, no. 6 (2009): R27.

[13] Coussios, Constantin C., and Ronald A. Roy. "Applications of acoustics and cavitation to noninvasive therapy and drug delivery." Annu. Rev. Fluid Mech. 40 (2008): 395-420.

[14] Brenner, Michael P., Sascha Hilgenfeldt, and Detlef Lohse. "Single-bubble sonoluminescence." Reviews of modern physics 74, no. 2 (2002): 425.

[15] Esche R 1952 Untersuchung der Schwingungskavitation in Flussigkeiten (Investigation of acoustic cavitation in liquids) Acustica 2 AB208–18

[16] Holt, R. Glynn, and D. Felipe Gaitan. "Observation of stability boundaries in the parameter space of single bubble sonoluminescence." Physical review letters 77, no. 18 (1996): 3791.

[17] Holt, R. Glynn, D. Felipe Gaitan, Anthony A. Atchley, and Joachim Holzfuss. "Chaotic sonoluminescence." Physical review letters 72, no. 9 (1994): 1376.

[18] Lauterborn, Werner, and Claus-Dieter Ohl. "Cavitation bubble dynamics." Ultrasonics sonochemistry 4, no. 2 (1997): 65-75.

[19] R. Lauterborn, Werner, and Andreas Koch. "Holographic observation of period-doubled and chaotic bubble oscillations in acoustic cavitation." Physical Review A 35, no. 4 (1987): 1974.

[20] Lauterborn, Werner, and Eckehart Cramer. "Subharmonic route to chaos observed in acoustics." Physical Review Letters 47, no. 20 (1981): 1445.

[21] Parlitz, U., V. Englisch, C. Scheffczyk, and W. Lauterborn. "Bifurcation structure of bubble oscillators." The Journal of the Acoustical Society of America 88, no. 2 (1990): 1061-1077.

[22] Haghi, H., Sojahrood, A.J. and Kolios, M.C., 2019. Collective nonlinear behavior of interacting polydisperse microbubble clusters. Ultrasonics sonochemistry, 58, p.104708.

[23] Sojahrood, A.J., Wegierak, D., Haghi, H., Karshfian, R., & Kolios, M. C. A simple method to analyze the super-harmonic and ultra-harmonic behavior of the acoustically excited bubble oscillator. *Ultrasonics sonochemistry* 54 (2019):99-109

[24] A.J. Sojahrood et al., Influence of the pressure-dependent resonance frequency on the bifurcation structure and backscattered pressure of ultrasound contrast agents: a numerical investigation, *Nonlinear Dynamics* 80 (2015): 889-904.

[25] F. Hegedűs, Topological analysis of the periodic structures in a harmonically driven bubble oscillator near Blake's critical threshold: Infinite sequence of two-sided Farey ordering trees, *Physics Letters A* 380-10 (2016): 1012-1022.

[26] F. Hegedűs and K. Klapcsik, The effect of high viscosity on the collapse-like chaotic and regular periodic oscillations of a harmonically excited gas bubble. *Ultrasonics sonochemistry* 27, (2015): 153-164

[27] S.A. Suslov, A.Ooi, and R. Manasseh, Nonlinear dynamic behavior of microscopic bubbles near a rigid wall, *Physical Review E* 85 (2012): 066309.

[28] Zhang, Yuning. "Chaotic oscillations of gas bubbles under dual-frequency acoustic excitation." Ultrasonics sonochemistry 40 (2018): 151-157.

[29] Zhang, Yuning, and Shengcai Li. "Combination and simultaneous resonances of gas bubbles oscillating in liquids under dual-frequency acoustic excitation." Ultrasonics sonochemistry 35 (2017): 431-439.

[30] Klapcsik, Kálmán, and Ferenc Hegedűs. "Study of non-spherical bubble oscillations under acoustic irradiation in viscous liquid." Ultrasonics sonochemistry 54 (2019): 256-273.

[31] Caflish, R.E., Miksis, M.J., Papanicolaou, G.C., Ting L., Effective equations for wave propagation in bubbly liquids, *J. Fluid Mech.* 153 (1985): 259–273.

[32] Wijngaarden, L.V., On the equation of motion for mixtures of liquid and gas bubbles, *J. Fluid Mech.*33 132(1) (1968): 465–474.

[33] Commander, Kerry W., and Andrea Prosperetti. ”Linear pressure waves in bubbly liquids: Comparison between theory and experiments.” The Journal of the Acoustical Society of America 85, no. 2 (1989): 732-746.

[34] Louisnard, Olivier. ”A simple model of ultrasound propagation in a cavitating liquid. Part I: Theory, nonlinear attenuation and traveling wave generation.” Ultrasonics sonochemistry 19, no. 1 (2012): 56-65..

[35] Jamshidi, Rashid, and Gunther Brenner. ”Dissipation of ultrasonic wave propagation in bubbly liquids considering the effect of compressibility to the first order of acoustical Mach number.” Ultrasonics 53, no. 4 (2013): 842-848.

[36] AJ. Sojahrood, H. Haghi, R. Karshafian and M.C. Kolios Critical corrections to formulations of nonlinear energy dissipation of ultrasonically excited bubbles and a unifying parameter to asses and enhance bubble activity in applications, (2019) arXiv:1909.04864.

[37] Dogan, Hakan, and Viktor Popov. ”Numerical simulation of the nonlinear ultrasonic pressure wave propagation in a cavitating bubbly liquid inside a sonochemical reactor.” Ultrasonics sonochemistry 30 (2016): 87-97.

[38] Hoff, L., Sontum, P. C., & Hovem, J. M. Oscillations of polymeric microbubbles: Effect of the encapsulating shell. *The Journal of the Acoustical Society of America* 107(4) (2000): 2272-2280.

[39] Segers, T., de Jong, N., & Versluis, M. Uniform scattering and attenuation of acoustically sorted ultrasound contrast agents: Modeling and experiments. *The Journal of the Acoustical Society of America* 140(4) (2016): 2506-2517.

[40] Goertz, David E., Nico de Jong, and Antonius FW van der Steen. ”Attenuation and size distribution measurements of Definity™ and manipulated Definity™ populations.” Ultrasound in medicine & biology 33, no. 9 (2007): 1376-1388.

[41] Shekhar, Himanshu, Nathaniel J. Smith, Jason L. Raymond, and Christy K. Holland. ”Effect of temperature on the size distribution, shell properties, and stability of Definity®.” Ultrasound in medicine & biology 44, no. 2 (2018): 434-446.

[42] Raymond, Jason L., Kevin J. Haworth, Kenneth B. Bader, Kirthi Radhakrishnan, Joseph K. Griffin, Shao-Ling Huang, David D. McPherson, and Christy K. Holland. ”Broadband attenuation measurements of phospholipid-shelled ultrasound contrast agents.” Ultrasound in medicine & biology 40, no. 2 (2014): 410-421.

[43] Sojahrood, A. J., Q. Li, H. Haghi, R. Karshafian, T. M. Porter, and M. C. Kolios. ”Pressure dependence of the ultrasound attenuation and speed in bubbly media: Theory and experiment.” arXiv preprint arXiv:1811.07788 (2018).

[44] Holt, R. Glynn, and Ronald A. Roy. ”Measurements of bubble-enhanced heating from focused, MHz-frequency ultrasound in a tissue-mimicking material.” Ultrasound in medicine & biology 27, no. 10 (2001): 1399-1412.

[45] Segers, Tim, Pieter Kruizinga, Maarten P. Kok, Guillaume Lajoinie, Nico De Jong, and Michel Versluis. ”Monodisperse versus polydisperse ultrasound contrast agents: Non-linear response, sensitivity, and deep tissue imaging potential.” Ultrasound in medicine & biology 44, no. 7 (2018): 1482-1492.

[46] Plesset, M.S. The dynamics of cavitation bubbles. *ASME J. Appl. Mech.* 16 (1949): 228–231.

[47] Keller, J.B. & Miksis M., Bubble oscillations of large amplitude, *J. Acoust. Soc. Am.* 68 (1980) 628–633.

[48] Marmottant, Philippe, Sander Van Der Meer, Marcia Emmer, Michel Versluis, Nico De Jong, Sascha Hilgenfeldt, and Detlef Lohse. ”A model for large amplitude oscillations of coated bubbles accounting for buckling and rupture.” The Journal of the Acoustical Society of America 118, no. 6 (2005): 3499-3505.

[49] Toegel, Ruediger, Bruno Gompf, Rainer Pecha, and Detlef Lohse. ”Does water vapor prevent upscaling sonoluminescence?.” Physical review letters 85, no. 15 (2000): 3165.

[50] Prosperetti, Andrea, Lawrence A. Crum, and Kerry W. Commander. ”Nonlinear bubble dynamics.” The Journal of the Acoustical Society of America 83, no. 2 (1988): 502-514.

[51] Stricker, Laura, Andrea Prosperetti, and Detlef Lohse. ”Validation of an approximate model for the thermal behavior in acoustically driven bubbles.” The Journal of the Acoustical Society of America 130, no. 5 (2011): 3243-3251.

[52] B.D. Storey, A.J. Szeri, A reduced model of cavitation physics for use in sonochemistry, Proc. Roy. Soc. Lond. A 457 (2001) 1685–1700.

[53] T.J. Matula, P.R. Hilmo, B.D. Storey, A.J. Szeri, Radial response of individua bubbles subjected to shock wave lithotripsy pulses in vitro, Phys. Fluids 14 (2002) 913–921.

[54] Morgan, Karen E., John S. Allen, Paul A. Dayton, James E. Chomas, A. L. Klibaov, and Katherine W. Ferrara. "Experimental and theoretical evaluation of microbubble behavior: Effect of transmitted phase and bubble size." IEEE transactions on ultrasonics, ferroelectrics, and frequency control 47, no. 6 (2000): 1494-1509.

[55] Lide, D.R., and Kehiaian, H. V., CRC Handbook of Thermophysical and Thermochemical Data, *CRC Press, Boca Raton, FL,* (1994)

[56] http://detector-cooling.web.cern.ch/Detector-Cooling/data/C3F8_Properties.pdf

[57] Vokurka, K. On Rayleigh's model of a freely oscillating bubble. I. Basic relations. Czechoslovak Journal of Physics B, 35(1), (1985): 28-40.

[58] Hilgenfeldt, S., Lohse, D., & Zomack, M. Response of bubbles to diagnostic ultrasound: a unifying theoretical approach. The European Physical Journal B-Condensed Matter and Complex Systems, 4(2), (1998):247-255.

[59] Flynn, H.G., Church, C.C.: Transient pulsations of small gas bubbles in water. J. Acoust. Soc. Am. 84, 985–998 (1988)

[60] Sojahrood, A.J., Earl, R.E., Kolios, M.C. and Karshafian, R., 2019. Notes on the two main routes of period doubling and 1/2 order subharmonic oscillations in a bubble oscillator. arXiv preprint arXiv:1909.02694.

[61] Sojahrood, A.J., Earl, R., Li, Q., Porter, T.M., Kolios, M.C. and Karshafian, R., 2019. Nonlinear dynamics of acoustic bubbles excited by their pressure dependent subharmonic resonance frequency: oversaturation and enhancement of the subharmonic signal. arXiv preprint arXiv:1909.05071.

[62] Sojahrood, Amin Jafari, and Michael C. Kolios. ”Classification of the nonlinear dynamics and bifurcation structure of ultrasound contrast agents excited at higher multiples of their resonance frequency.” Physics Letters A 376, no. 33 (2012): 2222-2229.

[63] Hegedűs, F., Cs Hős, and L. Kullmann. ”Stable period 1, 2 and 3 structures of the harmonically excited Rayleigh–Plesset equation applying low ambient pressure.” The IMA Journal of Applied Mathematics 78, no. 6 (2012): 1179-1195.

[64] Alexander A., and Ayache Bouakaz. ”Theoretical investigation of shear stress generated by a contrast microbubble on the cell membrane as a mechanism for sonoporation.” The Journal of the Acoustical Society of America 128, no. 1 (2010): 11-19.

[65] Bouakaz, Ayache, Nico De Jong, and Christian Cachard. ”Standard properties of ultrasound contrast agents.” Ultrasound in medicine & biology 24, no. 3 (1998): 469-472.

[66] Tang, M-X., H. Mulvana, T. Gauthier, A. K. P. Lim, D. O. Cosgrove, R. J. Eckersley, and E. Stride. ”Quantitative contrast-enhanced ultrasound imaging: a review of sources of variability.” Interface focus 1, no. 4 (2011): 520-539.

[67] van der Meer, Sander M., Benjamin Dollet, Marco M. Voormolen, Chien T. Chin, Ayache Bouakaz, Nico de Jong, Michel Versluis, and Detlef Lohse. ”Microbubble spectroscopy of ultrasound contrast agents.” The Journal of the Acoustical Society of America 121, no. 1 (2007): 648-656.

[68] Li, Qian, Thomas J. Matula, Juan Tu, Xiasheng Guo, and Dong Zhang. ”Modeling complicated rheological behaviors in encapsulating shells of lipid-coated microbubbles accounting for nonlinear changes of both shell viscosity and elasticity.” Physics in Medicine & Biology 58, no. 4 (2013): 985.

[69] O’Reilly, M.A. and Hynynen, K., 2018. Ultrasound and microbubble-mediated blood-brain barrier disruption for targeted delivery of therapeutics to the brain. In Targeted Drug Delivery (pp. 111-119). Humana Press, New York, NY.

[70] O’Reilly, M.A. and Hynynen, K., 2012. Blood-brain barrier: Real-time feedback-controlled focused ultrasound disruption by using an acoustic emissions–based controller. Radiology, 263(1), pp.96-106.

[71] Sojahrood, Amin Jafari, Raffi Karshafian, and Michael C. Kolios. ”Numerical and experimental classification of the oscillations of single isolated microbubbles: Occurrence of higher order subharmonics.” In 2012 IEEE International Ultrasonics Symposium, pp. 402-405. IEEE, 2012.

[72] Sojahrood, Amin Jafari, Raffi Karshafian, and Michael C. Kolios. ”Detection and characterization of higher order nonlinearities in the oscillations of Definity at higher frequencies and very low acoustic pressures.” In 2012 IEEE International Ultrasonics Symposium, pp. 1193-1196. IEEE, 2012.

[73] Jafari Sojahrood, Amin, Raffi Karshafian, and Michael C. Kolios. ”Bifurcation structure of the ultrasonically excited microbubbles undergoing buckling and rupture.” In Proceedings of Meetings on Acoustics ICA2013, vol. 19, no. 1, p. 075097. ASA, 2013.

Chapter 8

Classification of the mechanisms of ultrasound energy dissipation from the nonlinear oscillations of coated and uncoated bubbles

8.1 Abstract

Acoustic waves are dissipated when they pass through bubbly media. Dissipation by bubbles takes place through thermal damping (Td), radiation damping (Rd) and damping due to the friction of the liquid (Ld) and friction of the coating (Cd). Knowledge of the contributions of the Td, Rd, Ld and Cd during nonlinear bubble oscillations will help in optimizing the bubble and ultrasound exposure parameters for relevant applications by maximizing a desirable parameter. In this work we investigate the mechanisms of dissipation in bubble oscillations and their contributions to the total damping (W_{total}) in various nonlinear regimes. By using bifurcation analysis, we have classified nonlinear dynamics of bubbles that are sonicated with their 3rd superharmonic (SuH) and 2nd SuH resonance frequency (f_r), pressure dependent resonance frequency (PDf_r), f_r, subharmonic (SH) resonance ($f_{sh} = 2f_r$), pressure dependent SH resonance (PDf_{sh}) and $\frac{1}{3}$ order SH resonance. The corresponding Td, Rd, Ld, Cd, W_{total}, scattering to dissipation ratio (STDR), maximum wall velocity and maximum back-scattered pressure from non-destructive oscillations of bubbles were calculated and analyzed using bifurcation diagrams. We classified different regimes of dissipation and provided parameter regions in which a particular parameter of interest (e.g. Rd) can be enhanced. Afterwards enhanced bubble activity is linked to some relevant applications in ultrasound. This paper represents the first comprehensive analysis of the nonlinear bubble

oscillations regimes and the mechanisms of dissipations in bubble oscillations.[1].

8.2 Introduction

An ultrasonically excited bubble is a highly nonlinear oscillator in which deterministic chaos manifests itself [1, 2, 3]. When a high pressure acoustic field is generated in an aqueous medium, the rare faction cycle may exceed the attractive forces among liquid molecules generating cavitation bubbles. Bubbles begin oscillating and emit sound [4, 5, 6]. The spectral components of the emitted sound consist of harmonics and subharmonics of the incident sound wave center frequency and broadband noise (Lauterborn & Holzfuss 1991 [3]). The nonlinear frequency content of the emitted sound by bubbles has found its applications in contrast enhanced diagnostic ultrasound to visualize the vascular structure [7,8,9] with superior contrast. Bubbles signatures are also used for monitoring treatments in therapeutic ultrasound [10,11,12].

The pressure emitted by collapsing bubbles may form a shock wave (Radek 1972; Vogel et al. 1986) [5,13], that can mechanically damage nearby nearby structures. Bubble oscillations generate micro-streaming in the liquid which results in shear stresses on the objects in its vicinity and micro-mixing in the liquid [14, 15]. The induced shear stresses and the emitted shock-waves has found their applications in industry (cleaning the micro-structures [14,15,16]) and medicine (e.g. enhanced drug and gene delivery [17,18,19], blood brain barrier opening [20,21] and shock wave lithotripsy and histotripsy [22, 23]).

Ultrasonically excited bubbles can focus and concentrate the acoustic energy from the macro-scale (acoustic wave) to the micro-scale and nano-scale [19,24] generating extremely high temperatures and pressures as the bubbles collapse. This leads to molecular disassociation which triggers the production of highly reactive free radicals [24, 25, 26] which then interact with other substances in the solution. This phenomenon has been shown useful in numerous industrial processing applications ranging from sonochemistry [24, 25, 26] (chemical reaction rate enhancement and treatment of organic compounds) to the food industry [27] and medicine (sonodynamic therapy [28]). Bubbles can focus and amplify the energy of the sound field by more than 11 orders of magnitude, which is sufficient not only to break chemical bonds but also to induce luminescence

[1]To be submitted as: A.J. Sojahrood, H. Haghi, R. Karshafian and M.C. Kolios, Classification of the mechanisms of ultrasound energy dissipation from the nonlinear oscillations of coated and uncoated bubbles.

[29]. Local sound amplification and enhanced dissipation of acoustic energy by bubbles been used to enhance the heating generated by ultrasound during ultrasound thermal therapies and high intensity focused ultrasound (HIFU) tumor ablation [30].

Understanding and enhancing a specific type of bubble oscillatory pattern can help in enhancing the outcome of the relevant application. For example, in contrast enhanced ultrasound the goal is maximizing the radiated pressure by the bubbles while keeping the dissipation of energy due to bubble attenuation minimum [31, 32, 33]. This will lead to enhanced contrast and better visualization of the target and eliminating the shadowing in ultrasonic images [31, 32, 33]. Shadowing [34, 35] is caused by the dissipation of the ultrasonic energy by bubbles which leads to a weaker signal intensity from underlying tissue. In HIFU the goal is to increase the dissipation at the focus while reducing pre-focal shielding and energy dissipation by bubble oscillations. Here, knowledge of the pressure dependent dissipation effects and the advantage of the sharp pressure gradients of HIFU transducers facilitate the desired effect [32, 33, 36].

Bubbles dissipate the acoustic energy through radiation damping (Rd), thermal damping (Td), damping due to the viscosity of the liquid (Ld) and damping due to the friction of the coating (Cd) [37, 38, 39, 40, 41]. Despite the importance of detailed knowledge of the energy dissipation mechanisms in bubble oscillations, the majority of previous studies have been limited by linear approximations [37, 42, 43, 44, 45]. Linear studies simplify the bubble oscillations to very small amplitudes at low excitation pressures (e.g. 1 kPa) [37, 42]. However, bubble oscillations are nonlinear and energy dissipation depends highly on the excitation pressure [39, 40, 41, 46]. Moreover, the majority of the applications are based on sending ultrasound pulses of high pressure amplitude; thus, linear approximations are inappropriate to model bubble oscillations.

Despite the importance of the knowledge on nonlinear energy dissipation by bubbles; however, there are only few recent studies that explored the pressure dependent effects on energy dissipation [38, 39, 40, 41, 46, 47]. Louisnard [38] derived the pressure dependent energy equations by considering the conservation of mass and momentum in a bubbly media and used the Rayleigh-Plesset equation for bubble oscillations [48]. He derived the dissipation equations for Ld and Td. His analysis showed that energy dissipation is pressure dependent and predictions of the linear model can be orders of magnitude smaller than the pressure dependent model. Jamshidi & Brenner used Louisnard's approach and Keller-Miksis equation [49] to incorporate the compressibility effects

up to the first order of Mach number. They were able to derive Ld, Td and Rd. Their analysis showed that Rd has an important role in energy dissipation and as is typically done cannot be neglected [39]. In our recent work, we showed that equations derived by Jamshidi & Brenner need to be corrected as their model predicts non-physical values for Rd near resonance and predictions of Rd are not consistent with the predictions of the scattered pressured energy (Sd) by bubbles [40]. We presented the corrected forms of Ld, Rd and Td. We showed that dissipation terms are highly pressure dependent and as pressure increases Rd may grow faster than Td and Ld; thus, there exist optimum pressure and frequency ranges where the scattering to dissipation ratio (STDR) can be maximized [40, 41]. Moreover, we showed that the STDR which can be used as standardization parameter to assess the efficacy of bubble oscillations [40] in applications is pressure dependent. STDR should be used in conjunction with Rd and the maximum scattered (re-radiated) pressure by bubbles for a more complete assessment of a given control parameter for bubble oscillation optimization [40].

Using the same approach as in [40], we derived the nonlinear energy dissipation equations for a coated bubble [41]. We analyzed the resonance power curves for free and encapsulated bubbles and showed that Td can be neglected for coated bubbles that have C3F8-like gas cores. We also showed that although Td is the dominant dissipation mechanism for large uncoated bubbles; at higher pressures Rd can supersede Td. Moreover, Cd is the strongest dissipation mechanism in the oscillations of the coated bubbles; pressure increase however, there are instances in which Rd is stronger than Ld and Td.

In this paper we provide a detailed analysis of the pressure dependent dissipation mechanisms by bubble oscillations and role of each of the dissipation components (Td, Ld,Rd and Cd) at various nonlinear regimes. Knowledge of the pressure dependent dissipation effects and the examination of each contributing component will help us better understand bubble related phenomena and enhance a desirable effect in bubble oscillations.

In this paper we have classified major nonlinear regimes of the oscillations for free and coated bubbles. In this regard, our recent comprehensive approach is used to analyze the bubble oscillations [50] as a function of pressure. The major nonlinear regimes that are considered here are 2nd and 3rd SuH resonant oscillations, $\frac{3}{2}$, $\frac{5}{2}$ and $\frac{7}{2}$ UH regimes, pressure dependent resonance effects, excitation with linear resonance (f_r), pressure dependent resonance(PDf_r), $\frac{1}{2}$, $\frac{1}{3}$ and higher order

SH resonance. Afterwards, the pressure dependent dissipation mechanism and the role of each contributing factor to the total dissipation is analyzed in detail for each category of oscillations. STDR, maximum bubble wall velocity and maximum re-radiated pressure amplitude are analyzed for each regime. We show that depending on the specific oscillation regime, there is a exposure condition in which a particular parameter (e.g. maximum wall velocity, the maximum re-radiated pressure amplitude, Rd, W_{total}) can be maximized or minimized. These findings are then related to some of the current applications of bubbles.

8.3 Methods

8.3.1 Coated bubble model

The dynamics of a coated bubble oscillator including compressibility effects to the first order of Mach-number can be modeled using the Keller-Miksis-Church-Hoff (KMCH) model [41, 42, 49]:

$$\rho\left[\left(1-\frac{\dot{R}}{c}\right)R\ddot{R}+\frac{3}{2}\dot{R}^2\left(1-\frac{\dot{R}}{3c}\right)\right]= \\ \left(1+\frac{\dot{R}}{c}+\frac{R}{c}\frac{d}{dt}\right)\left(P_g-\frac{4\mu_L\dot{R}}{R}-\frac{12\mu_{sh}\epsilon R_0^2\dot{R}}{R^4}-12G_s\epsilon R_0^2\left(\frac{1}{R^3}-\frac{R_0}{R^4}\right)-P_0-P\right) \tag{8.1}$$

Where ρ and c are respectively the density and sound speed of the medium, R is the radius at time t, $\dot{R}$ is the bubble wall velocity, $\ddot{R}$ is the bubble wall acceleration, R_0 is the initial radius of the bubble, μ and μ_{sh} are the viscosity of the liquid and shell (coating) respectively, ϵ is the thickness of the coating, G_s is the shell shear modulus, P_g is the gas pressure inside the bubble, P_0 is the atmospheric pressure (101.325 kPa) and P is the acoustic pressure given by $P = P_a sin(2\pi ft)$ with P_a and f are respectively the excitation pressure and frequency. In this paper for all of the simulations of the coated bubbles G_s=50 MPa and $\mu_{sh} = \frac{1.49(R_0(\mu m)-0.86)}{\theta(nm)}$ [51] with $\theta = 4nm$. The gas inside the bubble was chosen to be C3F8 and the surrounding medium water.

Thermal parameters of the gases at 1 atm				
Gas type	L($\frac{W}{mK}$)	$c_p(\frac{kJ}{kgK})$	c_v $(\frac{kJ}{kgK})$	ρ_g $(\frac{kg}{m^3})$
Air [53]	$0.01165 + C \times T^2$	1.0049	0.7187	1.025
C3F8 [54]	0.012728	0.79	0.7407	8.17

Table 8.1: Thermal properties of the gases used in simulations.[2] C=5.528×10^{25} $\frac{W}{mK^2}$.

8.3.2 Uncoated Bubble model

The dynamics of the uncoated bubble including the compressibility effects to the first order of Mach number can be modeled using Keller-Miksis (KM) equation [49]:

$$\rho[(1-\frac{\dot{R}}{c})R\ddot{R}+\frac{3}{2}\dot{R}^2(1-\frac{\dot{R}}{3c})] = (1+\frac{\dot{R}}{c})(G)+\frac{R}{c}\frac{d}{dt}(G) \tag{8.2}$$

where $G = P_g - \frac{4\mu_L\dot{R}}{R} - \frac{2\sigma}{R} - P_0 - P_a sin(2\pi ft)$.

In this equation, R is radius at time t, R_0 is the initial bubble radius, $\dot{R}$ is the wall velocity of the bubble, $\ddot{R}$ is the wall acceleration, ρ is the liquid density (998 $\frac{kg}{m^3}$), c is the sound speed (1481 m/s), P_g is the gas pressure, σ is the surface tension (0.0725 $\frac{N}{m}$), μ is the liquid viscosity (0.001 Pa.s), and P_a and f are the amplitude and frequency of the applied acoustic pressure. The values in the parentheses are for pure water at 293 K. In this paper the gas inside the uncoated bubble is air and water is the host media.

8.3.3 Thermal effects

If thermal effects are considered, P_g is given by Eq. 5 [49, 50, 51, 52, 53]:

$$P_g = \frac{N_g K T}{\frac{4}{3}\pi R(t)^3 - N_g B} \tag{8.3}$$

Where N_g is the total number of the gas molecules, K is the Boltzman constant and B is the molecular co-volume of the gas inside the bubble. The average temperature inside the gas can be calculated using Eq. 6 [49]:

$$\dot{T} = \frac{4\pi R(t)^2}{C_v}\left(\frac{L\,(T_0 - T)}{L_{th}} - \dot{R}P_g\right) \tag{8.4}$$

where C_v is the heat capacity at constant volume, T_0=293K is the initial gas temperature, L_{th} is the thickness of the thermal boundary layer. L_{th} is given by $L_{th} = min(\sqrt{\frac{aR(t)}{|\dot{R}(t)|}}, \frac{R(t)}{\pi})$ where a is the thermal diffusivity of the gas which can be calculated using $a = \frac{L}{c_p \rho_g}$ where L is the gas thermal conductivity and c_p is specific heat capacity at constant pressure and ρ_g is the gas density.

Predictions of the full thermal model have been shown to be in good agreement with predictions of the models that incorporate the thermal effects using the PDEs [55] that incorporate the temperature gradients within the bubble. To calculate the radial oscillations of the coated bubble and uncoated bubble while including the thermal effects Eqs. 1 and Eq. 2 are respectively coupled with Eq. 3 and 4 and then solved using the ode45 solver of Matlab.

8.3.4 Nonlinear terms of dissipation for the KMCH model

We have derived the equations for the average power loss in the oscillations of the KMCH model [41]:

$$
\begin{cases}
Td = \dfrac{-4\pi}{T} \displaystyle\int_0^T R^2 \dot{R} P_g dt \\[2ex]
Ld = \dfrac{16\pi\mu_L}{T} \displaystyle\int_0^T R\dot{R}^2 dt \\[2ex]
Cd = \dfrac{48\pi\mu_{sh}\varepsilon R_0^2}{T} \displaystyle\int_0^T \frac{\dot{R}^2}{R^2} dt \\[2ex]
Gd = \dfrac{48\pi G_s \varepsilon R_0^2}{T} \displaystyle\int_0^T \left(\frac{\dot{R}}{R} - \frac{R_0 \dot{R}}{R^2} \right) dt \\[2ex]
Rd = \dfrac{1}{T} \displaystyle\int_0^T \left(4\pi \left[\frac{R^2\dot{R}^2}{c} (P - P_g) + \frac{R^3 \dot{R}}{c} \left(\dot{P} - \dot{P}_g \right) + \frac{4\mu_L R^2 \dot{R}\ddot{R}}{c} \right.\right. \\
\quad \left. + 12\mu_{sh}\varepsilon R0^2 \left(\frac{\dot{R}\ddot{R}}{cR} - \frac{3\dot{R}^3}{cR^2} \right) + 12 G_s \varepsilon R0^2 \left(\frac{-2\dot{R}^2}{cR} + \frac{3R_0\dot{R}^2}{cR^2} \right) \right] \\
\left. - \frac{\rho R^2 \dot{R}^4}{2c} - \frac{\rho R^3 \dot{R}^2 \ddot{R}}{c} \right) dt
\end{cases}
\tag{8.5}
$$

Where Td,Ld,Cd,Rd and Gd are the dissipated power due to thermal, Liquid viscosity , coating viscosity, re-radiation and stiffness of the coating. In simulations we did not present the values for

Gd since it is always zero for a full cycle. T is the integration time and can be given as n/f where n=1,2..... . In this paper the integrals are performed over the last 20 cycles of a 500 cycles pulses to avoid the transient bubble behavior.

8.3.5 Nonlinear terms of dissipation for the KM model

We have derived the dissipation power terms of the KM model as follows [40]:

$$\begin{cases} Td = \dfrac{-1}{T}\displaystyle\int_0^T (P_g)\,\frac{\partial V}{\partial t}dt \\ \\ Ld = \dfrac{16\pi\mu_L}{T}\displaystyle\int_0^T \left(R\dot{R}^2\right)dt \\ \\ Rd = \dfrac{1}{T}\displaystyle\int_0^T \left[\frac{4\pi}{c}\left(R^2\dot{R}\left(\dot{R}P + R\dot{P} - \frac{1}{2}\rho\dot{R}^3 - \rho R\dot{R}\ddot{R}\right)\right)\right. \\ \qquad \left. -\left(\dfrac{\dot{R}}{c}P_g + \dfrac{R}{c}\dot{P}_g\right)\dfrac{\partial V}{\partial t} + \dfrac{16\pi\mu_L R^2\dot{R}\ddot{R}}{c}\right]dt \end{cases} \tag{8.6}$$

All the dissipated powers were calculated for the last 20 cycles of pulses with 500 cycles length. Simulations were carried out in Matlab using ODE45 with the highest possible relative and absolute tolerance. The time steps for integration in each simulation were $\leq \frac{10^{-4}}{f}$.

8.3.6 Bifurcation diagrams

Bifurcation diagrams are valuable tools to analyze the dynamics of nonlinear systems where the qualitative and quantitative changes of the dynamics of the system can be investigated effectively over a wide range of the control parameters. In this paper, we employ a more comprehensive bifurcation analysis method introduced in [50, 56].

2.3.a) Conventional bifurcation analysis

When dealing with systems responding to a driving force, to generate the points in the bifurcation diagrams vs. the control parameter, one option is to sample the R(t) curves using a specific point

in each driving period. The approach can be summarized by:

$$P \equiv (R(\Theta))\{(R(t), \dot{R}(t)) : \Theta = \frac{n}{f}\} \quad where \quad n = 480, 481...500 \tag{8.7}$$

Where P denotes the points in the bifurcation diagram, R and $\dot{R}$ are the time dependent radius and wall velocity of the bubble at a given set of control parameters of (R_0, P_0, P_A, c, k, μ, G_s, μ_{sh}, θ, σ, f) and Θ is given by $\frac{n}{f}$. Points on the bifurcation diagram are constructed by plotting the solution of $R(t)$ at time points that are multiples of the driving acoustic period. The results are plotted for $n = 480 - 500$ to ensure a steady state solution has been reached.

2.3.b) Method of peaks

As a more general method, bifurcation points can be constructed by setting one of the phase space coordinates to zero:

$$Q \equiv max(R)\{(R, \dot{R}) : \dot{R} = 0\} \tag{8.8}$$

In this method, the steady state solution of the radial oscillations for each control parameter is considered. The maxima of the radial peaks ($\dot{R} = 0$) are identified (determined within $n = 480 - 500$ cycles of the stable oscillations) and are plotted versus the given control parameter in the bifurcation diagrams. The bifurcation diagrams of the normalized bubble oscillations ($\frac{R}{R_0}$) are calculated using both methods a) and b). When the two results are plotted alongside each other, it is easier to uncover more important details about the SuH and UH oscillations, as well as the SH and chaotic oscillations.

8.4 Results

In this section various nonlinear oscillation regimes of coated and uncoated bubbles are introduced by visualizing the radial oscillations of the bubble as a function of pressure at various frequencies. Then we build a link between different nonlinear oscillation regimes and the dissipated powers.
In the simulations, the uncoated bubbles that enclose air and have initial radii of 10 μm and 2 μm. The bubble with $R_0 = 10\mu m$ is chosen as it will have strong thermal damping due to its bigger size. The bubble with $R_0 = 2\mu m$ is chosen as viscous effects are strong due to its size. For the coated

bubbles we investigated the bubbles with initial radii of 1 and $4\mu m$. This is because the bubble with $R_0 = 4\mu m$ is probably the largest bubble that can be used in medical applications (as the capillaries have diameters around $8\mu m$ [8]). This bubble possibly also has the highest possible size dependent Td. The bubble with $R_0 = 1\mu m$ is also chosen as it is in the typical range of the contrast agents that are used in medical applications and viscous effects strongly influence its dynamics.

8.4.1 Bifurcation structure and dissipation mechanisms of uncoated bubbles

8.4.1.1 The case of an uncoated air bubble with $R_0 = 10\mu m$

Figure 8.1 shows the bifurcation structure of the normalized oscillations ($\frac{R}{R_0}$) as a function of acoustic pressure of an uncoated air bubble with $R_0 = 10\mu m$ and the corresponding dissipated powers due to Ld, Td and Rd for ($0.25f_r \leq f \leq 1$). Throughout the manuscript and in this Figure the blue diagram is constructed using the method of maxima and the red diagram is constructed through conventional analysis. When f=$0.25f_r$ (Fig. 8.1a) an increase in pressure results in the generation of 3rd order SuH oscillations at $P_a \approxeq 63kPa$ (the blue curve shows three maxima for a period one oscillation (1 solution in the red graph)). The red curve undergoes a period doubling (Pd) bifurcation concomitant with 3 Pds in the blue graph at $P_a \approxeq 90kPa$. This results in $\frac{7}{2}$ UH oscillations. The period 2 (P2) oscillations undergo symmetry breaking to period one (P1) oscillations with thee maxima at $P_a \approxeq 100kPa$. With a slight pressure increase a saddle node bifurcation takes place to P1 oscillations with 3 maxima of higher amplitude. At this point the bubble may not sustain stable oscillations as $\frac{R}{R_0} > 2$ (black horizontal line) [57] (for further discussion on the minimum threshold for bubble destruction please refer to [32]). Further pressure increase results in period doubling cascades to chaos. The corresponding power losses are presented in Fig. 8.1b. For $P_a \leq 63kPa$, Rd is the weakest damping mechanism with Td the strongest mechanism (approximately 2 orders of magnitude larger). Rd grows faster than other damping mechanisms with increasing pressure and at $P_a \approxeq 90kPa$ concomitant with the appearance of 3rd SuH oscillations, Rd becomes equal to Ld. Rd becomes stronger than Ld when UH oscillations occur; later, simultaneous with the saddle node bifurcation Rd undergoes a large increase and becomes the strongest damping mechanism. Td is the dominant mechanism for pressures below 100 kPa (the saddle node bifurcation) and at ≈ 130 kPa $Rd > Td = Ld$.

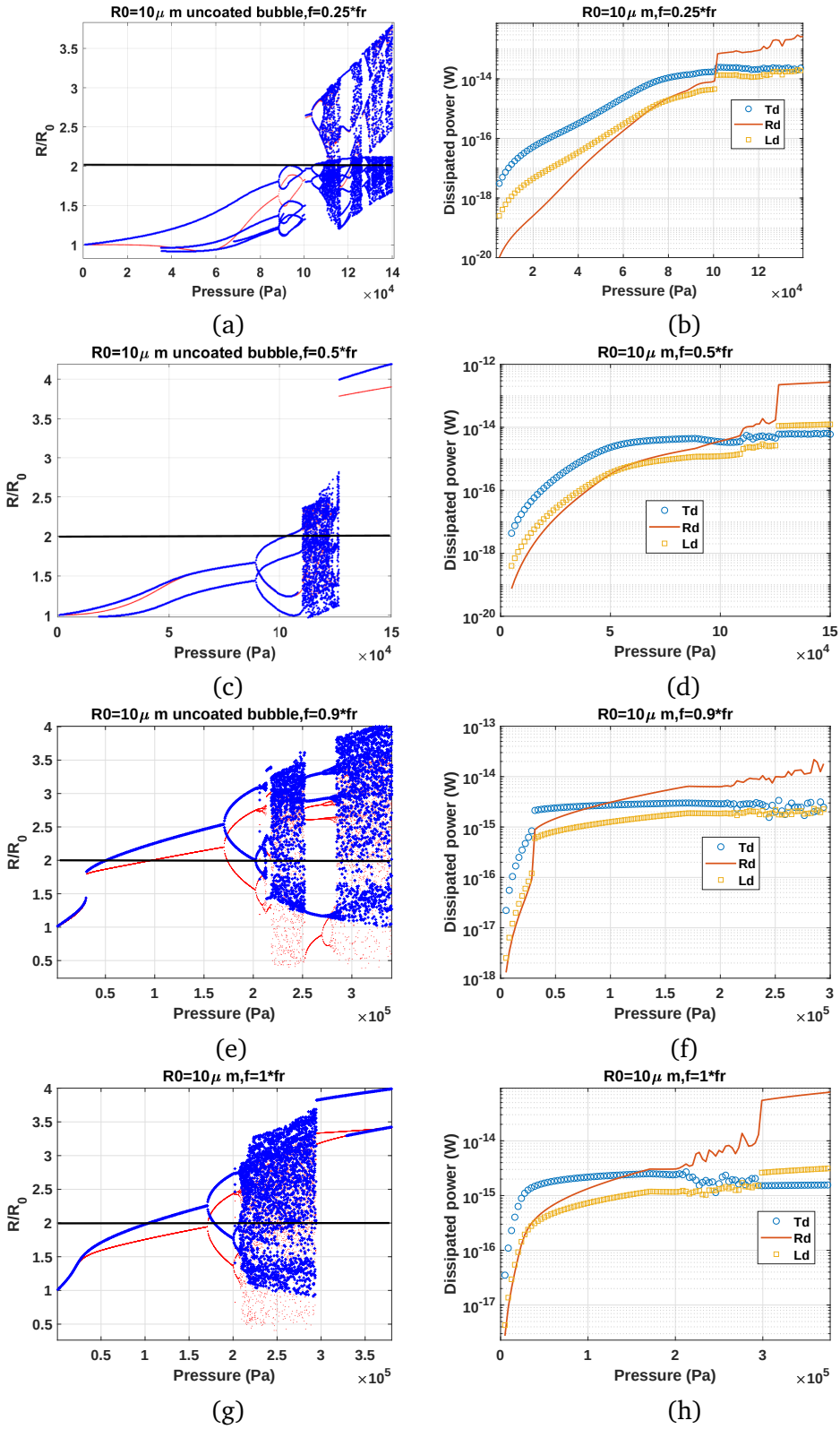

Figure 8.1: Bifurcation structure (left column) and the dissipated power as a function of pressure (right column) of the oscillations of an uncoated air bubble with $R_0 = 10\mu m$ for $f = 0.25f_r$ (a-b),$f = 0.5f_r$ (c-d), $f = 0.9f_r$ (e-f) & $f = f_r$ (g-h).

When $f = 0.5f_r$ (Fig 8.1c); 2nd order SuH occurs in the oscillations of the bubble at $P_a \approxeq 20kPa$; this manifests itself as a P1 oscillation (1 red line) with 2 maxima (two solutions for the blue curve). Radial oscillations grow with increasing pressure and at $P_a \approxeq 90kPa$ the red curve undergoes a Pd which is coincident with 2 Pds for the blue curve; this results in $\frac{5}{2}$ order UH oscillations. Oscillations become chaotic (sudden unset of chaos at $P_a \approxeq 110kPa$); further at $P_a \approxeq 125kPa$ a giant P1 resonance emerges out of chaos. Possible bubble destruction occurs at $\approx 110kPa$ (black horizontal line ($\frac{R}{R_0} > 2$)). For pressures below 50 kPa $Td > Ld > Rd$. Later, concomitant with saturation of 2nd order SuH oscillations at $\approx 50kPa$ (red line becomes equal to one of the maxima indicating resonant oscillations as the wall velocity becomes in phase with the driving acoustic pressure). Rd becomes equal to Td and gets stronger than Ld during UH oscillations. Td is the dominant mechanism at $P_a < 90kPa$; however, when UH oscillations are saturated, Rd supersedes Td and stays higher during the chaotic oscillation regime. Occurrence of the giant resonance is concomitant with a large increase in Rd as it becomes approximately two orders of magnitude higher than Td.

When $f = 0.9f_r$ (Fig. 8.1e), P1 oscillations (with 1 maxima) undergo a saddle node bifurcation to P1 oscillations of higher amplitude at $P_a \approxeq 40kPa$. The bubble possibly is destroyed at $Pa \approxeq 50kPa$ (black horizontal line). Further increase in pressure results in Pd at 175 kPa; P2 oscillations undergo a cascade of Pds to chaos at 210 kPa. The corresponding dissipated power is presented in Fig. 8.1f. For pressures below the saddle node (SN) bifurcation Td is the strongest damping mechanism (an order of magnitude larger) with $Td > Ld \approxeq Rd$. Concomitant with the SN, (note that at this pressure the wall velocity becomes in phase with the driving pressure) Rd becomes stronger than Ld and at 100 kPa it surpasses the initially larger Td. Further increase in pressure results in the fastest growth rate in Rd and the slowest growth rate in Td. Simultaneous with Pd and during majority of the P2 oscillation regime, Rd, Ld and Td stay approximately constant (this can be due the decrease in wall velocity concomitant with Pd when bubble is sonicated with a frequency near its resonance frequency [32]). During chaotic oscillations $Rd > Td > Ld$ with fluctuations due to sporadic oscillations.

For $f = f_r$ (Fig. 8.1g), at lower pressures ($P_a < 25kPa$) oscillations are P1 and the wall velocity is in phase with the driving acoustic force (blue and red curve are on top of each other) indicating resonant oscillations. Further pressure increases result in possible bubble destruction at $P_a =$

$100kPa$ (black horizontal line meets the blue line $\frac{R}{R_0} > 2$). At $P_a \approxeq 175kPa$, Pd occurs and choas appears for $205 < P_a < 295$ followed by the emergence of a giant P2 resonance. The corresponding power graph is presented in Fig. 8.1h. For $P_a < 25kPa$ where wall velocity is in phase with the driving pressure $Td > Rd = Ld$ and there is a very sharp growth for all the damping factors (possibly due to the resonant nature of oscillations). Rd becomes bigger than Ld above 25 kPa and grows faster than both Ld and Td until it becomes equal to Td at At $P_a \approxeq 150kPa$. Rd becomes sightly higher than Td when Pd occurs; however, the occurrence of Pd decreases the rate of growth of the damping powers and they which stays relatively constant during P2 oscillations (due to possibly the decrease of the wall velocity during P2 oscillations when $f = f_r$ [32, 58]). Chaotic oscillations result in a slight decrease in Td but Rd keeps growing and at the giant resonance Rd undergoes a large increase and becomes approximately two orders of magnitude larger than the other damping factors. Occurrence of the P2 giant resonance is concomitant with a decrease in Td. The reduction in Td is concomitant with the occurrence of the giant resonance may lead to better sonochemical efficacy as higher temperatures are created while at the same time their escape becomes more limited.

Figure 8.2a shows the case of sonication with $f = 1.2f_r$. We have chosen this frequency to allow the bubble to undergo non-destructive Pd ($\frac{R}{R_0} < 2$). We have previously [58] shown that for uncoated bubbles sonication with $f = f_r$ most likely results in bubble destruction before development of any P2 oscillations. This was also seen in Fig. 8.1g ($f = f_r$). Fig. 8.2a shows that when $f = 1.2f_r$ radial oscillations are initially of P1 and monotonically increase in amplitude as excitation pressure increases. At $P_a \approxeq 180kPa$ Pd takes place; P2 oscillations then undergo a SN bifurcation to a P3 oscillations (properties of this P3 oscillation has been studied in [58]) which can be concomitant with bubble destruction as $\frac{R}{R_0} > 2$. The bubble oscillations return to P2 after a very small window of chaos. Another chaotic window appears through successive Pd. A giant P2 resonance emerges out of the chaotic window when $P_a > 220kPa$ which later undergo successive Pds to chaos. The dissipated powers are shown in Fig. 8.2b. Td is the strongest damping factor for pressures below 190 kPa. For $P_a < 80$ kPa, $Td > Rd \approxeq Ld$. Rd becomes stronger than Ld as increasing pressure above 80 kPa. At P_a=190 kPa, Rd becomes stronger than Td simultaneous with the SN bifurcation for P3 oscillations; however, as soon as P3 converts to P2, Td becomes larger than Rd. Emergence of the P2 giant resonance is simultaneous with a large increase in Rd and Ld and a subsequent

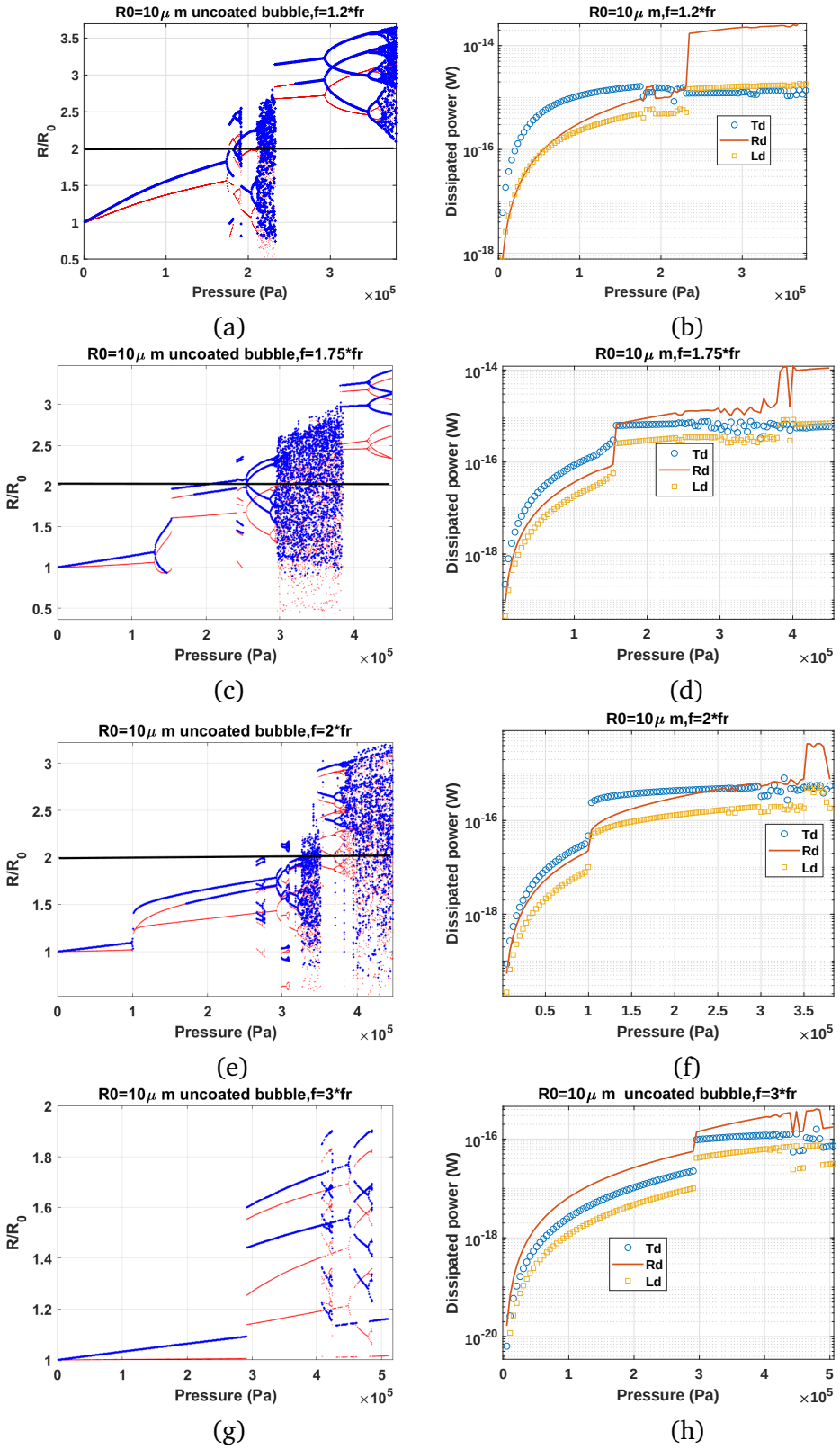

Figure 8.2: Bifurcation structure (left column) and the dissipated powers (right column) of the oscillations of an uncoated air bubble with $R_0 = 10\mu m$ for $f = 1.2f_r$ (a-b),$f = 1.75f_r$ (c-d), $f = 2f_r$ (e-f) & $f = 3f_r$ (g-h).

decrease in Td. This can be due to the faster collapse with higher wall velocity and acceleration resulting in an increase in Rd and Ld; however, due to the fast collapse there is not enough time for temperature conduction thus Td decreases. In this region Rd is an order of magnitude larger than Ld and Td and its the only region in this pressure range where Ld is stronger than Td.

Fig. 8.2c displays the case of sonication $f = 1.75 f_r$ which is the pressure dependent SH resonance frequency of the bubble (PDf_{sh} [59]). This freqeuncy is chosen so that the SN bifurcation leads to non-destructive oscillations. Oscillations are of P1 initially; pressure increase results in Pd at $\approxeq 130kPa$. P2 oscillations (with two maxima) undergo a SN bifurcation to P2 oscillations (with one maximum) of higher amplitude $\approxeq 130kPa$. At $\approxeq 180kPa$ second maxima re-emerges with the same amplitude of the smaller solution in the red curve (indicating that wall velocity is in phase with the excitation pressure once every two acoustic cycles). At $\approxeq 200kPa$ $\frac{R}{R_0} = 2$ (black horizontal line); beyond this pressure the bubble may not sustain non-destructive oscillations. P2 oscillations undergo Pds to a P4 solution which later undergoes successive Pds to chaos at $P_a = 300kPa$. A giant P3 (with two maxima) resonance emerges out of the chaotic window at $\approxeq 390kPa$. Fig. 8.2d shows that for $P_a < 130kPa$ $Td > Rd > Ld$. Occurrence of the SN bifurcation (over-saturation of SH signal [59]) results in a fast increase in Rd and enhancement in the STDR. Rd grows with pressure increase during the P2 oscillations; however Td and Ld do not increase. Rd, Td and Ld undergo sporadic fluctuations during chaos. Emergence of giant resonance results in a sharp increase in Rd and Ld and a small decrease in Td. $Rd > Ld > Td$ for the P3 giant resonance oscillations regime. The decrease in Td and the faster and larger radial collapses indicate that higher temperatures are generated while the heat conduction becomes limited. The higher temperatures can have consequences in enhancing chemical reactions within the bubble.

When sonicated with $f = 2f_r$ (f_{sh}) oscillations undergo a Pd at $P_a = 100kPa$; P2 oscillations increase in amplitude and evolve in a shape of a bow-tie (Chapter 4) [59]. Consistent with previous observations [59] sonication with f_{sh} results in the largest pressure range with stable P2 oscillations. At $P_a \approxeq 280kPa$ a small window of P6 oscillations appear through a SN bifurcation with each solution undergoing Pds to P12 (the properties of this rare oscillation regime have been studied in the appendix of (Chapter 4) [59]). Oscillations return to P2 which then undergo Pd to P4 oscillations. For a small window of excitation pressure P12 oscillations appear through a SN bifurcation; however, here because $\frac{R}{R_0} > 2$ the bubble most likely undergoes destruction. P12

oscillations undergo P24 oscillations for a small window and then disappear as P4 oscillations emerge. At $\approxeq 320kPa$ chaos appears. A P3 giant resonance emerges out of the chaotic window which later undergo successive Pds to chaotic oscillations. For $P_a < 220kPa$, $Td > Rd > Ld$. After the occurrence of Pd, Td remains relatively constant with increasing pressure while Rd grows faster than Ld as pressure increases. Eventually at $P_a \approxeq 200kPa$ Rd becomes equal to Td. The occurrence of giant resonance results in sharp increase in Rd and Ld and Rd becomes the strongest damping factor with $Rd > Ld > Td$. Regeneration of chaos results in a decrease in Rd and Ld with $Rd \approxeq Td > Ld$.

When $f = 3f_r$ (Fig. 8.2g); radial oscillations grow very slowly and monotonically with pressure; at $P_a \approxeq 300kPa$ a SN bifurcation takes place and oscillations become P3 (3 solutions for the red curve with 2 maxima). Properties of these oscillations have been studied in [60, 61, 62]. At $\approxeq 410kPa$ oscillations undergo a SN bifurcation to P6 oscillations for small excitation pressure window which then transition to P12 and then back to P3 oscillations. P12 occurs at $\approx 450kPa$ through Pds. P12 oscillations then switch to P1 oscillation with pressure increase. Power dissipation curve is shown in Fig. 8.2h. Here Rd is the strongest damping mechanism for all the studied pressure ranges with $Rd > Td > Ld$. SN bifurcation results in a sharp increase in the dissipated powers at 300 kPa with Td exhibiting the largest increase.

8.4.1.2 The case of an uncoated air bubble with $R_0 = 2\mu m$

The same nonlinear oscillations regimes are also studied for an uncoated air bubble with $R_0 = 2\mu m$. Due to the smaller size of the bubble, a larger contribution from viscous effects and a smaller contribution for thermal effects are expected.

Fig. 8.3a shows the case of sonication with $f = 0.3f_r$. P1 oscillations undergo a 3rd SuH resonance at $P_a \approxeq 60kPa$ (P1 oscillations with 3 maxima). At $P_a \approxeq 62kPa$, the amplitude of one of the maxima coincides with the amplitude of the red curve indicating that the wall velocity becomes in phase with the driving pressure every acoustic cycle. At $P_a \approxeq 133kPa$ the red curve undergoes a Pd and P1 oscillations become P2. At the same time three concomitant Pds occur in the blue curve and UH oscillations of 7/2 order develop. The red curve grows fast within increasing pressure with the occurrence of 3rd order SuH and Pd, the amplitude of the red curve becomes the same as the highest amplitude of the blue curve right when Pd takes place, indicating an UH resonance. During

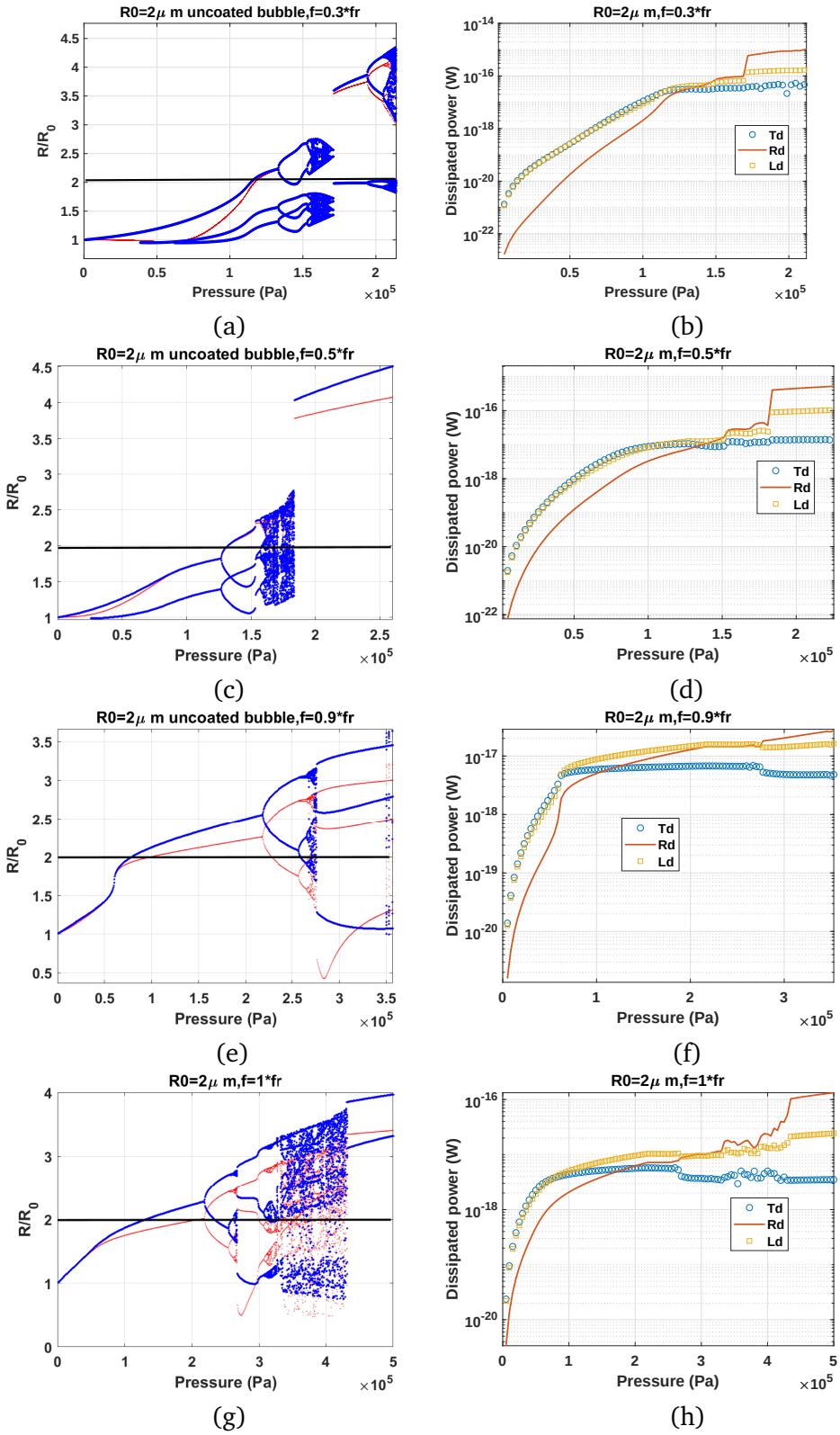

Figure 8.3: Bifurcation structure (left column) and the dissipated powers (right column) of the oscillations of an uncoated air bubble with $R_0 = 2\mu m$ for $f = 0.3f_r$ (a-b),$f = 0.5f_r$ (c-d), $f = 0.9f_r$ (e-f) & $f = f_r$ (g-h).

UH oscillations the value of the upper and lower branch of P2 oscillations in red curve are exactly the same as the two highest amplitudes of the blue curve. A small chaotic window appears at 170 kPa and then a 2nd order SuH giant (P1 with 2 maxima) resonance emerges out of the chaotic window which later undergoes successive Pds to chaos. Due to the smaller bubble size compared tothe 10 μm bubble oscillations analyzed in Fig. 8.1b, Ld and Td have the same value for pressures below 120 kPa and Td is no longer the dominant power dissipation mechanism. Rd grows faster a pressure increases and the contributions of Td, Ld and Rd become similar when Pd takes place. $Rd > Ld > Td$ for the UH regime of oscillations. The giant resonance is concomitant with a sharper increase in Rd making Rd the dominant damping mechanism during giant resonant oscillations.

When $f = 0.5f_r$ (Fig. 8.3c) oscillations are of P1 with one maximum for $P_a < 25kPa$; 2nd order SuH oscillations occur at $\approxeq 25kPa$ (2 maxima appear in the blue curve). At $P_a = 90kPa$, the amplitude of the red curve becomes equal to the highest amplitude maximum of the blue curve. This is concomitant with the saturation of 2nd order SuH frequency component of the scattered pressure (P_{sc}). At 127 kPa, the red curve undergoes a Pd concomitant with two Pds in the blue curve resulting in a P2 oscillation with 4 maxima ($\frac{3}{2}$ UH resonance [50]). At $\approxeq$ 140 kPa $\frac{R}{R_0} = 2$ and the bubble possibly can not sustain non-destructive oscillations beyond this pressure. For $P_a > 150kPa$ a chaotic window emerges and later at $P_a \approxeq 184kPa$ a giant period one resonance emerges out of the chaotic window. Fig. 8.2d shows the corresponding dissipated powers. Ld and Rd are approximately equal for pressures below the occurrence of Pd and UH resonance. Simultaneous with the $\frac{3}{2}$ UH resonance, Rd becomes stronger than Ld and Td with $Rd > Ld > Td$. Rd undergoes the sharpest increase concomitant with the generation of giant resonance, making it the strongest dissipation mechanism at higher pressures.

When $f = 0.9f_r$ (Fig. 8.3e), which is a PDf_r [32], the oscillations are of P1 and grow monotonically with increasing pressure and at $P_a \approxeq 60kPa$ (the pressure of the PDf_r) the oscillation amplitude undergo a sharp increase with the red and blue curve coinciding with each other. Above $P_a \approxeq 75kPa$ $\frac{R}{R_0}$ exceeds 2 (black horizontal curve) and beyond this point bubble destruction is likely. Oscillations undergo Pd at $\approxeq$ 220 kPa and a small chaotic window occurs at $P_a \approxeq 260kPa$ through successive Pds. At $\approxeq$ 275 kPa a P3 oscillations with 3 maxima emerges out of the chaotic window until $P_a \approxeq$ 350 kPa where chaos is regenerated. The power dissipation graph in Fig. 3f indicates that $Td > Ld > Rd$ before the SN bifurcation takes place. Above $P_a \approxeq 60kPa$ (pressure

for SN bifurcation) Ld becomes stronger and the dissipation order is $Ld > Td > Rd$. After SN, Rd grows faster with pressure increase while Td stays constant. Rd supersedes Td at $P_a \approxeq$ 125 kPa and becomes equal to Ld when Pd takes place. Ld, Rd and Td then stay relatively constant for the P2 oscillations regimes (this can be due to the decrease in wall velocity and acceleration when Pd takes place in cases where the bubble is sonicated with a frequency near $f = f_r$ [32]). Emergence of the P3 oscillations of the chaotic window with high amplitude is concomitant with an increase in Rd and decrease in Ld and Td; this will lead to an increase in the STDR, however, with the possible trade off the loss of stable oscillations.

When $f = f_r$ (Fig. 8.3g); at lower pressures ($P_a < 60kPa$) oscillations are of P1 and the wall velocity is in phase with the driving acoustic force (blue and red curve are on top of each other) indicating resonant oscillations. Further pressure increase results in possible bubble destruction at $P_a = 120kPa$ (black horizontal line meets the blue line). At $P_a \approxeq 220kPa$, occurrence of Pd results in P2 oscillations for $220 < P_a < 260$ followed by the emergence of a small chaotic window through successive Pds. Similar to the previous case, a P3 emerges from the chaotic window followed by regeneration of chaos for $320kPa < P_a < 425kPa$. At $\approxeq 425kPa$ a giant P2 resonance emerges out of the chaotic window. The corresponding dissipated powers illustrated in Fig. 8.3h show that for pressures below $\approx 60kPa$, $Td > Ld > Rd$. Above this pressure $Ld > Td > Rd$ until the excitation pressure reaches $\approxeq$ 190 kPa and Rd becomes equal to Td. When Pd occurs, Rd overcomes Td; then Rd, Ld and Td stay constant during P2 oscillations. Generation of P4 results in an increase in Rd and a subsequent decrease in Ld and Td. Emergence of P3 results in an increase in Rd making the order as $Rd > Ld > Td$ followed by a sharp increase of Rd when giant resonance takes place. Similar to previous cases Td decreases when giant resonance occurs, and Ld increases however with a smaller percentage compared to Rd. Once again, the giant resonance can lead to a significant increase in STDR; however this may lead to bubble destruction. The generation of higher temperatures due to stronger collapses and the decrease in Td may have consequences in enhancing chemical reactions within the bubble.

The case of $f = 1.2f_r$ is shown in Fig. 8.4a. Oscillation amplitude increases monotonically with pressure and bubble undergoes Pd at $\approxeq 225kPa$. Unlike the case of sonication with $f = f_r$, (and similar to the uncoated air bubble with $R_0 = 10\mu m$) Pd occurs when $\frac{R}{R_0} < 2$ thusthe bubble is more likely to sustain P2 oscillations. At $\approxeq 225kPa$ oscillations become chaotic through successive Pds

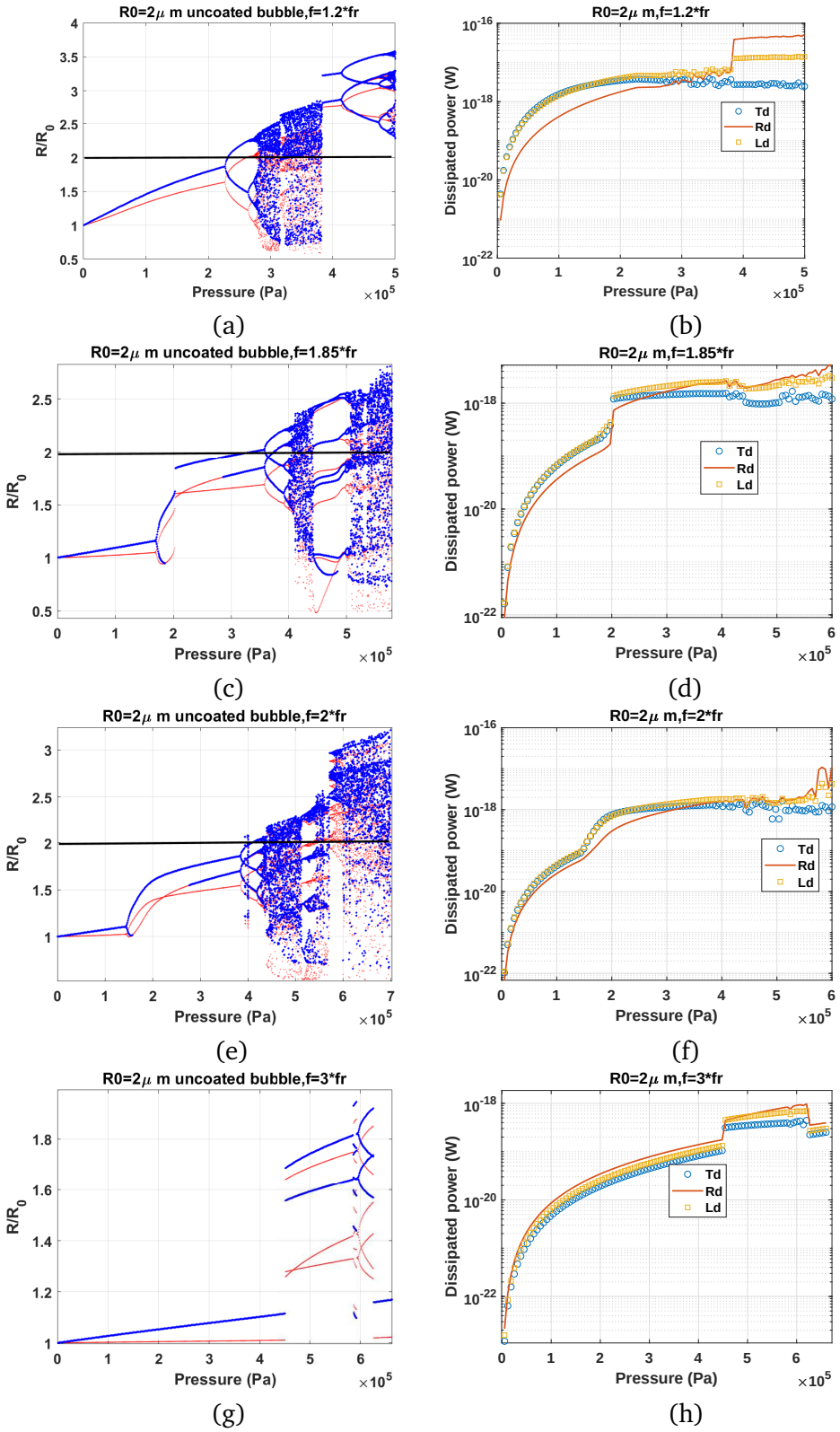

Figure 8.4: Bifurcation structure (left column) and the dissipated power (right column) of the oscillations of an uncoated air bubble with $R_0 = 2\mu m$ for $f = 1.2f_r$ (a-b),$f = 1.85f_r$ (c-d), $f = 2f_r$ (e-f) & $f = 3f_r$ (g-h).

and chaos stretches until $P_a \approxeq 390kPa$. At this pressure a P2 giant resonant oscillation emerges out of the chaotic window (the solution with the higher amplitude in red curve is exactly equal to the smaller maximum indicating wall velocity becomes in phase with the driving acoustic pressure once every two acoustic cycles). The P2 giant resonance undergoes successive Pds to chaos at $\approxeq 500kPa$. The corresponding dissipated power graphs (Fig. 8.4b) show that $Ld \approxeq Td > Rd$ for $P_a \lesssim$ 225 kPa. When Pd occurs, Ld becomes stronger than Td with $Ld > Td > Rd$; once again, during P2 oscillations, Ld, Td and Rd stay relatively constant as pressure increases. Generation of P4 and chaos is concomitant with an increase in Rd making $Ld \approxeq Rd > Td$. This is similar to the previous cases when the giant resonance emerges Rd and Ld undergo a sharp increase (Rd exhibits the sharpest increase), while Td decreases slightly. This makes the contribution order of the dissipation mechanisms as $Rd > Ld > Td$.

When $f = 1.85f_r$ (the PDf_{sh} [59]) the P1 oscillation amplitude grows slowly with increasing pressure and the bubble undergoes a Pd at $\approxeq 190kPa$. Generation of Pd is concomitant with a sharp increase in the oscillation amplitude (oscillations are P2 and have two maxima). At 200 kPa P2 oscillations undergo a SN bifurcation to P2 oscillations of higher amplitude (here the signal looses one of its maxima [59]). As pressure increases the second maxima is generated at $\approxeq 290kPa$. At 300 kPa, $\frac{R}{R_0}$ becomes larger than 2 (black line). P2 oscillations undergo period doubling to P4-2 oscillations and a chaotic window appears at 405 kPa through successive Pds of the P4-2 signal. Later at 440 kPa, a P6 oscillation with 6 maxima emerges out of the chaotic window which through successive Pds translate to P12 and chaos at $\approxeq 500 - 505kPa$. The corresponding power graphs (Fig. 8.4d) show that $Td = Ld > Rd$ below $P_a \approxeq 190kPa$ where Pd takes place. Generation of Pd results in a decrease in Td and Ld becomes stronger than Td. Simultaneous with the SN bifurcation at $P_a = 200kPa$, Rd, Ld and Td undergo a sharp increase (with Rd exhibiting the highest increase). This makes Rd approximately equal to Ld and for the rest of the P2 oscillations, power dissipation stays relatively constant with increasing pressure and $Rd = Ld > Td$. Generation of chaos results in some sporadic fluctuations and when P6 emerges out of chaos Ld and Td decrease resulting in $Rd > Ld > Td$.

When $f = f_{sh}$ ($f = 2f_r$ in Fig. 8.4e), P1 oscillations slowly grow with increasing pressure and at $P_a \approxeq 140kPa$, a Pd takes place, and concomitant with Pd, oscillation amplitude start growing quickly. P2 oscillations evolve in the form of a bow-tie. We have shown in (Chapter 4) [58] that this

is the characteristic of micron size bubbles when they are sonicated with $f = 2f_r$. Right when Pd occurs, oscillations have two maxima, one of the maxima disappears shortly after Pd but reemerges with a value equal to the higher amplitude of the red curve at $\approxeq 290kPa$ (in [58] we have shown that this may be the point where $\frac{1}{2}$ SH frequency component of the P_{sc} gets saturated). Oscillations undergo Pds at 395 kPa to P4-2 oscillations and when $P_a \approxeq 410kPa$ $\frac{R}{R_0}$ exceeds 2 (black horizontal line collides with the blue curve). A small window of P6-2 ([58]) occurs right before 400 kPa. Later chaos appears at $\approxeq 440kPa$. For $P_a < 300kPa$, $Td = Ld = Rd$ and simultaneous with Pd, dissipation powers undergo a fast increase; but, they quickly plateau with pressure increase. At $P_a = 300kPa$ Td=Ld=Rd. Further increase in pressure results in a slight decrease in Td and a slight increase in Rd and Ld. At $P_a \approxeq 580kPa$ where the amplitude of the chaotic oscillations sharply increases; Rd becomes stronger than Ld.

When $f = 3f_r$ (Fig. 8.4g), oscillations grow very slowly with pressure increase until at $\approxeq 420kPa$ at which P1 oscillations undergo a SN bifurcation to P3 oscillations with 2 maxima. Oscillation amplitude increase slowly with increasing pressure and a small P6 window appears at ≈ 590-598 kPa followed by a return to P3 oscillations and then 3 simulations Pds to P6 oscillations. P6 oscillations return to P1 oscillations at $P_a \approxeq 610kPa$. The corresponding dissipated power graphs (Fig. 8.4h) show that similar to the case of unacoated air bubble with $R_0 = 10\mu m$, $Rd > Ld > Td$ before the occurrence of the SN bifurcation. Occurrence of SN bifurcation is concomitant with a sharp increase in Rd and Ld and Td with ($Rd > Ld > Td$). As pressure increases the difference between Rd, Ld and Td diverges. A return to P1 oscillations is concomitant with a decrease in the dissipation. Due to the larger increase in Td when P3 occurs, the STDR decreases. The increase in Td is due to the large average surface area of the bubbles and a slower rebound during P3 oscillations.

8.4.2 Bifurcation structure and power dissipation of the oscillations of the coated bubbles

8.4.2.1 The case of a coated C3F8 bubble with $R_0 = 4\mu m$

In this subsection we analyze the dynamics of the coated bubbles that are often used in medical ultrasound. The gas core is chosen to be C3F8 as it is typically used in coated bubbles and the

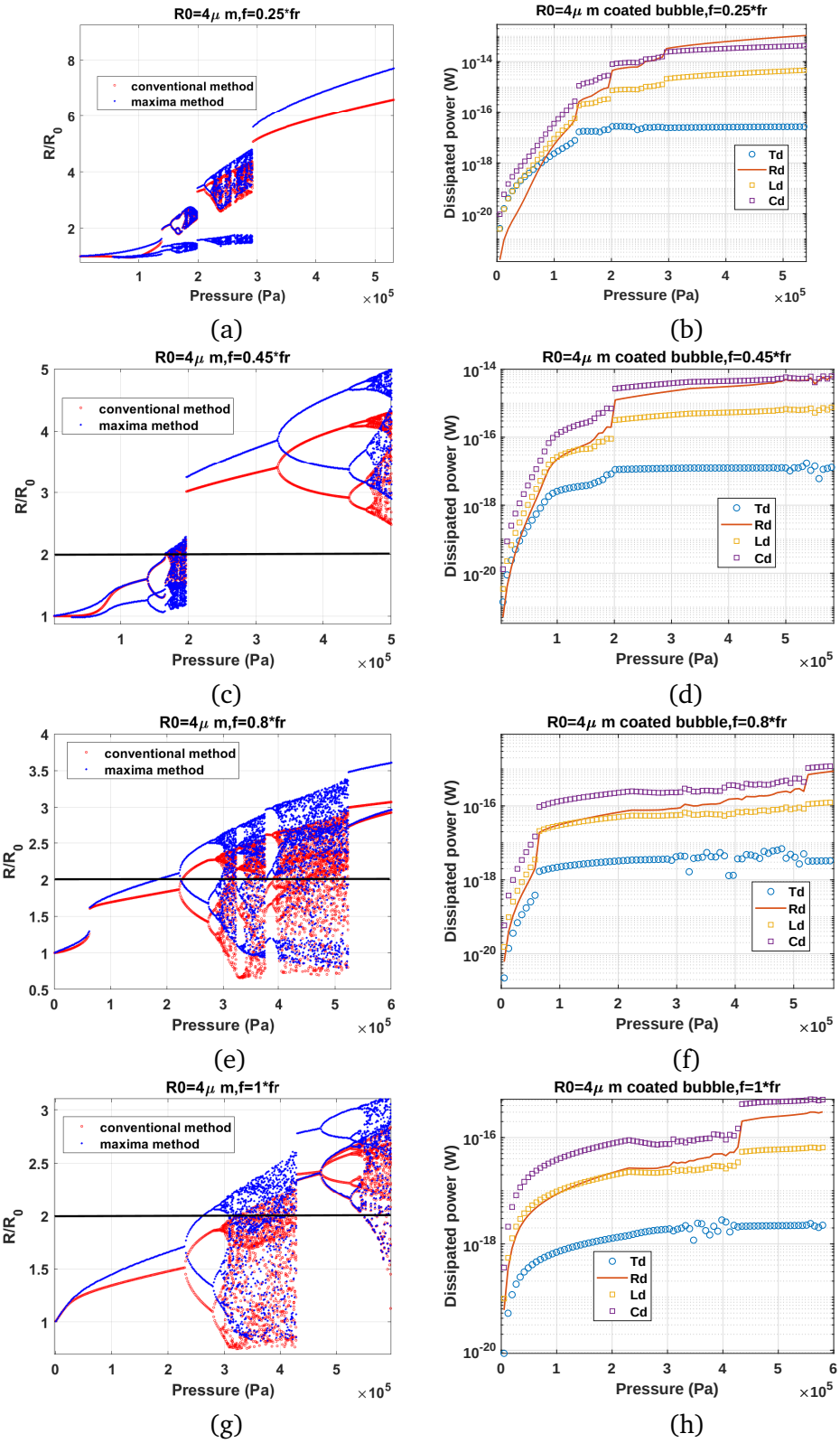

Figure 8.5: Bifurcation structure (left column) and the dissipated power as a function of pressure (right column) of the oscillations of a coated C3F8 bubble with $R_0 = 4\mu m$ for $f = 0.25f_r$ (a-b),$f = 0.45f_r$ (c-d), $f = 0.8f_r$ (e-f) & $f = f_r$ (g-h).

maximum size of the bubbles that are chosen for our study is $8\mu m$ ($R_0 = 4\mu m$) since capillaries are typically below 8 μm in diameter [8].

Figure 8.5a displays the bifurcation structure of a coated bubble with $R_0 = 4\mu m$ when $f = 0.25 f_r$. The oscillation amplitude grows with pressure and at $P_a = 80kPa$, 3 maxima appear in the P1 oscillations (3rd order SuH [50]). The 3rd order SuH undergoes a SN bifurcation to another 3rd order SuH oscillations at $P_a \approxeq 140kPa$. The signal is still P1 with 3 maxima and at $P_a \approxeq 160kPa$ Pd takes place in the red curve (concomitant with 3 Pds for each maxima in the blue curve) and $\frac{7}{2}$ order UH oscillations are generated. A small chaotic window appears before $P_a = 200kPa$ followed by a P1 signal of 2nd order SuH, then $\frac{5}{2}$ UH resonance and later again chaos. At approximately 295 kPa a giant P1 resonance with one maximum emerges out of the chaotic window. The corresponding power dissipation curves are shown in Fig. 8.5b. Cd is the strongest dissipation mechanism with $Cd > Ld > Td$ for $P_a < 80kPa$. When SuH oscillations occur, Rd becomes equal to Td and keeps growing faster than other dissipation mechanisms until Pd takes place where Rd undergoes the sharpest increase and becomes larger than Ld. Rd keeps growing faster with the SN bifurcation to 2nd order SuH oscillations, Rd undergoes another sharp increase and becomes equal to Cd during chaotic oscillations. Emergence of the giant resonance out of chaos is concomitant with another sharp increase in Rd, making Rd the strongest dissipation mechanism afterwards.

Figure 8.5c shows the case of sonication with $f = 0.45 f_r$. As pressure increases, the P1 oscillation amplitude increases and at $\approxeq 25kPa$ two maxima appear in the P1 oscillations. At approximately 105 kPa; bubble collapses two times in each acoustic cycles with the wall velocity of one of the collapses in phase with the driving acoustic pressure (red and blue line have the same value). Pd takes place at $\approxeq 140kPa$ ($\frac{5}{2}$ UH oscillations are generated (signal is P2 with 4 maxima)) and $\frac{R}{R_0}$ becomes equal to 2 at the pressure at which chaos is generated at $P_a \approxeq 180kPa$. Slightly below 200 kPa a giant P1 resonance emerges out of the chaotic window which later undergoes successive Pds to chaos at $P_a \approxeq 470kPa$. The corresponding power dissipation curves in Fig. 8.5d shows that for pressures below the SuH oscillations, $Cd > Ld > Td \approxeq Rd$. After the generation of SuH oscillations Rd supersedes Td and becomes equal to Ld at about 105 kPa (when red curve meets the blue curve in Fig. 8.5c). Power dissipation curves plateau and when Pd occurs. Rd, Cd, Ld and Td increase. During $\frac{5}{2}$ UH oscillations $Cd > Rd > Ld > Td$. Emergence of giant resonance is concomitant with an increase in all the dissipation mechanisms with Rd exhibiting the sharpest growth. Afterwards

Rd grows faster and becomes $\approxeq$ to Cd during chaotic oscillations. Similar to Fig. 8.5b, Rd and Cd are 3 orders of magnitude larger than Td and about an order of magnitude stronger than Ld.

When $f = 0.8f_r$ (PDf_r [32]) a SN bifurcation takes place at $P_a = 80kPa$ and the oscillation amplitude $\frac{R}{R_0}$ exceeds at $P_a \approxeq 190kPa$ (black line meets the blue curve). At $\approxeq 220kPa$, Pd takes place and afterwards P2 oscillations undergo successive period doubling to chaos at $\approxeq 280kPa$. A P2 giant resonance with 2 maxima emerges out of the chaotic window at 520 kPa. The corresponding dissipation curves in Fig. 8.5f reveal that when the SN occurs, Cd, Ld, Rd and Td undergo a sharp increase with Td exhibiting the smallest increase. Before the SN, $Cd > Ld > Rd > Td$ and after the SN, $Cd > Ld = Rd > Td$. When $\frac{R}{R_0}$ exceeds 2, Rd becomes stronger than Ld and power dissipation contribution is in the following order for the rest of the pressure range that studied: $Cd > Rd > Ld > Td$. Emergence of the giant resonance is simultaneous with an increase in Rd, Cd and Ld (with Rd demonstrating the largest increase) and Td decreases.

When $f = f_r$ (Fig. 8.5g) the oscillation amplitude grows monotonically with pressure. For excitation pressures below 50 kPa, the red curve and blue curves have the same value (wall velocity is in phase with the driving acoustic pressure). The two curves diverge as pressure increases and at 230 kPa Pd takes place. P2 oscillations amplitudes exceed $\frac{R}{R_0} = 2$ at 260 kPa; afterwards successive Pds take place in the bifurcation structure resulting in chaotic oscillations at $\approx 300kPa$. The chaotic window continues up to 420 kPa; whereby, large amplitude P2 oscillations emerge out of the chaotic window (one of the red solutions is equal to the smallest maxima in blue curve). Chaos is then generated through successive Pds at 520 kPa. Power dissipation curves in Fig. 8.5h show that $Cd > Rd \approxeq Ld > Td$; however, when Pd occurs, Rd slightly exceeds Ld due to the fact that both Cd and Ld undergo a slightly higher decrease compared to Rd. This is possibly due to decrease in the wall velocity when Pd takes place when bubble is sonicated with a frequency close to its resonance frequency (Chapters 2 and 4) [32]. Emergence of the giant P2 oscillations is concomitant with a very sharp increase in Rd and Cd, a slight increase in Ld and minimal changes in Td.

When $f = 1.2f_r$ (Fig. 8.6a), the oscillation amplitude grows monotonically with pressure. A Pd takes place at $\approxeq 230kPa$. Bubbling bifurcation takes place in each of the branches of the P2 regime and a small window of chaos appears followed by a small P3 window which undergoes Pd to P12 after which there is an interesting symmetry breaking leading to a sudden onset of chaos. The

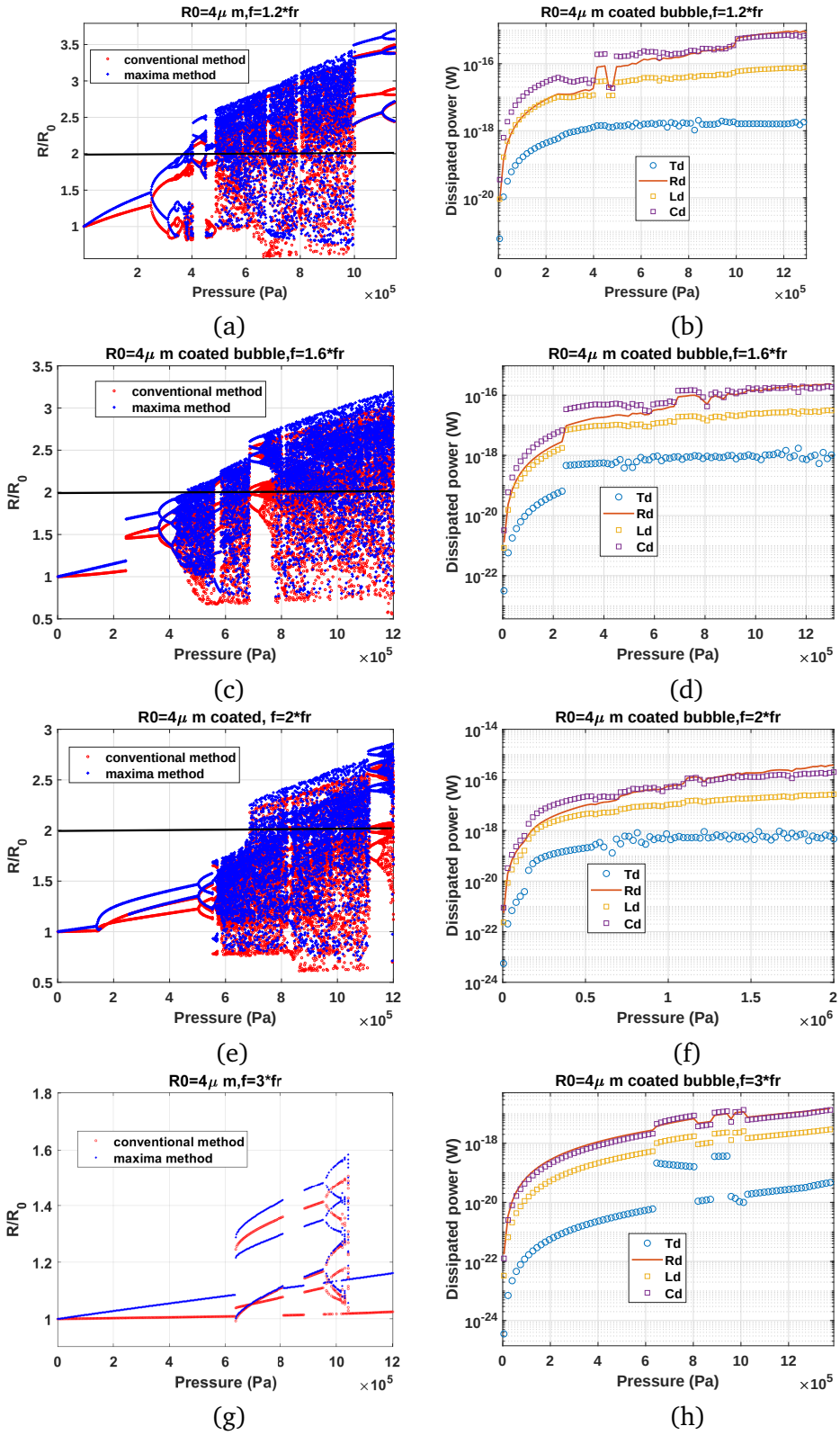

Figure 8.6: Bifurcation structure (left column) and the dissipated powers (right column) of the oscillations of a coated C3F8 bubble with $R_0 = 4\mu m$ for $f = 1.2f_r$ (a-b),$f = 1.6f_r$ (c-d), $f = 2f_r$ (e-f) & $f = 3f_r$ (g-h).

oscillation amplitude exceeds $\frac{R}{R_0} = 2$ at $\approxeq 390kPa$. The chaotic window extends until $P_a = 1MPa$ where a giant P3 emerges out of the chaotic window which then undergoes Pd to P12 oscillations. The corresponding dissipation curves in Fig. 8.6b show that $Cd > Ld = Rd > Td$ until Pd after which Rd becomes slightly larger than Ld. Pd results in a notable decrease in Cd and Ld. Td remains two orders of magnitude less than Cd (Fig. 8.5b). When the first P3 oscillation occurs, Cd, Rd and Ld undergo a sharp increase with the most notable increase in Rd. Symmetry breaking bifurcation results in a decrease in dissipation due to lower oscillation amplitudes. Initiation of chaos leads to a sharp increase in dissipation with $Cd > Rd > Ld > Td$. Rd grows faster than other mechanisms as pressure increases and becomes equal to Cd at $\approx 820kPa$. Finally when the P3 giant resonance occurs Cd, Rd and Ld undergo an increase with Rd experiencing the largest growth. Td undergoes a small decrease during P3 giant resonance oscillations.

Fig. 8.6c represents the case of sonication with $f = 1.6f_r$ (PDf_{sh} [59]). P1 oscillations grow slowly with pressure and at $\approxeq 230kPa$ a SN bifurcation from P1 oscillations of lower amplitude to P2 oscillations (with one maximum) of higher amplitude takes place. Second maxima emerges at $\approxeq 320kPa$; afterwards oscillations undergo Pd at $\approxeq 380kPa$ which are then followed by successive Pds to chaos at $\approxeq 400kPa$. Chaotic window stretches until $\approxeq 700kPa$ with a small window of P6 oscillations. A P6 oscillation regime with high amplitude emerges out of the chaotic window; later undergoing Pds to P12 and then chaos. The corresponding dissipation curves are shown in Fig. 8.6d. For pressures below the SN bifurcation $Cd > Rd > Ld > Td$. Occurrence of SN bifurcation is concomitant with a sharp increase in the dissipated powers. $Cd > Rd > Ld > Td$ until at higher pressures (> 1 MPa) Rd surpasses Cd.

$f = 2f_r$ (Fig. 8.6e) is the f_{sh} of the bubble [58]. P1 oscillations undergo Pd at $\approxeq 180kPa$. The P2 oscillations loose one maxima right after the generation of Pd and then evolve in a form of a bow-tie with the second maxima re-emerging with an amplitude equal to the larger branch of the red curve $\approxeq 280kPa$. Consistent with previous observations in [58], sonication with $f = 2f_r$ results in the largest pressure range of stable P2 oscillations. Oscillations undergo Pd to P4 oscillations followed by a SN bifurcation to P4 oscillations of higher amplitude at $\approxeq 570kPa$; before successive Pds to chaos. Amplitude of the chaotic oscillations increases at $\approxeq 710kPa$ which can possibly lead to bubble destruction as $\frac{R}{R_0} > 2$. Chaos continues until 1.1 MPa where a P6 oscillation of large amplitude emerges out of chaos which later undergoes successive Pds to P12 and chaos. The

corresponding dissipation curves are depicted in Fig. 8.6f. $Cd > Rd > Ld > Td$ with dissipated powers undergoing a fast growth concomitant with Pd. When chaos appears Rd becomes equal to Cd and later at 1.5 MPa onward $Rd > Cd > Ld > Td$. When $f = 2f_r$, Td is in average two orders of magnitude smaller than Cd and Rd.

The case of sonication with $f = 3f_r$ is shown if Fig. 8.6g. Oscillations grow slightly with pressure and at $\approxeq 620kPa$ a SN bifurcation takes place and P1 oscillations turn into P3 oscillations of higher amplitude. P3 then grows in amplitude until it turns to P1 oscillations for a small pressure window and then again re-emerges through a SN bifurcation. P3 oscillations undergo Pds to P6 and then return to P1 oscillations for $P_a \approxeq 1.04MPa$. Corresponding dissipated power curves are shown in Fig. 8.6h. Unlike previous cases here $Rd > Cd > Ld > Td$. The SN bifurcation results in a large increase in dissipated powers specially in case of Td. This is because during these P3 oscillations the bubble collapses 3 times out of which two are very gentle and thus a large average bubble radius is maintained during oscillations. This increases the surface area for the heat exchange and Td increases. Moreover, bubble collapses strongly only once in every three cycles; thus high velocity and re-radiated pressure are achieved only once in every three acoustic cycles. This is why the average for Ld, Cd and Rd are small. During P3 and P6 oscillations $Cd > Rd > Ld > Td$ and elsewhere $Rd > Cd > Ld > Td$.

8.4.2.2 The case of a coated C3F8 bubble with $R_0 = 1\mu m$

Fig. 8.7a shows the dynamics of a C4F8 coated bubble with $R_0 = 1\mu m$ when $f = 0.25f_r$. Oscillations are initially P1 with one maximum, later at about $P_a = 160kPa$, 3 maxima are generated in the bubble oscillations which grow in amplitude as pressure increases, undergoing a SN bifurcation to higher amplitude oscillations at about 320 kPa. In this region (P1 with 3 maxima) the 3rd harmonic of the backscattered pressure is maximum and the bubble is in the 3rd order SuH oscillation mode. Pd occurs at about 350 kPa, leading to a P2 signal with 6 maxima and $\frac{7}{2}$ UH oscillations. Oscillations become chaotic through successive Pds at $\approxeq 365kPa$; at the same time $\frac{R}{R_0}$ exceeds 2 thus, the bubble may not sustain long lasting non-destructive oscillations beyond this pressure. At 405 kPa, a P2 oscillation regime with large amplitude emerges out of the chaotic window. Oscillations become chaotic again through successive Pds of the P2 signal and the chaotic

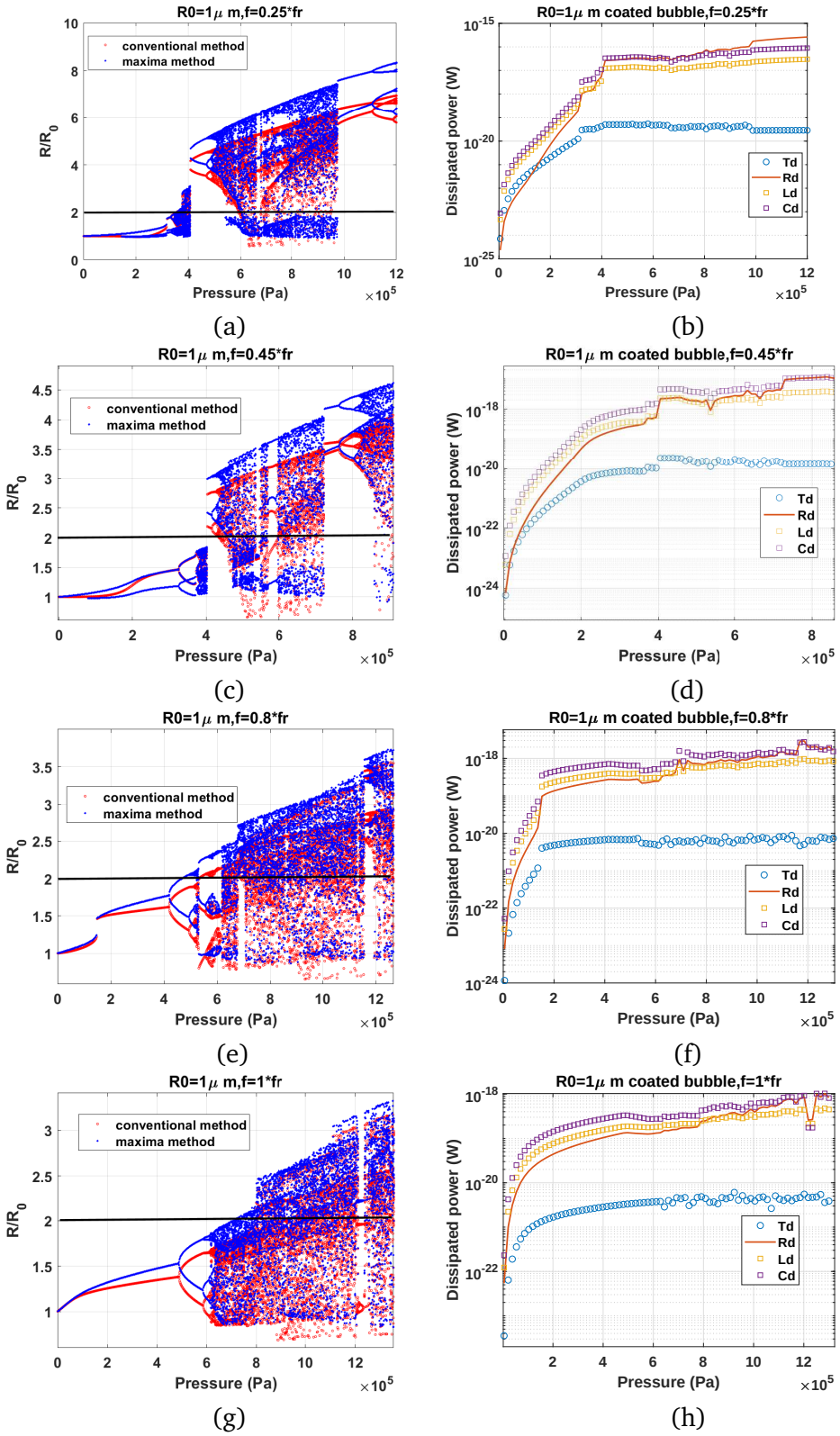

Figure 8.7: Bifurcation structure (left column) and the dissipated power as a function of pressure (right column) of the oscillations of a coated C3F8 bubble with $R_0 = 1\mu m$ for $f = 0.25f_r$ (a-b),$f = 0.45f_r$ (c-d), $f = 0.8f_r$ (e-f) & $f = f_r$ (g-h).

window extends until $\approx 970kPa$. Above this pressure a P2 giant resonance emerges out of chaos, and later undergoes successive Pds to chaos. Fig. 8.7b shows that at pressures lower than 160 kPa (generation of 3 maxima in the osculations) $Cd > Ld > Td > Rd$. Above 160 kPa, Rd increases beyond Td and $Cd > Ld > Rd > Td$ until SN bifurcation occurs at about 320 kPa. Rd grows faster and when SN occurs it undergoes a sharp increase alongside Ld and Cd. $Cd > Ld = Rd > Td$ above SN bifurcation and during UH oscillations. Rd exceeds Ld when $\frac{R}{R_0} > 2$ and during the chaotic oscillations. When the large amplitude P2 oscillations are generated Rd undergoes the sharpest increase and becomes equal to Cd. Thereafter $Cd = Rd > Ld > Td$ until about 900 kPa where Rd slightly exceeds Cd. Emergence of the giant P2 resonance leads to a sharp increase in Rd and a decrease in Td similar to previous cases.

When $f = 0.45f_r$ (Fig. 8.7b) P1 oscillations increase in amplitude with pressure and at about 85 kPa a second maxima appear in the bubble oscillations. Oscillations keep growing and at about 300 kPa the red curve becomes equal in amplitude to the highest amplitude maxima (indicating the wall velocity of one of the maxima becomes in phase with the driving acoustic field). At about 320 kPa, Pd occurs and oscillations become P2 with 4 maxima indicating the generation of $\frac{5}{2}$ UH resonance. A small chaotic window appears, and at about 400 kPa a P2 oscillation regime with higher amplitude emerges out of the chaotic window. At this point, since $\frac{R}{R_0}$ exceeds 2 the bubble possibly undergoes destruction. The dissipation curves are shown in Fig. 8.7d. For lower pressures $Cd > Ld > Rd = Td$; however, due to the faster growth of Rd compared to other dissipation mechanisms, it supersedes Td at about 40 kPa and becomes equal to Ld when Pd takes place. When the P2 oscillations with higher amplitude emerge out of the chaotic window, the dissipation powers undergo a sharp increase with $Cd > Rd = Ld > Td$.

The case of sonication with $f = 0.8f_r$ (PDf_r) is presented in Fig. 8.7e. P1 oscillations undergo SN bifurcation to higher amplitude at $\approxeq 150kPa$ and at the same time the value of the red curve becomes equal to the maxima in the blue curve (indicating the wall velocity is in phase with the driving signal). Oscillations grow with pressure increase and at 410 kPa, Pd takes place leading to P2 oscillations until 500 kPa. Chaos is then generated through successive period doubling bifurcations at 510 kPa. For this frequency $Cd > Ld > Rd > Td$ in the studied pressure range. There is a sharp increase in the dissipation power when SN takes place. Furthermore concomitant with Pd, Cd, Ld and Rd decrease due to reduced wall velocities [32].

Fig. 8.7g displays the case of sonication with $f = f_r$. Initially value of the red curve is equal to the oscillation amplitude in the blue curve and above 100 kPa the two curve diverge (this is because f_r shifts to PDf_r as pressure increases [32] and when $f = f_r$ oscillations are only resonant at lower pressures) and Pd takes place at $\approxeq 480kPa$. P2 oscillations undergo successive Pds to chaos at 620 kPa. Chaos stretches beyond 1 MPa with oscillation amplitudes exceeding $\frac{R}{R_0} = 2$ at 700 kPa. The dissipated power curves are presented in Fig. 8.7h. Similar to the case of $f = 0.8f_r$, $Cd > Ld > Rd > Td$ and occurrence of Pd leads to a slight decrease in Cd, Rd and Ld.

Fig. 8.8a displays the case of sonication with $f = 1.2f_r$. The P1 oscillation amplitude increases with pressure and Pd occurs at about 570 kPa. A small period bubbling window takes place for $\approxeq 760 - 800kPa$ and initiation of chaos is at about 860 kPa. When chaos is initiated, $\frac{R}{R_0} > 2$. The corresponding power curves in Fig. 8.8b show that similar to the case of $f = 0.8f_r$ and f_r, $Cd > Ld > Rd > Td$ for $P_a < 760kPa$ where period bubbling takes place. Occurrence of Pd at 570 kPa is concomitant with a decrease in Cd, Ld and Rd and when bubbling occurs $Cd \approxeq Ld \approxeq Rd > Td$. Generation of sudden chaos at $\approx 880kPa$ is simultaneous with a sudden increase in Cd, Ld and Rd with $Cd > Ld > Rd > Td$ right after the onset of chaos.Further increases in pressure result in a faster growth in Rd making Rd $\approxeq$ Cd at $\approx$ 1.1 MPa.

Figure 8.8c shows the dynamics of the bubble in case of sonication with $f = 1.6f_r$ (Pdf_{sh}). P1 oscillation amplitude grow with pressure increase and at 580 kPa a SN bifurcation from P1 oscillations to P2 oscillations of higher amplitude takes place. P2 oscillations then grow with pressure increase and undergo further Pds. After a small window of P6-P12 oscillations chaos is generated. At 1.2 MPa oscillation amplitude exceeds 2 and possible bubble destruction may take place. The corresponding power graphs are depicted in Fig. 8.8d. $Cd > Ld \approxeq Rd > Td$ for $P_a < 800kPa$. Occurrence of the SN results in a sharp increase in Cd, Rd, Ld and Td with Td exhibiting the highest increase.

When $f = 2f_r$ (Fig. 8.8c) P1 oscillations undergo Pd at 400 kPa; P2 oscillations later evolve in a form of a bow-tie (Chapter 4) [58] (red curve) undergoing successive Pd to chaos. For P_a less than the pressure threshold of Pd, $Rd \approxeq Cd > Ld > Td$. When Pd occurs, Cd grows larger than Rd and Rd becomes equal to Ld. Td exhibits the largest growth when Pd occurs. During P2 oscillations Rd grows faster than other damping factors exceeding Ld at $\approxeq 900kPa$.

When $f = 3f_r$ (Fig. 8.8g) P1 oscillations undergo a SN bifurcation to P3 oscillations of higher

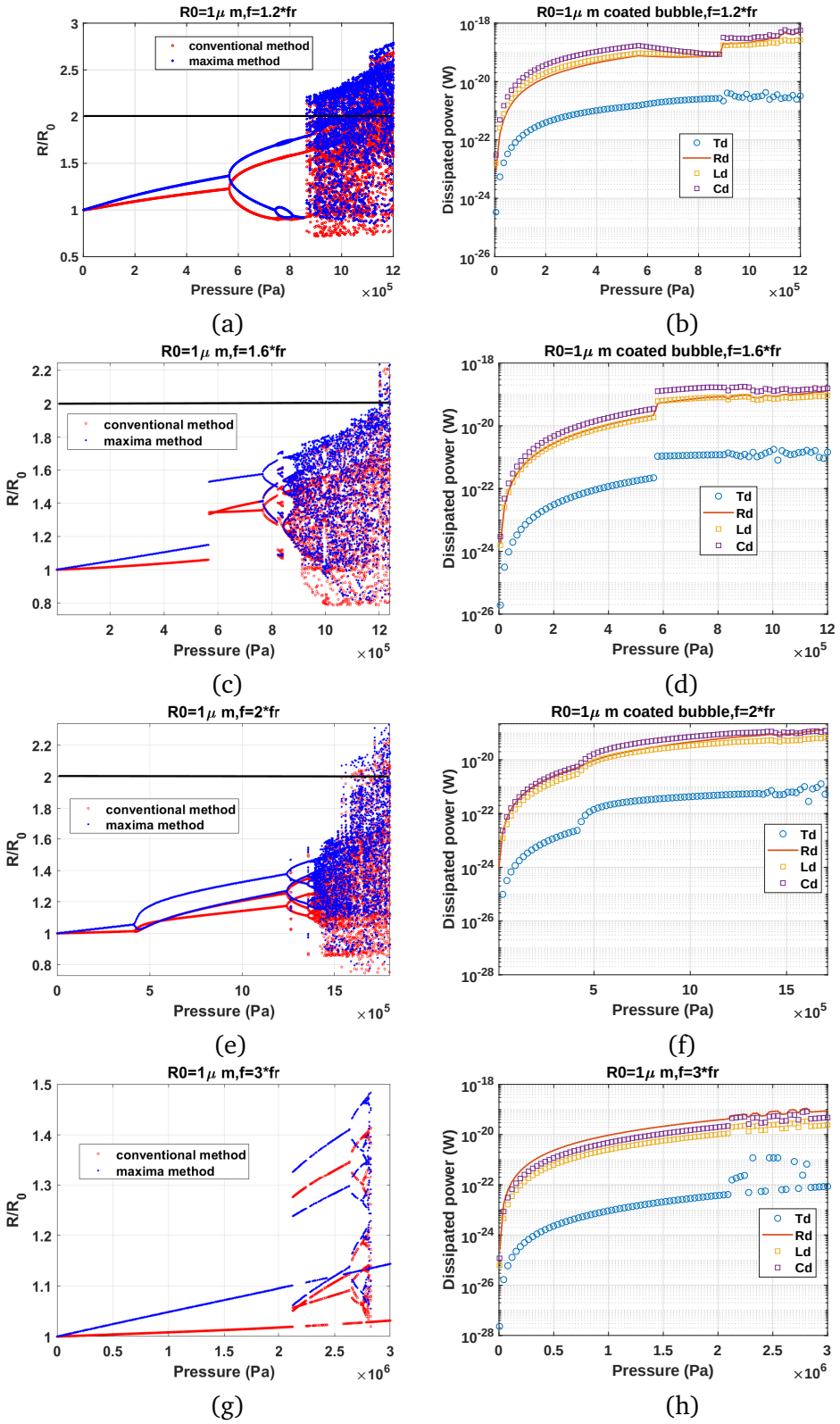

Figure 8.8: Bifurcation structure (left column) and the dissipated power as a function of pressure (right column) of the oscillations of a coated C3F8 bubble with $R_0 = 1\mu m$ for $f = 1.2f_r$ (a-b),$f = 1.6f_r$ (c-d), $f = 2f_r$ (e-f) & $f = 3f_r$ (g-h).

amplitude. Pressure increase results in an increase in the amplitude of the P3 oscillations and at $\approxeq 2.7MPa$ Pd takes place and oscillations become P12. Later through multiple Pds a small chaotic window appears which is followed by a sudden onset of P1 oscillations for the rest of the pressures studied here. The corresponding dissipated power graphs are shown in Fig. 8.8h. Rd is the strongest dissipated power for the studied pressure range here with $Rd > Cd > Ld > Td$. When SN takes place, similar to the case of $R_0 = 4\mu m$ all dissipated powers undergo a sharp increase; however, Td exhibits the largest growth potentially due to more surface area available for heat transfer.

8.4.3 Concluding graphs of $|\dot{R(t)}|_{max}$, $|P_{sc}|_{max}$, total dissipated power and STDR

In the previous subsection section we investigated the evolution of the Cd, Ld, Rd and Td as a function of pressure at different frequencies and related their changes to the nonlinear behavior of the bubble. In this section we consider only stable non-destructive bubble oscillations ($\frac{R_{max}}{R_0} \leq 2$ [57] and for a more thorough review on bubble destruction threshold please refer to [32]). Here we study maximum wall velocity amplitude ($|\dot{R(t)}|_{max}$), maximum amplitude of the re-radiated pressure ($|P_{sc}|_{max}$), total dissipated power ($W_{total} = Rd + Ld + Td + Cd$), scattering to dissipation ratio (STDR) when bubble is sonicated with the frequencies that are studied in Figs. 8.1-8.8 and for excitation pressures below the bubble destruction threshold. $|\dot{R(t)}|_{max}$ is abbreviated with V_m from here on for simplicity and $|P_{sc}|_{max}$ is abbreviated with P_m. $STDR = \frac{Rd}{Rd+Ld+Td+Cd}$ where Cd is equal to zero for the uncoated bubble.

Figure 8.9a plots V_m as a function of pressure for different frequencies for an uncoated air bubble with $R_0 = 10\mu m$. V_m is only presented for the oscillation regimes that most probably results in non-destructive bubble oscillations $\frac{R}{R_0} \leq 2$ [57]. Results show that when bubble is sonicated with $f = 0.5f_r$, V_m reaches the maximum value for non-destructive oscillations. This can have advantages in drug delivery applications since higher wall velocity results in faster streaming and lower frequency of oscillations leads to smaller values for the thickness of the boundary layer [63]. Since shear stress on the nearby objects is proportional to wall velocity and inversely proportional to the thickens of the boundary layer [64] sonication in this regime may result in higher shear stress values compared to other frequencies.

Fig. 8.9b shows P_m as a function of pressure for the studied frequencies in Figs. 8.1-8.2. Sonication

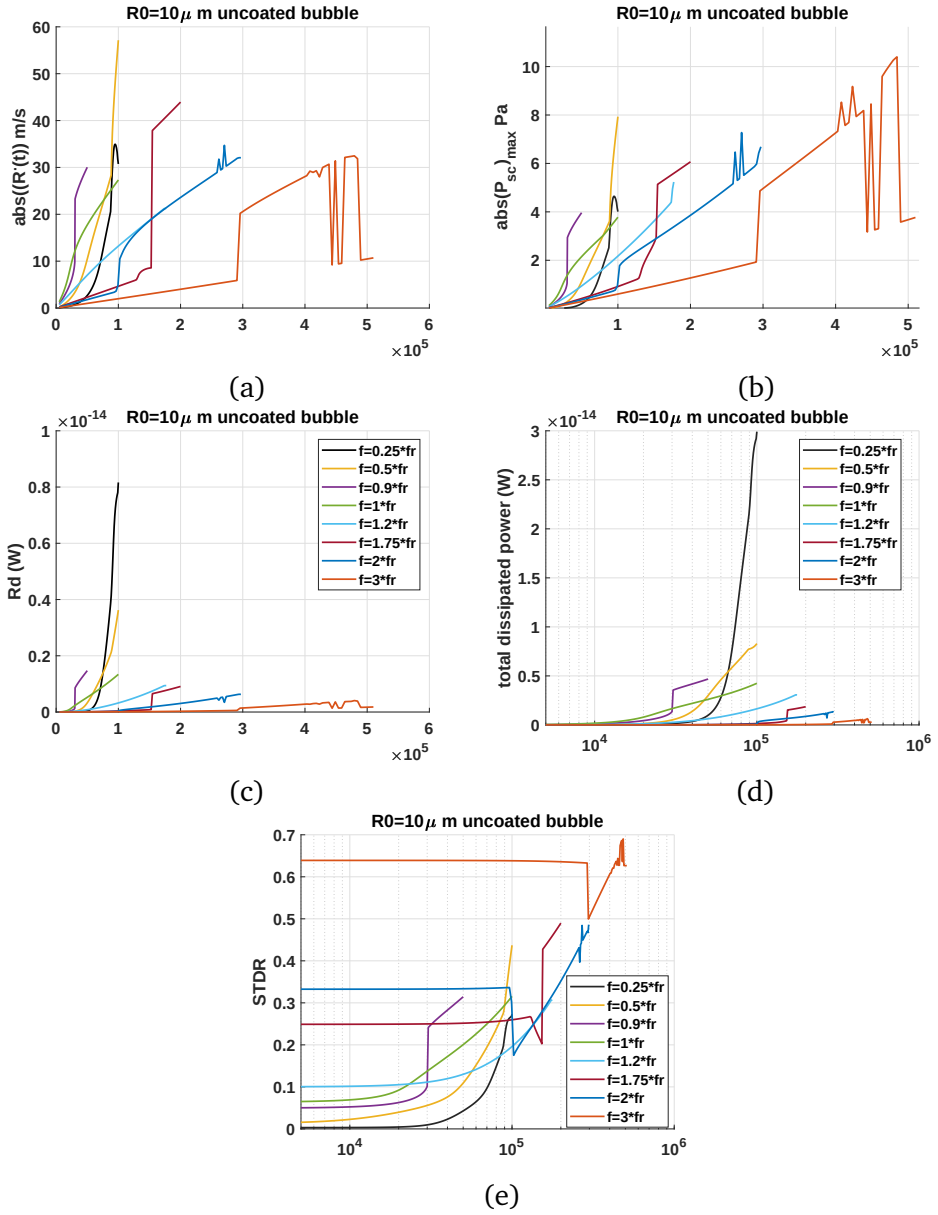

Figure 8.9: Nondestructive ($\frac{R}{R_0} \leq 2$) values of: a)$|\dot{R(t)}|_{max}$ (V_m), b) $|P_{sc}|_{max}$ (P_m), c)Rd, d)W_{total} and e)STDR as a function of pressure in the oscillations of an uncoated air bubble with $R_0 = 10\mu m$.

with $f = 3f_r$ leads to the highest P_m; thus if the goal of the application is to increase the absolute amplitude of P_{sc} and enhance echogenecity then sonication with $f = 3f_r$ and pressures above the pressure threshold for generation of P3 oscillations will be the optimized frequency and pressure.

Rd can be used as a measure for continuous bubble activity. In contrast to P_m which denotes the maximum spontaneous back-scattered (re-radiated) pressure, Rd is a measure of sustained bubble activity as it is averaged over time. Fig. 8.9c shows that the maximum non-destructive Rd occurs for $f = 0.25f_r$ and frequencies below resonance display the largest non-destructive Rd.

The total dissipated power ($W_{total} = Rd + Ld + Td$) is shown in Fig. 8.9d. Maximum dissipated power occurs for $f = 0.25f_r$. Sonication below resonance have the advantage of higher dissipated powers. This is useful in applications where bubbles are used to enhance the power deposition by ultrasound to increase the generated heating. Furthermore, when compared to $f = f_r$, below 100 kPa, the dissipated power is lower when $f = 0.3f_r$ and above 100 kPa the dissipated power undergoes a sharp increase and becomes approximately 4.8 times larger than the case of sonication with $f = f_r$. This has advantages in focused ultrasound heating enhancement; by taking advantage of the sharp pressure gradients of the focused ultrasound transducers, spatial heating prior to the focal point is limited and heating at the focal region can be enhanced.

Fig. 8.9e displays the STDR as a function of pressure. Frequencies above f_r have larger STDR; the higher the freqeuncy the larger is the STDR which leads to the maximum STDR at $f = 3f_r$. It is interesting to note that for frequencies above resonance the onset of non-linear oscillations results in a decrease in STDR; STDR then grows as pressure increases. This is mainly due to the increase in other damping parameters especially Td. As pressure increases, due to the faster growth rate of Rd, STDR raises again. Freqeuncies below resonance have lower STDRs compared to $f = f_r$. This is because of the increased Td and decreased Rd; however, the onset of SN bifurcation is concomittant with an increase in STDR for $f = 0.8f_r$ (PDfr) and $f = 0.5f_r$ (2nd SuH) oscillations.

Figure 8.10 represents the uncoated air bubble with $R_0 = 2\mu m$. The exact same behavior of the previous case ($R_0 = 10\mu m$) is observed here. Maximum non-destructive V_m and P_m occurs for $f = 0.5f_r$ (2nd SuH) and $f = 3f_r$ respectively. Maximum Rd and W_{total} are achieved when $f = 0.25f_r$ (3rd SuH). STDR is higher for higher frequencies with the maximum at $f = 3f_r$. Similar to Fig. 8.9e, the onset of nonlinear oscillations results in a decrease and then increase in STDR if the bubble is sonicated above resonance.

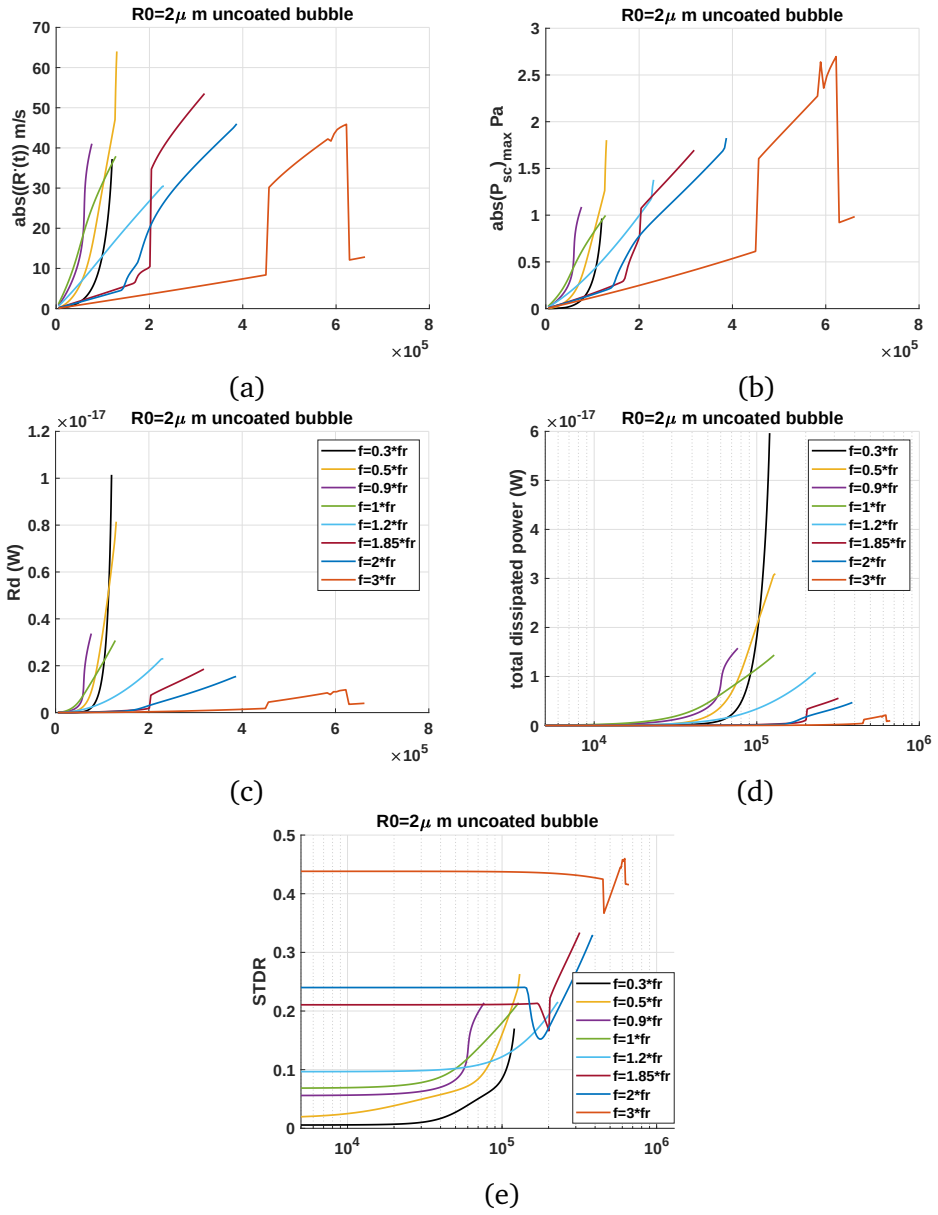

Figure 8.10: Nondestructive ($\frac{R}{R_0} \leq 2$) values of: a)$|\dot{R(t)}|_{max}$ (V_m), b) $|P_{sc}|_{max}$ (P_m), c)Rd, d)W_{total} and e)STDR as a function of pressure in the oscillations of an uncoated air bubble with $R_0 = 2\mu m$.

The case of the C3F8 coated bubble with $R_0 = 4\mu m$ is shown in Fig. 8.11. The same conclusions can be drawn as the two previous cases (Figs. 8.9 and 8.10). The case of the C3F8 coated bubble with $R_0 = 1\mu m$ is shown in Fig. 8.11. Same conclusions can be drawn as the three previous cases in (Figs. 8.9, 8.10 and 8.11).

8.5 Discussion and summary

Acoustic waves are highly dissipated when they pass through bubbly media. Dissipation by bubbles takes place through thermal damping (Td), radiation damping (Rd) and damping due to the friction of the liquid (Ld) and friction of the coating (Cd). Td, Rd, Ld and Cd are nonlinear and depend on the complex dynamics of the bubbles. The correct estimation of dissipation events in the bubble oscillations will help in optimizing the relevant applications by maximizing a desirable parameter. Most previous studies were limited by linear approximations [37, 66, 67, 68, 69, 70, 71]. These approximations lead to inaccurate estimation of the dissipation phenomenon in applications as they are only valid for low pressures and linear regimes of low amplitude oscillations. Despite the importance of understanding the nonlinear dissipation events; only a few recent studies have attempted to investigate the problem accounting for the full non-linearity of the subject [38,39,40, 41,46,47].

At present, the pressure dependence of the dissipation events is not well understood. Thus, in this paper we attempt to classify the bubble oscillations at various excitation frequencies as a function of pressure. Using a recent comprehensive approach [50, 56] in studying the nonlinear bubble dynamics we have classified the nonlinear oscillations of the uncoated and coated bubbles as a function of pressure excited with frequencies that result in 3rd and 2nd SuH regimes, pressure dependent (PD) resonance (f_r) oscillations, bubbles sonicate with f_r (linear resonance frequency), PD subharmonic (SH) resonance (PDf_{sh}), $\frac{1}{2}$ order SH resonance (f_{sh}) and $\frac{1}{3}$ order SH resonance ($f = 3f_r$). We have considered the nonlinear thermal and radiation effects in modeling the oscillations of the bubbles. Dynamics of the bubble including the generation of (2nd and 3rd order) SuH and ($\frac{7}{2}$ and $\frac{5}{2}$ order) UH oscillations, P1 resonant oscillations, cases of the occurrence of different types of giant resonances as well as different SH regimes of oscillations were revealed. Moreover, nonlinear dissipated powers due to Rd, Ld, Td and Cd were calculated and results were

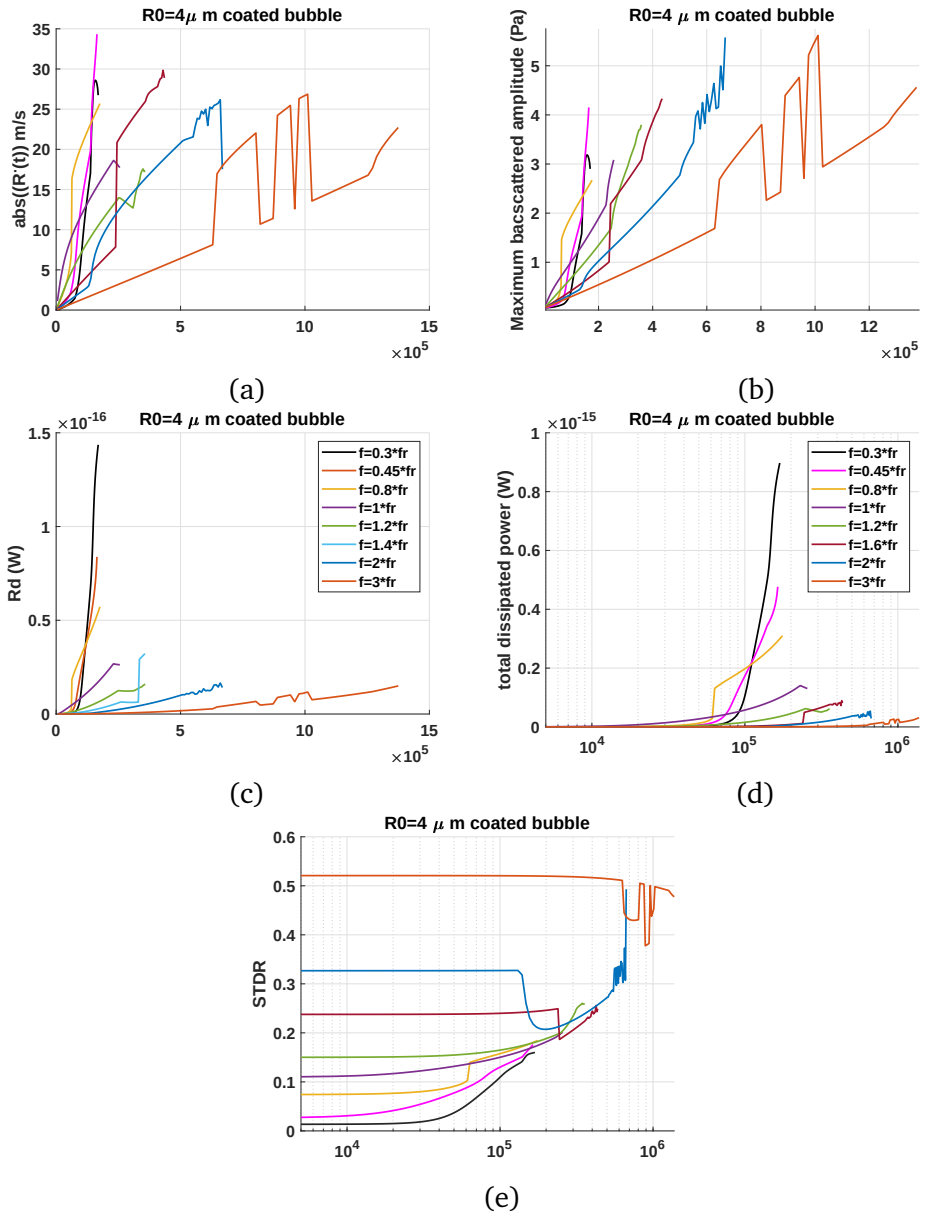

Figure 8.11: Nondestructive ($\frac{R}{R_0} \leq 2$) values of: a)$|\dot{R(t)}|_{max}$ (V_m), b) $|P_{sc}|_{max}$ (P_m), c)Rd, d)W_{total} and e)STDR as a function of pressure in the oscillations of a coated C3F8 bubble with $R_0 = 4\mu m$.

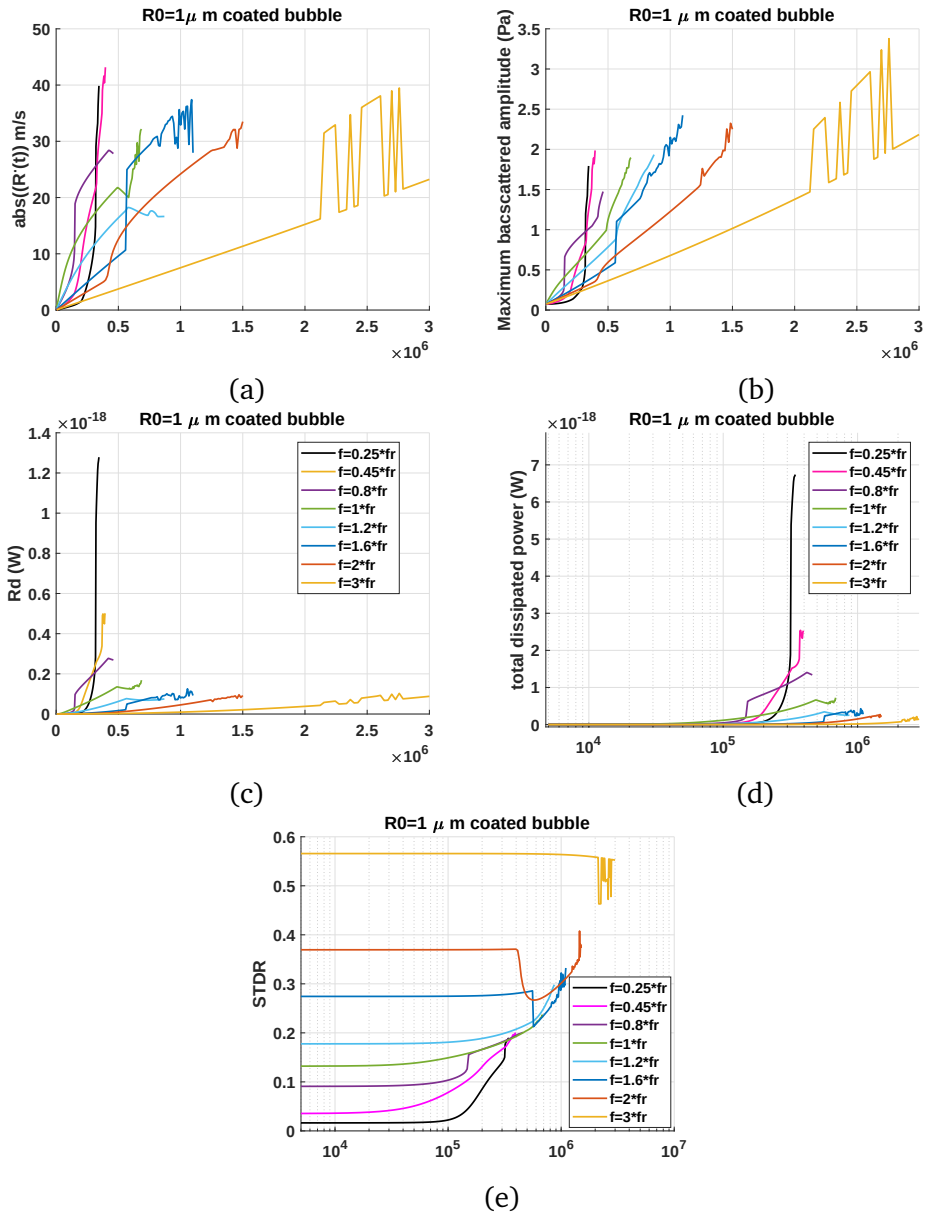

Figure 8.12: Nondestructive ($\frac{R}{R_0} \leq 2$) values of: a)$|\dot{R(t)}|_{max}$ (V_m), b) $|P_{sc}|_{max}$ (P_m), c)Rd, d)W_{total} and e)STDR as a function of pressure in the oscillations of a coated C3F8 bubble with $R_0 = 2\mu m$.

presented in tandem with the bifurcation curves. Using this approach different regimes of the evolution of the dissipative phenomena are linked to the responsible nonlinear effect in the bubble oscillations.

Our main results can be summarized as follows:

8.5.1 Classification of the main nonlinear regimes of oscillations and the corresponding dissipative powers

1- When a bubble (coated or uncoated) is sonicated with a frequency which is approximately between $\frac{f_r}{4}$ and $\frac{f_r}{3}$, and above a pressure threshold 3 maxima occur in the P1 oscillations. The third harmonic component of the backscattred pressure (P_{sc}) is larger than other frequency components. This is suitable for applications like SuH imaging [72, 73]. Above a second pressure threshold period doubling (Pd) takes place and oscillations become P2 with 6 maxima. At this point the $\frac{7}{2}$ UH component of the P_{sc} is larger than the SH and other UHs components of the signal. This frequency and pressure range is suitable for high resolution UH imaging [74, 75, 76] and passive cavitation mapping techniques [77]. Further pressure increases beyond this region most probably results in bubble destruction as $\frac{R}{R_0}$ exceeds 2. Pressure increase also result in the generation of chaos and periodic oscillations of higher amplitudes. At higher pressures a giant resonance (2nd order SuH) emerges out of the chaotic window. The corresponding evolution of the dissipative powers at different nonlinear regimes are summarized in table 2.

2- When $f \approxeq 0.4 - 0.6 f_r$ both of the cases of the coated and uncoated bubbles start with P1 oscillations and above a pressure threshold a second maxima occur in the P1 oscillations. This is simultaneous with a fast growth of the 2nd harmonic component of the P_{sc} (2nd harmonic component becomes the strongest frequency component in the spectra). This frequency and pressure range is suitable for 2nd harmonic imaging applications of ultrasound [72, 73]. Above a second pressure threshold Pd happens and oscillations become P2 with 4 maxima. At this point between the SH and UH components of the frequency spectrum of the P_{sc}, the $\frac{5}{2}$ has the highest amplitude. This can be used to enhance contrast and resolution in UH imaging applications of ultrasound [74,75,76] and passive cavitation mapping techniques [77] or high resolution treatment

Dissipation mechanisms when $f = 0.25 - 0.35 f_r$					
Oscillation shape	Linear	P1(3 maxima)	P2(6 maxima)	chaos	giant 2nd SuH resonance
Oscillation type	fundamental	3rd SuH	$\frac{7}{2}$ UH	broadband	P1/p2
Uncoated air bubble with $R_0 = 10\mu m$	$Td > Ld > Rd$	$Td > Rd = Ld$	$Td = Rd > Ld$	$Rd > Td > Ld$	$Rd > Ld > Td$
Uncoated air bubble with $R_0 = 2\mu m$	$Td \approxeq Ld > Rd$	$Td \approxeq Ld \approxeq Rd$	$Ld \approxeq Rd > Td$	$Rd > Ld > Td$	$Rd > Ld > Td$
coated C3F8 bubble with $R_0 = 4\mu m$	$Cd > Ld \approxeq Td > Rd$	$Cd > Ld \approxeq Rd > Td$	$Cd > Rd \approxeq Ld > Td$	$Cd \approxeq Rd > Ld > Td$	$Rd > Cd > Ld > Td$
coated C3F8 bubbles with $R_0 = 4\mu m$	$Cd > Ld > Td > Rd$	$Cd > Ld > Rd > Td$	$Cd > Rd \approxeq Ld > Td$	$Cd \approxeq Rd > Ld > Td$	$Rd > Cd > Ld > Td$

Table 8.2: Evolution of dissipation powers at different nonlinear regimes for uncoated air and coated C3F8 bubbles when $f = 0.25 - 0.3 f_r$

monitoring using UH emissions [78]. Further pressure increase results in chaos and $\frac{R}{R_0}$ exceeding 2. Pressure increase beyond this point leads to emergence of a P1 giant resonance out of the chaotic window. The corresponding evolution of the dissipative powers at different nonlinear regimes are summarized in table 3.

3- When $f = 0.7 - 0.9 f_r$ (the pressure dependent resonance frequency (PDf_r (Chapter 2) [32])), at lower pressures oscillations are P1 with 1 maximum. Above a pressure threshold, a saddle node (SN) bifurcation takes place and P1 oscillations undergo a large increase in amplitude to another P1 oscillation with 1 maximum. Higher amplitude oscillations after the SN are resonant at this frequency as the maxima curve and the conventional curve has the same value (the wall velocity is in phase with the excitation force). The conventional and maxima curve diverge from each other as pressure increases beyond the SN. The occurrence of the SN can have significant advantages in imaging techniques based on amplitude modulation [32, 74, 79, 80]. Beyond the SN, the increase in excitation pressure leads to a monotonic increase in oscillation amplitude and above a second pressure threshold Pd takes place and oscillations become P2 with 2 maxima.

Dissipation mechanisms when $f = 0.45 - 0.55 f_r$					
Oscillation shape	Linear	P1(2 maxima)	P2(4 maxima)	chaos	P1 giant resonance
Oscillation type	fundamental	2nd SuH	$\frac{5}{2}$ UH	broadband	P1/P2
Uncoated air bubble with $R_0 = 10\mu m$	$Td > Ld > Rd$	$Td > Rd \approxeq Ld$	$Td \approxeq Rd > Ld$	$Rd > Td > Ld$	$Rd > Ld > Td$
Uncoated air bubble with $R_0 = 2\mu m$	$Td \approxeq Ld > Rd$	$Td \approxeq Ld > Rd$	$Ld \approxeq Rd > Td$	$Rd > Ld > Td$	$Rd > Ld > Td$
coated C3F8 bubble with $R_0 = 4\mu m$	$Cd > Ld \approxeq Td > Rd$	$Cd > Ld \approxeq Rd > Td$	$Cd > Rd \approxeq Ld > Td$	$Cd > Rd > Ld > Td$	$Rd \approxeq Cd > Ld > Td$
coated C3F8 bubble with $R_0 = 1\mu m$	$Cd > Ld > Td > Rd$	$Cd > Ld > Rd > Td$	$Cd > Rd \approxeq Ld > Td$	$Cd > Rd > Ld > Td$	$Rd \approxeq Cd > Ld > Td$

Table 8.3: Evolution of dissipation powers at different nonlinear regimes for uncoated air and coated C3F8 bubbles when $f = 0.45 - 0.55 f_r$.

Apart from the coated bubble with $R_0 = 1\mu m$, other studied bubbles in this frequency range most probably destroyed as $\frac{R_{max}}{R_0}$ exceeds 2 before any P2 is generated. Further pressure increase leads to successive Pds to chaos with a possible window (of P3/P6 oscillations with 3/6 maxima) which is located inside chaotic window. At higher pressures a P2 giant resonance may emerge out of the chaotic window. The corresponding evolution of the dissipative powers at different nonlinear regimes are summarized in table 4.

4- When $f = f_r$ (linear resonance frequency of the bubbles) oscillations are P1 with 1 maxima at lower pressures. At the beginning of the bifurcation diagrams; the curve that is constructed with the method of peaks has the exact value as the conventional method. This indicates that the wall velocity is in phase with the driving signal and oscillations are resonant. As the pressure increases the two curves start diverging as the resonance frequency changes with pressure. At higher pressures resonance frequency shifts to smaller values [32] (Pdf_r). Above a pressure threshold, bubbles undergo Pd and oscillations become P2 with two maxima. For coated bubbles when, Pd can occur when $\frac{R_{max}}{R_0} < 2$ (bubbles may sustain non-destructive oscillations); however, in case of uncoated bubbles Pd only occurs when $\frac{R_{max}}{R_0} > 2$ (uncoated bubbles may not sustain

Dissipation mechanisms when $f = 0.7 - 0.9 f_r$					
Oscillation shape	Linear	SN-P1(1 maxima)	P2(2 maxima)	chaos	P2 giant resonance
Oscillation type	fundamental (F)	2nd SuH/F	$\frac{3}{2}$ UH/ $\frac{1}{2}$ SH	broadband	P1/P2
Uncoated air bubble with $R_0 = 10\mu m$	$Td > Ld > Rd$	$Td > Rd \approxeq Ld$	$Td \approxeq Rd > Ld$	$Rd > Td > Ld$	$Rd > Ld > Td$
Uncoated air bubble with $R_0 = 2\mu m$	$Td \approxeq Ld > Rd$	$Td \approxeq Ld > Rd$	$Ld \approxeq Rd > Td$	$Rd > Ld > Td$	$Rd > Ld > Td$
coated C3F8 bubble with $R_0 = 4\mu m$	$Cd > Ld > Rd > Td$	$Cd > Ld \approxeq Rd > Td$	$Cd > Rd > Ld > Td$	$Cd > Rd > Ld > Td$	$Rd \approxeq Cd > Ld > Td$
coated C3F8 bubble with $R_0 = 1\mu m$	$Cd > Ld > Rd > Td$	$Cd > Ld > Rd > Td$	$Cd > Ld > Rd > Td$	$Cd > Rd > Ld > Td$	$Rd \approxeq Cd > Ld > Td$

Table 8.4: Evolution of dissipation powers at different nonlinear regimes for uncoated air and coated C3F8 bubbles when $f = 0.7 - 0.9 f_r$.

non-destructive P2 oscillations when they are sonicated with their f_r). The two main routes of Pd has been extensively studied in our previous work [58] without the inclusion of thermal damping effects. P2 oscillations undergo successive Pd to chaos. At higher pressures a P2 (with two maxima) giant resonance may emerge out of the chaotic window. The giant resonance oscillations undergo successive Pds to chaotic oscillations of higher amplitude. The corresponding evolution of Cd, Rd, Ld and Td are summarized in table 5.

5- When $f = 1.2 f_r$, at lower excitation pressures, oscillations are P1 with 1 maximum. Contrary to the case of $f = f_r$, the conventional curve and the curve constructed by method of peaks start diverging right at the beginning of the bifurcation diagram. Increasing pressure leads to Pd and oscillations becomes P2 with two maxima. At this frequency P2 oscillations can be non-destructive (in case of both coated and uncoated bubbles) as when Pd occurs since $\frac{R_{max}}{R_0}$ is below 2. Sonication with this frequency and in pressure ranges responsible for P2 oscillations may lead to $\frac{3}{2}$ UH resonant oscillations. Further pressure increase results in successive Pds to chaos. At higher pressures a P2 giant resonance may emerge out of the chaotic window, undergoing successive Pds to chaotic

Dissipation mechanisms when $f = f_r$					
Oscillation shape	Linear resonance	Linear	P2(2 maxima)	chaos	P2 giant resonance
Oscillation type	fundamental	fundamental	$\frac{3}{2}$ UH/$\frac{1}{2}$ SH	broadband	$\frac{1}{2}$ SH &$\frac{3}{2}$ UH
Uncoated air bubble with $R_0 = 10\mu m$	$Td > Ld > Rd$	$Td > Rd \approxeq Ld$	$Td \approxeq Rd > Ld$	$Rd > Td > Ld$	$Rd > Ld > Td$
Uncoated air bubble with $R_0 = 2\mu m$	$Td > Ld > Rd$	$Ld > Rd$	$Ld \approxeq Rd > Td$	$Rd > Ld > Td$	$Rd > Ld > Td$
coated C3F8 bubble with $R_0 = 4\mu m$	$Cd > Ld > Rd > Td$	$Cd > Ld \approxeq Rd > Td$	$Cd > Rd > Ld > Td$	$Cd > Rd > Ld > Td$	$Rd \approxeq Cd > Ld > Td$
coated C3F8 bubble with $R_0 = 1\mu m$	$Cd > Ld > Rd > Td$	$Cd > Ld > Rd > Td$	$Cd > Ld > Rd > Td$	$Cd > Rd > Ld > Td$	$Rd \approxeq Cd > Ld > Td$

Table 8.5: Evolution of dissipation powers at different nonlinear regimes for uncoated air and coated C3F8 bubbles when $f = f_r$.

oscillations of higher amplitude. The lower amplitude branch of the curve that is generated by the method of peaks has the same value as the higher amplitude branch of the curve created by the conventional method. This is suggests that wall velocity is in phase with excitation frequency once every two acoustic cycles. The corresponding evolution of the dissipative powers are summarized in table 6.

6- When $f = 1.6 - 1.8 f_r$ (pressure dependent subharmonic (SH) resonance frequency PDf_{sh} Chapter 5 [58]) at lower pressures oscillations are P1 with 1 maxima. Pressure increase leads to one of the following scenarios: 1- generation of Pd above a pressure threshold; then, a SN bifurcation from P2 oscillations of lower amplitude to P2 oscillations (1 maximum) of higher amplitude. 2- SN bifurcation above a pressure threshold from P1 oscillations with 1 maxima to P2 oscillations with 1 maxima. This happens while $\frac{R_{max}}{R_0}$ is below 2; therefore, the bubbles may sustain non-destructive P2 oscillations when insonated with frequencies $f = 1.6 - 1.8 f_r$. Further pressure increases lead to the generation of a second maximum (with the same amplitude of the higher branch of the conventional curve). Occurrence of the SN can provide significant advantages for amplitude modulation techniques [78, 79, 80] and in this case because of the higher sonication

Dissipation mechanisms when $f = 1.2f_r$					
Oscillation shape	Linear	Linear	P2(2 maxima)	chaos	chaos/P2 giant resonance
Oscillation type	fundamental	fundamental	$\frac{3}{2}$ UH/$\frac{1}{2}$ SH	broadband	broadband/$\frac{1}{2}$ SH &$\frac{3}{2}$ UH
Uncoated air bubble with $R_0 = 10\mu m$	$Td > Ld \approxeq Rd$	$Td > Rd > Ld$	$Td > Rd > Ld$	$Rd \approxeq Td > Ld$	$Rd > Ld > Td$
Uncoated air bubble with $R_0 = 2\mu m$	$Td > Ld > Rd$	$Ld > TD > Rd$	$Ld > Td > Rd$	$Ld \approxeq Rd > Td$	$Rd > Ld > Td$
coated C3F8 bubble with $R_0 = 4\mu m$	$Cd > Ld > Rd > Td$	$Cd > Ld \approxeq Rd > Td$	$Cd > Rd > Ld > Td$	$Cd > Rd > Ld > Td$	$Cd \approxeq Rd > Ld > Td$
coated C3F8 bubble with $R_0 = 1\mu m$	$Cd > Ld > Rd > Td$	$Cd > Ld > Rd > Td$	$Cd > Ld > Rd > Td$	$Cd > Rd > Ld > Td$	$Rd \approxeq Cd > Ld > Td$

Table 8.6: Evolution of dissipation powers at different nonlinear regimes for uncoated air and coated C3F8 bubbles when $f = 1.2f_r$.

frequency, we can expect higher resolution. Moreover, we have shown in [59] that occurrence of SN leads to oversaturation of the $\frac{1}{2}$ SH and $\frac{3}{2}$ UH frequency content of the P_{sc}. This can provide higher contrast to tissue and signal to noise ratio in SH imaging techniques [81,82,83] and possibly SH and UH monitoring of treatments [77,78,84,85]. Oscillations undergo successive Pds to chaos. Further pressure increase may lead to the emergence of a P3 giant resonance which will undergo successive Pds to chaotic oscillations of higher amplitude. The dynamics of the bubble sonicated with their PDf_{sh} (in the absence of thermal damping) has been extensively studied in our previous work [59]. The corresponding evolution of dissipative powers are summarized in table 7.

7- when $f = 2f_r$ (linear SH resonance frequency f_{sh} [58]) oscillations are P1 with 1 maximum at lower pressures. Above a pressure threshold Pd takes place and oscillations become P2 with 2 maxima. As pressure increases one of the maxima disappears with pressure increase and the P2 oscillations evolve in the form of a bowtie (the curve that is constructed using the conventional method). Later the second maxima re-appears with an amplitude equal to the higher branch of the conventional curve. Oscillations undergo successive Pds to chaos. When $f = 2f_r$, P2

Dissipation mechanisms when $f = 1.6 - 1.8 f_r$					
Oscillation shape	Linear	P2 through SN	P4(4 maxima)	chaos	chaos/P3 giant resonance(Gf_r)
Oscillation type	fundamental	$\frac{1}{2}$ SH/$\frac{3}{2}$ UH	$\frac{1}{4}, \frac{1}{2}, \frac{3}{4} SH$&UHs	broadband	P1/P2
Uncoated air bubble with $R_0 = 10\mu m$	$Td > Rd > Ld$	$Rd > TD > Ld$	$Rd > Td > Ld$	$Rd > Td > Ld$	$Rd > Ld > Td(Gf_r)$
Uncoated air bubble with $R_0 = 2\mu m$	$Td \approxeq Ld > Rd$	$Ld > Rd > Td$	$Ld \approxeq Rd$¿Td	$Ld \approxeq Rd > Td$	$Rd > Ld > Td$
coated C3F8 bubble with $R_0 = 4\mu m$	$Cd > Rd > Ld > Td$	$Cd > Rd > Td$	$Cd > Ld \approxeq Rd > Ld > Td$	$Cd > Rd > Ld > Td$	$Cd \approxeq Rd > Ld > Td$
coated C3F8 bubble with $R_0 = 1\mu m$	$Cd > Ld \approxeq Rd > Td$	$Cd > Ld \approxeq Rd > Td$	$Cd > Ld \approxeq Rd > Td$	$Cd > Ld \approxeq Rd > Td$	$Cd > Rd > Ld > Td$

Table 8.7: Evolution of dissipation powers at different nonlinear regimes for uncoated air and coated C3F8 bubbles when $f = 1.6 - 1.8 f_r$.

oscillations occur for the widest excitation pressure range and $\frac{R_{max}}{R_0}$ is below 1.5; therefore, bubbles have the highest probability of sustaining non-destructive P2 oscillations. Analytical solutions [86,87,88,89,90,91] predict the generation of P2 oscillations at the lowest pressure threshold when the bubble is sonicated with $f = 2f_r$. Later, it was shown in [92,93] in case of smaller bubbles (e.g. $R_0 = 0.6\mu m$) that the lowest pressure threshold occurs when bubble is sonicated with a frequency near its f_r. They concluded that the increased damping is responsible for shift the lowest frequency threshold. However, none of the previous studies included both of the pressure dependent thermal and radiation damping effects. In this work, we have included both of these effects with their full non-linearity and observed that the lowest pressure threshold of P2 oscillations occurs at none of the $f = f_r$ or $f = 2f_r$, but it occurs at frequencies below $PDF f_r$. As an instance, for the uncoated air bubble $R_0 = 10\mu m$ pressure thresholds for P2 oscillations are 87.5, 82, 88, 170 and 96kPa respectively at f=0.25, 0.35, 0.5, 1 and $2f_r$. Thus for this bubble lowest P2 pressure threshold is $0.35 f_r$. This may be explained with the increased damping effects due to thermal damping and pressure dependent non-linear coupling. The study of the lowest pressure threshold for P2 oscillations and the reasons behind it is not within the scope of this paper and can be the subject of future studies. The corresponding evolution of dissipation powers are summarized in table 8.

Dissipation mechanisms when $f = 2f_r$					
Oscillation shape	Linear	P2 through SN	P4(4 maxima)	chaos	chaos/P3 giant resonance(Gf_r)
Oscillation type	fundamental	$\frac{1}{2}$ SH/$\frac{3}{2}$ UH	$\frac{1}{4}, \frac{1}{2}, \frac{3}{4} SH\&$UHs	broadband	P1/P2
Uncoated air bubble with $R_0 = 10\mu m$	$Td > Rd > Ld$	$TD > Rd > Ld$	$Td \approxeq Rd > Ld$	$Td \approxeq Rd > Ld$	$Rd > Ld > Td(Gf_r)$
Uncoated air bubble with $R_0 = 2\mu m$	$Td \approxeq Ld > Rd$	$Td \approxeq Ld > Rd$	$Ld \approxeq Rd$¿Td	$Ld \approxeq Rd > Td$	$Rd > Ld > Td$
coated C3F8 bubble with $R_0 = 4\mu m$	$Cd > Rd > Ld > Td$	$Cd > Rd > Ld > Td$	$Cd > Rd > Ld > Td$	$Cd \approxeq Rd > Ld > Td$	$Rd > Cd > Ld > Td$
coated C3F8 bubble with $R_0 = 1\mu m$	$Cd \approxeq Rd > Ld > Td$	$Cd > Ld \approxeq Rd > Td$	$Cd > Rd > Ld > Td$	$Cd \approxeq Rd > Ld > Td$	$Cd \approxeq Rd > Ld > Td$

Table 8.8: Evolution of dissipation powers at different nonlinear regimes for uncoated air and coated C3F8 bubbles when $f = 2f_r$.

8- When $f = 3f_r$ oscillations are P1 with 1 maximum at lower pressures. Oscillation amplitude grow very slowly withe the excitation pressure increase and above a pressure threshold P3 oscillations of higher amplitude are generated through a SN bifurcation. Later P3 oscillations undergo Pd to P12 followed by successive Pds to a small chaotic window before the oscillations convert to P1 with lower amplitude. The corresponding evolution of the dissipative powers is summarized in table 9. The SN bifurcation is concomitant with a sharp increase in P_{sc}. This has advantages for amplitude modulation imaging techniques [74, 79, 80] at higher frequencies [94]. The pressure amplitudes for the pulses shoudl be chosen below and above the SN pressure.

9- within the pressure ranges that were investigated here, occurrence of the giant resonances were in the form of a large amplitude periodic oscillations that emerge out of the chaotic window at higher pressures. These oscillations were concomitant with a sharp increase in Rd, Ld and Cd (in case of coated bubbles) and at the same time concomitant with a decrease in Td. This implies that oscillations have larger wall velocity amplitudes and acceleration; moreover due to the larger instantaneous changes of the R_{max} to R_{min} higher core temperatures are expected. The faster

Dissipation mechanisms when $f = 3f_r$					
Oscillation shape	Linear	P3 through SN	P6(6 maxima)	chaos	linear
Oscillation type	fundamental	$\frac{1}{3}$ & $\frac{2}{3}$ SH&$\frac{3}{4}$UHs	$\frac{1}{6}$, $\frac{1}{3}$&..SHs&higher order UHs	broadband	fundamental
Uncoated air bubble with $R_0 = 10\mu m$	$Rd > Td > Ld$	$Rd > Td > Ld$	$Rd > Td > Ld$	$Rd > Td > Ld$	$Rd > Td > Ld$
Uncoated air bubble with $R_0 = 2\mu m$	$Rd > Ld > Td$	$Rd \approxeq Ld > Td$	$Rd > Ld > Td$	$Rd > Ld > Td$	$Rd > Ld > Td$
coated C3F8 bubble with $R_0 = 4\mu m$	$Rd > Cd > Ld > Td$	$Cd > Rd > Ld > Td$	$Cd > Rd > Ld > Td$	$Cd \approxeq Rd > Ld > Td$	$Rd \approxeq Cd > Ld > Td$
coated C3F8 bubble with $R_0 = 1\mu m$	$Rd > Cd > Ld > Td$	$Rd > Cd > Ld > Td$	$Rd > Cd > Ld > Td$	$Rd > Cd > Ld > Td$	$Rd > Cd > Ld > Td$

Table 8.9: Evolution of dissipation powers at different nonlinear regimes for uncoated air and coated C3F8 bubbles when $f = 3f_r$.

collapses and rebound in these oscillation regimes leaves very little time for heat transfer thus Td decreases. This approach has advantages for sonochemical applications of ultrasound as higher core temperatures are achieved and thermal loss is decreased.

8.5.2 $|\dot{R(t)}|_{max}$, $|P_{sc}|_{max}$, Rd, W_{total} and STDR during non-destructive $\frac{R_{max}}{R_0} \leq 2$ and their possible applications

In this section we summarize some important parameters related to the bubble behavior and link them to possible medical and sonochemical applications. These parameters are extracted for excitation pressures that leads to non-destructive regime of oscillations ($\frac{R_{max}}{R_0} \leq 2$) and for excitation frequency range of $f = 0.25f_r - 3f_r$.

1- The maximum wall velocity amplitude ($|\dot{R(t)}|_{max}$) was the largest for the bubbles that were sonicated with $f = 0.45 - 0.5f_r$. Higher wall velocities results in faster micro-streaming. The shear stress induced by bubbles on nearby objects is proportional to the micro-streaming velocity and to the thickness of the boundary layer [63, 64, 96]. The thickness of the boundary layer is inversely proportional to frequency [63, 64, 96]. Thus, sonication with $f = 0.45 - 0.5f_r$ not only can produce the highest non-destructive micro-streaming, but it also has a small boundary layer. Sonication in

this frequency range may therefore enhance the shear stress and drug delivery efficacy. Moreover, non-destructive and non-inertial high shear stresses in this frequency may enhance the surface cleaning [97, 98, 99] while avoiding damage to delicate micro-structures (e.g. semi-conductor industry, optical devices & precision apparatus) usually stemming from violent inertial collapse of bubbles [98, 99]. Quantification of the shear stress at various non-linear regimes is a complex task and is the subject of future studies.

2- The maximum amplitude of the back-scattred pressure ($|P_{sc}|_{max}$) from bubbles was the largest for bubbles sonicated with $3f_r$. Echogencity of the ultrasound images is directly proportional to $|P_{sc}|_{max}$. Thus, in applications like B-Mode imaging [82] using contrast agents, higher frequencies ($f = 1.6 - 3f_r$) may be desired. However, one must also note that the higher $|P_{sc}|_{max}$ occurs at a higher pressure for $f = 3f_r$; thus, the signal intensity from the background tissue can be higher. In the absence of any non-linear signal acquisition (as an instance amplitude modulation [74, 79, 80] or phase inversion [100]) that suppresses the tissue response in the final image, the effect of higher scattering from tissue at higher pressures should also be considered. On the other hand the abrupt increase in the $|P_{sc}|_{max}$ of the bubble when SN bifurcation takes place (e.g. at $f = 1.6f_r$ or $f = 3f_r$ (Fig. 8.12b)) can be used to increase the residual signal in amplitude modulation techniques and increase the contrast to tissue ratio and signal to noise ratio. In amplitude modulation technique two pulses are sent to the target with different amplitudes. The received signals from the target are then scaled and subtracted; due to the linear tissue response the two signals cancel each other after subtraction. However, the nonlinear response of the bubbles with respect to increase in pressure results in a considerable residue which leads to enhanced CTR. Another application for the non-inertial higher P_{sc} can be in drug delivery or surface cleaning. The increased pressure radiated by the bubbles can increase the permeability [96] of the cells or objects in their vicinity and contribute to the drug delivery enhancement or cleaning.

3- Rd and W_{total} were maximum for bubbles that were sonicated with $0.25 - 0.3f_r$. Higher Rd and W_{total} are of great importance for applications related to bubble enhanced heating in high intensity focused ultrasound (HIFU) [30, 101, 102] and ultrasound thermal therapies and hyperthermia. Enhanced heating is of particular interest especially in cases like liver and brain where there is strong cooling of tissue due to high blood perfusion and the presence of skull [103] and rib cage limits the amount of ultrasound energy that can be delivered to target. In [104], it was shown

that enhancing the deposited power by increasing the wave dissipation or enhancing the pressure amplitude can decrease the effect blood flow cooling until full necrosis takes place. Sonication with $f = 0.25 - 0.3f_r$ can provide Rd and W_{total} of at least 6 times greater when compared to the case of sonication with f_r. Moreover, the higher frequency component of the P_{sc} signal (e.g. 3rd SuH, $\frac{7}{2}$ UHs) increases the absorption of the Rd in tissue and furthermore enhances the localized heating. Another advantage of sonication with $f = 0.25 - 0.3f_r$ is that Rd and W_{total} are very small for low pressures; however, above a pressure threshold (concomitant with the generation of UHs and SHs in the P_{sc}) Rd and W_{total} significantly increase. This finding is in line with experimental observation [30], where enhanced heating was concomitant with SH and UH emissions and broadband noise. The lower dissipation of acoustic waves below the pressure threshold leads to minimum enhanced heating and wave dissipation in the pre-focal tissue [32, 105, 106, 107, 108]. This allows higher energy delivery for bubbles in the target (especially in cases where delivery of higher acoustic energy is challenging) and enhances the safety of the treatment as the off-target bubble activity is minimized. Moreover, the generation of UHs at the target can be used to monitor and control the treatment using methods like passive cavitation detection [77, 85]. W_{total} and Rd were minimum for higher frequencies $f = 1.6 - 3f_r$. Thus, in addition to higher P_{sc} which leads to higher echogenecity in ultrasonic imaging, sonication with these frequencies results in lower heating due to bubble activity. This is another reason why higher frequencies may be more suitable for contrast enhanced ultrasound imaging. Moreover, enhanced absorption (W_{total}) in the target can be used to shield [34] structures with higher ultrasound attenuation (as an instance post-target bone [104] in brain).

4- The STDR as a function of pressure is nonlinear. The highest STDR belongs to $f = 3f_r$. In the absence of super-harmonic resonance, generation of SHs and UHs are concomitant with a decrease in STDR. As it was discussed in previous sections for $f = 1.6 - 3f_r$, Td undergoes a large increase when SHs are generated which consequently leads to a decrease in STDR. Despite the decrease, STDR still remains higher than $f < 2f_r$. The higher STDR have great advantages for contrast enhanced imaging. Higher STDR means bubble scatters more and dissipates less. This has consequences in increasing the echogenecity of the target and the underlying tissue. However, higher STDR by itself does not imply that a set of exposure parameters are suitable for imaging applications. As an instance when $f = 3f_r$ STDR is very high at lower pressures (e.g. 10 kPa);

however, at the same time P_{sc} is very small. This means that despite a high STDR, because of the weaker scattering by the bubble, the contrast signal may not be distinguishable from the background noise. Thus, STDR should be used in tandem with the P_{sc} and Rd curves to study the suitable exposure parameters for the relevant application.

8.6 conclusion

In this work we investigated the mechanisms of energy dissipation in bubble oscillations and their contribution to the total damping (W_{total}) at various nonlinear regimes of bubble oscillations. By using a comprehensive bifurcation analysis, we have classified the nonlinear dynamics of the bubbles and the corresponding dissipative mechanisms. The bifurcation structure of the uncoated and coated bubbles including the full thermal and radiation effects have been classified for the first time. Using our recently developed equations for energy dissipation in the oscillations of coated and uncoated bubbles [40, 41], the pressure dissipation mechanisms of ultrasonic energy were analyzed in detail. Results were presented in tandem with the bifurcation diagrams and several nonlinear features of dissipation phenomenon were revealed and classified. We have shown that by choosing suitable frequency and pressure a particular bubble related effect can be enhanced. Possible applications that could benefit from these oscillation regimes were presented.

8.7 Acknowledgments

The work is supported by the Natural Sciences and Engineering Research Council of Canada (Discovery Grant RGPIN-2017-06496), NSERC and the Canadian Institutes of Health Research (Collaborative Health Research Projects) and the Terry Fox New Frontiers Program Project Grant in Ultrasound and MRI for Cancer Therapy (project #1034). A. J. Sojahrood is supported by a CIHR Vanier Scholarship.

Bibliography

[1] Lauterborn, Werner, and Thomas Kurz. ”Physics of bubble oscillations.” Reports on progress in physics 73, no. 10 (2010): 106501.

[2] Parlitz, U., V. Englisch, C. Scheffczyk, and W. Lauterborn. ”Bifurcation structure of bubble oscillators.” The Journal of the Acoustical Society of America 88, no. 2 (1990): 1061-1077.

[3] Lauterborn, Werner, and Joachim Holzfuss. ”Acoustic chaos.” International Journal of bifurcation and Chaos 1, no. 01 (1991): 13-26.

[4] Holzfuss, Joachim, Matthias Rüggeberg, and Andreas Billo. ”Shock wave emissions of a sonoluminescing bubble.” Physical review letters 81, no. 24 (1998): 5434.

[5] Holzfuss, Joachim. ”Acoustic energy radiated by nonlinear spherical oscillations of strongly driven bubbles.” Proceedings of the Royal Society A: Mathematical, Physical and Engineering Sciences 466, no. 2118 (2010): 1829-1847.

[6] Dollet, Benjamin, Philippe Marmottant, and Valeria Garbin. ”Bubble dynamics in soft and biological matter.” Annual Review of Fluid Mechanics 51 (2019): 331-355.

[7] D’Onofrio, Mirko, Stefano Crosara, Riccardo De Robertis, Stefano Canestrini, and Roberto Pozzi Mucelli. ”Contrast-enhanced ultrasound of focal liver lesions.” American journal of roentgenology 205, no. 1 (2015): W56-W66.

[8] K. Ferrara, R. Pollard, and M. Borden, Ultrasound microbubble contrast agents: fundamentals and application to gene and drug delivery, *Annu. Rev. Biomed. Eng.* 9 (2007): 415-447.

[9] Schinkel, Arend FL, Mathias Kaspar, and Daniel Staub. ”Contrast-enhanced ultrasound: clinical applications in patients with atherosclerosis.” The international journal of cardiovascular imaging 32, no. 1 (2016): 35-48.

[10] C.C Coussios, et al. Role of acoustic cavitation in the delivery and monitoring of cancer treatment by high-intensity focused ultrasound (HIFU), *International Journal of Hyperthermia* 23(2) (2007) 105-120.

[11] M.A. O'Reilly and K. Hynynen, Blood-brain barrier: real-time feedback-controlled focused ultrasound disruption by using an acoustic emissions-based controller, *Radiology* 263, (2012)96–106

[12] K.J. Haworth, et al., Passive imaging with pulsed ultrasound insonations, *The Journal of the Acoustical Society of America*, 132(1) (2012) 544-553.

[13] Soluian, Stepan Ivanovich. Theoretical foundations of nonlinear acoustics. Consultants Bureau, 1977.

[14] Rivas, David Fernandez, Bram Verhaagen, James RT Seddon, Aaldert G. Zijlstra, Lei-Meng Jiang, Luc WM van der Sluis, Michel Versluis, Detlef Lohse, and Han JGE Gardeniers. "Localized removal of layers of metal, polymer, or biomaterial by ultrasound cavitation bubbles." Biomicrofluidics 6, no. 3 (2012).

[15] Maisonhaute, Emmanuel, Cesar Prado, Paul C. White, and Richard G. Compton. "Surface acoustic cavitation understood via nanosecond electrochemistry. Part III: Shear stress in ultrasonic cleaning." Ultrasonics sonochemistry 9, no. 6 (2002): 297-303..

[16] Ohl, Claus-Dieter, Manish Arora, Rory Dijkink, Vaibhav Janve, and Detlef Lohse. "Surface cleaning from laser-induced cavitation bubbles." Applied physics letters 89, no. 7 (2006): 074102.

[17] Roovers, Silke, Tim Segers, Guillaume Lajoinie, Joke Deprez, Michel Versluis, Stefaan C. De Smedt, and Ine Lentacker. "The role of ultrasound-driven microbubble dynamics in drug delivery: from microbubble fundamentals to clinical translation." Langmuir (2019).

[18] Kooiman, Klazina, Hendrik J. Vos, Michel Versluis, and Nico de Jong. "Acoustic behavior of microbubbles and implications for drug delivery." Advanced drug delivery reviews 72 (2014): 28-48.

[19] Marmottant, Philippe, and Sascha Hilgenfeldt. "Controlled vesicle deformation and lysis by single oscillating bubbles." Nature 423, no. 6936 (2003): 153.

[20] M.A. O'Reilly and K. Hynynen, Blood-brain barrier: real-time feedback-controlled focused ultrasound disruption by using an acoustic emissions-based controller, *Radiology* 263, (2012)96–106

[21] O'Reilly, Meaghan A., Adam C. Waspe, Milan Ganguly, and Kullervo Hynynen. "Focused-ultrasound disruption of the blood-brain barrier using closely-timed short pulses: influence of sonication parameters and injection rate." Ultrasound in medicine & biology 37, no. 4 (2011): 587-594.

[22] Pishchalnikov, Yuriy A., Oleg A. Sapozhnikov, Michael R. Bailey, James C. Williams Jr, Robin O. Cleveland, Tim Colonius, Lawrence A. Crum, Andrew P. Evan, and James A. McAteer. "Cavitation bubble cluster activity in the breakage of kidney stones by lithotripter shockwaves." Journal of endourology 17, no. 7 (2003): 435-446.

[23] Johnsen, Eric, and Tim Colonius. "Shock-induced collapse of a gas bubble in shockwave lithotripsy." The Journal of the Acoustical Society of America 124, no. 4 (2008): 2011-2020.

[24] Gong, Cuiling, and Douglas P. Hart. "Ultrasound induced cavitation and sonochemical yields." The Journal of the Acoustical Society of America 104, no. 5 (1998): 2675-2682.

[25] Suslick, Kenneth S. "Sonochemistry." science 247, no. 4949 (1990): 1439-1445.

[26] Suslick, Kenneth S., S. J. Doktycz, and E. B. Flint. "On the origin of sonoluminescence and sonochemistry." Ultrasonics 28, no. 5 (1990): 280-290.

[27] Mason, Timothy J., Larysa Paniwnyk, and J. P. Lorimer. "The uses of ultrasound in food technology." Ultrasonics sonochemistry 3, no. 3 (1996): S253-S260.

[28] Canavese, Giancarlo, Andrea Ancona, Luisa Racca, Marta Canta, Bianca Dumontel, Federica Barbaresco, Tania Limongi, and Valentina Cauda. "Nanoparticle-assisted ultrasound: a special focus on sonodynamic therapy against cancer." Chemical Engineering Journal 340 (2018): 155-172.

[29] Holt, R. Glynn, D. Felipe Gaitan, Anthony A. Atchley, and Joachim Holzfuss. "Chaotic sonoluminescence." Physical review letters 72, no. 9 (1994): 1376.

[30] Holt, R. Glynn, and Ronald A. Roy. "Measurements of bubble-enhanced heating from focused, MHz-frequency ultrasound in a tissue-mimicking material." Ultrasound in medicine & biology 27, no. 10 (2001): 1399-1412.

[31] Bouakaz, Ayache, Nico De Jong, and Christian Cachard. "Standard properties of ultrasound contrast agents." Ultrasound in medicine & biology 24, no. 3 (1998): 469-472.

[32] Sojahrood, Amin Jafari, Omar Falou, Robert Earl, Raffi Karshafian, and Michael C. Kolios. ”Influence of the pressure-dependent resonance frequency on the bifurcation structure and backscattered pressure of ultrasound contrast agents: a numerical investigation.” Nonlinear Dynamics 80, no. 1-2 (2015): 889-904..

[33] Segers, Tim, Pieter Kruizinga, Maarten P. Kok, Guillaume Lajoinie, Nico De Jong, and Michel Versluis. ”Monodisperse versus polydisperse ultrasound contrast agents: Non-linear response, sensitivity, and deep tissue imaging potential.” Ultrasound in medicine & biology 44, no. 7 (2018): 1482-1492.

[34] Zderic, Vesna, Jessica Foley, Wenbo Luo, and Shahram Vaezy. ”Prevention of post-focal thermal damage by formation of bubbles at the focus during high intensity focused ultrasound therapy.” Medical physics 35, no. 10 (2008): 4292-4299.

[35] Soetanto, Kawan, and Man Chan. ”Fundamental studies on contrast images from different-sized microbubbles: analytical and experimental studies.” Ultrasound in medicine & biology 26, no. 1 (2000): 81-91.

[36] Sojahrood, Amin Jafari, and Michael C. Kolios. ”The utilization of the bubble pressure dependent harmonic resonance frequency for enhanced heating during high intensity focused ultrasound treatments.” In American Institute of Physics Conference Series, vol. 1481, pp. 345-350. 2012.

[37] Commander, Kerry W., and Andrea Prosperetti. ”Linear pressure waves in bubbly liquids: Comparison between theory and experiments.” The Journal of the Acoustical Society of America 85, no. 2 (1989): 732-746.

[38] Louisnard, Olivier. ”A simple model of ultrasound propagation in a cavitating liquid. Part I: Theory, nonlinear attenuation and traveling wave generation.” Ultrasonics sonochemistry 19, no. 1 (2012): 56-65.

[39] Jamshidi, Rashid, and Gunther Brenner. ”Dissipation of ultrasonic wave propagation in bubbly liquids considering the effect of compressibility to the first order of acoustical Mach number.” Ultrasonics 53, no. 4 (2013): 842-848.

[40] Sojahrood, A.J., Haghi, H., Karshafian, R. and Kolios, M.C., 2020. Critical corrections to models of nonlinear power dissipation of ultrasonically excited bubbles. Ultrasonics Sonochemistry, 66, pp.105089-105089.

[41] Sojahrood, A.J., Haghi, H., Li, Q., Porter, T.M., Karshafian, R. and Kolios, M.C., 2020. Nonlinear power loss in the oscillations of coated and uncoated bubbles: Role of thermal, radiation and encapsulating shell damping at various excitation pressures. Ultrasonics sonochemistry, 66, p.105070.

[42] Hoff, Lars, Per C. Sontum, and Jens M. Hovem. ”Oscillations of polymeric microbubbles: Effect of the encapsulating shell.” The Journal of the Acoustical Society of America 107, no. 4 (2000): 2272-2280.

[43] Mantouka, Agni, Hakan Dogan, P. R. White, and T. G. Leighton. ”Modelling acoustic scattering, sound speed, and attenuation in gassy soft marine sediments.” The journal of the acoustical society of America 140, no. 1 (2016): 274-282.

[44] Dogan, Hakan, Paul R. White, and Timothy G. Leighton. ”Acoustic wave propagation in gassy porous marine sediments: The rheological and the elastic effects.” The Journal of the Acoustical Society of America 141, no. 3 (2017): 2277-2288.

[45] Segers, T. J., N. de Jong, and Michel Versluis. ”Uniform scattering and attenuation of acoustically sorted ultrasound contrast agents: Modeling and experiments.” Journal of the Acoustical Society of America 140, no. 4 (2016): 2506-2517.

[46] Dogan, Hakan, and Viktor Popov. ”Numerical simulation of the nonlinear ultrasonic pressure wave propagation in a cavitating bubbly liquid inside a sonochemical reactor.” Ultrasonics sonochemistry 30 (2016): 87-97.

[47] Sojahrood, A. J., Q. Li, H. Haghi, R. Karshafian, T. M. Porter, and M. C. Kolios. ”Pressure dependence of the ultrasound attenuation and speed in bubbly media: Theory and experiment.” arXiv preprint arXiv:1811.07788 (2018).

[48] Plesset, Milton S. ”The dynamics of cavitation bubbles.” Journal of applied mechanics 16 (1949): 277-282.

[49] Keller, Joseph B., and Michael Miksis. ”Bubble oscillations of large amplitude.” The Journal of the Acoustical Society of America 68, no. 2 (1980): 628-633.

[50] Sojahrood, A. J., D. Wegierak, H. Haghi, R. Karshfian, and M. C. Kolios. ”A simple method to analyze the super-harmonic and ultra-harmonic behavior of the acoustically excited bubble oscillator.” Ultrasonics sonochemistry 54 (2019): 99.

[51] Morgan, Karen E., John S. Allen, Paul A. Dayton, James E. Chomas, A. L. Klibaov, and Katherine W. Ferrara. ”Experimental and theoretical evaluation of microbubble behavior: Effect of transmitted phase and bubble size.” IEEE transactions on ultrasonics, ferroelectrics, and frequency control 47, no. 6 (2000): 1494-1509.

[52] Toegel, Ruediger, Bruno Gompf, Rainer Pecha, and Detlef Lohse. ”Does water vapor prevent upscaling sonoluminescence?.” Physical review letters 85, no. 15 (2000): 3165.

[53] Lide, David R., and Henry V. Kehiaian. CRC handbook of thermophysical and thermochemical data. Crc Press, 1994.

[54] http://detector-cooling.web.cern.ch/Detector-Cooling/data/C3F8_Properties.pdf

[55] Stricker, Laura, Andrea Prosperetti, and Detlef Lohse. ”Validation of an approximate model for the thermal behavior in acoustically driven bubbles.” The Journal of the Acoustical Society of America 130, no. 5 (2011): 3243-3251.

[56] Sojahrood, A.J., Wegierak, D., Haghi, H., Karshafian, R. and Kolios, M.C., 2018. A comprehensive bifurcation method to analyze the super-harmonic and ultra-harmonic behavior of the acoustically excited bubble oscillator. arXiv preprint arXiv:1810.01239.

[57] Flynn, H.G., Church, C.C.: Transient pulsations of small gas bubbles in water. J. Acoust. Soc. Am. 84, 985–998 (1988)

[58] Sojahrood, A.J., Earl, R., Kolios, M.C. and Karshafian, R., 2020. Investigation of the 1/2 order subharmonic emissions of the period-2 oscillations of an ultrasonically excited bubble. Physics Letters A, p.126446.

[59] A.J. Sojahrood, R.E. Earl, M.C. Kolios and R. Karshafian, Nonlinear dynamics of acoustic bubbles excited by their pressure dependent subharmonic resonance frequency: oversaturation and enhancement of the subharmonic signal, arxiv: 2019

[60] Sojahrood A.J. & M.C. Classification of the nonlinear dynamics and bifurcation structure of ultrasound contrast agents excited at higher multiples of their resonance frequency. Physics Letters A, 376(33), pp.2222-2229.

[61] Hegedűs, F., Hős, C. and Kullmann, L., 2012. Stable period 1, 2 and 3 structures of the harmonically excited Rayleigh–Plesset equation applying low ambient pressure. The IMA Journal of Applied Mathematics, 78(6), pp.1179-1195.

[62] Hegedűs, F., 2016. Topological analysis of the periodic structures in a harmonically driven bubble oscillator near Blake's critical threshold: Infinite sequence of two-sided Farey ordering trees. Physics Letters A, 380(9-10), pp.1012-1022.

[63] J.A. Rooney, Hemolysis near an ultrasonically pulsating gas bubble, Science 169 (1970) 869–871.

[64] J. Wu, W.L. Nyborg, Ultrasound, cavitation bubbles and their interaction with cells, Adv. Drug Deliv. Rev. 60 (2008) 1103–1116.

[65] Bouakaz, A., De Jong, N. and Cachard, C., 1998. Standard properties of ultrasound contrast agents. Ultrasound in medicine & biology, 24(3), pp.469-472.

[66] Goertz, D.E., de Jong, N. and van der Steen, A.F., 2007. Attenuation and size distribution measurements of Definity™ and manipulated Definity™ populations. Ultrasound in medicine & biology, 33(9), pp.1376-1388.

[67] Raymond, J.L., Haworth, K.J., Bader, K.B., Radhakrishnan, K., Griffin, J.K., Huang, S.L., McPherson, D.D. and Holland, C.K., 2014. Broadband attenuation measurements of phospholipid-shelled ultrasound contrast agents. Ultrasound in medicine & biology, 40(2), pp.410-421.

[68] Shekhar, H., Smith, N.J., Raymond, J.L. and Holland, C.K., 2018. Effect of temperature on the size distribution, shell properties, and stability of Definity®. Ultrasound in medicine & biology, 44(2), pp.434-446.

[69] Shekhar, H., Kleven, R.T., Peng, T., Palaniappan, A., Karani, K.B., Huang, S., McPherson, D.D. and Holland, C.K., 2019. In vitro characterization of sonothrombolysis and echocontrast agents to treat ischemic stroke. Scientific reports, 9(1), p.9902.

[70] Helfield, B.L., Leung, B.Y., Huo, X. and Goertz, D.E., 2014. Scaling of the viscoelastic shell properties of phospholipid encapsulated microbubbles with ultrasound frequency. Ultrasonics, 54(6), pp.1419-1424.

[71] Xia, L., Porter, T.M. and Sarkar, K., 2015. Interpreting attenuation at different excitation amplitudes to estimate strain-dependent interfacial rheological properties of lipid-coated monodisperse microbubbles. The Journal of the Acoustical Society of America, 138(6), pp.3994-4003.

[72] Bouakaz, A., Frigstad, S., Ten Cate, F.J. and de Jong, N., 2002. Super harmonic imaging: a new imaging technique for improved contrast detection. Ultrasound in medicine & biology, 28(1), pp.59-68.

[73] Cherin, E., Yin, J., Forbrich, A., White, C., Dayton, P.A., Foster, F.S. and Démoré, C.E., 2019. In Vitro Superharmonic Contrast Imaging Using a Hybrid Dual-Frequency Probe. Ultrasound in medicine & biology. 45(9), pp.2525-2539.

[74] Perera, R., Hernandez, C., Cooley, M., Jung, O., Jeganathan, S., Abenojar, E., Fishbein, G., Sojahrood, A.J., Emerson, C., Stewart, P.L. and Kolios, M., 2019. Contrast Enhanced Ultrasound Imaging by Nature-Inspired Ultrastable Echogenic Nanobubbles. Nanoscale.

[75] Shekhar, H., Rowan, J.S. and Doyley, M.M., 2017. Combining subharmonic and ultraharmonic modes for intravascular ultrasound imaging: A preliminary evaluation. Ultrasound in medicine & biology, 43(11), pp.2725-2732.

[76] De Jong, N., Emmer, M., Van Wamel, A. and Versluis, M., 2009. Ultrasonic characterization of ultrasound contrast agents. Medical & biological engineering & computing, 47(8), pp.861-873.

[77] Haworth, K.J., Salgaonkar, V.A., Corregan, N.M., Holland, C.K. and Mast, T.D., 2015. Using passive cavitation images to classify high-intensity focused ultrasound lesions. Ultrasound in medicine & biology, 41(9), pp.2420-2434.

[78] Alli, S., Figueiredo, C.A., Golbourn, B., Sabha, N., Wu, M.Y., Bondoc, A., Luck, A., Coluccia, D., Maslink, C., Smith, C. and Wurdak, H., 2018. Brainstem blood brain barrier disruption using focused ultrasound: A demonstration of feasibility and enhanced doxorubicin delivery. Journal of controlled release, 281, pp.29-41.

[79] Eckersley, R.J., Chin, C.T. and Burns, P.N., 2005. Optimising phase and amplitude modulation schemes for imaging microbubble contrast agents at low acoustic power. Ultrasound in medicine & biology, 31(2), pp.213-219.

[80] Phillips, P.J., 2001, October. Contrast pulse sequences (CPS): imaging nonlinear microbubbles. In 2001 IEEE Ultrasonics Symposium. Proceedings. An International Symposium (Cat. No. 01CH37263) (Vol. 2, pp. 1739-1745). IEEE.

[81] Goertz, D.E., Frijlink, M.E., Tempel, D., Bhagwandas, V., Gisolf, A., Krams, R., de Jong, N. and van der Steen, A.F., 2007. Subharmonic contrast intravascular ultrasound for vasa vasorum imaging. Ultrasound in medicine & biology, 33(12), pp.1859-1872.

[82] Goertz, D.E., Cherin, E., Needles, A., Karshafian, R., Brown, A.S., Burns, P.N. and Foster, F.S., 2005. High frequency nonlinear B-scan imaging of microbubble contrast agents. IEEE transactions on ultrasonics, ferroelectrics, and frequency control, 52(1), pp.65-79.

[83] Forsberg, F., Piccoli, C.W., Merton, D.A., Palazzo, J.J. and Hall, A.L., 2007. Breast lesions: imaging with contrast-enhanced subharmonic US—initial experience. Radiology, 244(3), pp.718-726.

[84] M.A. OReilly, et al, Focused-ultrasound disruption of the blood-brain barrier using closely-timed short pulses: inflence of sonication parameters and injection rate, Ultrasound in medicine & biology 37 (2011): 587-594.

[85] Haworth, K.J., Bader, K.B., Rich, K.T., Holland, C.K. and Mast, T.D., 2016. Quantitative frequency-domain passive cavitation imaging. IEEE transactions on ultrasonics, ferroelectrics, and frequency control, 64(1), pp.177-191.

[86] Eller, Anthony, and H. G. Flynn. ”Generation of subharmonics of order one-half by bubbles in a sound field.” The Journal of the Acoustical Society of America 46.3B (1969): 722-727.

[87] Prosperetti, Andrea. ”Nonlinear oscillations of gas bubbles in liquids: steady-state solutions.” The Journal of the Acoustical Society of America 56.3 (1974): 878-885.

[88] Prosperetti, Andrea. ”Application of the subharmonic threshold to the measurement of the damping of oscillating gas bubbles.” The Journal of the Acoustical Society of America61.1 (1977): 11-16.

[89] Prosperetti, Andrea. ”A general derivation of the subharmonic threshold for non-linear bubble oscillations.” The Journal of the Acoustical Society of America 133.6 (2013): 3719-3726

[90] P. D., P. M. Shankar, and V. L. Newhouse. ”Subharmonic generation from ultrasonic contrast agents.” Physics in Medicine & Biology 44.3 (1999): 681.

[91] Shankar, P. M., P. D. Krishna, and V. L. Newhouse. ”Subharmonic backscattering from ultrasound contrast agents.” The Journal of the Acoustical Society of America106.4 (1999): 2104-2110.

[92] Katiyar, Amit, and Kausik Sarkar. ”Effects of encapsulation damping on the excitation threshold for subharmonic generation from contrast microbubbles.” The Journal of the Acoustical Society of America 132.5 (2012): 3576-3585.

[93] Katiyar, Amit, and Kausik Sarkar. ”Excitation threshold for subharmonic generation from contrast microbubbles.” The Journal of the Acoustical Society of America 130.5 (2011): 3137-3147.

[94] Jafari Sojahrood, A. and Kolios, M., 2011. Theoretical considerations for ultrasound contrast agent amplitude modulation techniques at high frequencies. The Journal of the Acoustical Society of America, 129(4), pp.2511-2511.

[95] Wang, M. and Zhou, Y., 2018. Numerical investigation of the inertial cavitation threshold by dual-frequency excitation in the fluid and tissue. Ultrasonics sonochemistry, 42, pp.327-338.

[96] Kooiman, K., Vos, H.J., Versluis, M. and de Jong, N., 2014. Acoustic behavior of microbubbles and implications for drug delivery. Advanced drug delivery reviews, 72, pp.28-48.

[97] T.J. Mason, Ultrasonic cleaning: a historical perspective, Ultrason. Sonochem. 29 (2016) 519–523.

[98] Maisonhaute, E., Prado, C., White, P.C. and Compton, R.G., 2002. Surface acoustic cavitation understood via nanosecond electrochemistry. Part III: Shear stress in ultrasonic cleaning. Ultrasonics sonochemistry, 9(6), pp.297-303.

[99] Yamashita, T. and Ando, K., 2019. Low-intensity ultrasound induced cavitation and streaming in oxygen-supersaturated water: Role of cavitation bubbles as physical cleaning agents. Ultrasonics sonochemistry, 52, pp.268-279.

[100] BURNS, P.N., WILSON, S.R. and SIMPSON, D.H., 2000. Pulse inversion imaging of liver blood flow: improved method for characterizing focal masses with microbubble contrast. Investigative radiology, 35(1), p.58.

[101] Zhang, P. and Porter, T., 2010. An in vitro study of a phase-shift nanoemulsion: a potential nucleation agent for bubble-enhanced HIFU tumor ablation. Ultrasound in medicine & biology, 36(11), pp.1856-1866.

[102] Razansky, D., Einziger, P.D. and Adam, D.R., 2006. Enhanced heat deposition using ultrasound contrast agent-modeling and experimental observations. ieee transactions on ultrasonics, ferroelectrics, and frequency control, 53(1), pp.137-147.

[103] O'Reilly, M.A. and Hynynen, K., 2012. Ultrasound enhanced drug delivery to the brain and central nervous system. International Journal of Hyperthermia, 28(4), pp.386-396.

[104] Behnia, S., Jafari, A., Ghalichi, F. and Bonabi, A., 2008. Finite-element simulation of ultrasound brain surgery: effects of frequency, focal pressure, and scanning path in bone-heating reduction. Open Physics, 6(2), pp.211-222.

[105] Jafari Sojahrood, A., Haghi, H., Karshafian, R. and Kolios, M.C., 2016. Propagation of low amplitude focused ultrasound waves in a bubbly medium: Finite element simulation and theoretical considerations for optimization of the treatment parameters. The Journal of the Acoustical Society of America, 140(4), pp.3371-3371.

[106] Sojahrood, A.J. and Kolios, M.C., 2012, October. The utilization of the bubble pressure dependent harmonic resonance frequency for enhanced heating during high intensity focused ultrasound treatments. In AIP Conference Proceedings (Vol. 1481, No. 1, pp. 345-350). AIP.

[107] Sojahrood, A.J., Haghi, H., Karshafian, R. and Kolios, M.C., 2015, October. Nonlinear model of acoustical attenuation and speed of sound in a bubbly medium. In 2015 IEEE International Ultrasonics Symposium (IUS) (pp. 1-4). IEEE.

[108] Segers, T., Kruizinga, P., Kok, M.P., Lajoinie, G., De Jong, N. and Versluis, M., 2018. Monodisperse versus polydisperse ultrasound contrast agents: Non-linear response, sensitivity, and deep tissue imaging potential. Ultrasound in medicine & biology, 44(7), pp.1482-1492.

Chapter 9

Universal classification of the nonlinear dynamics of acoustically excited bubbles and the corresponding nonlinear changes in the attenuation and sound speed of the bubbly media: Theory, experiments, and applications

9.1 Abstract

Attenuation and sound speed of bubbly media are one of the fundamental problems in acoustics. The problem is of general interest due to the wide range of applications related to the physics of the bubbly media including but not limited to underwater acoustics & oceanography, sonochemistry, and several medical applications (e.g. contrast-enhanced imaging of vasculature, enhanced drug delivery, etc). However, the problem has remained unsolved; data regarding pressure-dependent changes of the attenuation and sound speed of a bubbly medium are not available. Our theoretical understanding of the problem is limited to linear or semi-linear models; thus predictions are not accurate in the regime of large amplitude bubble oscillations. Secondly, the nonlinear dynamics of bubbles are complex and not fully understood. We propose a universal and straightforward attenuation-sound speed model that is not restricted to any linear approximations. The model is global; it is valid for free bubbles, bubbles encapsulated with different shell types and bubbles immersed in elastic mediums (e.g., sediments, tissue, etc.). The predictions of the model are verified against the linear and semi-linear models for all the mentioned cases above. Predictions

of the model are tested with the results of experiments using monodispersions of lipid-coated microbubbles. We report for the first time, observations of the pressure dependence of sound speed in a bubbly medium. The nonlinear radial oscillations of the bubbles are universally classified utilizing our recently proposed comprehensive bifurcation analysis of the radial oscillations of the bubbles. Radial oscillations were studied as a function of pressure at various frequencies including pressure dependent resonance, linear resonance, $\frac{1}{2}$ & $\frac{1}{3}$ order SHs, super harmonic & ultra-harmonic resonance oscillations. Using the classified regimes of oscillations, the nonlinear attenuation and sound speed of the bubbly media are characterized. By taking advantage of the characterized scheme and finite element simulation of the propagation of focused ultrasonic waves, it is shown that the attenuation and sound speed of the bubbly media can be engineered through adjusting the sonication frequency; through which, the pre-focal acoustic loss can be minimized. Thus ultrasonic waves can tunnel through dense populations of bubbles with minimum loss[1].

9.2 Introduction

Acoustically excited microbubbles (MBs) are present in a wide range of phenomena; they have applications in sonochemistry [1]; oceanography and underwater acoustics [2,3]; material science [4], sonoluminescence [5] and in medicine [6,7,8,9,10,11,12]. Due to their broad and exciting biomedical applications, it has been stated that ″ The future of medicine is bubbles ″ [12]. MBs are used in ultrasound molecular imaging [6,7] and recently have been used for the non-invasive imaging of the brain microvasculature [7]. MBs are being investigated for site-specific enhanced drug delivery [8,9,10,11] and for the non-invasive treatment of brain pathologies (by transiently opening the impermeable blood-brain barrier (BBB) to deliver macromolecules [9]; with the first in human clinical BBB opening reported in 2016 [8]). However several factors limit our understanding of MB dynamics which consequently hinder our ability to optimally employ MBs in these applications. The MB dynamics are nonlinear and chaotic [13,14,15]; furthermore, the typical lipid shell coating adds to the complexity of the MBs dynamics due to the nonlinear behavior of the shell (e.g., buckling and rupture [16]). Importantly, the presence of MBs changes the sound speed

[1]Part one of this chapter is under review as: AJ. Sojahrood, Q. Li, H. Haghi, R. Karshafian, T.M. Porter and M.C. Kolios, Development of a universal model for pressure dependence of sound speed and attenuation of the bubbly media: Theory and experiments. Part two will be submitted as: A.J. Sojahrood, H. Haghi, R. Karshafian and M.C. Kolios, Classification of the nonlinear attenuation and sound speed in bubbly media with applications.

and attenuation of the medium [17,18,19,20,21]. These changes are highly nonlinear and depend on the MB nonlinear oscillations which in turn depend on the ultrasound pressure and frequency, MB size and shell characteristics [17, 18, 19, 20]. The increased attenuation due to the presence of MBs in the beam path may limit the pressure at the target location. This phenomenon is called pre-focal shielding (shadowing) [20,21]. Additionally, changes in the sound speed can change the position and dimensions of the focal region; thus, reducing the accuracy of focal placement (e.g., for targeted drug delivery). In imaging applications, MBs can limit imaging in depth due to the shadowing caused by prefocal MBs [14, 20, 21, 23]. In sonochemistry, changes in the attenuation and the sound speed impact the pressure distribution inside the reactors and reduces the procedure efficacy [18,19].

An accurate estimation of the pressure dependent attenuation and sound speed in bubbly media remains one of the unsolved problems in acoustics [25]. Most current models are based on linear approximations which are only valid for small amplitude MB oscillations [17]. Linear approximations, however, are not valid for the typical exposure conditions encountered in biomedical applications. In an effort to incorporate the nonlinear MB oscillations in the attenuation estimation of bubbly media, a pressure-dependent MB scattering cross-section has been introduced [2, 26]. While the models introduce a degree of pressure dependency (e.g. only the pressure dependance of the scattering cross section were considered while the damping factors were estimated using the linear model), they still incorporate linear approximations for the calculation of the rest of the damping factors (e.g. liquid viscous damping, shell viscous damping and thermal damping). Additionally, they neglect the nonlinear changes of the sound speed in their approximations. We have shown in [27,28], that the changes in liquid and shell viscous damping and thermal damping are pressure dependent and significantly deviate from linear predictions even at moderate pressures (e.g. 40 kPa).

Louisnard [18] and Holt and Roy [29] have derived models based on employing the energy conservation principle. In Louisnard´s approach [18] the pressure dependent imaginary part of the wave number is calculated by computing the total nonlinear energy loss during bubble oscillations. However, this method still uses the linear approximations to calculate the real part of the wave number; thus, it is unable to predict the changes of the sound speed with pressure. Holt and Roy calculated the energy loss due to MB nonlinear oscillations and then calculated the attenuation

by determining the extinction cross-section. Both approaches in [18] and [29] use the analytical form of the energy dissipation terms. In the case of coated MBs with nonlinear shell behavior, such calculations are complex and can result in inaccuracies. The existing approaches for sound speed computations based on the Woods model [29, 30] are either limited to bubbles whose expansion are essentially in phase with the rarefaction phase of the local acoustic pressure, or encounter difficulties in nonlinear regimes of oscillations because of their dependence on $\frac{dP}{dV}$ (e.g. [31]) where P is pressure and V is the MB volume.

Experimental investigation of the pressure and frequency dependence of the attenuation of bubbly media has been limited to few studies of coated MBs suspensions [23, 26, 32]. The pressure dependence of the sound speed in bubbly media has not been experimentally investigated. In the absence of a comprehensive and nonlinear model to calculate the sound speed and attenuation, the relationship between the changes in the pressure and variations in the sound speed and attenuation has remained incomplete.

The objective of this work is to provide a universal comprehensive model describing the relationship between the acoustic pressure and the sound speed and attenuation in a bubbly medium, as well as testing the predictions experimentally. Here, we report on our controlled observations on the pressure dependence of the sound speed of a bubbly medium for the first time. A theoretical model is derived that can predict the pressure dependent attenuation and sound speed; the model is free from any linear approximations and treats the MB oscillations with their full nonlinearity. We have first proposed this model in [33, 34], and reported its initial experimental validation in [35]; initial results were featured as conference papers in [34, 36].

In the second part of this paper, we will classify the nonlinear regimes of bubble oscillations and apply the classification to characterize the changes of the sound speed and attenuation in a bubbly media over a wide range of acoustic exposure parameters. Afterwards, we will apply the characterized scheme to optimize the sonication conditions to reduce the high attenuation of sound waves during focused ultrasound exposures (e.g. using the pressure dependent resonance frequency).

9.3 Methods

9.3.1 Derivation of the comprehensive model

To drive the model, we start with the Caflisch equation [37] for the propagation of the acoustic waves in a bubbly medium:

$$\nabla^2 (P) = \frac{1}{C_l^2}\frac{\partial^2 P}{\partial t^2} - \sum_{i=1}^{N} \rho_l \frac{\partial^2 \beta_i}{\partial t^2} \tag{9.1}$$

In this equation, P is pressure, C_l is the speed of sound in the liquid in the absence of bubbles, ρ_l is the liquid density and β_i is the local volume fraction occupied by the gas at time t of the *ith* MBs. $\beta_i$is given by $\beta_i(t) = \frac{4}{3}\pi R_i(t)^3 N_i$ where R_i *(t)* is the instantaneous radius of the MBs with initial radius of R_{0i} and N_i is the number of the corresponding MBs per unit volume in the medium. The summation is performed over the whole population of the MBs. Eq. 9.1 can also be written in terms of the complex conjugate of the acoustic pressure as in equation 9.2:

$$\nabla^2 \left(\bar{P}\right) = \frac{1}{C_l^2}\frac{\partial^2 \bar{P}}{\partial t^2} - \sum_{i=1}^{N} \rho_l \frac{\partial^2 \beta_i}{\partial t^2} \tag{9.2}$$

where $\bar{P}$ is the complex conjugate of P. To calculate the attenuation and sound speed we need to determine the wave number (k=k_r-$i\alpha$); the sound speed can be calculated from k_r which is the real part of the wave number, and the attenuation α from the imaginary part of the wave number. To obtain the expressions for the imaginary and real part of the wave number, we first need to write Eq. 9.1 and its complex conjugate in the form of the Helmholtz equation; then the nonlinear wave number will be given by: $k^2 = -\frac{\nabla^2(P)}{P}$.

To achieve this, Eq. 9.1 was multiplied by $\frac{\bar{P}}{P\bar{P}}$ and Eq. 9.2 was multiplied by $\frac{P}{P\bar{P}}$ where $\bar{P}$ is the complex conjugate of P. The pressure dependent real and imaginary parts of k^2 were derived using the time average of the results of the addition and subtraction of the new equations and applying the boundary conditions of the problem:

$$\langle \Re(k^2) \rangle = \frac{-\omega^2}{C_l^2} - \frac{2\rho_l}{T|P|^2} \sum_{i=1}^{N} \int_0^T \Re(P) \frac{\partial^2 \beta_i}{\partial t^2} dt \tag{9.3}$$

$$\langle \Im(k^2) \rangle = -\frac{2\rho_l}{T|P|^2} \sum_{i=1}^{N} \int_0^T \Im(P) \frac{\partial^2 \beta_i}{\partial t^2} dt \tag{9.4}$$

where $\Re$ and $\Im$ denote the real and imaginary parts respectively, $<>$ denotes the time average, ω is the angular frequency of a propagating wave, and T is the time averaging interval. The contribution of each MB with β_i is summed. Using Eqs. 9.3 and 9.4, we can now calculate the pressure-dependent sound speed and attenuation in a bubbly medium. To do this, the radial oscillations of the MBs in response to an acoustic wave need to be calculated first. Then equation 3 and 4 were solved by integrating over the β_i of each of the MBs in the population.

9.3.2 The bubble models

The volume fraction occupied by a bubble with β_i depends on the $R(t)$ of each bubble. $R(t)$ of each bubble is determined by solving the model that describe the bubble oscillations. The predictions of equations 3 and 4, will be numerically verified in case of an uncoated free bubble model, a coated bubble model and a model of a bubble immersed in sediment or tissue. In each case the model predictions are validated against the linear regime of oscillations at very low pressures ($1kPa$) by comparing the predictions with the linear models. Linear models are derived using the Commander $\&$ Porspereti approach in [17]. Afterwards, predictions of the imaginary part of the wave number are verified numerically with modifications to the Louisnard model [18] at different pressures. The Louisnard model was modified by Jamshidi $\&$ Brenner [19] to include the compressibility effects to the first order of Mach number. Using this approach, they were able to present the nonlinear terms that describe the power loss due to radiation effects. In chapter 6 [27] we provided critical corrections to the derived terms in [19] for uncoated bubbles. Using our approach in chapter 6 ([27]), we have derived the terms describing the nonlinear power loss in the case of the coated bubbles in chapter 7([28]). Here, we will also derive the terms describing the nonlinear power loss for bubbles that are immersed in sediments or tissues using our approach in [27].

9.3.2.1 Uncoated free bubble

Radial oscillations of an uncoated bubble can be modeled to the first order of Mach number by solving the Keller-Miksis [22] (KM) model:

$$\rho\left((1-\frac{\dot{R}}{C_l})R\ddot{R}+\frac{3}{2}\dot{R}(1-\frac{R}{3C_l})\right)=(1+\frac{\dot{R}}{C_l})(G)+\frac{R}{C_l}\frac{d}{dt}(G) \tag{9.5}$$

where $G=P_g-\frac{4\mu_L\dot{R}}{R}-\frac{2\sigma}{R}-P_0-P_asin(2\pi ft)$.

In this equation, R is radius at time t, R_0 is the initial bubble radius, $\dot{R}$ is the wall velocity of the bubble, $\ddot{R}$ is the wall acceleration, ρ is the liquid density (998 $\frac{kg}{m^3}$), C_l is the sound speed (1481 m/s), P_g is the gas pressure, σ is the surface tension (0.0725 $\frac{N}{m}$), μ is the liquid viscosity (0.001 Pa.s), P_0 is the atmospheric pressure (101.325 kPa), and P_a and f are the amplitude and frequency of the applied acoustic pressure. The values in the parentheses are for pure water at 293 K. In this paper the gas inside the bubble is either air or C3F8 and water is the host media.

9.3.2.2 Coated bubble

The dynamics of the coated bubble can be modeled using the Keller-Miksis-Church-Hoff model (KMCH) [28]. We have derived this model by adding the compressibility effects to the first order of Mach number in [28]. The model is presented in Eq. 9.6:

$$\begin{gathered}\rho\left(\left(1-\frac{\dot{R}}{C_l}\right)R\ddot{R}+\frac{3}{2}\dot{R}^2\left(1-\frac{\dot{R}}{3C_l}\right)\right)=\\ \left(1+\frac{\dot{R}}{C_l}+\frac{R}{C_l}\frac{d}{dt}\right)\left(P_g-\frac{4\mu_L\dot{R}}{R}-\frac{12\mu_{sh}\epsilon R_0^2\dot{R}}{R^4}-12G_s\epsilon R_0^2\left(\frac{1}{R^3}-\frac{R_0}{R^4}\right)-P_0-P\right)\end{gathered} \tag{9.6}$$

in this equation μ_{sh} is the viscosity of the shell (coating), ϵ is the thickness of the coating, G_s is the shell shear modulus, P_g is the gas pressure inside the bubble, P_0 is the atmospheric pressure (101.325 kPa) and P is the acoustic pressure given by $P=P_asin(2\pi ft)$ with P_a and f are respectively the excitation pressure and frequency. In this paper for all of the simulations related to coated bubbles G_s=45 MPa and $\mu_{sh}=\frac{1.49(R_0(\mu m)-0.86)}{\theta(nm)}$ [38] (sh stands for shell (coating)) with $\theta=4nm$ (unless otherwise stated).

9.3.2.3 Bubble in sediment or tissue

The Yang and Church model [39] describes the radial oscillations of an uncoated bubble in a viscoelastic medium (e.g. marine sediments or tissue):

$$\rho\left(1-\frac{\dot{R}}{C_l}\right)R\ddot{R}+\frac{3}{2}\rho\dot{R}^2\left(1-\frac{\dot{R}}{3C_l}\right)= \\ \left(1+\frac{\dot{R}}{C_l}+\frac{R}{C_l}\frac{d}{dt}\right)\left(P_g-\frac{2\sigma}{R}-\frac{4\mu_s\dot{R}}{R}-\frac{4G}{3R^3}\left(R^3-R_0^3\right)-P_0-P_a sin(2\pi ft)\right) \tag{9.7}$$

This equation, similar to Eq. 9.5 and 9.6 accounts for compressibility effects to the first order of Mach number, thus inherits the acoustic radiation losses. Several approaches for the incorporation of such losses into a Rayleigh-Plesset type equation were outlined in [26]. The introduced new constant G describes the shear modulus and μ_s describes the shear viscosity of the sediment or tissue. In this paper we considered a tissue with $G = 0.5MPa$, $\mu_s = 0.00287Pa.s$ and $\sigma = 0.056N/m$ (blood surface tension) [39].

9.3.2.4 Gas pressure and thermal effects

4a-Linear thermal model

The linear thermal model [17, 40] is a popular model that has been widely used in studies related to oceanography [4, 5] and the modeling and charecterization of coated bubble oscillations [41, 42, 43, 44, 45]. In this model through linearization, thermal damping is approximated by adding an artificial viscosity term to the liquid viscosity. Furthermore, a variable isoentropic index is used instead of the polytropic exponent of the gas.

In this model P_g is given by:

$$P_g = P_{g0}\left(\frac{R_0}{R}\right)^{3k_i} \tag{9.8}$$

Where the polytropic exponent γ is replaced by isoentropic indice (k_i):

$$k_i = \frac{1}{3}\Re(\phi) \tag{9.9}$$

The liquid viscosity is artificially increased by adding a thermal viscosity (μ_{th}) to the liquid viscosity. This thermal viscosity (μ_{th}) is given by:

$$\mu_{th} = \frac{P_{g0}\Im(\phi)}{4\omega} \tag{9.10}$$

In the above equations the complex term ϕ is calculated from

$$\phi = \frac{3\gamma}{1 - 3\left(\gamma - 1\right) i\chi \left[\left(\frac{i}{\chi}\right)^{\frac{1}{2}} coth\left(\frac{i}{\chi}\right)^{\frac{1}{2}} - 1\right]} \tag{9.11}$$

where γ is the polytropic exponent and $\chi = \frac{D}{\omega R_0^2}$ represents the thermal diffusion length where D is the thermal diffusivity of the gas. $D = \frac{L}{\gamma C_p \rho_g}$ where C_p, ρ_g, and L are specific heat in constant pressure, density and thermal conductivity of the gas inside the bubble.

To calculate the radial oscillations of the coated bubble and uncoated bubble while including the linear thermal effects Eqs.11.3 , 9.6 & 9.7 are coupled with Eq. 8 and the liquid viscosity is increased by μ_{th}. The linear thermal model is used to derive the attenuation and sound speed terms in the regime of linear oscillations. In case of the uncoated bubble and the uncoated bubble in viscoelastic medium (Eq.11.3 &9.7) $P_g = P_0 + \frac{2\sigma}{R_0}$. In the case of the coated bubble (Eq.9.6) $P_g = P_0$.

4b- Full thermal model

If thermal effects are considered, P_g is given by Eq. 9.12 [47]:

$$P_g = \frac{N_g K T}{\frac{4}{3}\pi R(t)^3 - N_g B} \tag{9.12}$$

here N_g is the total number of the gas molecules, K is the Boltzman constant and B is the molecular co-volume. The average temperature inside the gas can be calculated using Eq. 13 [47]:

$$\dot{T} = \frac{4\pi R(t)^2}{C_v}\left(\frac{L\left(T_0 - T\right)}{L_{th}} - \dot{R}P_g\right) \tag{9.13}$$

here C_v is the heat capacity at constant volume, T_0=300K is the initial gas temperature, L_{th} is the thickness of the thermal boundary layer. L_{th} is given by $L_{th} = min(\sqrt{\frac{DR(t)}{|\dot{R}(t)|}}, \frac{R(t)}{\pi})$ where D is the thermal diffusivity of the gas. D can be calculated using $D = \frac{L}{c_p \rho_g}$ where L is the gas thermal

Thermal parameters of the Air at 1 atm [42]			
L ($\frac{W}{mK}$)	$c_p(\frac{kJ}{kg^0C})$	$c_v(\frac{kJ}{kgK})$	ρ_g ($\frac{kg}{m^3}$)
0.01165+C×T	1.0049	0.7187	1.025

Table 9.1: Thermal properties used in simulations. (C=5.528×10^{25} $\frac{W}{mK^2}$)

conductivity, c_p is specific heat at constant pressure and ρ_g is the gas density.

Predictions of the full thermal model have been shown to be in good agreement with predictions of the models that incorporate the thermal effects using the PDEs [48]. To calculate the radial oscillations of the coated bubble and uncoated bubble while including the full thermal effects Eqs.11.3 (coated bubble) or Eq.9.6 (uncoated bubble) or Eq. 9.7 (bubble in sediment or tissue) are coupled with Eq. 12 & 13 and then solved using the ode45 solver in Matlab.

9.3.3 Attenuation and sound speed equations for linear regime of oscillations

The linear thermal equations (Eqs.9.8,9.9, 9.10 & 9.11) were coupled to the bubble models (Eqs.11.3,9.6 & 9.7) to derive the attenuation and sound speed terms.

For the linear regime, radial oscillations can be considered as $R = R_0(1 + x)$ where x is a small displacement amplitude. Thus, $\dot{R} = R_0\dot{x}$ and $R^{-n} = R_0(1 - nx)$ (higher order small terms are neglected in the Taylor series expansion of R^{-n}). We also define a function $g(t) = e^{i\omega t}$. The incident pressure can be linearized as [2, 51]:

$$P_a g(t) = \frac{\rho \ddot{R} R_0}{\left(1 - \frac{i\omega R_0}{C_l}\right)} \tag{9.14}$$

Using these linear approximations we can provide a linear analytical solution to Eqs. 5, 6 and 7. These solutions can be written in the following general form of forced damped oscillations:

$$\alpha\ddot{x} + 2\beta\dot{x} + \gamma x = -P_a e^{i\omega t} \tag{9.15}$$

where constants α, β and γ can be defined by solving the appropriate equations. We can transfer Eq.9.15 to the frequency domain by setting $x(t) = x(\omega)e^{i\omega t}$:

$$-\alpha\omega^2 x(\omega)e^{i\omega t} + 2i\beta\omega x(\omega)e^{i\omega t} + \gamma x(\omega)e^{i\omega t} = -P_a e^{i\omega t} \tag{9.16}$$

Eq.9.16 can be simplified by dividing both sides by $\alpha e^{i\omega t}$ and inputting $\omega_0 = \frac{\gamma}{\alpha}$ (ω_0 is resonance angular frequency). Thus:

$$x(\omega)\left[\omega_0^2 - \omega^2 + \frac{2i\beta}{\alpha}\omega\right] = -\frac{P_a}{\alpha} \tag{9.17}$$

9.3.3.1 Free uncoated bubble (KM model) constants

In case of the uncoated bubble model Eq. 11.3, the constants α, β and γ of Eq.9.16 can be derived using an approach similar to [2, 51]:

$$\begin{cases} \alpha = \rho R_0^2 + \dfrac{4\mu R_0}{C_l} \\ \beta = 2\mu_{th} - \dfrac{\sigma}{C_l} + 2\mu + \dfrac{\left(\frac{\omega R_0}{C_l}\right)}{1+\left(\frac{\omega R_0}{C_l}\right)^2}\dfrac{\omega}{2}\left(\rho R_0^2\right) \\ \gamma = P_{g0}\Re(\phi) - \dfrac{2\sigma}{R_0} + \dfrac{\omega^2\rho R_0^2}{1+\left(\frac{\omega R_0}{C_l}\right)^2} \end{cases} \tag{9.18}$$

and the angular resonance frequency $\omega_0 = 2\pi f_r$ (f_r is the linear resonance frequency) is given by:

$$\omega_0 = \sqrt{\frac{P_{g0}\Re(\phi) - \frac{2\sigma}{R_0} + \frac{\omega^2\rho R_0^2}{1+\left(\frac{\omega R_0}{C_l}\right)^2}}{\rho R_0^2 + \frac{4\mu\ R_0}{C_l}}} \tag{9.19}$$

The constant δ_{total} is the total damping and is defined as $\delta_{total} = \frac{\beta}{\alpha}$ (in left hand side of equation 9.17). Thus:

$$\delta_{total} = \frac{\beta}{\alpha} = \frac{2\mu_{th} - \frac{\sigma}{C_l} + 2\mu + \frac{\left(\frac{\omega R_0}{C_l}\right)}{1+\left(\frac{\omega R_0}{C_l}\right)^2}\frac{\omega}{2}\left(\rho R_0^2\right)}{\rho R_0^2 + \frac{4\mu R_0}{C_l}} \tag{9.20}$$

where δ_{Vis}, δ_{th}, δ_{Rad} & δ_{int} are damping constants due to liquid viscosity, thermal loss, re-radiation and interfacial effects.

$$\begin{cases} \delta_{Vis} = \dfrac{2\mu}{\rho R_0^2 + \frac{4\mu R_0}{C_l}} \\ \\ \delta_{th} = \dfrac{2\mu_{th}}{\rho R_0^2 + \frac{4\mu R_0}{C_l}} \\ \\ \delta_{Rad} = \dfrac{\frac{\left(\frac{\omega R_0}{C_l}\right)}{1+\left(\frac{\omega R_0}{C_l}\right)^2}\frac{\omega}{2}\left(\rho R_0^2\right)}{\rho R_0^2 + \frac{4\mu R_0}{C_l}} \\ \\ \delta_{int} = \dfrac{-\sigma}{\rho R_0^2 + \frac{4\mu R_0}{C_l}} \end{cases} \tag{9.21}$$

9.3.3.2 Coated bubble (KMCH) model

Linearzing Eq. 9.6 for coated bubbles we can arrive in an analytical solution in the form of Eq. 9.17 where the angular linear resonance frequency is given by

$$\omega_0 = \sqrt{\frac{P_{g0}\Re(\phi) + \frac{12G_s\epsilon}{R_0} + \frac{\omega^2\rho R_0^2}{1+\left(\frac{\omega R_0}{C_l}\right)^2}}{\rho R_0^2 + \frac{4\mu R_0}{C_l} + \frac{12\mu_{sh}\epsilon}{C_l}}} \tag{9.22}$$

and

$$\begin{cases} \alpha = \rho R_0^2 + \dfrac{4\mu R_0}{C_l} \\ \\ \beta = 2\mu_{th} + 2\mu + \dfrac{\left(\frac{\omega R_0}{C_l}\right)}{1+\left(\frac{\omega R_0}{C_l}\right)^2}\dfrac{\omega}{2}\left(\rho R_0^2\right) - 2GR_0 \\ \\ \gamma = P_{g0}\Re(\phi) - \dfrac{2\sigma}{R_0} + \dfrac{\omega^2\rho R_0^2}{1+\left(\frac{\omega R_0}{C_l}\right)^2} + 4G \end{cases} \tag{9.23}$$

In this case, due to the addition of the shell due to the addition of shell we have an extra term for damping due to shell viscosity δ_{shell}. Thus $\delta_{total} = \delta_{liquid} + \delta_{radiation} + \delta_{shell} + \delta_{thermal}$ where:

$$\begin{cases} \delta_{liquid} = \dfrac{2\mu}{\rho R_0^2 + \frac{4\mu R_0}{C_l} + \frac{12\mu_{sh}\epsilon}{C_l}} \\ \delta_{radiation} = \dfrac{\frac{\left(\frac{\omega R_0}{C_l}\right)}{1+\left(\frac{\omega R_0}{C_l}\right)^2}\frac{\omega}{2}\left(\rho R_0^2\right)}{\rho R_0^2 + \frac{4\mu R_0}{C_l} + \frac{12\mu_{sh}\epsilon}{C_l}} \\ \delta_{shell} = \dfrac{\frac{6\mu_{sh}\epsilon}{R_0} + \frac{6G_s\epsilon}{C_l}}{\rho R_0^2 + \frac{4\mu R_0}{C_l} + \frac{12\mu_{sh}\epsilon}{C_l}} \\ \delta_{thermal} = \dfrac{2\mu_{th}}{\rho R_0^2 + \frac{4\mu R_0}{C_l} + \frac{12\mu_{sh}\epsilon}{C_l}} \end{cases} \tag{9.24}$$

9.3.3.3 Bubble immersed in tissue or sediment

The linear analytical solution to Eq.9.7 for bubbles immersed in tissue or sediments can be written again in the form of Eq. 9.17. The constants of the equation can be written as follows [2, 51]:

$$\omega_0^2 = \frac{P_{g0}\Re(\phi) - \frac{2\sigma}{R_0} + \frac{\omega^2\rho R_0^2}{1+\left(\frac{\omega R_0}{C_l}\right)^2} + 4G}{\rho R_0^2 + \frac{4\mu R_0}{C_l}} \tag{9.25}$$

and

$$\begin{cases} \alpha = \rho R_0^2 + \dfrac{4\mu R_0}{C_l} \\ \beta = 2\mu_{th} - \dfrac{\sigma}{C_l} + 2\mu + \dfrac{\left(\frac{\omega R_0}{C_l}\right)}{1+\left(\frac{\omega R_0}{C_l}\right)^2}\dfrac{\omega}{2}\left(\rho R_0^2\right) - 2GR_0 \\ \gamma = P_{g0}\Re(\phi) - \dfrac{2\sigma}{R_0} + \dfrac{\omega^2\rho R_0^2}{1+\left(\frac{\omega R_0}{C_l}\right)^2} + 4G \end{cases} \tag{9.26}$$

The total damping this case has a term related to the elasticity of the sediment or the tissue (δ_{Sed}). Thus the total damping is: $\delta_{total} = \delta_{liquid} + \delta_{radiation} + \delta_{Sed} + \delta_{thermal}$ where:

$$\begin{cases} \delta_{Vis} = \dfrac{2\mu}{\rho R_0^2 + \frac{4\mu R_0}{C_l}} \\ \delta_{th} = \dfrac{2\mu_{th}}{\rho R_0^2 + \frac{4\mu R_0}{C_l}} \\ \delta_{Rad} = \dfrac{\frac{\left(\frac{\omega R_0}{C_l}\right)}{1+\left(\frac{\omega R_0}{C_l}\right)^2}\frac{\omega}{2}\left(\rho R_0^2\right)}{\rho R_0^2 + \frac{4\mu R_0}{C_l}} \\ \delta_{int} = \dfrac{-\sigma}{\rho R_0^2 + \frac{4\mu R_0}{C_l}} \\ \delta_{Sed} = \dfrac{2GR_0}{\rho R_0^2 + \frac{4\mu R_0}{C_l}} \end{cases} \tag{9.27}$$

9.3.3.4 Derivation of the linear equations of attenuation and sound speed

Using the linear formulations for R, $\frac{\partial^2 \beta}{\partial t^2} = 4\pi {R_0}^3 \ddot{x}$. Moreover $x(\omega)$ can be calculated from Eq. 9.17 :

$$x(\omega) = \frac{-\frac{P_a}{\alpha}}{\left[\omega_0^2 - \omega^2 + 2i\delta_{total}\omega\right]} \tag{9.28}$$

and $\dot{x}(\omega) = -\omega x(\omega)$ & $\ddot{x}(\omega) = \omega^2 x(\omega)$. Inputting these into equation 1 and eliminating $e^{i\omega t}$ yields:

$$\nabla^2 (P) + k^2 P = 0 \tag{9.29}$$

where k is the complex wave number ($k = \frac{\omega}{C} - i\alpha$):

$$k^2 = (\frac{\omega}{C_l})^2 + 4\pi\omega^2 \sum_{j=1}^{N} \frac{R_{0j}^2}{\omega_0^2 - \omega^2 + 2i\delta_{total}\omega} \tag{9.30}$$

where R_{0j} is the initial radius of the bubble number j. Attenuation and sound speed can easily be obtained from equation 9.29.

9.3.4 Derivation of the equations of the sound speed and attenuation using the semi-linear approach of Louisnard

The wave number (k) in equation 9.30 does not depend on pressure. Linear approximations are not valid at large bubble oscillation amplitudes due to pressure dependent non-linear microbubble oscillations. Louisnard [18] derived the pressure dependent term for the imaginary part of the wave number. In this approach, firstly, the terms for the nonlinear energy dissipation are derived accounting for large bubble oscillation amplitude. He started with the mass and momentum conservation equations in a bubbly media [37]:

$$\begin{cases} \dfrac{1}{\rho C_l^2}\dfrac{\partial P}{\partial t} + \nabla.v = \dfrac{\partial \beta}{\partial t} \\ \rho\dfrac{\partial v}{\partial t} = -\nabla P \end{cases} \tag{9.31}$$

here $P(r,t)$ & $v(r,t)$ are the pressure and velocity field. He arrived at:

$$\frac{\partial}{\partial t}\left(\frac{1}{2}\frac{P^2}{\rho C_l^2} + \frac{1}{2}\rho v^2\right) = NP\frac{\partial V}{\partial t} \tag{9.32}$$

Where $V(r,t)$ is the instantaneous volume of the bubbles at time t and N is the number of bubbles per unit volume. V can be calculated by solving the related bubble model. In order to get an energetic interpretation of the bubble radial motion, both sides of the bubble model (e.g. Eq. 11.3 or 9.6 or 9.7) can be multiplied by the time derivative of the bubble volume $\frac{\partial V}{\partial t}$ and using the equation of the kinetic energy of the liquid [18] $K_l = 2\pi\rho R^3\dot{R}^2$ and Eq.9.32, we can arrive at:

$$\frac{\partial}{\partial t}\left(\frac{1}{2}\frac{P^2}{\rho C_l^2} + \frac{1}{2}\rho v^2 + NK_l + 4N\pi R^2\sigma\right) + \nabla.(Pv) = -N\left(\pi_{total}\right) \tag{9.33}$$

where π_{total} is total dissipated energy term. Because Louisnard used the plain Rayleigh-Plesset equation that does not incorporate the compressibility effects of the liquid; he was not able to derive the terms that describe the nonlinear loss due to radiation effects. Jamshidi & Brenner [19] used the K-M equation (Eq. 11.3) that incorporates the compressibility effects up to the first order

of Mach number. Thus, they were able to derive the nonlinear radiation loss terms. In [27] we provided critical corrections to the terms derived in [19].

By taking a time average of both sides of Eq.9.33 and eliminating terms that are zero:

$$\nabla . < Pv >= -N\left(\Pi_{Total}\right) \tag{9.34}$$

Where Π_{Total} is the total dissipated power. Eq. 9.34 expresses the conservation of mechanical energy averaged over one or many periods of oscillations. The physical interpretation of this equation is that the the acoustic energy leaving a volume of bubbly liquid is always smaller than the one incident on it [18]. This is due to the losses during the bubble oscillations. Each bubble therefore acts as a dissipator of acoustic energy. The physical origin of wave attenuation is thus self-contained in the Caflish model, even for nonlinear oscillations, provided that a correct model is used to describe the losses in the bubble oscillation. In [37], Caflish et. al proposed a conservation equation similar to Eq. 35; however, since they disregarded viscosity and assumed isothermal oscillations, mechanical energy was conserved. Eq. (35) as derived by Louisnard [18] reverts the same equation solved in 1D by Rozenberg [52] in the case of purely traveling waves, but in the latter work, the dissipated power was fitted from experimental data, rather than being calculated from single bubble dynamics as done by Louisnard [18].

9.3.4.1 Nonlinear dissipation terms of the uncoated free bubble

In case of the uncoated bubble model Eq.11.3, Π_{Total} is the sum of the following dissipated powers [27]:

$$\begin{cases} \Pi_{Thermal} = \dfrac{-4\pi}{T}\displaystyle\int_0^T R^2\dot{R}P_g dt \\ \\ \Pi_{Liquid} = \dfrac{16\pi\mu_L}{T}\displaystyle\int_0^T R\dot{R}^2 dt \\ \\ \Pi_{Radiation} = \dfrac{1}{T}\displaystyle\int_0^T \left[\dfrac{4\pi}{C_l}\left(R^2\dot{R}\left(\dot{R}P + R\dot{P} - \dfrac{1}{2}\rho\dot{R}^3 - \rho R\dot{R}\ddot{R}\right)\right)\right. \\ \qquad\qquad \left. - \left(\dfrac{\dot{R}}{C_l}P_g + \dfrac{R}{C_l}\dot{P}_g\right)\dfrac{\partial V}{\partial t} + \dfrac{16\pi\mu_L R^2\dot{R}\ddot{R}}{C_l}\right] dt \end{cases} \tag{9.35}$$

where T is the integration time interval.

9.3.4.2 Nonlinear dissipation terms of the coated bubble

For the coated bubble Eq.9.6, Π_{Total} is the sum of the following dissipated powers [28]:

$$
\begin{cases}
\Pi_{Thermal} = \dfrac{-4\pi}{T}\displaystyle\int_0^T R^2\dot{R}P_g dt \\[2ex]
\Pi_{Liquid} = \dfrac{16\pi\mu_L}{T}\displaystyle\int_0^T R\dot{R}^2 dt \\[2ex]
\Pi_{Shell} = \dfrac{48\pi\mu_{sh}\varepsilon R_0^2}{T}\displaystyle\int_0^T \frac{\dot{R}^2}{R^2} dt \\[2ex]
\Pi_{Gs} = \dfrac{48\pi G_s\varepsilon R_0^2}{T}\displaystyle\int_0^T \left(\frac{\dot{R}}{R} - \frac{R_0\dot{R}}{R^2}\right) dt \\[2ex]
\Pi_{Radiation} = \dfrac{1}{T}\displaystyle\int_0^t \left(4\pi\left[\frac{R^2\dot{R}^2}{C_l}\left(P - P_g\right) + \frac{R^3\dot{R}}{C_l}\left(\dot{P} - \dot{P}_g\right) + \frac{4\mu_L R^2\dot{R}\ddot{R}}{C_l}\right.\right. \\
\left. +12\mu_{sh}\varepsilon R0^2\left(\frac{\dot{R}\ddot{R}}{C_l R} - \frac{3\dot{R}^3}{C_l R^2}\right) + 12G_s\varepsilon R0^2\left(\frac{-2\dot{R}^2}{cR} + \frac{3R_0\dot{R}^2}{C_l R^2}\right)\right] \\
\left. -\frac{\rho R^2\dot{R}^4}{2C_l} - \frac{\rho R^3\dot{R}^2\ddot{R}}{C_l}\right) dt
\end{cases}
\tag{9.36}
$$

9.3.4.3 Nonlinear dissipation terms of the bubble in sediment or tissue

And in case of the bubbles immersed in sediments or tissue Eq.9.7, Π_{Total} is derived using the same approach in [27, 28]:

$$\begin{cases} \Pi_{Thermal} = \dfrac{-4\pi}{T}\displaystyle\int_0^T R^2\dot{R}P_g dt \\ \\ \Pi_{Liquid} = \dfrac{16\pi\mu_L}{T}\displaystyle\int_0^T R\dot{R}^2 dt \\ \\ \Pi_{Radiation} = \dfrac{1}{T}\displaystyle\int_0^T \left[\dfrac{4\pi}{C_l}\left(R^2\dot{R}\left(\dot{R}P + R\dot{P} - \dfrac{1}{2}\rho\dot{R}^3 - \rho R\dot{R}\ddot{R} + \dfrac{4G\dot{R}}{3C_l R^3}\left(R^3 - R_0^3\right)\right)\right)\right. \\ \qquad\qquad \left. - \left(\dfrac{\dot{R}}{C_l}P_g + \dfrac{R}{C_l}\dot{P}_g\right)\dfrac{\partial V}{\partial t} + \dfrac{16\pi\mu_L R^2\dot{R}\ddot{R}}{C_l}\right] dt \\ \\ \Pi_{Sediment} = \dfrac{-1}{T}\displaystyle\int_0^T \dfrac{16G\pi\dot{R}}{3R}\left(R^3 - R_0^3\right) dt \end{cases} \tag{9.37}$$

9.3.4.4 Pressure dependent attenuation and sound speed in Louisnard model

Louisnard [18] used the equations of energy dissipation and obtained the imaginary part of the k^2. In this model Imaginary part of the k^2 is pressure dependent; however, real part of the k^2 is still calculated by the linear model.

$$\Im(k^2) = 2\rho\omega\sum_{j=1}^{N}\frac{\Pi(R_{0j})_{Total}}{|P|^2} \tag{9.38}$$

where $\Pi(R_{0j})_{Total}$ is the total dissipated power due to the oscillations of the jth bubble with initial radius of $R_0 j$. The real part of the k^2 can be calculated from Eq. 9.30 as follows:

$$\Re(k^2) = (\frac{\omega}{C_l})^2 + 4\pi\omega^2\sum_{j=1}^{N}\frac{R_{0j}(\omega_{0j}^2 - \omega^2)}{(\omega_{0j}^2 - \omega^2)^2 - 4\delta_{totalj}^2\omega^2} \tag{9.39}$$

The Louisnard model [18] (Eq. 33 & 34) incorporates the pressure effects in the imaginary part of the wave number. However, because the real part of the wave number is still estimated from the

linear approximations it loses accuracy in predicting the sound speed and attenuation, especially in oscillation regimes where the sound speed changes are significant.

9.4 Results

9.4.1 Validation of the model at linear regimes against the linear models

The relevant models (Eq.11.3 (uncoated bubble), Eq.9.6 (coated bubble) and Eq. 9.7 (bubble in tissue or sediment)) for large amplitude MB oscillations were coupled with the ordinary differential equations describing the thermal damping effects (Eq.9.12 and Eq.9.13). The new set of differential equations were solved to calculate the MB radial oscillations. Constants of the linear models were calculated from Eq. 9.21 (uncoated bubble), Eq.9.24 (coated bubble) and Eq.9.27 (bubble in tissue or sediment). Attenuation and sound speed were then calculated for each case using Eq.9.30.
Since the linear model is only valid for narrowband pulses with small pressure amplitudes, pulses of *1kPa* amplitude with 60 cycles were chosen at each frequency, and the last 20 cycles of the bubble oscillations were used (to eliminate the transient behavior) for the integration using Eqs.9.3 and 9.4. For the linearized model, the initial MB radius is 2 μm; the gas inside the MB is *air* and the thermal properties are chosen from [49] (Table 1) and β was set to 10^{-5}. Figures 9.1a-f compare the attenuation and sound speed predictions between the linear model and the non-linear model given by Eq.9.3 and 9.4. Model predictions are in excellent agreement with the linear model for small amplitude radial oscillations ($R_{max}/R_0 < 1.01$). The simple model given by Eq. 3 and 4 predicted the attenuation and sound speed of the medium for the uncoated bubble, the coated bubble and the bubble in tissue. The model only requires as input the radial oscillations of the bubbles and reduces the complexity of deriving the linear terms in each cases. Fig. 9.1 also shows that the the effect of encapsulating shell (added viscosity and stiffness) reduced the bubble expansion ratio which translated to smaller changes in attenuation and sound speed when compared to the uncoated counterpart.

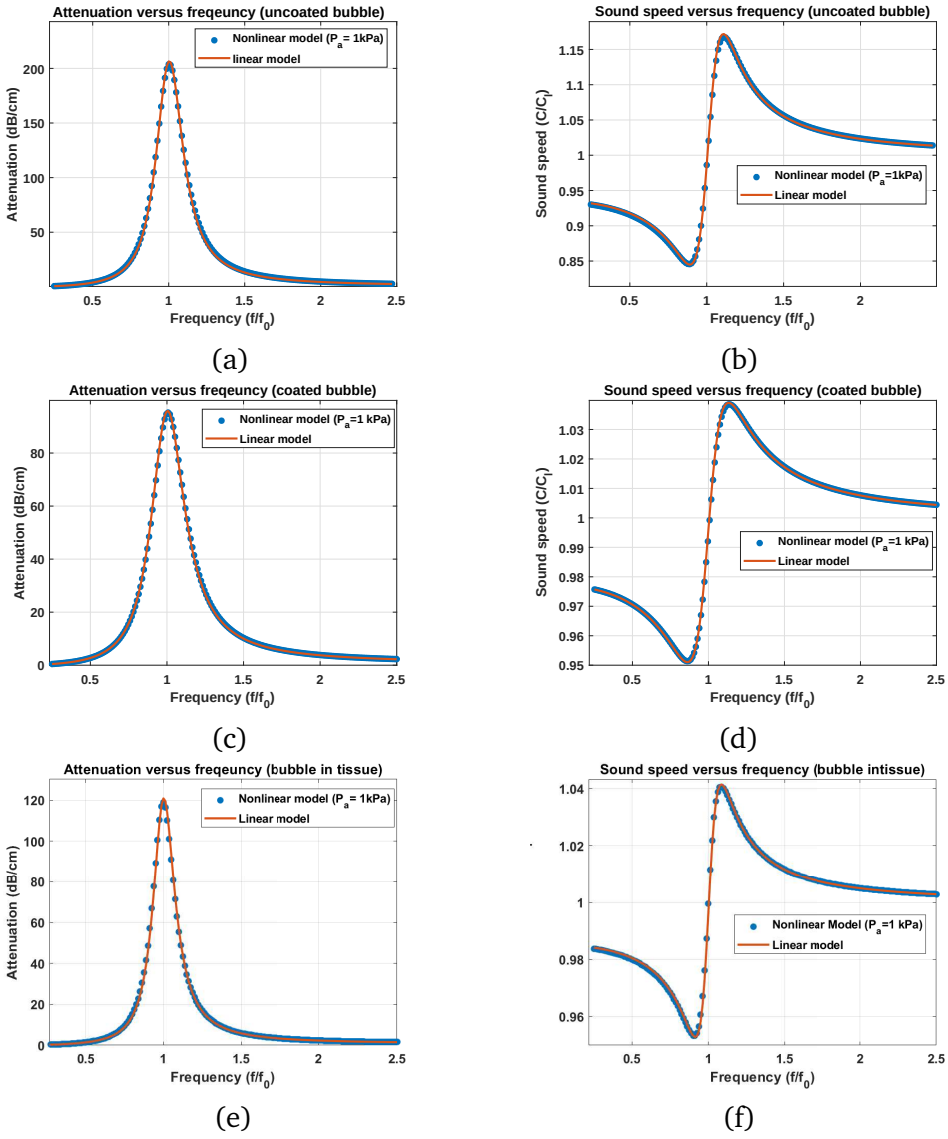

Figure 9.1: Case of a bubbly medium with MBs with $R_0 = 2\mu m$ and $\beta = 10^{-5}$. Attenuation calculated using the linear model and nonlinear model (left) and sound speed calculated using the linear model and the nonlinear model at (P= 1kPa) (Right) for: uncoated bubbles in water (a & b), coated bubbles in water (c & d) and uncoated bubbles in tissue ($\rho = 1060 \frac{kg}{m^3}$, $C_l = 1540 \frac{m}{s}$, $\mu_s = 0.00287 Pa.s$, $G = 0.5 MPa$, $\sigma = 0.056$ N/m [39]) (e & f).

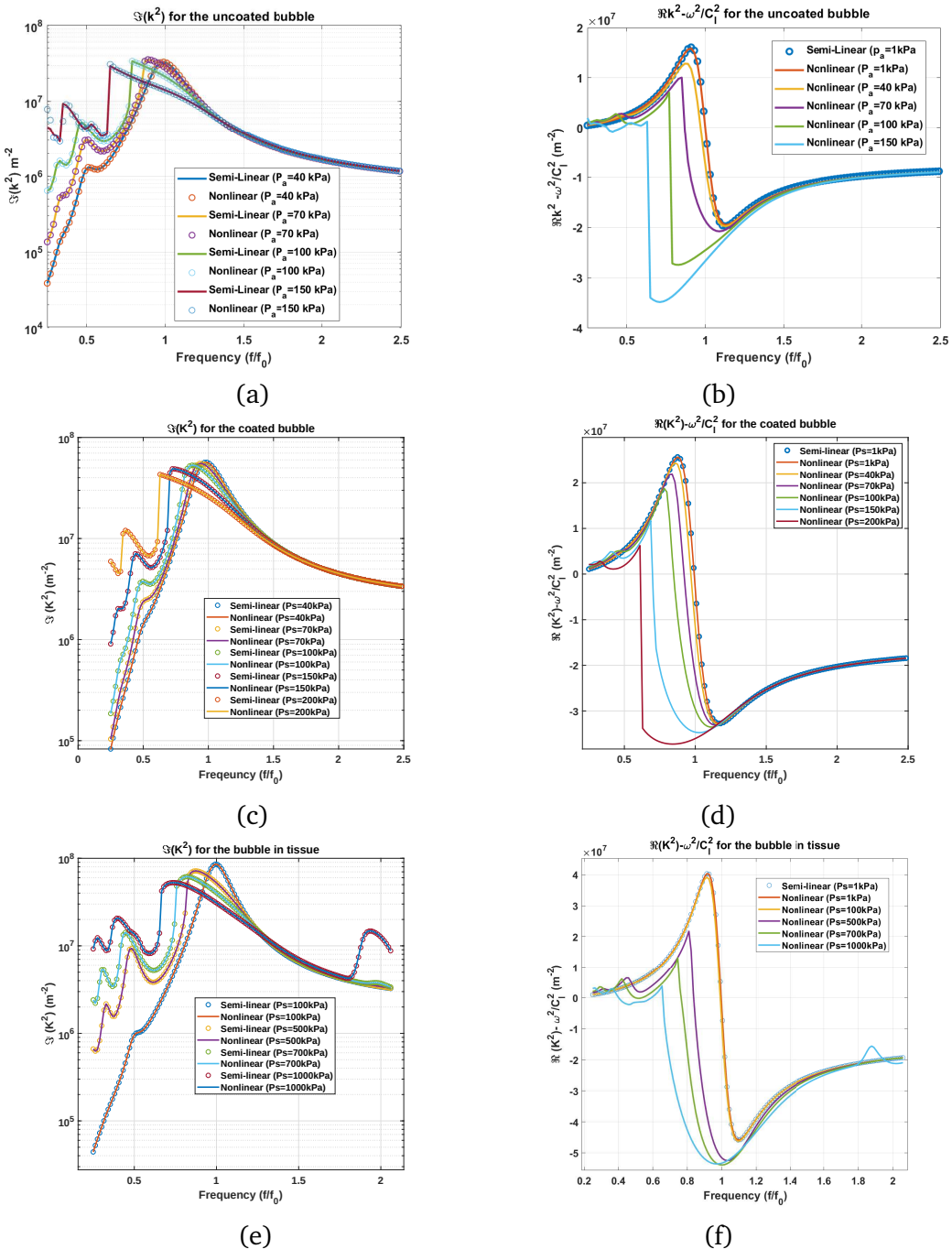

Figure 9.2: Case of a bubbly medium with MBs with $R_0 = 2\mu m$ and $\beta = 10^{-5}$ sonicated at various pressures. Left: $\left\langle \Im\left(k^2\right)\right\rangle$ calculated using the nonlinear model (Eqs.9.4) and Louisnard model (Eq.9.38) and Right: $\left\langle \Re\left(k^2\right)\right\rangle$ calculated using the nonlinear model (Eqs.9.3) and the Louisnard model (Eq.9.39) (Louisanrd model employs the linear model for the real part; thus it is pressure independent) for: uncoated bubbles in water (a & b), coated bubbles in water (c & d) and uncoated bubbles in tissue ($\rho = 1060 \frac{kg}{m^3}$, $C_l = 1540 \frac{m}{s}$, $\mu_s = 0.00287 Pa.s$, $G = 0.5 MPa$, $\sigma = 0.056$ N/m [39]) (e & f).

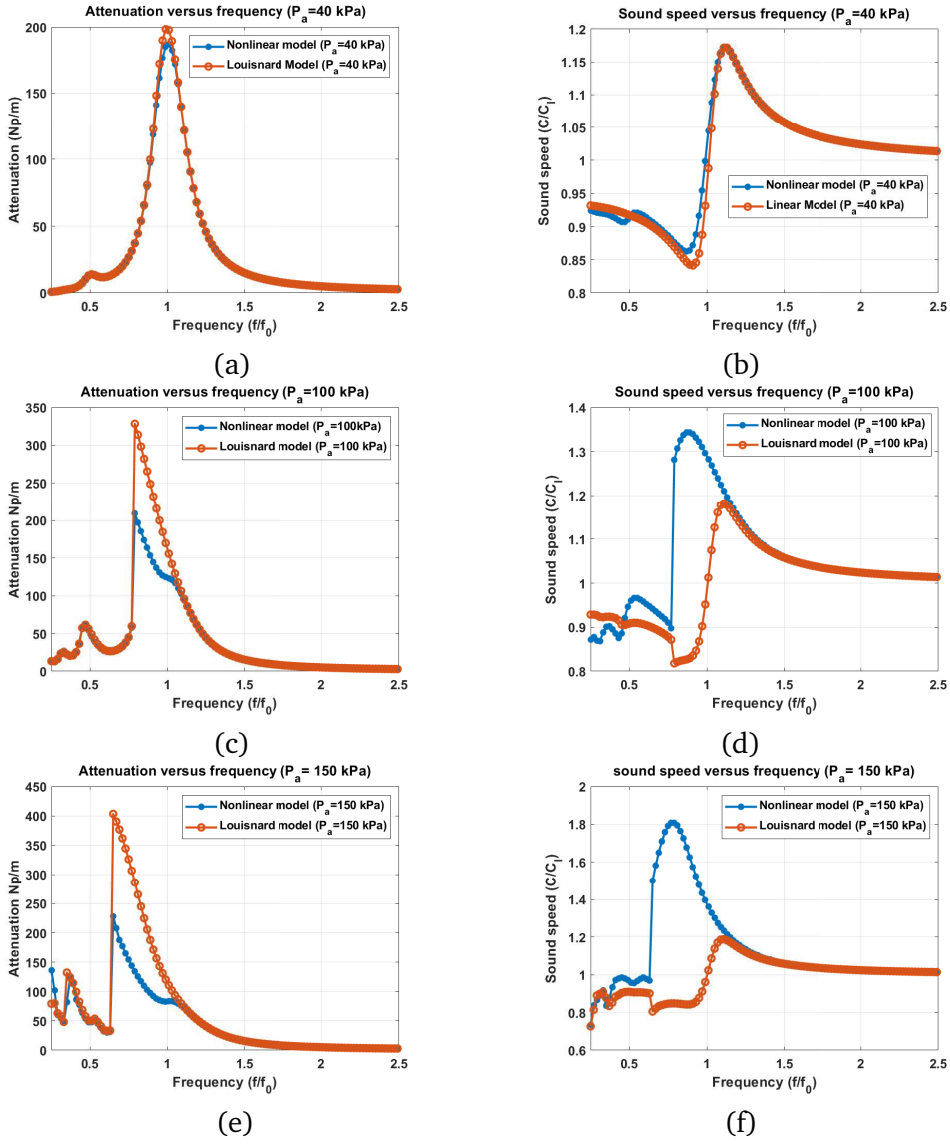

Figure 9.3: Comparison between the predictions the Louisnard & the nonlinear model for sound speed and attenuation. Case of a bubbly medium with uncoated MBs with $R_0 = 2\mu m$ and $\beta = 10^{-5}$. a) attenuation at $P_a = 40kPa$, b) sound speed at $P_a = 40kPa$, c) attenuation at $P_a = 100kPa$ d) sound speed at $P_a = 100kPa$, e) attenuation at $P_a = 150kPa$ and f) sound speed at $P_a = 150kPa$

9.4.2 Validation of the model at higher pressures against the semi-linear Louisnard model

As the pressure increases, assumptions (e.g. small amplitude MB oscillations) on which the linear model is based on are no longer valid. To investigate the effect of pressure, the radial oscillations of the MBs were simulated for exposures of various acoustic pressure amplitudes. For the uncoated bubble $P_a = 40, 70, 100, 150kPa$, for the coated bubble $P_a = 40, 70, 100, 150, 200kPa$ and for the bubble in tissue $P_a = 100, 500, 700, 1000kPa$ were chosen. The power dissipation expressions for nonlinear damping effects which are given by Eq.9.35 (for uncoated bubble), Eq.9.36 for coated bubble and Eq.9.37 for the bubble in tissue were used to calculated the total dissipated power. The imaginary and real part of the wave number were then calculated using Eqs.9.4 and 9.3 in case of our nonlinear model and Eq.9.38 and Eq.9.39 in case of the Louisnard model [18]. The predictions of the two models are illustrated in Figs. 9.2a-f.

The left column of Fig. 9.2 shows that the $\langle \Im (k^2) \rangle$ calculated by Eq.9.3 is in excellent agreement with the Louisnard model (Eq.9.38) for all the acoustic pressures and the bubble models that investigated. Our simple model only needs the radial oscillations of the bubble as input and reduces the complexity of the Louisnard model where the equations for different dissipation mechanisms must be derived for each bubble case. Variations of $\langle \Im (k^2) \rangle$ with pressure shows the importance of the considerations of the pressure effects as the linear model fails to predict phenomena like the resonance shift (e.g. [14]), changes in the amplitude of the $\langle \Im (k^2) \rangle$ with pressure and the generation of SuH (e.g. [53]) and subharmonic (SH) resonances (e.g. [54, 55]). As an instance in case of the uncoated bubble in Fig. 9.2a $\langle \Im (k^2) \rangle \approxeq 8.5 * 10^8 m^{-2}$ at pressure dependent resonance($\frac{f}{f_r} \approxeq 0.98$) when $P_a = 40kPa$. However, as pressure increases to $P_a = 150kPa$ resonance shifts to $\frac{f}{f_r} \approxeq 0.64$ and $\langle \Im (k^2) \rangle \approxeq 7.3 * 10^8 m^{-2}$. Moreover, a SuH occurs at $\frac{f}{f_r} \approxeq 0.34$ with $\langle \Im (k^2) \rangle \approxeq 2.4 * 10^8 m^{-2}$. When $P_a = 40kPa$ and at $\frac{f}{f_r} \approxeq 0.34$, $\langle \Im (k^2) \rangle \approxeq 3.9 * 10^6 m^{-2}$. Thus, the pressure increase has a significant influence on the resonances of the system and the magnitude of the $\langle \Im (k^2) \rangle$.

The Louisnard model uses the linear assumptions (Eq.9.39) to calculate the $\langle \Re (k^2) \rangle$. The predictions of the nonlinear model Eq.9.3 for $\langle \Re (k^2) \rangle - (\frac{\omega}{C_l})^2$, are compared with the predictions of Eq.9.39 in the right hand column of Fig. 9.2 and for 9.3 bubble cases (uncoated, coated

and bubble in tissue). We have subtracted the constant $(\frac{\omega}{C})^2$ from $\langle \Re\left(k^2\right)\rangle$ to better highlight the pressure dependent changes. In each case, pressure increase leads to significant changes in $\langle \Re\left(k^2\right)\rangle$, and predictions of Eq. 9.3 significantly deviate from the linear values (Eq.9.39). As an instance for the uncoated bubble (Fig. 9.2b) the linear model predicts a maximum for $\langle \Re\left(k^2\right)\rangle - (\frac{\omega}{C_l})^2 \approxeq 4.1 * 10^7 m^{-2}$ at $\frac{f}{f_r} \approxeq 0.9$ and a minimum for $\langle \Re\left(k^2\right)\rangle - (\frac{\omega}{C_l})^2 \approxeq -5 * 10^7 m^{-2}$ at $\frac{f}{f_r} \approxeq 1.12$. However, when $P_a = 100kPa$ the maximum is $\langle \Re\left(k^2\right)\rangle - (\frac{\omega}{C_l})^2 \approxeq 1.9 * 10^7 m^{-2}$ at $\frac{f}{f_r} \approxeq 0.761$ and the minimum is $\langle \Re\left(k^2\right)\rangle - (\frac{\omega}{C_l})^2 \approxeq -8.5 * 10^7 m^{-2}$ at $\frac{f}{f_r} \approxeq 0.773$.

Our model incorporates the pressure-dependent changes in $\langle \Re\left(k^2\right)\rangle$ and thus can be used to predict the changes of the $\langle \Re\left(k^2\right)\rangle$ with pressure. To our best knowledge this is the first time that the frequency-pressure dependence of the $\langle \Re\left(k^2\right)\rangle$ in a bubbly medium has been calculated. The ability of our model to calculate both the $\langle \Im\left(k^2\right)\rangle$ & $\langle \Re\left(k^2\right)\rangle$ with pressure changes increase the accuracy of the predictions of the medium attenuation and sound speed changes.

Fig. 9.3 compares the attenuation and sound speed that are calculated using the nonlinear model and the Louisnard model. The values are calculated for the uncoated bubble in Fig. 9.2a-b and at $P_a = 40kPa$, $P_a = 100kPa$ and $P_a = 150kPa$. At 40 kPa (Fig. 9.3a-b), the Louisnard model fails to capture the sound speed fluctuation around $\frac{f}{f_r} \approxeq 0.5$ due to the occurrence of 2nd order superharmonic (SuH) regime. Moreover, the Louisnard model over-estimates the attenuation at the resonance frequency by about 10 $\%$. The deviation in the predicted values between the two models increases with increasing pressure. At $P_a = 100kPa$ (Fig. 9.3c-d), Louisnard model overestimates the attenuation by about 40 $\%$. Moreover, Louisnard model can not capture the the shift in the maximum sound speed to lower frequencies as well as the $\approx 15\%$ increase in its magnitude. At 150 kPa (Fig. 9.3e-f) the Louisnard model overestimates the attenuation peak by 77 $\%$ and underestimates the sound speed peak by about 52 $\%$. The nonlinear model predicts a shift in the frequency of the sound speed peak by about 42 $\%$. Once again, the frequency at which the attenuation peaks ($\frac{f}{f_r} = 0.65$) corresponds to the frequency at which $\frac{C}{C_l} = 1$.

This, shows that pressure dependent effects of $\langle \Re\left(k^2\right)\rangle - (\frac{\omega}{C_l})^2$ can not be neglected and must be included in the calculation of sound speed and attenuation. Our proposed model has the advantage of calculating both of the pressure dependent $\langle \Re\left(k^2\right)\rangle - (\frac{\omega}{C_l})^2$ and $\langle \Im\left(k^2\right)\rangle$.

As the pressure increases, the resonance frequency of the bubbles decreases [14], which is observed as the peak of $\Im(k^2)$ in Fig. 9.2 and attenuation curve in Fig. 9.3 shift towards lower frequencies;

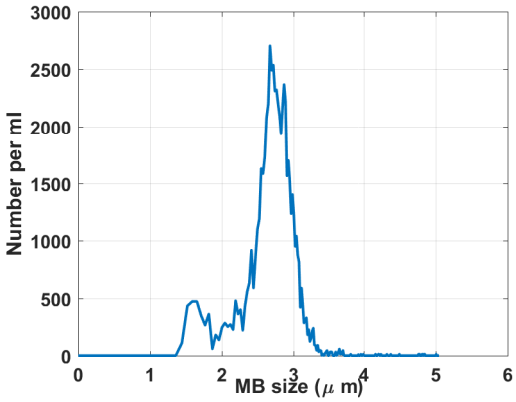

Figure 9.4: Size distribution of the MBs in the experiments measured by coulter counter

this corresponds to the frequencies at which the sound speed in the bubbly medium is equal to the sound speed in the absence of the bubbles. This is seen in Fig. 9.3 where the frequency in which attenuation peaks corresponds to the frequency in which $\frac{C}{C_l} = 1$ in the blue curves that can only be captured by our proposed model. At pressure dependent resonances, the oscillations are in phase with the driving acoustic pressure similar to the case of linear resonance(when $f = f_r$ and at $P_a \cong< 1kPa$ $\frac{C}{C_l} = 1$ page 290 [56]). As the pressure increases, the maximum sound speed of the bubbly medium increases and occurs at a lower frequency, which depends on the driving acoustic pressure amplitude. The abrupt increases in the sound speed and attenuation at particular frequencies in Fig 9.3c-d and in $\langle \Im \left(k^2\right) \rangle$ in Figs. 9.2a, 2c & 2d are due to the pressure dependent resonance frequency which is described in detail in [14]. We have previously shown that when MBs are sonicated with their pressure dependent resonance frequency, the radial oscillation amplitude of the MBs undergo a saddle node bifurcation (rapid increase in amplitude) as soon as the pressure increases above threshold [14] and the maximum stable scattered pressure increases considerably.

9.4.3 Experiments

To experimentally explore the pressure-dependent changes of the sound speed and attenuation for coated MBs, monodisperse lipid shell MBs were produced using flow-focusing in a microfluidic device as previously described [32, 57]. Fig. 9.4 shows the size distribution of the MBs in our experiments. The setup for the attenuation and sound speed measurements is the same as the one used in [57]. Fig. 9.5 shows the setup for the measurements of the attenuation and sound speed.

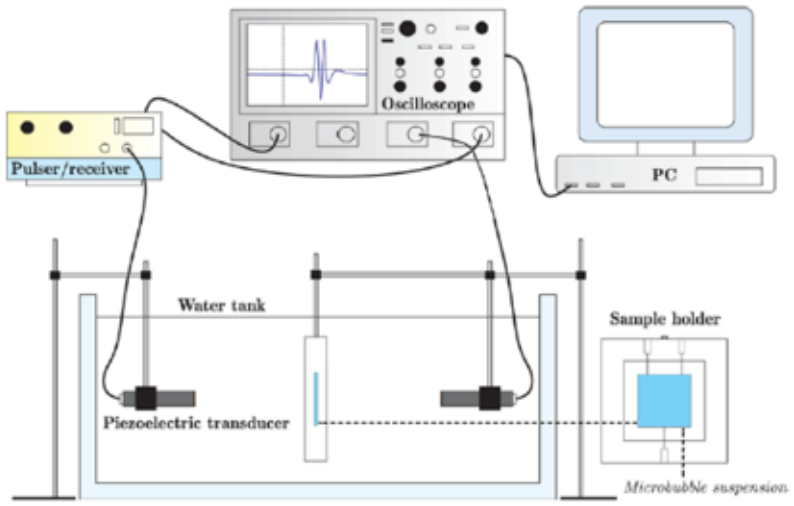

Figure 9.5: The schematic of the setup for the measurements. A broadband pulse with 2.25 MHz center frequency is transmitted by the transducer on the right hand. After propagation through the chamber, the pulse will be revived by the transducer on the left hand side.

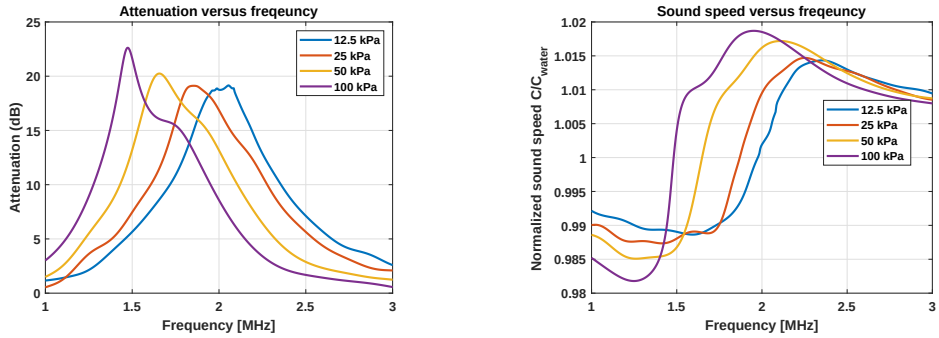

Figure 9.6: Experimentally measured a) attenuation and b) sound speed of the bubbly medium for four different pressures.

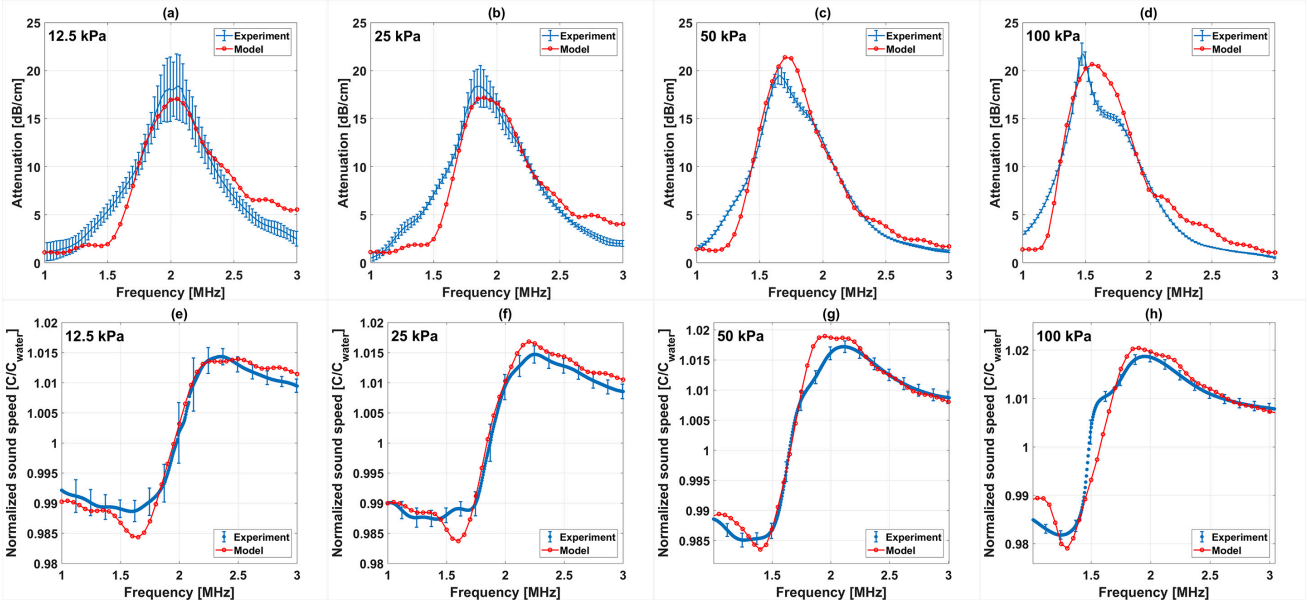

Figure 9.7: Experimentally measured (blue) and simulated (red) attenuation of the sample for a) 12.5 kPa, b) 25 kPa, c) 50 kPa and d) 100 kPa . Sound speed of the sample for e) 12.5 kPa, f) 25 kPa, g) 50 kPa and h) 100 kPa . Errors bars represent the standard deviation.

The thermal properties for the gas can be found in the Table 9.1 ([50]). However, the thermal effects are neglected in the simulations as we have shown in chapter 7 that in case of coated bubbles with C3F8 as the gas core, thermal effects can be neglected. A pair of single-element 2.25-MHz unfocused transducers (Olympus, Center Valley,≈ PA; bandwidth 1-3.0 MHz) were aligned coaxially in a tank of deionized water and oriented facing each other. Monodisperse MBs were injected into a sample chamber that was made with a plastic frame covered with an acoustically transparent thin film. The dimensions of sample chamber were 1.4 x 3.5 x 3.5 cm (1.4 cm acoustic path length), and a stir bar was used to keep the MBs dispersed. The transmit transducer was excited with a pulse generated by a pulser/receiver (5072PR, Panametrics, Waltham, MA) at a pulse repetition frequency (PRF) of 100 Hz. An attenuator controlled the pressure output of the transmit transducer (50BR-008, JFW, Indianapolis, IN), which was calibrated with a 0.2-mm broadband needle hydrophone (Precision Acoustics, Dorset, UK). Electric signals generated by pulses acquired by the receive transducer were sent to the Gagescope (Lockport, IL) and digitized at a sampling frequency of 50MHz. All received signals were recorded on a desktop computer (Dell, Round Rock, TX) and processed using Matlab software (The MathWorks, Natick, MA). The peak negative pressures of the acoustic pulses that are used in experiments were 12.5, 25 and 50 and 100 kPa.
Figs. 9.6a-b show representative samples of the experimentally measured attenuation and sound speed of the mixture respectively. The attenuation of the bubbly medium increases as the pressure increases from 12.5 kPa to 100 kPa and the frequency of the maximum attenuation decreases from 2.045 MHz to 1.475 MHz. Maximum sound speed of the medium increases with pressure and the corresponding frequency of the maximum sound speed decreases by pressure increases. To our best knowledge this is the first experimental demonstration of the pressure dependence of the sound speed. It is also interesting to note that at the pressure dependent resonance frequencies (measured attenuation peaks) the sound speed is equal to the sound speed of the water in the absence of bubbles.

9.5 Comparison of the model predictions against experimental observations

9.5.0.1 Lipid coated bubble model including bubble-bubble interaction

To numerically simulate the attenuation and sound speed, the Marmottant model [16], which accounts for radial-dependent shell properties, was modified to include MB multiple scattering using the approach introduced in [58]:

$$\begin{aligned} R_i\ddot{R}_i + \frac{3}{2}\dot{R_i}^2 = \frac{1}{\rho}([P_0 + \frac{2\sigma(R_{0i})}{R_{0i}}](\frac{R_i}{R_{i0}})^{3k}(1 - \frac{3k}{C_l}\dot{R}_i) \\ -\frac{2\sigma(R_i)}{R_i} - \frac{4\mu\dot{R}_i}{R_i} - \frac{4\kappa_s\dot{R}_i}{R_i^2} - P_{ac}(t)) - \\ \sum_{j\neq i}\frac{R_j}{d_{ij}}(R_j\ddot{R}_j + 2\dot{R_j}^2), i = 1, .., N \end{aligned} \tag{9.40}$$

In this equation R_{i0} is the initial radius of the ith bubble, P_0 is the atmospheric pressure C_l is the sound speed, k is the polytropic exponent, μ is the viscosity of the liquid. σ is the surface tension which is a function of bubble radius and is given by :

$$\sigma = \begin{cases} 0 & if \quad R <= R_b \\ \chi\left((\frac{R}{R_b})^2 - 1\right) & if \quad R_b < R < R_r \\ \sigma_{water} & if \quad R >= R_r \end{cases} \tag{9.41}$$

where σ_{water} is the water surface tension, $R_b = \frac{R_0}{\sqrt{1+\frac{R_0}{\chi}}}$ is the buckling radius, R_r is the rupture radius (=break up radius in this paper) and χ is the shell elasticity. κ_s in equation9.40, is the surface diltational viscosity .

Using our approach in [59], Eq.9.40 can be written in a matrix format as:

$$\begin{pmatrix} \ddot{R}_1 \\ \ddot{R}_2 \\ \dots \\ \ddot{R}_N \end{pmatrix} = \begin{pmatrix} R_1 & \frac{R_2^2}{d_{12}} & \dots & \frac{R_N^2}{d_{1N}} \\ \frac{R_1^2}{d_{21}} & R_1 & \dots & \frac{R_N^2}{d_{2N}} \\ \dots & \dots & \dots & \dots \\ \frac{R_1^2}{d_{N1}} & \frac{R_2^2}{d_{N2}} & \dots & R_N \end{pmatrix}^{-1} \begin{pmatrix} A_1 \\ A_2 \\ \dots \\ A_N \end{pmatrix} \tag{9.42}$$

where:

$$A_i = \frac{1}{\rho}\left(\left[P_0 + \frac{2\sigma(R_{0i})}{R_{0i}}\right]\left(\frac{R_i}{R_{i0}}\right)^{3k}\left(1 - \frac{3k}{C_l}\dot{R}_i\right) - \frac{2\sigma(R_i)}{R_i} - \frac{4\mu\dot{R}_i}{R_i} - \frac{4\kappa\dot{R}_i}{R_i^2} - P_{ac}(t) - \frac{3\rho}{2}\dot{R}_i{}^2\right) - \sum_{j\neq i}\frac{2R_j\dot{R}_j{}^2}{d_{ij}} \tag{9.43}$$

The gas inside the bubble is C3F8 and the properties are given in Table 9.1. We have neglected the thermal effects in the numerical simulations in this part. In [28] we have shown that in case of the coated bubbles that enclose C3F8 gas cores, thermal dissipation has negligible contribution to the overall dissipated power. Thus, thermal effects are neglected to reduce the complexity of the multiple scattering equation that is used in the simulations (Eq.9.40).

9.5.0.2 Simulation procedure

At each frequency and pressure, 63 MBs were selected from the size distribution in Fig. 9.4 and were randomly distributed in a cube with sides of 0.1 mm in length (to simulate the concentration of 63000 MBs/ml in the experiments). The results were weighted by the number density of the MBs in Fig. 9.4 and were implemented in Eqs.9.3 & 9.4. This procedure was repeated by iterating different values for the shell elasticity (0.1N/m$<\chi<$2.5 N/m), initial surface tension (0

N/m $< \sigma(R_0) <$ 0.072 N/m), shell viscosity (1e-9 *Pa.s* $<\mu_s<$ $1e-7$ $Pa.s$), and break up radius ($R_0 < R_{breakup} < 2R_0$) to fit the experimental curves.

To compare the predictions of the model with experiments, Figs. 9.7a-h illustrate the results of the experimentally measured (blue) (with standard deviations of the 100 data points at each condition) and numerically simulated (red) sound speed of the medium as a function of frequency, for 4 different pressure exposures of (12.5, 25, 50 and 100 kPa). The shell parameters that were used to fit the experimental results are χ=1.1 N/m, $\sigma(R_0)$= 0.016N/m, μ_s=7e-9 $Pa.s$ and $R_{breakup}$=1.1R_0.

Figs. 9.7a-d show the results of the experimentally measured (blue) and numerically simulated (red) medium attenuation for peak acoustic pressures of 12.5, 25, 50 and 100 kPa. As the pressure increases, the frequency at which the maximum attenuation occurs (which indicates the resonance frequency) decreases (from 2.02 MHz at 12.5 kPa to 1.475 MHz at 100 kPa) and the magnitude of the attenuation peak increases (from 16.5 dB/cm at 2 MHz to 21.8 dB/cm at 1.475 MHz). At 12.5 kPa and for frequencies below $\sim$ 2 MHz, the speed of sound in the bubbly medium is smaller than the sound speed of water. Above 2 MHz, speed of sound increases and reaches a maximum at 2.25 MHz with a magnitude of $\sim$ 1.015C_l. At $\sim$ 2MHz the sound speed is equal to C_l. This is also the frequency where the attenuation is maximum. According to the linear theory [56] at the resonance frequency the sound speed of the bubbly medium is equal to the sound speed of the medium without the bubbles. As the pressure increases to 25, 50 and 100 kPa the frequency at which the speed of sound in the bubbly sample is equal to C_l decreases to 1.87, 1.65 and 1.48 MHz respectively. The frequency at which the maximum sound speed occurs decreases as the pressure increases and the magnitude of the maximum sound speed increases to $\sim$ 1.019C_l at 100 kPa. The minimum sound speed decreases from $\sim$ 0.989C_l at 12.5 kPa (peak at1.6 MHz) to $\sim$ 0.981C_l at 100 kPa and (1.25 MHz). At each pressure, the frequency at which attenuation is maximized (the pressure dependent resonance) is approximately equal to the frequency where the sound speed becomes equal to C_l. Thus, it can be observed that, even at the pressure dependent resonance frequency (PDf_r) which is a nonlinear effect [14], the velocity is in phase with the driving force and $\frac{C}{C_l} = 1$ (page 290 [56]). This observation is also consistent with the numerical results of the uncoated bubble in Figs. 9.1a-f and Figs. 9.3a-d (blue curves).

9.6 classification of the main nonlinear regime of oscillations and the corresponding changes in the attenuation and sound speed

Knowledge of the changes of the attenuation and sound speed due to bubble pulsations is key to optimize the applications involving bubble dynamics. The attenuation and sound speed changes are dependent on the nonlinear bubble dynamics. MB oscillators can exhibit stable nonlinear oscillations (e.g. period 2, 3, 4 or superharmonics, ultra harmonics and chaotic oscillations) [13, 14, 15, 53, 54, 55, 60, 61, 62, 63, 64, 65, 66]. However, our knowledge of the attenuation and sound speed of the medium during nonlinear bubble oscillations is limited.

In this section, first we will introduce some main nonlinear oscillation regimes. Then, the sound speed and attenuation changes are classified in these regimes for the first time. We then introduce an optimization case where the lost focus due to ultrasound attenuation is reconstructed.

9.6.1 Bifurcation diagrams

Understanding the complex dynamics of nonlinear systems over extended control parameter regions is easier when using bifurcation diagrams where the qualitative and quantitative changes of the dynamics of the system can be investigated. In this section, we employ a more comprehensive bifurcation analysis using the method introduced in chapter 3 ([53]).

9.6.2 Nonlinear oscillation regimes of the coated bubble

A coated bubble in water with $R_0 = 2\mu m$ with a C3F8 gas core is considered. The shell parameters are $G_s = 20MPa$, $\epsilon = 4nm$ and $\mu_{sh} = 0.265Pa.s$. The number of the bubbles is calculated to represent a clinical situation as follows:

Definity® bubbles are one of the coated bubbles that are used clinically (e.g. [67,68]). The dosage of Definity® bubbles is $10\mu l$ per kg weight of the human body and each ml of Definity® has 1.2×10^{10} bubbles [67, 68]. Thus, for a 100 kg patient with approximately 7500 ml total blood volume, bubble density in blood will be $1.6 * 10^{12}\ bubbles/m^3$. Since approximately 7% of the

body is blood and considering homogeneous distribution of blood in the body for simplicity, this number will be diluted to 7% for the simulations of the wave propagation through a sample of tissue. It should be noted that the final value is only an approximation and in real cases factors like different blood perfusion at different locations of the body as well as the presence of large blood vessels in the beam path should be considered. Incorporation of these factors are beyond the scope of this study. Moreover, we assumed no interaction between bubbles and possible effects of the surrounding tissue is neglected.

In the next sections we present the bifurcation structure of a coated bubble irradiated at different frequencies of interest (e.g. f_r, f_{sh}, ..)

9.6.2.1 Case of $f = 0.3f_r$

Fig. 9.8a shows the bifurcation structure of the coated bubble as a function of the pressure. The blue line is constructed using the method of peaks and the red line is constructed using the conventional method. At $\approx 50kPa$, 3 maxima appear in the period-1 bubble oscillations (blue line has 3 branches while the red line consists of only one branch); this indicates the generation of 3rd order SuH in the oscillations of the bubble [53]. Oscillations amplitude grows with increasing pressure and at $\approx 140kPa$, the red graph experiences period doubling (Pd). The Pd in red graph is concomitant with 3 Pds in the blue graph, indicating a $\frac{7}{2}$ UH regime of oscillations [53]. A further pressure increase above 168 kPa results in oscillations with $\frac{R_{max}}{R_0} > 2$ and bubble may most likely undergo destruction [69] (for a detailed review of bubble destruction threshold please refer to [14]). At about 168 kPa a saddle node bifurcation results in 2nd order superharmonic (SuH) resonance (P1 with 2 maxima) which undergo Pd and chaos. At about 270 kPa a P1 giant resonance emerges out of the chaotic window which undergoes Pd above 500 kPa. Finally chaotic oscillations appear at $P_a \approx 750kPa$ through successive Pds.

At lower pressures the attenuation of the bubbly medium is 0.24 Np/m (smallest compared to the other frequencies ($0.3f_r < f \leq 3f_r$) studied here). Concomitant with the appearance of the 3 solutions in the blue curve (3rd order SuH) attenuation increases rapidly with pressure and reaches 12.8 Np/m at $\approx 168kPa$. The occurrence of saddle node bifurcation at 168 kPa is concomitant with an abrupt increase in attenuation to 53 Np/m. Attenuation increases to $\approx 83Np/m$ before the emergence of the giant resonance. The giant resonance is concomitant with another abrupt

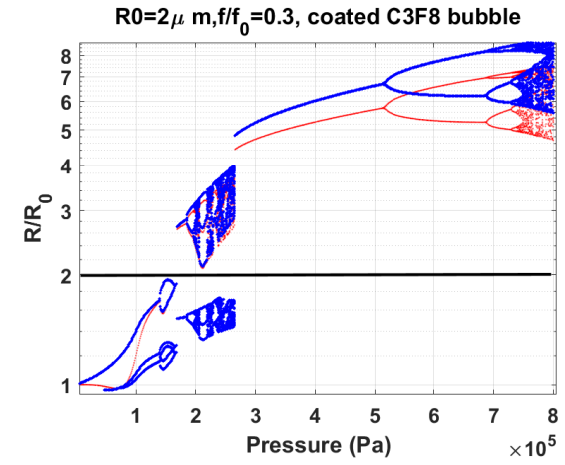

(a)

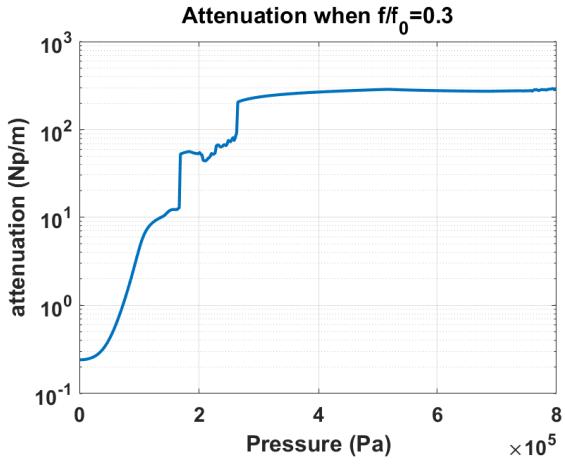

(b)

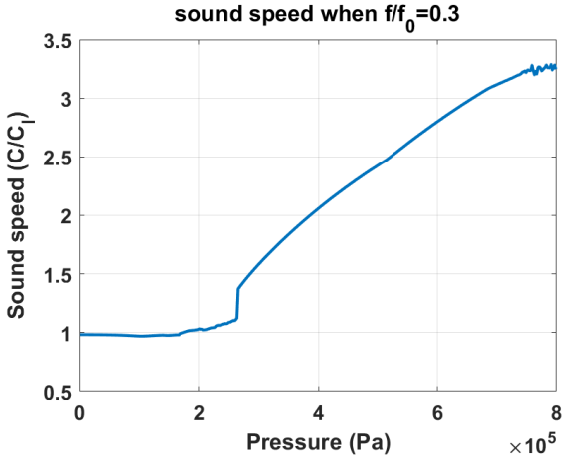

(c)

Figure 9.8: a) Bifurcation structure of the coated bubble as a function of pressure when $f = 0.3f_r$, b) the corresponding attenuation of the bubbly water and c) sound speed of the bubbly water.

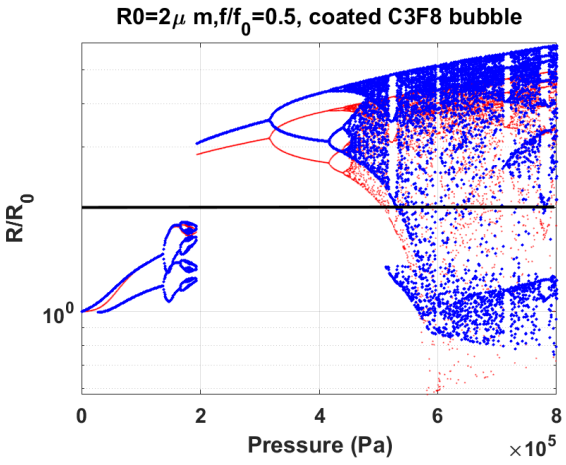

(a)

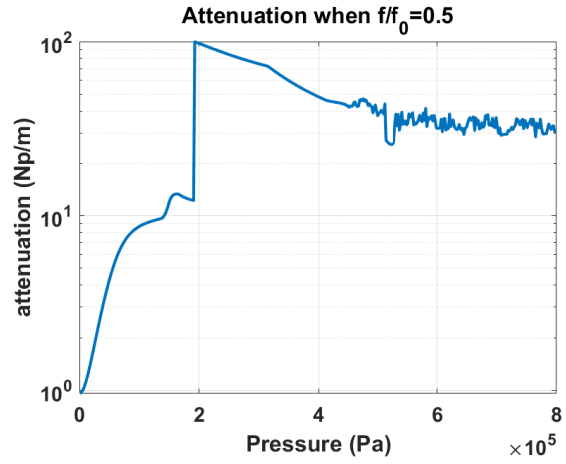

(b)

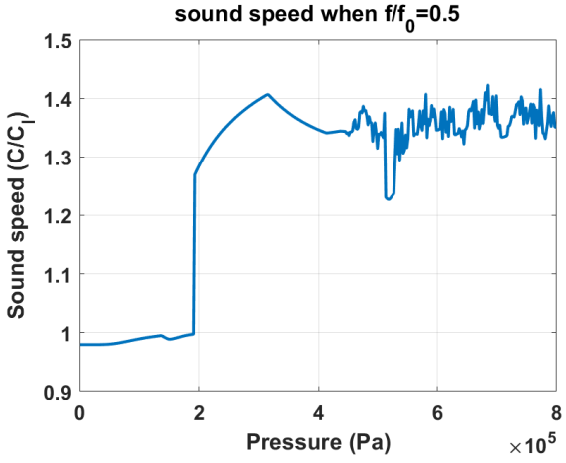

(c)

Figure 9.9: a) Bifurcation structure of the coated bubble as a function of pressure when $f = 0.5f_r$, b) the corresponding attenuation of the bubbly water and c) sound speed of the bubbly water.

increase in attenuation to $\approx 212Np/m$ at $P_a \approxeq 269kPa$. Attenuation grows very slowly with pressure increase and reaches $\approx 292Np/m$ at 800 kPa.

Sound speed $\frac{C}{C_l} = 0.982 - 0.980$ barely changes for pressure below the occurrence of saddle-node bifurcation at $P_a = 168kPa$. After the occurrence of saddle-node bifurcation $\frac{C}{C_l}$ increases with pressure and reaches 1.12 at 263 kPa. Emergence of the giant resonance results in an abrupt increase in $\frac{C}{C_l}$ to 1.34. Afterwards, $\frac{C}{C_l}$ increases rapidly with pressure and reaches ≈ 3.3 during the chaotic oscillations at 800 kPa.

9.6.2.2 Case of $f = 0.5f_r$

Bifurcation structure of the bubble when $f = 0.5f_r$ is shown in Fig. 9a. At $P_a = 28kPa$ two maxima occur (2 branches in the blue curve) for P1 (1 branch in red curve) oscillations. This indicates the 2nd harmonic regime of oscillations [53]. Oscillations amplitude increases with pressure and a Pd occur at $\approx 137kPa$. This results in a P2 oscillations (two branches in red curve) with 4 maxima (4 branches in the blue curve) which indicates the $\frac{5}{2}$ order UH resonance [53]. Oscillations undergo further Pds to P4 oscillations with 8 maxima and at $\approx 200kPa$ a giant P1 resonance appear. Occurrence of the giant P1 resonance is most likely concomitant with bubble destruction $\frac{R}{R_0} > 2$. Further pressure increase results in multiple Pds to chaos at $\approx 455kPa$.

Attenuation of the bubbly medium increases with pressure increases and reaches $\approx 9.6Np/m$ at 137 kPa. The occurrence of the UHs is concomitant with fast increase in attenuation as it reaches $13.3Np/m$ at 165 kPa. A further Pd decreases the attenuation to $12.2Np/m$ right before the generation of giant resonance. The giant resonance is concomitant with a sharp increase in attenuation to $\approx 100Np/m$. A further pressure increase results in a steady decline in attenuation. The occurrence of Pd further decreases the attenuation until attenuation plateaus to small fluctuations around $\approx 37Np/m$ during chaotic oscillations.

Sound speed remains at $\frac{C}{C_l} = 0.98 - 0.99$ until the incident pressure approximately reaches to 200 kPa. Concurrent with the giant resonance, the sound speed abruptly increases to $\frac{C}{C_l} = 1.27$. The sound speed keeps increasing with pressure and reaches $\frac{C}{C_l} = 1.4$ at $P_a \approx 317kPa$. Concomitant with the Pd at $P_a \approx 318kPa$, the sound speed start decreasing with pressure increase and plateaus to fluctuating values around $\frac{C}{C_l} \approx 1.37$ during the chaotic oscillations.

9.6.2.3 Case of $f = 0.75 f_r$

Fig. 9.10 shows the bifurcation structure of the bubble sonicated with $f = 0.75 f_r$. This frequency is referred to as the pressure dependent resonance frequency of the bubble [14, 70]. Initially, the bubble oscillations are of P1 with one maxima and the oscillation amplitude grows with increasing pressure. At $P_a = 85kPa$ the radial oscillations undergo a saddle node bifurcation to P1 oscillations with higher amplitude.At the saddle node point, the red curve meets the blue curve; this indicates that the wall velocity is in phase with the incoming wave and the bubble oscillations are at resonance [56]. This also confirms our experimental observations in Fig. 9.6 and 9.7 in which the frequency at which the sound speed becomes equal to the sound speed of the pure water at pressure dependent resonances of the system. The pressure increase results in a monotonic increase in oscillation amplitude and $\frac{R_{max}}{R_0} \approxeq 2$ at $P_a \approxeq 128kPa$; thus any pressure increase above 128 kPa most likely results in non-stable bubble oscillations. Pd occurs at $P_a \approxeq 229kPa$ with the emergence of chaos at about 310 kPa through successive Pds. A P2 giant resonance emerges out of the chaotic window just above 600 kPa and later undergoes two Pds to P4 oscillations.

Attenuation of the medium slowly increases with pressure; however in the vicinity of the pressure for saddle-node bifurcation attenuation increases abruptly ($\alpha \approxeq 16Np/m$ at $P_a = 81kPa$ and increases to approximately 80 Np/m at 85 kPa). After the occurrence of saddle-node bifurcation attenuation decreases with increasing pressure until it plateaus to a fluctuating value around 11.5 Np/m during the chaotic oscillations. Concomitant with the generation of the giant resonance, attenuation abruptly increases and plateaus to $\approx 21.5Np/m$.

For pressures below the generation of saddlenode (SN) bifurcation the $\frac{C}{C_l} \approxeq 0.968$. Just before the occurrence of SN, sound speed decreases slightly, then it undergoes an abrupt increase. $\frac{C}{C_l} \approxeq 0.962$ at $P_a = 83kPa$ and increases to $\frac{C}{C_l} \approxeq 1.05$ at $P_a = 85kPa$ and plateaus to 1.1 at 159 kPa. Concomitant with the Pd at 229 kPa, sound speed starts decreasing with pressure increase to $\frac{C}{C_l} \approxeq 1.08$ right before the occurrence of chaos. Sound speed fluctuates during chaotic oscillations and then increases with the emergence of giant resonance.

In [14] we have shown that when the bubble is sonicated with its pressure dependent resonance frequency (PDf_r) the generation of Pd is concomitant with a decrease in the bubble wall velocity

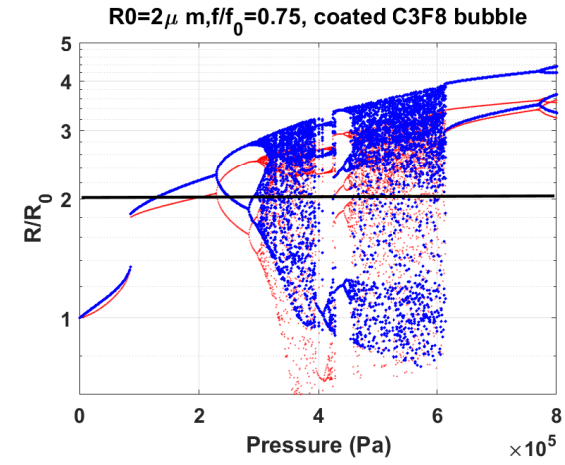

(a)

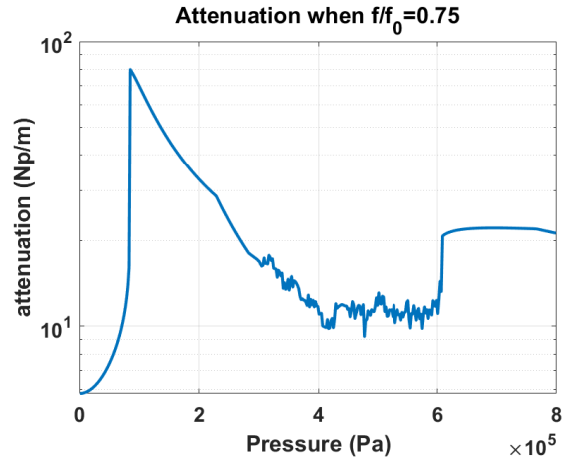

(b)

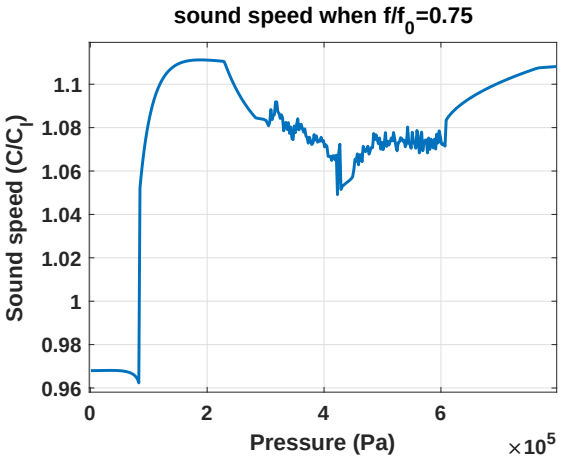

(c)

Figure 9.10: a) Bifurcation structure of the coated bubble as a function of pressure when $f = 0.75 f_r$, b) the corresponding attenuation of the bubbly water and c) sound speed of the bubbly water.

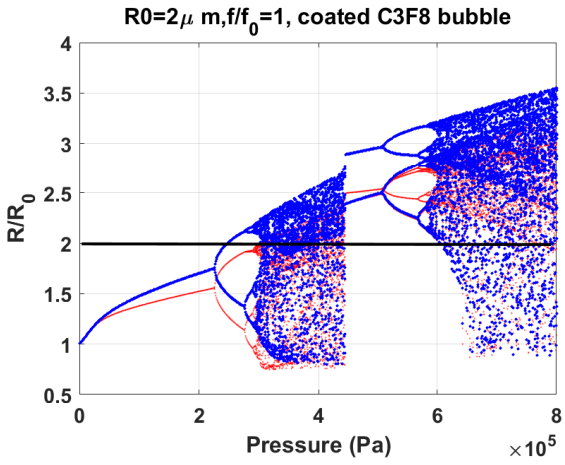

(a)

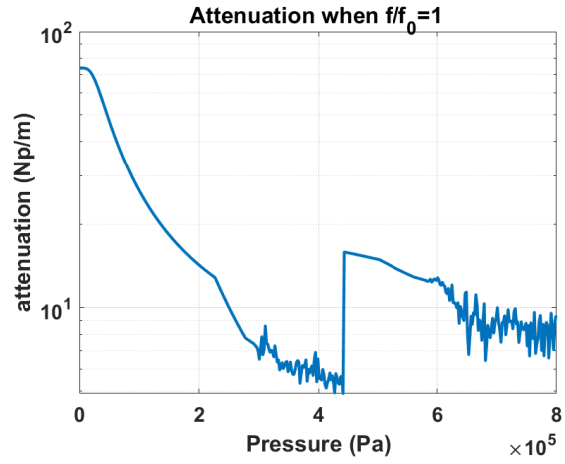

(b)

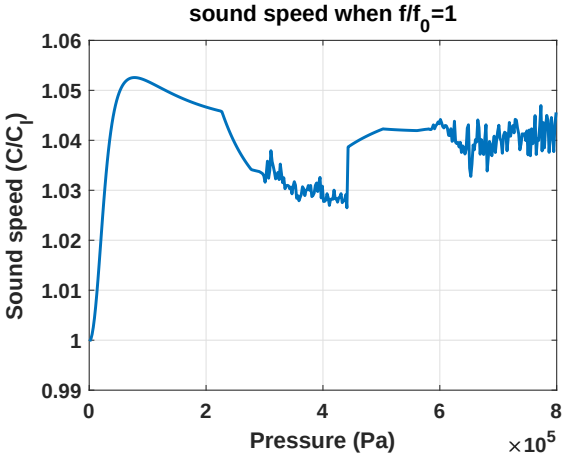

(c)

Figure 9.11: a) Bifurcation structure of the coated bubble as a function of pressure when $f = f_r$, b) the corresponding attenuation of the bubbly water, c) and sound speed of the bubbly water.

amplitude and scattered pressure. Here, we show that generation of Pd is also concomitant with the decrease in sound speed of the bubbly medium. Moreover, Fig. 9.10b show that the rate of attenuation decrease further increases when Pd occurs.

9.6.2.4 Case of $f = f_r$

When the bubble is sonicated with its resonance frequency, the oscillation amplitude increases monotonically with increasing pressure (Fig 9.11a). The red curve and blue curve have the same value for $P_a < 23kPa$. This indicates that the wall velocity is in phase with the incoming acoustic waves. This is expected as the bubble is sonicated with its linear resonance frequency. As the pressure increases the two curves diverge because of the change in the resonance frequency with pressure. Oscillations undergo a Pd at 226 kPa; $\frac{R_{max}}{R_0}$ exceeds 2 at 248 kPa (possible bubble destruction above this point) and chaos is generated through multiple Pds at 300 kPa. At 444 kPa a giant P2 resonance emerges out of the chaotic window and subsequently undergoes a Pd cascade to chaos at about 600 kPa.

The attenuation decreases as pressure increases. Attenuation is 74 Np/m at 1 kPa and decreases to 12.4 Np/m at 231 kPa. Concomitant with Pd, the rate of attenuation decrease with pressure increases and attenuation further drops to 7.7 Np/m at 279 kPa. Within the chaotic window, the pressure increase results in a further decrease of the attenuation in a fluctuating manner to 4.8 Np/m right before the emergence of the giant resonance. The giant resonance is concomitant with an abrupt increase in attenuation to 15.8 Np/m at 445 kPa. Afterwards, the attenuation decreases slowly with pressure and plateaus to a fluctuating value around 8.9 Np/m within the second chaotic window.

At $P_a = 1kPa$, $\frac{C}{C_l} = 1$ (Fig. 9.11c). The sound speed rises very fast with pressure increase and reaches $\frac{C}{C_l} = 1.052$ at 79 kPa. Further pressure increase results in a slow and steady decrease of the sound speed. Concomitant with Pd, the rate of the sound speed decrease increases and speed reaches $\frac{C}{C_l} = 1.034$ right before the generation of chaos. Sound speed fluctuates around 1.03 within the chaotic window and concurrent with the generation of giant resonance sound speed increases abruptly to $\frac{C}{C_l} = 1.038$. Sound speed plateaus to a fluctuating value around $\frac{C}{C_l} = 1.041$.

9.6.2.5 Case of $f = 1.5f_r$

The bifurcation structure of the bubble sonicated with $f = 1.5f_r$ (Pressure dependent SH resonance frequency PDf_{sh}) is shown in Fig. 9.12a. The oscillations amplitude increases monotonically with pressure and Pd occurs at $\approxeq 249kPa$. P2 oscillations undergo a SN bifurcation to P2 oscillations of higher amplitude at $P_a \approxeq 290kPa$. In [55], we have shown that SN bifurcation is concomitant with the over saturation of the SH component of the scattered pressure by the bubble. P2 oscillations undergo another Pd and P4 oscillation amplitude increases beyond the destruction threshold of $\frac{R_{max}}{R_0} = 2$ [69] at $P_a = 377kPa$. Chaos appears at $P_a \approxeq 426kPa$ and extends to $P_a \approxeq 768kPa$ with a small window of periodic behavior. A giant P3 resonance emerges out of the chaotic window at $P_a = 767kPa$.

The attenuation (Fig. 9.12b) decreases very slowly with increasing pressure (from 3.5 at 1kPa to 3.2 Np/m at 249 kPa). Concurrent with Pd at 249 kPa, the attenuation decreases rapidly to 2.3 Np/m at $P_a = 285kPa$. SN occurrence results in an abrupt increase in the attenuation to 9.4 Np/m at 291 kPa. The attenuation then decreases with pressure increase and fluctuates around a mean value of 3.3 Np/m within the chaotic window and then abruptly increases to 6.5 Np/m when a giant resonance occurs.

The sound speed remains constant around $\frac{C}{C_l} = 1.01$ until Pd takes place under which the sound speed decreases to $\frac{C}{C_l} = 1.009$. Concomitant with SN, sound speed abruptly increases to $\frac{C}{C_l} = 1.013$ and fluctuates within the chaotic oscillations. Sound speed changes are much smaller compared to the resonance and below resonance oscillations.

9.6.2.6 Case of $f = 2f_r$

Bifurcation structure of the bubble when $f = 2f_r$ (linear SH resonance frequency of the bubble f_{sh}) is shown in Fig. 9.13a. The oscillation amplitude grows slowly with pressure increase and Pd occurs at 140 kPa. At this point oscillations have two maxima. One of the maxima quickly disappears. At about 200 kPa Pd occurs and evolve in the shape of a bow-tie (chapter 4) [54] and at $P_a = 263kPa$ the second maxima re-emerges with a value equal to the higher branch of the red curve. This indicates that wall velocity is in phase with the driving pressure once every two acoustic

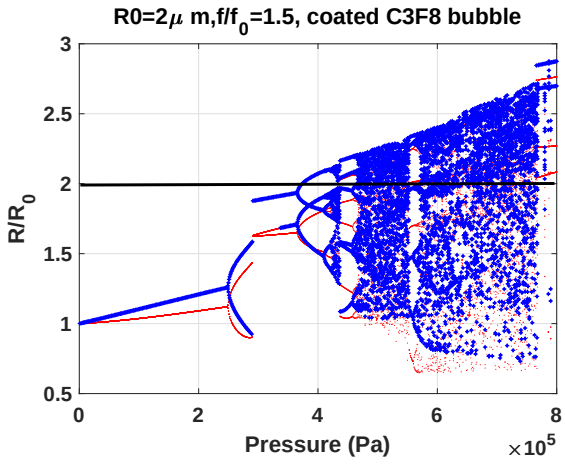

(a)

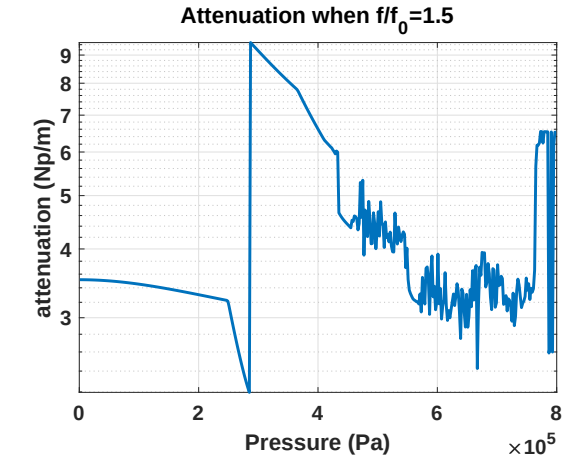

(b)

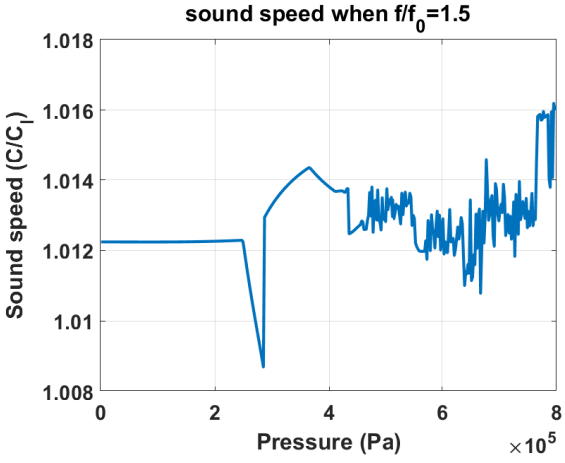

(c)

Figure 9.12: a) Bifurcation structure of the coated bubble as a function of pressure when $f = 1.5 f_r$, b) the corresponding attenuation of the bubbly water c) and sound speed of the bubbly water.

cycles and full SH resonance is developed. Oscillations undergo successive Pds to chaos and bubble destruction may occur at $P_a > 700$ kPa for the chaotic oscillations.

The attenuation of the medium stays constant around 1.3 Np/m below the pressure for Pd. As soon as Pd takes place the attenuation starts increasing rapidly until it reaches a maximum of 3.15 Np/m coincident with re-emergence of the second maximum in the bifurcation diagram. After that attenuation decreases and fluctuates during the chaotic oscillations.

Sound speed changes are small. Sound speed decreases with Pd and starts increasing as soon as one of the maxima disappears. Occurrence of the second Pd is also concomitant with a decrease in sound speed. Sound speed fluctuates within the chaotic window and never increases above $\frac{C}{C_l} = 1.0075$ for the chaotic regime of oscillations.

9.6.2.7 Case of $f = 3f_r$

The bifurcation structure of the bubble when $f = 3f_r$ is shown in Fig. 9.14a. The oscillation amplitude increases slowly with pressure and at $P_a \approxeq 632kPa$, P3 oscillations develop. P3 oscillations result in the generation of 1/3, 2/3 SHs in the scattered pressure of the bubble [62]. Occurrence of P3 oscillations are concomitant with a rapid increase in attenuation in Fig. 9.14b and sound speed in Fig. 9.14c. P3 oscillations become P1 at $P_a \approxeq 789kPa$ and subsequently attenuation and sound speed decreases abruptly. Contrary to the common belief, attenuation of the bubbly medium when the bubble is sonicated with multiples of its resonance frequency is very small even when the P2 or P3 oscillations are generated.

9.6.2.8 Simulation of the propagation of focused waves through bubbly media

In the previous subsection, we revealed some major nonlinear regimes of oscillations by the analysis of bifurcation diagrams. Attenuation and sound speed changes of the medium were investigated alongside the bifurcation diagrams and the changes of the attenuation and sound speed were classified in each category. In this section, propagation of the focused ultrasonic waves through a bubbly medium is numerically simulated using finite element method. The Comsol® software is used for numerical simulations. The knowledge obtained in the previous section is used to optimize the exposure parameters for ultrasound wave propagation.

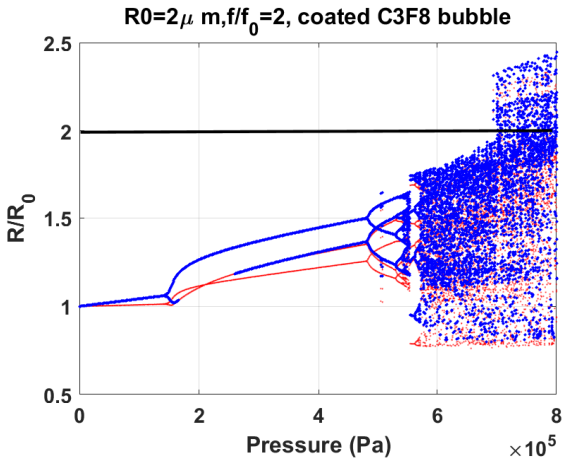

(a)

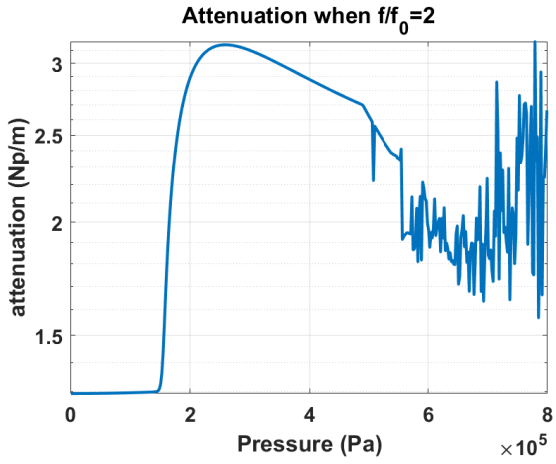

(b)

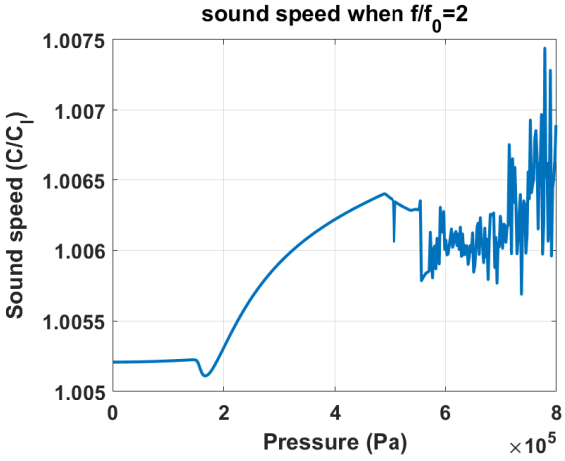

(c)

Figure 9.13: a) Bifurcation structure of the coated bubble as a function of pressure when $f = 2f_r$, b) the corresponding attenuation of the bubbly water (b) and c) sound speed of the bubbly water.

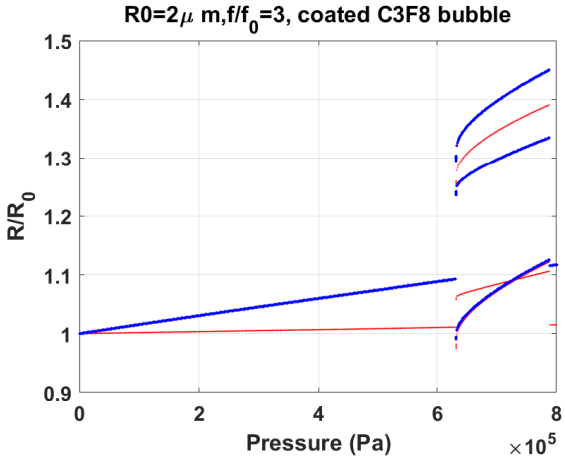

(a)

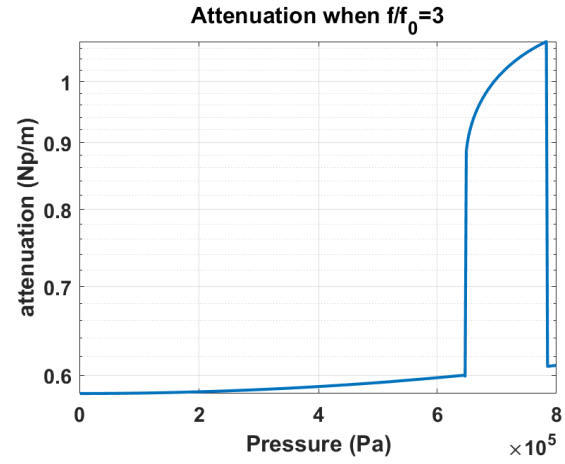

(b)

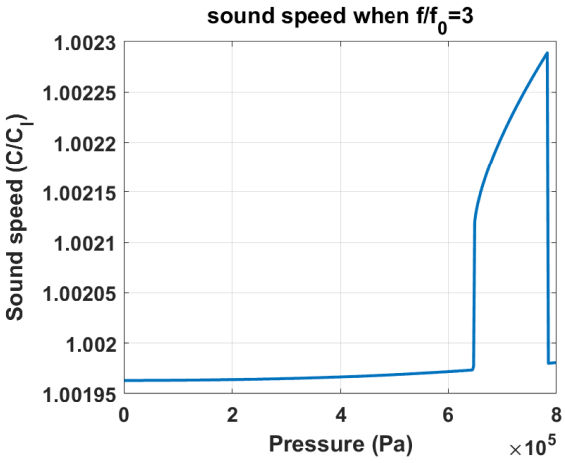

(c)

Figure 9.14: a) Bifurcation structure of the coated bubble as a function of pressure when $f = 3f_r$, b) the corresponding attenuation of the bubbly water and c) sound speed of the bubbly water.

In applications pertaining to bubble dynamics, the increased attenuation of the bubbly media hinders the efficacy of applications by limiting the ultrasonic energy that can be delivered to the target. We have proposed in [14, 71] that application of the pressure dependent resonance or SuH resonance may help us to decrease the attenuation caused by bubbles in the pre-focal region. Moreover, in focused ultrasound applications like high intensity focused ultrasound (HIFU), the sharp pressure gradient by focused transducers can be used to only activate the focal bubbles which may result in significant decrease in the attenuation as the pre-focal bubbles are non-resonant [14, 71]. In [23], Pdf_r is used to sonicate narrow size distribution of bubbles and it is shown that this method enhances the ability of penetrating through a bubbly medium with minimum loss.

Here we first compare the attenuation and sound speed of the medium at the classified stages below resonance oscillations. Then, the frequency and pressure of the sonication is optimized to maximize the gain at the focus. Fig. 9.15a-b, compares the attenuation and sound speed changes of the medium as a function of pressure and for frequencies equal to resonance and below resonance. The higher frequencies are omitted from the figure for the simplicity of the comparison. Attenuation and sound speed changes at $f = 2f_r$ & $3f_r$ are negligible compared to resonance and below resonance oscillations even when SH resonances occur. These frequencies are often used for nonlinear imaging at 1/2 order SHs; however, due to stronger bubble activity frequencies around resonance and below resonance are used for most applications.

Fig. 9.15a shows that the attenuation changes can be divided in 5 different regions. In region A, $P_a < 95kPa$ sonication with $f = f_r$ results in the highest attenuation. Thus, pressure waves will be attenuated in the pre-focal region and the ultrasound focus may be destroyed. If one desires to set the focal pressure at 100 kPa and have strong bubble activity, $f = 0.75f_r$ (PDf_r) should be the ultrasound frequency. Moreover, if the goal of the application is SuH harmonic imaging or UH harmonic imaging at 100-170 kPa; $f = 0.5f_r \& 0.3f_r$ are more suitable as not only are the SuH and the UH component of the scattered pressure stronger, but also the pre-focal attenuation is orders of magnitude smaller than when $f = f_r$ or $f = 0.75f_r$. Thus, undesirable image artifacts like shadowing would be minimized.

Sonication with $f = 0.3f_r$ and $f = 0.5f_r$ are desirable in case of achieving a target focal pressure withing 100-170 kPa range. For higher bubble activity at the focus and to achieve effects like enhanced heating within the 170-200 kPa range $f = 0.3f_r$ is the desirable frequency due to an

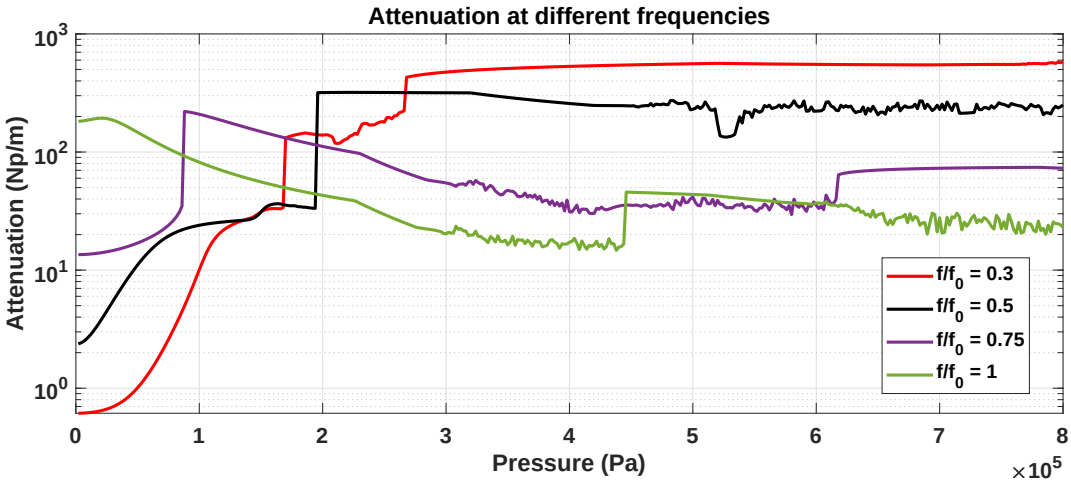

(a)

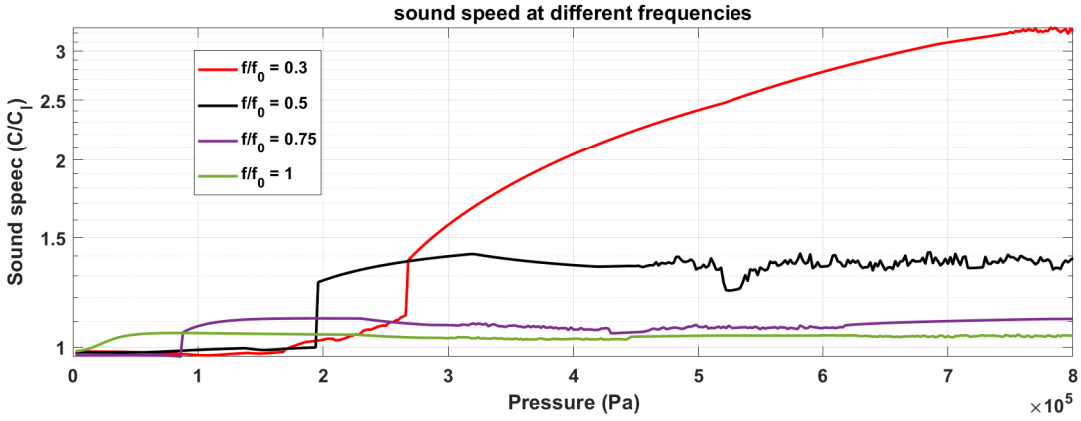

(b)

Figure 9.15: Comparison between the pressure dependent attenuation and sound speed of the medium at different resonance and below resonance for a bubbly medium composed of MBs with $R_0 = 2\mu m$. a) attenuation b) sound speed.

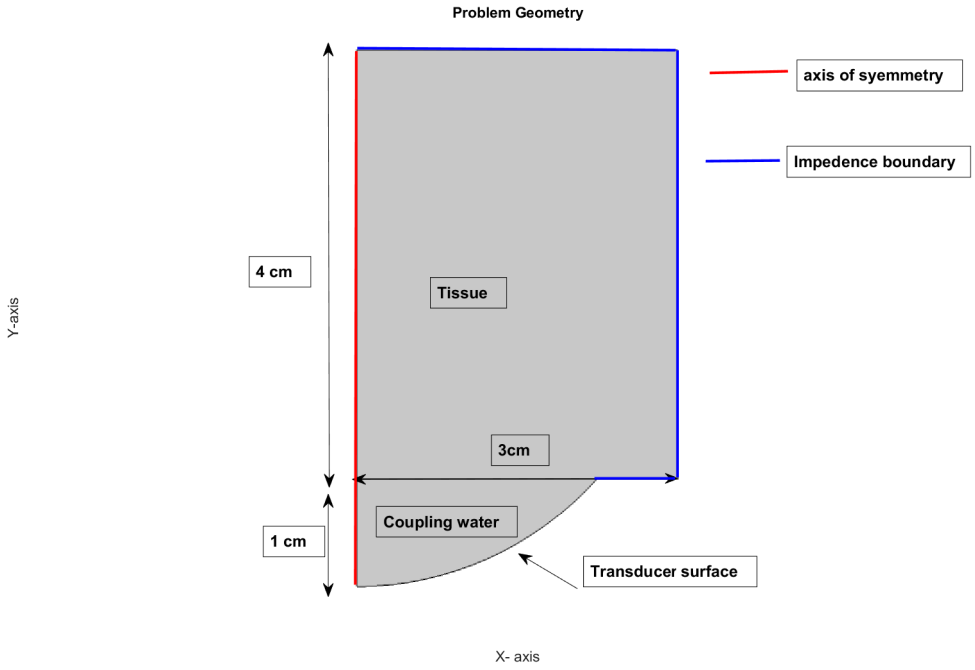

Figure 9.16: Geometry of the problem for the finite element simulations.

order of magnitude stronger bubble activity in this range.

Sonication with $f = 0.3f_r$ results in the highest attenuation for $P_a > 266kPa$ with possible application of enhanced heating at low ultrasound powers. When $f = f_r$, the attenuation at 300 kPa is $\approxeq 240Np/m$. This can reduce the pressure required to achieve the same therapeutic pressure by $\approx$ 14-15 times. Fig 9.15b shows that sound speed changes are pressure dependent and highest sound speed in each category corresponds to the 5 different identified regions in Fig. 9.15a. As an instance, when $f = 0.75f_r$ occurrence of SN is concomitant with a large increase in sound speed; thus the maximum sound speed in region B belong to the case of $f = 0.75f_r$.

Fig. 9.16 shows the geometry and boundary conditions of the problem for simulation of the wave propagation through the bubbly medium. The transducer has an aperture of 4.8 cm and a focal point at 3 cm. We have considered a small geometry to reduce the computation time and memory requirements. The problem has a cylindrical symmetry. The coupling medium between the transducer and the tissue is water. The sound speed an density of the tissue are set as 1530 m/s and 1030 kg/m^3 and the attenuation of the tissue is set as 5 Np/m. We have neglected the small changes of the tissue attenuation with frequency. 4 frequencies of $f = f_r$, $0.75f_r$, $0.5f_r$ & $0.3f_r$

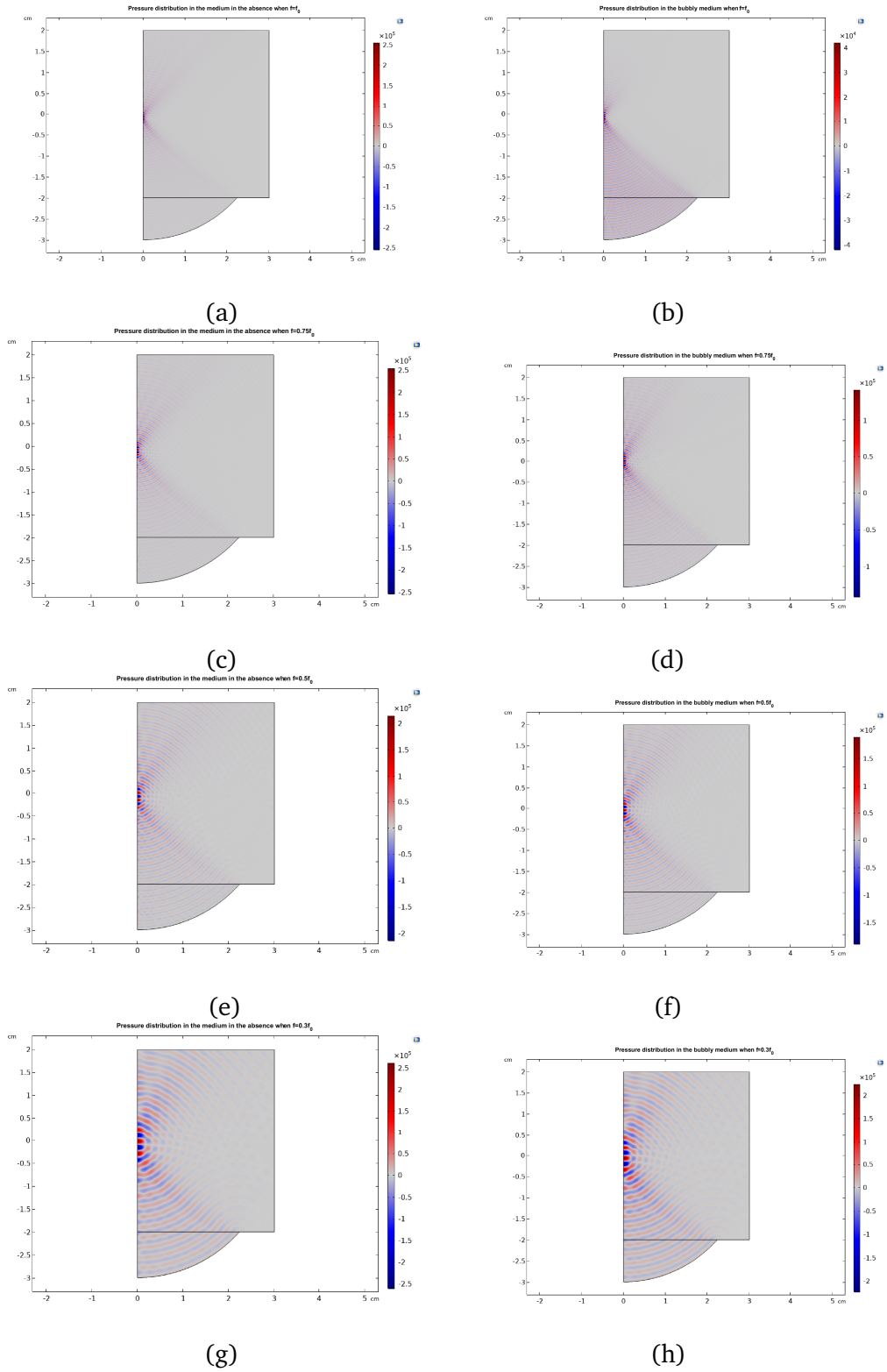

Figure 9.17: Pressure distribution in the medium in the absence of bubbles (Left column) and in the presence of bubbles (Right column) for: $a\&b) f = f_r$, $c\&d) f = 0.75 f_r$, $e\&f) f = 0.5 f_r$ and $g\&h) f = 0.3 f_r$

are considered. When using the FEM to solve the Helmholtz equation the density of discretization points should be at least ten points per wavelength in order to achieve a reasonable accuracy (i.e., $\frac{\lambda}{h} = 10$, where λ is the wavelength and h the side length of a finite element). Also, the density of discretization points per wavelength must increase with the wave number to maintain a fixed level of accuracy [72]. In this paper, similar to [73] the maximum element size of meshing was chosen to satisfy $\frac{\lambda}{h} \geq 12$ in each case. At each sonication the pressure at the surface of the transducer is chosen so that the focal pressure in the tissue in the absence of bubbles is $250kPa < P < 255kPa$. In the next step, we consider the case of the bubbly tissue by updating the pressure dependent attenuation and sound speed using the data in Fig. 9.15.

Fig. 9.17 shows the pressure distribution in the medium before and after the addition of the bubbles. When $f = f_r$ and in the absence of bubbles, there is sharp focus at Z=0 cm with $\approx 250kPa$ (Fig. 9.17a). However, after the addition of bubbles the focus is attenuated heavily. Due to the very large attenuation at lower pressures when $f = f_r$, ultrasonic waves encounter large absorption in the pre-focal path with low pressure. This results in weakening of the focal pressure to $\approx 40kPa$ (Fig. 9.17b).

To reconstruct the focus, the attenuation in the pre-focal region with low pressures should be decreased. This can be achieved to some degrees by using the PDf_r ($f = 0.75f_r$). Fig. 9.17d shows that when $f = 0.75f_r$ a stronger focal pressure of $\approx 145kPa$ is achieved. The shape and location of the focus are slightly different due to the higher sound speed at $\approx 145kPa$. To increase the focal pressure further, we need to further decrease the pre-focal attenuation. This can be achived either by using $f = 0.5f_r$ or $f = 0.3f_r$. Figures 9.17f and 9.17h shows that when $f = 0.5f_r$ $\&$ $f = 0.3f_r$ the focal pressure can be recovered to ≈ 188 $\&$ $\approx 226kPa$ respectively.

To better compare the focal pressure before and after addition of the bubbles, Fig. 9.18 displays the pressure variations along the Z axis from the center of the transducer (highlighted by red color in Fig. 9.16). When $f = f_r$ the focal pressure decreases by 84% due to the presence of bubbles (Fig. 9.18a). Moreover, the focal point remains more or less at the same location the sound speed changes for most of the beam path is very close to that of the pure medium. When $f = 0.75f_r$ (Fig. 18b), bubbles decrease the focal pressure by $\approx 45\%$ and due to the large changes of the sound speed in the vicinity and at the focal region, the center of the focal region moves 0.1cm along the z-direction. When $f = 0.5f_r$ (Fig. 9.18c) bubbles decrease the focal pressure by 28% and

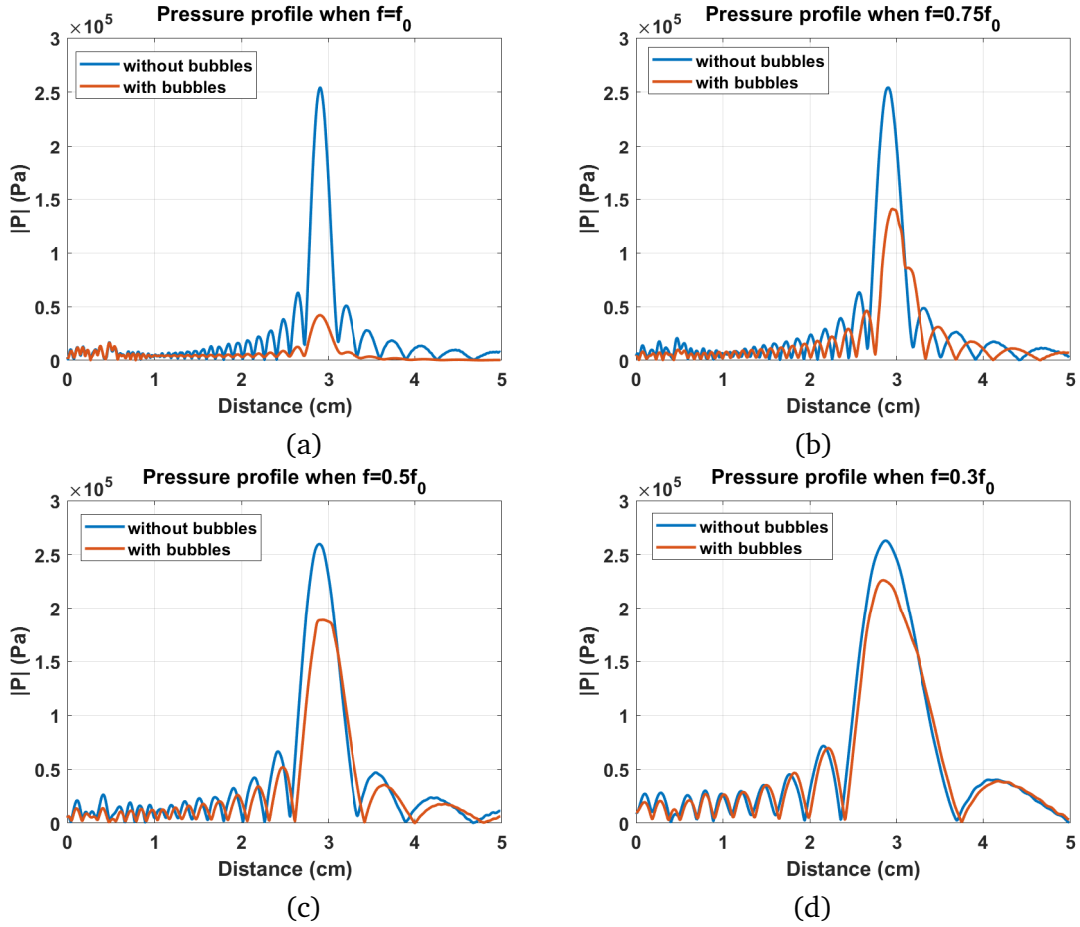

Figure 9.18: Pressure profiles along the center axis of the geometry before (blue line) and after (red line) the addition of bubbles for four different excitation frequencies: a)$f = f_r$, b)$f = 0.75f_r$, c)$f = 0.5f_r$ and d)$f = 0.3f_r$.

the center of the focal region moves a small distance in the positive z-direction. Fig. 9.18d shows that when $f = 0.3f_r$ the strongest focal pressure is achieved as the presence of bubbles results only in 14% decrease in the focal pressure. The shift in the focal region is not noticeable as within the pressure range in the medium, the changes of the sound speed were negligible. These results further support the experimental observations in [23] that application of PDf_r and narrow size distribution of bubbles increase the focal pressure and enhances deep penetration in bubbly media. Moreover, here we show for the first time that applications of 2nd SuH, 3rd SuH and etc can further facilitate the reduction in pre-focal shielding, thus enhancing our ability to penetrate deeper target.

9.7 Discussion

Pressure dependent changes of the attenuation and sound speed in bubbly media is one of the open problems in acoustics [25]. The bubble activity in the target heavily depends on the acoustic pressure that can reach the target. Thus, understanding the bubble related phenomena as well as optimizing the applications related to bubble oscillations requires a detailed understanding of the pressure distribution in the bubbly media. 'Due to the many applications of bubbles (ranging from underwater acoustics [2, 3], sonochemsitry and material sciences [1, 4, 5] to medical applications [7, 8, 9, 10, 11, 12]) the problem is of general interest and findings will be beneficial to a large field of physical and engineering applications.

There is no comprehensive model that can be used to estimate attenuation and sound speed changes for large amplitude bubble oscillations. The majority of published work employs linear models that are derived using the Comander & Prosperetti approach [17]. Since these models are developed under the assumption of very small amplitude bubble oscillations ($R = R_0(1 + x)$ where $x \ll 1$), they are not valid for most applications. On the other hand recent semi-linear models [2, 18, 26] are able to address some pressure dependent effects. However, because of some linear inherent assumptions (e.g. in Lousinard model [18] the real part of the wave number squared is calculated from the linear model and the Segers Model employs the linear dissipation constant for the liquid viscosity, thermal effects and shell viscosity [26]; and in all models, sound speed changes are neglected) these models do not predict the attenuation and sound speed changes accurately.

Another factor that increases the complexity of the problem is the nonlinear dynamics of bubbles which are pressure dependent and influences the attenuation and sound speed of the medium. Thus, for a better understanding of the bubble phenomenon and to take full advantage of the bubble dynamics in applications, not only do we need to develop a model that is not limited by linear assumptions but also we need to have a detailed understating of the nonlinear dynamics of the bubble in the medium.

We developed a nonlinear model that is not restrained by linear assumptions. The model predictions were validated against linear models at a very small pressure excitation ($P_a = 1kPa$) and for three different cases of the uncoated bubble, the coated bubble and the bubble in viscoelastic

media. At higher pressures, the predictions of the Imaginary part of k^2 were validated by comparing the predictions of the model with the Louisnard model [18] and for the three different cases mentioned above. Advantages of the developed model in this paper are its simplicity and its ability to calculate the pressure dependent real part and imaginary part of the k^2. We showed that pressured dependent effects of the real part of the k^2 that are neglected in semi-linear models are important. Attenuation and sound speed estimations using the Louisnard model that does not take into account the pressure dependent effects of the real part of the k^2 deviate significantly from the predictions of the nonlinear model in this paper; and these deviations increase with increasing pressure.

Predictions of the model were validated against experimentally measured attenuation and sound speed of mono-dispersions of lipid coated bubbles, with good agreement. Here, we showed for the first time, experimental observations of the pressure dependent sound speed in bubbly media. Despite the good agreement between theory and experiment, there were small discrepancies between the model predictions and experimental measurements. The small discrepancies can be due to the fact that we have not considered pressure variations within the MB chamber. Additionally we assumed that all the MBs have the identical shell composition and properties, and effects like strain softening or shear thinning of the shell [41], and possible MB destruction, were neglected. As the purpose of the current work was to investigate the pressure dependence of the sound speed and attenuation and to develop a model to accurately predict these effects, we have used the simplest model for lipid coated MBs. Investigation of models that incorporate more complex rheological behaviors of the shell which takes into account the effect of shell properties on sound speed and attenuation is the subject of future work.

The changes of the magnitude of sound speed in our experiments were quite small; this is due to the low concentration of the MBs in our experiments, as well as the small size of the microbubbles. Bigger microbubbles have stronger effects on the sound speed changes of the medium because of their higher compressibility as well as their more rapid changes in resonance frequency with increasing acoustic pressure [14]. In many applications (e.g. drug delivery, ultrasound imaging) much higher concentrations of microbubbles are employed, thus greater changes in the sound speed amplitude is expected (e.g. please refer to Fig. 9.1 with $\beta = 10^{-5}$). Nevertheless, although the changes of the sound speed amplitude are small, we were able to measure these changes in

experiments consistent with model predictions.

When fitting the shell parameters ([22, 43, 44, 45, 46]), sound speed values are of great help for more accurate characterizations of the shell parameters, especially in case of microbubbles with more complex rheology [16, 41]. There may exist multiple combination of values of the initial surface tension, shell elasticity and shell viscosity that fits well with measured attenuation curves; however, only one combination provides good fit to both the measured sound speed and attenuation values. Sound speed curves provide more accurate information on the effect of shell parameters on the bulk modulus of the medium (e.g. Shell elasticity) while attenuation graphs are more affected by damping parameters; thus the attenuation and sound speed curves can be used in parallel in order to achieve a more accurate characterization of the shell parameters.

We have classified the sound speed and attenuation of bubbly media in some of the main regimes of oscillations that are often used in applications. We can summarize the main findings as follows:

1- At lower pressures, the maximum attenuation occurs when $f = f_r$ (f_r is the linear resonance frequency of the bubble). When $f = f_r$ attenuation decreases with increasing pressure. Sound speed initially increases with pressure and then starts decreasing. Occurrence of Pd, increases the rate of decrease in attenuation and sound speed. The emergence of the giant resonance is concomitant with abrupt increase in attenuation and sound speed.

2- At lower pressure, the minimum attenuation occurs for the lowest frequency (here $f = 0.3f_r$). Attenuation abruptly increases when a SN bifurcation takes place. Sound speed changes are minimum before the occurrence of the SN. The SN is concurrent with an abrupt increase in the sound speed. Maximum changes of sound speed occur in the vicinity of giant resonance and for frequencies below resonance.

3- The attenuation of the medium in the regime of UH or SuH resonance is an order of magnitude smaller than when fundamental resonance takes place ($P_a = 1kPa$ and $f = f_r$ or $f = PDf_r$ and pressure$\geq SN$ pressure).

4- For $f > 1.5f_r$, the attenuation is orders of magnitude smaller than the attenuation in case of $f = f_r$ or $f = Pdf_r$. Even after the generation of 1/2 or 1/3 order SHs, the attenuation and sound speed changes of the medium are orders of magnitude smaller compared to the cases of sonication with resonance or Pdf_r. Attenuation in the regime of 1/2 order SHs is comparable to the UH resonance at $f \leq 0.5f_r$.

5- During nonlinear oscillations, the lowest changes in attenuation and sound speed occurs when $f \approxeq 3f_r$ & 1/3 SHs are generated. Thus, this condition may be exploited for contrast enhanced imaging with higher scattering to attenuation ratio and higher resolution. Moreover, due to the stability of the oscillations, higher wall velocities and scattered pressures [60,74,75], this condition may be applied for enhanced drug delivery for higher concentrations of bubbles and to target deeper regions.

6- Depending on the focal pressure and the resonance frequency of the bubbles, the frequency of the sonication can be chosen so that the attenuation of the pre-focal bubbles is reduced. This was shown through finite element simulations of focused ultrasonic waves through a bubbly medium. In this regard, the focal pressure can be set as the pressure above the SN pressure.

7- Sonication with frequencies $\leq 0.5f_r$ has the potential of achieving a very high focal attenuation and bubble activity while minimizing the pre-focal attenuation. The higher focal attenuation may aid in decreasing the focal pressure in HIFU applications by more than an order of magnitude while delivering therapeutic temperatures. This can be of great importance in the treatment of regions in the body where the presence of obstacles like pre-focal bone (e.g. skull and rib-cage) limit the energy that can be delivered to target. Moreover, the higher attenuation in the target and lower focal pressure can significantly reduce artifacts like post-target bone heating [73,76,77,78].

9.8 Conclusion

In summary, we have presented a nonlinear model for the calculation of the pressure-dependent attenuation and sound speed in a bubbly medium. The model is free from any linearization in the MB dynamics. The accuracy of the model was verified by comparing it to the linear model [17] at low pressures and the semilinear Lousinard model [18] at higher-pressure amplitudes. The relationship between the sound speed and pressure was established both theoretically and verified experimentally. The predictions of the model are in good agreement with experimental observations. To our best knowledge, unlike current sound speed models, the model introduced in this paper does not have a $\frac{dP}{dV}$ term (e.g. [28]); thus it does not encounter difficulties addressing the nonlinear oscillations. To accurately model the changes of the attenuation and sound propagation in a bubbly medium we need to take into account how the sound speed changes with pressure and

frequency. Another advantage of the model is that it uses as input only the radial oscillations of the MBs. There is no need to calculate the energy loss terms, and thus our approach is simpler and faster. Moreover, for the case of nonlinear shell behavior (e.g. [16, 41]) it may provide more accurate estimates since there is no need for simplified analytical expressions. MB oscillator exhibits stable nonlinear oscillations [14, 15, 53, 54, 55, 60, 61, 62, 63, 64, 65, 66] (e.g. period 3, 4 or super and ultra harmonics) and the effect of these nonlinear oscillations on the changes of sound speed and attenuation is now revealed with this approach. Application of this model will help to shed light on the effect of nonlinear oscillations on the acoustical properties of the bubbly medium (we initially reported on this in [31]) and explore new potential parameters to further optimize and improve the current applications.

Acknowledgments

The work is supported by the Natural Sciences and Engineering Research Council of Canada (Discovery Grant RGPIN-2017-06496), NSERC and the Canadian Institutes of Health Research (Collaborative Health Research Projects) and the Terry Fox New Frontiers Program Project Grant in Ultrasound and MRI for Cancer Therapy (project #1034). A. J. Sojahrood is supported by a CIHR Vanier Scholarship and Qian Li is supported by NSF CBET grant #1134420.

Bibliography

[1] K.C. Suslick Science, **247**, 1439(1990.)

[2] A. Mantouka, H. Dogan, P.R. White and T.G. Leighton , The Journal of the Acoustical Society of America, **140**(1), 274 (2016).

[3] P.C. Etter. *Underwater acoustic modeling and simulation*, (CRC Press, 2013).

[4] Maisonhaute, E., Prado, C., White, P.C. and Compton, R.G., Ultrasonics sonochemistry, **9**(6), 297 (2002).

[5] Flannigan, D.J. and Suslick, K.S. , Nature, **434**(7029), 52 (2005).

[6] K. Ferrara, R. Pollard, and M. Borden. Ann. Rev. of Biomed. Eng., **9**, 415 (2007).

[7] C. Errico, J. Pierre, S. Pezet, Y. Desailly, Z. Lenkei, O. Couture, and M. Tanter. Nature, **527**(7579), 499 (2015).

[8] A. Carpentier, et.al, Science translational medicine, **8**(343) 343re2 (2016).

[9] A. Burgess, K. Shah, O. Hough, and K. Hynynen, Expert Review of Neurotherapeutics **15**(5), 477 (2015).

[10] P. Marmottant, and S. Hilgenfeldt. Nature, **423**(6936), 153 (2003).

[11] P. Prentice, A. Cuschieri, K. Dholakia, M. Prausnitz, and P. Campbell. Nature physics, **1**(2), 107 (2005).

[12] T. Matula t al. Acoustics Today, **1** 14 (2013).

[13] U. Parlitz, V. Englisch, C. Scheffczyk, and W. Lauterborn. The Journal of the Acoustical Society of America, **88**(2), 1061 (1990).

[14] A.J., Sojahrood, O. Falou, R. Earl, R. Karshafian, and M.C. Kolios. Nonlinear Dynamics, **80**, 889 (2015).

[15] F. Hegedűs, Physics Letters A, **380**(9), 1012 (2016).

[16] P. Marmottant, S. van der Meer, M. Emmer, M. Versluis, N. de Jong, S. Hilgenfeldt, and D. Lohse, The Journal of the Acoustical Society of America, **118**(6), 3499 (2005).

[17] K.W. Commander, and A. Prosperetti. **85**(2), 732 (1989).

[18] O. Louisnard. Ultrasonics sonochemistry, **19**(1), 56 (2012).

[19] R. Jamshidi and G. Brenner. Ultrasonics, **53**(4), 842 (2013).

[20] Sojahrood, A.J., Haghi, H., Karshafian, R. and Kolios, M.C., 2019. Sojahrood, A.J., Haghi, H., Karshafian, R. and Kolios, M.C., 2020. Critical corrections to models of nonlinear power dissipation of ultrasonically excited bubbles. Ultrasonics Sonochemistry, 66, pp.105089-105089.

[21] M.X. Tang, H. Mulvana, T. Gauthier, A.K.P. Lim, D.O. Cosgrove, R.J. Eckersley and E. Stride. Interface Focus, **1**(4), 520 (2011).

[22] J.B. Keller, and M. Miksis. The Journal of the Acoustical Society of America, **68**(2), 628 (1980).

[23] Segers, T., Kruizinga, P., Kok, M.P., Lajoinie, G., De Jong, N. and Versluis, M., 2018. Monodisperse versus polydisperse ultrasound contrast agents: Non-linear response, sensitivity, and deep tissue imaging potential. Ultrasound in medicine & biology, 44(7), pp.1482-1492.

[24] J.M. Escoffre, A. Novell, J. Piron, A. Zeghimi, A. Doinikov and A. Bouakaz. IEEE transactions on ultrasonics, ferroelectrics, and frequency control, **60**(1) (2013).

[25] K. Yasui. *Unsolved Problems in Acoustic Cavitation*. Handbook of Ultrasonics and Sonochemistry, (Springer 2016).

[26] Segers, T. J., de Jong, N., & Versluis, M. (2016). Uniform scattering and attenuation of acoustically sorted ultrasound contrast agents: Modeling and experiments. Journal of the Acoustical Society of America, 140(4), 2506-2517.

[27] Sojahrood, A.J., Haghi, H., Karshafian, R. and Kolios, M.C., 2019. Sojahrood, A.J., Haghi, H., Karshafian, R. and Kolios, M.C., 2020. Critical corrections to models of nonlinear power dissipation of ultrasonically excited bubbles. Ultrasonics Sonochemistry, 66, pp.105089-105089.

[28] Sojahrood, A.J., Haghi, H., Li, Q., Porter, T.M., Karshafian, R. and Kolios, M.C., 2020. Nonlinear power loss in the oscillations of coated and uncoated bubbles: Role of thermal, radiation and encapsulating shell damping at various excitation pressures. Ultrasonics sonochemistry, 66, p.105070.

[29] G. Holt and R. Roy. Bubble dynamics in therapeutic ultrasound, in "Bubble and Particle Dynamics in Acoustic Fields: Modern Trends and Applications, 2005, ISBN 81-7736-284-4, edited by Doinikov. A.

[30] A.B. Wood, *A Textbook of Sound* (Bell, London, 1946)

[31] T.G. Leighton, S.D. Meers, and P.R. White. In Proceedings of the Royal Society of London A: Mathematical, Physical and Engineering Sciences **460**, 2521 (2004).

[32] Y. Gong, M. Cabodi, and T.M. Porter. Applied Physics Letters, **104**(7), 074103 (2014).

[33] A.J Sojahrood, R. Karshafian, and M. C. Kolios. The Journal of the Acoustical Society of America **137**, 2398 (2015).

[34] A.J. Sojahrood, H. Haghi, R. Karshafian, and M.C. Kolios. "Nonlinear model of acoustical attenuation and speed of sound in a bubbly medium." In Ultrasonics Symposium (IUS), (2015) IEEE International, DOI: 10.1109/ULTSYM.2015.0086

[35] A.J Sojahrood, Q. Li, M. Burgess, R. Karshafian, T. Porter, and M.C. Kolios. The Journal of the Acoustical Society of America **text 139**, 2175 (2016).

[36] A.J. Sojahrood et al. Investigation of the nonlinear propagation of ultrasound through a bubbly medium including multiple scattering and bubble-bubble interaction: Theory and experiment. Ultrasonics Symposium (IUS), (2017), IEEE International, 10.1109/ULTSYM.2017.8092528

[37] R.E. Caflisch, M.J. Miksis, G.C. Papanicolaou, and L. Ting. Journal of Fluid Mechanics, **153**, 259 (1985).

[38] Morgan, K.E., Allen, J.S., Dayton, P.A., Chomas, J.E., Klibaov, A.L. and Ferrara, K.W., 2000. Experimental and theoretical evaluation of microbubble behavior: Effect of transmitted phase and bubble size. IEEE transactions on ultrasonics, ferroelectrics, and frequency control, 47(6), pp.1494-1509.

[39] Yang, X. and Church, C.C., 2005. A model for the dynamics of gas bubbles in soft tissue. The Journal of the Acoustical Society of America, 118(6), pp.3595-3606.

[40] Prosperetti, A., Crum, L.A. and Commander, K.W., 1988. Nonlinear bubble dynamics. The Journal of the Acoustical Society of America, 83(2), pp.502-514.

[41] A.A. Doinikov, J.F. Haac, and P.A. Dayton. Ultrasonics, **49**(2), 269 (2009).

[42] B.L. Helfield, X. Huo, R. Williams, and D.E. Goertz. Ultrasound in medicine & biology, **38**(7), 1298 (2012).

[43] H. Shekhar, N.J. Smith, J.L. Raymond, & C.K. Holland. Ultrasound in medicine & biology, 44(2), 434 (2018).

[44] B.L. Helfield, et al. Ultrasonics **54**(6) 1419 (2014).

[45] D.E. Goertz, N. de Jong, and A.F.W. van der Steen. Ultrasound in medicine & biology **33**(9) 1376 (2007).

[46] J.L. Raymond, K.J. Haworth, K.B. Bader, K. Radhakrishnan, J.K. Griffin, S.L. Huang, D.D. McPherson, and C.K. Holland, Ultrasound in medicine & biology **40**(2) 410 (2014).

[47] R. Toegel, S. Luther, and D. Lohse. Physical Review Letters, **96**(11), 114301 (2006).

[48] Stricker, L., Prosperetti, A. and Lohse, D., 2011. Validation of an approximate model for the thermal behavior in acoustically driven bubbles. The Journal of the Acoustical Society of America, 130(5), pp.3243-3251.

[49] Lide, D.R. and Kehiaian, H.V., 1994. CRC handbook of thermophysical and thermochemical data. Crc Press.

[50] $https://detector-cooling.web.cern.ch/detector-cooling/data/C3F8_{P}roperties.pdf$

[51] Dogan, H., White, P.R. and Leighton, T.G., 2017. Acoustic wave propagation in gassy porous marine sediments: The rheological and the elastic effects. The Journal of the Acoustical Society of America, 141(3), pp.2277-2288.

[52] L. D. Rozenberg, in: L. D. Rozenberg (Ed.), High-intensity ultrasonic fields, Plenum Press, New-York, 1971.

[53] Sojahrood, A.J., Wegierak, D., Haghi, H., Karshfian, R. and Kolios, M.C., 2019. A simple method to analyze the super-harmonic and ultra-harmonic behavior of the acoustically excited bubble oscillator. Ultrasonics sonochemistry, 54, pp.99-109.

[54] Sojahrood, A.J., Earl, R., Kolios, M.C. and Karshafian, R., 2020. Investigation of the 1/2 order subharmonic emissions of the period-2 oscillations of an ultrasonically excited bubble. Physics Letters A, p.126446.

[55] Sojahrood, A.J., Earl, R., Li, Q., Porter, T.M., Kolios, M.C. and Karshafian, R., 2019. Nonlinear dynamics of acoustic bubbles excited by their pressure dependent subharmonic resonance frequency: oversaturation and enhancement of the subharmonic signal. arXiv preprint arXiv:1909.05071.

[56] T. Leighton. *The acoustic bubble*, (Academic press, 2012). Pages 290 and 301.

[57] M.A. Parrales, J.M. Fernandez, M. Perez-Saborid, J.A. Kopechek and T.M. Porter. The Journal of the Acoustical Society of America, **136**(3), 1077 (2014).

[58] H. Takahira, S. Yamane, T. Akamatsu. JSME International Journal Series B Fluids and Thermal Engineering, **38**(3), 432 (1995).

[59] Haghi, H., Sojahrood, A.J. and Kolios, M.C., 2019. Collective nonlinear behavior of interacting polydisperse microbubble clusters. Ultrasonics sonochemistry, 58, p.104708.

[60] A.J Sojahrood R. Karshafian, and M.C. Kolios. Bifurcation structure of the ultrasonically excited microbubbles undergoing buckling and rupture, *Proceedings of Meetings on Acoustics ICA2013* **19**(1) ASA, (2013).

[61] A.J. Sojahrood et al. The Journal of the Acoustical Society of America **141**.5 3493 (2017).

[62] A.J. Sojahrood & M.C. Kolios. Physics Letters A, **376**(33), 2222 (2012).

[63] F. Hegedűs, Physics Letters A, **380**(10) 1012 (2016)

[64] F. Hegedűs, C. Hős, and L. Kullmann, The IMA Journal of Applied Mathematics **78** 1179 (2012).

[65] Y. Zhang. Ultrasonics sonochemistry **40** 151 (2018).

[66] S.A. Suslov, A.Ooi, and R. Manasseh. Physical Review E **85** 066309 (2012).

[67] McDannold, N., Vykhodtseva, N. and Hynynen, K., 2007. Use of ultrasound pulses combined with Definity for targeted blood-brain barrier disruption: a feasibility study. Ultrasound in medicine & biology, 33(4), pp.584-590.

[68] O'Reilly, M.A., Jones, R.M. and Hynynen, K., 2014. Three-dimensional transcranial ultrasound imaging of microbubble clouds using a sparse hemispherical array. IEEE Transactions on Biomedical Engineering, 61(4), pp.1285-1294.

[69] Flynn, H.G., Church, C.C.: Transient pulsations of small gas bubbles in water. J. Acoust. Soc. Am. 84, 985–998 (1988)

[70] Doinikov, A.A., Haac, J.F. and Dayton, P.A., 2009. Resonance frequencies of lipid-shelled microbubbles in the regime of nonlinear oscillations. Ultrasonics, 49(2), pp.263-268.

[71] Sojahrood, A.J. and Kolios, M.C., 2012, October. The utilization of the bubble pressure dependent harmonic resonance frequency for enhanced heating during high intensity focused ultrasound treatments. In AIP Conference Proceedings (Vol. 1481, No. 1, pp. 345-350). AIP.

[72] F. Ihlenburg (Ed.), Finite Element Analysis of Acoustic Scattering (Springer, New York, 1998)

[73] Behnia, S., Jafari, A., Ghalichi, F. and Bonabi, A., 2008. Finite-element simulation of ultrasound brain surgery: effects of frequency, focal pressure, and scanning path in bone-heating reduction. Open Physics, 6(2), pp.211-222.

[74] Sojahrood, A.J., Karshafian, R. and Kolios, M.C., 2012, October. Detection and characterization of higher order nonlinearities in the oscillations of Definity at higher frequencies and very low acoustic pressures. In 2012 IEEE International Ultrasonics Symposium (pp. 1193-1196). IEEE.

[75] Sojahrood, A.J., Karshafian, R. and Kolios, M.C., 2012, October. Numerical and experimental classification of the oscillations of single isolated microbubbles: Occurrence of higher order subharmonics. In 2012 IEEE International Ultrasonics Symposium (pp. 402-405). IEEE.

[76] Zderic, V., Foley, J., Luo, W. and Vaezy, S., 2008. Prevention of post-focal thermal damage by formation of bubbles at the focus during high intensity focused ultrasound therapy. Medical physics, 35(10), pp.4292-4299.

[77] Lin, W.L., Liauh, C.T., Chen, Y.Y., Liu, H.C. and Shieh, M.J., 2000. Theoretical study of temperature elevation at muscle/bone interface during ultrasound hyperthermia. Medical physics, 27(5), pp.1131-1140.

[78] Lin, W.L., Liauh, C.T., Yen, J.Y., Chen, Y.Y. and Shieh, M.J., 2000. Treatable domain and optimal frequency for brain tumors during ultrasound hyperthermia. International Journal of Radiation Oncology* Biology* Physics, 46(1), pp.239-247.

Chapter 10

Intensified non-linearity at very low amplitudes high frequency ultrasound excitations of lipid coated microbubbles

10.1 Abstract

Polydisperse solutions of lipid coated Definity® microbubbles (MBs) were sonicated with 30 cycles pulses of 25 MHz frequency and pressure amplitudes of 70kPa-300kPa. Here, we report the first time observation and characterization of higher order subharmonics in the scattered signals of single MB events at very low amplitude high frequency ultrasound excitations. Period 2(P2), P3, and two different P4 oscillations were observed. Experimental observations contradict the perceived behavior at such low excitations. To investigate the mechanism of the enhanced nonlinearity, the bifurcation structure of the lipid coated MBs is studied for the first time. Consistent with the experimental results, we show that this unique oscillator can exhibit chaotic oscillations and higher order subharmonics at very low excitation amplitudes. Buckling or rupture of the shell and the dynamic variation of the shell elasticity causes the intensified non-linearity at low excitations.[1]

10.2 Introduction

Even after over a decade of study, the dynamics of ultrasonically excited lipid coated microbubbles (MBs) are not fully understood, owing to the complex dynamical aspects of their behaviour. Inter-

[1]Under review as: A.J. Sojahrood, H. Haghi, T.M. Porter, R. Karshafian and M.C. Kolios, Intensified non-linearity at very low amplitudes high frequency ultrasound excitations of lipid coated microbubbles

estingly, lipid coated MBs have been shown to exhibit 1/2 order subharmonic (SH) oscillations even when the excitation amplitude is low (<30 kPa [1, 2, 3]). Despite the increased inherent damping due to the coating, such low threshold values contradict the predictions of the theoretical models as these values are even below the thresholds expected for uncoated free MBs [4, 5].

Bubbles are known to be a complex oscillators and addition of coating introduces additional nonlinearity to an already complex system. The lipid coating may cause compression dominated oscillations [6] or limit the MB oscillations to only above a certain pressure threshold [7]. Through experiments and numerical simulations it has been shown in [1] that the low pressure threshold for SH emissions is due to the compression only behavior of the MBs due to the buckling of the shell. More interestingly, Overvelde et al. [8] showed that the lipid coating may enhance the nonlinear MB response at acoustic pressures as low as 10 kPa. In addition, even a small ($\approx 10kPa$) increase in the acoustic pressure amplitude leads to a significant decrease in the main resonance frequency [8] resulting to a pronounced skewness of the resonance curve. The origin of the "thresholding [7]" behavior have been linked to the shift in resonance [8]. Nonlinear resonance behavior of the lipid coating has also been observed at higher frequencies (5-15 MHz [9]), (8-12 MHz [10]) and (11-25 MHz [11]). Through theoretical analysis of the Marmottant model for lipid coated MBs [12], Prosperetti [4] attributed the lower SH threshold of the lipid MBs to the variation in the mechanical properties of the coating in the neighborhood of a certain MB radius (e.g. the occurrence of buckling). Lipid coating may also result in expansion dominated behavior in liposome-loaded lipid coatings [13]. Expansion dominated oscillations happen when the initial surface tension of the lipid coated MB is close to that of the water [11, 13]. In this regime, in contrast to compression dominated behavior, the MB expands more than it compresses. Expansion-dominated behavior was used to explain the reason behind enhanced non-linearity at higher frequencies (25 MHz) [11]. The Marmottant model effectively captures the behavior of the MB including expansion-dominated behavior [11, 12, 14], compression only behavior [6], thresholding [7] and enhanced non-linear oscillations at low excitation pressures [1, 2, 8, 14, 15, 16].

Despite the numerous studies which employed the methods of nonlinear dynamics and chaos to investigate the dynamics of acoustically excited MBs [17, 18, 19, 20, 21, 22, 23, 24, 25, 26, 27, 28, 29, 30, 31, 32, 33, 34, 35, 36, 37, 38, 39, 40, 41, 42, 43, 44], the detailed bifurcation structure and nonlinear dynamics of the lipid coated MBs have not been studied.

Lipid coated MBs are being routinely used in diagnostic ultrasound [2, 45, 46, 47, 48]. Moreover, they have been used in cutting edge non-invasive treatments of brain disorders and tumors in humans [49]. Currently there are several investigations on the potential use of lipid coated microbubbles (MBs) in high resolution and high contrast imaging procedures [50] as well as non-invasive ultrasonic treatments and localized drug/gene delivery [51]. Despite the promising results of these investigations, the complex dynamics of the system makes it difficult to optimize the behavior of lipid coated MBs. Moreover, from nonlinear dynamics point of view, the lipid coated MB oscillator is a very interesting topic of investigation due to the highly nonlinear nature of the system. The complex behavior of the uncoated MB is interwoven with the nonlinear behavior of the lipid coating which enables unique dynamical properties for this oscillator.

In this work we study the bifurcation structure of the lipid coated MBs as a function of size and frequency at different pressure values. Numerical results are accompanied by experimental observations of single MB events at low pressure excitation. We show for the first time that in addition to 1/2 order SHs, higher order SHs (e.g. 1/3, 1/4) can be generated at very low excitation amplitudes. Moreover, analysis of the bifurcation structure of the system reveals a unique property of the lipid coated MB which is the generation of chaos at excitation pressures as low as 5kPa.

10.3 Methods

10.3.1 Experimental method

Very dilute solutions of Definity® MBs were sonicated with continuous pulse trains of 25 MHz using the Vevo 770 ultrasound imaging machine (VisualSonics Inc. Toronto, Ontario). The pulse length was held constant at 30 cycles while the applied acoustic pressure was varied over the range of $\approx 70 - 300kPa$. The backscattered signals from individual MBs were extracted and different nonlinear modes of oscillations were identified. Acquisition of signals from single MB were similar to the approach in [52]. Fig. 10.1 shows a schematic of an acquired signal from a single MB event ($\approx 250kPa$ and $f = 25MHz$).

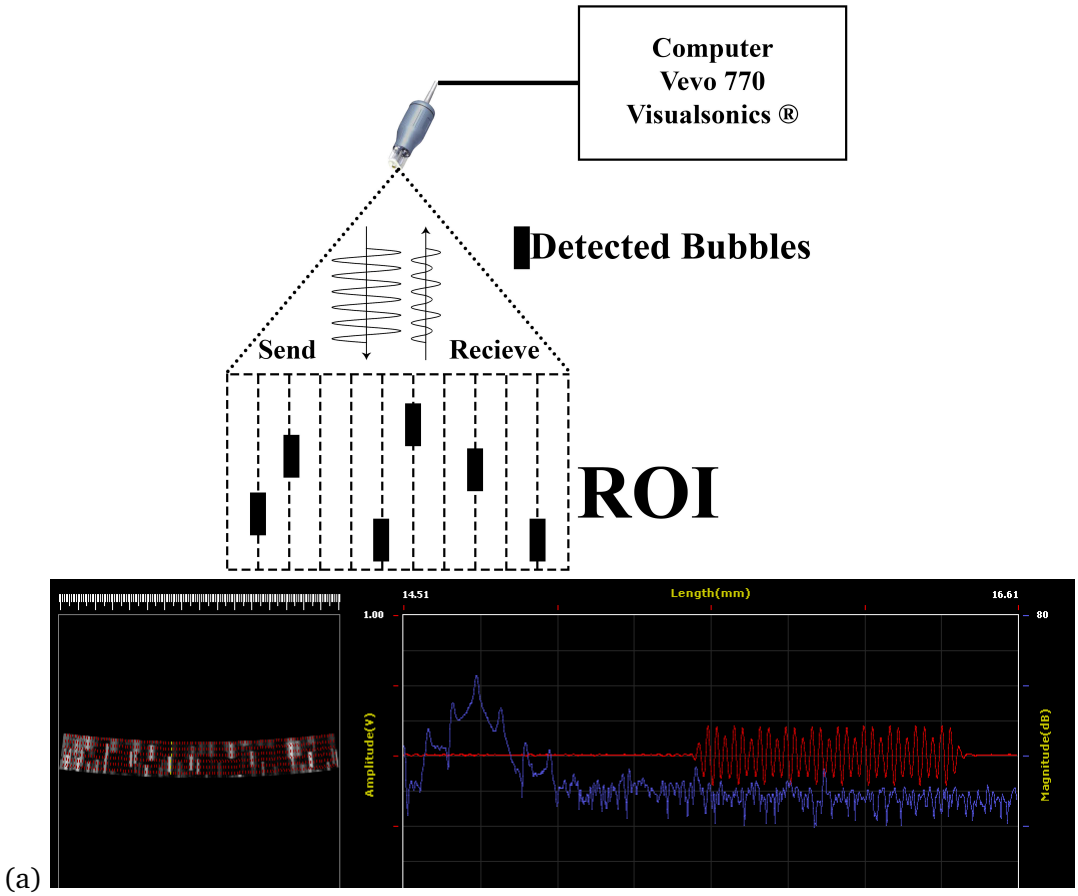

Figure 10.1: a) Schematic of the Vevo 770 (Visualsonics®) machine which was used in the experiments to detect the signals from single MB events in the region of interest (ROI). b) Left: ROI as seen by the machine for an ultrasound pulse train at 25 MHz and 250 kPa of pressure, and Right: Signal (red) from a single P3 MB event. The frequency spectrum of the received signal is shown in blue.

10.3.2 Numerical procedure

10.3.2.1 Marmottant Model

Dynamics of coated MBs undergoing buckling and rupture can be effectively modeled using the Marmottant equation [12]:

$$\rho\left(R\ddot{R}+\frac{3}{2}\dot{R}^2\right)= \left[P_0+\frac{2\sigma(R_0)}{R_0}\right](\frac{R}{R_0})^{-3k}\left(1-\frac{3k}{c}\dot{R}\right)-P_0-\frac{2\sigma(R)}{R}-\frac{4\mu\dot{R}}{R^2}-\frac{4k_s\dot{R}}{R^2}-P_a(t) \tag{10.1}$$

In this equation, R is radius at time t, R_0 is the initial MB radius, $\dot{R}$ is the wall velocity of the bubble, $\ddot{R}$ is the wall acceleration, ρ is the liquid density (998 $\frac{kg}{m^3}$), c is the sound speed (1481 m/s), P_0 is the atmospheric pressure, $\sigma(R)$ is the surface tension at radius R, μ is the liquid viscosity (0.001 Pa.s), k_s is the coating viscosity and $P_a(t)$ is the amplitude of the acoustic excitation ($P_a(t) = P_a sin(2\pi f t)$) where P_a and f are the amplitude and frequency of the applied acoustic pressure. The values in the parentheses are for pure water at 293 K. In this paper the gas inside the MB is C3F8 and water is the host media.

The surface tension $\sigma(R)$ is a function of radius and is given by:

$$\sigma(R)=\begin{cases}0 & if \quad R\le R_b\\ \chi(\frac{R^2}{R_b^2}-1) & if \quad R_b\le R\le R_{breakup}\\ \sigma_{water} & if \quad Ruptured \quad R\ge R_r\end{cases} \tag{10.2}$$

σ_{water} is the water surface tension (0.072 N/m), $R_b = \frac{R_0}{\sqrt{1+\frac{R_0}{\chi}}}$ is the buckling radius, $R_r = R_b\sqrt{1+\frac{\sigma_{brak-up}}{\chi}}$ is the rupture radius (=break up radius in this paper similar to [11]) and χ is the shell elasticity. Shear thinning of the coating is included in the Marmottant model using [53]:

$$k_s=\frac{4k_0}{1+\alpha\frac{|\dot{R}|}{R}}; \tag{10.3}$$

where k_0 is the shell viscous parameter and α is the characteristic time constant associated with the shear rate. In this work shell parameters of $\chi = 0.975N/m$, $k_0 = 2.98\times10^{-10}kgs^{-1}$ and

$\alpha = 1 \times 10^{-6}s$ are used for the $Definity^{®}$ MBs. These values are adopted from the estimated parameters in [53, 54].

10.3.2.2 Keller-Miksis model

The dynamics of the uncoated MBs were also visualized alongside the lipid coated MBs to highlight the contributions of the coating to the nonlinear bheavior of the bubble. To model the uncoated MB dynamics the Keller-Miksis model [55] is used:

$$\rho[(1-\frac{\dot{R}}{c})R\ddot{R}+\frac{3}{2}\dot{R}(1-\frac{R}{3c})] = (1+\frac{\dot{R}}{c})(G)+\frac{R}{c}\frac{d}{dt}(G) \tag{10.4}$$

where $G = \left(P_0 + \frac{2\sigma_{water}}{R_0}\right)(\frac{R}{R_0})^{-3k} - \frac{4\mu_L\dot{R}}{R} - \frac{2\sigma}{R} - P_0 - P_a sin(2\pi ft)$.

10.3.2.3 Scattered pressure by MBs

The pressure scattered (re-radiated) by the oscillating MB can be calculated using [56, 57]:

$$P_{sc} = \rho\frac{R}{r}(R\ddot{R}+2\dot{R}^2) \tag{10.5}$$

here r is the distance from the MB center. The scattered pressure (P_{sc}) at 15 cm (approximate path length of the MBs in experiments) is calculated for 30 cycle pulses to match experimental conditions. The calculated P_{sc} is then convolved with the one way transducer response accounting for attenuation effects in water ($0.000221\frac{dB}{mmMHz^2}$ [58]). Moreover, to better compare with experimental observations, sample frequency for simulations is chosen to be equal to the sample frequency in experiments which is $460MHz$.

10.3.2.4 Investigation tools

The results of the numerical simulations were visualized using a comprehensive bifurcation analysis method [43]. In this method the bifurcation structure of the normalized MB oscillations ($\frac{R}{R_0}$) are plotted in tandem versus a control parameter using two different bifurcation methods (Poincaré

section at each driving period and method of peaks).

2.2.4.a) Poincaré section (conventional method)

When dealing with systems responding to a driving force, to generate the points in the bifurcation diagrams vs. the control parameter, one option is to sample the R(t) curves using a specific point in each driving period. The approach can be summarized in:

$$P \equiv (R(\Theta))\{(R(t), \dot{R}(t)) : \Theta = \frac{n}{f}\} \tag{10.6}$$

Where P denotes the points in the bifurcation diagram, R and $\dot{R}$ are the time dependent radius and wall velocity of the MB at a given set of control parameters of (R_0, P_A and f), Θ is given by $\frac{n}{f}$ and n=1,2,....440. Points on the bifurcation diagram are constructed by plotting the solution of $R(t)$ at time points that are multiples of the driving acoustic period. The results are plotted for $n = 400 - 440$ to ensure a steady state solution has been reached for all MBs and thus 40 Poincaré point are stored for each solution. Due to smaller viscous effects, bigger MBs require longer cycles to reach steady state.

2.2.4.b) Method of peaks

Another way of constructing bifurcation points is by setting one of the phase space coordinates to zero:

$$Q \equiv max(R)\{(R, \dot{R}) : \dot{R} = 0\} \tag{10.7}$$

In this method, the steady state solution of the radial oscillations for each control parameter is considered. The maxima of the radial peaks ($\dot{R} = 0$ and $\ddot{R} > 0$) are identified (determined within 400-440 cycles of the stable oscillations) and are plotted versus the given control parameter in the bifurcation diagrams.

The bifurcation diagrams of the normalized MB oscillations (R/R_0) are calculated using both methods a) and b). When the two results are plotted alongside each other, it is easier to uncover more important details about the superharmonic (SuH) and ultraharmonic (UH) oscillations, as well as the SH and chaotic oscillations. This gives insight into the nonlinear behavior over a wide range of parameters, and enables the detection of SuH and UH oscillations alongside SH and chaotic oscillations [43]. This approach reveals the intricate details of the oscillations. In this paper the

bifurcation diagrams of the normalized radial oscillations of the $Definity^{®}$ MBs were plotted versus the MBs initial diameter for fixed frequencies of 25 MHz and for the range of the pressure values studied in the experiments.

10.4 Results

10.4.1 Bifurcation structure

10.4.1.1 Bifurcation of $\frac{R}{R_0}$ as a function of frequency for uncoated and coated MBs with different $\sigma(R_0)$

In order to visualize the dynamics of the MBs at low pressures, the bifurcation structure of a $2\mu m$ MB is plotted as a function of frequency when $P_a = 5kPa$ (Fig. 10.2). The blue graph represents the results using the maxima method and the red graph represents the results using the conventional method (Poincaré section at each period). The uncoated MB (Fig. 10.2a) exhibits a P1 signal over 1-30 MHz with one maximum and resonant oscillations at $\approx 4.7MHz$. Contrary to Fig. 10.2a, the lipid MB with $\sigma(R_0) = 0$ exhibits significant non-linearity at 5 kPa (Fig. 10.2b). Higher order SuHs ($5th - 2nd$ order) are seen for $f <\approx 2.88MHz$. For example the 5th order SuH at 1MHz is a P1 signal with 5 maxima. P1 resonance occurs at $f \cong 4.63MHz$ with P2 oscillations over a wide frequency range of $\approx 6.9MHz < f < 12.22MHz$ with a small window of P4-2 and chaos. We call this a P4-2 oscillations as it occurs when P2 oscillations undergo a period doubling (PD) to P4 [23, 44]. P3 occurs between $\approx 12.85MHz < f < 18.2MHz$. P4-1 happens in the frequency range between $18.2MHz < f < 19.5MHz$ (highlighted in subplot within Fig. 10.2b). We call this a P4-1 regime as it occurs when P1 oscillations undergo a saddle node bifurcation to P4 oscillations [26, 29, 30].

The Lipid MB with $\sigma(R_0) = 0.01N/m$ (Fig. 10.2c) exhibits P1 oscillations with one maximum. The pressure dependent resonance frequency (PDf_r [42]) occurs at $f \approx 9.15MHz$. The MB behavior is of P1 with one maximum for all the studied frequencies.

The lipid MB with $\sigma(R_0) = 0.03N/m$ (Fig. 10.2d) exhibits P1 behavior with 1 maximum and a resonance at $\approx 10.66MHz$.

The behavior of the MB with $\sigma = 0.062N/m$ (Fig. 10.2e) is similar to $\sigma = 0.01N/m$ with

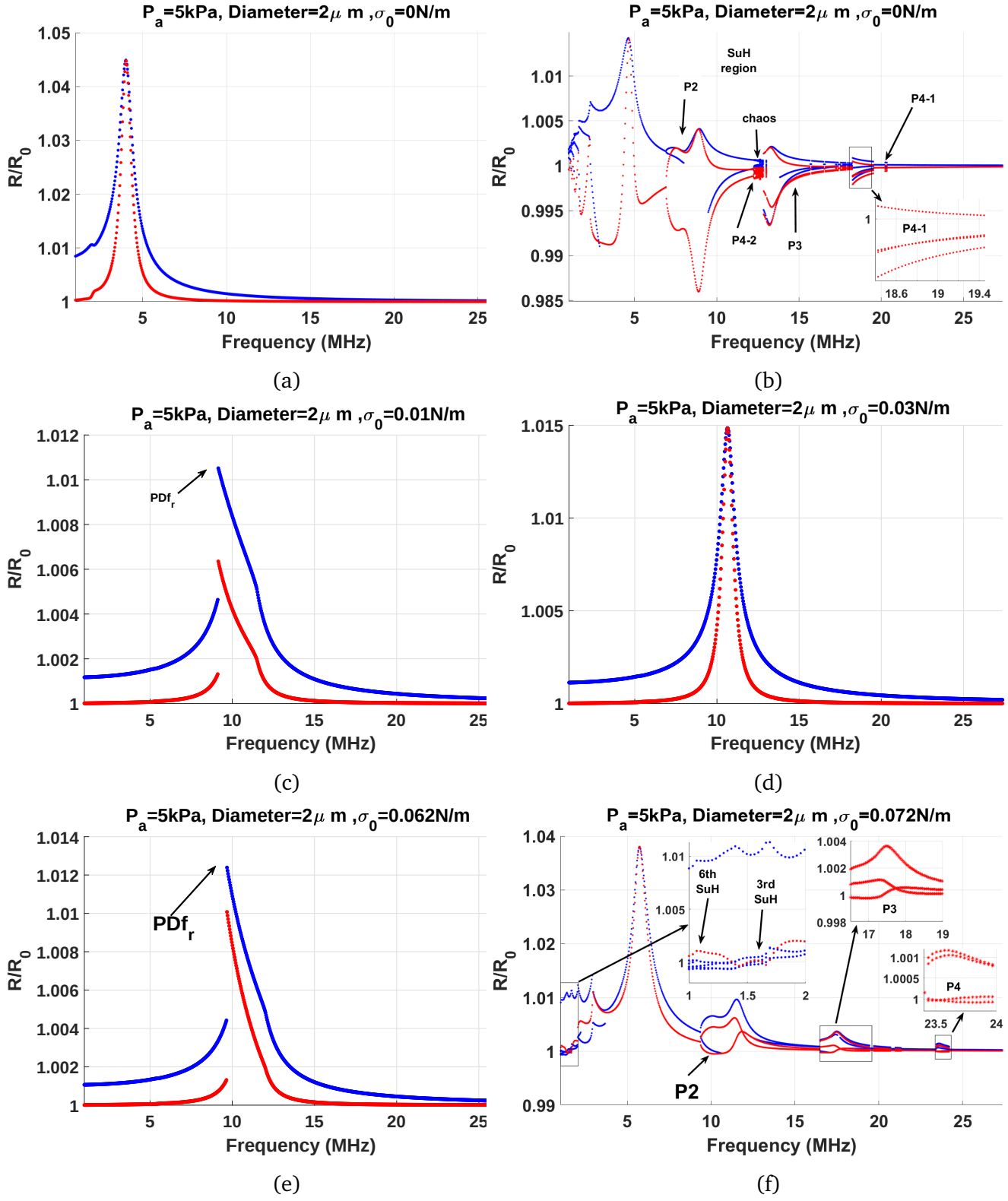

Figure 10.2: The bifurcation structure (blue represent the maxima and the red represents the conventional method) of the $\frac{R}{R_0}$ of a $2\mu m$ MB as a function of frequency for $P_a = 5kPa$ for the: a) uncoated MB and for the lipid MB with b) $\sigma(R_0) = 0N/m$, c) $\sigma(R_0) = 0.01N/m$, d) $\sigma(R_0) = 0.03N/m$, e) $\sigma(R_0) = 0.062N/m$ and f) $\sigma(R_0) = 0.072N/m$.

$PDf_r \cong 9.6MHz$.

The MB with $\sigma(R_0) = 0.072N/m$ exhibits a similar behavior to the MB with $\sigma(R_0) = 0N/m$ demonstrating $6th - 2nd$ order SuHs between the freqeuncy range of 1-3.7 MHz. Some of the SuH between $1MHz < f < 2MHz$ are highlighted in a subplot within Fig. 10.2f). P2 occurs between $9.3MHz < f < 16.5MHz$. P3 occurs between $16.5MHz < f < 19MHz$ (highlighted as a subplot inside Fig. 10.2f), between $19.7 < f < 20.7MHz$ and between $20.3MHz < f < 21.3MHz$. P4-1 regime occurs between $23.4MHz < f < 24MHz$ (highlighted within a subplot in Fig. 10.2f). The MB also demonstrates P1 resonance frequency at $\approx 5.7MHz$.

When Fig. 10.2a and 10.2f are compared, despite the higher damping due to the coating, the coated MB undergoing shell rupture exhibits a higher oscillation amplitude.

10.4.1.2 Bifurcation $\frac{R}{R_0}$ as a function of size (initial diameter) for uncoated and coated MBs with different $\sigma(R_0)$

In order to investigate the nonlinear behavior of the commercially available $Definity^{®}$ MBs for the experimental exposure conditions, the bifurcation structure of the $\frac{R}{R_0}$ is studied as a function of size when $P_a = 250kPa$ and $f = 25MHz$. This is because of the polydisperse nature of the $Definity^{®}$ MBs, and since we are limiting our analysis to the focal zone with small variations in pressure and the fixed sonication frequency. The size distribution in the simulations replicates the distribution of the native $Definity^{®}$ [54] Thus, the $\frac{R}{R_0}$ plot versus size will provide insight relevant to the experimental conditions in this study.

Fig. 10.3a, shows the bifurcation structure of an uncoated MB as a function of size. MB with sizes between $0.27\mu m$-$0.28\mu m$ exhibit 2nd order SuH (P1 oscillation with 2 maxima as highlighted in a subplot) and MBs with sizes $0.54\mu m$ are resonant. Fig. 10.3a shows that at $f = 25MHz$ and $P_a = 250kPa$ the uncoated MB cannot produce SHs.

Fig. 10.3b, shows the bifurcation structure of the $Definity^{@}$ MBs with $\sigma(R_0) = 0N/m$. In stark contrast to the uncoated MB (Fig. 10.3a), an abundance of nonlinear behavior is observed. This includes 4th, 3rd and 2nd order SuHs for MB sizes smaller than $0.345\mu m$ (some are highlighted in a subplot within Fig. 10.3b), P1 resonance for $\approx 0.59\mu m$ MBs , P2, P4-2 and chaotic behavior for MB sizes of $\approx 0.74\mu m < 2R_0 < 1.13\mu m$, P3 oscillations for $\approx 1.13\mu m < 2R_0 < 1.49\mu m$, and intermittent P4-1 oscillations for $\approx 1.49\mu m < 2R_0 < 1.7\mu m$ (P4-1 is highlighted in a subplot within

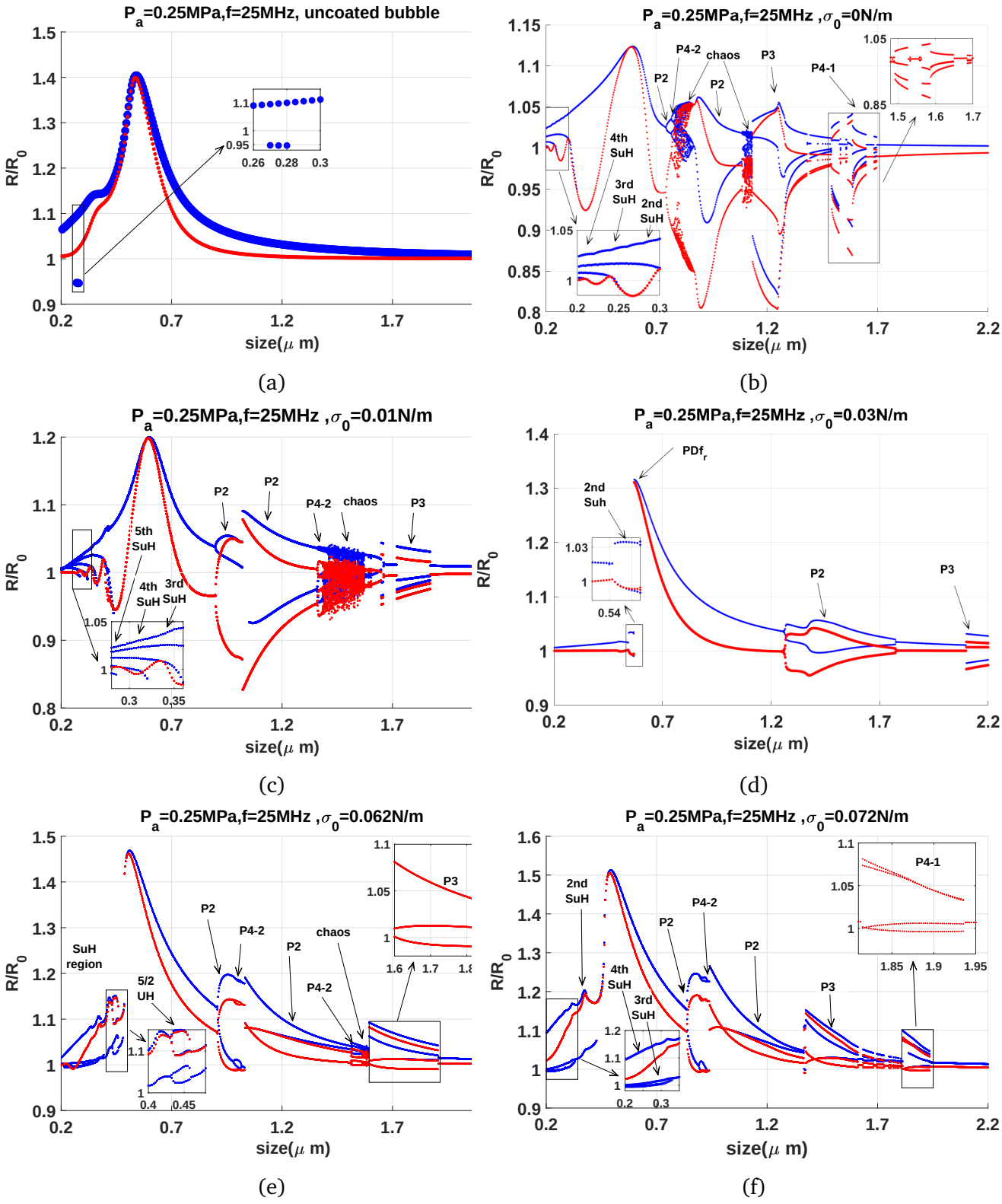

Figure 10.3: The bifurcation structure of the $\frac{R}{R_0}$ (blue represent the maxima and the red represents the conventional method) as a function of size (MB diameter) at $P_a = 250kPa$ and $f = 25MHz$ for the: a) uncoated MB and for the lipid MBs with b)$\sigma(R_0) = 0N/m$, c)$\sigma(R_0) = 0.01N/m$, d)$\sigma(R_0) = 0.03N/m$, e) $\sigma(R_0) = 0.062N/m$ and f) $\sigma(R_0) = 0.072N/m$.

Fig. 10.3b).

$Definity^{®}$ MBs with $\sigma(R_0) = 0.01N/m$ (Fig. 10.3c), exhibit enhanced nonlinear behavior including $5th - 2nd$ order SuHs (highlighted in a subplot), P2, P4-2, P3 and chaos. Fig. 10.3d represents the behavior of MBs with $\sigma(R_0) = 0.03N/m$. 2nd order SuH (highlighted in a subplot), PDf_r, P2 and P3 oscillations are observed.

Fig. 10.3e-f represent the MBs with initial surface tension close to that of water and thus with a higher tendency for rupture and expansion dominated behavior. For $\sigma(R_0) = 0.062N/m$ and for MB sizes $0.2\mu m < 2R_0 < 0.5\mu m$, 3rd and 2nd order SuH and 5/2 UH regimes are observed. 5/2 UH is a P2 with 4 maxima and is highlighted in a subplot within Fig. 10.3e. PDf_r, P2, P4-2 and P3 (highlighted in a subplot) oscillations are observed for MB sizes $2R_0 > 0.5\mu m$. When $\sigma(R_0) = 0.072N/m$ (Fig. 10.3f), in addition to the nonlinear behavior we observe in Fig. 10.3e, we observe 4th order SuH regime (highlighted in a subplot as a P1 with 4 maxima) and P4-1 and the absence of 5/2 UHs.

Results indicate that the nonlinear behavior of the MBs is highly sensitive to the initial surface tension as well as the MB size. The closer the surface tension to 0 or that of water ($\sigma_{water} = 0.072N/m$), the greater is the tendency of the MB to exhibit nonlinear behavior. In Fig. 10.3, P4-1 oscillations *were only observed* when $\sigma(R_0) = 0$ and $0.072N/m$.

The MBs with $\sigma(R_0) = 0.062$ (Fig. 10.3e) and $\sigma(R_0) = 0.072$ (Fig. 10.3f), exhibit higher oscillation amplitude compared to uncoated MBs of the same size.

In order to better visualize the effect of the $\sigma(R_0)$ on the MB behavior, the bifurcation structure of the $\frac{R}{R_0}$ of the MB is plotted as a function of $\sigma(R_0)$ for two different MB sizes in Fig. 10.4. Bifurcation structure of a MB with an initial diameter of $0.92\mu m$ is depicted in Fig. 10.4a. The nonlinear behavior occurs only for the two extreme ends of the $\sigma(R_0)$. P2 occurs for $\sigma(R_0) < 0.011N/m$ and $\sigma(R_0) > 0.061N/m$ with P4-2 happening for $0.0032N/m < \sigma(R_0) < 0.048N/m$ and $\sigma(R_0) > 0.069N/m$. For a MB with initial diameter of $1.89\mu m$, the same general behavior is observed. For initial surface tension values between $0.0127 < \sigma(R_0) < 0.057N/m$ we observe P1 behavior with 1 maximum. As we approach to the lower and higher $\sigma(R_0)$, nonlinear behavior manifests itself in the bifurcation diagrams. P4-1 oscillations occurs for $0.0035N/m < \sigma(R_0) < 0.0041N/m$ and $\sigma(R_0) > 0.07N/m$. P3 occurs for $0.009N/m < \sigma(R_0) < 0.012N/m$ and $0.058N/m < \sigma(R_0) < 0.069N/m$.

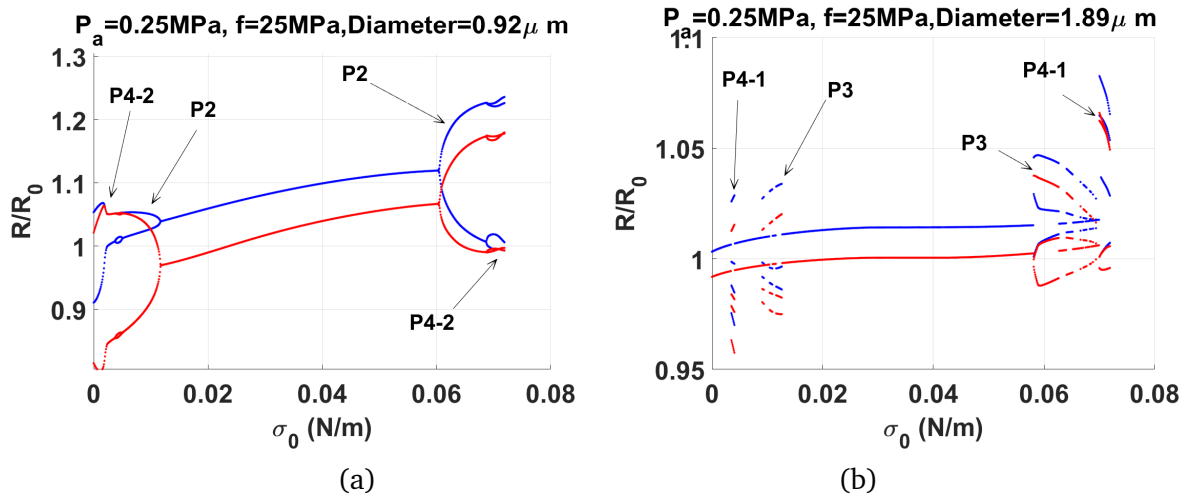

Figure 10.4: The bifurcation structure of $\frac{R}{R_0}$ as a function of $\sigma(R_0)$ at $f = 25MHz$ and $P_a = 250kPa$ for a MB size of: a) 0.92 μm & b) 1.89 μm

10.4.1.3 Experiments

In experiments at $P_a \approx 250kPa$ and $f = 25MHz$ we observed 5 main types of backscattered signals in the data collected from single MB events. A representative of each category is shown in Fig. 10.5a (P1), Fig. 10.5d (P2), Fig. 10.5g (P3) , Fig. 10.5j (P4-2) and Fig. 10.5m (P4-1). The results of the numerical simulations are presented in the second column and the frequency spectrum of the experimental signals and the numerical simulations are plotted in the third column (blue:experiments, red:simulations). Numerical simulations are for the $Definity^{®}$ MBs with $\sigma(R_0) = 0.072N/m$ with the corresponding sizes chosen from the bifurcation diagram (Fig. 10.3f) to match the observed behavior in the experiments.

Fig. 10.5a displays a typical P1 signal observed in experiments. The calculated P_{sc} for a 2 μm $Definity^{®}$ MB is displayed in Fig. 10.5b (in red color for distinction) and the power spectrum of the signals in Fig. 10.5a and 5b are shown in Fig. 10.5c. The scattered pressure has one maximum and the frequency spectrum has a peak at 25 MHz.

A representative signal of the P2 oscillations is displayed in the second row of Fig. 10.5. Both experimental and simulated (initial size of $0.955\mu m$) signals have two maxima revealing a P2 oscillation regime. The power spectra in Fig. 10.5f consist of a SH peak at 12.5MHz and a 3/2 UH peak at 32.5 MHz. Good agreement between experiments and simulations can be achieved when selecting the appropriate values for size and $\sigma(R_0)$.

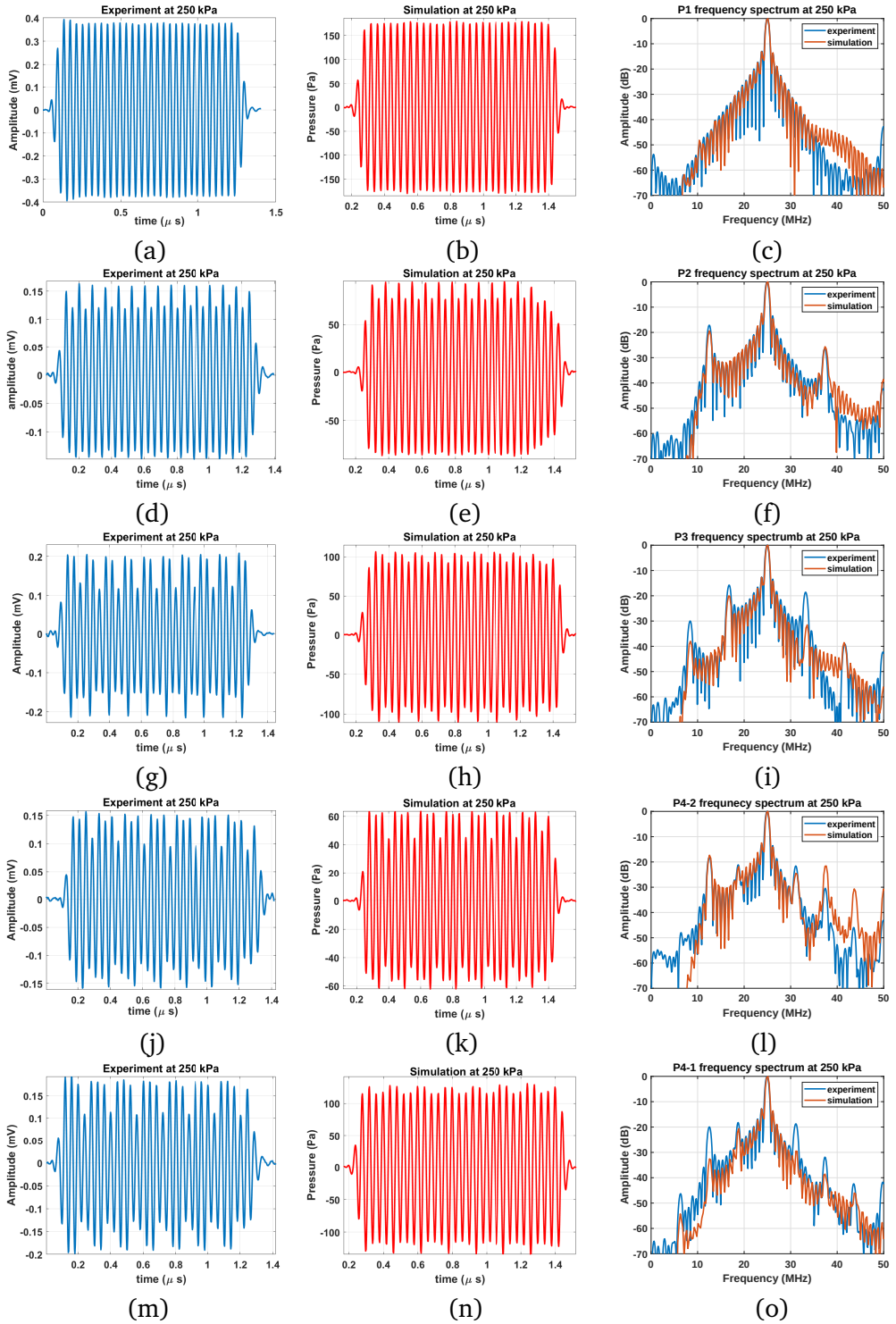

Figure 10.5: Demonstration of 5 main oscillation regimes acquired experimentally (blue) and simulated (red) choosing MB sizes based on the feature similarity in Fig. 3f. Representative experimental data and simulations of: 1st row P1, 2nd row P2, 3rd row P3, 4th row P4-2 and 5th row P4-1.

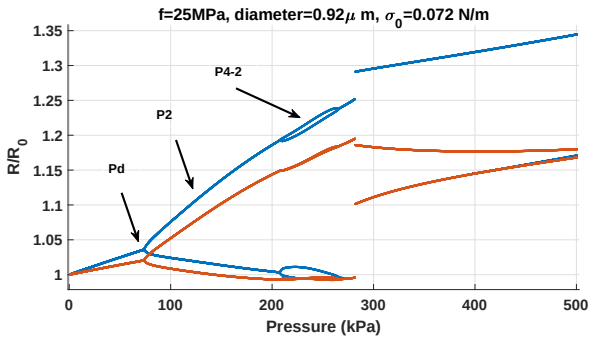

(a)

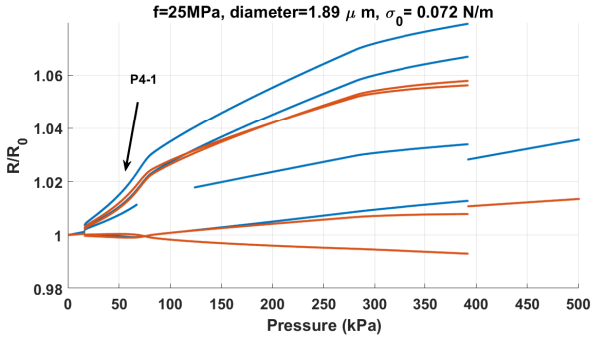

(b)

Figure 10.6: The bifurcation structure of the $\frac{R}{R_0}$ of the MB as a function of pressure for excitation with $f = 25MHz$ for a lipid MB with $\sigma(R_0) = 0.072N/m$ and a diameter of : a) 0.92 μm & b) 1.89 μm

A representative of the P3 signal is shown in the third row of Fig. 10.5. The experimental and simulated (initial size of $1.39\mu m$) signals have 3 maxima and the order of the maxima are consistent between experiments and simulations. The power spectra shown in Fig. 10.5i shows a good agreement between experiments and simulations with SHs at (1/3 order) 8.33 MHz, (2/3 order) 16.66 MHz and UHs at (4/3 order) 33.33 MHz and (5/3 order) 41.66 MHz.

P4-2 oscillations are shown in the 4th row of Fig. 10.5. There is a good agreement between the experimental and the simulated signals (initial size of $0.92\mu m$). Both signals have 4 peaks in two envelopes and each envelope repeats itself once every two acoustic cycles. In each envelope there are two peaks and the peaks repeat themselves in an amplitude order of (largest, small, large, smallest). The frequency spectra of the signals are shown in Fig. 10.5l. There are 3 SHs at (1/4 order) 6.25 MHz, (1/2 order) 12.5 MHz and (3/4) order at 18.75 MHz. The 1/2 order SH is the strongest detected SH and due to the weakness of the 1/4 SH, this peak is hardly detectable. This is because the transducer sensitivity drops sharply away from the center frequency and especially below 12.5 MHz (transducer bandwidth is 100%). While the numerically simulated P_{sc} in the

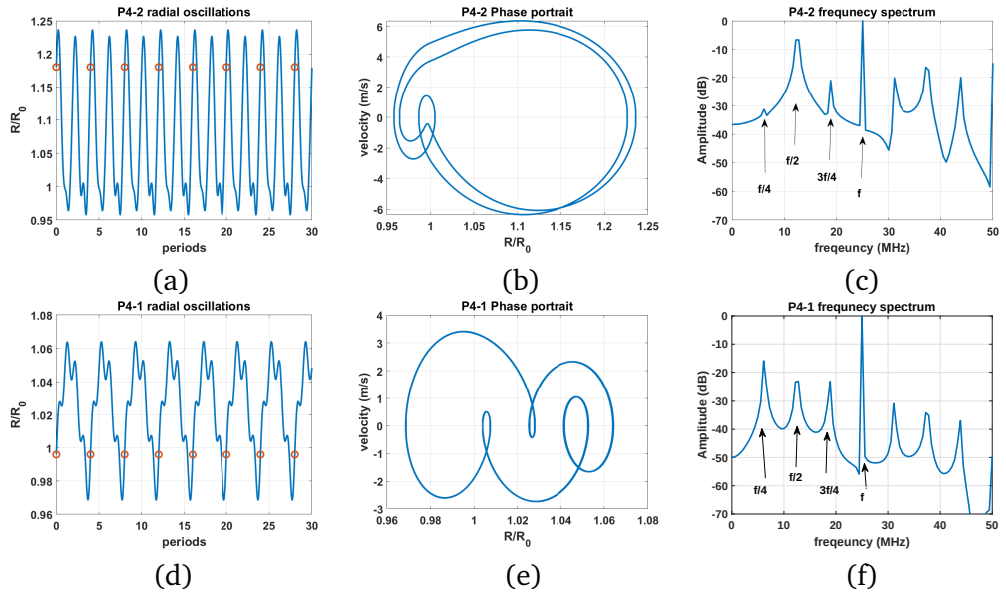

Figure 10.7: Characteristics of the two P4 oscillations identified: a) P4-2 radial oscillations, b) P4-2 phase portrait, c) power spectrum of the P4-2 P_{sc}, d)P4-1 radial oscillations, e)P4-2 phase portrait and f) power spectrum of P4-2 P_{sc}. Here P_{sc} is not convolved with the transducer response. (red circles shows the location of the R every 4 acoustic cycles)

abscense of convolution with transducer response had a clear peak at 6.25 MHz, however, after the signal is convolved with the transducer response, the signal drops below the noise level of -70 dB in our experiments.

The last row of Fig. 10.5 depicts the case of the P4-1 oscillations. Simulations are for a MB with initial size of $1.89\mu m$. The signals have one envelope with 4 maxima that repeats itself once every 4 acoustic cycles. Amplitudes repeats themselves in the order of smallest, largest, large and small. Both experimental and simulated signals demonstrate the same pattern of peaks and their orders. The power spectra in Fig. 10.5o shows a good agreement between the orders of the SHs and their locations. There are 3 SHs at (1/4 order) 6.25 MHz, (1/2 order) 12.5 MHz and (3/4 order) at 18.75 MHz. The 3/4 order SH is the strongest detected SH. It should be noted that 1/4 order SH is the strongest peak in the calculated P_{sc} in the absence of convolution with transducer response (see Fig. 10.7f). Due to the reduced sensitivity of the transducer at 6.25 MHz, the detected strength of the 1/4 order SH diminishes strongly and it drops below all the other SHs.

10.4.1.4 Difference between P4-1 and P4-2

Fig. 10.6a shows the bifurcation structure of a 0.92 μm $Definity^{®}$ MB as a function of pressure when $f = 25MHz$. At low pressures there are linear oscillations with period doubling (Pd) at $\approx 70kPa$. P2 oscillations undergo further Pd to P4-2 oscillations at $\approx 210kPa$. The process of P4-2 generation and disappearance is through a bubbling bifurcation. In case of the $1.89\mu m$ $Definity^{@}$ (Fig. 10.6b), P4 oscillations are generated through a direct period quadrupling via a saddle node bifurcation similar to [26]. This is the reason why we named this a P4-1 oscillations. Models for uncoated MBs or coated MBs with pure viscoelastic behavior predict very high pressures for the generation of P4-1 oscillations; however, here we show, for the first time, that the dynamic variation of the shell elasticity including buckling and rupture enhances the generation of the P4-1 oscillations at very low acoustic pressures ($P_a = 16.625kPa$ in Fig. 10.6b).

Fig. 10.7 compares the radial oscillations, phase portraits and the power spectra of the P_{sc} for both P4 oscillation classification at $f = 25MHz$ and $P_a = 250kPa$. P4-2 radial oscillations consist of two envelops, with each envelope having 2 maxima or one with 2 maxima and the other with a maxima and a critical point. These envelopes repeat themselves once every two acoustic cycles in Fig. 10.7a. The phase portrait of the P4-2 oscillations consists of a loop undergoing two internal loops with the largest loop undergoing another internal loop. The power spectrum depicts SHs with strength order of $1/2 > 3/4 > 1/4$. P4-1 oscillations in Fig. 10.7d have one envelope with 4 maxima which repeats itself once every 4 acoustic cycles. The phase portrait consist of a main loop that has undergone 3 bends to create 3 internal loops. The frequency spectrum of P_{sc} depicts SHs in the strength order of $1/4 > 1/2 > 3/4$. It should be noted that due to the lower sensitivity of the transducer as we move away from central frequency, the strength order of the SHs that are detected in experiments were different. After, convolving the simulations results with the one way transducer response, experiments and simulations were in good agreement. To our best knowledge, this is the first time that the two types of P4 oscillations are detected experimentally and characterized numerically for a MB oscillator.

10.5 Discussion

A MB oscillator is an extremely complex system that has beneficial applications in a wide range of fields including material science and sonochemistry [59, 60, 61], food technology [62] underwater acoustics [63, 64] and medical ultrasound (ranging from imaging blood vessels [65], drug delivery [51] to thrombolysis [66] and the treatment of brain through intact skull [49, 67]). In addition to these important applications, the complex dynamical properties of the MB system make it a very interesting subject in the field of nonlinear dynamics. It is well known that an ultrasonically excited MB is a highly nonlinear oscillator. Due to the importance of the understanding of the MB behavior in several applications, numerous studies have employed the methods of nonlinear dynamics and chaos to study the complex behavior of the system. Pioneering works of [18, 19, 20, 61, 68] have revealed several nonlinear and chaotic properties of the MB oscillations (both numerically and experimentally). Recent extensive studies on the nonlinear behavior of MBs in water [23, 24, 25, 26, 27, 43, 44], coated MBs [26, 27, 42], MBs in highly viscous media [28, 29, 30, 31, 32, 33], MBs sonicated with asymmetrical driving acoustic forces [33, 34, 35, 36, 37, 38, 39, 40, 41] and MBs in non-Newtonian fluids [37] have revealed many nonlinear features in the MB behavior. Occurrence of P2, P3, P4-2, P4-1 and higher periods, as well as chaotic oscillations, has been shown in these works. Moreover, the effect of nonlinear dynamics of MBs on the propagation of sound waves in a bubbly medium is under recent investigation [26, 69, 70, 71].

Despite these studies that employed the methods of chaos physics to investigate the nonlinear dynamics of the uncoated and coated MBs with viscoelastic behavior, the effect of the lipid coating on the dynamics of the MB especially in the realm of nonlinear dynamics and chaos has not been investigated.

In this study we investigated the bifurcation structure of the lipid coated MBs and used the numerical results to help interpret unique signals that we observed experimentally. In stark contradiction to the results of classical theory of uncoated MBs, and despite the increased damping of the coated MBs, lipid coated MBs exhibited higher order nonlinear behavior at low excitation amplitudes (shown here both experimentally and numerically). The numerical and experimental findings can be summarized as follows:

a- We have shown that even at pressures as low as $5kPa$, $6th-2nd$ order SuHs, P4-2, P2, P3 P4-1

and chaotic regimes manifest themselves in the MB behavior. To our best knowledge the existence of higher order SHs and chaotic behavior at such low excitation amplitudes is first reported here.

b- The initial surface tension of the MB plays a critical role in the enhanced nonlinear behavior. We have shown that the closer $\sigma(R_0)$ is to 0 (leading to buckling and compression only behavior) or to σ_{water} (leading to shell rupture and expansion dominated behavior), the lower is the excitation threshold for nonlinear behavior and the higher is the order of non-linearity.

c- Despite the increased damping of the lipid coated MBs we show that, the MBs with surface tension $\geq 0.062N/m$ may have higher radial oscillation amplitude compared to the uncoated bubble.

d- We have experimentally shown that single $Definity^{®}$ MBs, can exhibit, P2, P3, P4-2 and P4-1 oscillations at high frequencies (25 MHz) and low pressures (250 kPa). These results can not be predicted using conventional coated MB models (pure viscoelastic behavior) and they are even in contrast with the predictions of the uncoated MB models with less damping effects.

e- Through numerical simulations of Marmottant model [12] and visualization of the results using bifurcation diagrams we showed that $Definity^{®}$ MBs, can exhibit enhanced nonlinear behavior. Using this model and assuming MBs with initial surface tension close to 0 N/m or σ_{water} could be used to explain experimental observations.

f- The 5 main regimes of oscillations were identified as P1, P2, P3, P4-2 and P4-1. Simulation results of the scattered pressure were in good agreement with experimental observations both in terms of the shape of the amplitude versus time signal and also its frequency content and when a MB size is used based on the exploration of the relevant parameter space.

g- For the first time, the two different P4 oscillations of the MB system were identified and characterized experimentally and numerically. P4-2 oscillations are the result of two consecutive well known period doublings while P4-1 oscillations occur through a single period quadrupling via a saddle node bifurcation. The distinct features of the signal shapes and their unique frequency spectrum were identified both experimentally and numerically. In general P4-1 oscillations require larger MBs compared to P4-2 oscillations

Previous studies have shown that lipid coated MBs can exhibit 1/2 order subharmonic oscillations even when the excitation amplitude is low (<30 kPa [1, 2, 3]) where such low pressure thresholds are below the thresholds expected even for uncoated free MBs [4,5]. The low pressure threshold for

SH emissions has been attributed to the buckling of the coating and compression only behavior [1]. Compression dominated oscillations [6] occur when the coating buckles and the effective surface tension on the MB drops to zero. In such an instance, the MB compresses more than it expands. In addition to compression only behavior, lipid coating may also result in expansion dominated behavior where the MB expands more than it compresses [11, 13]. Expansion-dominated behavior occurs when the shell ruptures. This effect was used to explain the enhanced non-linearity at at higher frequencies (25 MHz) [11, 72]. Theoretical analysis of the Marmottant model for lipid coated MBs [12] by Prosperetti [4] attributed the lower SH threshold of the lipid MBs to the variation in the mechanical properties of the coating in the neighborhood of a certain MB radius (e.g. occurrence of buckling). In this work we show that there is a symmetry for enhanced non-linearity in the bifurcation structure of the $\frac{R}{R_0}$ of the MB as a function of $\sigma(R_0)$. Both buckling and rupture can be responsible for enhanced non-linearity, where the closer the $\sigma(R_0)$ to the buckling state (0 N/m) or rupture threshold (0.072 N/m), the lower the excitation threshold required for the generation of nonlinear oscillations. Moreover, the closer the $\sigma(R_0)$ to these two limit values, the higher the order of the nonlinearity.

Using the estimated parameters for the $Definity^{®}$ MB in [54] and considering the shear thinning [53], the observed experimental behavior was only replicated for MBs with initial surface tension close to the two limit values of 0 and 0.072 N/m. However, it should be noted that during the sonication of a polydisperse solution of lipid MBs different values in initial surface tension and coating properties (coating elasticity and viscosity) are expected. It is been reported that even for MBs of the same size, the lipid coating can be different from MB to MB and are shown to be heterogeneous for MBs smaller than 10 μm [73, 74]. Despite the better homogenity of lipid distribution in lipid coated MBs similar to $Definity^{®}$ [73, 74], the small differences in the lipid distribution in the coating influences the effective coating properties, thus changing the MB response [75, 76, 77]. Moreover, its shown that the coating elasticity and coating viscoity changes with the MB size [78, 79, 80]. Despite assuming the same coating properties for all MB sizes in this work, we were still be able to replicate the observed behavior in experiments. Moreover, we used the simplest model for lipid coated MBs and we neglected the possible stiffness softening [81] or higher viscoelastic effects. Implementation of these effects are outside of the focus of this study but can be used to better characterizing the coating. In addition, simulation results only

implemented a monofreqeuncy ultrasound source, and the effects of nonlinear propagation of sound waves in the medium are neglected. The generation of the SHs and UHs were not due to the nonlinear propagation of waves as nonlinear propagation manifests itself through generation of only harmonics.

Effects of the shape oscillations on the MBs response were also neglected in this paper. Holt and Crum observed significant effects of shape oscillations on the nonlinear behavior of the larger MBs with initial radii between $20\mu m < R_0 < 100\mu m$ [82]. Versluis et al. [83] using high speed optical observations identified time-resolved shape oscillations of mode n= 2 to 6 in the behavior of single air bubbles with radii between $10\mu m$ and 45 μm. [83] concludes that the close to resonance bubbles were found to be most vulnerable toward shape instabilities. Effect of non-spherical bubble oscillations on nonlinear bubble behavior is studied in [84] through GPU accelerated large parameter investigations. The active cavitation threshold has been shown to depend on the shape instability of the bubble [84]. [84] also shows that shape instability can affect the subharmonic threshold and nonlinear behavior of bubbles. Nonspherical oscillations of ultrasound contrast agent coated MBs are investigated in [85] through high speed optical observations. They showed that non-spherical bubble oscillations are significantly present in medically relevant ranges of bubble radii and applied acoustic pressures. Non-spherical oscillations develop preferentially at the resonance radius and may be present during SH oscillations [85]. Thus, for a more accurate modeling of the MB oscillations, deeper theoretical modeling of bubble coating, accounting for membrane shear and bending is required [85].

Generation of higher order SHs at low pressures may have potential in high resolution SH imaging due to their higher frequencies, higher contrast to tissue and signal to noise ratio. A SH of order 2/3 or 3/4 can be detected more effectively by the transducer as they are closer to the transducer center frequency when compared to 1/2 order SHs. Moreover, the higher scattered pressures, faster oscillations and the lower frequency contents of the oscillations of the higher order SHs may enhance the nondestructive shear stress on cells for enhanced drug delivery or in cleaning applications. Mixing applications are another category of applications that can take advantage of higher order SHs at high frequencies.

10.6 conclusion

We have shown experimentally and for the first time that higher order SHs (e.g. 1/3,1/4,..) can be generated in the oscillations of lipid coated MBs when insonated at high frequencies and low excitation amplitudes. The bifurcation structure of a simple model of lipid coated MBs were studied as function of frequency and size for the first time. We showed that compression only behavior or expansion dominated oscillations respectively due to buckling and rupture of the coating and dynamic variation of the effective surface tension can explain the observed enhanced non-linearity in MBs oscillations.

Acknowledgments

The work is supported by the Natural Sciences and Engineering Research Council of Canada (Discovery Grant RGPIN-2017-06496), NSERC and the Canadian Institutes of Health Research (Collaborative Health Research Projects) and the Terry Fox New Frontiers Program Project Grant in Ultrasound and MRI for Cancer Therapy (project #1034). A. J. Sojahrood is supported by a CIHR Vanier Scholarship and Qian Li is supported by NSF CBET grant #1134420.

Bibliography

[1] Frinking, P.J., Gaud, E., Brochot, J. and Arditi, M., 2010. Subharmonic scattering of phospholipid-shell microbubbles at low acoustic pressure amplitudes. IEEE transactions on ultrasonics, ferroelectrics, and frequency control, 57(8), pp.1762-1771.

[2] Sijl, J., Dollet, B., Overvelde, M., Garbin, V., Rozendal, T., de Jong, N., Lohse, D. and Versluis, M., 2010. Subharmonic behavior of phospholipid-coated ultrasound contrast agent microbubbles. The Journal of the Acoustical Society of America, 128(5), pp.3239-3252.

[3] Biagi, E., Breschi, L., Vannacci, E. and Masotti, L., 2007. Stable and transient subharmonic emissions from isolated contrast agent microbubbles. IEEE transactions on ultrasonics, ferroelectrics, and frequency control, 54(3), pp.480-497.

[4] Prosperetti, A., 2013. A general derivation of the subharmonic threshold for non-linear bubble oscillations. The Journal of the Acoustical Society of America, 133(6), pp.3719-3726.

[5] O. Lotsberg, J. M. Hovem, and B. Aksum, "Experimental observation of subharmonic oscillations in Infoson bubbles," J. Acoust. Soc. Am., vol. 99, no. 3, pp. 1366–1369, 1996

[6] De Jong, N., Emmer, M., Chin, C.T., Bouakaz, A., Mastik, F., Lohse, D. and Versluis, M., 2007. "Compression-only" behavior of phospholipid-coated contrast bubbles. Ultrasound in medicine & biology, 33(4), pp.653-656.

[7] Emmer, M., Van Wamel, A., Goertz, D.E. and De Jong, N., 2007. The onset of microbubble vibration. Ultrasound in medicine & biology, 33(6), pp.941-949.

[8] Overvelde, M., Garbin, V., Sijl, J., Dollet, B., De Jong, N., Lohse, D. and Versluis, M., 2010. Nonlinear shell behavior of phospholipid-coated microbubbles. Ultrasound in medicine & biology, 36(12), pp.2080-2092.

[9] Helfield, B.L. and Goertz, D.E., 2013. Nonlinear resonance behavior and linear shell estimates for Definity™ and MicroMarker™ assessed with acoustic microbubble spectroscopy. The Journal of the Acoustical Society of America, 133(2), pp.1158-1168.

[10] Faez, T., Emmer, M., Docter, M., Sijl, J., Versluis, M., & de Jong, N. (2011). Characterizing the subharmonic response of phospholipid-coated microbubbles for carotid imaging. Ultrasound in medicine & biology, 37(6), 958-970.

[11] Helfield, B.L., Cherin, E., Foster, F.S. and Goertz, D.E., 2012. Investigating the subharmonic response of individual phospholipid encapsulated microbubbles at high frequencies: A comparative study of five agents. Ultrasound in medicine & biology, 38(5), pp.846-863.

[12] Marmottant, P., Van Der Meer, S., Emmer, M., Versluis, M., De Jong, N., Hilgenfeldt, S. and Lohse, D., 2005. A model for large amplitude oscillations of coated bubbles accounting for buckling and rupture. The Journal of the Acoustical Society of America, 118(6), pp.3499-3505.

[13] Luan, Y., Faez, T., Gelderblom, E., Skachkov, I., Geers, B., Lentacker, I., van der Steen, T., Versluis, M. and de Jong, N., 2012. Acoustical properties of individual liposome-loaded microbubbles. Ultrasound in medicine & biology, 38(12), pp.2174-2185.

[14] Jafari Sojahrood, A., Karshafian, R. and C. Kolios, M., 2013, June. Bifurcation structure of the ultrasonically excited microbubbles undergoing buckling and rupture. In Proceedings of Meetings on Acoustics ICA2013 (Vol. 19, No. 1, p. 075097). ASA.

[15] Sojahrood, A.J., Karshafian, R. and Kolios, M.C., 2012, October. Detection and characterization of higher order nonlinearities in the oscillations of Definity at higher frequencies and very low acoustic pressures. In 2012 IEEE International Ultrasonics Symposium (pp. 1193-1196). IEEE.

[16] Versluis, M., 2010, December. Nonlinear behavior of ultrasound contrast agent microbubbles and why shell buckling matters. In Proceedings of 20th International Congress on Acoustics, Sydney, Australia.

[17] Lauterborn, Werner, and Thomas Kurz. ”Physics of bubble oscillations.” Reports on progress in physics 73, no. 10 (2010): 106501.

[18] Parlitz, U., V. Englisch, C. Scheffczyk, and W. Lauterborn. ”Bifurcation structure of bubble oscillators.” The Journal of the Acoustical Society of America 88, no. 2 (1990): 1061-1077.

[19] Lauterborn, Werner, and Joachim Holzfuss. ”Acoustic chaos.” International Journal of bifurcation and Chaos 1, no. 01 (1991): 13-26.

[20] Prosperetti, A., 1974. Nonlinear oscillations of gas bubbles in liquids: steady-state solutions. The Journal of the Acoustical Society of America, 56(3), pp.878-885.

[21] Lauterborn, W. and Koch, A., 1987. Holographic observation of period-doubled and chaotic bubble oscillations in acoustic cavitation. Physical Review A, 35(4), p.1974.

[22] Ohl, C.D., Kurz, T., Geisler, R., Lindau, O. and Lauterborn, W., 1999. Bubble dynamics, shock waves and sonoluminescence. Philosophical Transactions of the Royal Society of London. Series A: Mathematical, Physical and Engineering Sciences, 357(1751), pp.269-294.

[23] Sojahrood, A.J., Earl, R., Kolios, M.C. and Karshafian, R., 2020. Investigation of the 1/2 order subharmonic emissions of the period-2 oscillations of an ultrasonically excited bubble. Physics Letters A, p.126446.

[24] Behnia, S., Sojahrood, A.J., Soltanpoor, W. and Sarkhosh, L., 2009. Towards classification of the bifurcation structure of a spherical cavitation bubble. Ultrasonics, 49(8), pp.605-610.

[25] Varga, R. and Hegedűs, F., 2016. Classification of the bifurcation structure of a periodically driven gas bubble. Nonlinear Dynamics, 86(2), pp.1239-1248.

[26] Sojahrood, A.J., Haghi, H., Karshafian, R. and Kolios, M.C., 2020. Critical corrections to models of nonlinear power dissipation of ultrasonically excited bubbles. Ultrasonics Sonochemistry, 66, pp.105089-105089.

[27] Sojahrood, A.J. and Kolios, M.C., 2012. Classification of the nonlinear dynamics and bifurcation structure of ultrasound contrast agents excited at higher multiples of their resonance frequency. Physics Letters A, 376(33), pp.2222-2229.

[28] Hegedűs, F., 2014. Stable bubble oscillations beyond Blake’s critical threshold. Ultrasonics, 54(4), pp.1113-1121.

[29] Hegedűs, F., Hős, C. and Kullmann, L., 2012. Stable period 1, 2 and 3 structures of the harmonically excited Rayleigh–Plesset equation applying low ambient pressure. The IMA Journal of Applied Mathematics, 78(6), pp.1179-1195.

[30] Hegedűs, F., 2016. Topological analysis of the periodic structures in a harmonically driven bubble oscillator near Blake's critical threshold: Infinite sequence of two-sided Farey ordering trees. Physics Letters A, 380(9-10), pp.1012-1022.

[31] Hegedűs, F. and Klapcsik, K., 2015. The effect of high viscosity on the collapse-like chaotic and regular periodic oscillations of a harmonically excited gas bubble. Ultrasonics sonochemistry, 27, pp.153-164.

[32] Klapcsik, K. and Hegedűs, F., 2019. Study of non-spherical bubble oscillations under acoustic irradiation in viscous liquid. Ultrasonics sonochemistry, 54, pp.256-273.

[33] Behnia, S., Sojahrood, A.J., Soltanpoor, W. and Jahanbakhsh, O., 2009. Suppressing chaotic oscillations of a spherical cavitation bubble through applying a periodic perturbation. Ultrasonics sonochemistry, 16(4), pp.502-511.

[34] Klapcsik, K., Varga, R. and Hegedűs, F., 2018. Bi-parametric topology of subharmonics of an asymmetric bubble oscillator at high dissipation rate. Nonlinear Dynamics, 94(4), pp.2373-2389.

[35] Hegedűs, F., Lauterborn, W., Parlitz, U. and Mettin, R., 2018. Non-feedback technique to directly control multistability in nonlinear oscillators by dual-frequency driving. Nonlinear Dynamics, 94(1), pp.273-293.

[36] Hegedűs, F. and Kalmár, C., 2018. Dynamic stabilization of an asymmetric nonlinear bubble oscillator. Nonlinear Dynamics, 94(1), pp.307-324.

[37] Zhang, Y., 2018. Chaotic oscillations of gas bubbles under dual-frequency acoustic excitation. Ultrasonics sonochemistry, 40, pp.151-157.

[38] Zhang, Y. and Li, S., 2017. Combination and simultaneous resonances of gas bubbles oscillating in liquids under dual-frequency acoustic excitation. Ultrasonics sonochemistry, 35, pp.431-439.

[39] Zhang, Y., Du, X., Xian, H. and Wu, Y., 2015. Instability of interfaces of gas bubbles in liquids under acoustic excitation with dual frequency. Ultrasonics sonochemistry, 23, pp.16-20.

[40] Zhang, Y. and Li, S., 2016. The secondary Bjerknes force between two gas bubbles under dual-frequency acoustic excitation. Ultrasonics sonochemistry, 29, pp.129-145.

[41] Zhang, Y. and Li, S., 2015. Acoustical scattering cross section of gas bubbles under dual-frequency acoustic excitation. Ultrasonics sonochemistry, 26, pp.437-444.

[42] Sojahrood, A.J., Falou, O., Earl, R., Karshafian, R. and Kolios, M.C., 2015. Influence of the pressure-dependent resonance frequency on the bifurcation structure and backscattered pressure of ultrasound contrast agents: a numerical investigation. Nonlinear Dynamics, 80(1-2), pp.889-904.

[43] Sojahrood, A.J., Wegierak, D., Haghi, H., Karshfian, R. and Kolios, M.C., 2019. A simple method to analyze the super-harmonic and ultra-harmonic behavior of the acoustically excited bubble oscillator. Ultrasonics sonochemistry, 54, pp.99-109.

[44] A.J. Sojahrood, R.E. Earl, M.C. Kolios and R. Karshafian Nonlinear dynamics of acoustic bubbles excited by their pressure dependent subharmonic resonance frequency: oversaturation and enhancement of the subharmonic signal. arxiv 2019

[45] Forsberg, F., Merton, D.A., Liu, J.B., Needleman, L. and Goldberg, B.B., 1998. Clinical applications of ultrasound contrast agents. Ultrasonics, 36(1-5), pp.695-701.

[46] Albrecht, T. and Hohmann, J., 2003. Ultrasound contrast agents. Der Radiologe, 43(10), pp.793-804.

[47] Feinstein, S.B., 2004. The powerful microbubble: from bench to bedside, from intravascular indicator to therapeutic delivery system, and beyond. American Journal of physiology-heart and circulatory physiology, 287(2), pp.H450-H457.

[48] Kaufmann, B.A. and Lindner, J.R., 2007. Molecular imaging with targeted contrast ultrasound. Current opinion in biotechnology, 18(1), pp.11-16.

[49] Abrahao, A., Meng, Y., Llinas, M., Huang, Y., Hamani, C., Mainprize, T., Aubert, I., Heyn, C., Black, S.E., Hynynen, K. and Lipsman, N., 2019. First-in-human trial of blood–brain barrier opening in amyotrophic lateral sclerosis using MR-guided focused ultrasound. Nature communications, 10(1), pp.1-9.

[50] Cherin, E., Yin, J., Forbrich, A., White, C., Dayton, P.A., Foster, F.S. and Démoré, C.E., 2019. In Vitro Superharmonic Contrast Imaging Using a Hybrid Dual-Frequency Probe. Ultrasound in medicine & biology, 45(9) pp. 2525-2539.

[51] Roovers, S., Segers, T., Lajoinie, G., Deprez, J., Versluis, M., De Smedt, S.C. and Lentacker, I., 2019. The role of ultrasound-driven microbubble dynamics in drug delivery: from microbubble fundamentals to clinical translation. Langmuir. 35, 31, 10173-10191

[52] Falou, O., Rui, M., El Kaffas, A., Kumaradas, J.C. and Kolios, M.C., 2010. The measurement of ultrasound scattering from individual micron-sized objects and its application in single cell scattering. The Journal of the Acoustical Society of America, 128(2), pp.894-902.

[53] Doinikov, A.A., Haac, J.F. and Dayton, P.A., 2009. Modeling of nonlinear viscous stress in encapsulating shells of lipid-coated contrast agent microbubbles. Ultrasonics, 49(2), pp.269-275.

[54] Goertz, D.E., de Jong, N. and van der Steen, A.F., 2007. Attenuation and size distribution measurements of Definity™ and manipulated Definity™ populations. Ultrasound in medicine & biology, 33(9), pp.1376-1388.

[55] Keller, J.B. & Miksis M., Bubble oscillations of large amplitude, ., *J. Acoust. Soc. Am.* 68 (1980) 628–633.

[56] Vokurka, K. On Rayleigh's model of a freely oscillating bubble. I. Basic relations. Czechoslovak Journal of Physics B, 35(1), (1985): 28-40.

[57] Hilgenfeldt, S., Lohse, D., & Zomack, M. Response of bubbles to diagnostic ultrasound: a unifying theoretical approach. The European Physical Journal B-Condensed Matter and Complex Systems, 4(2), (1998):247-255.

[58] Goertz, D.E., Cherin, E., Needles, A., Karshafian, R., Brown, A.S., Burns, P.N. and Foster, F.S., 2005. High frequency nonlinear B-scan imaging of microbubble contrast agents. IEEE transactions on ultrasonics, ferroelectrics, and frequency control, 52(1), pp.65-79.

[59] Suslick, Kenneth S. "Sonochemistry." science 247, no. 4949 (1990): 1439-1445.

[60] Crum, Lawrence A., Timothy J. Mason, Jacques L. Reisse, and Kenneth S. Suslick, eds. Sonochemistry and sonoluminescence. Vol. 524. Springer Science & Business Media, 2013.

[61] Holt, R. Glynn, D. Felipe Gaitan, Anthony A. Atchley, and Joachim Holzfuss. "Chaotic sonoluminescence." Physical review letters 72, no. 9 (1994): 1376.

[62] Mason, Timothy J., Larysa Paniwnyk, and J. P. Lorimer. "The uses of ultrasound in food technology." Ultrasonics sonochemistry 3, no. 3 (1996): S253-S260.

[63] Loewen, M., 2002. Physical oceanography: Inside whitecaps. Nature, 418(6900), p.830.

[64] Leighton, T.G., 2004. From seas to surgeries, from babbling brooks to baby scans: The acoustics of gas bubbles in liquids. International Journal of Modern Physics B, 18(25), pp.3267-3314.

[65] Liu, J.B., Merton, D.A., Forsberg, F. and Goldberg, B.B., 2019. Contrast-enhanced ultrasound imaging. In Diagnostic Ultrasound (pp. 51-74). CRC Press.

[66] Holland, C.K., Kleven, R.T., Karani, K.B., Salido, N.G., Shekhar, H. and Haworth, K.J., 2019. Sonothrombolysis: Effect of 220kHz insonation scheme. Ultrasound in Medicine & Biology, 45, p.S39.

[67] O'Reilly, M.A. and Hynynen, K., 2018. Ultrasound and microbubble-mediated blood-brain barrier disruption for targeted delivery of therapeutics to the brain. In Targeted Drug Delivery (pp. 111-119). Humana Press, New York, NY.

[68] R. Esche, "Investigations on oscillating cavities in liquids," Acustica 2, 208–218 1952.

[69] Sojahrood, A.J., Li, Q., Haghi, H., Karshafian, R., Porter, T.M. and Kolios, M.C., 2018. Pressure dependence of the ultrasound attenuation and speed in bubbly media: Theory and experiment. arXiv preprint arXiv:1811.07788.

[70] Louisnard, O., 2012. A simple model of ultrasound propagation in a cavitating liquid. Part I: Theory, nonlinear attenuation and traveling wave generation. Ultrasonics sonochemistry, 19(1), pp.56-65.

[71] Sojahrood, A.J., Haghi, H., Li, Q., Porter, T.M., Karshafian, R. and Kolios, M.C., 2020. Nonlinear power loss in the oscillations of coated and uncoated bubbles: Role of thermal, radiation and encapsulating shell damping at various excitation pressures. Ultrasonics sonochemistry, 66, p.105070.

[72] Shekhar, H. and Doyley, M.M., 2013. The response of phospholipid-encapsulated MBsto chirp-coded excitation: Implications for high-frequency nonlinear imaging. The Journal of the Acoustical Society of America, 133(5), pp.3145-3158.

[73] Kooiman, K., Kokhuis, T.J., van Rooij, T., Skachkov, I., Nigg, A., Bosch, J.G., van der Steen, A.F., van Cappellen, W.A. and de Jong, N., 2014. DSPC or DPPC as main shell component influences ligand distribution and binding area of lipid-coated targeted microbubbles. European journal of lipid science and technology, 116(9), pp.1217-1227.

[74] Kooiman, K., Emmer, M., Kokhuis, T.J., Bosch, J.G., de Gruiter, H.M., van Royen, M.E., van Cappellen, W.A., Houtsmuller, A.B., van der Steen, A.F. and de Jong, N., 2010, October. Lipid distribution and viscosity of coated microbubbles. In 2010 IEEE International Ultrasonics Symposium (pp. 900-903). IEEE.

[75] van Rooij, T., Luan, Y., Renaud, G., van der Steen, A.F., Versluis, M., de Jong, N. and Kooiman, K., 2015. Non-linear response and viscoelastic properties of lipid-coated microbubbles: DSPC versus DPPC. Ultrasound in medicine & biology, 41(5), pp.1432-1445.

[76] T. Faez, M. Emmer, M. Doctor, J. Sijl, M. Versluis, and N. de Jong, "Subharmonic spectroscopy of ultrasound contrast agents," presented at IEEE Ultrasonics Symposium Proceedings, 2010.

[77] D. H. Kim, M. J. Costello, P. B. Duncan, and D. Needham, "Mechanical properties and microstructure of polycrystalline phospholipid monolayer shells: Novel solid microparticles," Langmuir, vol. 19, pp. 8455-8466, 2003.

[78] Helfield, B.L., Leung, B.Y., Huo, X. and Goertz, D.E., 2014. Scaling of the viscoelastic shell properties of phospholipid encapsulated microbubbles with ultrasound frequency. Ultrasonics, 54(6), pp.1419-1424.

[79] Parrales, M.A., Fernandez, J.M., Perez-Saborid, M., Kopechek, J.A. and Porter, T.M., 2014. Acoustic characterization of monodisperse lipid-coated microbubbles: Relationship between size and shell viscoelastic properties. The Journal of the Acoustical Society of America, 136(3), pp.1077-1084.

[80] Segers, T., Gaud, E., Versluis, M. and Frinking, P., 2018. High-precision acoustic measurements of the nonlinear dilatational elasticity of phospholipid coated monodisperse microbubbles. Soft matter, 14(47), pp.9550-9561.

[81] Paul, S., Katiyar, A., Sarkar, K., Chatterjee, D., Shi, W.T. and Forsberg, F., 2010. Material characterization of the encapsulation of an ultrasound contrast microbubble and its subharmonic response: Strain-softening interfacial elasticity model. The Journal of the Acoustical Society of America, 127(6), pp.3846-3857.

[82] Holt, R.G. and Crum, L.A., 1992. Acoustically forced oscillations of air bubbles in water: Experimental results. The Journal of the Acoustical Society of America, 91(4), pp.1924-1932.

[83] Versluis, M., Goertz, D.E., Palanchon, P., Heitman, I.L., van der Meer, S.M., Dollet, B., de Jong, N. and Lohse, D., 2010. Microbubble shape oscillations excited through ultrasonic parametric driving. Physical review E, 82(2), p.026321.

[84] Klapcsik, K. and Hegedűs, F., 2019. Study of non-spherical bubble oscillations under acoustic irradiation in viscous liquid. Ultrasonics sonochemistry, 54, pp.256-273.

[85] Dollet, B., Van Der Meer, S.M., Garbin, V., De Jong, N., Lohse, D. and Versluis, M., 2008. Nonspherical oscillations of ultrasound contrast agent microbubbles. Ultrasound in medicine & biology, 34(9), pp.1465-1473.

Chapter 11

Bifurcation structure of ultrasonically excited lipid coated microbubbles

11.1 Abstract

An ultrasonically excited micro-bubble (MB) is an example of a highly nonlinear oscillator. In many applications, MBs are encapsulated by a lipid coating to increase their stability. However, the complex behavior of the lipid coating including buckling and rupture significantly influences the dynamics of the MBs and increases the nonlinearity of the system. The dynamics of the lipid coated MBs (LCMBs) are not well understood. In this paper, we investigate the nonlinear behavior of the LCMBs by analyzing their resonance curves and bifurcation diagrams as a function of incident ultrasound pressure. We show that, the lipid coating can enhance the generation of period 2 (P2), period 3 (P3), higher order subharmonics (SH), superharmonics and chaos at very low excitation frequencies (as low as 1 kPa). For LCMBs sonicated by their SH resonance frequency and in line with experimental observations with increasing pressure, P2 oscillations exhibit three stages: generation at very low excitation pressures, disappearance and re-generation. Within non-destructive oscillation regimes and by pressure increase, LCMBs can also exhibit two saddle node (SN) bifurcations resulting in possible sudden enhancement of the scattered pressure. The first SN resembles the pressure dependent resonance phenomenon in uncoated MBs and the second SN resembles the pressure dependent SH resonance. Moreover, for a given frequency, non-destructive P2 and P3 oscillations can coexist. Depending on the initial surface tension of the LCMBs, the nonlinear behavior may also be suppressed for a wide range of excitation pressures[1].

[1]To be submitted as: A.J. Sojahrood, H. Haghi, R. Karshafian and M.C. Kolios, Bifurcation structure of ultrasonically excited lipid coated microbubbles

11.2 Introduction

A bubble excited by an ultrasound pressure wave is an instance of a complex nonlinear dynamical system with resonances, several attractors and their basins, multiple bifurcations and chaotic behavior and not "yet fully describable behavior" due to its infinite complexity [1, 2, 3]. In spite of the complexity, bubbles behavior are used in industrial applications like cleaning [4, 5], food production [6], sonochemistry [7, 8, 9], sono-luminescence [9, 10], mixing [11, 12], therapeutic [13, 14, 15, 16] and diagnostic [17, 18, 19, 20] ultrasound.

One of the first nonlinear phenomena detected with bubbles in sound fields was through historical observations of Esche [21]. Esche reported the generation of a frequency peak at half the excitation frequency (f) in the power spectrum of the received signal [21]. In his investigation of bubbles driven with 3Hz-3.3 MHz, he found the appearance of spectral lines at f/2 and in some cases f/3 for sufficiently high acoustic pressures. In a continuation of Esche's work, Bohn reported spectral lines down to f/4 [22]. In the chaotic (broadband noise) region of the sound emitted by the bubble, Holzfuss & Lauterborn [3] observed a surprisingly low-dimensional attractor with correlation dimension of about 2.5 which is the characteristic for driven damped nonlinear oscillators. Several other experimental studies investigated the nonlinear dynamics of ultrasonically excited bubbles [23, 24, 25, 26, 27, 28, 29]; observing subharmonics, ultraharmonics and chaotic behavior. Numerical investigations have demonstrated the existence of multiple resonance peaks [2, 30, 31], period doubling route to chaos [32, 33, 34], strange attractors and chaotic behavior (e.g. [1, 2, 3, 28, 29]).

Within the last decade several studies have employed the methods of dynamical systems to study the behavior of bubbles. There have been successful attempts in classification of some of the nonlinear dynamics of the bubble oscillator [35,36,37,38]. Hegedűs [39] found numerical evidence for the existence of stable period 1 solutions beyond Blake's threshold [39]. Occurrence of higher order SHs (f/3, f/4, f/5 etc) has been extensively investigated in [38, 40] and for the case of ambient pressures slightly below the vapor pressure [39]. They are experimentally observed and numerically modelled in [41, 42, 43].

Hegedus [44] studied the topology of stable periodic solutions near Blake's threshold. The effect of high dissipation on the nonlinear evolution of the bubble behavior is considered in [45, 46]

and it has been shown that bubble becomes an over-damped oscillator suppressing collapse-like behavior. Moreover, they reported the existence of transient chaos [45]. Using two frequencies was proposed in [47] and extended in [48, 49, 50, 51] to control the chaotic behavior of the bubbles. The effect of multiple frequencies on the resonance behavior and nonlinear dynamics of the system was investigated in [52, 53, 54, 55].

Influence of the pressure on the resonance frequency and bifurcation structure of the bubble which is driven by its resonance frequency is studied in [56]. It is shown that increasing the incident ultrasound pressure decreases the resonance frequency of the bubble; when the bubble is sonicated with its pressure dependent resonance frequency a saddle node bifurcation takes place at the corresponding pressure which enhances the nondestructive back-scattered pressure by the bubbles. Non-spherical bubble oscillations in a viscous liquid is studied in detail in [46] and its been shown that the increased rate of dissipation can significantly extend the stable domains in the acoustic excitation parameter planes. We have studied the ultraharmonic (UH) and super harmonic (SuH) behavior of the bubble oscillator by introducing a more comprehensive method of construction of bifurcation diagrams [57]. Using this method, the bifurcation structure of the bubbles undergoing period doubling and 1/2 order sub-harmonic emissions have been extensively studied [34]. It was found that sonication of bubbles with twice their linear resonance frequency results in period doubling at a lower excitation and leads to non-destructive stable period 2 oscillations, however, sonication with resonance will most likely result in bubble destruction before the appearance of period 2 oscillations. We showed in Chapter 5 ([58]) that SH resonance frequency decreases with increasing pressure; and maximum SH strength is generated when the sonication frequency is 1.5-1.6 times the resonance frequency of the bubble.

In spite of numerous studies on the complex behavior of free (uncoated) bubbles, the dynamics of the coated bubbles have not been thoroughly studied. Bubbles stabilized by a coating in the form of phospho-lipid (e.g. $Definity^{®}$ [59]), or albumin (e.g. Optison [60]) or polymer (Point [61]) are designed to be used in clinical and pre-clinical medical ultrasound applications. Addition of the coating (more specifically in case of phospho-lipid coating) immensely increases the complexity of the bubble oscillator. During bubble oscillations phospho-lipid shell can undergo buckling and rupture [62] resulting in a dynamical system with varying stiffness. The dynamic stiffness of the nonlinear oscillator enhances the generation of nonlinear signatures in the oscillation of the coated

bubbles.

Buckling of the lipid shell has been shown to be one of the possible reasons for enhanced non-linearity [62,63,64,65,66,67,68,69,70,71]. Phospho-lipid shell bubbles exhibit compression only behavior [67] during which bubbles compress more than they expand. There exists a threshold behavior for the onset of oscillations [72]; the bubble starts to oscillate only above a pressure threshold. It has been experimentally observed that phospholipid shell bubbles can generate SH oscillations even at very low acoustic pressures (<30 KPa [64, 66, 73]). Such low threshold values not only contradict the predictions of the theoretical models for coated bubbles [65,74,75], they are even below the threshold values expected for uncoated free bubbles [65, 76]. The low pressure thresholds are despite the increased damping due to the presence of the shell. Through experiments and numerical simulations it has been shown in [64] that the low pressure threshold for SH emissions is due to the compression only behavior of the bubbles due to the buckling of the shell.

In [68] the lipid shell was found to enhance the nonlinear bubble response at acoustic pressures as low as 10 kPa. The increase in acoustic pressure lead to a substantial decrease of the frequency of the maximum response even at very low acoustic pressures [68] resulting in a pronounced skewness of the resonance curve. Such shift in resonance has been postulated in [68] to be the origin of the "thresholding [72]" behavior. Nonlinear resonance behavior of the lipid shell bubbles was also observed in higher frequencies (5-15 MHz) in [77]. It is shown in [66] that the shell elasticity of the phospholipid shell varies with bubble oscillation amplitude and the magnitude of "compression only" behavior depends on the initial phospholipid concentration on the bubble surface [66]. Prosperetti [65] through theoretical analysis of the Marmottant model [62] attributed the lower SH threshold of the lipid bubbles to the variation in the mechanical properties of the shell in the neighborhood of a certain bubble radius (e.g. the occurrence of buckling).

In addition to the widely studied 1/2 order SHs, we have experimentally detected higher order SHs (1/3,1/4 and 1/5) in the oscillations of lipid coated bubbles at very low acoustic pressures and high frequencies (e.g. 25 MHz) [41, 42, 43, 59]. Through analyzing bifurcation diagrams we concluded that buckling or rupture of the shell is responsible for the enhanced nonlinear behavior [59]. The closer the initial surface tension of the water to the two limit values of the buckling and rupture of the shell, the lower the pressure threshold for nonlinear oscillations.

Variation of the mechanical properties of the shell can also manifest itself in expansion dominated behavior in liposome-loaded lipid shells [69]. Expansion dominated oscillations occur for bubbles with an initial surface tension near the water [69, 77]. Upon expansion, the stiffness of the coating weakens and the bubble expands more than it compresses. Expansion-dominated behavior was used to explain the enhanced non-linearity at higher frequencies (25 MHz) [78]. The Marmottant model effectively captures the behavior of the bubble including expansion-dominated behavior [43, 59, 77], compression only behavior [67], thresholding [72] and enhanced non-linear oscillations at low excitation pressures [41, 43, 63, 64, 66, 68].

In this paper we perform a comprehensive analysis of the bifurcation structure of ultrasonically excited lipid coated microbubbles. Knowledge of the effect of the shell behavior on the nonlinear response of the bubble is essential to optimize the bubble response to an ultrasonic field. Moreover, the comprehensive knowledge that can be obtained through analyzing the bifurcation diagrams of the lipid coated bubbles may help in revealing potential parameter spaces in which bubble behavior can be beneficial to various applications. Last but not least, revealing the intricate behavior of the system and enhanced nonlinear effects is of potential interest in the field of nonlinear and chaotic dynamical systems.

11.3 Methods

11.3.1 Marmottant Model

The dynamics of the coated bubbles undergoing buckling and rupture can be effectively modeled using the Marmottant equation [59]:

$$\rho\left(R\ddot{R}+\frac{3}{2}\dot{R}^2\right)= \left[P_0+\frac{2\sigma(R_0)}{R_0}\right](\frac{R}{R_0})^{-3k}\left(1-\frac{3k}{c}\dot{R}\right)-P_0-\frac{2\sigma(R)}{R}-\frac{4\mu\dot{R}}{R^2}-\frac{4k_s\dot{R}(R)}{R^2}-P_a(t) \tag{11.1}$$

In this equation, R is the bubble radius at time t, R_0 is the initial bubble radius, $\dot{R}$ is the wall velocity of the bubble, $\ddot{R}$ is the wall acceleration, ρ is the liquid density (998 $\frac{kg}{m^3}$), c is the sound speed (1481 m/s), P_0 is the atmospheric pressure, $\sigma(R)$ is the surface tension at radius R, μ is the liquid viscosity (0.001 Pa.s), k_s is the viscosity of the coating, and $P_a(t)$ is the acoustic driving

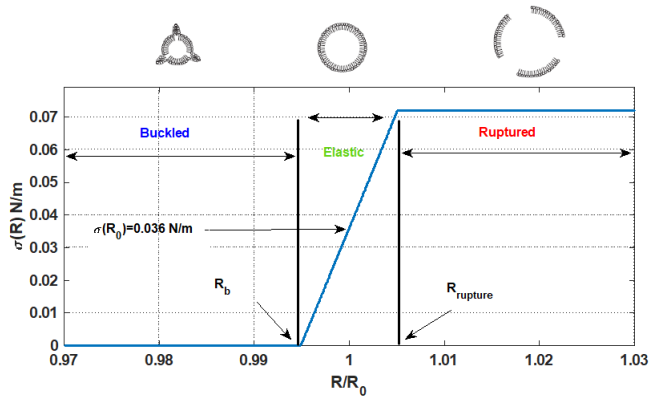

Figure 11.1: Schematic of the effective surface tension on a coated bubble with $R_0 = 2\mu m$, $\chi = 3.5N/m$ & $\sigma_0 = 0.036N/m$. The coating buckles when $R \leq R_b$ making the surface tension zero. The coating behaves elastically for $R_b \leq R \leq R_{breakup}$. When $R \geq R_{break-up}$, the coating ruptures and exposes the gas to water, thus effective surface tension becomes equal to σ_{water} (0.072 N/m).

force $P_a(t) = P_a sin(2\pi ft)$ where P_a and f are the amplitude and frequency of the applied acoustic pressure. The values in the parentheses are for pure water at 293^0K. In this paper the gas inside the bubble is C3F8 and water is the host media.

The surface tension $\sigma(R)$ is a function of radius and is given by:

$$\sigma(R) = \begin{cases} 0 & if \quad R \leq R_(b) \\ \chi(\frac{R^2}{R_b^2} - 1) & if \quad R_b \leq R \leq R_{breakup} \\ \sigma_{water} & if \quad Ruptured \quad R \geq R_r \end{cases} \tag{11.2}$$

where σ_{water} is the water surface tension and χ is the shell elasticity. R_r and R_b are the rupture and the buckling radius respectively where $R_b = \frac{R_0}{\sqrt{1+\frac{R_0}{\chi}}}$ and $R_r = R_b\sqrt{1 + \frac{\sigma_{brakup}}{\chi}}$. In this work similar to [78], $R_{breakup} = R_r$.

11.3.2 Keller-Miksis model

Dynamics of the uncoated bubbles were also visualized alongside the lipid coated bubbles to highlight the effect of the lipid shell on the bubble dynamics. To model the uncoated bubble dynamics the Keller-Miksis model [79] is used:

$$\rho[(1 - \frac{\dot{R}}{c})R\ddot{R} + \frac{3}{2}\dot{R}(1 - \frac{R}{3c})] = (1 + \frac{\dot{R}}{c})(G) + \frac{R}{c}\frac{d}{dt}(G) \tag{11.3}$$

where $G = \left(P_0 + \frac{2\sigma_{water}}{R_0}\right)(\frac{R}{R_0})^{-3k} - \frac{4\mu_L \dot{R}}{R} - \frac{2\sigma}{R} - P_0 - P_A sin(2\pi f t)$.

In both models we have neglected the effects of thermal damping. This is to decrease the problem complexity and to better highlight only the shell effects. Moreover, We have shown in Chapter 7 ([88]) that in case of C3F8 gas cores thermal damping is significantly smaller compared to air. Moreover, in case of coated bubbles with C3F8 gas cores, thermal effects maybe be fully neglected. However, in case of the uncoated bubble effects of thermal damping at higher pressures should be considered using full ODEs [89] that account for the thermal damping. We have shown in Chapter 7 [88] that the generally used linear assumptions [90] for thermal effects may lead to inaccuracies at pressures as low as $\approx 40kPa$. However, since the main focus of the paper is to highlight the coating effects and because the thermal effects of the C3F8 are weak [88], we have neglected the thermal effects in this paper.

11.3.3 Investigation tools

Bifurcation diagrams are valuable tools to analyze the dynamics of nonlinear systems since qualitative and quantitative changes of the dynamics of the system can be investigated effectively over a wide range of control parameters. In this paper, we employ a more comprehensive bifurcation analysis method introduced in [73, 74].

2.3.a) Conventional bifurcation analysis (Poincaré cross section at each driving period)

When dealing with systems responding to a driving force, to generate the points in the bifurcation diagrams vs. the control parameter, one option is to sample the R(t) curves using a specific point in each driving period. The approach can be summarized in:

$$P \equiv (R(\Theta))\{(R(t), \dot{R}(t)) : \Theta = \frac{n}{f}\} \quad where \quad n = 100, 101...150 \tag{11.4}$$

where P denotes the points in the bifurcation diagram, R and $\dot{R}$ are the time dependent radius and wall velocity of the bubble at a given set of control parameters of (R_0, P_0, P_A, c, k, μ, σ, f) and Θ is given by $\frac{n}{f}$. Points on the bifurcation diagram are constructed by plotting the solution of $R(t)$ at time points that are multiples of the driving acoustic period. In this work, the results are plotted for $n = 160 - 200$ to ensure a steady state solution has been reached.

2.3.b) Method of peaks As a more general method, bifurcation points can be constructed by

setting one of the phase space coordinates to zero:

$$Q \equiv max(R)\{(R, \dot{R}) : \dot{R} = 0\} \tag{11.5}$$

In this method, the steady state solution of the radial oscillations for each control parameter is considered. The maxima of the radial peaks ($\dot{R} = 0$) are identified (determined within 160-200 cycles of the stable oscillations) and are plotted versus the given control parameter in the bifurcation diagrams. The bifurcation diagrams of the normalized bubble oscillations ($\frac{R}{R_0}$) are calculated using both methods a) and b). When the two results are plotted alongside each other, it is easier to uncover more important details about the SuH and UH oscillations, as well as the SH and chaotic oscillations.

11.4 Results

11.4.1 Resonance curves

Compared to uncoated bubbles and coated bubbles with pure viscoelsatic behavior (e.g. Keller-Miksis model [79], Hoff model [80], Morgan model [81]), the resonance behavior of lipid coated bubbles are more complex. This is due to the buckling and rupture of the shell and dynamic variation of the effective surface tension of the bubble. As an example [68, 77] have shown numerically and experimentally that a pressure increase leads to a significant displacement of the main resonance (frequency of maximum response) of the bubble leading to a significant shift of the resonance curve.

Fig. 11.2 compares the resonance curves of a $2\mu m$ bubble at excitation pressure amplitudes 1, 6, 11, 16 & 21 kPa. In order to better understand the effect of the initial surface tension we have presented the case of the uncoated bubble in Fig. 11.2a & the coated bubbles with σ_0 of 0, 0.01, 0.036, 0.062 & 0.072 N/m in Figs. 11.2b-f respectively. The parameters for the bubble model are $\chi = 3.5N/m$ & $k_s = 4 * 10^{-9}kg/s$ [82, 83].

Upon a first glance at Fig. 11.2, the high sensitivity of the coated bubble to σ_0 is evident. While the resonance frequency of the uncoated bubble decreases slightly from $\approx 1.77MHz$ to $\approx 1.69MHz$,

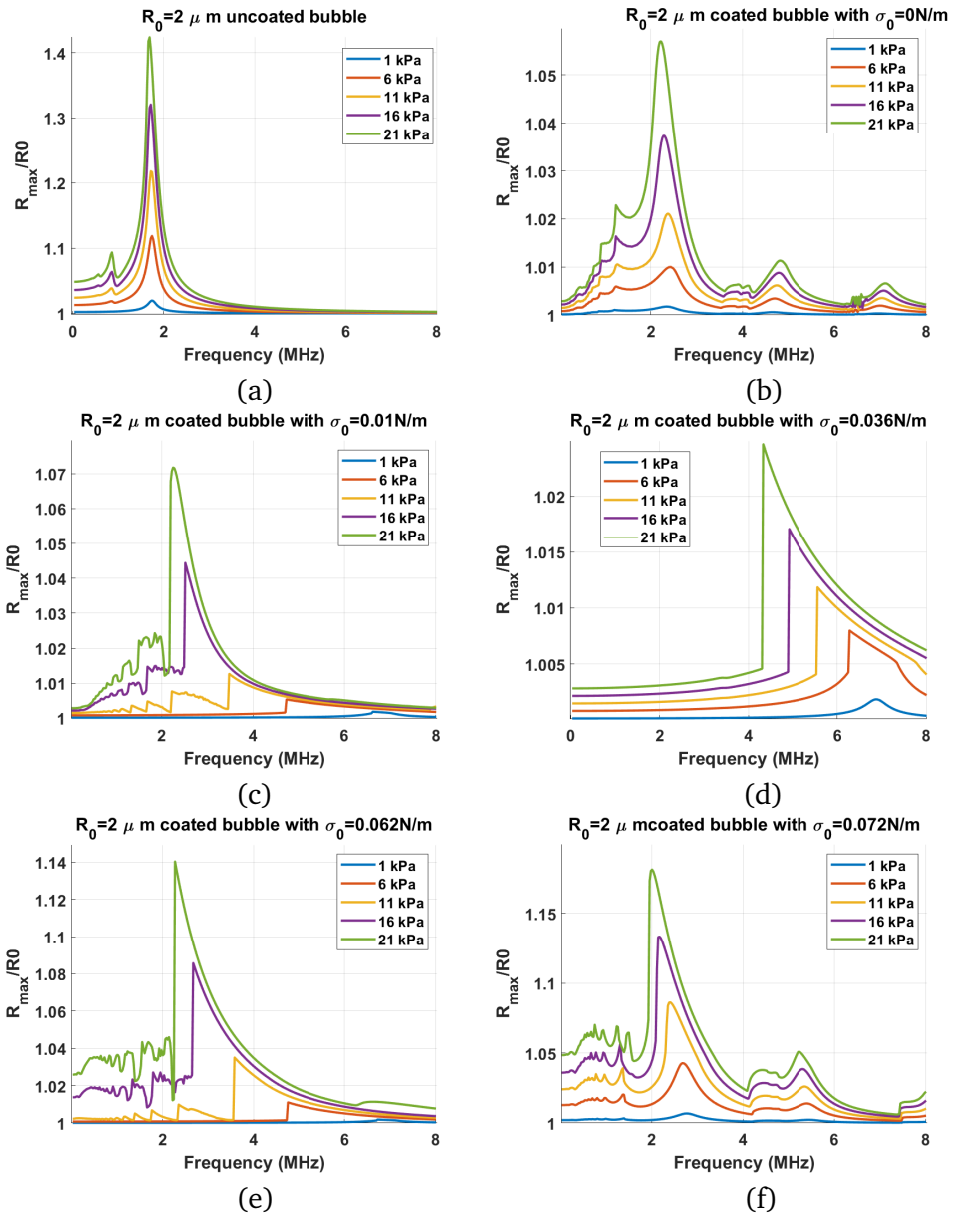

Figure 11.2: Resonance curves of a bubble with $R_0 = 2\mu m$ at different pressures for: a) uncoated bubble, and the coated bubble with b)$\sigma_0 = 0N/m$, c)$\sigma_0 = 0.01N/m$, d)$\sigma_0 = 0.036N/m$, e) $\sigma_0 = 0.062N/m$ & f) $\sigma_0 = 0.072N/m$.

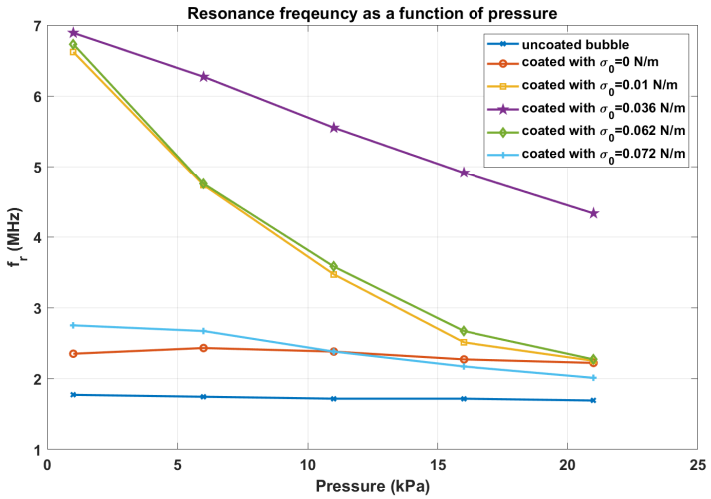

Figure 11.3: Resonance frequency as a function of pressure for the bubbles in Fig. 1.

the resonance frequency of the lipid coated bubble changes considerably over this relatively small pressure range (1 kPa-21 kPa). The resonance frequency (f_r) change as a function of P_A significantly depends on the σ_0. The bubbles with $\sigma_0 = 0.01$ & $0.062N/m$ display the largest change in f_r (fundamental frequency of the maximum response) which manifests itself in a skewness [68] in the resonance curve (Fig. 11.2c & Fig. 11.2e). Meanwhile, the coated bubbles with $\sigma_0 = 0N/m$ (at buckling stage) & $\sigma_0 = 0.072N/m$ (at rupture state) display the least change in the resonance frequency; however, in both cases 1/2 and 1/3 subharmonic (SH) resonances are generated at the lowest pressure thresholds. The reason for large change in the f_r of the bubble with $\sigma_0 = 0.01$ & $0.062N/m$ is that a very small change in pressure changes the state of the coating and changes the coating in a manner that leads to buckle or rupture.

The resonance frequency (f_r) as function of pressure is shown in Fig. 11.3. At 1 kPa, the bubble with $\sigma_0 = 0.035N/m$ has the highest resonance frequency. A pressure increase to 11 kPa results in a large change in the f_r of the bubbles with $\sigma_0 = 0.01N/m$ (6.62 to 3.47 MHz), $\sigma_0 = 0.062N/m$ (from 6.73 to 3.58 MHz) & for $\sigma_0 = 0.036N/m$ (6.89 MHz to 5.55 MHz). The uncoated bubble, and the bubbles with $\sigma_0 = 0$ & $\sigma_0 = 0.072N/m$ display very small changes in the f_r as pressure increases from 1 kPa to 5 kPa. This can be explained by the values of the buckling and rupture (break-up) radii. Fig. 11.4 displays the buckling and the break-up radii as a function of σ_0. The bubble with $\sigma_0 = 0N/m$ is initially at the buckled state, and has the largest break up radius of

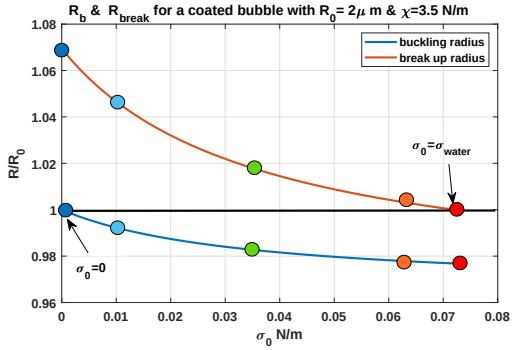

Figure 11.4: R_b (blue curve) and $R_{breakup}$ (red curve) as a function of σ_0. The circles mark the R_b & $R_{break-up}$ with ones in blue corresponding to $\sigma_0 = 0N/m$, light blue corresponding to $\sigma_0 = 0.01N/m$, green corresponding to $\sigma_0 = 0.036N/m$, orange corressponding to $\sigma_0 = 0.062N/m$ & red circles corresponding to $\sigma_0 = 0.072N/m$.

$\approx 1.07R_0$. The bubble with $\sigma_0 = 0.072N/m$ is initially at the ruptured state and has the lowest buckling radius of $\approx 0.97R_0$. Thus, for these two bubbles higher acoustic pressures are required to change the state of the coating and consequently the rates of change of their main resonance (f_r) with pressure are the smallest. The bubble with $\sigma_0 = 0.01N/m$ buckles at $R_b = 0.99R_0$ and the bubble with $\sigma_0 = 0.062N/m$ ruptures at $\approx 1.003R_0$, thus a very small pressure excitation is able to change the state of the coating to buckled or ruptured respectively. Hence, these two bubbles display the highest rates of change of f_r with increasing pressure.

Similar to our previous work in [34, 37, 38, 48, 56], in this work we will attempt to classify the nonlinear dynamics of the lipid bubbles as a function of pressure when they are sonicated with fractions or multiples of their f_r. However, the initial sharp decrease of the resonance frequency with pressure will make the classification difficult. Moreover, characterization of the coating parameters of the bubbles in experiments are generally through attenuation measurements of the bubble solution when there is an excitation pressure amplitude above 1kPa is applied. As an instance negative peak pressure of 25 kPa, 12.5 kPa, 30 kPa, 10 kPa & 5 kPa were applied respectively in [84], [85], [86], [82] & [83] and Peak to peak pressures of 33 kPa were applied in [86]. Very low pressures can not be applied experimentally due to the signal to noise constraints of the measurements systems.

To simplify the classification method and to have a better comparison with experimental data published we have calculated the resonance frequency at $P_a = 10kPa$ and used it for further study. Thus, in this paper for coated bubbles f_r refers to the resonance frequency at $P_a = 10kPa$.

11.4.2 Radial oscillations as a function of time and the corresponding changes in the $\sigma(R)$

In Fig. 11.2, we observed the generation of SuH as well as SH resonances at very low pressures in case of the coated bubbles. In this section, the enhanced nonlinear oscillations and their relationship with the bubble surface tension are briefly investigated to have a better insight on the mechanisms of enhanced nonlinearity. Fig. 11.5 shows the radial oscillations of the uncoated bubble as a function of 10 acoustic driving periods (100-110). The left column shows the radial oscillations when $P_a = 1kPa$ and $f = 0.3f_r$, $2f_r$ and $3f_r$ in Figs. 11.5a, 11.5c and 11.5e respectively. the right column shows the radial oscillations when $P_a = 60kPa$ and $f = 0.3f_r$, $2f_r$ and $3f_r$ in Figs. 11.5b, 11.5d and 11.5f respectively. The red circles locate the amplitude of the radial oscillations at each period. This is the Poincaré cross section at each driving period which is used to generate the bifurcation diagram using the method introduced in 2.3.a. The bubble oscillations in Fig. 11.5 are period 1 (P1) and the red circles have the same value at each driving periods. This indicates the absence of any SHs. Only 3rd order SuHs are seen (P1 oscillations with 3 maxima) when pressure is 60 kPa in Fig. 11.5b.

Fig. 11.6, depicts the case of the coated bubble with $R_0 = 2\mu m$ when $f = 0.3f_r$ and $P_a = 1kPa$. Top row is for $\sigma_0 = 0N/m$ with radial oscillations in Fig. 11.6a and the corresponding $\sigma(R)$ in Fig. 11.6b. The oscillations are P1 (red circle only represents one value), however, the radial oscillations have two maxima, indicating a 2nd order SuH regime of oscillations. The corresponding $\sigma(R)$ drops to zero and stay zero in the buckled state until the bubble expands above the buckling radius and again drops to zero when the bubble buckles upon compression. The bubble with $\sigma(R) = 0.072N/m$ (Fig. 11.6c) exhibits P1 oscillation with 3 maxima and thus a 3rd order SuH regime. When the bubble expands, $\sigma(R)$ can not grow beyond the surface tension of water ($0.072N/m$) thus the $\sigma(R)$ curve becomes flat(Fig. 11.6d). Upon contraction $\sigma(R)$ decreases and upon expansion it grows until the coating breaks and surface tension becomes equal to $0.072N/m$. In both cases, the buckling and rupture of the shell results in the enhanced nonlinearity (in these cases enhanced SuHs). For the bubble with $\sigma_0 = 0N/m$ there is compression dominated behavior and for the bubble with $\sigma_0 = 0.072N/m$ expansion dominated behavior is observed.

Fig. 11.7, depicts the case of the coated bubble with $R_0 = 2\mu m$ when $f = 2f_r$ and $P_a = 1kPa$. For

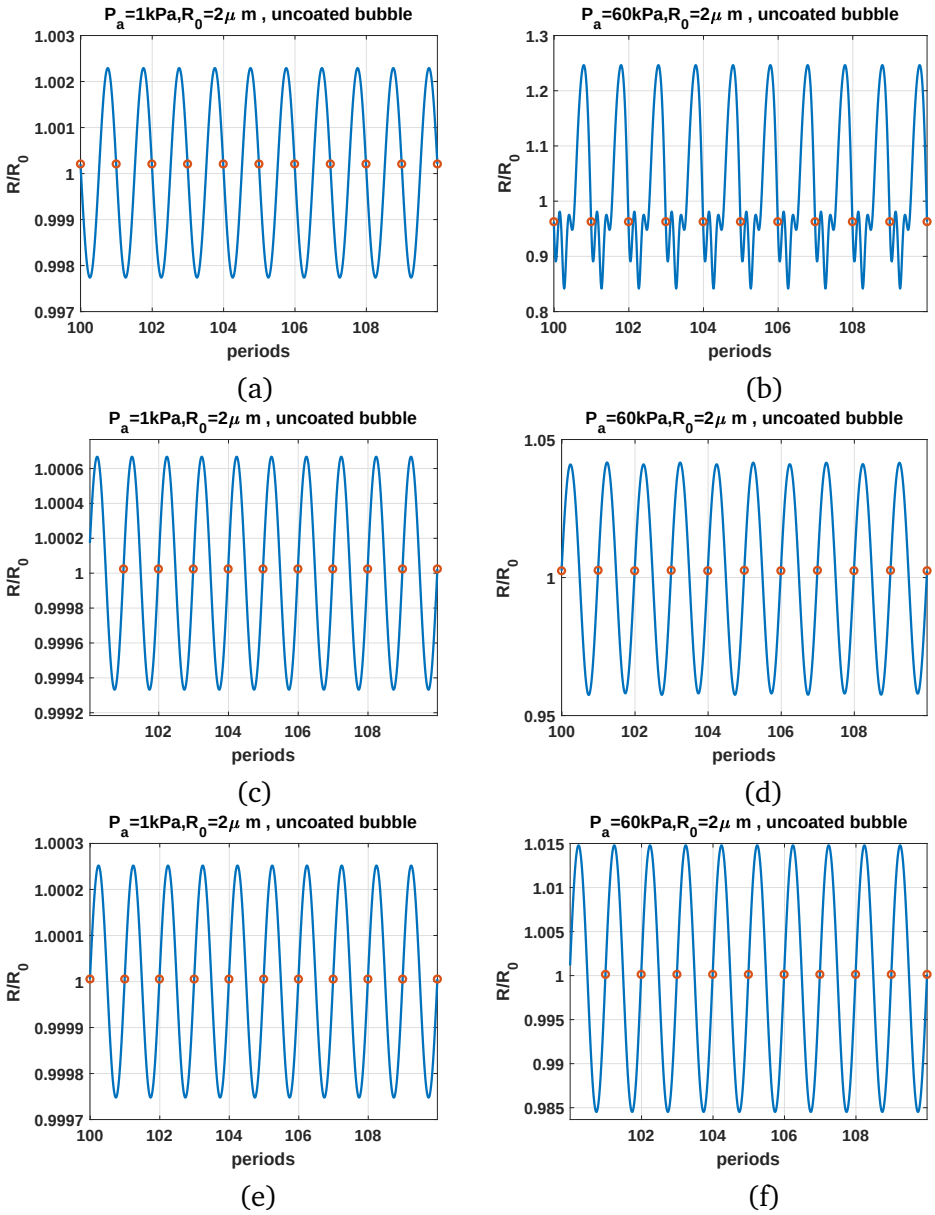

Figure 11.5: R/R_0 as function of the driving periods for a C3F8 uncoated bubble with $R_0 = 2\mu m$ when: a)$f = 0.3f_r$ & $P_a = 1kPa$, b)$f = 0.3f_r$ & $P_a = 60kPa$, c)$f = 2f_r$ & $P_a = 1kPa$, d)$f = 2f_r$ & $P_a = 60kPa$, e)$f = 3f_r$ & $P_a = 1kPa$ & f)$f = 3f_r$ & $P_a = 60kPa$. (Red circles correspond to the location of R(t) at each period)

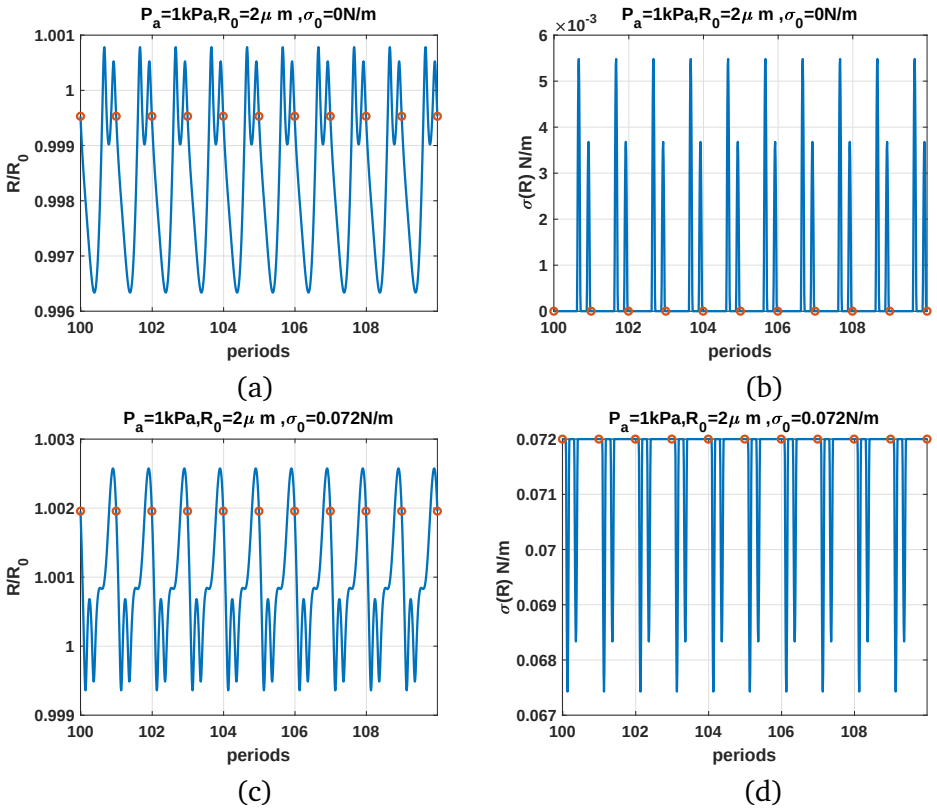

Figure 11.6: R/R_0 (left) & $\sigma(R)$ (right) as function of the driving periods for a C3F8 coated bubble with $R_0 = 2\mu m$ when $f = 0.3f_r$ & $P_a = 1kPa$ for: $a\&b$-$\sigma_0 = 0N/m$, $c\&d$-$\sigma_0 = 0.072N/m$. (Red circles correspond to the location of R(t) at each period)

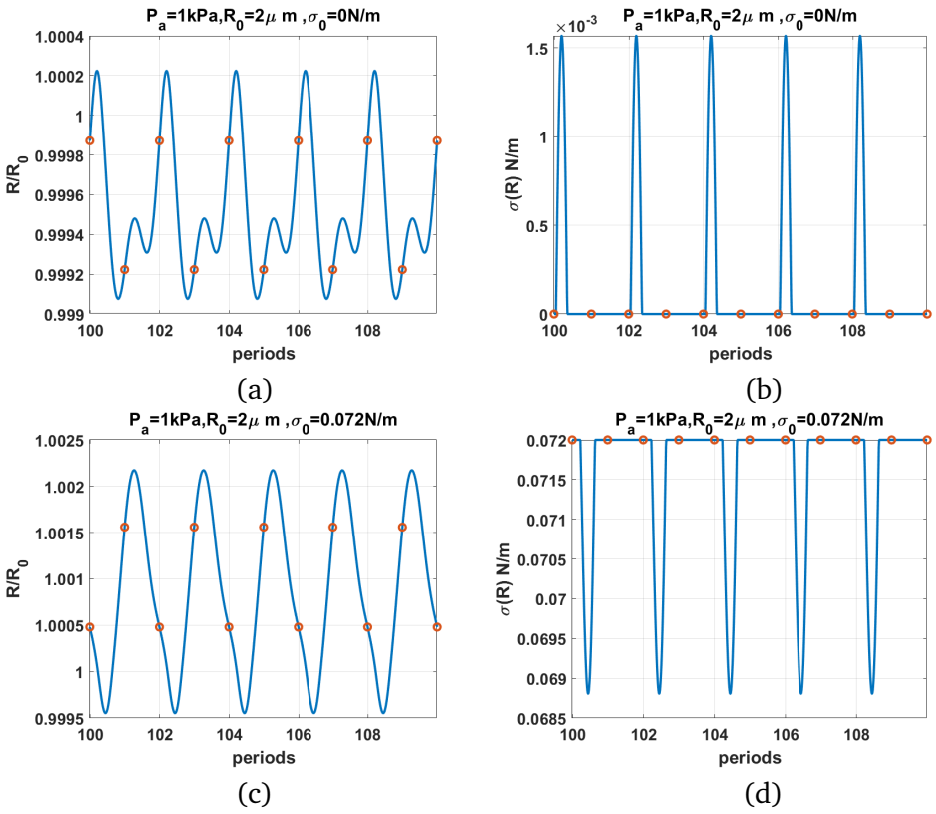

Figure 11.7: R/R_0 (left) & $\sigma(R)$ (right) as function of the driving periods for a C3F8 coated bubble with $R_0 = 2\mu m$ when $f = 2f_r$ & $P_a = 1kPa$ for: $a\&b$-$\sigma_0 = 0N/m$, $c\&d$-$\sigma_0 = 0.072N/m$. (Red circles correspond to the location of R(t) at each period)

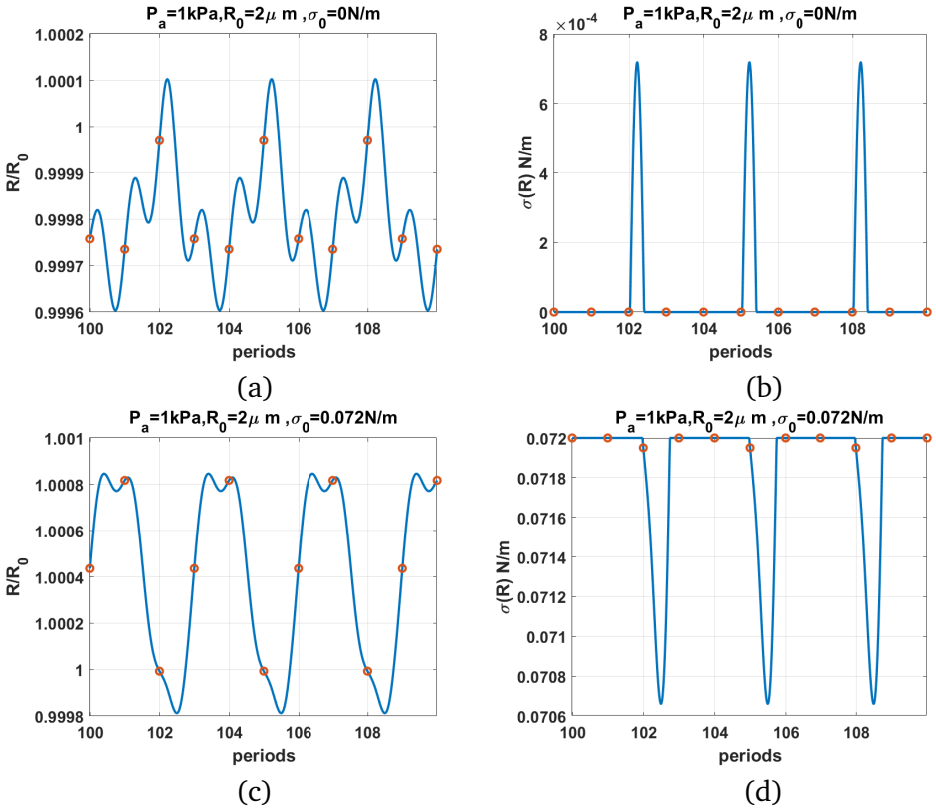

Figure 11.8: R/R_0 (left) & $\sigma(R)$ (right) as function of the driving periods for a C3F8 coated bubble with $R_0 = 2\mu m$ when $f = 3f_r$ & $P_a = 1kPa$ for: $a\&b$-$\sigma_0 = 0N/m$, $c\&d$-$\sigma_0 = 0.072N/m$. (Red circles correspond to the location of R(t) at each period)

$\sigma_0 = 0N/m$ (Fig. 11.7a) compression dominated radial oscillations are P2 (red circle corresponds to two values). The corresponding $\sigma(R)$ (Fig. 11.7b) remains equal to zero for a time duration of more than two periods followed by a short spike when the bubble expands above the buckling radius. The surface tension exhibits 5 spikes for the duration of 10 cycles. The bubble with $\sigma(R) = 0.072N/m$ (Fig. 11.7c) exhibits expansion dominated P2 oscillation with 1 maximum. The $\sigma(R)$ curve (Fig. 11.7d) exhibits the same behavior of Fig. 11.7b with an inverted shape. The surface tension displays 5 inverted spikes within 10 cycles.

Fig. 11.8, depicts the case of the coated bubble with $R_0 = 2\mu m$ when $f = 3f_r$ and $P_a = 1kPa$. For $\sigma_0 = 0N/m$ (Fig. 11.8a) compression dominated radial oscillations are P3 (red circle corresponds to three values) with 3 maxima. The corresponding $\sigma(R)$ (Fig. 11.8b) remains zero for a time duration of more than three periods followed by a short spike when the bubble expands above buckling radius. The surface tension exhibits 3 spikes for the duration of 10 cycles. The bubble with $\sigma(R) = 0.072N/m$ (Fig. 11.8c) exhibits expansion dominated P3 oscillation with 2 maxima.

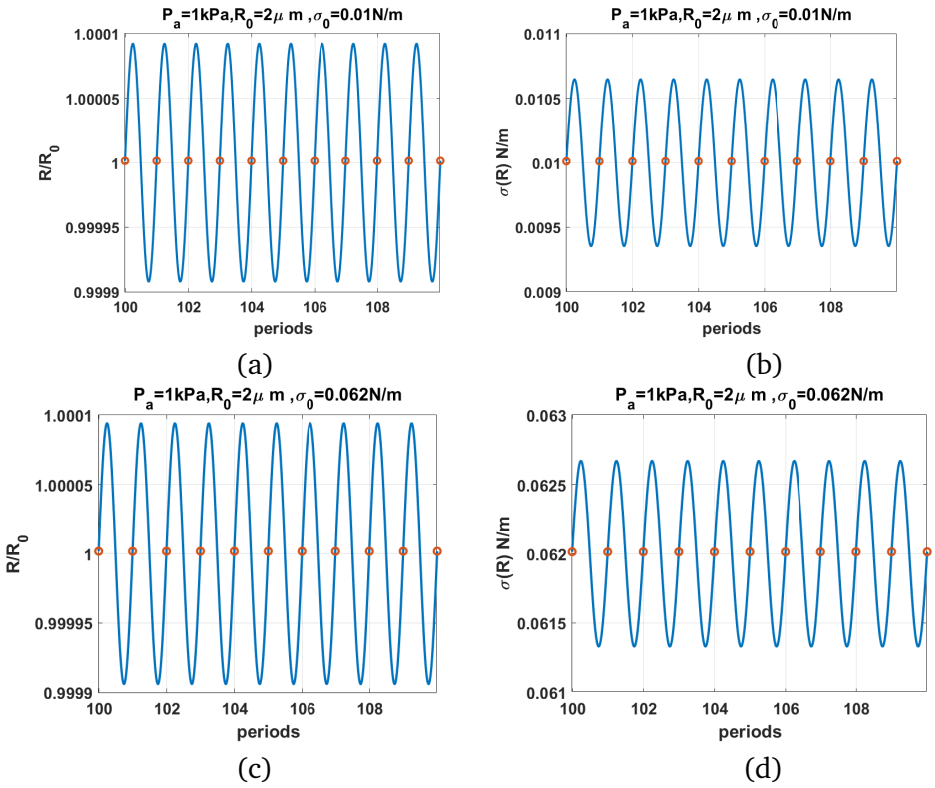

Figure 11.9: R/R_0 (left) & $\sigma(R)$ (right) as function of the driving periods for a C3F8 coated bubble with $R_0 = 2\mu m$ when $f = 3f_r$ & $P_a = 1kPa$ for: $a\&b$-$\sigma_0 = 0.01N/m$, $c\&d$-$\sigma_0 = 0.062N/m$. (Red circles correspond to the location of R(t) at each period)

The $\sigma(R)$ curve (Fig. 11.8d) exhibits the same behavior of Fig. 11.8b with an inverted shape. The surface tension displays 3 inverted spikes within 10 cycles.

Fig. 11.9 shows the radial oscillations and the surface tension of the coated bubble with $R_0 = 2\mu m$ at $P_a = 1kPa$ as a function of periods for bubbles with $\sigma_0 = 0.01N/m$ (Figs. 11.9a-b) and $\sigma_0 = 0.062N/m$ (Figs. 11.9c-d). Both cases display a P1 oscillations with symmetric amplitude around the initial bubble radius. The $\sigma(R)$ curves display symmetric oscillations and absence of sharp spikes that are seen in Figs. 11.6-8. When P_a increases the coating can buckle or rupture. Fig. 11.10 shows the the radial oscillations and surface tension of the coated bubble with $R_0 = 2\mu m$ at $P_a = 60kPa$ as a function of periods for bubbles with $\sigma_0 = 0.01N/m$ (Figs. 10a-b) and $\sigma_0 = 0.062N/m$ (Figs. 11.10c-d). Both cases display P3 oscillations and 3 spikes in the $\sigma(R)$ within 10 periods.

Comparison between Figs. 11.5-10 shows that the sharp variations of the $\sigma(R)$ in the neighborhood of the buckling or rupture radii enhances the nonlinear behavior. The coated bubbles initially at

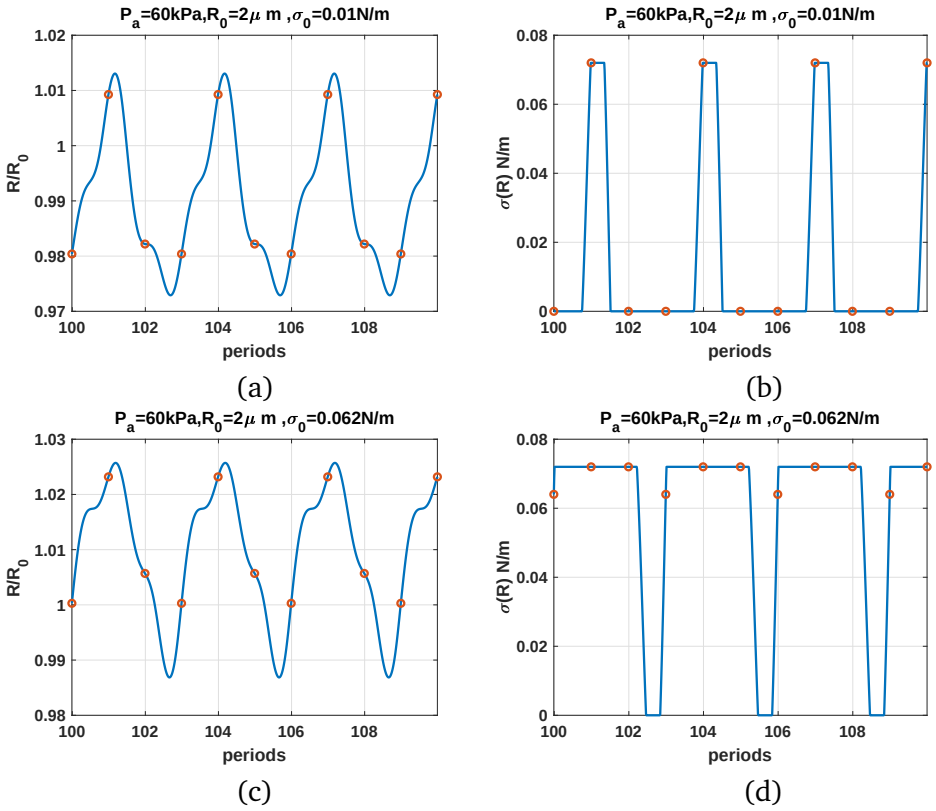

Figure 11.10: R/R_0 (left) & $\sigma(R)$ (right) as function of the driving periods for a C3F8 coated bubble with $R_0 = 2\mu m$ when $f = 2f_r$ & $P_a = 60kPa$ for: $a\&b$-$\sigma_0 = 0.01N/m$, $c\&d$-$\sigma_0 = 0.062N/m$. (Red circles correspond to the location of R(t) at each period)

buckled or ruptured state display this behavior at a pressure as low as 1 kPa. The coated bubbles with $\sigma_0 = 0.01N/m$ and $\sigma_0 = 0.062N/m$ need slightly higher pressures for the enhanced nonlinear oscillations. The uncoated did not show any enhanced nonlinearity.

11.4.3 Bifurcation structure of the uncoated bubble

In this section, we briefly highlight the main nonlinear regimes of the dynamics of the uncoated bubble as a function of pressure at different frequencies. This data will be useful when analyzing the behavior of the lipid coated bubble by highlighting the shell effects on the coated bubble dynamics. Figure 11.11a shows the bifurcation structure of the uncoated bubble with $R_0 = 2\mu m$ sonicated with $f = 0.3f_r$. Pressure increase above $\approx 50kPa$ leads to the generation of 3 maxima in the bubble oscillations (3 blue lines) for a period 1 (P1) oscillation regime. Thus 3rd SuH regime [57] is generated. Oscillations undergo period doubling (PD) at about 124 kPa. The blue curve with 3 maxima undergoes 3 PDs concomitant with the 1 PD in the red curve; thus oscillations become

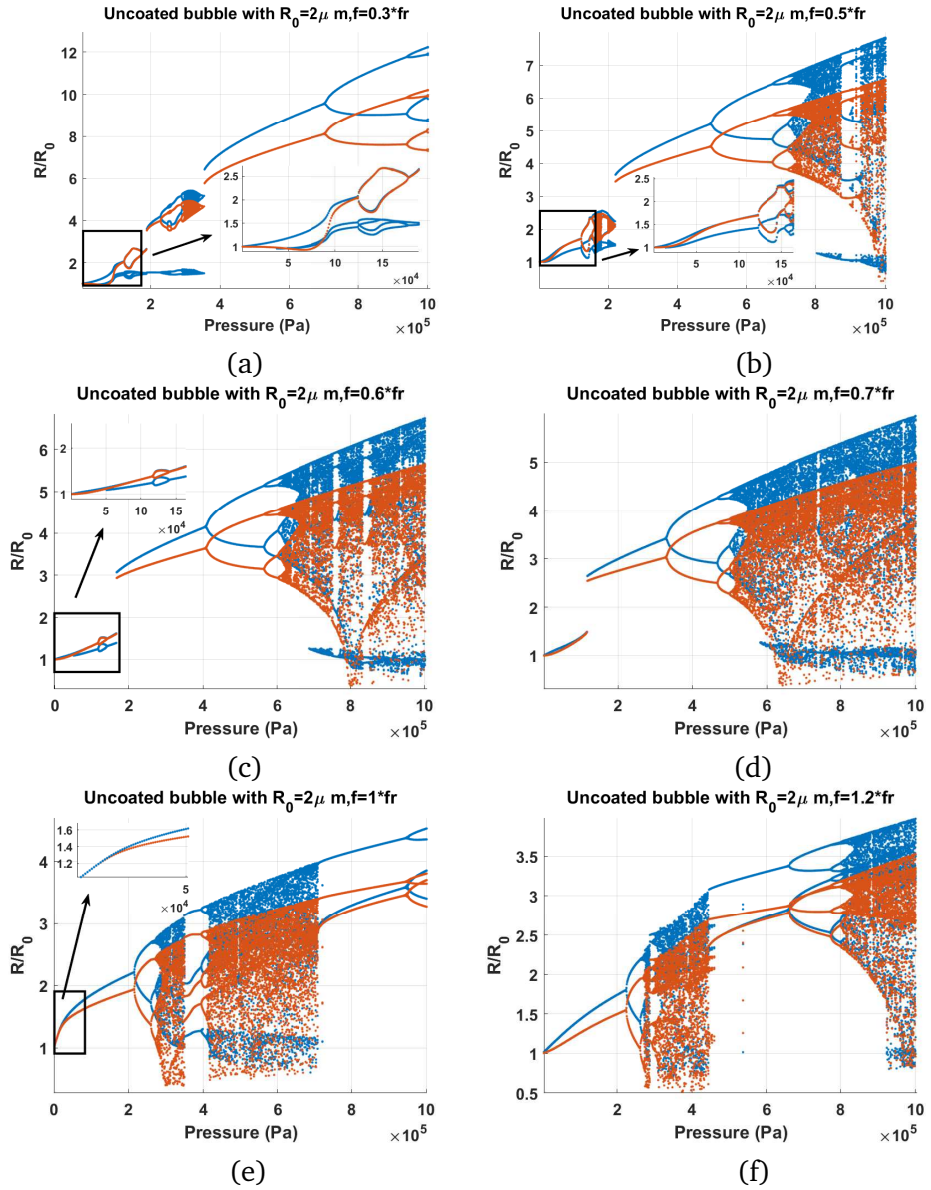

Figure 11.11: Bifurcation structure of the R/R_0 of the C3F8 uncoated bubble with $R_0 = 2\mu m$ as a function of pressure when: a)$f = 0.3f_r$, b)$f = 0.5f_r$, c)$f = 0.6f_r$, d)$f = 0.7f_r$, e)$f = f_r$ & f)$f = 1.2f_r$.

P2 with 6 maxima and 7/2 UH oscillations are generated ($124kPa < P_a < 178kPa$). The 3rd SuH region and the 7/2 UH region are highlighted as an inset in Fig. 11.11a. Further pressure increase leads to SN bifurcation to 2nd order SuH oscillations of higher amplitude, followed by 5/2 UHs, and a small chaotic window. Finally a giant P1 resonance emerges out of the chaotic window undergoing further PDs at higher pressures.

When $f = 0.5f_r$ (Fig. 11.11b), as pressure increases above 14 kPa, 2 maxima are generated in the P1 oscillation regime (2nd SuH). Further pressure increase results in a PD in both the blue and red graphs leading to a P2 oscillation with 4 maxima (5/2 UH oscillations). This region is highlighted as an inset in Fig. 11.11b. Chaos occurs in a small window above 160 kPa with a tiny window of periodic (P3 with 5 maxima) behavior within. Afterwards, a giant P1 resonance emerges out of the chaotic window. The P1 oscillations undergo a multiple cascades of PDs to chaos.

When $f = 0.6f_r$ (Fig. 11.11c) 5/2 UH oscillations (P2 with 4 maxima) are developed and then transition to P1 oscillations through a bubble in the pressure window of 116-150 kPa (highlighted in an inset). P1 oscillations then undergo a saddle node bifurcation to a P1 oscillation with higher amplitude at $P_a \approx 166kPa$. This is due to the pressure dependent resonance behavior that has been discussed in detail in [56]. Further pressure increase leads to a PD to P2 oscillations (at 406 kPa) which is followed by a cascade of PDs to chaos at $\approx 614kPa$.

The dynamics of the bubble sonicated with $f = 0.7f_r$ (Fig. 11.11d) is similar to the case of $f = 0.6f_r$; however, 5/2 UH oscillations are not generated and SN bifurcation occurs at a slightly lower pressure (117 kPa). At this pressure the red curve meets the blue curve. This is the pressure dependent resonance and the wall velocity becomes in phase with the driving signal. This is discussed in detail with numerical and experimental observations in [85]. PD occurs at 326 kPa which is lower than the PD threshold in Fig. 11.11c. Chaos settles through a cascade of PDs at 504 kPa.

When $f = f_r$ (Fig. 11.11e) oscillations are P1 and the blue line and the red line have the same value (highlighted in the inset) which indicates that the wall velocity is in phase with the acoustic driving force due to the resonance (page 290 in [91]). The two curves start diverging as soon as pressure increases above 18 kPa and at 215 kPa the oscillations undergo PD. Oscillations become chaotic above 400 kPa with a small window of periodic behavior (P3 with 3 maxima).

When $f = 1.2f_r$ (Fig. 11.11f), we witness the similar behavior as the case of $f = f_r$; however, P2

oscillations are developed for $R_{max}/R_0 < 2$, thus P2 oscillations are more likely stable [92].

When $f = 1.5f_r$ (Fig. 11.12a), P1 oscillations undergo PD with 2 maxima at 236 kPa. P2 oscillations undergo a SN bifurcation to P2 oscillations of higher amplitude at 347 kPa. Right at the SN point the lower branch of the red curve meets the lower branch of the blue curve indicating wall velocity is in phase with the driving acoustic pressure once very two acoustic cycles. The SN bifurcation is coincident with the pressure dependent SH resonance (Pdf_{sh}) [58]. This results in the over-saturation and enhancement of the SH signal from the pressure scattered by bubbles [58]. P2 oscillations undergo successive PDs to chaos at $\approx 494kPa$.

When $f = 1.8f_r$ (Fig. 11.12b) P1 oscillations undergo a SN bifycation to P2 oscillations of higher amplitude at 155 kPa. The P2 oscillations amplitude $\frac{R_{max}}{R_0} < 2$ thus bubbles may have higher stability compared to Fig. 11.12a. Further pressure increase leads to chaos through successive PDs. At 931 kPa a giant P3 resonance emerges out of the chaotic window.

When $f = 2f_r$ (linear SH resonance frequency), PD occurs at the lowest pressure threshold of 77 kPa (highlighted in an inset) [34]. P2 oscillations undergo successive PDs and chaos appears at 400 kPa and extends to $\approx 600kPa$ where giant P3 resonance emerges out of the chaotic window. Oscillations later become chaotic again through successive PDs.

When $f = 2.2f_r$ (Fig. 11.12d), PD occurs at 189 kPa which is higher than the PD threshold when $f = 2f_r$. This is an expected result from linear theory. P2 oscillations undergo PD to P4-2 at 445 kPa and then are followed by chaos through consecutive PDs at 482 kPa .

The case of $f = 2.8f_r$ is depicted in Fig. 11.12e. P1 oscillations undergo a SN to P3 oscillations at 390 kPa. P3 oscillations undergo PD to P6 at 489 kPa and a small chaotic window appears at 587 kPa. Chaos disappears and low amplitude P1 emerges out of the chaotic window at 588 kPa which later undergo a PD similar to Fig. 11.12d at 661 kPa. Further pressure increase results in the occurrence of P4 through a SN at 819 kPa. P4 oscillations undergo PD to P8 at about 900 kPa.

When $f = 3f_r$ (Fig. 11.12f), P3 occurs at 353 kPa through SN bifurcation. P3 extends to 567 kPa where P6 oscillations are generated through a PD. A small chaotic window appears before the low amplitude P1 which then undergoes a SN to P8 oscillations. Finally chaos is generated at $\approx 800kPa$.

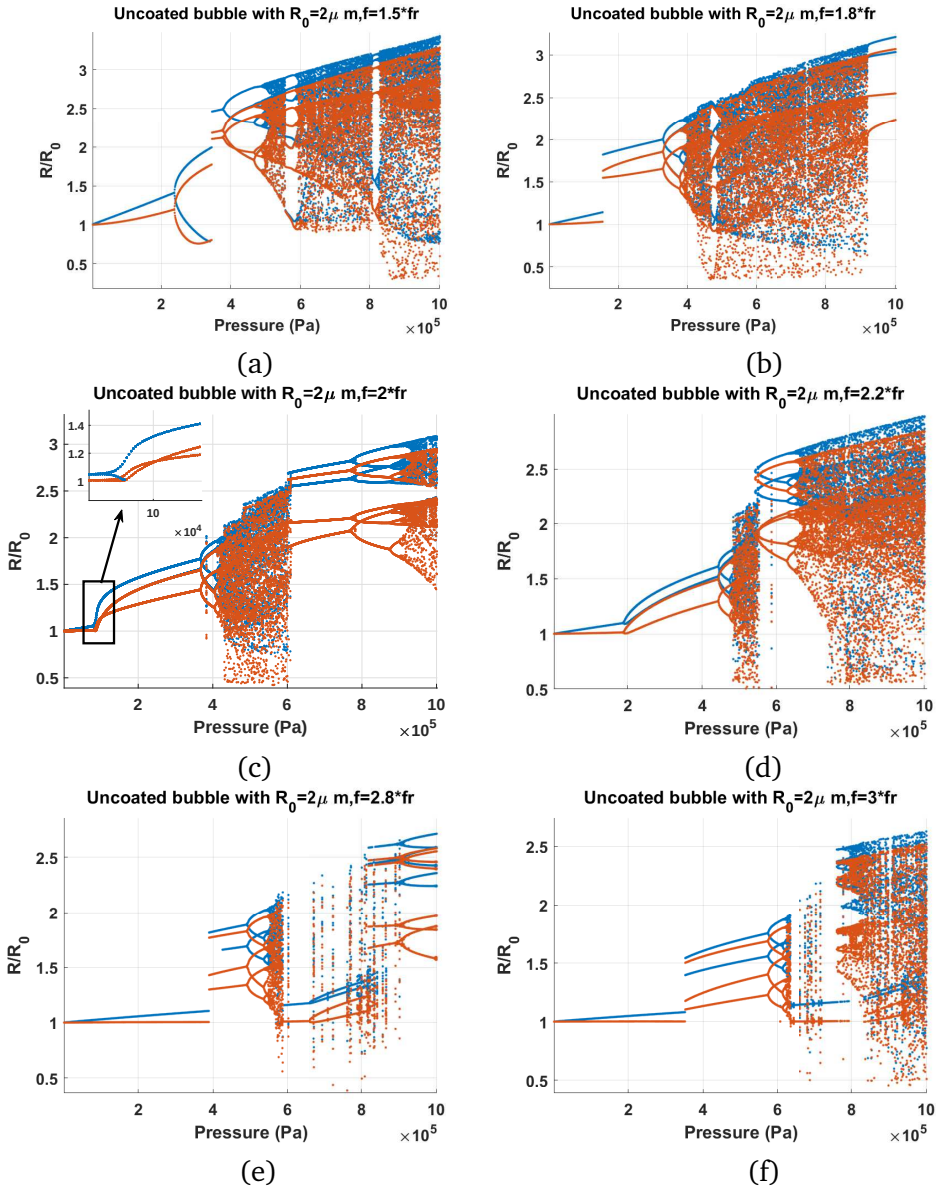

Figure 11.12: Bifurcation structure of the R/R_0 of the C3F8 uncoated bubble with $R_0 = 2\mu m$ as a function of pressure when: a)$f = 1.5f_r$, b)$f = 1.8f_r$, c)$f = 2f_r$, d)$f = 2.2f_r$, e)$f = 2.8f_r$ & f)$f = 3f_r$.

11.4.4 Bifurcation structure of the coated bubble with $\sigma_0 = 0$ & $\sigma_0 = 0.072N/m$

Due to the sharp decrease of resonance frequency with pressure and for simplification of the comparisons, as well as to consider the experimental constrains f_r is chosen to be the frequency of maximum response at 10 kPa. For the bubble with $\sigma_0 = 0N/m$, $f_r = f_{10kPa} = 1.012 f_{1kPa}$ which is due to a slight stiffness hardening behavior of the buckled bubble at low pressures. For the bubble with $\sigma_0 = 0.072N/m$, $f_r = f_{10kPa} = 0.865 f_{1kPa}$.

Figs. 11.13a-b show the bifurcation structure of the coated bubble when $f = 0.3 f_r$ & $\sigma_0 = 0$ (a) and $\sigma_0 = 0.072$ (b). This assumes the coatings are initially in the buckled and ruptured states receptively. The bubbles start oscillation in a P1 with two maxima (2nd SuH) right from $P_a = 1kPa$. The following evolution 2nd SuH $\rightarrow$ 3rd SuH (P1-3 maxima) $\rightarrow$ 4th SuH (P1 4 maxima) appears as pressure increases (these are highlighted as insets in Figs. 11.13a-b). Compared to the uncoated bubble case, the 2nd SuH appears at a very small pressure threshold ($P_a = 1kPa$). Wall velocity is in phase with the driving acoustic pressure for most of the pressures below 200 kPa. Further pressure increases results in the gradual disappearance of the maxima, and above 210 kPa, only two maxima remain in the bubble oscillations for both cases. The radial oscillation amplitude increases, until PD occurs in both graphs and 5/2 UH resonance occur (P2 oscillations with 4 maxima which is highlighted as an inset in Fig. 11.13b). For $\sigma_0 = 0$ N/m, 5/2 UH resonance exists for $P_a = 431 - 450kPa$ & for $\sigma_0 = 0.072$ N/m, 5/2 UH resonance exist for $P_a = 330 - 365kPa$. The UH resonance occurs and disappears through a bubbling bifurcation. 2nd maxima is annihilated soon after the disappearance of UH. Further pressure increase results in PD at very large oscillation amplitudes $\frac{R_{max}}{R_0} > 5$ where the bubble may not sustain non-destructive oscillations.

When $f = 0.5 f_r$ (Figs. 13c-d), oscillations start with 2nd order SuH oscillations (P1 with 2 maxima) right from the start at 1kPa and this stretches to $\approx 50kPa$ in both cases at which point 2nd maxima disappears (highlighted as insets in Figs. 11.13c-d). For the case of $\sigma_0 = 0N/m$ (Fig. 13c), second maxima re-appear at 147 kPa. At 190-231 kPa a bubbling bifurcation occurs where the oscillations become P2 with 4 maxima (5/2 UH regime which is highlighted as an inset). The second maxima disappears again at 230 kPa. Wall velocity stay in phase for most of the pressure range of $P_a < 262kPa$ for $\sigma_0 = 0N/m$ & $P_a < 151kPa$ for $\sigma_0 = 0.072N/m$. Further pressure increase results in PD ($P_a = 660kPa$ for $\sigma_0 = 0N/m$ & $P_a = 473kPa$ for $\sigma_0 = 0.072N/m$).

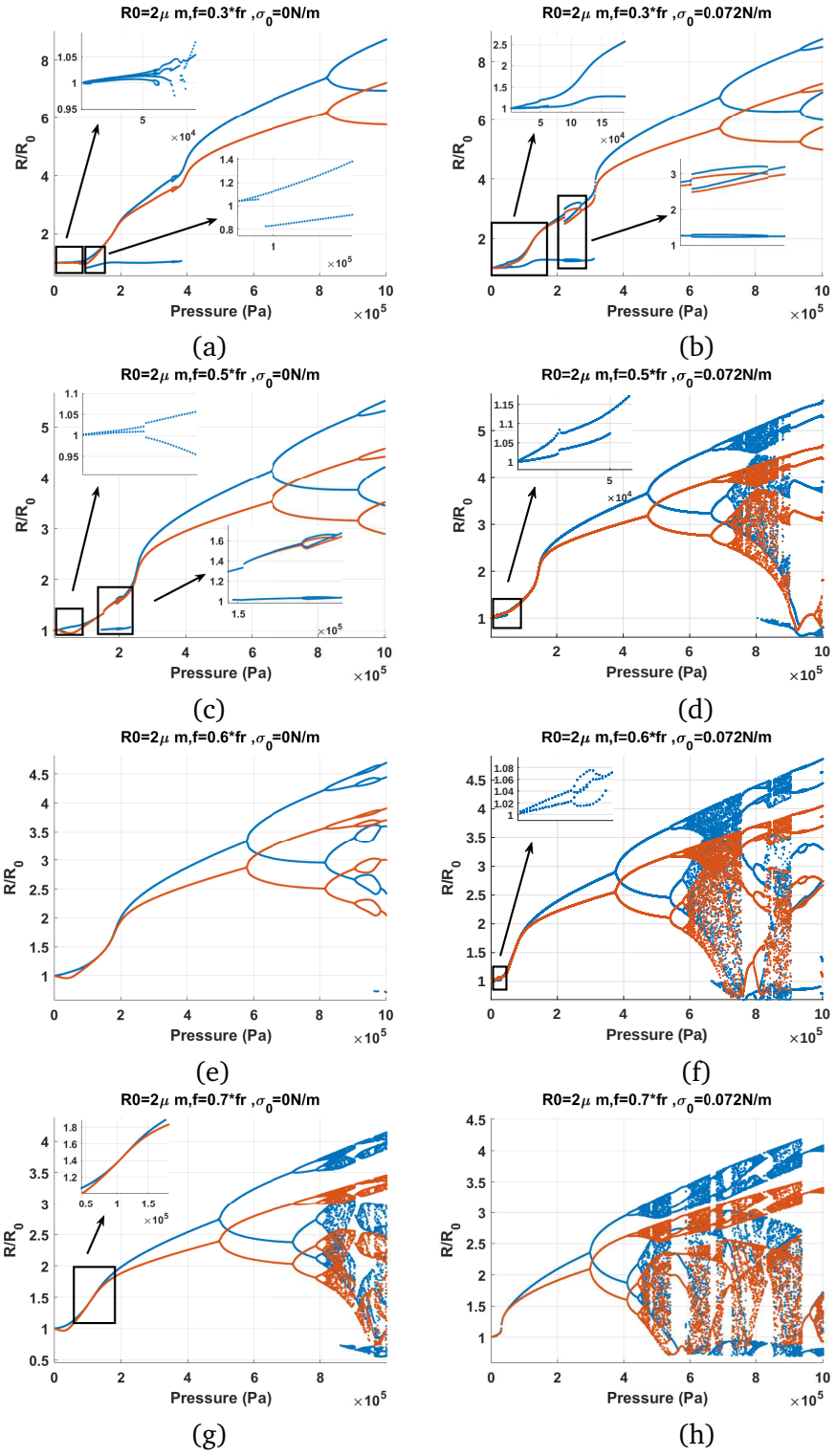

Figure 11.13: Bifurcation structure of the R/R_0 of the C3F8 coated bubble with $R_0 = 2\mu m$ as a function of pressure (left: $\sigma_0 = 0N/m$ and right: $\sigma_0 = 0.072N/m$): a-b)$f = 0.3f_r$, c-d)$f = 0.5f_r$, e-f)$f = 0.6f_r$, g-h)$f = 0.7f_r$.

Compared to the uncoated bubble case, the coating at its ruptured or buckled state reduces the pressure threshold for SuH oscillations. UH oscillations, however, are suppressed and only occur at higher pressures and for a much shorter range of excitation pressure. The pressure threshold for the giant PD increases and chaotic oscillations are suppressed within the excitation pressure range that is examined here. This can be due to the increased damping due to the coating.

When $f = 0.6f_r$ (Figs. 11.13e-f), oscillations are P1 and above a pressure threshold (100 kPa for $\sigma_0 = 0N/m$ & 40 kPa $\sigma_0 = 0.072N/m$), the rate of the growth of the oscillations amplitude with pressure increases abruptly. This point is similar to a inflection point. When this occurs, the wall velocity becomes in phase with the driving acoustic pressure as the red curve has the same value of the blue curve ($100kPa < P_a < 189kPa$ for $\sigma_0 = 0N/m$ & $41kPa < P_a < 90kPa$ & $\sigma_0 = 0.072N/m$). The bubble with $\sigma_0 = 0.072N/m$ undergoes a PD with 4 maxima (5/2 UHs) at $\approx$ 30 kPa which is highlighted as an inset in Fig. 11.13f. Further pressure increases results in the divergence of the blue and red curve and PD occurs at $P_a = 576kPa$ for $\sigma_0 = 0N/m$ & 369 kPa for $\sigma_0 = 0.072N/m$. Oscillations undergo further PDs to P4 as pressure increases. In case of the bubble $\sigma_0 = 0N/m$ a P8 regime is created and then annihilated through a bubbling bifurcation within the P4 window. Oscillations of the bubble with $\sigma_0 = 0.072N/m$ becomes chaotic through successive PDs with intermittent windows of period behavior within.

When $f = 0.7f_r$ (Figs. 11.13g-h), oscillations start in a similar manner to the case of $f = 0.6f_r$. The growth rate of the P1 oscillation amplitude increases abruptly above a pressure threshold which is lower than the case of the $f = 0.6f_r$ (90 kPa for $\sigma_0 = 0N/m$ & 29 kPa $\sigma_0 = 0.072N/m$). Consequently, wall velocity becomes in phase with the driving pressure (highlighted as an inset in Fig. 11.13g) and further pressure increases result in the divergence of the blue and the red curve. PD occurs at $P_a = 495kPa$ for $\sigma_0 = 0N/m$ & 295 kPa for $\sigma_0 = 0.072N/m$. Chaotic oscillations are finally generated through successive PDs with some periodic windows within.

The cases of the coated bubbles in Figs. 11.13e-h are similar to the case of the uncoated bubble sonicated with $f = 0.8f_r$ & $f = 0.9f_r$ (PDf_r [56]). However, the pressure threshold for the SN bifurcation or the increase in the growth rate of the oscillations (inflection point) is much lower in case of the coated bubble with $\sigma_0 = 0.072N/m$ despite being excited with lower frequencies. Moreover, the pressure threshold for PD and chaotic oscillations are higher for the coated bubbles with PD occurring at a higher The $\frac{R_{max}}{R_0}$. This can be due to the increased damping in the bubble

oscillations.

When $f = f_r$ (Fig. 11.14a-b) (note that in this paper in case of the lipid coated bubbles f_r was considered the frequency of maximum response at 10 kPa) the red and blue curve have the same value for $P_a < 20kPa$. The P1 oscillations amplitude grows as pressure increases and the two curves diverge with pressure increase. PD occurs at at $P_a = 267kPa$ for $\sigma_0 = 0N/m$ & 317 kPa for $\sigma_0 = 0.072N/m$ which is higher than the PD pressure for the uncoated bubble ($P_a = 215kPa$ Fig. 11.11e). $\frac{R_{max}}{R_0}$ of the P2 oscillations of the coated bubble however, are below 2 while the oscillation amplitude of the P2 oscillations in uncoated bubble are above 2. In case of the bubble with $\sigma_0 = 0N/m$ a further pressure increase leads to P4 oscillations through another PD. P4 oscillations become P8 and then again P4 through a bubbling bifurcation; P4 oscillations later undergo a PD cascade to chaos. At $P_a \approx 915kPa$ a P4 oscillation emerges out of the chaotic window through symmetry breaking (SB) bifurcation. P4 becomes P2 through another SB. For the bubble with $\sigma_0 = 0.072N/m$, P4 oscillations are generated twice inside the P2 window through bubbling bifurcation. At $P_a = 600kPa$ the P2 oscillations undergo a SN bifurcation to P2 oscillations of higher amplitude. This is similar to the behavior of the uncoated bubble sonicated by its $Pdf_{sh} =\approx 1.5 - 1.9f_r$ (Chapter 5) [58] & Fig. 11.12a ($f = 1.5f_r$). Thus, in case of the lipid coated bubble the buckling and rupture of the coating significantly decreases the Pdf_{sh}.

When $f = 1.2f_r$ (Fig. 11.14c-d), the P1 oscillation amplitude increases with increasing pressure and PD occurs at $P_a = 314kPa$ for $\sigma_0 = 0N/m$ & 238 kPa for $\sigma_0 = 0.072N/m$. Pressure thresholds for PD are higher than the pressure threshold of PD (218 kPa) in the uncoated bubble case in Fig. 11.11f. In both cases, with increasing pressure a SN bifurcation from P2 to another P2 with higher amplitude ($P_a = 796kPa$ for $\sigma_0 = 0N/m$ & 314 kPa for $\sigma_0 = 0.072N/m$). This is similar to the dynamics of the uncoated bubble bubble sonicated by its Pdf_{sh} [58] & Figs. 11.12a-b ($f = 1.5f_r$ & $1.8f_r$). This shows that the dynamic variations of the effective surface tension including buckling and rupture decreases the Pdf_{sh}. In the case of $\sigma_0 = 0.072N/m$ chaos appears through successive PDs, however, the bubble with $\sigma_0 = 0N/m$ does not exhibit chaotic oscillations in this pressure range. Additionally at a given pressure, $\frac{R_{max}}{R_0}$ is higher for the bubble with $\sigma_0 = 0.072N/m$ because of the expansion dominated behavior of the bubble. This can be one of the reasons for lower pressure threshold of P2 and chaotic oscillations in case of the bubble in ruptured state.

When $f = 1.5f_r$ (Fig. 11.14e-f), the bubble behavior is similar to the uncoated bubble sonicated

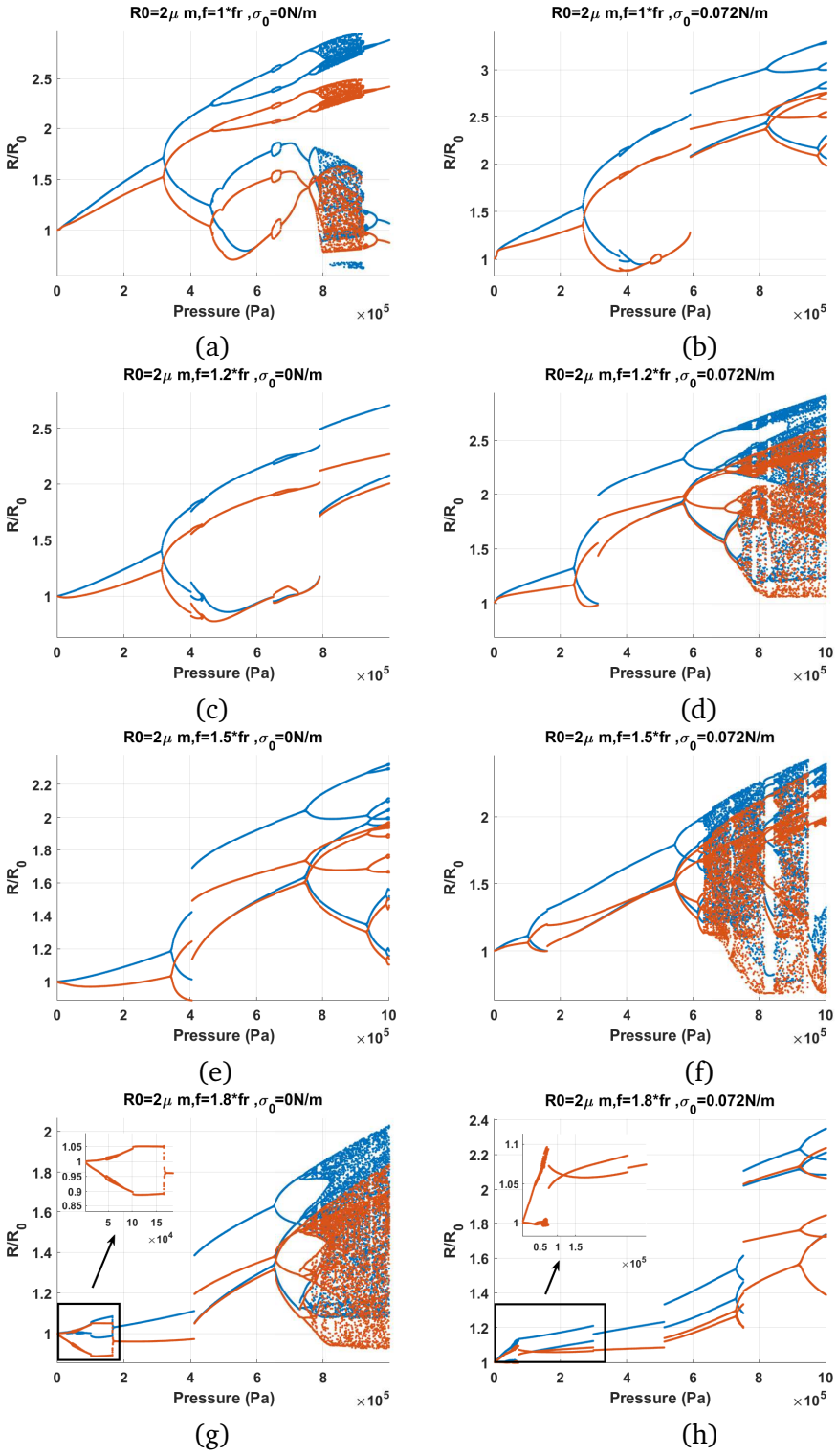

Figure 11.14: Bifurcation structure of the R/R_0 of the C3F8 coated bubble with $R_0 = 2\mu m$ as a function of pressure (left: $\sigma_0 = 0.0N/m$ and right: $\sigma_0 = 0.072N/m$): a-b)$f = f_r$, c-d)$f = 1.2f_r$, e-f)$f = 1.5f_r$, g-h)$f = 1.8f_r$.

with its PDf_{sh}. The pressure threshold for P2 oscillations are $P_a = 338kPa$ for $\sigma_0 - 0N/m$ & $P_a = 98kPa$ for $\sigma_0 = 0.072N/m$. In case of the bubble with $\sigma_0 = 0.072N/m$ pressure threshold for PD is lower than the case of the uncoated bubble (Fig. 11.12a). Increasing pressure results in a SN bifurcation from a P2 regime to a higher amplitude P2 regime only in case of the coated bubble with $\sigma_0 = 0N/m$. In case of the uncoated bubble the SN bifurcation results in $\frac{R_{max}}{R_0} > 2$, however, here P2 oscillations remain below 2 when SN occurs. The P2 oscillations undergo successive PDs to P8 in both bubbles (Fig. 11.14e-f). However, only the bubble with $\sigma_0 = 0.072N/m$, exhibits chaotic oscillations. Similar to the previous cases, $\frac{R_{max}}{R_0}$ is higher for the bubble in the ruptured state due to expansion dominated behavior.

When $f = 1.8f_r$ a very interesting phenomenon is observed (Fig. 11.14g-h). In both cases, the bubble starts oscillating in the P2 regime at the very low pressure threshold of 1kPa. To our best knowledge, such a low excitation threshold for P2 oscillations in nonlinear oscillators is first reported here. The dynamic of the bubble exhibits three interesting stages. The generation of P2 oscillations (at very low pressure), the disappearance of P2 oscillations and regeneration of P2 oscillations. Such behavior as been observed experimentally in [73,93]. In [73], the disappearance of SH oscillations is referred to as an "unexpected standstill" of SHs. This will be discussed further in discussion. Within the initial P2 window, a very small P4-2 window occurs for both bubbles. The pressure threshold for the initiation of the P4-2 oscillations is as low as 5 kPa for the bubble with $\sigma_0 = 0.072N/m$. The P2 oscillations disappear with increasing pressure above 173 kPa and 299 kPa for the bubbles with $\sigma_0 = 0$ & $0.072N/m$ respectively. A second P2 regime re-emerges through a SN bifurcation at 412 & 514 kPa for the bubbles with $\sigma_0 = 0$ & $0.072N/m$ respectively. This dynamical feature is similar to the case of uncoated bubble sonicated with its PDf_{sh} of $1.8f_r$ (Fig. 11.12b); however, the SN occurs at a higher pressure. Similar to the uncoated bubble, after the SN occurrence, the bubble with $\sigma_0 = 0N/m$ undergoes chaotic oscillations through successive PDs.

When $f = 2f_r$ (Figs. 11.15a-b), the dynamics are similar to Figs. 11.14g-h. P2 oscillations are generated at 1kPa, and they disappear above 200 kPa. For the bubble with $\sigma_0 = 0N/m$, P2 oscillations re-emerge at $\approx 600kPa$ and through a PD bifurcation. Similar to the coated bubble sonicated with its Pdf_{sh} in [58], P2 oscillations undergo a SN bifurcation to P2 oscillations with higher amplitude. Further pressure increase results in chaotic oscillations through successive PDs. In case of the bubble with $\sigma_0 = 0.072N/m$, soon after the disappearance of the P2 oscillations, a

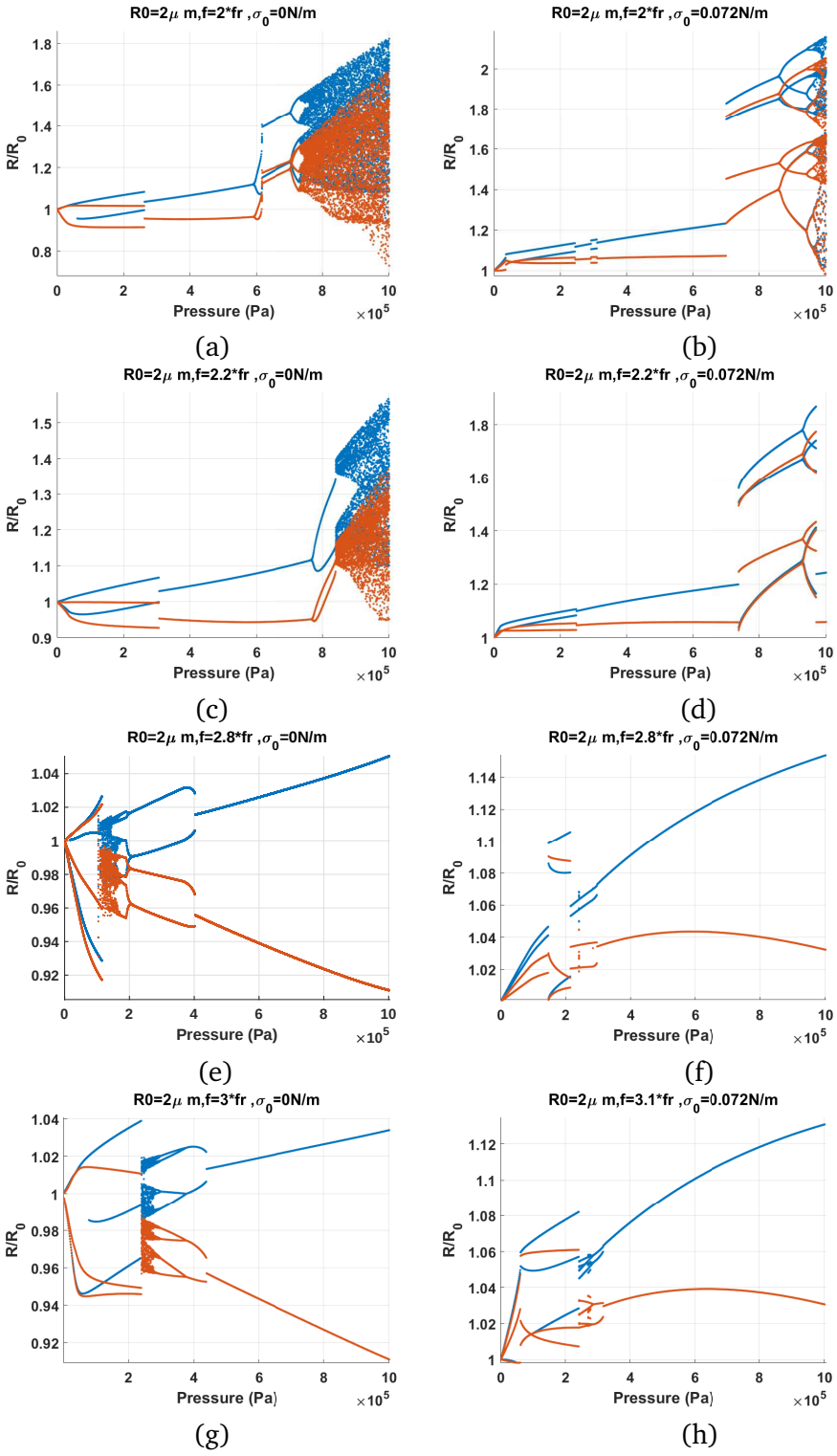

Figure 11.15: Bifurcation structure of the R/R_0 of the C3F8 coated bubble with $R_0 = 2\mu m$ as a function of pressure (left: $\sigma_0 = 0N/m$ and right: $\sigma_0 = 0.072N/m$): a-b)$f = 2f_r$, c-d)$f = 2.2f_r$, e-f)$f = 2.8f_r$, g)$f = 3f_r$ h)$f = 3.1f_r$.

rather small window (293-310 kPa) of P2 oscillations is generated through a SN. P2 oscillations disappear and P1 oscillations undergo a SN to P3 at 707 kPa.This dynamical feature is similar to Fig. 11.12f where the uncoated bubble is sonicated with $f = 3f_r$.

The dynamics of the bubble sonicated with $f = 2.2f_r$ (Figs. 11.15c-d) is similar to $f = 2f_r$ and the general dynamical features of the system stays the same.

The dynamics of the bubbles with $\sigma_0 = 0N/m$ & $0.072N/m$ sonicated with $1.8f_r \leq f \leq 2.2f_r$ exhibits three main stages. In stage one the bubble shows enhanced non-linearity by which P2 oscillations are generated at very low pressure thresholds. The P2 oscillations disappear by pressure increases however, they re-emerge as P2 or P3 oscillations above pressure threshold higher than the uncoated counterpart, and in a similar fashion to the uncoated bubble sonicated by its PDf_{sh} or $f = 2.8 - 3f_r$.

The bifurcation structure of the bubbles when $f = 2.8f_r$ is shown in Figs. 11.15e-f. Right at $P_a = 1kPa$, the bubble with $\sigma_0 = 0N/m$ starts P3 oscillations. The enhanced non-linearity of P3 at such a low excitation is reported for the first time here increases. Pressure increase leads to a sudden chaos at 104 kPa, with the P3 attractor coexisting with chaos until its disappearance at 112 kPa. Chaos stretches to 156 kPa. Chaotic oscillations become P2 through a cascade of symmetry breaking bifurcations.

Cases of $f = 3f_r$ & $\sigma_0 = 0N/m$ and $f = 3.1f_r$ & $\sigma_0 = 0.072N/m$ are shown in Figs. 11.18g & h respectively [2]. P3 oscillations start at $P_a = 1kPa$ for both cases. For $\sigma_0 = 0N/m$, sudden chaos appear at 240 kPa. With pressure increase P2 oscillations emerge out of the chaotic window through a cascade of symmetry breaking bifurcations. Lastly P1 oscillations appear above 400 kPa. For $\sigma_0 = 0.072N/m$, P4-2 oscillations emerge out of the P3 oscillations through a SN bifurcation and undergo symmetry breaking bifurcation to P2 and then P1.

11.4.5 Bifurcation structure of the coated bubble with $\sigma_0 = 0.01$ & $\sigma_0 = 0.062N/m$

Bifurcation structures in this section are also plotted at multiples and fractions of the resonance frequency. Similar to the previous section, the resonance frequency is set to be the frequency of

[2] case of $f = 3f_r$ and $\sigma_0 = 0.072N/m$ exhibits the similar dynamic as of Fig. 11.7h. Thus, here we decided to present $f = 3.1f_r$ to highlight the generation of P3 at $P_a = 1kPa$

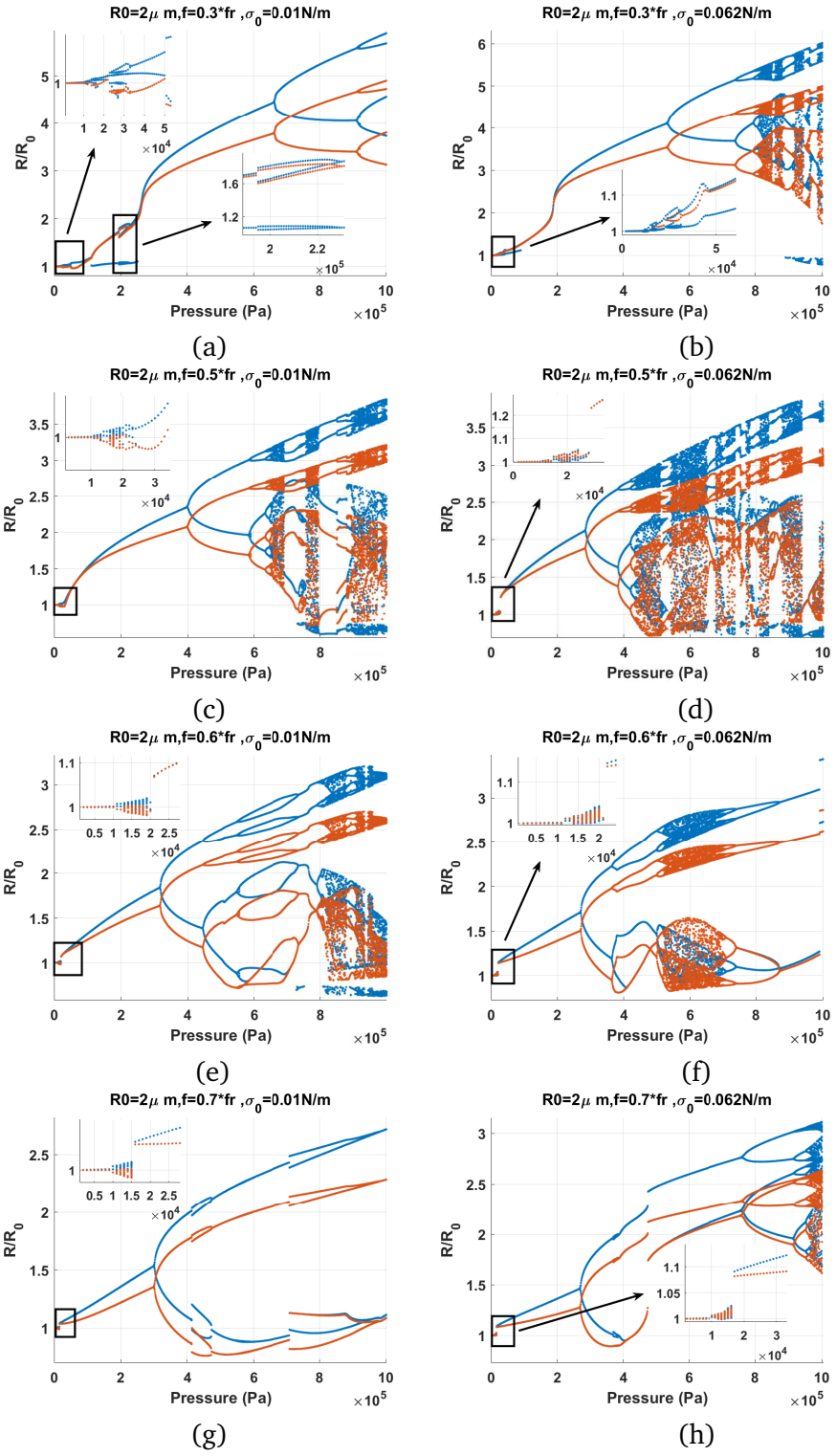

Figure 11.16: Bifurcation structure of the R/R_0 of the C3F8 coated bubble with $R_0 = 2\mu m$ as a function of pressure (left: $\sigma_0 = 0.01N/m$ and right: $\sigma_0 = 0.062N/m$): a-b)$f = 0.3f_r$, c-d)$f = 0.5f_r$, e-f)$f = 0.6f_r$, g-h)$f = 0.7f_r$.

maximum response at 10 kPa. For the bubble with $\sigma_0 = 0.01N/m$, $f_r = f_{10kPa} = 0.52f_{1kPa}$ & for the bubble with $\sigma_0 = 0.062N/m$, $f_r = f_{10kPa} = 0.53f_{1kPa}$.

The bifurcation structures of the bubbles with $\sigma_0 = 0.01N/m$ & $\sigma_0 = 0.062N/m$ insonified by $0.3f_r \leq f \leq 0.7f_r$ are shown in Fig. 11.16. Figs 11.16a-b shows the cases of sonication with $f = 0.3f_r$. The dynamics of the bubbles are very similar to their counterparts with $\sigma_0 = 0N/m$ & $0.072N/m$ sonicated with $f = 0.3 - 0.5f_r$ (Figs. 11.13a-d). However, there are two differences: 1) $\frac{R_{max}}{R_0}$ is in generally lower than the initially buckled or the ruptured bubble over all pressures studied and, 2) The threshold for the start of SuH oscillations is $\approx 11kPa$ which was 1 kPa in (Figs. 11.13a-d). The pressure threshold for SuH oscillations is still lower than the case of uncoated bubble in Figs. 11.11a-b.

Sonication with $f = 0.5f_r$ is depicted in Figs. 11.16c-d. There is a general similarity with the bubbles with $\sigma_0 = 0$ & $\sigma_0 = 0.072N/m$ sonicated with $f = 0.6f_r$ & $f = 0.7f_r$. Above a pressure threshold in all cases there is a SN bifurcation or an increase in the growth rate of the bubble oscillation amplitude (manifested in the form of an inflection point) which corresponds to the PDf_r. At this point the red and blue curve meet indicating the wall velocity with the acoustic excitation is in phase. Referring to Fig. 11.3, the rate of the decrease of f_r with pressure increase is higher for the bubbles with $\sigma_0 = 0.1$ & $0.072N/m$ compared to $\sigma_0 = 0$ & $\sigma_0 = 0.072N/m$. This manifests itself in the occurrence of the SN or the inflection point at lower frequencies and lower pressures in Figs. 11.16e-h.

The bubbles exhibit 2nd order SuH (P1- 2 maxima) and 5/2 UHs within the pressure range of 10-28 kPa. Above 28 kPa, the bubble with $\sigma_0 = 0.062N/m$ undergoes a SN bifurcation from a P1 oscillation to another P1 oscillation with higher amplitude. At the 57 kPa, the growth rate of the oscillations amplitude increases for the bubble with $\sigma_0 = 0.062N/m$. This indicates the PDf_r point. Further pressure increase results in PD and chaotic oscillations. The pressure threshold for PD and $\frac{R_{max}}{R_0}$ are smaller than their counter part with $\sigma_0 = 0$ and 0.072 N/m (Figs. 11.13c-f).

The dynamics of the bubbles with $\sigma_0 = 0.01$ & $0.062N/m$ sonicated with $f = 0.6f_r$ (Figs. 16e-f) are similar to the case of $f = 0.5f_r$ in Figs. 11.16c-d. A SN bifurcation takes place at $\approx 17kPa$ for both bubbles and the oscillations amplitude increases abruptly (PDf_r). Just before the occurrence of SN, a small amplitude chaotic window appears. When SN occurs, blue curve and red curve obtain the same value. As pressure increases oscillation amplitude increases and the two curve

diverge. PD occurs at $P_a = 300$ and $267kPa$ respectively for $\sigma_0 = 0.01$ and $\sigma_0 = 0.072N/m$. The bubble with $\sigma_0 = 0.01N/m$ exhibits the transition from P2 $\rightarrow$ P4 through a PD and P4 $\rightarrow$ P8 $\rightarrow$ P4 through a bubbling bifurcation and then chaos with increasing pressure. The bubble with $\sigma_0 = 0.062N/m$ undergoes P4 and chaos through multiple PDs which is followed by the emergence of P2 oscillations through multiple symmetry breaking bifurcations out of chaos. The case of sonication with $f = 0.7f_r$ is shown in Fig. 11.16g-h. There are two SN bifurcations with pressure increase. The initial SN occurs at $\approx$ 15 kPa and results in P1 oscillations of higher amplitude. After the first SN oscillation amplitude grows with increasing pressure and PD occurs in both cases. A small P4 window is generated within the P2 window. For the case of $\sigma_0 = 0.01N/m$ at $P_a = 710kPa$ P4 oscillations are regenerated and then transition to P2 via symmetry breaking at 982 kPa. For the bubble with $\sigma_0 = 0.062N/m$ at $P_a = 479kPa$ P2 oscillations undergo a SN bifurcation to P2 oscillations with higher amplitudes. This is similar to the dynamics of the uncoated bubble sonicated with its PDf_{sh} (Figs. 11.12a-b).

Case of the $f = f_r$ is shown in Fig. 11.17a-b. At $P_a = 10kPa$ a SN bifurcation takes place and oscillation amplitudes increase slightly (PDf_r at 10 kPa). Oscillation amplitude increases slowly with pressure and PD occurs at $P_a = 326kPa$ & $148kPa$ respectively for $\sigma_0 = 0.01N/m$ & $\sigma_0 = 0.062N/m$. After the SN, the dynamics of the bubble with $\sigma_0 = 0.01N/m$ (Fig. 11.17a) & $\sigma_0 = 0.062N/m$ (Fig. 11.17b) sonicated with $f = f_r$ are respectively similar to the dynamics of the bubble with $\sigma_0 = 0N/m$ (Fig. 11.14e) & $\sigma_0 = 0.072N/m$ (Fig. 11.14f) sonicated with $f = 1.5f_r$. For the bubble with $\sigma_0 = 0.01N/m$ increasing pressure results in a SN bifurcation from P2 oscillations to a higher amplitude P2 oscillations at 378 kPa. This is similar to the dynamics of the uncoated bubble sonicated with its PDf_{sh} (Fig. 11.12a) [58]. P2 oscillations then grow in amplitude with pressure increase and oscillations become P4-2 through a PD at 624 kPa. Bubble continues with P4-2 oscillations with a P8 window within, which is created and annihilated through a bubbling bifurcation. The dynamics of the bubble with $\sigma_0 = 0.062N/m$ resembles the case of the uncoated bubble sonicated with $f = 2f_r$ (Fig. 11.12c) [34]. P2 oscillations spread between $148 - 555kPa$. At 555 kPa, P4-2 oscillations are generated via a PD and later undergo successive PDs to chaotic oscillations at 638 kPa.

The case for $f = 1.2f_r$ is shown in Figs. 11.17c-d. In both cases we witness the generation of the P2 oscillations, their disappearance and re-generation which is similar to the dynamics of the initially

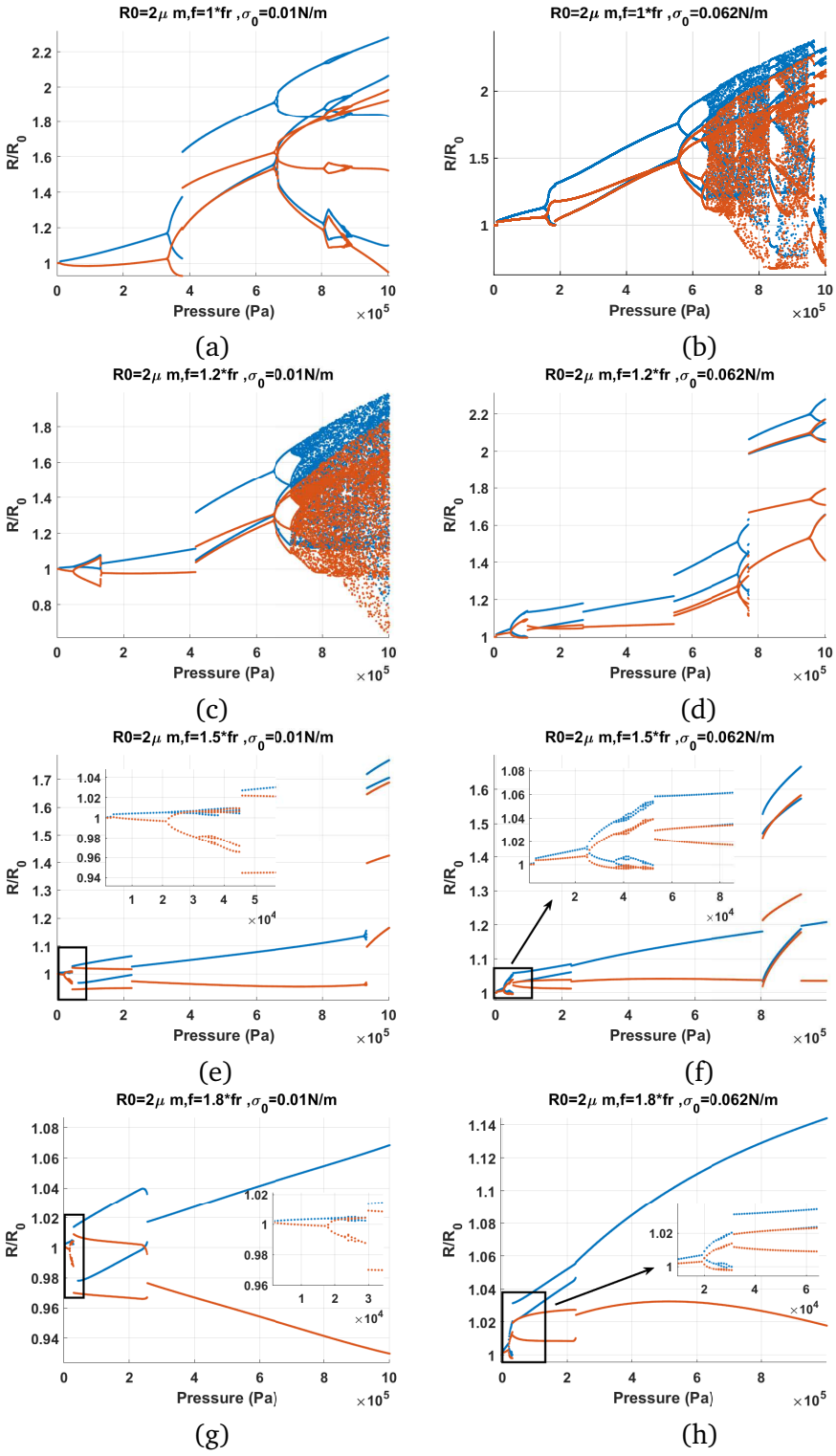

Figure 11.17: Bifurcation structure of the R/R_0 of the C3F8 coated bubble with $R_0 = 2\mu m$ as a function of pressure (left: $\sigma_0 = 0.01N/m$ and right: $\sigma_0 = 0.062N/m$) sonicated with: a-b)$f = f_r$, c-d)$f = 1.2f_r$, e-f)$f = 1.5f_r$, g-h)$f = 1.8f_r$.

buckled and ruptured bubble in Figs. 11.14g-h. For bubbles with $\sigma_0 = 0.01N/m$ (Fig. 11.17c) & $\sigma_0 = 0.062N/m$ (Fig. 11.17d) P2 oscillations occur via a PD at $P_a = 47$ & $48kPa$ respectively. With pressure increase P2 oscillations transition to P1 (disappearance of 1/2 order SHs) at $P_a = 140$ & $269kPa$ respectively. P2 oscillations are then re-appear at $P_a = 418$ & $545kPa$ respectively. Dynamics of the coated bubbles in this pressure region is similar to the dynamics of the uncoated bubble sonicated with its PDf_{sh} (Fig. 11.12b). In case of $\sigma_0 = 0.01N/m$, further pressure increase results in a cascade of PDs to chaos. In case of the $\sigma_0 = 0.062N/m$ further pressure increase results in the appearance of P3 oscillations which later undergo PD to P6 oscillations.

The dynamic variation of the effective surface tension due to the lipid coating decreased the frequency of Pdf_{sh} to frequencies close to resonance. Moreover, P3 oscillations are unexpectedly generated. Compared to the uncoated bubble, the pressure thresholds for P2 oscillations are smaller. Also, $\frac{R_{max}}{R_0}$ are generally smaller than both the uncoated bubble and the bubbles with $\sigma_0 = 0.0N/m$ & $\sigma_0 = 0.072N/m$.

When $f = 1.5f_r$ (Figs. 11.17e-f), PD occurs at $P_a = 16$ & $21kPa$ for $\sigma_0 = 0.01N/m$ & $\sigma_0 = 0.062N/m$ respectively and they stretch up to approximately 224 kPa where they transition to P1 oscillations via a SN bifurcation. Further pressure increase results in the generation of P3 oscillations via another SN bifurcation at $P_a = 834kPa$ & $P_a = 805kPa$ respectively for $\sigma_0 = 0.01N/m$ & $\sigma_0 = 0.062N/m$. The dynamics of the bubble in this region is similar to the dynamics of the uncoated bubble sonicated with $f = 2.8 - 3f_r$ (Figs. 11.12e-f).

For $f = 1.8f_r$ (Figs. 11.17g-h), P2 oscillations occur via a PD at $P_a = 14$ & $18\ kPa$, respectively for $\sigma_0 = 0.01N/m$ & $\sigma_0 = 0.062N/m$. At 30 kPa P2 oscillations undergo a SN bifurcation to P2 oscillations of higher amplitude. At 255 kPa, P2 oscillations transition to P1 oscillations via another SN. The bubble oscillates with P1 for the rest of the studied pressure range. In this case the dynamic variation of the effective surface tension of the lipid coating enhances the generation of P2 oscillations at very low pressures. The coating lowers the pressure threshold for the Pdf_{sh}; however, at higher pressures suppresses the nonlinear oscillations.

For $f = 2f_r$ (Figs. 11.18a-b), PD is initiated at $P_a = 17kPa$ for both bubbles. A SN bifurcations transition the P2 oscillations to P2 oscillations of higher amplitude at 26 kPa. P4-2 oscillations are generated and transition back to P2 oscillations through bubbling bifurcation. The P2 oscillations undergo SN bifurcation to P1 oscillations at $P_a = 268kPa$ & $230kPa$ respectively for the bubbles

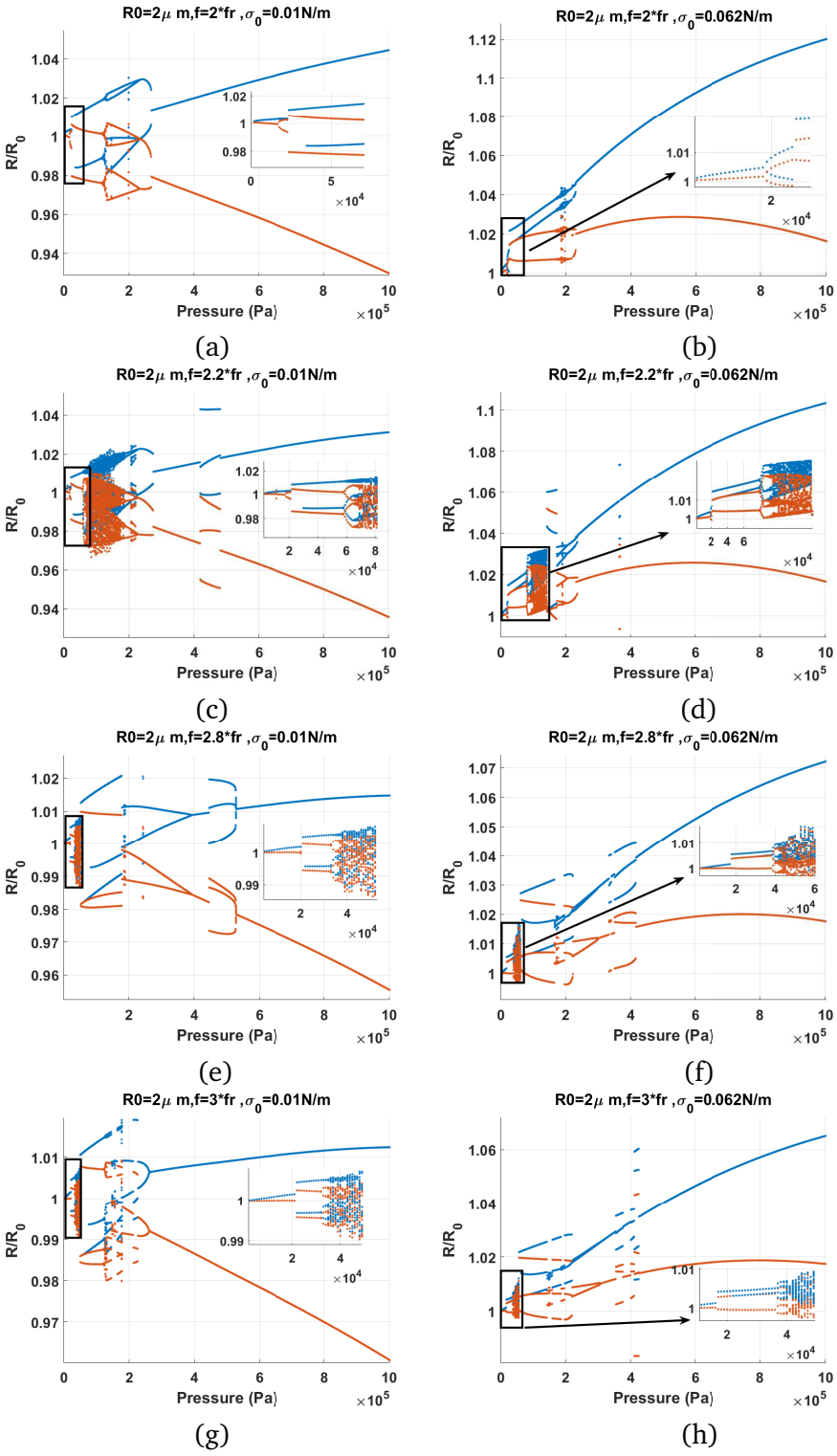

Figure 11.18: Bifurcation structure of the R/R_0 of the C3F8 coated bubble with $R_0 = 2\mu m$ as a function of pressure (left: $\sigma_0 = 0.01N/m$ and right: $\sigma_0 = 0.062N/m$) sonicated with: a-b)$f = 2f_r$, c-d)$f = 2.2f_r$, e-f)$f = 2.8f_r$, g-h)$f = 3f_r$.

with $\sigma_0 = 0.01N/m$ & $\sigma_0 = 0.062N/m$. Oscillations of the bubble stay at P1 for the rest of the pressure ranges that is studied here. Compared to the uncoated bubble in Fig. 11.12c the lipid coating enhances the P2 oscillations at low acoustic pressures; however, the P2 oscillations of the bubble is suppressed at higher pressures.

When $f = 2.2f_r$ (Figs. 11.18c-d), P2 oscillations are generated through a PD at $P_a = 17kPa$ and then at $P_a = 20kPa$ undergo a SN bifurcation to P2 oscillations of higher amplitude. Oscillations undergo a cascade of PDs to P4-2 and finally chaos at 71 and 95 kPa for the bubbles with $\sigma_0 = 0.01N/m$ & $\sigma_0 = 0.062N/m$ respectively. For the bubble with $\sigma_0 = 0.01N/m$ and through a cascade of reverse PDs starting at 175 kPa, bubble oscillations transition to a P2 regime, which later undergo a SN bifurcation to P1 at 274 kPa. For the bubble with $\sigma_0 = 0.062N/m$, the transition from chaos to P2 is via a SN bifurcation at 141 kPa. Oscillations transition to P4-2 via a SN at 173 kPa followed by reverse PD to P2 and SN to P1 at 236 kPa. P3 oscillations are generated via a SN bifurcation for a small window of pressure for both bubbles.

When $f = 2.8f_r$ (Figs. 11.18e-f), P2 oscillations are generated via SN bifurcations at $P_a \approx 20kPa$. Chaos sets in for a small pressure window of $\approx$ (39-51kPa) & (42-59kPa) for the bubbles with $\sigma_0 = 0.01N/m$ & $\sigma_0 = 0.062N/m$ respectively. P3 oscillations emerge out of the chaotic window via a SN bifurcation and then transition to P2 oscillations via another SN bifurcation at 179 kPa and 229 kPa for the bubbles with $\sigma_0 = 0.01N/m$ & $\sigma_0 = 0.062N/m$, respectively. For the bubble with $\sigma_0 = 0.01N/m$, P3 oscillations are re-generated through SN bifurcation at $447kPa$ and undergo a reverse period tripling at $P_a = 530kPa$ to P1 oscillations. For the bubble with $\sigma_0 = 0.062N/m$ P3 oscillations are generated at 334 kPa via a SN and the transition again to P1 oscillations via another SN at 416 kPa. The oscillations remain P1 for the rest of the studied pressure range. When compared to the uncoated bubble, the lipid coating enhanced the generation of P2 and P3 oscillations at lower pressures. The coating also, enhanced the onset of chaos at very low excitation amplitudes and suppressed the chaotic oscillations at higher pressures.

Figs. 11.18g-h represent the case of $f = 3f_r$. The dynamics at low pressures $P_a < 200kPa$ are similar to those in Figs. 11.18e-f. P2 oscillations are generated at low pressures through a SN which then undergo a cascade of PDs to chaotic oscillations. P3 oscillations then emerge out of the chaotic window through a SN at 49 and 55 kPa, respectively for bubbles with $\sigma_0 = 0.01$ & $\sigma_0 = 0.062N/m$. For the bubble with $\sigma_0 = 0.01N/m$, the pressure increase results in P6-3

oscillations via a PD at 124 kPa. At 144 kPa, P6-3 oscillations transition to P2 oscillations via a SN. P2 transition to P6 via another SN at 164 kPa. At 178 kPa, P6 transition to P2 via another SN. At 213 kPa, P2 becomes P3 via a SN which is then followed by a SN from P3 to P2 and reverse PD to P1 for the rest of the studied pressure range. For the bubble with $\sigma_0 = 0.062N/m$ within the pressure range of 140-376 kPa, there are intermittent transitions between P2 and P3 via SNs. At 401 kPa, P1 oscillations give birth to a P4-1 oscillations which then transition to P3 via a SN at 411 kPa. P1 oscillations emerge out of the P3 window via a SN at 425 kPa. Compared to the uncoated bubble, lipid coating enhances the P2, P3 and chaotic oscillations at very low acoustic pressures. Moreover, P4-1 oscillations appear at $3f_r$. In case of the uncoated bubble and for the same initial conditions however, P4-1 is expected to appear at frequencies near $4f_r$.

Compared to the case of $\sigma_0 = 0N/m$ & $\sigma_0 = 0.072N/m$, P2 and P3 oscillations are not generated right at the 1 kPa driving pressure and need pressures above 10 kPa. Moreover, the bubbles generally have lower $\frac{R_{max}}{R_0}$.

11.4.6 Bifurcation structure of the coated bubble with $\sigma_0 = 0.036N/m$

In this section and for the bubble with $\sigma_0 = 0.036N/m$, $f_r = f_{10kPa} = 0.824f_{1kPa}$. Bifurcation structure of the bubble with $\sigma_0 = 0.36N/m$ is shown in $Figs11.11\&11.12$.

Fig. 11.19a shows the case of sonication with $f = 0.3f_r$. P1 oscillations undergo a SN at $P_a = 44kPa$ and the bubble oscillations amplitude increases abruptly (This is similar to the dynamics of the bubble sonicated with its PDf_r in Fig. 11.11c-d). Wall velocities are in phase (blue curve meets the red curve) with the driving acoustic pressure for a range of acoustic excitation pressures and with increasing pressure the two curves diverge. PD occurs at 371 kPa followed by a cascade of PDs leading to chaos at $\approx 595kPa$. Further pressure increase results in the intermittent transition between chaos and periodic behavior. This behavior is similar to the dynamics of the uncoated bubble sonicated with its pressure dependent resonance frequency (PDf_r) in Figs. 11.11a-d. The presence of the coating thus lowers the pressure threshold for the SN bifurcation. However, the pressure threshold for PD is higher and the bubble oscillation amplitude is generally smaller than the uncoated bubble.

When $f = 0.5f_r$ (Fig. 11.19b) the bubble undergoes two bifurcations that leads to two abrupt

increases in the bubble oscillation amplitude. The first is a SN which takes place at 34 kPa transitioning the P1 oscillations to a P1 with higher amplitude. The second one is an inflection point at 460 kPa transitioning the P2 oscillations to P2 oscillations with slightly higher amplitude. Here, the system exhibits dynamics that are similar to two different regimes of the oscillations in the uncoated bubble. The low pressure transition is similar to the low pressure transition of the uncoated bubble sonicated with PDf_r (Figs. 11.11c-d). The second transition that occurs at a higher pressure resembles the dynamics of the bubble sonicated with its PDf_{sh} in Fig. 11.12b. When compared to the uncoated counterpart, for the coated bubble the first transition occurs at a lower pressure while the second transition occurs at a higher pressure.

When $f = 0.6f_r$ (Fig. 11.19c), we witness the same two pressure thresholds as the previous case. Two SN occur, one at $P_a = 29kPa$ and the second one at $327kPa$. The first SN transition P1 to a P1 oscillation of higher amplitude (PDf_r) while the second SN transition the P2 oscillations to P2 oscillations of higher amplitude (PDf_{sh}). Further pressure increases leads to P4-2 with bubbles of P8-4 inside. Right after the bubble 4 small windows of chaos appear which transition to P4 and then again to chaos.

When $f = 0.7f_r$ (Fig. 11.19d) two SN takes place; the first SN transitions a P1 oscillation to a P1 oscillation of higher amplitude at 25 kPa (PDf_r) and the second SN transition the P1 oscillation to P2 oscillations of higher amplitude at 277 kPa (Pdf_{sh}). Pressure increase leads to P4-2 through PD at $\approx 600kPa$ and later chaos at 671 kPa.

Looking at Figs. 11.19a-d, the dynamic variation of the surface tension of the lipid coating significantly decreases the frequencies of pressure dependent resonance (PDf_r) $\&$ and pressure dependent SH resonance frequency (PDf_{sh}). As an instance, PDf_{sh} typically occurs for $1/5f_r < f < 2f_r$ for the uncoated bubble ([58] and Figs. 11.12a-b) while PDf_{sh} occurred at frequencies as low as $0.5f_r$ for the coated bubble with $\sigma_0 = 0.036N/m$.

When $f = f_r$ (Fig. 11.19e), an unexpected behavior is observed. P1 oscillations undergo a SN to P3 oscillations at 833 kPa. In case of the uncoated bubble (Figs. 11.12e-f) or bubbles with pure viscoelastic coating [38], this behavior only occurs for frequencies close to $3f_r$. Thus the lipid coating here, decreased the P3 resonance frequency by 200 $\%$. The pressure threshold for P3 oscillations, however is higher for the coated bubble when compared to the uncoated counterpart.

When $f = 1.2f_r$ (Fig. 11.19f), nonlinear oscillations are suppressed to only a P1 oscillation for the

studied pressure range.

For $f = 1.5f_r - 2.2f_r$ (Figs. 11.20a-d), P3 oscillations are enhanced. Compared to the P3 oscillations in cased of the uncoated bubble (Figs. 11.12e-f), P3 occurs at lower pressure thresholds. For instance at $f = 2.2f_r$ P3 is generated at 157 kPa. This is however, higher than the pressure threshold for P3 oscillations in case of the coated bubbles with $\sigma_0 = 0, 0.01, 0.62$ & $0.072N/m$.

When $f = 2.8f_r$ (Fig. 11.20e), P3 is generated through a SN at 134 kPa and later transition to P1 via another SN at 269 kPa. P5 oscillations are generated at 373 kPa through a SN and transition to P1 at 433 kPa. P5 oscillations re-appear again for a short pressure window through the same mechanism at 647 kPa.

When $f = 3f_r$ (Fig. 20f), P3 oscillations start at 128 kPa and stretch up to 279 kPa with a short window of P1 oscillations within. P5 oscillations are generated at 351 and 592 kPa for two short pressure windows. Compared to the uncoated bubble sonicated with $3f_r$ (Fig. 11.12f), the pressure threshold of P3 oscillations is lowered by about 276 $\%$.

Coating with $\sigma_0 = 0.036N/m$ significantly reduced the frequency for P3 and P5 oscillations. Most interestingly, the coated bubble with $\sigma_0 = 0.036N/m$ exhibits enhanced P3 oscillations over a very large frequency range of $f_r \leq f \leq 3f_r$.

11.4.7 Investigation of the mechanism of the disappearance (standstill) and regeneration of P2

In section 3.2 we showed that the enhancement of P2 oscillations at lower pressures can be caused by the asymmetric variations of the effective surface tension due to buckling or rupture. Here, we look in to the possible reasons of the disappearance of the P2 oscillations when increasing pressure. Fig. 11.21a shows the radial oscillations as a function of the driving periods of the coated bubble in Fig. 11.17d ($R_0 = 2mum$ and $\sigma_0 = 0.062N/m$) at $P_a = 400kPa$. At this pressure the P2 oscillation regime disappeared. Radial oscillations are P1, and the red circles return only one value. The corresponding $\sigma(R)$ curve, depicts a rather symmetrical variations in the buckling and rupture, the bubble spends the same approximate time in the buckled stage as the ruptured stage. For 10 driving periods, the bubble buckles 10 times and ruptures 10 times.

As pressure increases, P2 is regenerated (Fig. 11.17d). At 650 kPa the radial oscillations vs period curves have two maxima (Fig. 11.21c) and the red circles have 2 distinct values. $\sigma(R)$ as a function

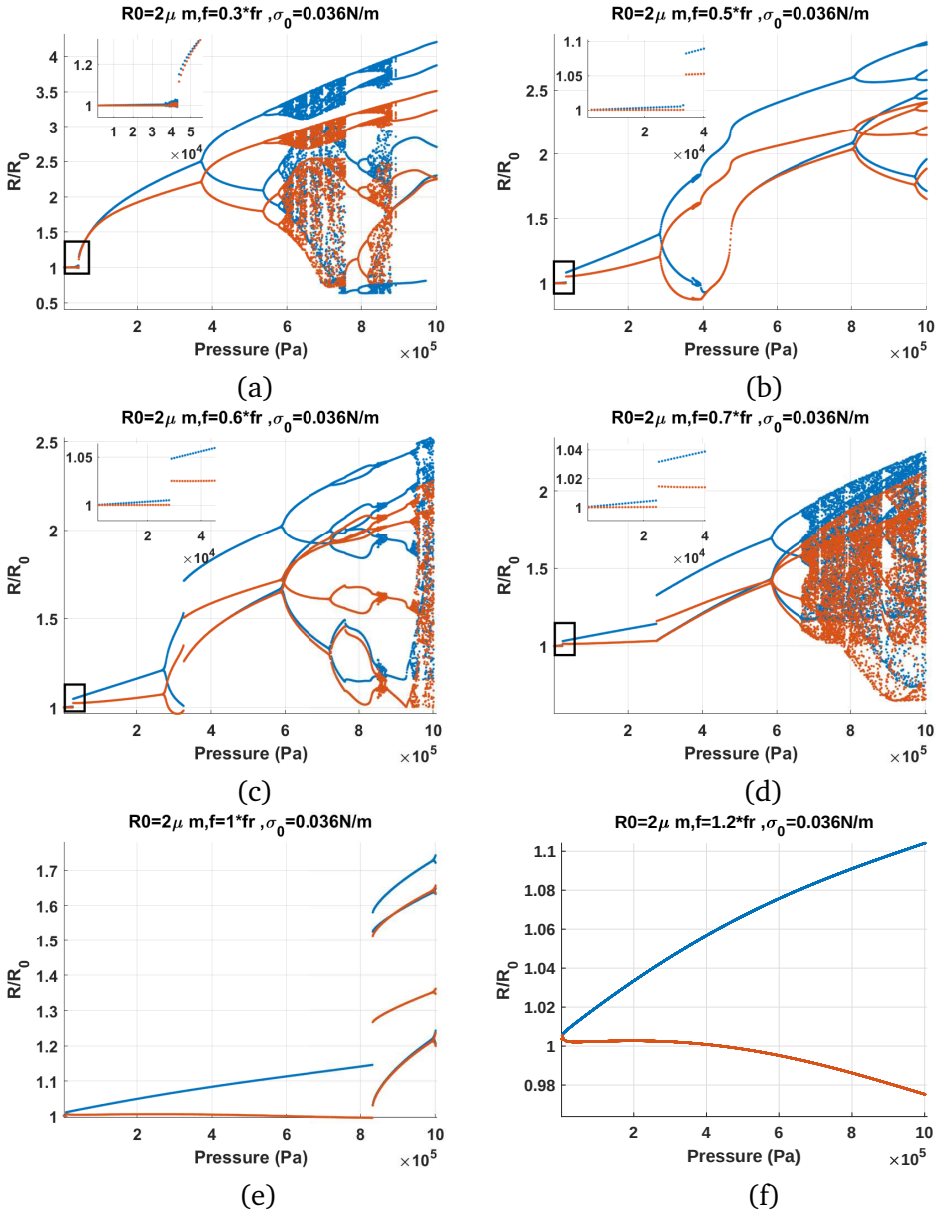

Figure 11.19: Bifurcation structure of the R/R_0 of the C3F8 coated bubble with $R_0 = 2\mu m$ and $\sigma_0 = 0.36N/m$ as a function of pressure when sonicated with: a)$f = 0.3f_r$, b)$f = 0.5f_r$, c)$f = 0.8f_r$, d)$f = 0.9f_r$, e)$f = f_r$ & f)$f = 1.2f_r$.

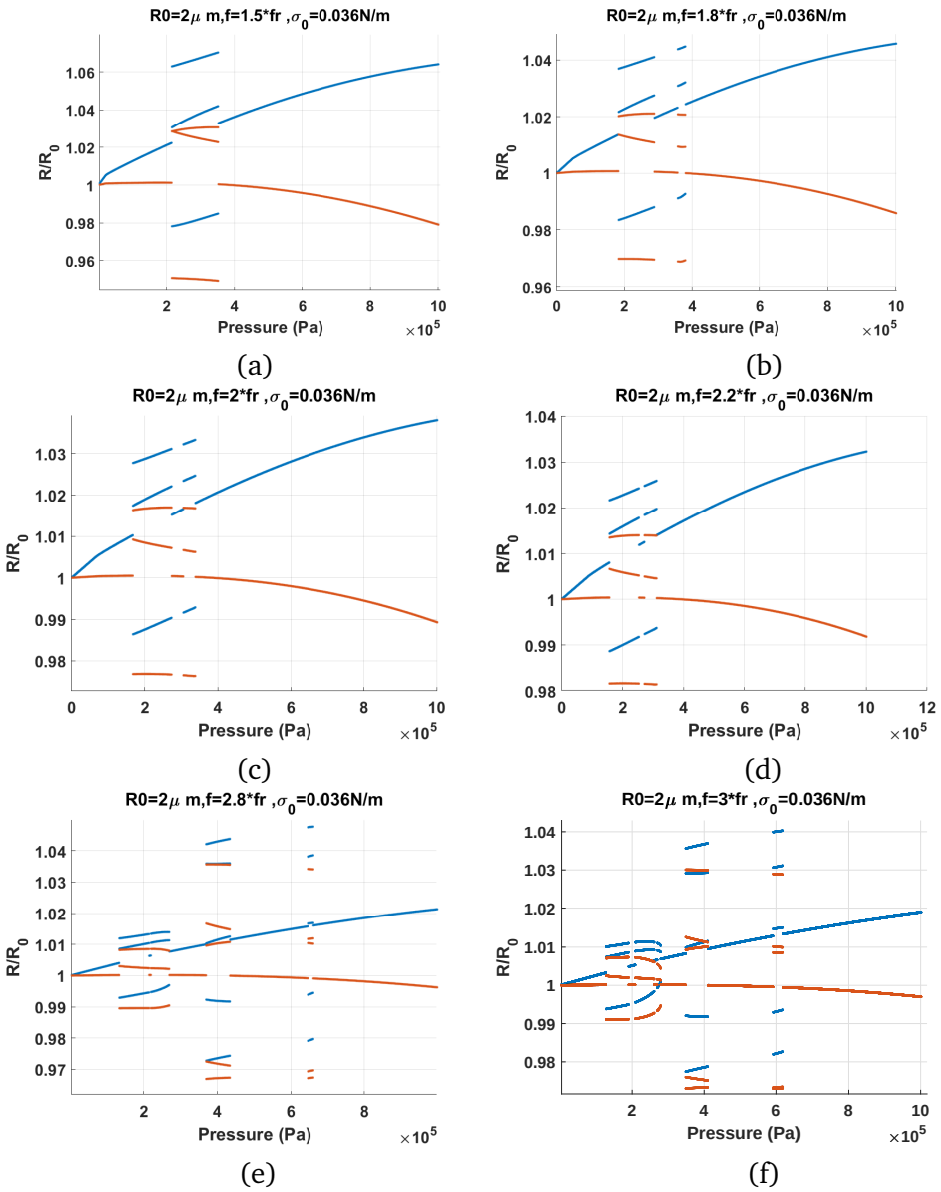

Figure 11.20: Bifurcation structure of the R/R_0 of the C3F8 coated bubble with $R_0 = 2\mu m$ and $\sigma_0 = 0.36N/m$ as a function of pressure when: a)$f = 1.5f_r$, b)$f = 1.8f_r$, c)$f = 2f_r$, d)$f = 2.4f_r$, e)$f = 2.8f_r$ & f)$f = 3f_r$.

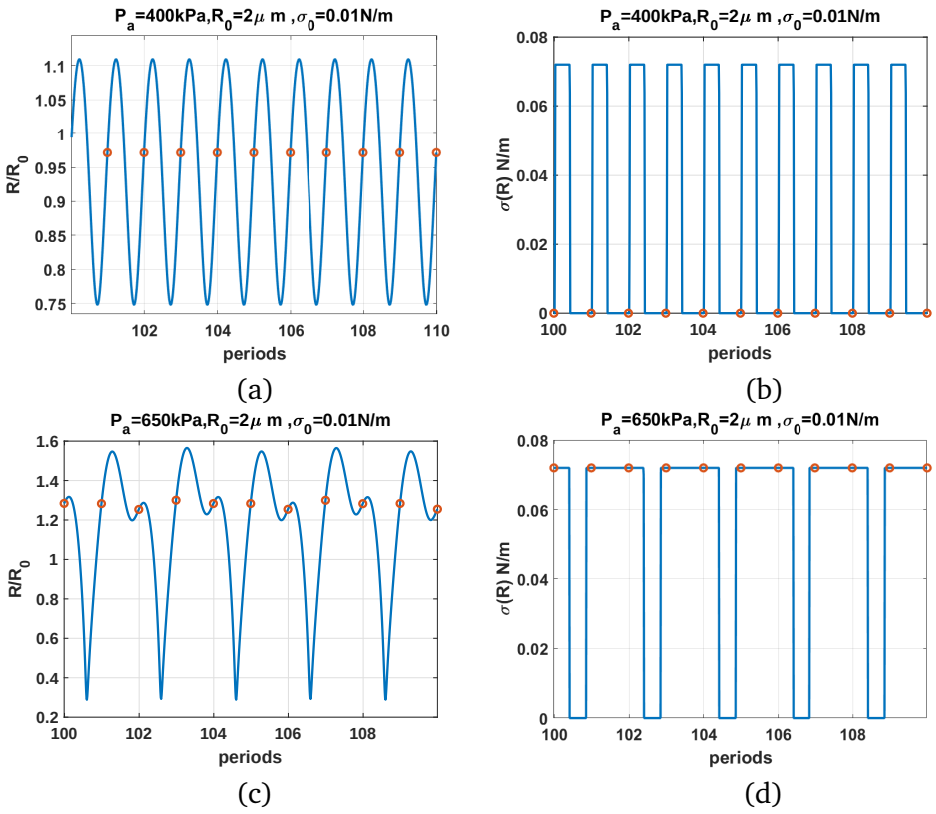

Figure 11.21: R/R_0 (left) & $\sigma(R)$ (right) as function of the driving periods for a C3F8 coated bubble with $R_0 = 2\mu m$ with $\sigma_0 = 0.062N/m$ when $f = 1.2f_r$ for: $a\&b$-$P_a = 400kPa$, $c\&d$-$P_a = 650kPa$. (Red circles correspond to the location of R(t) at each period)

of the driving periods (Fig. 11.21d) exhibits an asymmetrical behavior between the buckled and the ruptured state. The bubble spends a longer time duration at the ruptured stage than the buckled stage. As a result, the bubble buckles 5 times and ruptures 5 times within 10 driving periods. Thus oscillations become P2 again.

11.5 Summary of the results and discussion

11.5.1 Sonication with $f < f_r$

First the findings related to the sonications with frequencies smaller than resonance are presented.

11.5.1.1 $\sigma_0 = 0, 0.01, 0.062$ and $0.072N/m$

1- SuH regimes are generated at lower excitation thresholds compared to the uncoated bubbles. The bubbles initially at the buckled or the ruptured stages exhibit SuH regime of oscillations at the lowest pressure threshold of 1 kPa. Thus applications of coated bubbles with initial surface tension close to $0N/m$ or $0.072N/m$ have the potential to increase the contrast in super harmonic imaging (e.g. [94]). Due to the lower threshold of the SuH generation, the amplitude of the generated harmonics in tissue will be smaller. Therefore, the contrast to tissue ratio may be higher.

2- The sudden increase in the bubble oscillation amplitude (SN bifurcation or the inflection point in bifurcation diagrams) occurs at lower excitation amplitudes when compared to the uncoated bubble and coated bubbles with linear viscoelastic behavior [56]. The SN bifurcation is more pronounced in case of the bubbles with $\sigma_0 = 0.01N/m$ and $\sigma_0 = 0.062N/m$. The wall velocity stays in phase with the driving sound field for a larger pressure range. The reason for the lower pressure threshold for the SN and lower frequencies of PDf_r is the fast decrease of the resonance frequency with increasing pressure. Overvelde et al. [68] has experimentally and numerically shown that for coated microbubbles undergoing buckling, the nonlinear resonance behavior is enhanced at pressures as low as 10 kPa. Helfield and Goertz [77] experimentally observed the enhanced nonlinear resonance behavior of the lipid coated microbubbles at pressures of 13-25kPa. The SN bifurcation can have applications in amplitude modulation techniques [95].

3- For the coated bubble with $\sigma_0 = 0N/m$, PD occurs at a higher pressure threshold compared to the uncoated bubble, and for other cases, PD occurs at lower pressure thresholds.

4- For $0.6f_r \leq f \leq 0.7f_r$ and for coated bubbles with $\sigma_0 = 0.01$ & $0.062N/m$, P2 oscillations (with resonant 3/2 UHs) are generated within non-destructive regimes of oscillations $R_{max}/R_0 < 2$. For the uncoated bubble and coated bubbles with $\sigma_0 = 0$ & $0.072N/m$, PD most likely results in bubble destruction. In [34, 58] we have shown that in case of uncoated bubbles PD may be concomitant with bubble destruction when the bubble is sonicated with $f \leq f_r$. The stabilizing effect of the coating with $\sigma_0 = 0.01$ & $0.062N/m$ can enhance the non-destructive PD for the frequencies below resonance.

5- In case of coated bubbles with $\sigma_0 = 0.01$ & $0.062N/m$, PDf_{sh} can occur at frequencies as low as $0.6f_r$. In such cases two SN bifurcations are observed with increasing pressure. The first SN occurs at a lower pressure threshold and transfers a P1 oscillation to a P1 oscillation of higher amplitude. The second SN occurs at a higher pressure and transfers a P2 oscillation to a P2 oscillation of higher amplitude. In [58] we have shown that PDf_{sh} typically occurs at $1.5f_r < f < 2f_r$ and can lead to oversaturation of the 1/2 order SH component of the scattered signal. The enhanced nonlinear resonance behavior of the coating thus shifts the PDf_{sh} to frequencies below resonance. The occurrence of the two SNs may have potential applications in increasing the contrast in multi-pulse amplitude modulation techniques.

11.5.1.2 Case of the coated bubble with $\sigma_0 = 0.036N/m$

1- Compared to the uncoated bubble and coated bubbles with linear viscoelastic behavior (PDf_r is within $0.5f_r < f < f_r$ [56]), the frequency of PDf_r is much lower (as low as $0.3f_r$).

2- PDf_{sh} can occur even at $f = 0.5f_r$. In case of the uncoated bubble PDf_{sh} occurs at $1.5f_r < f < 2f_r$ [58].

3- For $0.5f_r \leq f \leq 0.7f_r$ and with increasing pressure, two SN occur; the first one transfers a P1 oscillation regime to a higher amplitude P1 and the second one which is at a higher pressure transfers a P1 or a P2 oscillation regime to a higher amplitude P2 regime.

11.5.2 $f \geq f_r$

In this section findings of the sonications with frequencies above resonance are summarized. Such a frequency range is typically used in SH imaging of microbubbles in contrast enhanced ultrasound [20, 68, 78, 96].

11.5.2.1 Cases of the coated bubbles wiht $\sigma_0 = 0, 0.01, 0.062$ and $0.072N/m$

1- For the coated bubbles with $\sigma_0 = 0N/m$ & $\sigma_0 = 0.072N/m$ sonicated with $f_r \leq f \leq 1.5f_r$ and for the ones with $\sigma_0 = 0.01N/m$ & $\sigma_0 = 0.062N/m$ sonicated with $f = f_r$, the bifurcation structure is similar to the case of sonication with PDf_{sh} in case of the uncoated bubbles. P2 oscillations undergo a SN from a P2 oscillation to a P2 oscillation of higher amplitude. The nonlinear behavior of the coating thus reduces the PDf_{sh} to frequencies below $1.5f_r$. Thus for the coated bubbles with $\sigma_0 = 0N/m$ & $\sigma_0 = 0.072N/m$, sonication with $f_r \leq f \leq 1.5f_r$ may result in a stronger 1/2 order SH component of the scattered signal because of the over-saturation that takes place when $f = PDf_{sh}$.

2- For the coated bubbles with $\sigma_0 = 0N/m$ & $\sigma_0 = 0.072N/m$ that are insonated with $1.8f_r \leq f \leq 2.2f_r$, with increasing pressure, P2 oscillations are generated through a PD (at a pressure threshold of 1 kPa), disappear and then are regenerated at a higher pressure as a higher amplitude P2 or P3. The second P2 is similar to the dynamics of the uncoated bubble undergoing a SN to P2 when $f = PDf_{sh}$. The second P3 is similar to the dynamics of the uncoated bubble undergoing a SN to P3 when $f = \approx 3f_r$. In [73], the disappearance of SH oscillations is referred to as an "unexpected standstill" of SHs. This means that, in the case of a bubble able to generate a stable subharmonic oscillation, the subharmonic emission disappears if the acoustic pressure is raised above a second pressure threshold. The subharmonic standstill however, is a reversible [73]; that is, if the acoustic pressure is decreased again, the bubbles start generating subharmonics one more time [73]. Thus, disappearance is not due to the bubble destruction. Prior works on subharmonics performed on a population of microbubbles did not report this kind of behavior because it was probably "masked" by the overall response of the several other bubbles within the same sample volume that experience different pressure amplitudes [73]. The standstill of subharmonic emission also was not explained by the numerical studies of the nonlinear models of the bubble dynamics. Here, we show that the

disappearance of the SHs is due to the symmetric buckling and rupture of the shell at moderate pressures. At higher pressures, similar to the lower pressures the buckling and rupture of the shell becomes asymmetric. This manifests itself in the re-generation of P2 signals. Above the second pressure threshold, the bubble spends more time in the ruptured stage than the buckling stage. This exposes the bare gas to water for a longer duration and thus can explain the reduced stability of SH oscillations when they were re-generated [73].

In sensitive therapeutic applications like blood-brain barrier opening, the SH components of the scattered pressure by microbubbles are commonly used as a signature for quantifying the nonlinear oscillations of the bubble cloud and treatment efficacy [97,98]. Due to the strong interplay between stable and inertial cavitation regimes, undersatning the origin and stability of P2 oscillation regimes is crucial. Thus, the information on the generation, disappearance, amplification and stability of the P2 oscillations that is obtained here, provides a framework for the analysis of the optimization of SH oscillations in applications.

3- For the coated bubbles with $\sigma_0 = 0.01N/m$ & $\sigma_0 = 0.062N/m$ sonicated with $f = 1.5f_r$, with increasing pressure, P2 oscillations are generated through a PD and then disappear via a SN. Above a second pressure threshold, a P3 oscillation regime occurs via a SN from a P1 regime. This is similar to the dynamics of the uncoated bubble undergoing a SN to P3 when $f \approx 3f_r$. The pressure threshold for PD is smaller than the uncoated bubbles [40] and the coated bubbles with linear viscoelastic behavior [38].

4- For the coated bubbles with $\sigma_0 = 0.01N/m$ & $\sigma_0 = 0.062N/m$ sonicated with $1.8f_r \leq f \leq 2f_r$, with increasing pressure, P2 oscillations are generated through a PD and then are amplified via a SN. P2 oscillations are then transfer to a P1 regime via another SN. Bubble oscillations remain P1 for the rest of the pressure range studied in this paper.

5- For the coated bubbles with $\sigma_0 = 0N/m$ & $\sigma_0 = 0.072n/m$ and for $2.8f_r \leq f \leq 3.1f_r$, P3 may occurs at very low pressure amplitudes (as low as 1 kPa). Chaos can emerge at pressures lower than 200 kPa.

6- The lowest pressure threshold for the chaotic oscillations are for the coated bubbles with $\sigma_0 = 0.01N/m$ & $\sigma_0 = 0.062N/m$ when sonicated with $2.8f_r \leq f \leq 3f_r$ which is followed by the emergence of P3 out of the chaotic window. To our best knowledge, such low pressure thresholds for chaotic oscillations has not been observed in a bubble oscillator. The pressure threshold for P3

is approximately 5 times smaller than the uncoated counterpart.

Here we identified several different types of SN that occur with increasing pressure in the oscillations of the lipid coated bubbles. This information, can provide the fundamental framework for the optimization of amplitude modulation techniques and SH imaging procedures. Moreover, the enhanced P3 and higher order oscillations may find potential in mixing applications and drug delivery.

In cases analyzed in this paper, $\frac{R_{max}}{R_0}$ was higher for the bubbles with a higher σ_0 because of the expansion dominated behavior of the bubble. This can be one of the reasons for the lower pressure threshold of P2 and chaotic oscillations in case of the bubble in the ruptured state.

11.5.2.2 Case of the coated bubble with $\sigma_0 = 0.036N/m$

1- For $1.5f_r \leq f \leq 3f_r$ with increasing pressure a P3 occurs via a SN through a P1 oscillation regime. The pressure threshold for P3 is about half of the uncoated counterpart. P3 disappears via a SN. A second or 3rd SN may occur with pressure increase that can lead to the regeneration of P3 or the generation of P5 or P7 oscillations. Due to the wide range of the pressure and frequency of P3 behavior for the bubbles with $\sigma_0 = 0.036N/m$, engineering of the coatings with such initial surface tensions may find potential in higher order SH imaging with potential higher resolution and contrast. In (Chapter 10) [99] we have shown that the 2/3 or 3/4 order SHs are stronger than 1/2 order SHs and due to their close proximity to the transducer central frequency they may be detected with superior sensitivity.

11.6 Conclusion and future work

In this work, the bifurcation structure of the lipid coated bubbles undergoing buckling and rupture was studied extensively. Our results further confirmed that the rapid variation of the effective surface tension and buckling and rupture of the coating enhances the generation of nonlinear behavior including higher order SHs, SuHs and chaos. We showed for the first time that P2 and P3 can occur at pressures as low as 1 kPa ($\approx 1\%$ of the ambient pressure). Existence of chaos was confirmed at pressures as low as 10 kPa. The closer the initial surface tension of the bubble to the

buckling stage or the ruptured stage, the lower the pressure threshold for the nonlinear behavior. We showed that rapid variations of the surface tension on the bubble may not be enough for enhanced non-linearity. In case of asymmetrical variations of the surface tension between buckling and rupture, nonlinear behavior is enhanced. However, symmetrical behavior of the effective surface tension may suppress the non-linearity.

In this paper and for simplicity we only analyzed the radial oscillations of the bubble. Future, work can be extended by analyzing the scattered pressure of the bubbles to find the regions of SH power enhancement. Bubble-bubble interaction should also be considered as in applications bubbles exist in poly-disperse clouds. We have shown in [100] that the bubble cluster may exhibit collective behavior dominated by the response of the larger bubbles. Future studies need to look into the potential collective behavior of the lipid coated bubbles at lower excitation pressure amplitudes.

Bibliography

[1] Lauterborn, Wernend Thomas Kurz. ”Physics of bubble oscillations.” Reports on progress in physics 73, no. 10 (2010): 106501.

[2] Parlitz, U., V. Englisch, C. Scheffczyk, and W. Lauterborn. ”Bifurcation structure of bubble oscillators.” The Journal of the Acoustical Society of America 88, no. 2 (1990): 1061-1077.

[3] Lauterborn, Werner, and Joachim Holzfuss. ”Acoustic chaos.” International Journal of bifurcation and Chaos 1, no. 01 (1991): 13-26.

[4] Maisonhaute, Emmanuel, Cesar Prado, Paul C. White, and Richard G. Compton. ”Surface acoustic cavitation understood via nanosecond electrochemistry. Part III: Shear stress in ultrasonic cleaning.” Ultrasonics sonochemistry 9, no. 6 (2002): 297-303.

[5] Yusof, Nor Saadah Mohd, Bandar Babgi, Yousef Alghamdi, Mecit Aksu, Jagannathan Madhavan, and Muthupandian Ashokkumar. ”Physical and chemical effects of acoustic cavitation in selected ultrasonic cleaning applications.” Ultrasonics sonochemistry 29 (2016): 568-576.

[6] Mason, Timothy J., Larysa Paniwnyk, and J. P. Lorimer. ”The uses of ultrasound in food technology.” Ultrasonics sonochemistry 3, no. 3 (1996): S253-S260.

[7] Suslick, Kenneth S. ”Sonochemistry.” science 247, no. 4949 (1990): 1439-1445.

[8] Mason, Timothy J., and Timothy J. Mason. Sonochemistry. Vol. 2. New York: Oxford University Press, 1999.

[9] Crum, Lawrence A., Timothy J. Mason, Jacques L. Reisse, and Kenneth S. Suslick, eds. Sonochemistry and sonoluminescence. Vol. 524. Springer Science & Business Media, 2013.

[10] Brenner, Michael P., Sascha Hilgenfeldt, and Detlef Lohse. ”Single-bubble sonoluminescence.” Reviews of modern physics 74, no. 2 (2002): 425.

[11] Liu, Robin H., Jianing Yang, Maciej Z. Pindera, Mahesh Athavale, and Piotr Grodzinski. ”Bubble-induced acoustic micromixing.” Lab on a Chip 2, no. 3 (2002): 151-157.

[12] Collis, James, Richard Manasseh, Petar Liovic, Paul Tho, Andrew Ooi, Karolina Petkovic-Duran, and Yonggang Zhu. ”Cavitation microstreaming and stress fields created by microbubbles.” Ultrasonics 50, no. 2 (2010): 273-279.

[13] Kooiman, Klazina, Hendrik J. Vos, Michel Versluis, and Nico de Jong. ”Acoustic behavior of microbubbles and implications for drug delivery.” Advanced drug delivery reviews 72 (2014): 28-48.

[14] Roovers, S., Segers, T., Lajoinie, G., Deprez, J., Versluis, M., De Smedt, S.C. and Lentacker, I., 2019. The role of ultrasound-driven microbubble dynamics in drug delivery: from microbubble fundamentals to clinical translation. Langmuir.

[15] Mainprize, T., Lipsman, N., Huang, Y., Meng, Y., Bethune, A., Ironside, S., Heyn, C., Alkins, R., Trudeau, M., Sahgal, A. and Perry, J., 2019. Blood-brain barrier opening in primary brain tumors with non-invasive MR-guided focused ultrasound: a clinical safety and feasibility study. Scientific reports, 9(1), p.321.

[16] McMahon, D., Poon, C. and Hynynen, K., 2019. Evaluating the safety profile of focused ultrasound and microbubble-mediated treatments to increase blood-brain barrier permeability. Expert opinion on drug delivery, 16(2), pp.129-142.

[17] Liu, J.B., Merton, D.A., Forsberg, F. and Goldberg, B.B., 2019. Contrast-enhanced ultrasound imaging. In Diagnostic Ultrasound (pp. 51-74). CRC Press.

[18] Nam, Kibo, Ji-Bin Liu, John R. Eisenbrey, Maria Stanczak, Priscilla Machado, Jingzhi Li, Zhaojun Li, Ying Wei, and Flemming Forsberg. ”Three-Dimensional Subharmonic Aided Pressure Estimation for Assessing Arterial Plaques in a Rabbit Model.” Journal of Ultrasound in Medicine 38, no. 7 (2019): 1865-1873.

[19] Haworth, K.J., Mast, T.D., Radhakrishnan, K., Burgess, M.T., Kopechek, J.A., Huang, S.L., McPherson, D.D. and Holland, C.K., 2012. Passive imaging with pulsed ultrasound insonations. The Journal of the Acoustical Society of America, 132(1), pp.544-553.

[20] Goertz, D.E., Frijlink, M.E., Tempel, D., Bhagwandas, V., Gisolf, A., Krams, R., de Jong, N. and van der Steen, A.F., 2007. Subharmonic contrast intravascular ultrasound for vasa vasorum imaging. Ultrasound in medicine & biology, 33(12), pp.1859-1872.

[21] Esche R 1952 Untersuchung der Schwingungskavitation in Flussigkeiten (Investigation of acoustic cavitation in liquids) Acustica 2 AB208–18

[22] Bohn L 1957 Schalldruckverlauf und Spektrum bei der Schwingungskavitation (Pressure and spectra in acoustic cavitation) Acustica 7 201–16

[23] Holt, R. Glynn, D. Felipe Gaitan, Anthony A. Atchley, and Joachim Holzfuss. "Chaotic sonoluminescence." Physical review letters 72, no. 9 (1994): 1376.

[24] Dam, J.S., Levinsen, M.T. and Skogstad, M., 2002. Period-doubling bifurcations from breaking the spherical symmetry in sonoluminescence: Experimental verification. Physical review letters, 89(8), p.084303.

[25] Lauterborn, W., Kurz, T., Mettin, R. and Ohl, C.D., 1999. Experimental and theoretical bubble dynamics. Advances in chemical physics, 110, pp.295-380.

[26] Lauterborn W and Cramer E 1981 On the dynamics of acoustic cavitation noise spectra Acustica 49 280–7

[27] Cramer E and Lauterborn W 1982 Acoustic cavitation noise spectra Appl. Sci. Res. 38 209–14

[28] Lauterborn W 1986 Acoustic chaos Physics Today 39 S-4–S-5

[29] Lauterborn W, Schmitz E and Judt A 1993 Experimental approach to a complex acoustic system Int. J. Bifurcation Chaos 3 635–42

[30] Lauterborn, W., 1976. Numerical investigation of nonlinear oscillations of gas bubbles in liquids. The Journal of the Acoustical Society of America, 59(2), pp.283-293.

[31] Prosperetti, A., 1974. Nonlinear oscillations of gas bubbles in liquids: steady-state solutions. The Journal of the Acoustical Society of America, 56(3), pp.878-885.

[32] Lauterborn, W. and Koch, A., 1987. Holographic observation of period-doubled and chaotic bubble oscillations in acoustic cavitation. Physical Review A, 35(4), p.1974.

[33] Ohl, C.D., Kurz, T., Geisler, R., Lindau, O. and Lauterborn, W., 1999. Bubble dynamics, shock waves and sonoluminescence. Philosophical Transactions of the Royal Society of London. Series A: Mathematical, Physical and Engineering Sciences, 357(1751), pp.269-294.

[34] Sojahrood, A.J., Earl, R., Kolios, M.C. and Karshafian, R., 2020. Investigation of the 1/2 order subharmonic emissions of the period-2 oscillations of an ultrasonically excited bubble. Physics Letters A, p.126446.

[35] Behnia, S., Sojahrood, A.J., Soltanpoor, W. and Sarkhosh, L., 2009. Towards classification of the bifurcation structure of a spherical cavitation bubble. Ultrasonics, 49(8), pp.605-610.

[36] Varga, R. and Hegedűs, F., 2016. Classification of the bifurcation structure of a periodically driven gas bubble. Nonlinear Dynamics, 86(2), pp.1239-1248.

[37] AJ sojahrood, H. Haghi, R. Karshafian and M.C. Kolios, Classification of the mechanisms of energy loss in the nonlinear oscillations of coated and uncoated bubbles, Arxiv 2020

[38] Sojahrood, A.J. and Kolios, M.C., 2012. Classification of the nonlinear dynamics and bifurcation structure of ultrasound contrast agents excited at higher multiples of their resonance frequency. Physics Letters A, 376(33), pp.2222-2229.

[39] Hegedűs, F., 2014. Stable bubble oscillations beyond Blake's critical threshold. Ultrasonics, 54(4), pp.1113-1121.

[40] Hegedűs, F., Hős, C. and Kullmann, L., 2012. Stable period 1, 2 and 3 structures of the harmonically excited Rayleigh–Plesset equation applying low ambient pressure. The IMA Journal of Applied Mathematics, 78(6), pp.1179-1195.

[41] Sojahrood, A.J., Karshafian, R. and Kolios, M.C., 2012, October. Detection and characterization of higher order nonlinearities in the oscillations of Definity at higher frequencies and very low acoustic pressures. In 2012 IEEE International Ultrasonics Symposium (pp. 1193-1196). IEEE.

[42] Sojahrood, A.J., Karshafian, R. and Kolios, M.C., 2012, October. Numerical and experimental classification of the oscillations of single isolated microbubbles: Occurrence of higher order subharmonics. In 2012 IEEE International Ultrasonics Symposium (pp. 402-405). IEEE.

[43] Jafari Sojahrood, A., Karshafian, R. and C. Kolios, M., 2013, June. Bifurcation structure of the ultrasonically excited microbubbles undergoing buckling and rupture. In Proceedings of Meetings on Acoustics ICA2013 (Vol. 19, No. 1, p. 075097). ASA.

[44] Hegedűs, F., 2016. Topological analysis of the periodic structures in a harmonically driven bubble oscillator near Blake's critical threshold: Infinite sequence of two-sided Farey ordering trees. Physics Letters A, 380(9-10), pp.1012-1022.

[45] Hegedűs, F. and Klapcsik, K., 2015. The effect of high viscosity on the collapse-like chaotic and regular periodic oscillations of a harmonically excited gas bubble. Ultrasonics sonochemistry, 27, pp.153-164.

[46] Klapcsik, K. and Hegedűs, F., 2019. Study of non-spherical bubble oscillations under acoustic irradiation in viscous liquid. Ultrasonics sonochemistry, 54, pp.256-273.

[47] Behnia, S., Sojahrood, A.J., Soltanpoor, W. and Jahanbakhsh, O., 2009. Suppressing chaotic oscillations of a spherical cavitation bubble through applying a periodic perturbation. Ultrasonics sonochemistry, 16(4), pp.502-511.

[48] Klapcsik, K., Varga, R. and Hegedűs, F., 2018. Bi-parametric topology of subharmonics of an asymmetric bubble oscillator at high dissipation rate. Nonlinear Dynamics, 94(4), pp.2373-2389.

[49] Hegedűs, F., Lauterborn, W., Parlitz, U. and Mettin, R., 2018. Non-feedback technique to directly control multistability in nonlinear oscillators by dual-frequency driving. Nonlinear Dynamics, 94(1), pp.273-293.

[50] Hegedűs, F. and Kalmár, C., 2018. Dynamic stabilization of an asymmetric nonlinear bubble oscillator. Nonlinear Dynamics, 94(1), pp.307-324.

[51] Zhang, Y., 2018. Chaotic oscillations of gas bubbles under dual-frequency acoustic excitation. Ultrasonics sonochemistry, 40, pp.151-157.

[52] Zhang, Y. and Li, S., 2017. Combination and simultaneous resonances of gas bubbles oscillating in liquids under dual-frequency acoustic excitation. Ultrasonics sonochemistry, 35, pp.431-439.

[53] Zhang, Y., Du, X., Xian, H. and Wu, Y., 2015. Instability of interfaces of gas bubbles in liquids under acoustic excitation with dual frequency. Ultrasonics sonochemistry, 23, pp.16-20.

[54] Zhang, Y. and Li, S., 2016. The secondary Bjerknes force between two gas bubbles under dual-frequency acoustic excitation. Ultrasonics sonochemistry, 29, pp.129-145.

[55] Zhang, Y. and Li, S., 2015. Acoustical scattering cross section of gas bubbles under dual-frequency acoustic excitation. Ultrasonics sonochemistry, 26, pp.437-444.

[56] Sojahrood, A.J., Falou, O., Earl, R., Karshafian, R. and Kolios, M.C., 2015. Influence of the pressure-dependent resonance frequency on the bifurcation structure and backscattered pressure of ultrasound contrast agents: a numerical investigation. Nonlinear Dynamics, 80(1-2), pp.889-904.

[57] Sojahrood, A.J., Wegierak, D., Haghi, H., Karshfian, R. and Kolios, M.C., 2019. A simple method to analyze the super-harmonic and ultra-harmonic behavior of the acoustically excited bubble oscillator. Ultrasonics sonochemistry, 54, pp.99-109.

[58] A.J. Sojahrood, R.E. Earl, M.C. Kolios and R. Karshafian Nonlinear dynamics of acoustic bubbles excited by their pressure dependent subharmonic resonance frequency: oversaturation and enhancement of the subharmonic signal. arxiv 2019

[59] Intensified non-linearity at very low amplitude high frequency excitation of nano-micron sized lipid coated bubbles, Arxiv 2019

[60] Kamaev, P.P., Hutcheson, J.D., Wilson, M.L. and Prausnitz, M.R., 2004. Quantification of optison bubble size and lifetime during sonication dominant role of secondary cavitation bubbles causing acoustic bioeffects. The Journal of the Acoustical Society of America, 115(4), pp.1818-1825.

[61] Chitnis, P.V., Lee, P., Mamou, J., Allen, J.S., Böhmer, M. and Ketterling, J.A., 2011. Rupture threshold characterization of polymer-shelled ultrasound contrast agents subjected to static overpressure. Journal of applied physics, 109(8), p.084906.

[62] Marmottant, P., Van Der Meer, S., Emmer, M., Versluis, M., De Jong, N., Hilgenfeldt, S. and Lohse, D., 2005. A model for large amplitude oscillations of coated bubbles accounting for buckling and rupture. The Journal of the Acoustical Society of America, 118(6), pp.3499-3505.

[63] Versluis, M., 2010, December. Nonlinear behavior of ultrasound contrast agent microbubbles and why shell buckling matters. In Proceedings of 20th International Congress on Acoustics, Sydney, Australia.

[64] Frinking, P.J., Gaud, E., Brochot, J. and Arditi, M., 2010. Subharmonic scattering of phospholipid-shell microbubbles at low acoustic pressure amplitudes. IEEE transactions on ultrasonics, ferroelectrics, and frequency control, 57(8), pp.1762-1771.

[65] Prosperetti, A., 2013. A general derivation of the subharmonic threshold for non-linear bubble oscillations. The Journal of the Acoustical Society of America, 133(6), pp.3719-3726.

[66] Sijl, J., Dollet, B., Overvelde, M., Garbin, V., Rozendal, T., de Jong, N., Lohse, D. and Versluis, M., 2010. Subharmonic behavior of phospholipid-coated ultrasound contrast agent microbubbles. The Journal of the Acoustical Society of America, 128(5), pp.3239-3252.

[67] De Jong, N., Emmer, M., Chin, C.T., Bouakaz, A., Mastik, F., Lohse, D. and Versluis, M., 2007. "Compression-only" behavior of phospholipid-coated contrast bubbles. Ultrasound in medicine & biology, 33(4), pp.653-656.

[68] Overvelde, M., Garbin, V., Sijl, J., Dollet, B., De Jong, N., Lohse, D. and Versluis, M., 2010. Nonlinear shell behavior of phospholipid-coated microbubbles. Ultrasound in medicine & biology, 36(12), pp.2080-2092.

[69] Luan, Y., Faez, T., Gelderblom, E., Skachkov, I., Geers, B., Lentacker, I., van der Steen, T., Versluis, M. and de Jong, N., 2012. Acoustical properties of individual liposome-loaded microbubbles. Ultrasound in medicine & biology, 38(12), pp.2174-2185.

[70] De Jong, N., Emmer, M., Van Wamel, A. and Versluis, M., 2009. Ultrasonic characterization of ultrasound contrast agents. Medical & biological engineering & computing, 47(8), pp.861-873.

[71] Shekhar, H., Awuor, I., Thomas, K., Rychak, J.J. and Doyley, M.M., 2014. The delayed onset of subharmonic and ultraharmonic emissions from a phospholipid-shelled microbubble contrast agent. Ultrasound in medicine & biology, 40(4), pp.727-738.

[72] Emmer, M., Van Wamel, A., Goertz, D.E. and De Jong, N., 2007. The onset of microbubble vibration. Ultrasound in medicine & biology, 33(6), pp.941-949.

[73] Biagi, E., Breschi, L., Vannacci, E. and Masotti, L., 2007. Stable and transient subharmonic emissions from isolated contrast agent microbubbles. IEEE transactions on ultrasonics, ferroelectrics, and frequency control, 54(3), pp.480-497.

[74] P. M. Shankar, P. D. Krishna, and V. L. Newhouse, “Subharmonic backscattering from ultrasound contrast agents,” J. Acoust. Soc. Am., vol. 106, no. 4, pp. 2101–2110, 1999.

[75] E. Kimmel, B. Krasovitski, A. Hoogi, D. Razansky, and D. Adam, “Subharmonic response of encapsulated microbubbles: Conditions for existence and amplification,” Ultrasound Med. Biol., vol. 33, no. 11, pp. 1767–1776, 2007.

[76] O. Lotsberg, J. M. Hovem, and B. Aksum, “Experimental observation of subharmonic oscillations in Infoson bubbles,” J. Acoust. Soc. Am., vol. 99, no. 3, pp. 1366–1369, 1996

[77] Helfield, B.L. and Goertz, D.E., 2013. Nonlinear resonance behavior and linear shell estimates for Definity™ and MicroMarker™ assessed with acoustic microbubble spectroscopy. The Journal of the Acoustical Society of America, 133(2), pp.1158-1168.

[78] Helfield, B.L., Cherin, E., Foster, F.S. and Goertz, D.E., 2012. Investigating the subharmonic response of individual phospholipid encapsulated microbubbles at high frequencies: A comparative study of five agents. Ultrasound in medicine & biology, 38(5), pp.846-863.

[79] Keller, J.B. & Miksis M., Bubble oscillations of large amplitude, ., *J. Acoust. Soc. Am.* 68 (1980) 628–633.

[80] Hoff, L., Sontum, P.C. and Hovem, J.M., 2000. Oscillations of polymeric microbubbles: Effect of the encapsulating shell. The Journal of the Acoustical Society of America, 107(4), pp.2272-2280.

[81] Morgan, K.E., Allen, J.S., Dayton, P.A., Chomas, J.E., Klibaov, A.L. and Ferrara, K.W., 2000. Experimental and theoretical evaluation of microbubble behavior: Effect of transmitted phase and bubble size. IEEE transactions on ultrasonics, ferroelectrics, and frequency control, 47(6), pp.1494-1509.

[82] Segers, T., Gaud, E., Versluis, M. and Frinking, P., 2018. High-precision acoustic measurements of the nonlinear dilatational elasticity of phospholipid coated monodisperse microbubbles. Soft matter, 14(47), pp.9550-9561.

[83] Segers, T., de Jong, N. and Versluis, M., 2016. Uniform scattering and attenuation of acoustically sorted ultrasound contrast agents: Modeling and experiments. The Journal of the Acoustical Society of America, 140(4), pp.2506-2517.

[84] Helfield, B.L., Leung, B.Y., Huo, X. and Goertz, D.E., 2014. Scaling of the viscoelastic shell properties of phospholipid encapsulated microbubbles with ultrasound frequency. Ultrasonics, 54(6), pp.1419-1424.

[85] Sojahrood, A.J., Li, Q., Haghi, H., Karshafian, R., Porter, T.M. and Kolios, M.C., 2018. Pressure dependence of the ultrasound attenuation and speed in bubbly media: Theory and experiment. arXiv preprint arXiv:1811.07788.

[86] Shekhar, H., Smith, N.J., Raymond, J.L. and Holland, C.K., 2018. Effect of temperature on the size distribution, shell properties, and stability of Definity®. Ultrasound in medicine & biology, 44(2), pp.434-446.

[87] Kopechek, J.A., Haworth, K.J., Raymond, J.L., Douglas Mast, T., Perrin Jr, S.R., Klegerman, M.E., Huang, S., Porter, T.M., McPherson, D.D. and Holland, C.K., 2011. Acoustic characterization of echogenic liposomes: Frequency-dependent attenuation and backscatter. The Journal of the Acoustical Society of America, 130(5), pp.3472-3481.

[88] Sojahrood, A.J., Haghi, H., Li, Q., Porter, T.M., Karshafian, R. and Kolios, M.C., 2020. Nonlinear power loss in the oscillations of coated and uncoated bubbles: Role of thermal, radiation and encapsulating shell damping at various excitation pressures. Ultrasonics sonochemistry, 66, p.105070.

[89] Toegel, Ruediger, Bruno Gompf, Rainer Pecha, and Detlef Lohse. "Does water vapor prevent upscaling sonoluminescence?." Physical review letters 85, no. 15 (2000): 3165.

[90] Prosperetti, A., Crum, L.A. and Commander, K.W., 1988. Nonlinear bubble dynamics. The Journal of the Acoustical Society of America, 83(2), pp.502-514.

[91] Leighton, T., 2012. The acoustic bubble. Academic press.

[92] Flynn, H.G., Church, C.C.: Transient pulsations of small gas bubbles in water. J. Acoust. Soc. Am. 84, 985–998 (1988)

[93] Perez, C., 2015. Characterization of Ultrasound Pressure Fields, Microbubbles and Their Interaction (Doctoral dissertation).

[94] Cherin, E., Yin, J., Forbrich, A., White, C., Dayton, P.A., Foster, F.S. and Démoré, C.E., 2019. In vitro superharmonic contrast imaging using a hybrid dual-frequency probe. Ultrasound in medicine & biology, 45(9), pp.2525-2539.

[95] Phillips, P. J. "Contrast pulse sequences (CPS): imaging nonlinear microbubbles." In 2001 IEEE Ultrasonics Symposium. Proceedings. An International Symposium (Cat. No. 01CH37263), vol. 2, pp. 1739-1745. IEEE, 2001.

[96] Goertz, D.E., Cherin, E., Needles, A., Karshafian, R., Brown, A.S., Burns, P.N. and Foster, F.S., 2005. High frequency nonlinear B-scan imaging of microbubble contrast agents. IEEE transactions on ultrasonics, ferroelectrics, and frequency control, 52(1), pp.65-79.

[97] M. A. O'Reilly and K. Hynynen, (2012) Blood-brain barrier: Real-time feedback-controlled focused ultrasound disruption by using an acoustic emission-based controller, Radiology 263, 96.

[98] C. H. Tsai, J. W. Zhang, Y. Y. Liao, and H. L. Liu, 2016. Real-time monitoring of focused ultrasound blood-brain barrier opening via subharmonic acoustic emission detection: Implementation of confocal dual-frequency piezoelectric transducers, Phys. Med. Biol. 61, 2926

[99] A.J. Sojahrood et al, 2020. Intensified non-linearity at very low amplitudes high frequency ultrasound excitations of lipid coated microbubbles, Arxiv 2020

[100] Haghi, H., Sojahrood, A.J. and Kolios, M.C., 2019. Collective nonlinear behavior of interacting polydisperse microbubble clusters. Ultrasonics sonochemistry, 58, p.104708.

Chapter 12

Discussion and Conclusions

12.1 Major contributions

In this thesis, the nonlinear dynamics of the uncoated and coated bubbles with linear visco-elasticity has been extensively studied and classified using the methods of nonlinear dynamics and chaos. Next, the complex influence of the coating undergoing buckling and rupture is investigated. Using the information of the classified dynamics of the uncoated bubbles, the complex influence of the coating on the bubble dynamics is analyzed and classified numerically and experimentally. The effects of the nonlinear bubble pulsations on the attenuation and sound speed of the medium are thoroughly investigated. A new nonlinear model for calculating the attenuation and sound speed of bubbly media is developed and verified experimentally and numerically. Using the nonlinear model and the information of the classified nonlinear behavior of the bubbles, the frequency and pressure dependent attenuation and sound speed of the bubbly media are calculated and classified as a function of pressure and frequency. The major contributions of this thesis to the field of ultrasound contrast agents and bubble dynamics are as follows:

1- In Chapter 2, the analysis of the bifurcation structure of the coated bubbles with linear viscoelastic behavior revealed the possibility of maximizing the non-destructive scattered pressure by bubbles when insonating them with their pressure dependent resonance frequency.
2- In Chapter 3 we introduced a comprehensive bifurcation method to analyze the nonlinear dynamics of the acoustically excited bubbles. Using this method, in addition to the higher periods (higher order subharmonics (SHs)) and chaotic oscillations, one can differentiate ultraharmonics (UHs) from SHs. Moreover, superharmonic (SuH) regimes of the oscillations are also revealed

within the same graph. Additionally, this method can reveal information about the phase of the wall velocity with respect to the driving sound field which can be used for applications in imaging and the identification of the nonlinear resonances of the system.

3- In Chapter 4, we investigate two main period 2 (P2) oscillation regimes (1/2 order SHs) of the uncoated bubble oscillator. We show that for uncoated bubbles sonicated with $f = f_r$, P2 oscillations may be concomitant with bubble destruction. However, sonication with the SH resonance frequency $f_{sh} = 2f_r$ results in the generation of SHs at very low oscillation amplitudes and very gentle wall velocities leading to non-destructive stable cavitation.

4- It is known that SHs grow as ultrasound pressure increases and get quickly saturated. In Chapter 5, we show that for an uncoated bubble, the SH resonance frequency is pressure dependent (PDf_{sh}) and decreases with increasing pressure. Sonication with $1.5f_r < PDf_{sh} < 1.7f_r$ results in the enhancement and over-saturation of the upper limit of the SH power for non-destructive regime of oscillations.

5- In Chapter 6, we provide critical corrections to the formulations of the nonlinear power dissipation through thermal, liquid viscosity and radiation damping for the oscillations of the uncoated bubbles. We then show the nonlinear behavior of the dissipated powers as a function of pressure and frequency for the first time. We show that linear approximations can loose accuracy even at pressures as low as 20 kPa.

6- In Chapter 7, we introduced a simple model for coated bubbles with linear visco-elasticity that accounts for the radiation effects. The nonlinear terms for power dissipation through damping due to the viscosity of the coating (Cd), liquid viscosity (Ld), thermal damping (Td) and radiation damping (Rd) were derived. Through analyzing linear thermal models and full thermal models we show that the commonly used linear thermal model losses accuracy at pressures as low as 20 kPa and thus studies related to uncoated bubbles must apply the full thermal models. However, in case of the coated bubbles enclosing C3F8 type gases that are commonly used as contrast agents, the thermal effects can be ignored. We show that Rd grows faster than the other damping mechanisms and can exceed Cd, Ld and Td. The faster growth of Rd can increase the scattering to dissipation ratio (STDR) for some frequency and pressure ranges. This has several potential applications in contrast enhanced imaging ultrasound (CEUS), enhanced heating in focused ultrasound applications (FUS), drug delivery and sonochemistry.

7- In Chapter 8, using the method that is developed in Chapter 3 and extending the analysis of the Chapters 2,4 and 5 we classified the dynamics of the uncoated bubbles and coated bubbles with linear viscoelasticity. Using the derived nonlinear equations for power dissipation in Chapters 5 and 6, the power dissipations in the nonlinear regime of the oscillations are classified. Exposure parameter domains where Rd is maximized as well as domains where Td can be maximized (or minimized) are identified. Results provide the fundamental framework for the optimization of the use of coated and uncoated bubbles in CEUS, focused ultrasound (FUS) applications, drug delivery and soncohemistry.

8- In Chapter 9, we present a simple nonlinear model for the calculation of the attenuation and sound speed changes in bubbly media. Unlike current models, there are no linear approximations in this model. The accuracy of the model is verified against linear and semi-linear models and experiments. Through controlled experiments on mondisperse bubble populations, the dependence of the sound speed on the excitation pressure amplitude is identified experimentally and verified numerically. Using the information of Chapter 7, we have calculated and classified the pressure dependent attenuation and sound speed changes of the bubbly media. Using this classification scheme, we examined the feasibility of focusing ultrasound through dense bubbly clouds with minimal loss, with important applications to CEUS, FUS, drug delivery and sonochemistry. The model derived here, has potential effects for accurate characterization of the complex rheological properties of the encapsulating shell in coated bubbles. This work won the 2nd **best paper award** in the 171st Meeting of the Acoustical Society of America in Salt Lake City, Utah in 2016 [1].

9- In Chapter 10, we show experimentally that in addition to the previously identified P2 oscillations, P3, P4-1 and P4-2 oscillations can also be generated for lipid coated bubbles at very low excitation amplitudes. There is strong evidence that the mechanism for the enhancement is due to the buckling or rupture of the shell that results in asymmetrical variations of the effective surface tension as a function of time. The effective surface tension on the bubble undergoes rapid changes in the neighborhood of the buckling or rupture radii. These new identified regimes have potential advantages in diagnostic and therapeutic ultrasound. This work won the **best paper award** in the joint congress of the 21st International Congress on Acoustics, 165th Meeting of the Acoustical Society of America and the 52nd meeting of the Canadian Acoustical Society in Montreal, Canada in 2013 [2].

10- In Chapter 11, the bifurcation structure of the coated bubbles are investigated. Using the information of chapters 2,4,5 and 7 we were able to classify the complex effects of the coating on the nonlinear behavior of the bubble. Here, we show that buckling and rupture may be needed to induce asymmetric behavior in the effective surface tension that enhances non-linearity. In the case of the symmetric variations in the effective surface tension, buckling and rupture may suppress the nonlinear behavior. This could be one of the physical reasons behind the generation, disappearance and regeneration of SH emissions in the oscillations of coated bubbles with increasing pressure. We show that higher order SuHs, P2 and P3 can be generated at pressures as low as 1 kPa. Such low pressure thresholds for nonlinear behavior have not been observed previously in a bubble oscillator. Results of this work can be used as a fundamental framework for the optimization of the CEUS, FUS, drug delivery and treatment monitoring applications of coated bubbles.

12.2 Detailed Contributions

12.2.1 Pressure dependent resonance

In most UCA applications, resonant UCA oscillations are of fundamental importance as they result in the highest energy transfer from the ultrasonic field to the UCAs [3] and thus they can generate a significant backscattered signal or wall velocities. Previous studies for uncoated and coated bubbles have shown a shift in the UCA resonance with increasing pressure [4, 5, 6, 7, 8], however, despite the well-known shift in the resonant frequency, the consequences of this shift in the UCA resonant frequency on the dynamical behavior of the UCAs has not been examined thoroughly. Maximization of the scattered pressure by resonant bubbles is of great importance in the stable cavitation and many biomedical applications.

In Chapter 2 we studied the resonance frequency (f_r) as a function of the pressure for different size coated bubbles with linear viscoelasiticity. The bifurcation structure of the oscillations of the UCAs was studied as a function of the driving pressure for excitation frequencies that were determined using the UCAs pressure dependent resonances (PDf_r). It was shown that when insonated with the PDf_r the radial oscillations of the bubble undergo a saddle-node (SN) bifurcation to radial oscillations of higher amplitude. Consequently the scattered pressure from UCAs undergoes a rapid increase. We show that using the optimum PDf_r as the insonation frequency, the maximum

possible non-destructive (ND) scattered pressure (P_{sc}) can be enhanced up to 9 fold. In Chapter 8 and 11, we extended the analysis of the PDf_r regime of oscillations to uncoated bubbles and lipid coated bubbles (undergoing buckling and rupture) respectively. It was shown that due to the reduced viscous damping of the uncoated bubbles, applications of the PDf_r for nondestructive scattered pressure (NDP_{sc}) are limited to frequencies close to f_r (e.g. $f > 0.8f_r$ for bubbles with $1\mu m < R_0$). In case of the lipid coated bubbles and due to the rapid changes of the f_r with increasing pressure, the SN occurs at pressures significantly smaller than the uncoated and coated bubbles with linear vsicoelastic behavior. This is due to the rapid changes of the f_r with increasing pressure (e.g. $f_{10kPa} = 0.5f_{1kPa}$) for the case of the lipid coated bubbles.

The sudden increase in the radial oscillations of the UCA at the SN pressure may provide advantages to current diagnostic and therapeutic applications of the UCA. One of the diagnostic ultrasound applications that can benefit from this phenomenon is the amplitude modulation (AM) UCA imaging technique [9, 10, 11]. The nonlinearity of the UCA system can be enhanced by choosing the first pressure slightly below the SN pressure and the second pressure above the SN. In case of the lipid coated bubbles, the bubble may exhibit two SNs with increasing pressure. The two SNs can be further exploited in AM techniques that use multiple pulses.

Another benefit may be in the case of imaging a region of interest (ROI) deep within the body. Because the UCAs are distributed within all the vessels among the pre-target tissue layers, they may shield the signals along the beam path and from the target tissue and the UCAs in the ROI. This tends to be more problematic in cases of deeper targets. This is because the signal encounters more UCAs on its path to the target and back, therefore the signal significantly loses its strength. The ultrasonic beams become attenuated by the superficial pre-focal tissue, which causes the loss of the strength of the signal from the UCAs at the target, thus limits the visualization of the tissue layers at deeper locations [12, 13]. The accuracy of tissue perfusion measurements are largely affected by this shadowing effect [12, 13]. To allow accurate quantification, removal of the shadowing artifact is crucial. Near resonance, the attenuation is higher because of increased scattering and energy absorption by the UCAs. This is was shown in Chapter 9 where we showed that near the linear resonance frequency and at lower pressures (close to the transducer surface) the attenuation is maximum. The imaging procedure can be optimized by using focused transducers that produce the pressures greater than the SN pressure in the ROI (focal region) and less than the SN pressure

at the superficial tissue. This will decrease the pre-focal shadowing effect (because pre-focal UCAs will be non-resonant) and at the same time increases the scattered pressure at the ROI (the UCAs at the ROI are resonant because the focal pressure is more than the SN pressure) which can ultimately improve the SNR and CTR. This was shown in Chapter 9 by analyzing the attenuation of the bubbles sonicated with their PDf_r both through numerical simulations and experimental observations. It was shown that compared to f_r, the pre-focal attenuation is smaller for the PDf_r. Above the SN pressure, attenuation abruptly increases. Thus application of the PDf_r can limit the pre-focal attenuation and increase the NDP_{sc}. Using finite element simulations of the propagation of the focused waves in a bubbly media, we showed that the altered focus due to strong dissipation of dense bubble clouds can be reconstructed by optimizing the insonation frequency to PDf_r. This phenomenon was experimentally observed in [14].

One of the therapeutic applications that can benefit from this nonlinear behavior of UCAs is microbubble enhanced drug delivery. In drug delivery, UCA oscillations are used to enhance the permeability of the cell to the drug [15]. These applications need higher concentrations of UCAs, and pre-focal regions will attenuate the ultrasonic beams. Pre-focal UCAs may have undesirable effects on the healthy (non-targeted) tissue while also distorting the focus at the target tissue [16]. Because of the steep pressure gradient of the highly focused therapy transducers, pressures above the SN pressure can be generated at the target while the pressure in the surrounding tissue can be kept below the SN pressure. This way, the microbubbles in the non-focal surrounding tissue will oscillate below resonance and therefore the pre-focal scattering effects and attenuation are minimized. In addition, the microbubble activity will be enhanced in the focal region, due to enhanced oscillations in the pressure dependent resonance regime. This can lead to a more effective and precise treatment and enhanced safety.

12.2.2 Superharmonic regime of oscillations

In Chapter 3, we showed that the conventional method of constructing the bifurcation diagrams misses the identification of the intricate details of the bubble oscillations like superharmoncis (SuH) and can not distinguish between ultraharmonics (UHs) and subharmonics (SHs). We have introduced a simple alternative method to generate the bifurcation diagrams; the method extracts

the peaks of the oscillations and plots them as a function of the given control parameter. When this method is applied alongside the conventional method one can reveal hidden details of the bubble oscillations and identify the parameter ranges where SuH, UH or SH oscillations occur. The method was later used in chapter 8, 9, 10 and 11 in the analysis of the dynamics of the coated and uncoated bubbles.

When the bubbles are sonicated with $f < 0.5f_r$, SuHs are generated more efficiently. In the case of the coated bubbles undergoing buckling and rupture, SuHs can be generated at pressures as low as 1 kPa. The lower pressure threshold for the generation of SuHs, results in weaker nonlinear propagation of the wave through the medium. Thus, this application of coated bubbles with initial surface tension close to the ruptured or buckled state may have the potential to increase the CTR in SuH imaging techniques [17]. It was shown in Chapter 10 and 11 that coated bubbles can emit SuHs of higher order (6th order) even at very low excitation pressures (e.g. 5 kPa).

In Chapter 9, we showed that when the bubbly medium is sonicated with $SuHf_r$ (3rd or 4th order) of the bubble, and for pressures below the generation of SuHs, the attenuation of the medium is the lowest. The higher the order of the SuHs, the smaller the attenuation. As soon as the pressure increases above the threshold of the generation of the SuHs, the attenuation of the medium increases abruptly and becomes orders of magnitude stronger than the case of sonication with f_r or PDf_r. The higher is the order of SuHs, the larger is the attenuation increase. This has potential applications in reducing the pressure needed for UCA mediated tissue heating in focused ultrasound. Through analysis of the classified attenuation diagrams in Chapter 9, we show that the pressure needed for the same therapeutic efficacy can be reduced by 14-15 times. Through FEM simulations of the propagation of the focused waves through a bubbly medium, we showed that the focus can be reconstructed more efficiently when insonation frequency is chosen as the SuH resonance frequency.

In Chapter 3, we show that as soon as the pressure is increased above the threshold for the generation of the SuHs, the SuH components of the P_{sc} undergo a rapid increase. For optimum frequencies the SuH oscillation regime can also undergo a SN bifurcation to SuH oscillations of higher amplitude. AM techniques can take advantage of this strong pressure dependence of the generation of SuHs or the pressure at which SuH SN occurs.

12.2.3 1/2 order SH regime of oscillations

Using the method developed in Chapter 3, we studied the bifurcation structure of the SH resonant uncoated and coated bubbles in Chapters 4,5,7 and 11. We showed that in case of uncoated bubbles sonicated by their f_r, period doubling (PD) only occurs when the bubble expansion ratio is very close to 2 or higher than 2. The expansion ratio of 2 is regarded as the lowest threshold for bubble destruction [18]. Thus, uncoated bubbles may not be able to produce stable 1/2 order SHs when sonicated with f_r. When sonicated with $f = 2f_r$, however, PD occurs at very small expansion ratios and gentler wall velocities. P2 oscillations extend over a larger pressure domain. For bubbles with initial radii bigger than 0.3 μm, the pressure threshold for PD is smaller when $f = 2f_r$. In case of sonication with $f = f_r$ wall velocity and P_{sc} undergo a rapid decrease when PD occurs; however, when $f = 2f_r$, PD is concomitant with a fast increase in the wall velocity and the P_{sc}. In therapeutic applications of the bubbles, the occurrence of 1/2 order SHs is used an indicator for the efficacy of the treatments (e.g. [19, 20]). In case of $f = f_r$, however, due to the decrease in P_{sc} and wall velocity amplitude, occurrence of SHs may not result in increased treatment efficacy.

In case of coated bubbles (Chapter 7 and 11), however, due to the additional damping of the coating, and at $f = f_r$, PD can occur at expansion ratios below 2. Thus, coated bubbles may produce nondestructive SHs when they are sonicated with f_r.

In case of the uncoated bubbles, with increasing pressure, the SH resonance frequency decreases. The pressure dependent SH resonance frequency (PDf_{sh}), however, can be used to enhance the SH component of the P_{sc}. It is known that when the bubble is sonicated with its $f_{sh} = 2f_r$, SHs are generated above a pressure threshold, they quickly grow with increasing pressure and saturate (e.g. [21]). Thus, there is an upper limit of SH strength that can not be enhanced by increasing the incident ultrasound pressure. To the contrary, we showed in Chapters 4 and 5 that pressure increase can lead to the generation of chaos which leads to a significant drop in the SH amplitude. In Chapter 5, we showed that when the bubble is sonicated with its PDf_{sh}, increasing pressure results in a SN bifurcation occurrence and transition of a P1 or P2 oscillation regime to a higher amplitude P2 oscillation regime. This is concomitant with an abrupt increase in the SH amplitude of the P_{sh} and over-saturation of the signal above the perceived upper limit of the SH strength. For the uncoated bubbles and for the ND regime of oscillations, the frequency at which the maximum

SH amplitude is generated is at $1.5f_r < f < 1.6f_r$. In case of lipid coated bubbles however, we showed in Chapter 11, that the PDf_{sh} may occur at frequencies as low as $0.5f_r$. Such a decrease in PDf_{sh} is because of the buckling and/or rupture of the shell.

In case of the lipid coated bubbles, SH oscillations can be generated at pressures as low as 1 kPa. In this study the minimum pressure threshold was observed for $1.8f_r < f < 2.2f_r$. The closer the initial stage of the coating to the buckled or ruptured states, the lower the pressure threshold for the P2 oscillations. Moreover, we numerically observed the unexpected disappearance of the SH emissions by bubbles that were reported experimentally in [22, 23]. In line with the experimental observations, our numerical results predicted the regeneration of SHs above a second pressure threshold. The physical reason for the disappearance of the SHs may be due to the symmetric buckling and rupture of the shell at moderate excitation pressures. Increasing the pressure above the second pressure threshold introduces the asymmetry that is caused at lower pressures. The bubble spends more time in the ruptured stage than the buckled stage (or vice versa) leading to the enhancement of the P2 oscillations.

The fundamental framework provided here, is of great importance for the understanding of the stable cavitation regimes used in the treatment monitoring especially in sensitive cases like the use of bubbles to treat the brain [19, 20]. Moreover, the unique P2 dynamics of the lipid coated bubbles that are revealed here can be used to better understand and optimize the SH emissions of the bubble in nonlinear CEUS.

12.2.4 Higher order SH regimes

In our previous work [24, 25], we have shown that higher order SHs (P3, P4, P5 ..) are generated when the UCAs (with linear viscoelastic behavior of the coating) are sonicated with frequencies that are around multiples of their f_r (e.g. $3f_r$). P3 or P4 need higher pressure thresholds to be generated. In [25], we presented results where we sonicated dilute solutions of $Artenga^{®}$ bubbles (coating is made of polymer and surfactants), and observed the generations of P3, P4 and P5 at very high excitation amplitudes (>1.5 MPa at 25 MHz). Here, we show both numerically and experimentally that higher order SHs can be generated at very low excitation amplitudes. We have shown experimentally that P3 and P4 can be generated in the oscillations of the $Definity^{®}$ bubbles at pressures as low as 250 kPa and at 25 MHz. Analysis of the bifurcation structure of

the $Definity^{®}$ showed that, consistent with the experimental results, P3 and P4 can be generated at very low acoustic pressures (e.g. 250 kPa) when the sonication frequency is 25 MHz. These experimental results were in good agreement with the simulations results. In Chapter 11 we show that P3 can also be generated at pressures as low as 1 kPa. Buckling or rupture of the shell is responsible for the enhanced non-linearity at such low excitation amplitudes. P3 oscillations show the similar dynamic of the P2 oscillations in case of the lipid coated bubbles. They are generated at very low acoustic pressures, they disappear with increasing pressure and they are regenerated above a second pressure threshold. P3 oscillations can be generated at frequencies as low as f_r and they exist over a much larger frequency range when compared to uncoated bubbles (e.g. for a lipid coated bubble with initial surface tension of 0.036 N/m, P3 exists in $f_r < f < 3f_r$).

In Chapter 8, we showed that the scattered pressure amplitude is maximum when $f = 3f_r$ and when P3 is developed. In Chapter 10, we showed that higher order SHs (2/3 order or 3/4 order) can be 5-10 dB stronger than the 1/2 order SHs. They are also closer to the transducer center frequency, thus the transducer has higher sensitivity in detecting them. The higher ordre SHs have the potential to be used in CEUS to improve CTR, signal to noise ratio and resolution. Moreover, for a fixed frequency, due to larger wall velocities of the higher order SHs and their stability, they have potential to enhance the nondestructive shear stresses on the nearby cells. Therefore, they may provide long lasting ND enhanced drug delivery. Mixing or surface cleaning are examples of other non-biomedical potential applications.

12.2.5 Nonlinear energy dissipation in the oscillations of bubbles

Current models [26] for calculating the nonlinear energy dissipation during the oscillations of acoustically excited bubbles generate non-physical values for the radiation damping (Rd) term for some frequency and pressure regions that include near resonance oscillations. Moreover, the ratio of the dissipated powers significantly deviate from the values that are calculated by the linear model at low amplitude oscillations (acoustic excitation pressure of $P_A = 1kPa$ and expansion ratio of $<\approxeq 1.01$). In high amplitude oscillation regimes ($P_a \geq 20kPa$), the dissipated power due to Rd significantly deviates from the dissipated power as calculated by the widely accepted approach that uses the scattered power by the bubbles. In Chapter 6, we provided critical corrections for the calculation of the power dissipation during the propagation of ultrasonic waves through a

bubbly medium. The accuracy of the proposed models were verified against the linear analytical expressions for low amplitude oscillation regimes and against acoustic power theory for higher amplitude oscillation regimes. The correct models can be used to study the dissipation mechanisms related to thermal damping, radiation loss and damping due to liquid viscosity. We show that damping due to thermal effects, liquid viscosity and radiation heavily depend on the excitation pressure and that the linear model estimations are not valid even at pressures as low as 20 kPa.

In Chapter 7, we introduced a simple model for the coated bubbles that accounts for radiation effects up to the first order of Mach number. We then used the corrected approach to derive the pressure dependent dissipation terms related to Rd, Td, Cd and Ld with no linear simplifications. Despite the importance of the radiation effects, the majority of the previous models for coated bubble oscillations neglected or simplified radiation effects. We showed that the often neglected radiation effect is very important and can not be neglected even at low acoustic pressures (e.g. 50 kPa). Radiation damping becomes more important for certain exposure parameters. Even at frequencies below resonance (where according to linear theory Td is the major dissipation effect), dissipation due to radiation can become the major dissipation mechanism as pressure increases. For the uncoated bubbles, thermal effects are very important and can not be neglected. Moreover thermal effects must be applied using the full thermal models. The linear thermal model [27, 28] which is typically used in studies related to bubble dynamics, loses accuracy even at pressures as low as 20 kPa. In case of coated bubbles that encapsulate gas cores similar to C3F8, thermal effects are not important and can be neglected even at higher pressures. We also showed that scattering to damping ratio (STDR) is pressure dependent. At specific frequencies and pressures, the dissipation due to radiation (scattering) becomes higher than the other dissipation mechanisms and the STDR is maximized. The basic equations and the results in Chapters 6 and 7 can be used to optimize the exposure parameters in applications that seek to enhance STDR and for more accurate characterization of the bubbly media and coated bubbles.

In Chapter 8, we used the equations derived in Chapter 6 and 7 to classify the dissipation regimes in the nonlinear oscillations of the coated and uncoated bubbles. The nonlinear oscillations of the bubbles and the related pressure dependent dissipation mechanisms were classified over a wide frequency range of $0.2f_r \leq f \leq 3f_r$. We showed that by choosing the suitable frequency and pressure, a particular bubble related effect can be enhanced (e.g. wall velocity, P_{sc} or Rd). These

results were then related to possible applications (e.g. drug delivery) that could benefit from these parameters.

12.2.6 Pressure dependent attenuation and sound speed of the bubbly media

Pressure dependent changes of the attenuation and sound speed in bubbly media is one of the open problems in acoustics [29]. The bubble activity in the target region heavily depends on the acoustic pressure at the target. Thus, understating the bubble related phenomenon as well as optimizing the applications related to bubble oscillations requires a detailed understanding of the pressure distribution in the bubbly media. However, most of the studies employ linear models [27, 28], or semi linear models [30, 31, 32, 33, 34] to study the attenuation and sound speed changes of the bubbly media.

In Chapter 9, we presented a simple nonlinear model for the calculation of the pressure-dependent attenuation and sound speed in a bubbly medium. The model is free from any linearization in the bubble dynamics. The accuracy of the model (in cases of the uncoated bubbles, coated bubbles and bubbles immersed in tissue or sediments) was verified by comparing it to the linear model [27, 28] at low pressures and the semilinear Lousinard approach [30] at higher-pressure amplitudes.

The pressure dependent relationship between the sound speed and pressure was established theoretically and verified experimentally. The predictions of the model were in good agreement with the experimental observations. Unlike current sound speed models, the model introduced in this paper does not have a $\frac{dP}{dV}$ term (e.g. [35]); thus it does not encounter difficulties addressing the nonlinear oscillations. We showed that, to accurately model the changes of the attenuation and sound propagation in a bubbly medium, we need to take into account how the sound speed changes with pressure and frequency. Otherwise, the prediction accuracy decreases, especially for ultrasound exposure parameter ranges where the sound speed undergoes larger deviations compared to linear predictions (e.g. at the SN pressure when bubble is sonicated with PDf_r). Another advantage of the model is that it uses as input only the radial oscillations of the bubbles. There is no need to calculate the energy loss terms, and thus our approach is simpler and faster.

Using the information in Chapter 8, we have classified the pressure dependent regimes of attenuation and sound speed over a wide frequency range ($0.3f_r \leq f \leq 3f_r$). The classified regimes are of fundamental importance in choosing the exposure parameters in bubble related applications. This

was shown through FEM simulations of the propagation of the focused ultrasonic waves through bubbly media.

12.3 Limitations of this study

In the models that were used for bubble oscillations non-spherical bubble oscillations were neglected. Non-spherical bubble oscillations may change the bubble behavior. Holt et al. [36] investigated the subharmonic behavior of larger bubbles ($\approx 100 - 200\mu m$ in size) and observed the shape oscillations concomitant with subharmonic oscillations. They showed that, since the frequency of the first shape oscillation is 1/2 of the driving frequency, its appearance could be phenomenologically mistaken for a simple period-doubling of the radial mode. At higher pressure amplitudes, the oscillations were shown to be very complex, with many subharmonic components that are thought to result from nonlinear volume resonances and shape oscillations of undetermined mode [36]. Recently Klapcsik and Hegedus [37] through GPU accelerated large parameter investigations and 2 dimensional bifurcation diagrams, have studied the dependence of the active cavitation threshold on the shape instability of the bubble. Shape instability can affect the subharmonic threshold and nonlinear behavior of bubbles. More accurate predictions of the oscillations requires the incorporation of the shape instability during bubble oscillations. Versluis et al. [38] through using high speed optical observations were able to identify shape oscillations of mode n= 2 to 6 in the behavior of single air bubbles with radii between $10\mu m$ and 45 μm. Their study [38] concluded that the bubbles that are oscillating close to resonance were found to be most vulnerable toward shape instabilities. For coated bubbles, nonspherical bubble oscillations were investigated in [39] through high speed optical observations. It was shown that non-spherical bubble oscillations are significantly present in medically relevant ranges of bubble radii and applied acoustic pressures. Non-spherical oscillations develop preferentially at resonance and may be present during SH oscillations [39]. Guerda et al [40] investigated the SH emissions of single spherical bubbles. Their results show that when an acoustic bubble is driven at sufficiently large pressure amplitudes, energy transfer from surface to volume oscillations results in triggering of subharmonic spherical oscillations. At higher pressures and specially for larger bubbles, for a more accurate modeling of the MB oscillations, more sophisticated theoretical modeling of the bubble

coating, accounting for membrane shear and bending is required [39].

In the experiments of Chapter 9 broadband pulses were used to sonicate the bubble population. Thus, the attenuation and sound speed analysis were only limited to transient bubble behavior regimes. Application of narrow-band pulses can reveal nonlinear behavior at the steady state regime of oscillations and may be better for estimating some shell parameters (e.g. shear thinning). However, the general conclusions of the study are still valid for broadband and narrow-band pulses. Moreover, the analysis was confined to near resonance bubble oscillations. A recent experimental study [41], have shown that the near resonance attenuation measurements are not affected by broadband or narrow-band excitations.

The analysis in this thesis was carried out by bubble models that are valid only at low mach numbers (e.g. Keller-Miksis [42], Keller-Miksis-Church-Hoff [43] or Marmottant model [44]). Moreover, the model developed in Chapter 9, was derived from the Caflisch model [45] which is only valid for small Mach numbers (e.g. < 1). Effects of nonlinear propagation of sound in the medium were also neglected. These assumptions were reasonable since the analysis in this thesis were limited to small Mach numbers (e.g. < 0.3). For bubble oscillation regimes at higher mach numbers where the bubble wall velocity approaches or exceeds the sound speed in the liquid, the appropriate models (e.g. the Glimore model [46], the Kreider model [47], etc) must be used to model the bubble behavior. Even in these cases the attenuation and sound speed should be derived by considering the nonlinear propagation of sound waves.

Bibliography

[1] Jafari Sojahrood, A., Li, Q., Burgess, M., Karshafian, R., Porter, T. and Kolios, M.C., 2016. Development of a nonlinear model for the pressure dependent attenuation and sound speed in a bubbly liquid and its experimental validation. The Journal of the Acoustical Society of America, 139(4), pp.2175-2175.

[2] Jafari Sojahrood, A., Karshafian, R. and C. Kolios, M., 2013, June. Bifurcation structure of the ultrasonically excited microbubbles undergoing buckling and rupture. In Proceedings of Meetings on Acoustics ICA2013 (Vol. 19, No. 1, p. 075097). Acoustical Society of America.

[3] Parlitz U, Englisch V, Scheczyk C, Lauterborn W Bifurcation structure of bubble oscillators. J. Acoust. Soc. Am. **88**(2) 106177 (1990).

[4] Lauterborn W Numerical investigation of nonlinear oscillations of gas bubbles in liquids, J. Acoust. Soc. Am. **59**(2) 283-293 (1976).

[5] Overvelde, M., Garbin, V., Sijl, J., Dollet, B., De Jong, N., Lohse, D. and Versluis, M., 2010. Nonlinear shell behavior of phospholipid-coated microbubbles. Ultrasound in medicine & biology, 36(12), pp.2080-2092.

[6] Doinikov AA, Haac JF and Dayton PA Resonance frequencies of lipid-shelled microbubbles in the regime of nonlinear oscillations , Ultrasonics **49**(2) 263-268 (2009).

[7] Gong Y, Cabodi M and Porter T Pressure-dependent Resonance Frequency for Lipid-coated Microbubbles at Low Acoustic Pressures, IEEE International Ultrasonics Symposium Proceedings, 10.1109/ULTSYM.2010.0488 (2010)

[8] Helfield BL and Goertz DE Nonlinear resonance behavior and linear shell estimates for Definity and MicroMarker assessed with acoustic microbubble spectroscopy, J. Acoust. Soc. Am. **133** 1158- 1168 (2013)

[9] Philips P and Gardner E Contrast-agent detection and quantification, Eur.Radiol Suppl **14**(8) 4-10 (2004).

[10] Brock-Fisher AG, Poland M and Rafter P Means for increasing sensitivity in nonlinear imaging systems. US Patent **5577505** (1996).

[11] Eckersley RJ, Chin CT and Burns PN Optimizing phase and amplitude modulation schemes for imaging microbubble contrast agents at low acoustic power, Ultrasound in Med. Biol. **6**(31) 213-219 (2005).

[12] Bos LJ , Piek JJ and Spaan JA Effects of shadowing on the time-intensity curves in contrast echocardiography: a phantom study., Ultrasound in Med. & Biol. **22**(2) 217-227 (1996).

[13] Tang MX, Eckersley RJ and Noble JA Regularized estimation of contrast agent attenuation to improve the imaging of microbubbles in small animal studies, Ultrasound in Med. & Biol. **34**(6) 938-948 (2008).

[14] Segers, T., Kruizinga, P., Kok, M.P., Lajoinie, G., De Jong, N. and Versluis, M., 2018. Monodisperse versus polydisperse ultrasound contrast agents: Non-linear response, sensitivity, and deep tissue imaging potential. Ultrasound in medicine & biology, 44(7), pp.1482-1492.

[15] Roovers, S., Segers, T., Lajoinie, G., Deprez, J., Versluis, M., De Smedt, S.C. and Lentacker, I., 2019. The role of ultrasound-driven microbubble dynamics in drug delivery: from microbubble fundamentals to clinical translation. Langmuir, 35(31), pp.10173-10191.

[16] Coussios CC, Farny CH, Ter Haar G and Roy RA Role of acoustic cavitation in the delivery and monitoring of cancer treatment by high-intensity focused ultrasound (HIFU), International Journal of Hyperthermia **23**(2) 105-120 (2007).

[17] Cherin, E., Yin, J., Forbrich, A., White, C., Dayton, P.A., Foster, F.S. and Démoré, C.E., 2019. In vitro superharmonic contrast imaging using a hybrid dual-frequency probe. Ultrasound in medicine & biology, 45(9), pp.2525-2539.

[18] Flynn, H.G., Church, C.C.: Transient pulsations of small gas bubbles in water.913 J. Acoust. Soc. Am. 84, 985–998 (1988)

[19] M. A. O'Reilly and K. Hynynen, (2012) Blood-brain barrier: Real-time feedback-controlled focused ultrasound disruption by using an acoustic emission-based controller, Radiology 263, 96.

[20] C. H. Tsai, J. W. Zhang, Y. Y. Liao, and H. L. Liu, 2016. Real-time monitoring of focused ultrasound blood-brain barrier opening via subharmonic acoustic emission detection: Implementation of confocal dual-frequency piezoelectric transducers, Phys. Med. Biol. 61, 2926

[21] Shi, WilliamT, et al. "Pressure dependence of subharmonic signals from contrast microbubbles." Ultrasound in medicine & biology 25.2 (1999): 275-283.

[22] Biagi, E., Breschi, L., Vannacci, E. and Masotti, L., 2007. Stable and transient subharmonic emissions from isolated contrast agent microbubbles. IEEE transactions on ultrasonics, ferroelectrics, and frequency control, 54(3), pp.480-497.

[23] Perez, C., 2015. Characterization of Ultrasound Pressure Fields, Microbubbles and Their Interaction (Doctoral dissertation). University of Washington in Seattle, Applied Physics department

[24] Sojahrood, A.J. and Kolios, M.C., 2012. Classification of the nonlinear dynamics and bifurcation structure of ultrasound contrast agents excited at higher multiples of their resonance frequency. Physics Letters A, 376(33), pp.2222-2229.

[25] Sojahrood, A.J., Karshafian, R. and Kolios, M.C., 2012, October. Numerical and experimental classification of the oscillations of single isolated microbubbles: Occurrence of higher order subharmonics. In 2012 IEEE International Ultrasonics Symposium (pp. 402-405). IEEE.

[26] Jamshidi, R. and Brenner, G., 2013. Dissipation of ultrasonic wave propagation in bubbly liquids considering the effect of compressibility to the first order of acoustical Mach number. Ultrasonics, 53(4), pp.842-848.

[27] Commander, K.W. and Prosperetti, A., 1989. Linear pressure waves in bubbly liquids: Comparison between theory and experiments. The Journal of the Acoustical Society of America, 85(2), pp.732-746.

[28] Prosperetti, A., Crum, L.A. and Commander, K.W., 1988. Nonlinear bubble dynamics. The Journal of the Acoustical Society of America, 83(2), pp.502-514.

[29] K. Yasui. *Unsolved Problems in Acoustic Cavitation*. Handbook of Ultrasonics and Sonochemistry, (Springer 2016).

[30] Louisnard, O., 2012. A simple model of ultrasound propagation in a cavitating liquid. Part I: Theory, nonlinear attenuation and traveling wave generation. Ultrasonics sonochemistry, 19(1), pp.56-65.

[31] Mantouka, A., Dogan, H., White, P.R. and Leighton, T.G., 2016. Modelling acoustic scattering, sound speed, and attenuation in gassy soft marine sediments. The journal of the acoustical society of America, 140(1), pp.274-282.

[32] Segers, T., De Rond, L., de Jong, N., Borden, M. and Versluis, M., 2016. Stability of monodisperse phospholipid-coated microbubbles formed by flow-focusing at high production rates. Langmuir, 32(16), pp.3937-3944.

[33] Helfield, B., Chen, X., Qin, B. and Villanueva, F.S., 2016. Individual lipid encapsulated microbubble radial oscillations: Effects of fluid viscosity. The Journal of the Acoustical Society of America, 139(1), pp.204-214.

[34] Shekhar, H., Smith, N.J., Raymond, J.L. and Holland, C.K., 2018. Effect of temperature on the size distribution, shell properties, and stability of Definity. Ultrasound in medicine & biology, 44(2), pp.434-446.

[35] Leighton, T.G., Meers, S.D. and White, P.R., 2004. Propagation through nonlinear time-dependent bubble clouds and the estimation of bubble populations from measured acoustic characteristics. Proceedings of the Royal Society of London. Series A: Mathematical, Physical and Engineering Sciences, 460(2049), pp.2521-2550.

[36] Holt, R.G. and Crum, L.A., 1992. Acoustically forced oscillations of air bubbles in water: Experimental results. The Journal of the Acoustical Society of America, 91(4), pp.1924-1932.

[37] Klapcsik, K. and Hegedus, F., 2019. Study of non-spherical bubble oscillations under acoustic irradiation in viscous liquid. Ultrasonics sonochemistry, 54, pp.256-273.

[38] Versluis, M., Goertz, D.E., Palanchon, P., Heitman, I.L., van der Meer, S.M., Dollet, B., de Jong, N. and Lohse, D., 2010. Microbubble shape oscillations excited through ultrasonic parametric driving. Physical review E, 82(2), p.026321.

[39] Dollet, B., Van Der Meer, S.M., Garbin, V., De Jong, N., Lohse, D. and Versluis, M., 2008. Nonspherical oscillations of ultrasound contrast agent microbubbles. Ultrasound in medicine & biology, 34(9), pp.1465-1473.

[40] Guédra, M., Cleve, S., Mauger, C. and Inserra, C., 2020. Subharmonic spherical bubble oscillations induced by parametric surface modes. Physical Review E, 101(1), p.011101.

[41] Shekhar, H., Smith, N.J., Raymond, J.L. and Holland, C.K., 2018. Effect of temperature on the size distribution, shell properties, and stability of Definity®. Ultrasound in medicine & biology, 44(2), pp.434-446.

[42] Keller, Joseph B., and Michael Miksis. "Bubble oscillations of large amplitude." The Journal of the Acoustical Society of America 68.2 (1980): 628-633.

[43] Sojahrood, A.J., Haghi, H., Li, Q., Porter, T.M., Karshafian, R. and Kolios, M.C., 2020. Nonlinear power loss in the oscillations of coated and uncoated bubbles: Role of thermal, radiation and encapsulating shell damping at various excitation pressures. Ultrasonics sonochemistry, 66, p.105070.

[44] Marmottant, P., Van Der Meer, S., Emmer, M., Versluis, M., De Jong, N., Hilgenfeldt, S. and Lohse, D., 2005. A model for large amplitude oscillations of coated bubbles accounting for buckling and rupture. The Journal of the Acoustical Society of America, 118(6), pp.3499-3505.

[45] Caflisch, R.E., Miksis, M.J., Papanicolaou, G.C., Ting L., Effective equations for wave propagation in bubbly liquids, *J. Fluid Mech.* 153 (1985): 259–273.

[46] Gilmore F.R., The growth or collapse of a spherical bubble in a viscous compressible fluid, Calif. Inst. Tech. Rep. 26-4 (1952).

[47] Kreider, W., Crum, L.A., Bailey, M.R. and Sapozhnikov, O.A., 2011. A reduced-order, single-bubble cavitation model with applications to therapeutic ultrasound. The Journal of the Acoustical Society of America, 130(5), pp.3511-3530.